The Modelling of Nematic Liquid Crystal Phase Devices

by
Norman James Powell

A Thesis
Submitted to the University of Durham
for the Degree of
Doctor of Philosophy.

December 1993

Abstract

The implementation of nematic liquid crystal optical devices, which exploit the voltage dependent, optical path length modification of the electrical Freedrichsz transition, is presented. By combining refractive elements in a diffractive zone structure, efficient and flexible devices with relatively high refractive powers can be constructed. Continuously variable optical properties can be achieved by scaling the optical profile of the refractive elements and applying a phase correction to ensure that the transition between adjacent zones is an integral number of wavelength, hence a continuous optical profile is constructed. Two such devices are postulated; a variable deflection angle prism and a variable focal length lens, though the approach may be extended to other devices.

The zones are addressed through combed electrode structures. The required voltage profile is produced by dropping the applied voltages across a shaped conductive strip. A sampling of the profile is transported along the length of the zone via discrete electrodes. In order to produce the required scalability and independent phase correction of the optical profile, it is necessary to restrict the design and operation of the electrodes to the approximately linear region of the response curve. Two-dimensional optical structures can either be achieved through the use of planar earth plates, to mask connections to the centre of the device, or by cascading devices with electrode structures open to connection at the edges.

In order to predict the optical profiles of these and other devices, a model was constructed which describes the director orientation through a two-dimensional electrode structure. The variational finite element method was employed to minimize the electrical Gibbs free energy of a liquid crystal cell, in order to find the equilibrium director orientation. A preliminary version of this model is presented which is restricted to rotation of the liquid crystal to within the plane of the solution.

Who is able to purify the dark till it becomes slowly light ?

Who is able to calm the turbid till it slowly clears ?

Who is able to quicken the stagnant till it slowly makes progress ?

Tao Tê Ching, Lao Tzu.

To

William Arthur, Lilian Irene,

George, Wanda Kay,

Richard Steven, Johanna Suzanne,

and all the children lost down many paths[1].

[1]Genesis, 'Supper's Ready', ***Foxtrot***, The Famous Charisma Label (1972)

Declaration

I declare that the work reported in this thesis, unless otherwise stated, was carried out by the candidate, that it has not previously been submitted for any degree and that it is not currently being submitted for any other degree.

Candidate's signature: _____

Norman James Powell

Supervisor's signature: _____

Dr. Alan Purvis

Acknowledgements

I would like to thank my supervisor Dr. Alan Purvis for securing the three year SERC studentship and two year GEC case award. I am also grateful to Dr. M. G. Clark, Dr. M. C. K. Wiltshire and Dr. L. Laycock for their contributions as my industrial supervisors, at GEC-Marconi Hirst Research Centre, and also Dr. David Wood as deputy supervisor. The funding provided for this research by the Science and Engineering Research Council (SERC) was most appreciated.

I am especially grateful to my friend and colleague Dr. Geoff Williams, with whom I have had many interesting and enlightening discussions and for the time he has given proof reading this thesis. I am also extremely grateful to Dr. Robert Kelsall and Dr. Jonathan Welch for introducing me to the finite element method and adaptive meshes, respectively. The advice, support and additional proof reading provided by Dr. Richard Hall and Dr. Gordon Love was also greatly appreciated. I would also like to thank Dr. J. V. Major and Dr. D. Evans for their time and several interesting discussions.

I would like to thank the staff of both SEAS/SECS and the computer service for the support provided during the project, including Judith and Olive from the coffee-bar.

I am indebted to Dr. Lee Gould, Ken Linton and Anita Vranch for their support and friendship during my time in Durham. I am also grateful to Brian, Ed, Shell, Sean, Steve, Michelle, Haluk, Graham, Tony, Thomas, José, Mary, Maria, and the many others who have put up with me over the years.

Contents

List of Figures

List of Tables

Symbols

Chapter 2

Section 2.1

$\mathbb{n}$	Unit vector describing orientation of director

Section 2.2

$\mathbb{D}$	Displacement field
$\mathbb{E}$	Electric field
$\mathbb{P}$	Polarization
ε	Electrical permittivity of free space
$\boldsymbol{\varepsilon}_r$	Relative permittivity tensor in global reference frame
$\boldsymbol{\varepsilon}_l$	Relative permittivity tensor in local reference frame orientated with the principle axis of the liquid crystal molecule
ε_o & ε_e	Ordinary and extraordinary relative permittivities
χ_o & χ_e	Ordinary and extraordinary susceptibilities
$\mathbb{R}(\theta, \phi)$	Rotational matrix relating the local and global reference frames
θ & ϕ	Tilt and orientation of the liquid crystal
f_e	Electrical free energy density
n_{eff}	Effective refractive index of cell
n_o & n_e	Ordinary and extraordinary refractive indices
d	Cell thickness

Section 2.3

$(\bar{0}, \iota, \kappa, \lambda)$	Local reference frame with λ-axis parallel to the director $\mathbb{n}$
a_i $(i = 1, \ldots, 6)$	Local elastic distortions of director orientation
$O(r^2)$	Second order elastic distortions of director orientation
f_K	Elastic free energy density
$\mathbb{K}$	Elasticity tensor
K_{11}, K_{22} & K_{33}	Splay, twist and bend elastic constants
∇	Vector operator *del*

Section 2.4

G_e	Electrical Gibbs free energy
$\mathcal{D}$	Volume of the system
V	Electrical potential
V_{th}	Threshold voltage
τ_{on} & τ_{off}	Switch on and off times
γ_1	Twist viscosity of liquid crystal

Chapter 3

Section 3.2

ψ_i $(i = 1, \ldots, m)$	Dependent variables of system
$\mathcal{G}$ & $\mathcal{H}$	Governing equation of system
R	Residual error
W	Weighting function
$f(R)$	Function of the residual errors
$\mathcal{D}$	Domain of system
$\mathcal{S}$	Surface of system
χ	Functional
$\mathcal{L}$	Lagrangian density
$\mathbb{N}^e$	Shape function of finite element e
k & l	Indices of element nodes
p & q	Indices of system nodes
α_1, α_2 & α_3	Parameters of the shape function
$\hat{\psi}$	Finite element approximation of dependent variable ψ
$\bar{\psi}_k$	Value of $\hat{\psi}$ at node k
b & c	x and y dimensions of finite element
$(\bar{0}, x, y, z)$	Local reference frame, aligned global reference frame and centred on centroid of element
N	Number of finite elements
M	Number of nodes in system
k_{qp}	Element of matrix describing finite element system equations
v_p	Constant terms of finite element system equations
$\mathbf{k}_{\text{sys}}$	The finite element matrix for whole system
$\mathbf{k}_{\text{ele}}$	The finite element matrix for a single element
s_j	Directional cosines normal to surface $\mathcal{S}$
d_p & e_p	Parameters of the boundary condition applied to node p
Q_p	Right-hand side of system equations for node p

Section 3.3

m	Order of derivative of dependent variable
p	Order of polynomial used in trial function
d	Number of dimensions the element is described
h	Size of finite element
ϵ	Error of finite element approximation
$\lvert\epsilon_x\rvert$ & $\lvert\epsilon_y\rvert$	Errors of x and y derivatives of finite element approximation
$\lvert\epsilon\rvert$	Total error of system
$\lvert\epsilon\rvert_e$	Error of an element
$\lvert\epsilon\rvert_r$	Required error in an element
$\mathcal{D}_e$	Domain of an element
δ^x & δ^y	Distance in x and y from a point $(\bar{x}, \bar{y})$
$O(h^n)$	Order of term with respect to power of element size
ψ°	Projected, higher order approximation of solution
η	Acceptable relative error
ξ_g	Global refinement parameter
$\bar{\xi}_e$	Element refinement paramenter
ξ_e	Overall refinement parameter
ξ	Scaling factor of element size required to achieve refinement
ξ_c	Corrected scaling factor
a & n	Relaxation constant and new power for scaling factor
λ	Singularity strength

Chapter 4

Section 4.2

λ	Wavelength of illuminating light
σ	Sheet resistivity
ρ	Bulk resistivity
t	Thickness of electrode

Section 4.5

ϑ	Deflection angle of diffraction grating
n	Number of diffraction order
l	Length of grating period
f	Focal length
ϵ	Relative error of approximation
R_n	Radius of zone n
λ' & f'	Different illuminating wavelength and resulting focal length
R_N & ΔR_{MIN}	Full radius of lens and minimum zone size

Section 4.6

Δn Birefringence
d Cell thickness
φ Deflection angle of prism
l Length of prism
V Voltage across prism electrode
$\mathcal{R}$ Resistance of electrode
R Radius of lens

Section 4.8

$\mathcal{I}$ & $\mathcal{J}$ Labels of alternate zones

Section 4.10

t_0 Decay time of phase change
Δ Phase change
α Decay constant
β Material constant
V_i Initial voltage

Chapter 5

Section 5.2

u_s Complex amplitude of secondary wavelet
a Initial amplitude of secondary wavelet
j $\sqrt{-1}$
k Wavelength constant $2\pi/\lambda$
r Propagation length of secondary wavelet
n Zone index
x Position in optical device
R Radial position in optical device
ϱ Optical path length profile through liquid crystal film
ϑ Deflection angle from liquid crystal device
u Complex amplitude
u_0 Complex amplitude due to liquid crystal device
l Length of zone
I Intensity distribution
z Distance along optical axis
o_n Obliquity factor
v An arbitrary scaling factor for the optical profile

Section 5.3

i Integer scaling factor of optical profile
m Maximum integer scaling factor

Section 5.4

i An arbitrary integer

Chapter 6

Section 6.4

L Length of zone in direction of constant optical path
ΔV Voltage drop across the zone
$\mathcal{R}_T$ Total resistance of electrode
w Width of conducting electrode strip
x Direction of changing optical profile
$V(x)$ Voltage profile produced by conducting strip
$V_0(x)$ Normalized Voltage profile designed into the conducting strip
V_C Arbitrary shift in applied voltage
$\varrho(V)$ Optical path length response to voltage
ϱ_{off} Optical path length of off-state
ϱ_{grad} Gradient of approximately linear of response
ϱ_{int} Intersect of approximately linear of response
V_l Voltage marking change from approximately linear region to reciprocal response region
C Curvature constant of reciprocal response
B Asymptote of reciprocal response
$\varrho_0(x)$ Normalized, required optical profile
$\Delta\varrho$ Scaling of optical profile
ϱ_C Independent phase correction to optical profile

Section 6.5

R & β Radius and angle of position in liquid crystal device
ϵ Error in approximation
ϱ_1 & ϱ_2 Optical profiles of component liquid crystal for conical lens

Chapter 7

g Size of inter-electrode gap
e Size of electrode

Chapter 8

Section 8.3

χ_e	Electrical free energy solved with respect to the potential distribution
$\hat{V}$	Finite element approximation of potential distribution
$\bar{\mathbb{V}}$	Array of nodel values of potential distribution
$\bar{V}_i$	Nodel value of potential distribution at node i
ϕ_c	Average director orientation of element, Orientation at centroid of element
Δ	Area of triangular element
$X(x)$ & $Y(y)$	Parts of potential distribution separated along the spatial co-ordinates of the system
a	A constant
k	General spatial wavelength constant
n	Harmonic number
k_n	Spatial wavelength constant of the nth harmonic
A_n, B_n, C_n & D_n	Amplitudes of nth harmonic of $X(x)$ & $Y(y)$
L_x	Length of periodic repetition in electrode structure
ϵ_d	Relative permittivity of isotropic dielectric

Section 8.4

$(\bar{0}, \mu, \nu, o)$	Local co-ordinate system which follows the director orientation
$\phi_v(x, y)$	Spatial variation of director from ϕ_c
θ_c	Tilt at centroid of element
F_e	Electrical free energy solved with respect to the director distribution
α_1 & α_2	Parameters for potential distribution
$\phi_o(x, y)$	Pre-set orientation of director distribution
$\delta\phi(x, y)$	Small angle variation from pre-set director orientation
$\hat{\phi}$	Finite element approximation of overall director orientation
$\delta\hat{\phi}$	Finite element approximation of variation in director orientation
β_0, β_1 & β_2	Parameters for pre-set director orientation
γ_0, γ_1 & γ_2	Parameters for variations in director orientation
$\bar{\phi}_{oi}$	Nodal value of pre-set director orientation
$\delta\bar{\phi}_i$	Nodal value of variation in director orientation

Section 8.6

$\delta\phi_c$	Variation in director at centroid of element
ω_1 & ω_2	Parameters for overall spatial variation of director orientation from overall centroid orientation
$\bar{\phi}_i$	Nodal value of overall director orientation
F_K	Elastic energy
f_e	Electrical energy density
A_{11}, A_{12} & A_{22}	Elastic terms contributing to the system equation
E_0, E_1 & E_2	Electrical terms contributing terms to the system equation
$\hat{\beta}$	Spatial variation of pre-set director orientation
$\hat{\gamma}$	Spatial variation of variation in director orientation
$\hat{\phi}_o$	Finite element approximation of pre-set director orientation
u	Polynomial up to second order with respect spatial variations variations of direction orientation
v	Sinusoidal function of spatial variation of pre-set director orientations
$\Delta\phi$	Shift in nodal values, spatial variation across element
N	Minus logarithm to base 10 of spatial variation across element
D	Number of decimal places
O	First order of the spatial variation term which produces a variation from the flat case

Section 8.7

K	Isotropic approximation elastic constant
E, E' & E''	Terms of a second order Taylor's expansion of the electrical energy density
$\delta\mathbb{m}$	Variation in director distribution
$\mathbb{m}_o$	Pre-set director distribution

Section 8.8

$\lvert\epsilon_{xx}\rvert$	Error of the x derivative of the finite element approximation in the x-direction
$\lvert\epsilon_{xy}\rvert$	Error of the x derivative of the finite element approximation in the y-direction
$\lvert\epsilon_{yx}\rvert$	Error of the y derivative of the finite element approximation in the x-direction
$\lvert\epsilon_{yy}\rvert$	Error of the y derivative of the finite element approximation in the y-direction
$\lvert\epsilon_{\beta_2}\rvert$	Error of small angle approximation in the x-direction
$\lvert\epsilon_{\beta_3}\rvert$	Error of small angle approximation in the y-direction
i & j	Column and row indices of mesh
λ	Singularity strength

Chapter 9

Section 9.3.2

N_x Number of columns

Section 9.3.3

$\mathbb{L}$ Lower unit triangular matrix
$\mathbb{U}$ Upper triangular matrix
$\mathbb{b}$ One-dimensional matrix of right-hand side values
$\mathbb{c}$ One-dimensional matrix
$\mathbb{P}$ Pivoting matrix
$\bar{\psi}$ One-dimensional matrix of dependent variable nodal values

Section 9.3.6

$\mathbb{a}$ One-dimensional contribution array
$\mathbb{b}$ One-dimensional contribution array
$\mathbb{c}$ Two-dimensional contribution array

Section 9.4.2

$\Psi(x, y)$ Displacement field line potential function
(x_0, y_0) Point of zero potential value
$\mathbb{r}$ Path from (x_0, y_0) to any point (x, y)

Section 9.4.5

$n_{normalized}$ Normalized effective refractive index

Chapter 10

Section 10.2

$\delta\phi_{\max}$	Maximum variation of director orientation from current iteration of finite element solution
ϕ_o	Pre-set director orientation at position maximum variation from current iteration of finite element solution
ϕ_s	Solution orientation
$\mathcal{A}$	Gradient of orientation variation with respect pre-set orientation at solution orientation
$\mathcal{C}$	Scaling factor of variation in director orientation
$\delta\phi'_{\max}$	Variation of director orientation from previous iteration of finite element solution at position of maximum variation in current iteration
ϕ'_o	Pre-set director orientation from previous iteration of finite element solution at position of maximum variation in current iteration
$\delta\phi_{\max'}$	Variation of director orientation from current iteration of finite element solution at position of maximum variation in previous iteration
$\delta\phi'_{\max'}$	Variation of director orientation from previous iteration of finite element solution at position of maximum variation in previous iteration
ϕ_n	Pre-set orientation distribution for next iteration
ϕ_o	Pre-set orientation distribution from current iteration
$\delta\phi$	Variation form pre-set orientation from current iteration
$N_{\mathcal{C}}$	Power of 3° for *controlled* step

Section 10.3

$\phi_o^{\mathcal{B}}$	Pre-set orientation distribution from *buckled* iteration
$\delta\phi^{\mathcal{B}}$	Variation form pre-set orientation from *buckled* iteration
$\mathcal{B}$	Scaling factor for variation in director orientation from *buckled* iteration
$N_{\mathcal{B}}$	Power of 3° for *buckled* step
λ'	Scaled λ-direction to produce isotropic equivalent geometry
ϵ_t	Truncation error
V_{app}	Applied voltage
N_t	Logarithm to the base 10 of the ratio between the row to column dimensions of an element

Chapter 12

$\hat{\theta}$	Finite element approximation of director tilt distribution
$\hat{\theta}_v$	Finite element approximation of the spatial variation of director tilt distribution
$\hat{V}_0$	Finite element approximation of pre-set potential distribution
$\delta\hat{V}$	Finite element approximation of variation from pre-set potential distribution
$\mathcal{M}$	Elastic and motor couple per unit volume
$\mathcal{Q}$	Resistive couple per unit volume

Appendix A

U	Internal energy
x_i	Extensive parameters
S	Entropy
$\mathcal{V}$	Volume
a	Proportion of system
X_i	Intensive parameters
$x^0_{1,\ldots,n}$	Specific set of extensive values
T	Temperature
P	Pressure
V	Relative electrical potential
Q	Charge of the system
G	Gibbs free energy
U_e	Electro-static free energy
U_0	Other energy contributions
G_e	Electrical Gibbs free energy
N	Number of conductors
q_i	Charges in the system
v_i	Potential in the system

Appendix B

$f(x_i)$ & $g(x_i)$	Functions of independent variables
x_j $(j = 1, \ldots, m)$	Independent variables
X^0	Position of stationary point of function
δ	Arbitrary variation
ψ_i $(i = 1, \ldots, m)$	Dependent variables
χ	Functional
$\eta_i(x_j)$	Set of linearly independent functions of x_j
$\mathcal{D}$	Special domain
$\mathcal{S}$	Piece-wise, smooth *orientable* surface bounding $\mathcal{D}$
s_j	Directional cosines
$\mathcal{D}'$	Orthogonal projection of $\mathcal{D}$ into x_k =*constant* plane
$a(x_j)$ & $b(x_j)$, $j \neq k$	Functions describing 'bottom' and 'top' surfaces of special domain $\mathcal{D}$ with respect to x_k

Appendix C

$k = 1, \ldots, s$	Node indexing of element

Appendix D

xu & xl	Upper and lower limits of x values in element
yu & yl	Upper and lower limits of y values in element
$\bar{\gamma}_i$	Nodal value of spatial variation of variation in orientation

Chapter 1

Introduction

Nematic liquid crystal devices have been successfully employed as electronic displays for many years. Consequently, the technology for the manufacture and development of these devices is very well established, leading to low cost and good reliability. Recently, interest has been generated in the extension of their application to voltage controlled optical devices, which exploit the voltage modification of optical path length through the device.

This thesis presents the possibility of implementing two such devices, a prism with a voltage controllable deflection angle and a lens with a voltage controllable focal length. In considering the possibility of constructing such devices, it became apparent that the prediction of the optical profiles produced by a liquid crystal in two-dimensional electrode structures would be extremely useful in development and design of these devices. The development and subsequent construction of a model which describes these optical profiles represents the main subject matter of this thesis.

The properties of nematic liquid crystals exploited in these devices are described in Chapter 2. The electrical and elastic properties of nematic liquid crystal are introduced. The combination of these properties to form the electrical Freedrichsz transition, which provides the voltage modification of the optical properties, is described. The electrical Gibbs free energy is presented, which when minimized describes the equilibrium state of a nematic liquid crystal system. It is this expression that will be used to describe the liquid crystal devices.

In order to minimize the electrical Gibbs free energy, the finite element method is employed, this is described in Chapter 3.

In Chapter 4, the basic liquid crystal cell is described and existing implementations of optical nematic liquid crystal devices presented. Two approaches have been employed to implement these devices; creating a diffractive phase structure or refractive optical profile. Both these approaches were observed to have limitations.

The idea of combining of these two approaches, in order to overcome the limitations of each, providing the possibility of constructing the variable prism and lens, is presented in Chapter 5. The devices postulated are referred to as diffractive/refractive devices.

Consideration of how the voltage profiles, required for the implementation of the diffractive/refractive devices can be produced is given in Chapter 6. The principle concern being how to obtain piece-wise continuous, two dimensional optical profiles.

The presence of fringing fields in two-dimensional electrode structures and consequent unpredictability of optical profile is brought to attention in Chapter 7. The issues surrounding the electrode structures of the various types of device are then discussed and the requirement for the model described in this thesis is then emphasised.

The use of the finite element method to find the optical profiles is presented in Chapter 8 and its computer implementation described in Chapter 9. The behaviour of the model in a variety of test situations is described in Chapter 10. The results of the model and the implications they have on the design of further devices are presented in Chapter 11. The conclusions of the project and suggestions of further work are given in Chapter 12.

Chapter 2

Electro-Optical and Elastic Properties of Nematic Liquid Crystal

2.1 Introduction

Thermotropic liquid crystals exist as a mesophase between the solid, crystalline phase and the isotropic liquid phase (figure 2.1). The fluid properties, with residual orientational ordering, are predominant in the liquid crystal phase. Unlike the positional ordering in the rigid crystalline phase the liquid crystal phase is depicted by a statistical spread of orientations about a mean direction, the average of which is defined as the director, $\mathbf{n}$. The nematic liquid crystal phase is usually formed by rod-shaped molecules which give rise to the orientational ordering, and the anisotropic physical properties, which have been exploited in many devices. In addition to nematic liquid crystals (figure 2.1), there also exist chiral nematic liquid crystals, whose director has a continual tilt so describing a helical structure through the liquid crystal (figure 2.2a). There also exist smectic phases which contain varying degrees of positional ordering, in addition to the orientation ordering. In the smectic phases the liquid crystals form layers, again there is a statistical spread of the centre of gravity of the molecules about these layered structures. Two well known smectic phases are the smectic A phase, where the director is perpendicular to the plane of the layer, and the smectic C phase, where the director is at an angle other than 90° to the layer (figure 2.2b&c). This chapter deals exclusively with nematic liquid crystal properties, which due to their high degree of symmetry are simpler in form to describe, and are the type used in this research project.

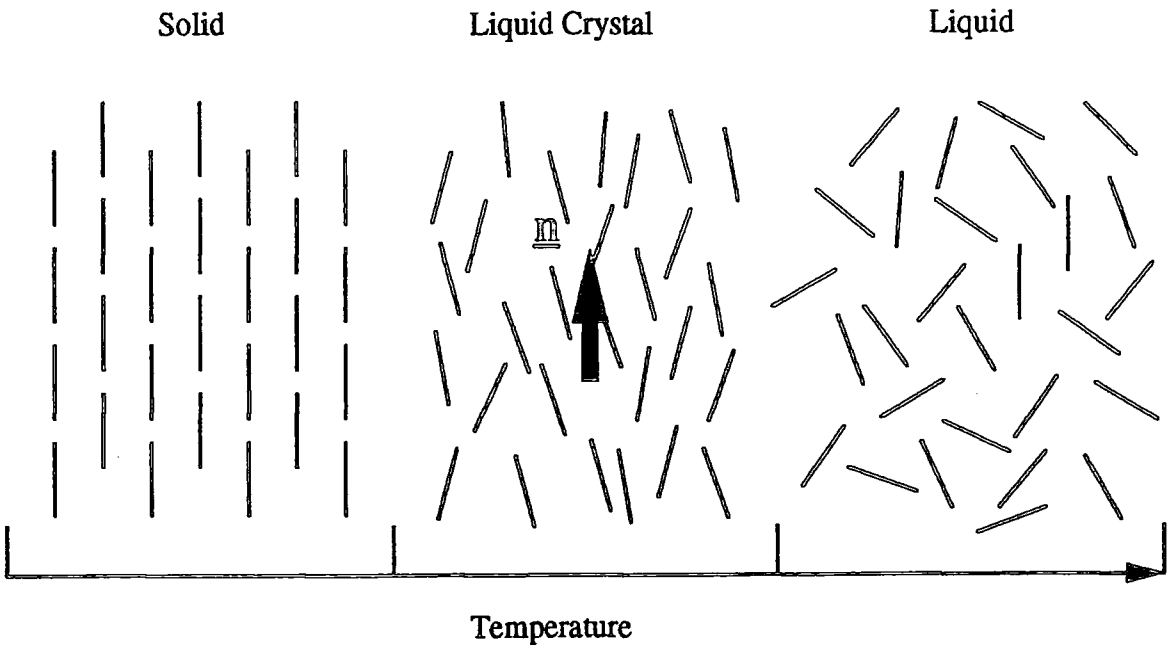

Figure 2.1: The Nematic Liquid Crystal Mesophase

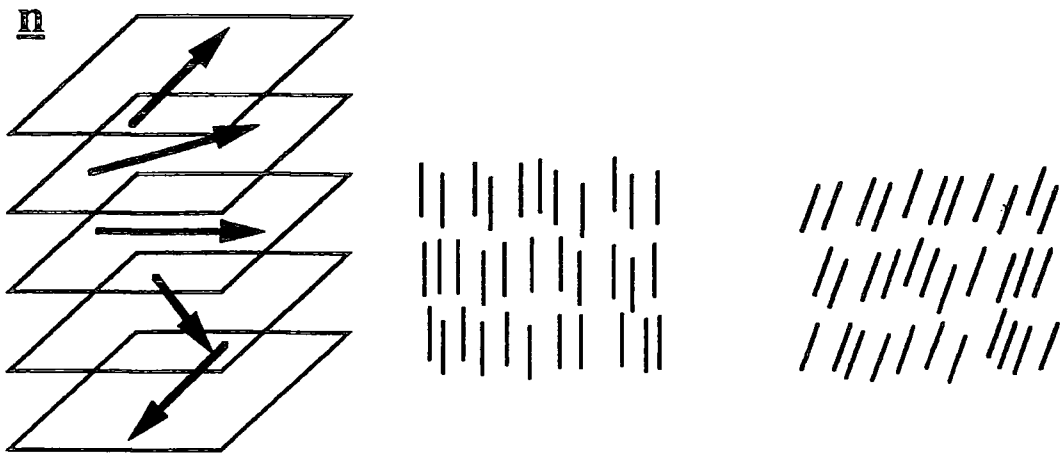

a) Chiral b) Smectic A c) Smectic C

Figure 2.2: Liquid Crystal Forms

2.2 Electro-Optical Properties

2.2.1 Anisotropic Dielectric Properties of Nematic Liquid Crystals

Nematic liquid crystals are uniaxial anisotropic dielectrics exhibiting an ordinary and extraordinary axis (figure 2.3). Each axis has a different susceptibility to induced dipoles and this is reflected in the expression for the dispacement field, $\mathbb{D}$;

$$\mathbf{D} = \varepsilon \boldsymbol{\varepsilon}_r \mathbf{E} \tag{2.1}$$

where ε is the permittivity of free space, and $\mathbf{E}$ the applied electric field, and $\boldsymbol{\varepsilon}_r$ is the relative permittivity tensor. If a local reference frame is considered, parallel to the principle axis of the molecule, the relative permittivity can be expressed as a diagonal matrix $\boldsymbol{\varepsilon}_l$;

$$\boldsymbol{\varepsilon}_l = \begin{bmatrix} \varepsilon_o & 0 & 0 \\ 0 & \varepsilon_o & 0 \\ 0 & 0 & \varepsilon_e \end{bmatrix} = \begin{bmatrix} 1 & 0 & 0 \\ 0 & 1 & 0 \\ 0 & 0 & 1 \end{bmatrix} + \begin{bmatrix} \chi_o & 0 & 0 \\ 0 & \chi_o & 0 \\ 0 & 0 & \chi_e \end{bmatrix} \tag{2.2}$$

where ε_o and ε_e are the ordinary and extraordinary relative permittivities, respectively, and χ_o and χ_e are the ordinary and extraordinary susceptibilities. To express the relative permittivity in a global reference frame the rotational matrix, $\mathbf{R}(\theta, \phi)$, which relates the two reference frames, needs to be applied;

$$\boldsymbol{\varepsilon}_r = \mathbf{R}^T(\theta, \phi)\, \boldsymbol{\varepsilon}_l\, \mathbf{R}(\theta, \phi) \tag{2.3}$$

where θ and ϕ represent the tilt and orientation of the liquid crystal (figure 2.4). A third rotation of the ordinary axis about the director is unnecessary, as the uniaxial symmetry ensures that the relative permittivities are invariant under such a rotation.

When an electric field is applied across the liquid crystal (figure 2.5), the components of polarization, $\mathbf{P}$, parallel and perpendicular to the extraordinary axis, are related to the components of electric field through different values of susceptibility;

$$\begin{aligned} P_e &= \varepsilon \chi_e E_e \\ P_o &= \varepsilon \chi_o E_o \end{aligned}$$

Consequently, the polarization is not parallel to the applied field, but shifted towards the axis of greater susceptibility. This will create a torque, pulling the induced dipole

towards alignment with the field. The angle the director is rotated by the torque is dependent on the relative values of χ_o and χ_e. In a positive dielectric, where $\chi_e > \chi_o$ the director is rotated towards alignment with the field, in a negative dielectric, where $\chi_e < \chi_o$ the director is rotated towards alignment normal to the field. The liquid crystals considered in this thesis are positive dielectrics.

It can be seen that the free electrical energy density of the liquid crystal, in an applied electric field;

$$f_e = \frac{1}{2}\mathbb{D} \cdot \mathbb{E} \tag{2.4}$$

is dependent on the orientation of the director to the applied field.

2.2.2 Anisotropic Refractive Index

A direct consequence of the anisotropic dielectric property of nematic liquid crystals is that the refractive index of liquid crystal is also anisotropic. The relative permittivity tensor can be represented by an ellipsoid which is the solution to;

$$\mathbb{D} \cdot \mathbb{E} = \frac{1}{\varepsilon}\mathbb{D} \cdot {\varepsilon_r}^{-1} \cdot \mathbb{D} = 1 \tag{2.5}$$

this is called the optical indicatrix, and is plotted in displacement field (figure 2.3). The refractive index n_{eff} for light with a polarization parallel to $\mathbb{D}$ is simply the radius of the indicatrix in that direction, and hence is given by;

$$n_{eff} = \frac{1}{d}\int_0^d \frac{dz}{\left(\frac{\cos^2\phi(z)}{n_e^2} + \frac{\sin^2\phi(z)}{n_o^2}\right)^{\frac{1}{2}}} \tag{2.6}$$

for light, appropriately polarized, passing through a depth d of liquid crystal, with $\phi(z)$ director orientation, and n_o and n_e ordinary and extraordinary refractive indices, respectively.

If there is a change of orientation in the liquid crystal, brought about by the application of an electric field, there is also a change in the effective refractive index for light polarized along the axis of the director. This is unlike the Pockel's effect [8], a first order non-linear optical phenomena in solid uniaxial crystals, which is due to the distortion of the refractive indicatrix, whereas the liquid crystal effect is due to the molecular movement changing the orientation of the indicatrix.

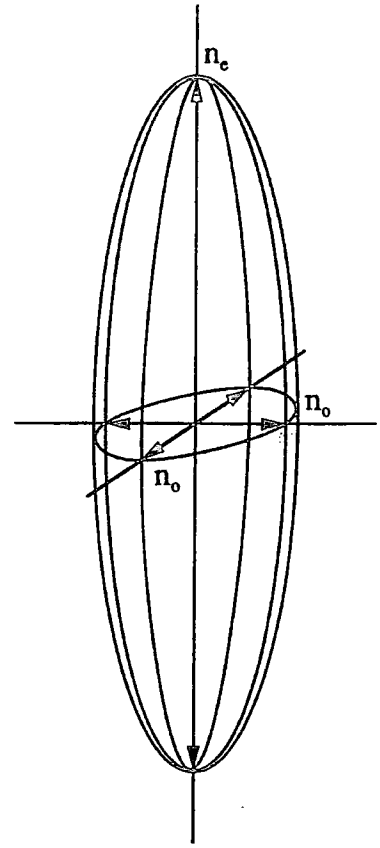

Ordinary Refractive Index: n_o
Extra-ordinary Refractive Index: n_e

Figure 2.3: Optical Indicatrix

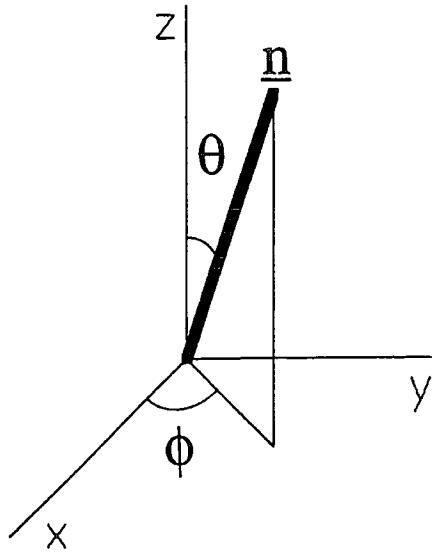

Figure 2.4: Rotation of Liquid Crystal to Global Reference Frame

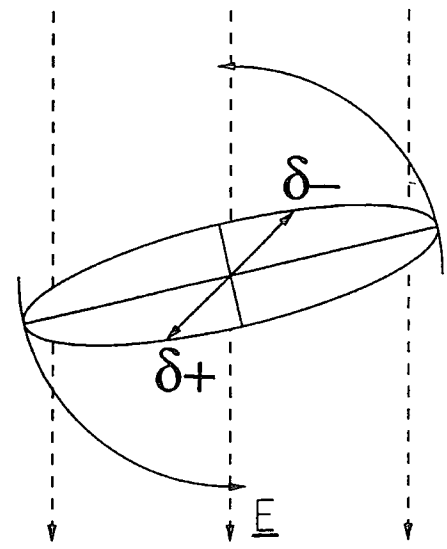

Figure 2.5: Polarization of Liquid Crystal in an Applied Electric Field

It is important to note that the frequencies of the applied electric field, applied to rotate the liquid crystal, and the electro-magnetic field, of the light which interacts with the indicatrix, are very different, typically $\sim$ 1 kHz and $\sim 10^{12}$ kHz respectively. Even though both the rotation of the liquid crystal in an applied electric field and the uniaxial indicatrix arise from the dielectric anisotropy of the liquid crystal, the relative permittivities are frequency dependent and so take different values to the applied field and the electro-magnetic frequencies.

2.3 Elastic Properties

The re-orientation promoted by the applied electric field is resisted by the elastic properties of the liquid crystal, which try to maintain its characteristic, orientational ordering. The difference between these distortions and the distortions in solid crystals is the absence of positional ordering, and hence the absence of translational distortions. The elasticity of isotropic liquids arises from changes of density, and whilst these are present in liquid crystals, the dominant distortions are those due to variation of the director orientation.

The observable distortions of the director orientation have a minimum spatial extent of the order of fractions of a micron, which greatly exceed the dimensions of the molecules. Due to this, for the elastic properties, the liquid crystal can be regarded as a continuum of smoothly varying director orientations, without reference to the molecules.

If we consider a local reference frame, $(\bar{0}, \iota, \kappa, \lambda)$ located with the λ-axis parallel to the director $\mathbf{n}$ at the local origin $\bar{0}$, then there are three types of elementary distortion; splay, twist and bend, with appropriate elastic constants, K_{11}, K_{22} and K_{33}, respectively (figure 2.6). The use of these three elastic constants in the expression for the elastic free energy density can be derived from consideration of these elementary distortions; a brief outline of the argument will be given.

The spatial components of the director can be expressed in terms of small, local distortions;

$$\left.\begin{array}{rcl} n_\iota &=& a_1\iota + a_2\kappa + a_3\lambda + O(r^2) \\ n_\kappa &=& a_4\iota + a_5\kappa + a_6\lambda + O(r^2) \\ n_\lambda &=& 1 + O(r^2) \end{array}\right\} \tag{2.7}$$

where

$$\frac{\partial n_\iota}{\partial \iota} = a_1; \qquad \frac{\partial n_\kappa}{\partial \kappa} = a_5$$

are splay deformations,

$$\frac{\partial n_\iota}{\partial \kappa} = a_2; \qquad \frac{\partial n_\kappa}{\partial \iota} = a_4$$

are twist deformations,

$$\frac{\partial n_\iota}{\partial \lambda} = a_3; \qquad \frac{\partial n_\kappa}{\partial \lambda} = a_6$$

are bend deformations, and $O(r^2)$ describes higher order terms.

Assuming Hooke's Law, the density of additional free energy caused by an arbitrary distortion can written;

$$f_K = \sum_i K_i a_i + \frac{1}{2} \sum_{ij} K_{ij} a_i a_j; \qquad i, j = 1, 2, \cdots 6. \tag{2.8}$$

providing a total of 42 elastic constants. These can be reduced by considering the following symmetries;

- The elasticity tensor, $\mathbf{K}$, is a symmetrical tensor; $K_{ij} = K_{ji}$.
- The cylindrical symmetry of uniaxial liquid crystals implies that the energy of the system is invariant to rotation about the λ-axis.
- There is no difference in the direction of the director; $\mathbf{n} = -\mathbf{n}$.
- The molecules have mirror symmetry.

to four independent elastic constants; K_{11}, K_{22}, K_{33} and K_{24}. It has been shown by Ericksen [9], using the divergence theorem, that K_{24} only contributes to the surface energy of the system and therefore can be ignored when dealing with the bulk properties of the material. The elastic energy density can then be expressed in terms of elementary distortions;

$$f_K = \frac{1}{2}\left[K_{11}\left(\frac{\partial n_\iota}{\partial \iota} + \frac{\partial n_\kappa}{\partial \kappa}\right)^2 + K_{22}\left(\frac{\partial n_\iota}{\partial \kappa} - \frac{\partial n_\kappa}{\partial \iota}\right)^2 + K_{33}\left(\frac{\partial n_\iota}{\partial \lambda} + \frac{\partial n_\kappa}{\partial \lambda}\right)^2\right] \tag{2.9}$$

This equation can be written in vector notation for an arbitrary deformation;

$$f_K = \frac{1}{2}\left[K_{11}\left(\nabla \cdot \mathbf{n}\right)^2 + K_{22}\left(\mathbf{n} \cdot \nabla \times \mathbf{n}\right)^2 + K_{33}\left(\mathbf{n} \times \nabla \times \mathbf{n}\right)^2\right] \tag{2.10}$$

which is known as Frank's equation [10], and is the principle equation in the continuum theory of liquid crystals.

Figure 2.6: Elementary Elastic Distortions

2.4 The Electrical Freedricksz Transition

2.4.1 The Homogeneously Aligned Cell

Consider a film of liquid crystal, sandwiched between two plates of glass (figure 2.7a). The surfaces of the glass are treated in such a way that the liquid crystal lies nearly flat to the surface, with a small pre-tilt angle, equal in size and sign on both surfaces, which ensures the liquid crystal is homogeneously aligned. An electric field applied across this cell will promote the re-orientation of the liquid crystal to align with the field. This re-orientation will be resisted by the elastic ordering properties of the liquid crystal. The resulting director distribution (figure 2.7b) will occur when the electrical free energy gained by the change in orientation is balanced by the elastic energy used in distorting the orientational ordering, and hence is the distribution which minimizes the electrical Gibbs free energy (Appendix A) [11] of the system;

$$G_e = \int_{\mathcal{D}} (f_K - f_e) d\mathcal{D} \tag{2.11}$$

where $\mathcal{D}$ is the volume of the system, since the cell is held at a constant voltage. This is the electrical equivalent to the thermodynamical system with its boundaries held at constant temperature.

The effective refractive index, equation (2.6), for light polarized in the direction of the director at the surface of the cell, is dependent on the resulting director distribution. Liquid crystal cells of this type are the basis of the research in Durham.

2.4.2 Voltage Dependence

Examining the terms of the energy equation (2.11), the principle relationship of the director distribution in the energy minimization can be established. The elastic energy density, equation (2.9), is expressed in terms of the square of the gradients of the director orientation. The electrical free energy density, equation (2.4), is in terms of the dot product of the electric and displacement fields, both of which are in terms of the gradient of the potential through space. This can be seen when the electrical energy is expressed in terms of electrical potential V, in the local

co-ordinate system, $(\bar{0}, \iota, \kappa, \lambda)$, parallel to the principle axes of the molecule;

$$f_e = \frac{\varepsilon}{2}\left\{\varepsilon_o\left(\frac{\partial V}{\partial \iota}\right)^2 + \varepsilon_o\left(\frac{\partial V}{\partial \kappa}\right)^2 + \varepsilon_e\left(\frac{\partial V}{\partial \lambda}\right)^2\right\} \tag{2.12}$$

Consequently, the director distribution $\mathbb{m}$ is dependent on the potential distribution through the system, and not the applied electric field.

Consider the case of two cells, of different thicknesses but with the same applied voltage. The electric fields through the cells will be different, but the orientation of the liquid crystal will be the same (figure 2.8). The electrical free energy, promoting the distortion, will be less in the thicker cell, as the fields will be scaled by the difference in thicknesses. The director distortions will be over a larger distance, thus scaling the elastic energy contribution as well. The thickness of the cell is scaled out, leaving the liquid crystal cell as a voltage dependent device.

2.4.3 The Threshold Voltage

As a consequence of the voltage dependence, the voltage at which the electrical forces overcome the elastic forces, and activation of the device begins, is a constant of the material. This is known as the threshold voltage and is given by;

$$V_{th} = \sqrt{\frac{\pi^2 K_{11}}{\varepsilon(\varepsilon_e - \varepsilon_o)}} \tag{2.13}$$

for homogeneously aligned cells [12].

2.4.4 Switching

When considering the use of liquid crystal cells as devices, the switching times are important. Liquid crystals are by their very nature viscous fluids, and their activation is through molecular rotation, which acts against the viscosity. The activation of the cell is driven by the applied voltage, and the switch on time [12] is given by;

$$\tau_{on} = \frac{d^2\gamma_1}{(V^2 - V_{th}^2)\varepsilon(\varepsilon_e - \varepsilon_o)} \tag{2.14}$$

where γ_1 is the liquid crystal twist viscosity, and d the cell thickness. The switch off time is much slower as it is not driven by the applied voltage: this the relaxation

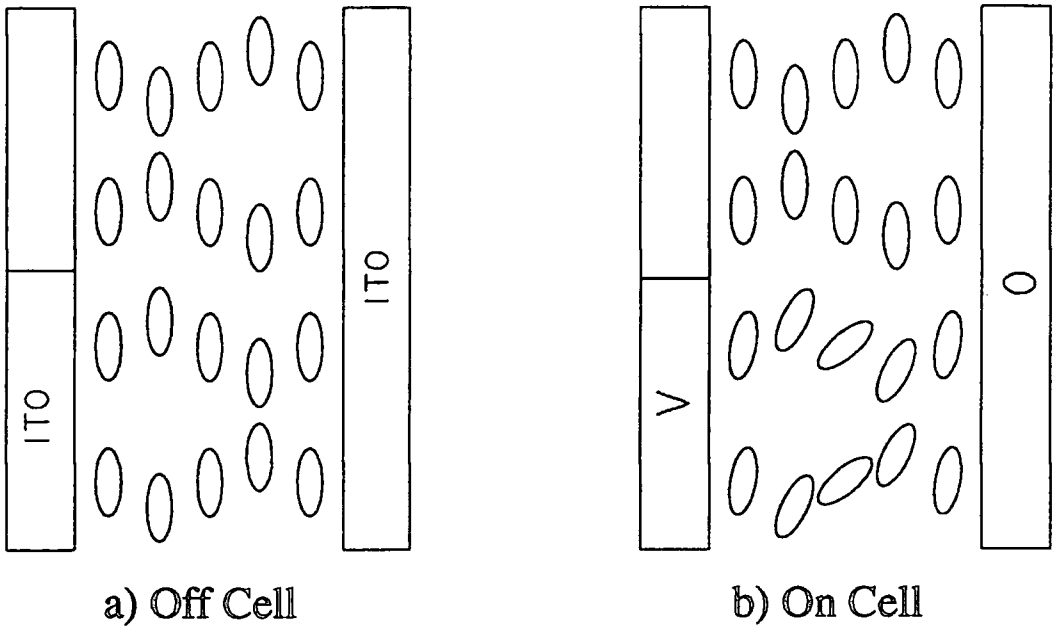

Figure 2.7: Homogeneously Aligned Cell

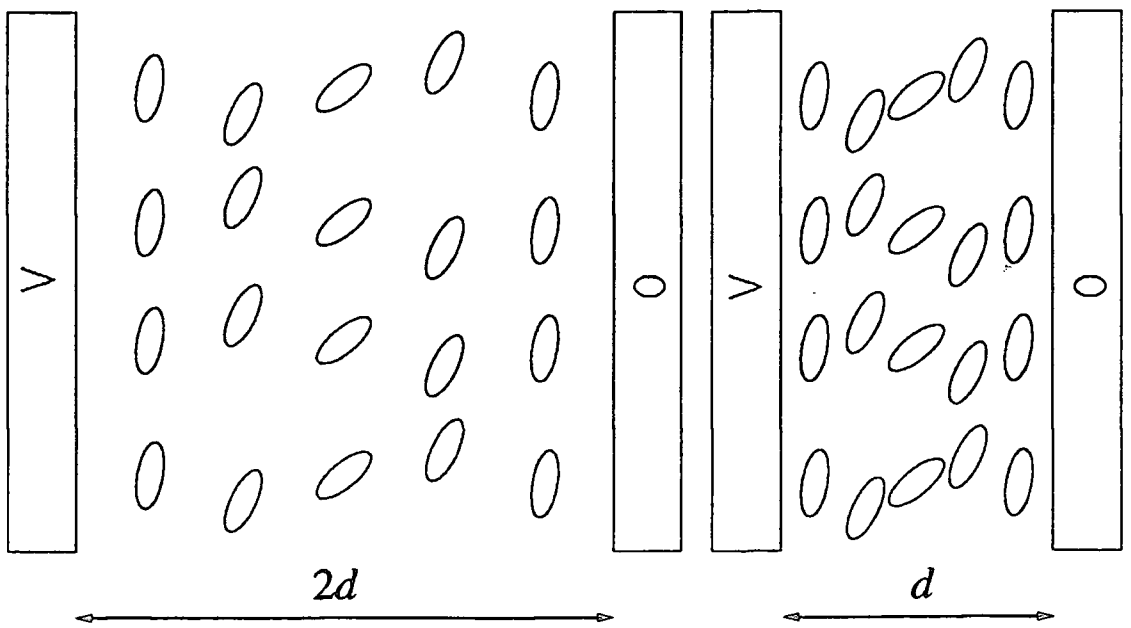

Figure 2.8: Director Distortion through Two Cells of Different Thickness, but with the same Applied Voltage.

time for the liquid crystal to return the inactive state, once the voltage has been removed, and is given by [12];

$$\tau_{off} = \frac{d^2\gamma_1}{K_{11}\pi^2} \tag{2.15}$$

These switching times are derived for a liquid crystal cell in which the central director is distorted by a low angle ($\leq 50°$). The switching times for nematic liquid crystal are very slow when compared to electro-optical effects of solid crystals.

2.5 Summary

The electro-optical properties of nematic liquid crystals have been introduced. The elastic properties have been shown to arise from three elementary types of distortions of the director ordering, splay, twist and bend, which are expressed in the elastic free energy density equations (2.9 & 2.10). The combination of these properties produce a voltage induced change in refractive index, equation (2.6), in a homogeneously aligned cell. The resulting director configuration can be considered as the distribution that minimizes the combination of elastic and electrical energies, equation (2.11). This effect is voltage dependent, and has a characteristic threshold voltage, equation (2.13). The switching times of liquid crystal devices are characteristically slow and are predominantly governed by the liquid crystals twist viscosity, equations (2.14 & 2.15).

This elementary, continuum theory view of nematic liquid crystal and the electrical Freedricksz transition, in a homogeneously aligned cell, is the basis of this research project, and the work in Durham, in the design of liquid crystal phase devices for optical applications.

The view of liquid crystals presented in this chapter is not complete or comprehensive, it is written to provide the reader with a platform from which this thesis and the research in Durham can be appreciated. Some important and central topics for a more general understanding of liquid crystal have been omitted, some of these topics are listed below:

- The chemical composition of the molecules, or mixtures of molecules which form a liquid crystal.

- The order parameters S and D which describe how well aligned the liquid crystal molecules are with the director. In continuum theory S is considered to be constant, and hence is ignored.
- The temperature dependence of liquid crystal properties and the phase changes between liquid crystal states and the crystalline and isotropic liquid states.
- Molecular models of the liquid crystal, which are useful in determining the temperature dependence of the liquid crystal properties and phases.
- The magneto-optical properties of liquid crystal, which are analogous to the electro-optical properties.
- In depth dynamical considerations, especially viscosity and back-flow of liquid crystal.
- Chiral nematic, smectic, discotic and polymer liquid crystals.
- The second order elastic distortions as included by Nehring and Saupe [13], in the continuum theory.

Further information about these topics may be found in any liquid crystal text [1, 2, 3, 4, 5].

2.6 References

[1] L. M. Blinov. *Electro-optical and magneto-optical properties of liquid crystals.* Wiley (1983).

[2] P. G. deGennes. *The properties of Liquid Crystals.* Clarendon Press, Oxford (1974).

[3] S. Chandraskhar. *Liquid Crystals.* Cambridge Press, Oxford (1977).

[4] P. J. Collings. *Liquid Crystals: Nature's Delicate Phase of Matter.* IOP Publishing Ltd (1990).

[5] W. M. de Jeu. *Physical Properties of Liquid Crystalline Materials.* Gordon and Breach (1980).

[6] W. J. Duffin. *Electricity and Magnetism.* 3rd edition, McGraw-Hill (1980).

[7] S. G. Lipson and H. Lipson. *Optical Physics.* 2nd edition, Cambridge University Press (1981).

[8] J. Wilson and J. F. B. Hawkes. *Optoelectronics: An Introduction.* Prentice-Hall (1983).

[9] J. L. Ericksen. *Arch. Rat. Mech. Anal.*, 10 (1962) 189.

[10] F. C. Frank. *Disc. Faraday Soc.*, 25 (1958) 19.

[11] R. N. Thurston and D. W. Berreman. 'Equilibrium and stability of liquid-crystal configurations in an electric field', *J. Appl. Phys.*, 52(1), (1981) 508-9.

[12] G. Labranie and J. Robert. 'Transient behaviour of the electrically controlled birefringence in a nematic liquid crystal', *J. Appl. Phys.*, 44 (11), (1973) 4869-74.

[13] J. Nehring and A. Saupe. 'On the Elastic Theory of Uniaxial Liquid' *J. Chem. Phys.*, 54 (1971) 337-343.

Chapter 3

The Finite Element Method

3.1 Introduction

In order to obtain the optical path profile of a liquid crystal device the director distribution which minimizes the electrical Gibbs free energy of these systems is required. The technique that will be employed for this task is the *finite element method.* This chapter provides an introduction to the concepts and techniques used in this thesis, further information is given in references [1-6]. The application of simple boundary conditions are described and the error estimator used in the design of an automatic adaptive mesh, which minimizes the errors expected in the calculation, is presented.

The finite element method originated in structural engineering; modelling structures consisting of discrete rods. The technique was then extended to continuous structures and continuous functions of physical and engineering problems. The principle features of the finite element method are:

- The physical region of the problem is subdivided into *finite elements.*
- One or more of the dependent variables are approximated in a polynomial form over each element and hence over the whole domain. The parameters of this approximation become the unknowns of the problem.
- Substitution of the approximations into the governing equations, or an alternative formularization of the system, yields a set of equations in terms of the unknown parameters. The solution of these equations produce an approximate solution to the problem.

If the resulting equations are linear with respect to the unknown parameters a computer implementation of a matrix inversion can be employed to solve them.

3.2 Principles of the Finite Element Method

3.2.1 Residual and Variational Methods

An approximate solution to a field problem can be found by approximating the m dependent variables ψ_i $(i = 1, \ldots, m)$, by trial solutions $\hat{\psi}_i$. Methods of applying such trial solutions fall into two groups; the *residual* and *variational* methods.

In residual methods the substitution of the trial solution into the governing field equations;

$$\mathcal{G}(\psi_i) = \mathcal{H}(\psi_i) \tag{3.1}$$

produces a residual error;

$$R = \mathcal{H}(\hat{\psi}_i) - \mathcal{G}(\hat{\psi}_i) \tag{3.2}$$

which is required to be small for a good approximation. In general, a weighted function of the residuals is required to obey a smallness criteria;

$$\int_{\mathcal{D}} W f(R)\, d\mathcal{D} = 0 \tag{3.3}$$

where W is a weighting function, $f(R)$ a function of the residuals such that $f(R) = 0$ when $R = 0$, and $\mathcal{D}$ is the problem domain. The Galerkin formulation is a residual method.

In variational methods the solution is the form of ψ_i which gives an extremum value of a *functional* $\chi(\psi_i)$, that is a function in the form of an integral;

$$\chi(\psi_i) = \int_{\mathcal{D}} \mathcal{L}\left(x_j, \psi_i, \frac{\partial \psi_i}{\partial x_j}\right) d\mathcal{D} \tag{3.4}$$

Substitution of the trial solution $\hat{\psi}_i$ into the functional and the requirement that it still satisfies the extremal condition leads to a set of equations from which $\hat{\psi}_i$ can be obtained.

In many cases *variational calculus* [1, 2, 7] (Appendix B.2) is used to relate the governing field equations to a functional. The Ritz formulation is a variational method.

When both the Ritz and Galerkin formulations of a problem are possible the resulting equations and obtained solutions are identical if the same trial solution is used.

As the problem being considered is an energy minimization, it lends itself directly to the variational method.

3.2.2 The Trial Solutions

In the finite element method the domain is split up into N finite elements. Nodes are established, usually at the vertices of the elements and at strategic positions (mid-sides, centroids etc.) in the interior or at the edges of the elements. Within a finite element e the dependent variables ψ_i are approximated by continuous functions;

$$\hat{\psi}_i^e = f_i^e(x_j, \bar{\psi}_{ik}^e) \tag{3.5}$$

in terms of x_j $(j = 1, \ldots, n)$ the independent variables and $\bar{\psi}_{ik}^e$ the nodal values of $\hat{\psi}_i$ and their derivatives at the nodes $(k = 1, \ldots, s)$ belonging to the element. The simplest form of the approximate function is linear with respect to the nodal values, $\bar{\psi}_{ik}$;

$$\hat{\psi}_i^e = \sum_{k=1}^{s} \mathbf{N}_{ik}^e(x_j)\bar{\psi}_{ik}^e \tag{3.6}$$

where $\mathbf{N}_{ik}^e$ are *Lagrangian* shape functions. If the functions are linear in terms of the nodal values and their derivatives then the shape functions are *Hermitian*, and the trial functions have higher order continuity across the domain. The shape functions are usually simple polynomials of the independent variables x_j. They must have the property of being zero at all the nodes of the element except the node it is associated with, where it is unity;

$$\mathbf{N}_{ik}^e(\text{at node } q) = \begin{cases} 1 & q = k \\ 0 & q \neq k \end{cases} \tag{3.7}$$

The trial functions $\hat{\psi}_i^e$ behave as either Lagrangian or Hermitian interpolation functions of the nodal values for any point within the element.

The trial function of the whole domain becomes a linear combination of these element functions;

$$\hat{\psi}_i = \sum_{e=1}^{N} \hat{\psi}_i^e = \sum_{e=1}^{N} \sum_{k=1}^{s} \mathbf{N}_{ik}^e(x_j)\bar{\psi}_{ik} \tag{3.8}$$

It is important to note that strictly speaking the elements do not share any points, but the nodal points where elements meet are made to have the same value, thus imposing the required order of continuity in the trial function across the domain.

An important criterion in the choice of shape function for a successful finite element formularization is *completeness*, that is the ability of the shape function to successfully approximate the function and its derivatives required to construct the functional.

The elements used in this thesis are some of the simplest conceivable for a two-dimensional problem, which still have variable dimensions. The problem is divided up into an irregular rectangular mesh, each rectangle is sub-divided into two right-angled triangles (figure 3.1), which form the finite elements. A linear shape function is used to describe the variation of the dependent variable across the element;

$$\hat{\psi}(x,y) = \alpha_0 + \alpha_1 x + \alpha_2 y \tag{3.9}$$

which can be simply expressed in terms of the nodal values at the vertices of the of the element;

$$\hat{\psi}(x,y) = \begin{bmatrix} \frac{1}{3} - \frac{x}{b} - \frac{y}{c}, & \frac{1}{3} + \frac{x}{b}, & \frac{1}{3} + \frac{y}{c} \end{bmatrix} \begin{bmatrix} \bar{\psi}_1 \\ \bar{\psi}_2 \\ \bar{\psi}_3 \end{bmatrix} \tag{3.10}$$

where b & c are the x & y dimensions of the element respectively, x & y being measured locally from the centroid of the triangle. This has the form of the *Lagrangian* interpolant of equation (3.6). The choice of this element will be discussed in Chapter 8.

3.2.3 The Functional

The problem concerning this thesis is an energy minimization which can be generally written as;

$$\chi = \int_{\mathcal{D}} \mathcal{L}\left(x_j, \psi, \frac{\partial \psi}{\partial x_j}\right) d\mathcal{D} + \int_{\mathcal{S}} \mathcal{L}\left(x_j, \psi, \frac{\partial \psi}{\partial x_j}\right) d\mathcal{S} \tag{3.11}$$

with domain $\mathcal{D}$ and surface $\mathcal{S}$. A system with a single dependent variable ψ is being considered but the argument can be extended to a system with m dependent variables ψ_i. The domain is broken down into N finite elements and trial functions $\hat{\psi}^e$ applied to each element. The functional can then be expressed as the combination

of all the elements;

$$\chi = \sum_{e=1}^{N} \chi^e \tag{3.12}$$

Substituting in the trial functions $\hat{\psi}^e$ into the functional gives an expression in terms of the nodal values $\bar{\psi}_p$. From variational calculus (Appendix B.1), the condition for a function to be stationary is that its first derivative with respect to each nodal value, separately, equals zero;

$$\frac{\partial \chi}{\partial \bar{\psi}_p} = 0 \tag{3.13}$$

providing an independent equation for each of the nodal values required to describe the approximate trial function over the M nodes ($p = 1, \ldots, M$) of the system.

If the functional is *quadratic-linear*, containing only quadratic and linear terms, with respect to the nodal values and their derivatives then the resulting equations form a set of linear independent equations of the form;

$$\frac{\partial \chi}{\partial \bar{\psi}_p} = k_{pq}\bar{\psi}_q + v_p = 0 \tag{3.14}$$

where p and q are system node numbers, and v_p represent constant terms independent of $\bar{\psi}_q$. As there are the same number of equations as unknown nodal values of the trial function and their derivatives, required to describe the trial function, the system is directly soluble. The matrix which describes the system is known as the k-system matrix, $\mathbf{k}_{\mathbf{sys}}$. The contribution from each element can be expressed separately;

$$\frac{\partial \chi^e}{\partial \bar{\psi}^e_k} = k^e_{kl}\bar{\psi}^e_l + v^e_k \tag{3.15}$$

where k and l are element node numbers, and added individually into the system equation;

$$\frac{\partial \chi}{\partial \bar{\psi}_p} = \sum_{e=1}^{N} \frac{\partial \chi^e}{\partial \bar{\psi}^e_k} \tag{3.16}$$

The matrix which describes the element is known as the k-element matrix, $\mathbf{k}_{\mathbf{ele}}$. The finite element approximations ensure that the dependence of each nodal value is local, dependent only on the nodes of the surrounding elements, hence the resulting matrix is *sparse*, mainly containing zeros. The resulting matrix is also *symmetrical*, $k_{pq} = k_{qp}$, and *banded* if the node numbering is appropriately ordered, the non-zero elements are restricted to a narrow band about the diagonal, all these properties are useful for reducing the calculation time required to solve the equations. The

solution to the equations can be regarded as a matrix inversion;

$$k_{pq}\bar{\psi}_q = -v_p \tag{3.17}$$

$$\bar{\psi}_q = -k_{pq}^{-1}v_p \tag{3.18}$$

By using the finite element method a system with an infinite number of degrees of freedom has been reduced to an approximate system with a finite number of degrees of freedom which can be solved as a set of linear independent equations.

3.2.4 Boundary Conditions

The boundary conditions fall into two groups, *principle* and *natural* boundary conditions. As a natural consequence of variational calculus the gradient of the dependent variables normal to the boundary surface is zero;

$$\frac{\partial \psi_i}{\partial s_j} = 0 \quad \text{on } \mathcal{S} \tag{3.19}$$

where s_j are the directional cosines of the outward normals to surface $\mathcal{S}$. This extends to the gradient of the trial solution normal to the boundary and is the natural boundary condition of the system. Consequently, only the principle boundary conditions need be applied.

The principle boundary conditions occur where the dependent varibles or its normal derivatives to the boundary are prescribed. The most frequently encountered boundary conditions are the Dirichlet, Neumann and Cauchy types, in which only the dependent variables and the first derivates, normal to the boundary are involved. More comlpex boundary conditions involving higher derivatives can also be constructed.

For the Dirichlet boundary condition, the dependent variable at the boundary is prescribed;

$$\bar{\psi}_p = e_p \quad p = p_1, \ldots, p_r \tag{3.20}$$

where p represents the r prescribed nodes on the boundary. For the Neumann boundary condition, the normal derivatives on the boundary are prescribed;

$$\frac{\partial \psi_p}{\partial s_j} = e_p \quad p = p_1, \ldots, p_r \tag{3.21}$$

The Cauchy boundary condition occurs when there is a prescribed relationship between the dependent varible and its derivative at the boundary;

$$\frac{\partial \psi_p}{\partial s_j} + e_p + d_p \psi_p = 0 \tag{3.22}$$

Only Dirichlet boundary conditions will be considered here.

A Dirichlet boundary condition may be directly applied by replacing some of the system equations with the boundary equations (3.20). For example, if a system is described by;

$$\begin{bmatrix} k_{11} & k_{12} & k_{13} & k_{14} & k_{15} \\ k_{21} & k_{22} & k_{23} & k_{24} & k_{25} \\ k_{31} & k_{32} & k_{33} & k_{34} & k_{35} \\ k_{41} & k_{42} & k_{43} & k_{44} & k_{45} \\ k_{51} & k_{52} & k_{53} & k_{54} & k_{55} \end{bmatrix} \begin{bmatrix} \bar{\psi}_1 \\ \bar{\psi}_2 \\ \bar{\psi}_3 \\ \bar{\psi}_4 \\ \bar{\psi}_5 \end{bmatrix} = \begin{bmatrix} Q_1 \\ Q_2 \\ Q_3 \\ Q_4 \\ Q_5 \end{bmatrix}$$

with prescribed values;

$$\begin{aligned} \bar{\psi}_1 &= e_1 \\ \bar{\psi}_4 &= e_4 \end{aligned}$$

the prescribed values may be inserted into the matrix;

$$\begin{bmatrix} 1 & 0 & 0 & 0 & 0 \\ k_{21} & k_{22} & k_{23} & k_{24} & k_{25} \\ k_{31} & k_{32} & k_{33} & k_{34} & k_{35} \\ 0 & 0 & 0 & 1 & 0 \\ k_{51} & k_{52} & k_{53} & k_{54} & k_{55} \end{bmatrix} \begin{bmatrix} \bar{\psi}_1 \\ \bar{\psi}_2 \\ \bar{\psi}_3 \\ \bar{\psi}_4 \\ \bar{\psi}_5 \end{bmatrix} = \begin{bmatrix} e_1 \\ Q_2 \\ Q_3 \\ e_4 \\ Q_5 \end{bmatrix}$$

breaking the symmetry of the system matrix, the symmetry can be restored by rearranging the terms associated with the prescribed nodes;

$$\begin{bmatrix} 1 & 0 & 0 & 0 & 0 \\ 0 & k_{22} & k_{23} & 0 & k_{25} \\ 0 & k_{32} & k_{33} & 0 & k_{35} \\ 0 & 0 & 0 & 1 & 0 \\ 0 & k_{52} & k_{53} & 0 & k_{55} \end{bmatrix} \begin{bmatrix} \bar{\psi}_1 \\ \bar{\psi}_2 \\ \bar{\psi}_3 \\ \bar{\psi}_4 \\ \bar{\psi}_5 \end{bmatrix} = \begin{bmatrix} e_1 \\ Q_2 - k_{21}e_1 - k_{24}e_4 \\ Q_3 - k_{31}e_1 - k_{34}e_4 \\ e_4 \\ Q_5 - k_{51}e_1 - k_{54}e_4 \end{bmatrix}$$

The prescribed nodes can be removed completely from the system matrix, reducing the size of the calculation;

$$\begin{bmatrix} k_{22} & k_{23} & k_{25} \\ k_{32} & k_{33} & k_{35} \\ k_{52} & k_{53} & k_{55} \end{bmatrix} \begin{bmatrix} \bar{\psi}_2 \\ \bar{\psi}_3 \\ \bar{\psi}_5 \end{bmatrix} = \begin{bmatrix} Q_2 - k_{21}e_1 - k_{24}e_4 \\ Q_3 - k_{31}e_1 - k_{34}e_4 \\ Q_5 - k_{51}e_1 - k_{54}e_4 \end{bmatrix}$$

These two boundary conditions are sufficient for the problem this thesis is concerned with.

3.3 Error Estimation and Adaptive Mesh Generation

The finite element method produces an approximate solution to the set of field equations. The difference between the *exact* and *approximate* solution; for example the error in the function or its mth derivative;

$$\epsilon = \psi^{(m)} - \hat{\psi}^{(m)} \tag{3.23}$$

decreases as the size of the finite elements, h, are reduced or the order of the polynomial, p, in the trial function is increased. For a well defined element the error should tend to disappear as the size of the element tends to zero; $\epsilon \rightarrow 0$ as $h \rightarrow 0$.

In order to establish how accurate a given approximate solution is an estimate of this error is required (an *a posteriori* error estimate), to find the true error the exact solution is required, which is not often available. With knowledge of the estimated error it is possible to improve the approximations of the finite element analysis, to achieve a specified accuracy economically with respect to computation. This refinement may be achieved by either reducing the size of the finite elements, h-adaption, increasing the order of the polynomial used in the trial functions, p-adaption, or combining both techniques, hp-adaption. The method used in this thesis is h-adaption, the reason for this choice will be discussed in Chapter 8.

This section will introduce the error norm used in this thesis and the convergence rate of the function and its derivatives, followed by the method of error estimation used and the adaptive mesh refinement strategy employed.

3.3.1 Error Norms and Convergence Rates

There are many error norms that can be used to quantify the difference between the *exact* and *approximate* solutions, in this thesis the L_2 norm [3, Chapter 14] of the first derivatives of the dependent variable will be used;

$$|\epsilon_x| = \left[\int_{\mathcal{D}} (\psi_x - \hat{\psi}_x)^T (\psi_x - \hat{\psi}_x) d\mathcal{D}\right]^{\frac{1}{2}} \tag{3.24}$$

$$|\epsilon_y| = \left[\int_{\mathcal{D}} (\psi_y - \hat{\psi}_y)^T (\psi_y - \hat{\psi}_y) d\mathcal{D}\right]^{\frac{1}{2}} \tag{3.25}$$

which can be constructed over the whole domain $\mathcal{D}$, subdomains, or the individual elements $\mathcal{D}_e$, and the squares of which combine additively;

$$|\epsilon|^2 = \sum_{e=1}^{N} |\epsilon|_e^2 \tag{3.26}$$

These error norms will be compared to the norms of the first derivates of the functions;

$$|\psi_x| = \left[\int_{\mathcal{D}} \psi_x^T \psi_x d\mathcal{D}\right]^{\frac{1}{2}} \tag{3.27}$$

$$|\psi_y| = \left[\int_{\mathcal{D}} \psi_y^T \psi_y d\mathcal{D}\right]^{\frac{1}{2}} \tag{3.28}$$

which can be constructed and combined as the error norms.

The exact solution can be expressed as a Taylor expansion in the vicinity of any point, $(\bar{x}, \bar{y})$ in two-dimensions;

$$\psi(x,y) = \bar{\psi} + \bar{\psi}_x \delta^x + \bar{\psi}_y \delta^y + \frac{1}{2}\bar{\psi}_{xx}(\delta^x)^2 + \frac{1}{2}\bar{\psi}_{yy}(\delta^y)^2 + \bar{\psi}_{xy}\delta^x\delta^y + \ldots \tag{3.29}$$

using notation $\delta^x = x - \bar{x}$, $\delta^y = y - \bar{y}$ and $\bar{\psi} = \psi(\bar{x}, \bar{y})$, $\bar{\psi}_x = \partial\psi(\bar{x}, \bar{y})/\partial x$, *etc.*. Within an element of size h described by a trial function of polynomial of degree p, the trial function can locally fit the Taylor expansion up to the same degree. The error is then the size of the truncated part of the expansion, hence of order $O(h^{p+1})$. The error with respect to the mth derivative of the finite element solution is of order $O(h^{p+1-m})$. This provides the convergence rate of a finite element solution to the exact solution. In the case of a linear element the function is of order $O(h^2)$ and its first derivative $O(h)$. A more mathematical argument for the convergence rate is presented in reference [6, p 106].

3.3.2 Error Estimation

Normally, the exact solution is not available to compare with the finite element solution to evaluate the error. A method of obtaining an a approximate solution, ψ^*, which is a higher order approximation of the exact solution, than that supplied by the finite element method is required. The error can then be estimated by comparing these two approximations;

$$\epsilon_x \approx \psi_x^* - \hat{\psi}_x \tag{3.30}$$

$$\epsilon_y \approx \psi_y^* - \hat{\psi}_y \tag{3.31}$$

There are points in a finite element at which the convergence rate for the derivatives are at an order, $O(h)$, higher than the global convergence, these points are known as *stress points* [6, p 151]. Reference [6, p 168-9] shows that the first derivatives of the function are in error at 'typical' points within the element of order $O(h^{p-1})$, but the average error of the element is of order $O(h^p)$, suggesting that the error must rapidly change sign in the element. With *a priori* knowledge of the positions of these sign changes, a higher approximation of the derivatives can be obtained. This property of improved accuracy is known as *superconvergence*, a brief summary of which is given in reference [8].

The error estimator employed in this thesis relies on the knowledge of the superconvergent points in linear triangular elements. It has been predicted [6, p 169] and proved [9] that the tangential derivatives have exceptionally accurate values at the midpoints of the element edge, but not the normal derivatives. An analysis of superconvergent points based an the use of Taylor series expansions has been presented [10], clearly demonstrating the improved accuracy of the tangential derivatives at the midpoints of the edges of linear triangular elements. This analysis applied to linear triangles is presented in Appendix C and applied to the shape function employed in this thesis (section 3.2.2).

Once these higher order values of the tangential derivatives at the edge midpoints have been obtained a piece-wise linear approximation function of these derivatives may be constructed by interpolation of the values to the nodal points of the elements. These *recovered gradient* functions are clearly a higher order approximation than the finite element approximation of the gradient, which is only a piece-wise constant function. The recovered gradients contain information about the curvature of the function, ψ_{xx}, ψ_{xy} & ψ_{yy}, which the linear finite element approximation cannot contain. As the finite element solution cannot describe this curvature, this represents the biggest error in the approximation. It is expedient to ensure that this error is divided up equally among all the elements and kept below certain limits. The strategy for achieving this is the topic of the next section.

The above argument is presented graphically for a one-dimensional situation in figure 3.2. If a function is approximated in one-dimension by a linear approximation;

$$\hat{\psi}(x) = \psi(\bar{x}) + \psi_x(\bar{x})\delta^x \tag{3.32}$$

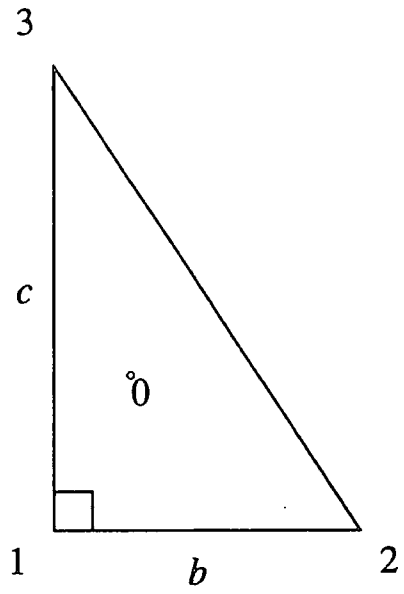

Figure 3.1: A Linear Right-Angled Triangular Element

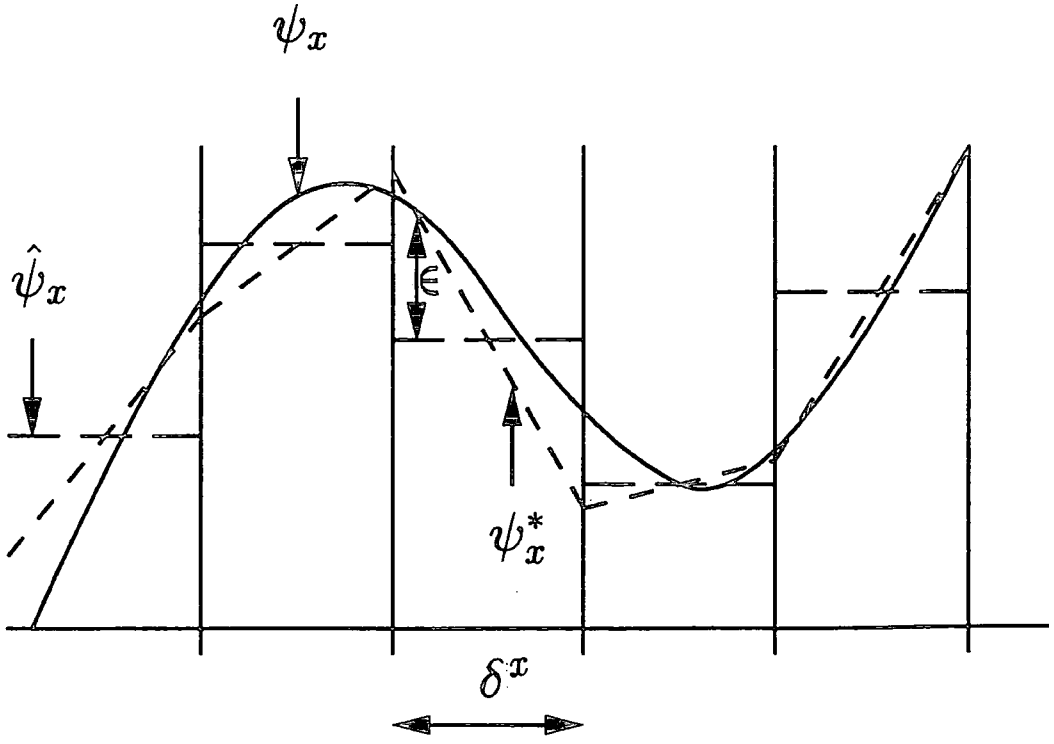

Figure 3.2: Gradient Recovery in a One-Dimensional Example

the first derivative is described by a constant within each element;

$$\hat{\psi}_x(x) = \psi_x(\bar{x}) \tag{3.33}$$

The projected gradient is described by a linear function within each element;

$$\psi_x^\circ(x) = \psi_x(\bar{x}) + \psi_{xx}(\bar{x})\delta^x \tag{3.34}$$

which includes a curvature term, ψ_{xx}. The error in the finite element approximation can be viewed in terms of this curvature;

$$\epsilon = \psi_x^* - \hat{\psi}_x = \psi_{xx}(\bar{x})\delta^x \tag{3.35}$$

which converges with order $O(h)$ (or $O(\delta^x)$) with respect to the first derivative of the function.

This method provides a very direct and easily calculable estimation of the error which is applicable to the model developed in this thesis.

3.3.3 Adaptive Mesh Refinement

Once an estimate of the local and global error has been made, knowledge of the convergence rate can be employed to redesign the mesh in order to achieve a required accuracy, *optimally* fulfilling any global and local error requirements. The strategy used to achieve this is presented in reference [3, Chapter 14]. The consensus of what accuracy is acceptable is between 5-10% for engineering problems.

The global requirement for an acceptable solution is that the error norm falls below a specified percentage of the L_2 norm upon which it is based;

$$|\epsilon| \leq \eta|\psi'| \tag{3.36}$$

where η is the specified value of permissible relative global error. A global parameter, ξ_g, can be defined;

$$\xi_g = \frac{|\epsilon|}{\eta|\psi'|} \tag{3.37}$$

where $\xi_g \leq 1$ indicates satisfaction of the global requirement and $\xi_g > 1$ that further refinement is necessary.

The local requirement for an acceptable solution is that the error is evenly distributed over all the elements, to ensure an *optimal* mesh;

$$|\epsilon|_e = |\epsilon|_r \tag{3.38}$$

where $|\epsilon|_e$ is the error norm of element e and $|\epsilon|_r$ is the 'required' element error norm. A local error parameter can be defined;

$$\bar{\xi}_e = \frac{|\epsilon|_e}{|\epsilon|_r} \tag{3.39}$$

where $\bar{\xi}_e = 1$ indicates an optimal element size, $\bar{\xi}_e > 1$ refinement is required and $\bar{\xi}_e < 1$ mesh depletion is required.

The criterion of the required element error norm $|\epsilon|_r$ used in this thesis is that of spreading the error evenly over all N elements, noting that the squares of the error norms are additive;

$$|\epsilon|_r = \frac{|\epsilon|}{\sqrt{N}} \tag{3.40}$$

where $|\epsilon|$ is the global error norm. Others can be used, such as the requirement that the error is distributed evenly for every unit area of the elements [11];

$$|\epsilon|_r = |\epsilon| \left(\frac{\mathcal{D}_e}{\mathcal{D}}\right)^{\frac{1}{2}} \tag{3.41}$$

where $\mathcal{D}$ is the problem domain and $\mathcal{D}_e$ the domain of the element.

Combining the global and local error requirements, a single element refinement parameter can be constructed;

$$\xi_e = \bar{\xi}_e \xi_g = \frac{|\epsilon|\,|\epsilon|_e}{\eta|\psi'|\,|\epsilon|_r} = \frac{|\epsilon|_e\sqrt{N}}{\eta|\psi'|} \tag{3.42}$$

This parameter, combined with knowledge of the convergence rate of the system, can be used to determine the size of the elements in a new mesh which fulfills both the global and local error requirements. It has been shown that the convergence rate of the mth derivate of a function described by a polynomial of order p over an element e of size h is $O(h^{p+1-m})$, hence the new element size which fulfills the local and global error requirements should be no larger than;

$$h_{\text{new}} = \frac{h}{\xi} \tag{3.43}$$

where

$$\xi = \xi_e^{\frac{1}{p+1-m}} \tag{3.44}$$

An adaptive strategy based on this was employed in this thesis.

It was reported in reference [11] that a modification of this refinement is often used;

$$\xi = (a\xi_e)^{\frac{1}{n}} \tag{3.45}$$

where a is a relaxation constant and n a new exponent, which is taken as $(p+1-m)$ except adjacent to singularities where the strength of the singularity is taken, $n = \lambda$. It was also reported that the use of $a = 1$ and $n = (p+1-m)$ led to inconsistent mesh refinement, which oscillated between over-refinement and over-depletion of areas of the domain in successive iterations of adaptive mesh refinement.

It was pointed out that the combination of $\bar{\xi}_e$ and ξ_g in equation (3.42) presumes that the convergence rate of the error within each element is the same as the global convergence rate;

$$|\epsilon| \simeq O(h^{p+1-m}) \tag{3.46}$$

This however does not account for the effect of the change of the element size on its contribution to the global error, remembering that the contribution of the squares of the error norms are additive, the convergence rate of an element can be written;

$$|\epsilon|_e \simeq O(h^{p+1-m})\mathcal{D}_e^{\frac{1}{2}} \simeq O(h^{p+1-m+d/2}) \tag{3.47}$$

This accounts for the 'sharing out' of the global convergence over elements of changing sizes, where d is the number of dimensions of the space considered. Consequently, the correct refinement parameter is given by the combination;

$$\xi_c = \bar{\xi}_e^{\frac{1}{p+1-m+d/2}} \xi_g^{\frac{1}{p+1-m}} \tag{3.48}$$

The oscillations are reported to disappear with the use of the correct mesh refinement parameter, ξ_c.

3.4 Summary

The principle features of a finite element method have been introduced. Finite element methods have been shown to fall into two groups, *residual* and *variational*, the variational method is used in this thesis. The division of the problem domain into finite elements, in which the dependent variables of the problem are approximated by either *Lagrangian* or *Hermitian* interpolation functions, was described, and the linear, right-angled triangular elements used in this thesis were provided for an example. Following the variational method it was shown that the application of finite element approximations to a functional, which is required to be extremal, provides a set of independent equations, in terms of the nodal values of the dependent function. If the functional is *quadratic-linear* with respect to these nodal values then the equations form a set of linear independent equations which can be solved by the computer implementation of matrix inversion. Two types of boundary conditions were considered; the *natural* boundary conditions, which are fulfilled as a consequence of variational calculus, and the *principle* (Dirichlet), prescribed boundary conditions, which can be imposed by substitution into and rearrangement of the set of system equations.

It was observed that the difference between the *exact* and *approximate* solution decreases as the size of the elements, h, decreases or the order of the approximation polynomial, p, increases. An error norm was introduced and the convergence rate of the approximate function and its derivatives was discussed. An *a posteriori* method of estimating the error of a finite element solution was described, exploiting the *superconvergence* of the tangential derivatives at the midpoints of the edges of linear triangular elements. The use of these estimates in the development of an *optimal* mesh which fulfills global and local error criteria was described, and it was observed that the adaptive mesh refinement strategy was inprecise and could be corrected.

The variational finite element method is directly applicable to the minimization of the electrical Gibbs free energy described in Chapter 2. The motivation for solving this energy minimization problem is described in Chapter 7. The use of the methods and techniques described in this chapter is described in Chapter 8, in the context of solving this problem.

3.5 References

[1] D. H. Norrie and G. de Vries. *An Introduction to Finite Element Analysis.* Academic Press (1978).

[2] D. H. Norrie and G. de Vries. *The Finite Element Method.* Academic Press (1973).

[3] O. C. Zienkiewicz and R. L. Taylor. *The Finite Element Method.* 4th edition, McGraw-Hill (1989).

[4] H. R. Schwarz. *Finite Element Methods.* Academic Press (1988).

[5] C. S. Desai and J. F. Abel. *Introduction to the Finite Element Method.* Van Nostrand Reinhold (1972).

[6] G. Strang and G. J. Fix. *An Analysis of the Finite Element Method.* Prentice Hall (1973).

[7] B. L. Moiseiwitsch. *Variational Principles.* Wiley (1966).

[8] M. Křížek and P. Neittaanmäki. 'On Superconvergence Techniques', *Acta Applicandae Mathematicae,* 9 (1987) 175-198.

[9] N. Levine. 'Superconvergent Recovery of the Gradient from Piecewise Linear Finite-element Approximations', *IMA J. Numer. Anal.,* 5 (1985) 407-427.

[10] R. J. MacKinnon and G. F. Carey. 'Superconvergent Derivatives: A Taylor Series Analysis', *Int. Numer. Meth. Engrg.,* 28 (1989) 489-509.

[11] E. Oñate and J. Castro. 'Adaptive Mesh Refinement Techniques for Structural Problems', *Finite Elements in the 90's,* edited by E. Oñate, J. Periaux and A. Samuelson, Springer-Verlag/CIMNE (1991) 133-145.

Chapter 4

Nematic Liquid Crystal Optical Devices

4.1 Introduction

Since the early 1970's twisted nematic liquid crystal devices have been used as electronic displays, initially in watches and calculators, and nowadays as flat panel colour liquid crystal television displays. Consequently, the technology for the manufacture and development of these devices is established, leading to low cost and good reliability. Research at Durham has concentrated on exploring the potential of using this existing technology to develop optical devices, exploiting the voltage controlled phase modulation of homogeneously aligned cells described in Chapter 2. By selectively applying voltages to regions of the liquid crystal, through designed electrodes, a variety of optical devices may be realised, including the potential of voltage controllability of the refractive index.

In this chapter a liquid crystal cell is described. A brief comparison is made between the use of twisted nematic and homogeneously aligned liquid crystal devices as optical devices. A general statement of the ideal requirements of the desirable optical devices is made, followed by an introduction to already existing devices, which fall into two groups, diffractive and refractive devices.

The possibility of cascading devices to create composite devices is mentioned. Methods of extending the operation of these devices from a single polarization of light to unpolarized light are presented. A summary is given of the techniques that may be employed to enhance the switching speeds of these devices.

4.2 The Liquid Crystal Cell

The liquid crystal cells investigated in Durham were constructed by various personnel at GEC-Marconi Hirst Research Centre laboratories. The following section reproduces almost verbatim the form of the cell which is described by Williams [1].

4.2.1 Basic Cell Components

Optically flat ($\sim \lambda/4$) Indium Tin Oxide (ITO) coated glass slides are used as the liquid crystal retaining bottle. Various thickness ITO coatings have been used, especially 25nm (200Ω/sq) and 125nm (30Ω/sq) thicknesses. The resistance per square, σ, is related to the resistivity of the material, ρ, by; $\sigma = \rho/t$, where t is the thickness of the conductor. A polyimide coating layer is added after the electrode structures have been etched in a solution of hydrochloric acid, de-ionized water and nitric acid (ITO etch). The purpose of this layer is twofold;

- It acts as a planarizing layer, producing a flat even surface above the etched electrode pattern ensuring a constant liquid crystal film thickness across the cell.
- This layer is buffed or scratched in one particular direction, to introduce alignment constraints in the liquid crystal. It has long been acknowledged that the rubbing of a surface induces uniform alignment of liquid crystals, with the nematic director nearly parallel (<2°) to the substrate surface [2].

Glass fibre spacing rods are used to maintain a constant separation of the glass slides. These are cylindrical in shape and very uniform in size. The liquid crystal employed throughout this project was E44 (supplied by Merck Chemicals, formerly BDH Ltd). It has a large, stable liquid crystal temperature range (-6°C to 106°C) and a high optical birefringence (0.262 @ 589.6nm).

4.2.2 Cell Operation

The model developed in this thesis assumes that the liquid crystal exists in an electro-static environment. Consequently, throughout the majority of this thesis the liquid crystal cells are described as being driven by a constant dc voltage, it is important to note that this is not strictly true. In practice, a low frequency ($\sim$1kHz) square wave is used, which prevents the electro-chemical breakdown of the liquid crystal. This square wave also negates the effect of the molecules' permanent dipole. The frequency is too high for the molecules to response to the change in polarity of the applied field, consequently they responds to the time average of the field, which is zero. The use of a 1kHz square wave illustrates the slow response of the liquid crystal, no switching could be expected on this time-scale. The electrically induced dipoles are able to flip their polarity at a much faster time-scale, keeping pace with the field's polarity. The frequency is low enough for the system to be considered to behave electro-statically. The dielectric properties are considered to be the driving mechanism of the cell, as described in Chapter 2. This assumption is made in the model developed in this thesis.

4.3 Twisted Nematic Liquid Crystal Display Devices

Twisted nematic liquid crystal displays [3] are constructed with a $\pi/2$ twist between the director at either surface of the cell (figure 4.1a). Polarisers are aligned with the director on each side of the cell. Light entering the cell is polarized along the director. The helix described by the director through the cell acts as a wave-guide, rotating the plane of polarized light through $\pi/2$. The second polarizer permits the transmission of the rotated light. The application of a voltage across the cell will cause the positive anisotropic liquid crystal to align with the field (figure 4.1b). The helical wave-guiding properties are destroyed. The light then passes through the cell, without alteration to its polarization, and is blocked by the second polarizer.

Displays are built up from small regions of the cell, which are addressed by independent voltages. For simple displays, such as watches and calculators, the elements are relatively large representing a segment of a digit, each digit being composed of eight segments including the decimal point. Each of these segments could

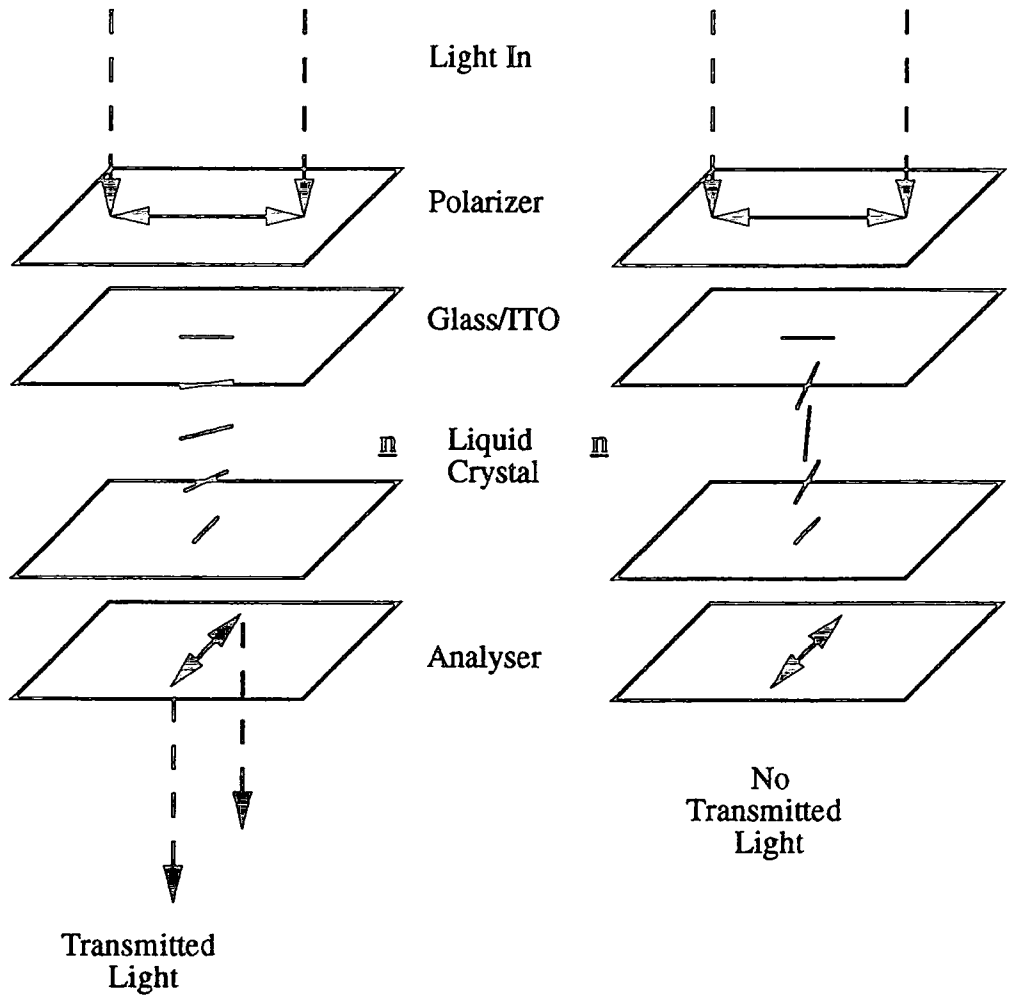

Figure 4.1: Twisted Nematic Liquid Crystal Cell

be addressed individually by a single connection. For larger displays the required connectivity becomes technologically impossible and time multiplexed addressing techniques are used. The amount of time multiplexing is limited by the response time of twisted nematic liquid crystal. The steep voltage response of supertwisted nematic liquid crystal configurations allows for a higher degree of multiplexing in non-grey scale display applications. For television applications where fast response, high contrast, wide viewing and a large number of grey levels have to be achieved, actively addressed twisted nematic liquid crystal displays which comprise an integrated solid state driver in each pixel are required. This is technologically very demanding. Therefore research presented in this thesis on liquid crystal optical devices is concerned with systems consisting of very simple connectivity. In future, it may be necessary to investigate more sophisticated and technologically demanding addressing techniques.

Twisted nematic liquid crystal devices could be used as amplitude blocking holographic elements, but with greater resolution and precision than that used in simple display devices [4]. Such devices have the immediate disadvantage over the phase holographic equivalents, since blocking the light reduces the optical through-put of the device by 50%, hence reducing its optical efficiency by four-fold.

Both twisted, and homogeneously aligned liquid crystal devices could be used as spatial light modulators. In this application the light passing through the modulating elements propagates rectilinearly, hence the resolution requirements are not as stringent as in holographic elements. To generate an array of spatial light modulators, time multiplexed addressing techniques are required.

4.4 Optical Devices

By careful design of the electrodes and applied voltages, a spatially varying phase surface may be produced in the plane of the cell. These voltages may be varied, so modifying the phase surface with time.

In order to achieve a successful liquid crystal optical device, the performance of that device should approach that of the solid state equivalent, or at least reach a level of performance which is acceptable for its intended application. More importantly,

there should be a justification for incorporating liquid crystalline materials into the devices, as opposed to simply etching the required phase surface in a passive medium. Hence, a useful voltage-dependent modification would be advantageous, the simplest manifestation of this is the ability to switch the device on and off. The performance requirement may be relaxed if a useful switchable effect is achieved which could not otherwise be realised.

The use of liquid crystal materials in electro-optical components have some advantages over the faster switching, solid state uniaxial crystals. The liquid crystal devices in question are activated by the application of relatively low voltages, typically a few volts. Consequently power consumption is very low. Liquid crystal materials can also exhibit large values of birefringence (0.262 @ 589.6nm for E44 at 20°C). Therefore thin liquid crystal films ($\sim$10 μm) can introduce several wavelengths of change in the optical path length. This is several orders of magnitude thinner than that required by solid crystals to produce only half a wavelength of change at much higher voltages, of the order of kV. Liquid crystal display technology is well established, providing good reliability and ease of manufacture.

Two approaches may be employed to implement an optical device in a liquid crystal cell:

- A diffractive phase structure can be produced by activating regions of different phase, incident light then diffracts about this structure.
- The phase surface may be varied spatially across the device to mimic the optical path profile of a solid, refractive device, for example a lens or a prism.

4.5 Diffractive Devices

The simplest diffractive phase structures are binary, where selected regions produce a phase change of π. These can be achieved in a thin film of liquid crystal ($\sim 2\mu$m), with the diffraction pattern etched onto one electrode and the other electrode left as a planar earth plate. These devices can be driven by one or two different applied voltages, making the addressing trivial. The diffractive properties are entirely determined by the electrode structure, the voltage determining whether the device is

switched on or off, or mix between the two states if a phase is applied which is not an integer number π. This makes these devices inflexible.

The diffraction pattern formed by any diffractive structure is scaled by the wavelength of the illuminating light. Any optical properties depending on the diffraction pattern will also be scaled. The change in scale across the visible spectrum can be quantified by;

$$\frac{\lambda(650nm) - \lambda(450nm)}{\lambda(650nm)} \times 100\% \sim 30\% \tag{4.1}$$

hence any diffractive device will exhibit strong chromatic aberration.

The performance of such devices is determined by how faithfully the liquid crystal reproduces the required phase surface, i.e. the contrast in phase between adjacent regions of liquid crystal which are switched on and those which are off. The limit of what scale these devices can be produced at is also important, the minimum feature size and the resolution of the features achievable in this technology being critical quantities.

Two examples of binary diffraction patterns are provided below;

- A diffraction grating, which relies on Fraunhofer, far field, diffraction.
- A Fresnel zone-plate lens, which relies on Fresnel, near field, diffraction.

4.5.1 Diffraction Gratings

The simplest holographic diffraction element is a diffraction grating. A voltage can be applied to a periodically etched electrode, such that the liquid crystal retards the phase of the light passing through by π. Such a device can be switched on and off. A development of this is the interlaced diffraction grating (figure 4.2), in which two dependent grating electrodes are etched. These can be selectively switched, changing the periodicity of the grating, so switching on and off various diffraction orders (figure 4.3).

Considering the interlaced diffraction grating structure (figure 4.2), the problem of connectivity in simple electrodes structures is evident. This being a one-dimensional pattern allows for the connecting of the grating lines at the top and

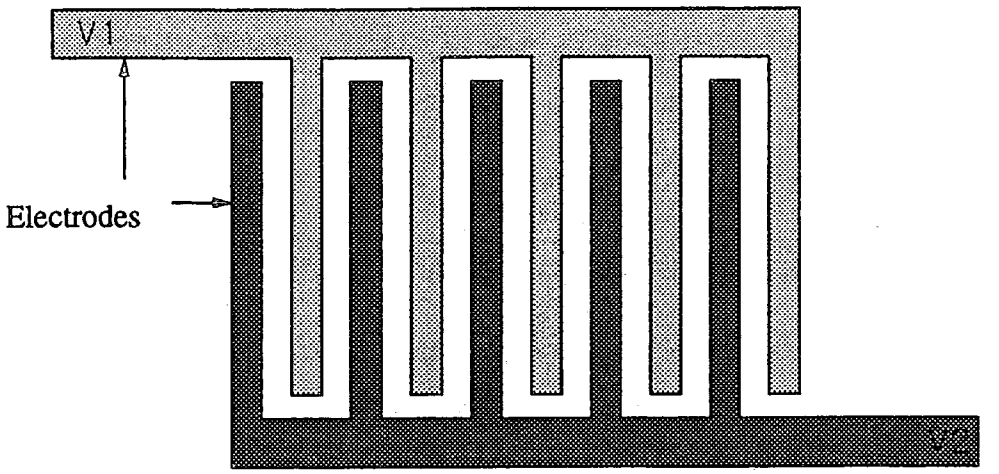

Figure 4.2: Interlaced Diffraction Grating Electrode

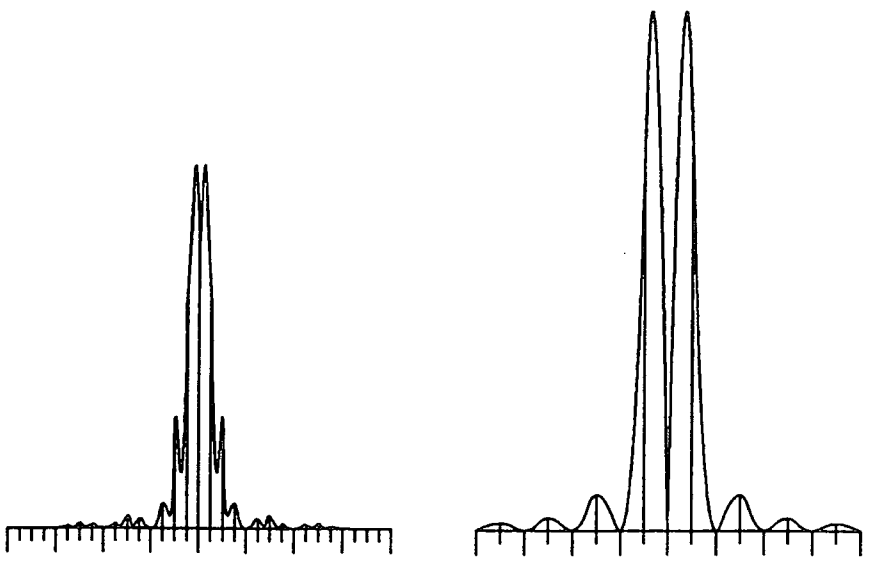

a) One Electrode On

b) Both Electrodes On

Figure 4.3: Diffraction Patterns from Interlaced Diffraction Gratings

bottom of the diffractive element. To implement a third switchable diffraction grating would require the independent addressing of each grating line. For a single layer of ITO with a two-dimensional diffraction structure, the implementation of one fully connected diffraction pattern is all that can be straightforwardly achieved.

The diffraction orders occur at angles of deflection given by;

$$\sin \vartheta = \frac{n\lambda}{l} \tag{4.2}$$

where n is the number of the diffraction order and l the length of the grating period. The deflection angles are dependent on the illuminating wavelength, λ, hence the gratings exhibit strong dispersion or chromatic aberration.

Equation (4.2) shows the limit of the diffraction patterns that can be achieved in a liquid crystal device, the broadest diffraction pattern being produced when the grating period is twice the minimum feature size that can be successfully incorporated in a liquid crystal cell.

The diffraction patterns for this section were obtained by analytically solving the one-dimensional Fraunhofer diffraction integral [6, section 11-3].

Devices consisting of six interlaced diffraction gratings, two geometries at three different scales, were manufactured by GEC-Marconi and investigated in Durham [5].

4.5.2 Fresnel Zone Plate Lenses

A binary, circular symmetric diffraction structure can be designed, which focuses light to a point at a focal length, f, from a diffraction screen (figure 4.4). The diffraction structure is based on Fresnel half-wavelength sub-divisions of a plane wavefront, incident on the zone-plate, with respect to the focal point. The zone boundaries occur when the optical path length from the zone-plate to the focus changes by half a wavelength. It can be shown, using Pythagoras's theorem, that the circular zone radii are given by [7];

$$R_n = \sqrt{n\lambda f + \frac{n^2\lambda^2}{4}} \tag{4.3}$$

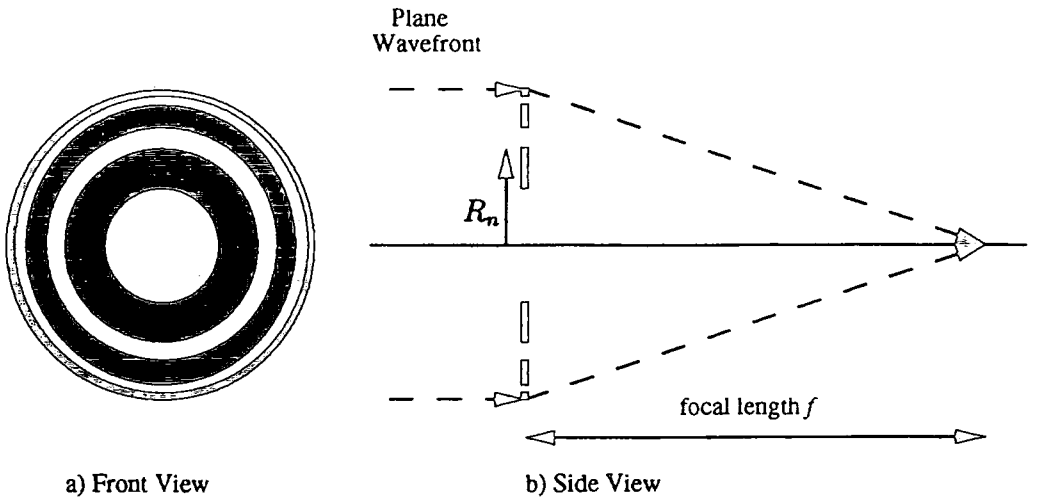

Figure 4.4: Binary Fresnel Zone-Plate

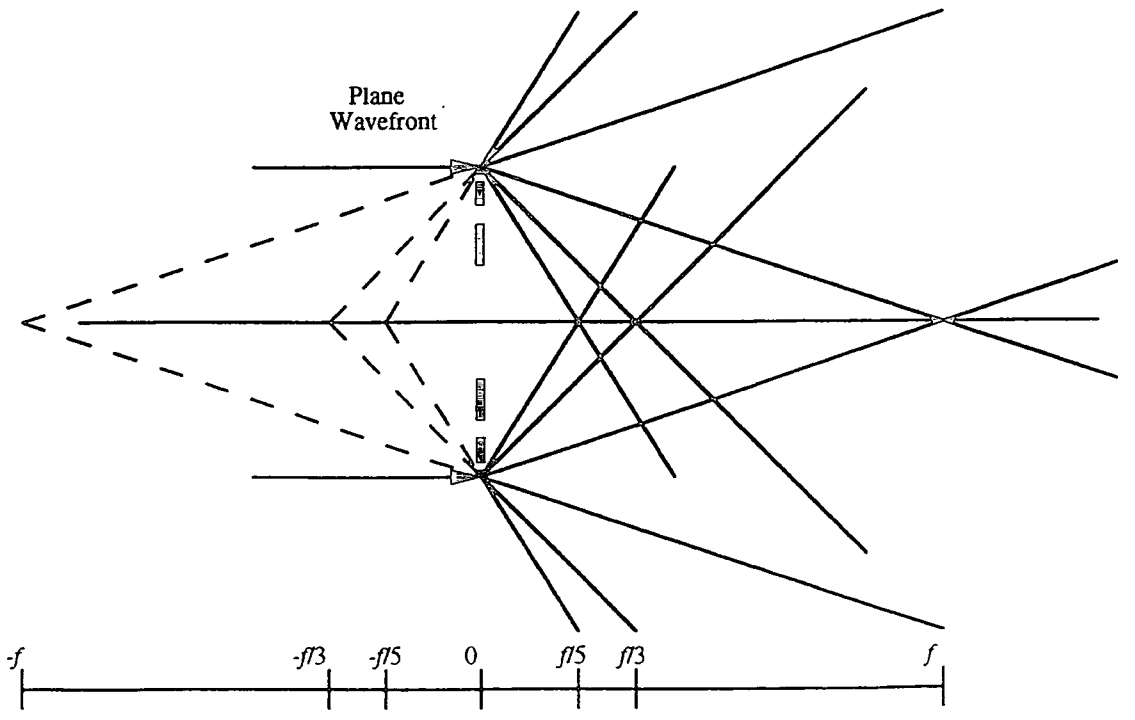

Figure 4.5: Converging and Diverging Foci

where λ is the wavelength of light the zone-plate is designed for and n is the index of the zone.

It can be shown [6, section 10-3] that the contribution from alternate zones are of opposite sign, with a slowly diminishing magnitude, varying slowly with the obliquity factor. The effect of consecutive zones is to nearly cancel each other out completely. A focus can be formed by blocking alternative zones, allowing for the constructive contribution of the remaining zones. This is known as an amplitude blocking, Fresnel zone-plate, which has efficiency with respect to intensity of $100/\pi^2\ \% \sim 10\%$.

The low efficiency is partly due to the fact that half the incident light is being blocked. The amplitude at the focus can be doubled by instead of blocking the incident light from alternate zones, phase retarding it by π, so reversing its contribution, thus increasing the efficiency with respect to intensity by four-fold. This illustrates the advantage of using phase-retardation instead of amplitude blocking in diffractive components.

The reason that phase-retarding Fresnel zone plates are only $\sim$ 40% efficient can be seen by considering the diffraction of the incident light by the Fresnel zones (figure 4.5). The zones behave as a diffraction grating of non-linear periodicity, whose first diffraction order is designed to converge to a focus. There also exists a diverging first order diffraction order, which corresponds to an imaginary focus, of the same focal length, behind the lens. In addition the higher orders of diffraction form additional foci, both converging and diverging, at the odd fractions of the focal length, $\pm f/3$, $\pm f/5$, ..., are formed.

The geometry of the Fresnel zones are dependent on the design wavelength, equation (4.3), which can be approximated by;

$$R_n \approx \sqrt{n\lambda f} \tag{4.4}$$

with a relative error given by;

$$\epsilon \sim \left(\frac{R_n}{4f}\right)^2 \tag{4.5}$$

Consequently, a zone-plate illuminated with a different wavelength, λ', behaves as a lens of a different focal length;

$$f' \approx \frac{\lambda}{\lambda'} f \tag{4.6}$$

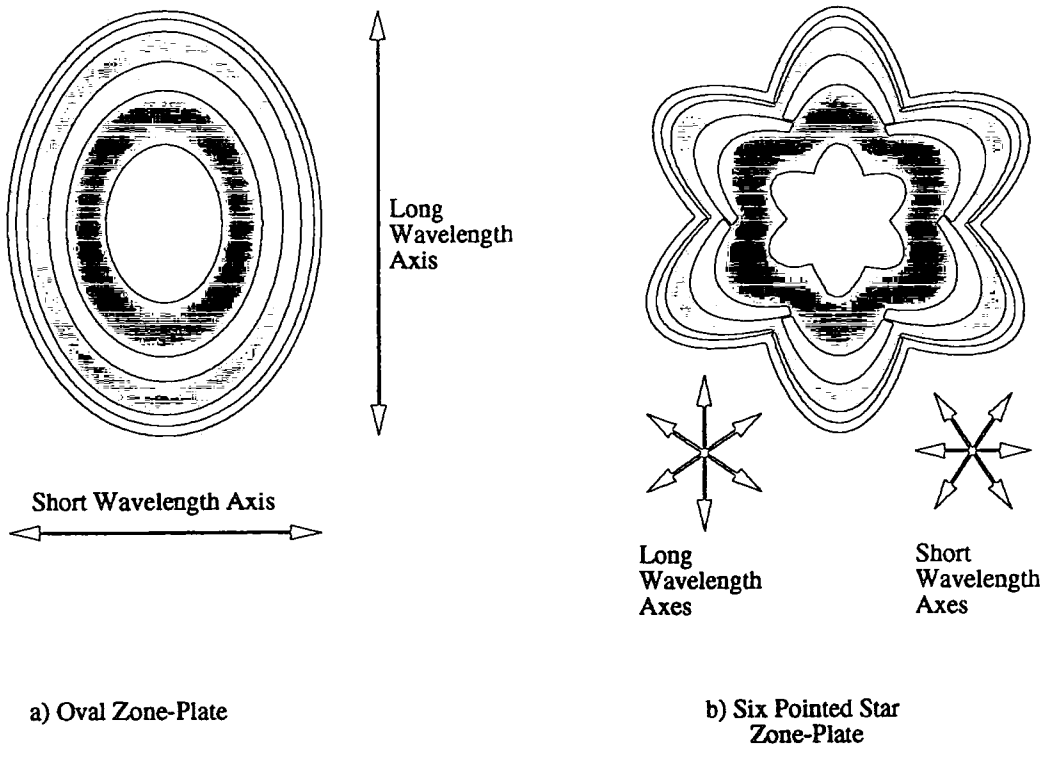

Figure 4.6: Polychromatic Zone-Plates

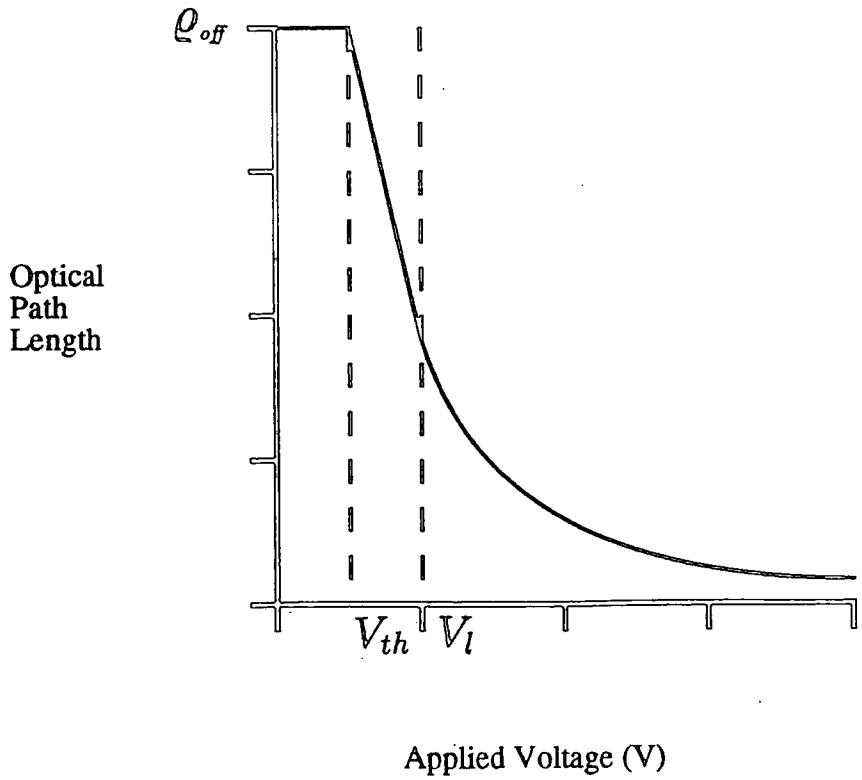

Figure 4.7: Optical Path Response Curve

hence zone-plates exhibit strong chromatic aberration.

A study has been made of the chromatic aberration of liquid crystal devices, and a poly-chromatic, binary Fresnel lens has been designed [8]. The radial zone period of a binary Fresnel lens was varied in such a way as to allow different wavelengths to couple into different axes of the lens. The resulting lens designs were shaped as an oval, or a six pointed star (figure 4.6), depending on the period of the radial variation. The result was a compromise between the bandwidth of light focused, and the proportion of incident light focused from each wavelength.

The aperture size of a Fresnel zone-plate lens is determined by the minimum feature size that can be achieved in the phase surface. As can be seen from the zone radius equation (4.3), the zones become progressively narrower the further out from the centre. The point where they can no longer be effectively implemented is an important design limit, and limits the f-number of the lenses that can be fabricated. It can be shown that this limit is given by;

$$\frac{f}{2R_N} \approx \frac{\Delta R_{MIN}}{\lambda} \tag{4.7}$$

using the approximation, equation (4.4), where R_N is the full radius of the lens and ΔR_{MIN} the minimum zone size that can successfully be implemented. The transition between the active and inactive regions becomes more significant the narrower the zones, as the proportion of the zone taken up by this transition becomes larger, degrading the performance of the device.

Two such lenses, $f/20$ and $f/10$, have been implemented as liquid crystal devices, and have been characterized and investigated by Williams *et al.* [1], [9], ..., [14], demonstrating spot sizes approaching the diffraction limit.

Recently, Tam *et al.* [4] have used a spatial light modulator with pixel size of 30μm $\times$ 60μm to produce an eight-phase-level $f/140$ Fresnel lens. The use of several phase levels increases the efficiency of the device as the resulting optical path profile more closely approximates that of an ideal lens. This idea will be explored further in Chapter 5.

4.6 Refractive Devices

The phase surface, produced by the liquid crystal, may be varied spatially across the device to mimic the optical path profile of a solid, refractive device. The total optical path change that can be achieved across the device is limited to the product of the birefringence and the liquid crystal film thickness, $\Delta n\, d$. Practical cell thicknesses are limited to the order of 20μm, thick cells ($>100\mu$m) suffer from poor liquid crystal alignment [15]. Thicker cells also have the disadvantage of increasing the switching times (equations (2.14 & 2.15)). So even with a highly birefringent liquid crystal, such as E44, liquid crystal refactive devices are limited to having low refractive powers.

It is important to note that even though the optical path length of $\Delta n\, d$ is used throughout this chapter this full optical path length change cannot usually be obtained, since the liquid crystal near the boundaries of the cell is never fully rotated, even at high voltages. A more realistic quantity would be between 90–95% of this value, but for the following discussion $\Delta n\, d$ is used for brevity.

To achieve a spatially varying optical path across the cell, a spatially varying voltage distribution needs to be applied. Consequently, the voltage addressing is less straightforward than in the binary, diffractive devices. Two alternative approaches are provided in the devices below;

- the monolithic prism uses a single current carrying electrode, which provides a continuous variation in voltage,
- the adaptive lens uses discrete electrodes, applying independent voltages, supplying a sampling of the ideal voltage distribution.

The optical properties of these refractive devices are dependent on the applied voltage, providing the attractive possibility of voltage controlled devices. Important properties of the devices may be modified, such as; the pitch of a prism, or the focal length and translational position of a lens.

Refractive devices do not have the disadvantage of strong chromatic aberration of diffractive devices, but liquid crystals are dispersive media, that is the birefringence

is wavelength dependent ($\Delta n \sim 0.33$ @ 450nm and $\Delta n \sim 0.25$ @ 650nm, for E44 [16, 17, 18]). This will lead to chromatic aberration, as any optical path change across the device using a proportion of the birefringence will vary with the birefringence. The change in birefringence across the visible spectrum can be quantified by;

$$\frac{\Delta n(450nm) - \Delta n(650nm)}{\Delta n(650nm)} \times 100\% \sim 30\% \tag{4.8}$$

Any optical property depending on the optical path length change across the device will vary accordingly, causing significant chromatic aberration. The dispersion in Crown Glass ($n \sim 1.528$ @ 434nm and $n \sim 1.514$ @ 656nm) would cause a variation of ~3%. It is important to note that the chromatic aberation due to refraction is in the opposite direction to that due to diffraction.

As in the diffractive devices, the performance is determined by the accuracy of the phase surface produced. The required phase surfaces are in this case continuous and smoothly varying.

4.6.1 Monolithic Prisms

A linear variation in voltage across the cell can be implemented by applying a potential drop across a planar electrode. This continuous variation in potential across the cell produces a continuous phase surface. Such a device can be used as a low angle prism whose pitch, the angle light is deflected through, is continuously variable with the applied voltages. The maximum deflection achievable by such a device is given by;

$$\varphi \approx \arctan\left(\frac{\Delta n\, d}{l}\right) \tag{4.9}$$

where Δn is the birefringence of the liquid crystal, d the cell thickness and l the length of the prism electrode. Even with a short, fat cell (10mm×20 μm) of highly birefringent E44 ($\Delta n \approx 0.262$ @ 589.6nm), only small deflection angles may be achieved (< 2 arcminutes).

The optical path response of any nematic liquid crystal to an applied voltage is non-linear. There is no response up to a threshold voltage (~0.9V), then there is an approximately linear response up to a higher voltage (~1.8V) and for the high voltage region there is a reciprocal relationship (figure 4.7). The phase surface produced

by a linear voltage distribution will reflect the non-linear phase response, degrading the performance of the liquid crystal prism. The operation of the device could be restricted to low voltages where the response is approximately linear, reducing the maximum prism pitch which can be attained.

Dropping a voltage across the planar electrode, will cause the dissipation of electrical energy to heat energy in the cell, at a rate of $V^2/\mathcal{R}$, where V is the applied voltage and $\mathcal{R}$ the resistance of the electrode. As the conductor is sandwiched between two plates of glass, which act as thermal insulators, there is a potential problem in the heating up of the device, changing or destroying the liquid crystal properties. Heating problems were observed in the first current carrying prism constructed in Durham [19]. Consequently, it is important to keep the resistance of such current carrying electrodes high.

Low angle, monolithic liquid crystal prisms of this type have been under investigation for their potential application in the astronomical adaptive image correction project, MARTINI, by Love *et al.* [16].

4.6.2 Adaptive Lenses

The cross-section of a lens can be approximated by applying an appropriate set of voltages to a series of strip electrodes, producing a cylindrical lens [20]. A two-dimensional, spherical lens can be produced using two one-dimensional, cylindrical lenses (figure 4.8), with the strip electrodes orthogonally aligned [21]. The focal length and translational lens position can be controlled by the applied voltages.

From geometrical optics, the optical path lengths of the rays converging on the focus are the same, hence by comparing the optical path lengths of light passing through the centre and the extreme edge of the lens, a limit on the minimum focal length can be found [20];

$$f \approx \frac{R^2}{2\Delta n\, d} \tag{4.10}$$

where R is the radius of the lens, this also limits the f-number attainable.

The use of strip electrodes to produce a one-dimensional phase surface illustrates the connectivity problem, to produce a two-dimensional surface would be difficult to

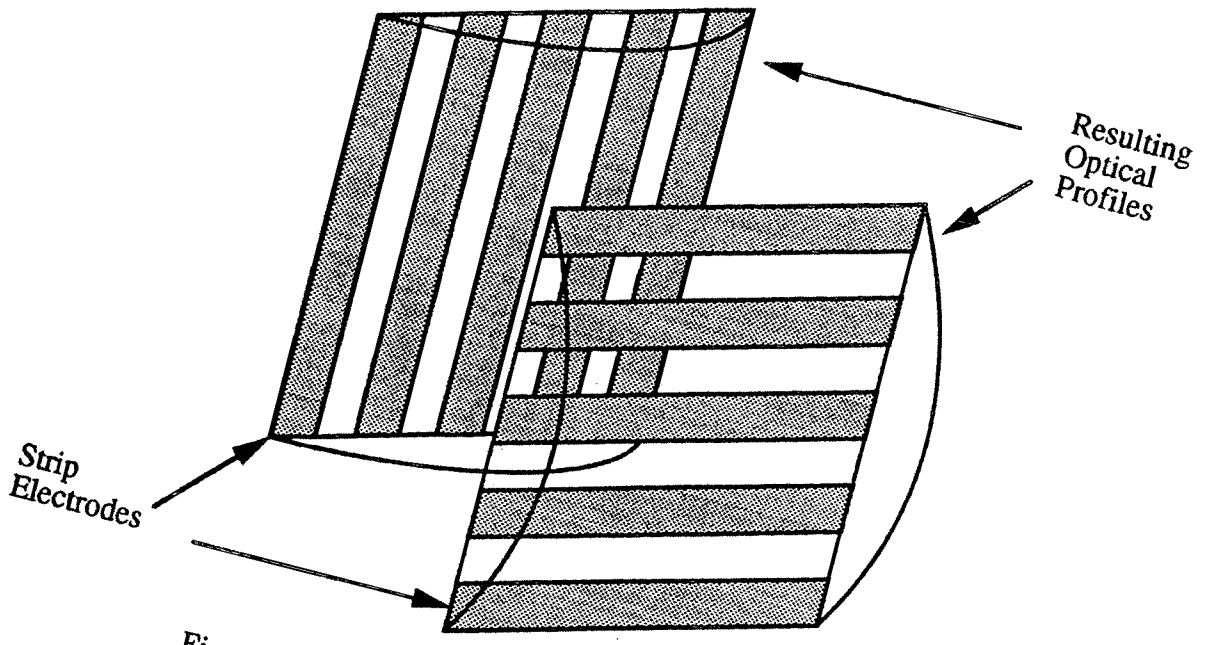

Figure 4.8: Crossing two Cylindrical Lenses

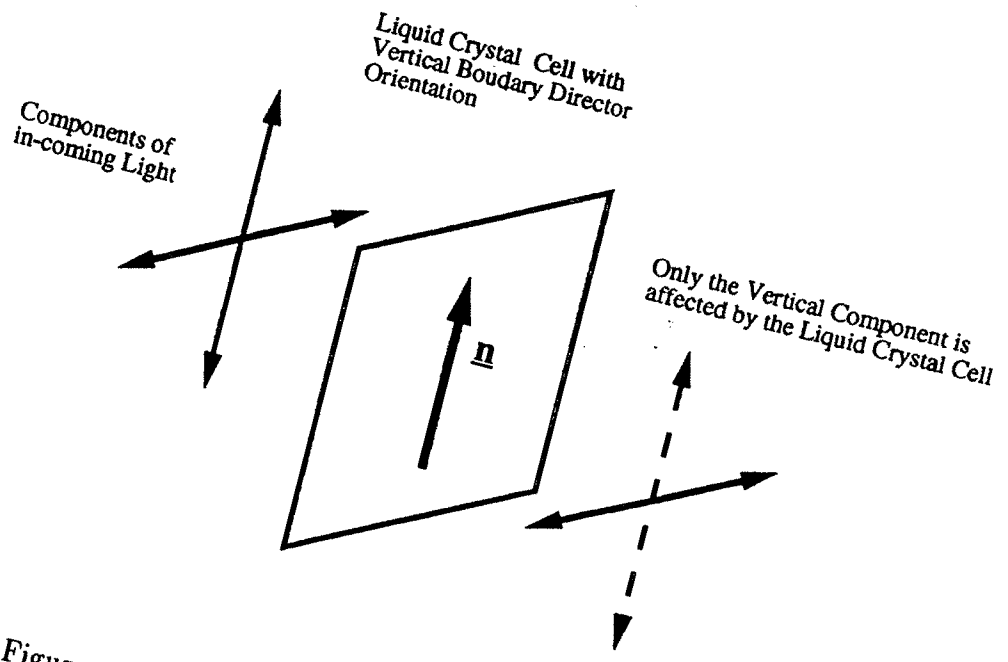

Figure 4.9: Polarization of a Nematic Liquid Crystal Cell

achieve by this method of direct addressing. The strip electrodes can only approximate the required phase surface by providing a sampling of it. In addition there are inter-electrode gaps, in which the required phase surface is not maintained. The problem of obtaining the required phase surface is the opposite to that of the diffractive devices. In the diffractive devices, a sharp transition is required between the activated regions under the electrode and the unactivated regions in the inter-electrode gaps. In these devices the phase surface is required to be smooth, and the inter-electrode gap is required to take the phase of the surrounding electrodes.

Research of these liquid crystal adaptive lenses has been conducted by Kowel *et al.* [20, 21, 15]. A lens constructed from 30μm electrodes with 30μm gaps, at various thicknesses, 25μm, 50μm & 75μm, with an aperture of 3.84mm, at two focal lengths, 5m and 7m, have been reported [15].

4.7 Cascading Devices

The physical thickness of these liquid crystal devices is relatively narrow, the two 1mm thick layers of containing glass making up the majority of the width. Consequently, several devices can be stacked in series, or cascaded, in very little space. This space can be further reduced if a cascaded device is built up from layers of liquid crystal separated by narrow layers of partitioning glass.

An example of the cascading of devices is the use of two cylindrical, adaptive lens to behave as a spherical lens [21]. Another example has been presented [22]; three binary Fresnel lenses where cascaded in series with a glass lens, in order to produce a system which could switch between 2^3 focal lengths, by the application of three independent voltages. Unfortunately, the low efficiency of the binary Fresnel lens caused the intensity of the focus to be successively reduced to $\sim$40% by each active lens. In addition, the other orders of focus combined with each other, creating foci of comparable intensity to the principle focus. It is important that the efficiency of each component is high to avoid these successive losses.

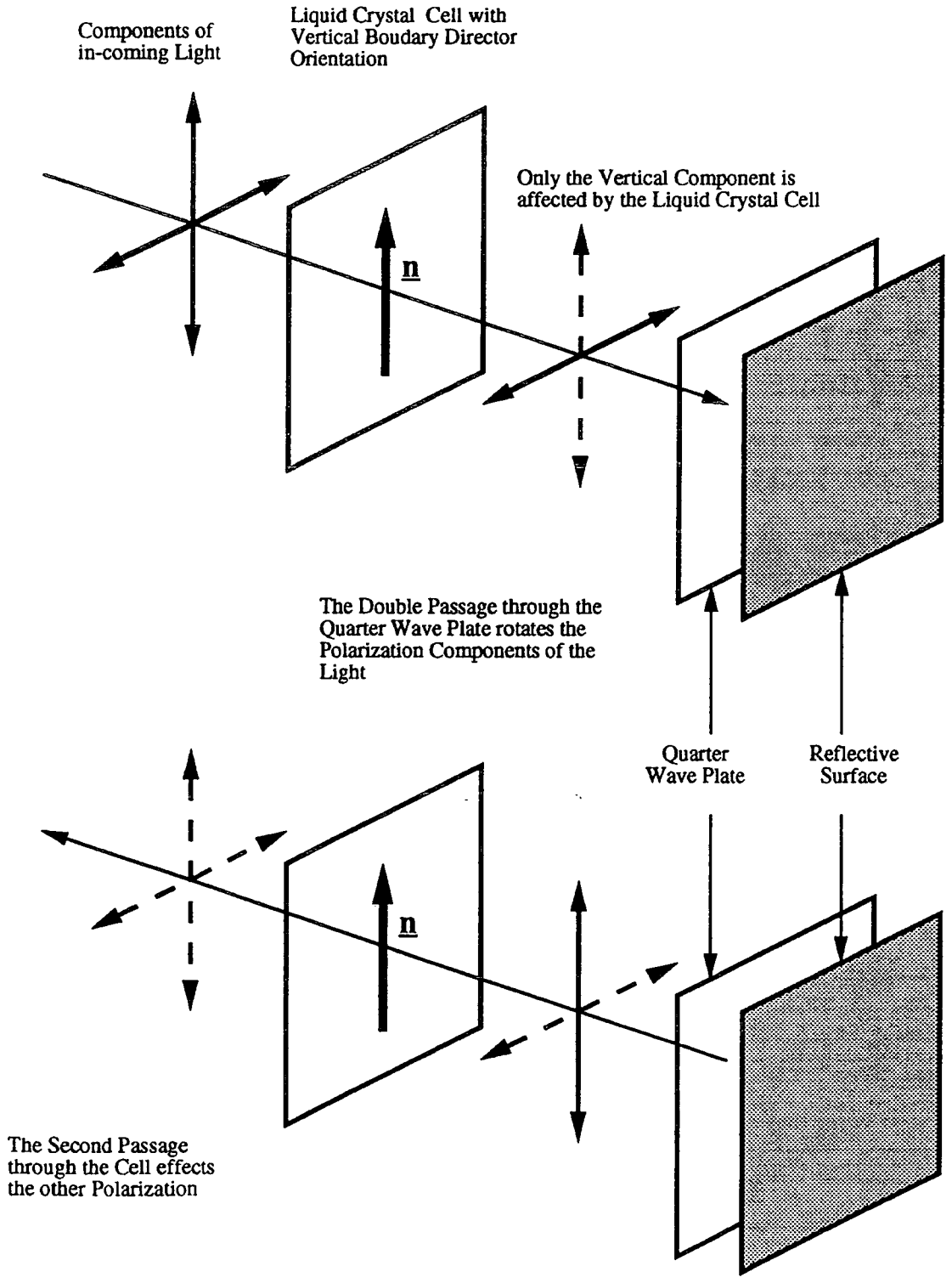

Figure 4.10: Using a Quarter-Wave Plate to Modulate Unpolarized Light with a Single Liquid Crystal Device

4.8 Unpolarized Light

The voltage modulation of the optical path exhibited by the liquid crystal only affects the component of the light parallel to the director orientation at the substrate interface (figure 4.9). This leads to the use of these liquid crystal devices with plane polarized light. The operation of these devices can be extended to unpolarized light by cascading two identically designed devices, fabricated with orthogonally aligned boundary director orientations. Each device operates on one of the orthogonal components of the incident light. The focusing of unpolarized light by liquid crystal adaptive lenses [20] and liquid crystal binary Fresnel lenses [1, 10] have been demonstrated using this technique.

A variation on this method using the double passage of a single liquid crystal cell and a quarter wave plate has been developed (figure 4.10) [23]. The first passage through the cell modulates the component of the unpolarized light parallel to the boundary director orientation. The double passage of through the quarter wave plate has the effect of rotating the orientation of the two component polarizations through $\pi/2$. On the second passage, the previously uneffected component is then appropriately orientated to be modulated by the liquid crystal cell and the previously modulated component can pass through unmodulated. In this way a single cell can be used for both components of the unpolarized light, thus avoiding any potential problems in aligning two cascaded devices.

Another single device method has been proposed [24] for binary diffractive devices. For the operation of a binary diffractive device only alternate zones need have the refractive index dependent on the applied voltage, for a single polarization. By aligning the boundary director of alternate zones to be orthogonal (figure 4.11a) the refractive index of zone $\mathcal{I}$ is dependent on the applied voltage and zone $\mathcal{J}$ is independent, for vertically polarized light. The reverse is true for horizontally polarized light. Consequently, the required binary diffractive structure is present for both components of arbitrarily polarized light in a single passage through the device, avoiding any alignment problems. Both polarizations are affected at the same point along the optical path unlike the previous two methods in which the position each polarization is affected is separated by the partitioning glass, and the double passage through the quarter-wave plate in the second case.

In such a device the zones are constructed by the boundary director orientation instead of the electrode geometry, a planar electrode is used for these devices. Consequently, the zone resolution is not limited by the restrictions of ITO wet-etching (section 6.2) and there will be no fringing fields between the zones (Chapter 7). This technique is however limited to binary diffractive devices.

In order to construct these devices the zone structures on both surfaces need to be carefully aligned. This can be avoided by the use of *homeotropic alignment* on the second surface, that is orientation of the molecules perpendicular to the surface (figure 4.11b). This halves the maximum optical path change of the device, but as only a phase change of π is required for operation this is not a serious problem.

4.9 Pixelated Devices

The practicalities and multiplexing considerations of pixelated optical devices are beyond the scope of this thesis, some of the considerations relating mainly to display applications may be found in [25, 26]. It is expected that requirements of high resolution and the continuum of activation levels may require the presence of an integrated solid state driver in each pixel.

It may appear that the use of a pixelated device may produce an extremely flexible device as it can take any arbitrary diffractive or refractive device form. The resolution of the pixels will determine the resolution of the optical path structure that the device can display. The pixel structure may have the additional effect of causing diffraction as a rectangular grating of the same period. A similar phenomena was observed in a binary, diffractive Fresnel zone-plate whose zones where approximated by rectangular regions of minimum dimension 20μm, consequently the curves contained 'jaggies' of 20μm (figure 4.12). This caused significant scattering into diffraction orders appropriate to a diffraction grating of period 20μm [1, 10]. The same effect was also observed in the spatial light modulator implementation of an eight-phase-level Fresnel lens [4]. It is clearly advantageous to reduce the pixel size to increase the resolution and move the diffraction orders away from the primary beam. The limit to the effective resolution of the pixels is restricted by the wet etching technique (section 6.2) to $\sim 2\frac{1}{2}\mu\text{m}\times 2\frac{1}{2}\mu\text{m}$, and the fringing fields which will be discussed in Chapter 7.

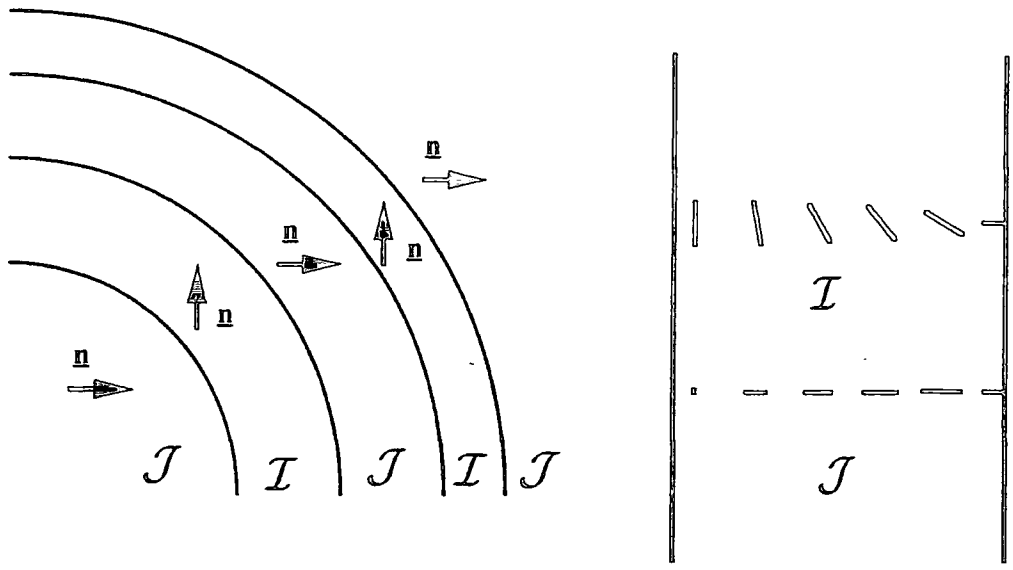

a) Alternate Zones have orthogonally aligned Boundary Director

b) Homeotropic Alignment on Second Surface

Figure 4.11: Using Orthogonally Aligned Boundary Directors to Modulate Unpolarized Light with a Single Liquid Crystal Device

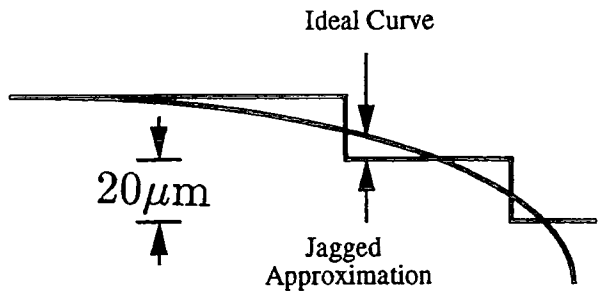

Figure 4.12: Curved Zone Constructed with Jaggies

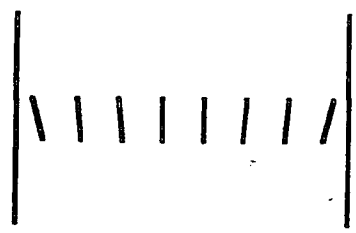

Director Boundary
Pre-Tilt has opposite
sign on opposite surface

Figure 4.13: Director Orientation through a π-Cell

4.10 Switching Speeds

The switch on and switch off times of a liquid crystal cell at low central angle ($\leq 50°$) distortions are given by [27], (section 2.4.4);

$$\tau_{on} = \frac{d^2\gamma_1}{(V^2 - V_{th}^2)\varepsilon(\varepsilon_e - \varepsilon_o)} \tag{4.11}$$

$$\tau_{off} = \frac{d^2\gamma_1}{K_{11}\pi^2} \tag{4.12}$$

and are relatively slow, the order of milliseconds, switching times of the order of microseconds are required for optical computing applications.

The equations ignore the effect of 'backflow', that is the movement of the centres of gravity of the liquid crystal molecules as they rotate. These effects are more dominant in the homogeneously aligned liquid crystal cells described in this thesis than in π-cells, which are cells whose boundary director orientation are π different on the opposite surfaces. In π-cells the director distribution does not follow a π twist through the cell, but remains parallel with the boundary directors (figure 4.13). The π-cells achieve the above switching times the device may need to be implemented as π-cells.

The switch on time is driven by the applied voltage, consequently faster switch on times can be achieved by applying voltages very much larger than required to achieve the on-state, to drive the cell quickly. When the on-state is reached a low voltage can be applied to maintain it. In this way the initial, rapid part of the activation to a high voltage state is used to obtain a lower voltage state at improved switching times. The switch off or relaxation of the cell is undriven and so cannot be improved in this way. It has been suggested that the cells could be driven off by the application of lateral fields to the cell [28].

4.10.1 The Transient Nematic Effect

In some applications a switching of π phase change, or half a wavelength, is required. Using the transient nematic effect improved switching speeds can be obtained for such small optical path changes. A liquid crystal amplitude modulator with response times of 1ms has been demonstrated [29, 30], using this effect in a homogeneously

aligned cell sandwiched between polarizers at $\pi/4$ to the boundary director of the cell. The cell is in a highly deformed on-state due to a large applied voltage. The voltage is removed and the liquid crystal allowed to freely relax until the required optical path change occurs, then an appropriate maintenance voltage is applied. This can be seen as using the initial, rapid part of the full decay to obtain a faster switching for a small part of the decay. This is different to the situation where the voltage is switched to the maintenance voltage which is present throughout the decay as this has the effect of providing an electrical breaking to the decay, thus slowing the switching.

It has been shown and experimentally demonstrated [31] that the decay time is given by;

$$t_0 \cong \left(\frac{\Delta/\pi}{2\pi\alpha}\right) \frac{1}{(1-\beta V_{th}/V_i)^2} \frac{\gamma_1 \lambda^2}{K_{11}\Delta n^2} \tag{4.13}$$

where Δ is the phase change, α (=1.10±0.02 for E7) is a decay constant found by experiment, β (≅0.60 for E7) is a constant of material and V_i (~10–50V) the initial voltage used. It is important to note that there is no dependence on cell thickness. Using the transient nematic effect, thick cells can be used to achieve faster switching between phases of odd and even multiples of π at a high levels of activation. The transient nematic effect has been demonstrated in the operation of a binary Fresnel lens [1].

4.10.2 Dual Frequency Addressing

An alternative method of driving off the liquid crystal is to exploit the dual frequency effect of some liquid crystal materials. The extraordinary relative permittivity, ε_e, is frequency dependent and relaxes at high frequencies (the order of kHz) to values less than the ordinary relative permittivity, ε_o, which remains about constant with frequency [32]. Consequently, at high frequencies the dielectric anisotropy $(\varepsilon_e - \varepsilon_o)$ changes sign, and can be used to drive the cell to an off-state [33].

Using the above techniques, some significant improvements on the switching times can be made. However, the achievement of switching times required for optical computing appears unlikely. The switching times will prove to be a significant limitation to the potential applications of the devices discussed in this thesis.

4.11 Summary

The components of a homogeneously aligned liquid crystal cell have been described. Its potential use as an optical device has been briefly compared to twisted nematic devices. The requirements of ideal liquid crystal optical devices were outlined; good optical performance, and the useful voltage modification of their optical characteristics.

Already existing liquid crystal optical devices were introduced, these fell into two groups; diffractive devices, including diffraction gratings and Fresnel lenses, and refractive devices, including monolithic prisms and adaptive lenses. The diffractive devices have been found to be inefficient, scattering light into several diffraction orders and limited in the voltage controllability to switching the devices on and off. The refractive devices were limited by the maximum optical path the device could achieve, $\Delta n\, d$; the maximum prism pitch given by equation (4.9), and the f-number of the lens limited by equation (4.10). The voltage controllability of refractive devices is very flexible, allowing for the continuous variation of prism pitch or focal length and the efficiency very high, theoretically approaching 100%.

The properties of devices based on diffraction vary with wavelength, which varies by ~30% across the visible spectrum. The properties of devices based on refraction suffer from the dispersive birefringence of liquid crystal, which varies by ~30% across the visible spectrum for E44, but in the opposite sense.

Due to the physical thickness of these flat liquid crystal devices, ~2mm including glass slides, several may be cascaded to produce a variety of composite devices. The efficiency of each component device is important as any inefficiencies will combine as each device is switched in.

The refractive index modulation of these devices only affects light polarized in the plane of the boundary liquid crystal director orientation. The operation of these devices can be extended to unpolarized light by cascading two identically designed devices, fabricated with orthogonally aligned boundary directors, each device operating on an orthogonal component of the incident light. A variation on this is reflecting the light through a single device and a quarter wave plate. The double passage through the latter has the effect of rotating the planes of the two com-

ponent polarizations of light through $\pi/2$, allowing the single liquid crystal device to modulate a component of the light with each passage. A single passage, single device method for binary devices has been proposed, in which alternate zones are constructed with orthogonal, boundary director alignments. Each zone is only active for one component of the incident light, together both components are modulated on a single passage.

The use of pixelated devices, though potentially much more flexible than the dedicated structures described, may suffer from diffraction about the pixels, and it may be too impractical to obtain the required resolution.

The switching times of homogeneously aligned liquid crystal cells are relatively slow. These could be improved by the use of π-cells to reduce the effects of backflow, the movement of the centres of gravity of the liquid crystal with rotation. The transient nematic effect, the initial rapid relaxation of the liquid crystal highly distorted by large applied voltages, could be used to obtain fast switching between two highly distorted states. The dual frequency effect, the changing of sign of the dielectric anisotropy of some positive dielectric liquid crystals at high frequencies, could also be used to drive off the devices. The employment of these techniques will improve the switching off times, but it is not expected that they will be sufficient to produce switching speeds for optical computing applications.

4.12 References

[1] G. Williams. *Electrically Controllable Liquid Crystal Fresnel Lenses.* PhD Thesis, Uni. of Durham (1991).

[2] J. Cognard. 'Alignment of nematic liquid crystals and their mixtures', *Mol. Cryst. Liq. Cryst.*, 1 (1982).

[3] M. Schadt. 'Plenary Lecture', *Liq. Crys.*, 5, 1 (1989) 57-71.

[4] E. C. Tam, S. Zhou and M. R. Feldman. 'Spatial-light-modulator-based electro-optical imaging system', *Appl. Opt.* 31, 5 (1992) 578-580.

[5] R. S. Longhurst. *Geometrical and Physical Optics.* 3rd edition, Longman (1973).

[6] A. J. Boyes. *Adaptive Image Processing Using An Electrically Controlled Hologram.* Undergraduate Project Report, Uni. of Durham (1988).

[7] Lord Rayleigh. 'Wave Theory', *Encyclopedia Britannica.* 9th edition, 24, 429 (1888).

[8] G. D. Love and A. Purvis. *Contract Report for GEC-Marconi,* (not open literature) Uni. of Durham (1992).

[9] A. Purvis, G. Williams and M. G. Clark. 'Liquid Crystal Lenses', *Int. Liquid Crystal Conf. Freiburg,* Paper A38 (1988).

[10] G. Williams, N. J. Powell, A. Purvis and M. G. Clark. 'Electrically controllable LC Fresnel lens', *SPIE Proc.,* 1168 (1989) 352-357.

[11] A. Purvis, G. Williams, M. G. Clark and M. C. K. Wiltshire. 'Spatial Light Phase Modulators and Fresnel Optical Components using LC's', *Applied Optics feature of OSA meeting* (1989).

[12] A. Purvis and G. Williams. 'Switchable Liquid Crystal Lenses', *Molecular Electronics News, SERC,* 5 (1989).

[13] G. Williams, A. Purvis and M. C. K. Wiltshire. 'Design Criteria and Fringing Field effects on the performance of LC Fresnel Lenses', *Applied Optics and Opto-Electronics Digest, Nottingham,* (1990) 225.

[14] A. Purvis, G. Williams, N. J. Powell, M. G. Clark and M. C. K. Wiltshire. 'Liquid crystal phase modulators for active micro-optic devices', *SPIE Proc.,* 1455 (1991) 145.

[15] P. F. Brinkley, S. T. Kowel and C, Chu. 'Liquid crystal adaptive lens: beam translation and field meshing', *Appl. Opt.,* 27, 21 (1984) 4578-4586.

[16] G. D. Love. *The use of liquid crystal adaptive optics devices in astronomy.* PhD Thesis, Uni. of Durham (1992).

[17] G. D. Love and J. V. Major. 'The application of Edser-Butler fringes to the measurement of the optical structure of liquid crystal prisms and the determination of dispersion characterists and thickness', *J. Phys. D.,* 24 (1991).

[18] G. D. Love and J. V. Major. 'A fast method to measure the voltage characteristics of liquid crystal using Edser-Butler fringes', *J. Meas. Sci. Technol.*, 3 (1992) 615-617.

[19] B. Margretts. *Production of a segment of a Fresnel lens in a liquid crystal cell.* Undergraduate Project Report, Uni. of Durham (1988).

[20] S. T. Kowel, D. S. Clevery and P. G. Kornreich. 'Focusing by electrical modulation of refraction in a liquid crystal cell', *Appl. Opt.*, 23, 2 (1984) 278-289.

[21] S. T. Kowel, P. G. Kornreich and A Nouhi. 'Adaptive Spherical Lens', *Appl. Opt.*, 23, 16 (1984) 2774-2777.

[22] A. Purvis, N. J. Powell and M. C. K. Wiltshire. 'Cascaded Liquid Crystal Fresnel Lenses', *Applied Optics and Opto-Electronics Digest, Leeds,* (1992) 229-233.

[23] G. D. Love. 'Liquid crystal phase modulator for unpolarized light', *Appl. Opt.*, 23, 13 (1993) 2222-2223.

[24] J. S. Patel and K. Rastani. 'Electrically controlled polarization-independent liquid-crystal Fresnel lens array', *Opt. Lett.*, 16, 7 (1991) 523-534.

[25] G. Baur. 'The influence of Material and Device Parameters on the Optical Characterists of Liquid Crystal Displays', *Mol. Cryst. Liq. Cryst.*, 63 (1981) 45-58.

[26] S. Matsumoto, H. Hotoh and H. Tomi. 'Material and Cell Parameters Considerations in a Highly Multiplexing TN Liquid Crystal', *Mol. Cryst. Liq. Cryst.*, 163 (1988) 87-99.

[27] G. Labranie and J. Robert. 'Transient behaviour of the electrically controlled birefringence in a nematic liquid crystal', *J. Appl. Phys.*, 44 (11), (1973) 4869-74.

[28] G. D. Love. *Private Communication,* Uni. of Durham.

[29] A. E. Perregaux. *US Patent.* No. 4 595 259 (1986).

[30] A. E. Perregaux, F. J. Stephany, E. C. Faux, R. A. Hudson, A. I. LaKatos, R. Narang and B. Richter. *SID International Symposium Digest,* 360 (1987).

[31] S-T. Wu and C-S. Wu. 'Small angle relaxation of highly deformed nematic liquid crystals' *Appl. Phys. Lett.*, 53, 19 (1988), 1794-1796.

[32] W. H. de Jeu, C. J. Gerritsma, P. VanZanten and W. J. A. Goosens. 'Relaxation of the dielectric constant and electro-dynamic instabilities in a liquid crystal' *Phys. Lett.*, 39A, 5 (1972) 335-356.

[33] H. K. Bücher, R. T. Klingbiel and J. P. Van Motor. 'Frequency-addressed liquid crystal field effect', *Appl. Phys. Lett.*, 25, 4 (1974) 186-188.

Chapter 5

Diffractive/Refractive Nematic Liquid Crystal Devices

5.1 Introduction

In Chapter 4 diffractive and refractive devices were presented with their limitations. This chapter explores the ideas developed during this research project of the type of optical path structures and device properties that might ideally be implemented in a liquid crystal device.

The limit of, $\Delta n\, d$, the change in optical path length was seen to be very restrictive in the implementation of refractive devices. The binary diffractive devices were seen to be very inflexible with respect to the possibility of the voltage modification of their optical structure. They also suffer from inefficiency, as light is lost to other diffraction orders. By combining these two approaches some of these disadvantages may be overcome in diffractive/refractive devices. The following discussion assumes spatially and temporally coherent light sources.

5.2 Wavelength Sampling of a Refractive Structure

Consider the effect of a solid, refractive device, for example a prism or a lens, on an incident plane wave of monochromatic light, wavelength λ (figure 5.1). The emerging wavefront is formed where light, passing through the spatially varying optical path of the device, has travelled the same optical path length. A prism forms a plane wave deflected through an angle φ, and a lens forms a converging spherical wave,

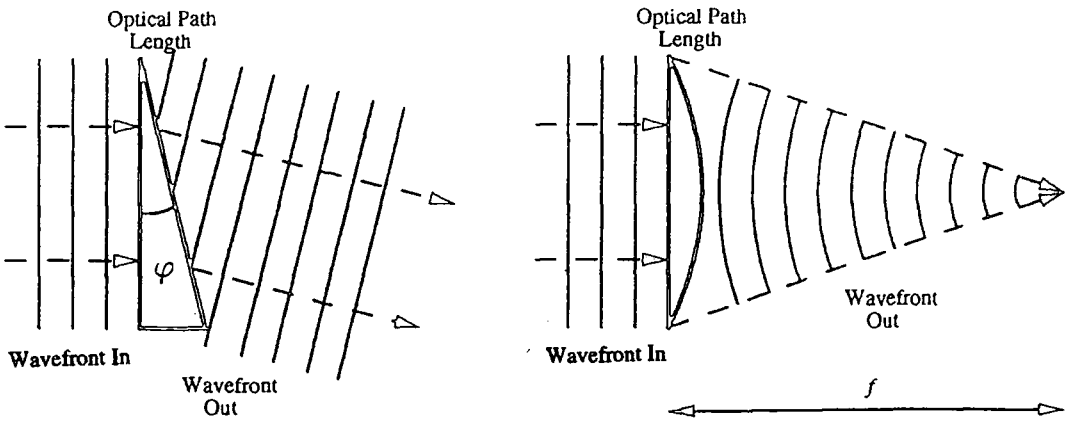

Figure 5.1: Refractive Prism and Lens

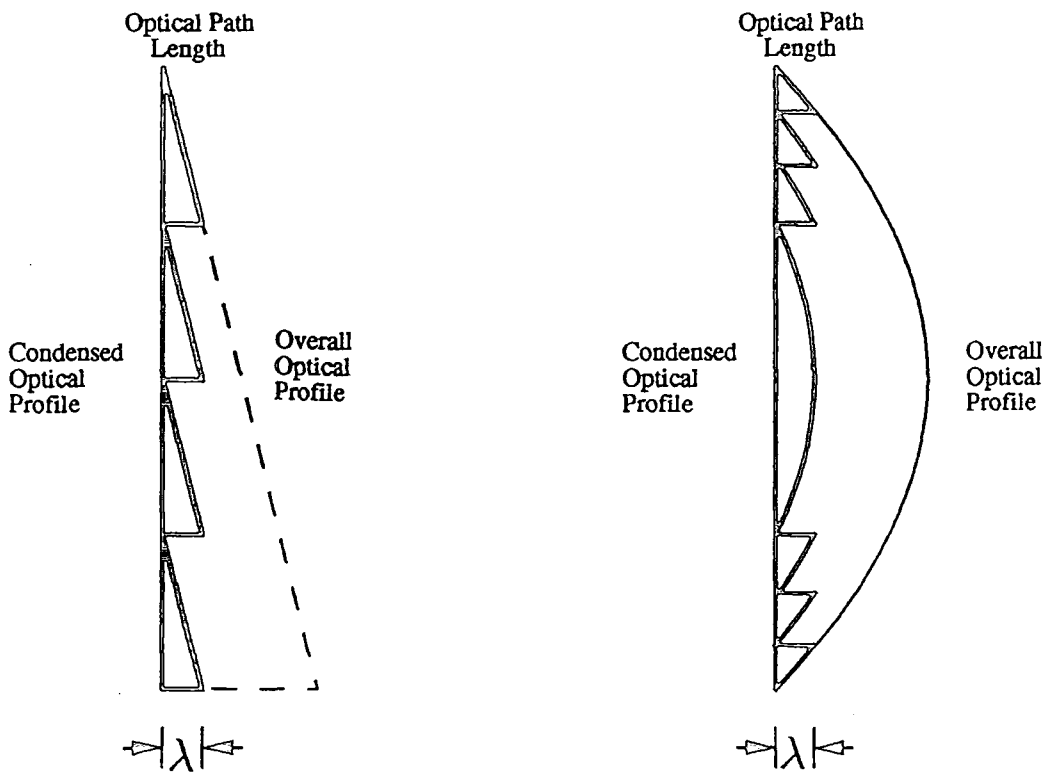

Figure 5.2: Condensed Prism and Lens

collapsing to a focus, f. Following Huygen [1, Chapter 10], the emerging wavefront can be constructed from the secondary expanding spherical wavelets;

$$u_s(r) = \frac{ae^{-jkr}}{r}$$

propagating through the device, where u_s is the complex amplitude, a the initial amplitude and r the distance propagated. The overall optical path traversed is not crucial in the construction of the emerging wavefront, it is the relative phase of the emerging wavelets that must be constant. Consequently, a wavefront may be constructed from light which has travelled optical path lengths with several whole-wavelengths difference in length. Exploiting this, a condensed refractive structure can be used to mimic the solid, refractive device by varying the optical path by the appropriate fractional wavelengths required to produce the appropriate wavefront. In other words, a Fresnel lens is produced as opposed to a Fresnel zone plate. In order to implement this an optical path change of one wavelength is required;

$$\Delta n\, d \approx \lambda \tag{5.1}$$

This can be achieved in relatively thin liquid crystal cells ($\sim 3\mu$m).

The resulting condensed refractive structures have a piece-wise continuous form, split into zones which represent surfaces where the optical path length changes by a whole-wavelength. The optical path is continuous within these zones and discontinuous at the zone boundaries. The optical path length profile in the n-th zone of a condensed prism is given by;

$$\varrho(x) = x \tan\varphi - n\lambda \tag{5.2}$$

where n is such that $\varrho(x) \leq \lambda$, x is the position in the prism and φ is the optical prism pitch (figure 5.2a). For a lens of focal length f the optical path depth of the n-th zone is given by;

$$\varrho(R) = \sqrt{f^2 + R^2} - f - n\lambda \tag{5.3}$$

where R is the radial position in the lens (figure 5.2b).

The efficiency of diffractive devices can be improved by blazing, that is the shaping of each zone so that the incident light is deflected into a single diffraction order, theoretically the efficiency of such devices can approach 100%.

The condensed refractive structures are identical in form to blazed diffractive structures. In the case of the condensed prism, the form of a blazed diffraction grating is taken, whose blazing angle is set to deflect all the incident light into the first diffraction order. This can be seen by considering the one-dimensional Fraunhofer diffraction integral, for a repeated structure of N zones, period length l;

$$u(\vartheta) = \sum_{n=0}^{N-1} \int_{nl}^{(n+1)l} u_0(x) \exp(-jkx \sin\vartheta) dx \tag{5.4}$$

where $u(\vartheta)$ is the complex amplitude in the far field image plane, at deflection angle, ϑ, and $u_0(x)$ is the complex amplitude at position x in the diffraction screen, for a general blazed diffraction structure;

$$\begin{aligned} u_0(x) &= \exp(jk\varrho(x)) \\ \varrho(x) &= (x - nl)\tan\varphi \end{aligned} \tag{5.5}$$

which produces the intensity distribution;

$$I = \left(\frac{\sin(kl(\sin\vartheta - \tan\varphi)/2)}{k(\sin\vartheta - \tan\varphi)/2}\right)^2 \left(\frac{\sin((Nkl\sin\vartheta)/2)}{\sin((kl\sin\vartheta)/2)}\right)^2 \tag{5.6}$$

The first term is a $sinc^2$ function, which has a central maxima at;

$$\sin\vartheta = \tan\varphi \tag{5.7}$$

($\vartheta \approx \varphi$ for small angles), and a series of minima at;

$$l(\sin\vartheta - \tan\varphi) = n\lambda \tag{5.8}$$

where n is an integer. The second term is a *comb* function which has a series of maxima at;

$$l\sin\vartheta = n\lambda \tag{5.9}$$

Consequently when;

$$l\tan\varphi = \lambda \tag{5.10}$$

the minima of the $sinc^2$ function coincide and hence cancel out the maxima of the *comb* function, with the exception of the central maxima, producing a single deflection angle.

In the case of the condensed lens, a blazed Fresnel lens is formed, with whole-wavelength zones instead of the half-wavelength zones of the binary zone-plate.

The blazing is such that all the incident light is deflected into the primary focus, producing a theoretically efficiency approaching 100% compared to the Fresnel lens which is approximately 40% efficient. This can be seen by considering the axial symmetric Fresnel integral, over the whole lens;

$$u(z) = 2\pi a \sum_{n=0}^{N-1} o_n(\vartheta) \int_{r_n}^{r_{n+1}} u_0(r) \exp(-jkr) dr \tag{5.11}$$

where r is the distance from a position in the lens, to a point of distance z along the optical axis and o_n is the obliquity factor. The complex amplitude of the blazed zone-plate is given by;

$$u_0(r) = \exp(jk\varrho(r))$$

By making a series of approximations, which are valid for relatively low refractive power lens, and positions of z, compatible with the focal lengths of the low refractive power lens assumption, the Fresnel integral can be expressed in a form analogous to the blazed diffraction grating, Fraunhofer integral, equation (5.4):

- The radial position of the zones for a whole-wavelength zone-plate can be approximated by;

$$R_n \approx \sqrt{2n\lambda f} \tag{5.12}$$

- The zone boundaries can be expressed in terms of the path length;

$$r_n \approx z + \frac{n\lambda f}{z} \tag{5.13}$$

- The optical path surface of the zone-plate, equation (5.3), can be approximated as a linear function of the optical path length, r;

$$\varrho(r) \approx \left(r - z - \frac{n\lambda f}{z}\right) \frac{\upsilon z}{\lambda f} \tag{5.14}$$

  where υ is a generalizing scaling factor, hence a spherical lens approximation is used within each zone,

- The effect of the obliquity factor can be ignored.

The relative errors associated with these approximations are given by;

$$\epsilon \sim \left(\frac{R}{2f}\right)^2 \tag{5.15}$$

$$\epsilon \sim \left(\frac{R}{2z}\right)^2 \tag{5.16}$$

The resulting intensity distribution is of the same form as the intensity of blazed diffraction grating, equation (5.6);

$$I = \left(2\pi a \frac{f}{z}\right)^2 \left(\frac{\sin(k\lambda(f/z - \upsilon/\lambda)/2)}{k(f/z - \upsilon/\lambda)/2}\right)^2 \left(\frac{\sin((Nk\lambda f/z)/2)}{\sin((k\lambda f/z)/2)}\right)^2 \tag{5.17}$$

producing a single focus at $z = f$ when $\upsilon = \lambda$.

As can be seen, the condensing of thick refractive structures, to increase the effective refractive power and the blazing of diffractive structures, to improve efficiency by deflecting the incident light into only one diffraction order, lead to the same diffractive/refractive structures.

A similar treatment of the Fresnel lens in terms of a phase surface has recently been independently published [2].

5.3 Multiple Wavelength Optical Path Switching

If it is assumed that a dedicated electrode structure is used, the zone boundaries will be reflected in this structure, restricting the possible voltage distributions that can be applied to the device. On the surface this appears to restrict these diffractive/refractive devices to having one operating state, as the diffractive devices were, with the only advantage over passive devices being that they can be switched on and off. Fortunately, there is a little more flexibility built into these structures.

Consider a refractive structure which is similar in form to these previously considered (figure 5.3), scaled to i times the thickness, where i is an integer. A condensed structure can be formed with the same zone boundaries, but with the optical path of each zone scaled by i and $i\lambda$ path length change at the boundaries. This can be seen as increasing the blazing depth to deflect light into the higher diffraction orders of the *comb* functions of equations (5.6 & 5.17). In the case of a condensed prism, several possible prism pitches can be attained;

$$\varphi = \arctan\left(\frac{i\lambda}{l}\right) \tag{5.18}$$

where l is the length of the blazed prism element, or period length, and i is the integer scaling factor. In the case of a condensed lens, several foci can be selected between, of focal length f/i. The limit to the possible variations on the device

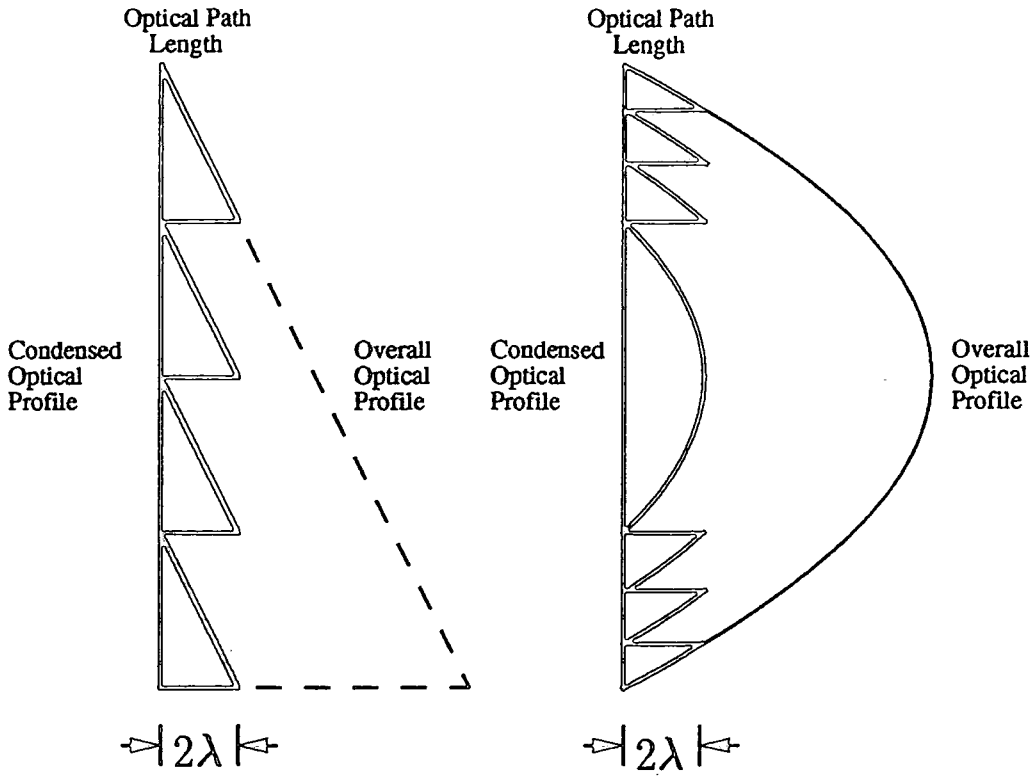

Figure 5.3: Scaled Prism and Lens

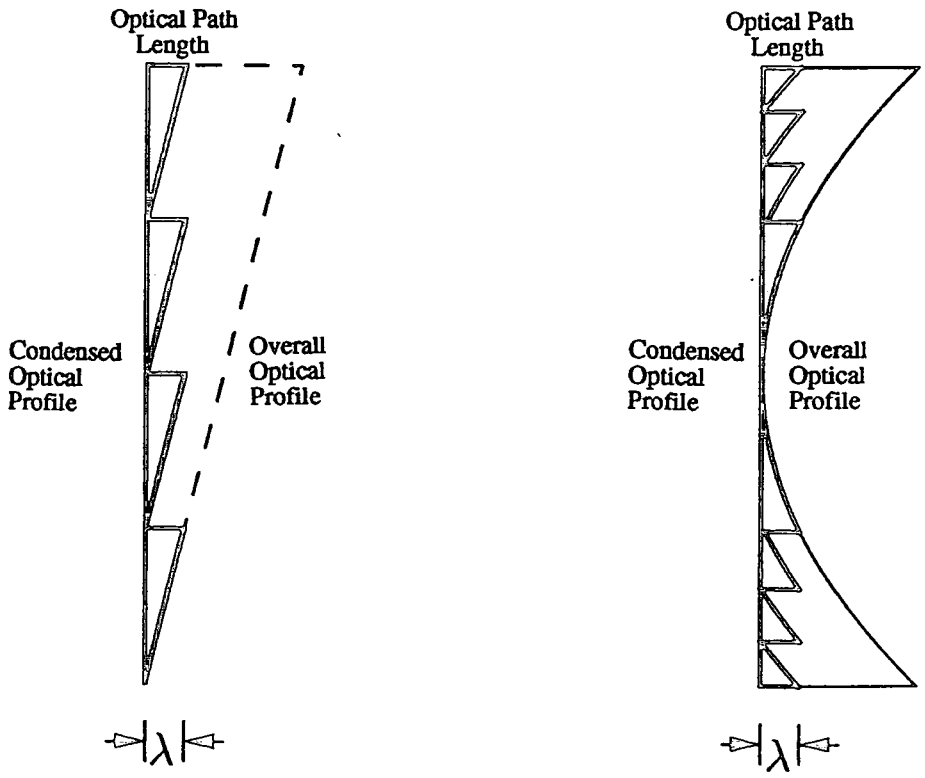

Figure 5.4: Negative Prism and Lens

is given by the number of wavelengths change which can be obtained across the devices;

$$m \sim \frac{\Delta n\, d}{\lambda} \tag{5.19}$$

where m is an integer, a 20μm cell of E44 can obtain $\sim$10 wavelengths.

By reversing the direction of the phase surface (figure 5.4), negative diffraction orders can be selected. Hence, the pitch of the prism can be reversed, deflecting light in the opposite direction, or the negative foci of the lens can be used.

5.4 Continuous Optical Path Modulation

The condensing of optical path surfaces to produce higher refractive power devices has been shown to produce optical components which can be switched between a limited number of discrete states. While this is an improvement on binary, diffractive devices, which could only operate at one state and off, the refractive devices could operate at a continuous set of states. The refractive prism could be varied through all the angles of deflection, from no deflection to its maximum angle of deflection, equation (4.9). The adaptive lens could take any focal length down to its minimum, equation (4.10). The question arises: is it possible to re-endow these diffractive/refractive devices with the same flexibility as the refractive devices?

Consider a diffractive/refractive structure that has been activated to a state lying between two integer or modular wavelength states (figure 5.5). Each individual blazed element is of the correct form for deflection into an intermediate deflection angle or focus. Unfortunately, the resulting phase surface is no longer continuous, discontinuities occur at the zone boundaries. As a consequence, the zones are not in phase with each other in order to constructively interfere at the intermediate deflection angle or focus. The diffraction structures, caused by the zone boundaries, diffract the incident light into the diffraction orders, the majority into the nearest diffraction order. This can be seen in equations (5.6 & 5.17) as the shifted $sinc^2$ minima no longer coincide with the stationary *comb* function diffraction orders, consequently they are not cancelled out.

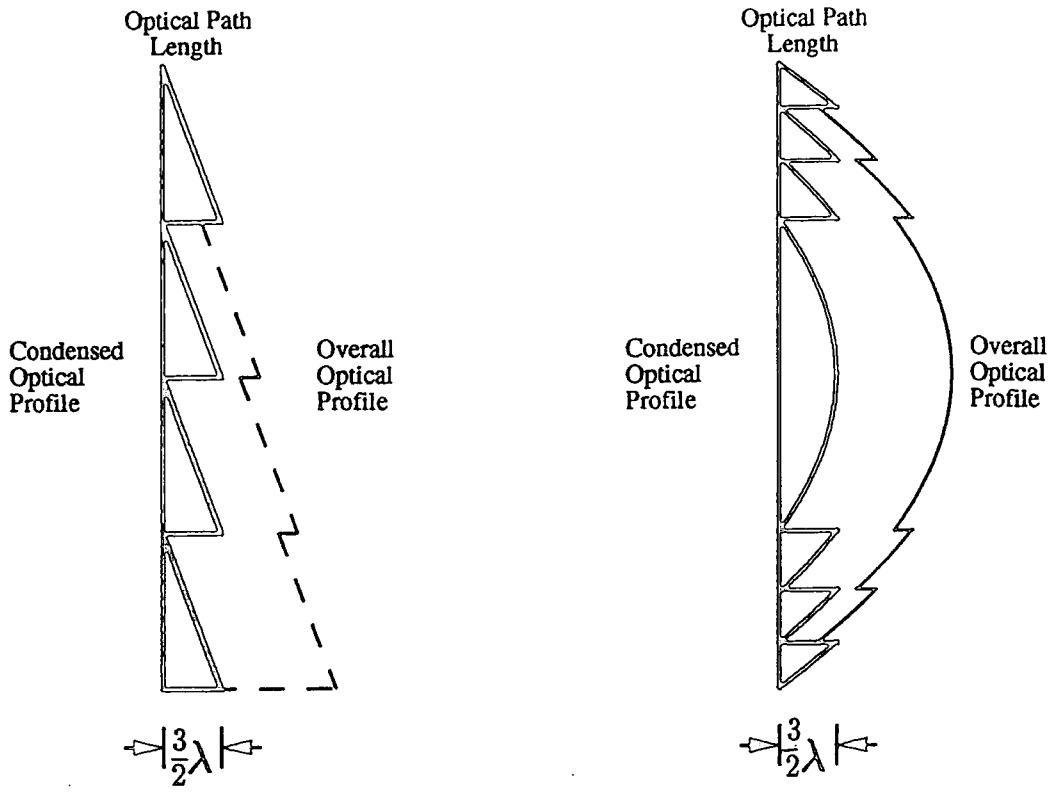

Figure 5.5: Partially Scaled Prism and Lens

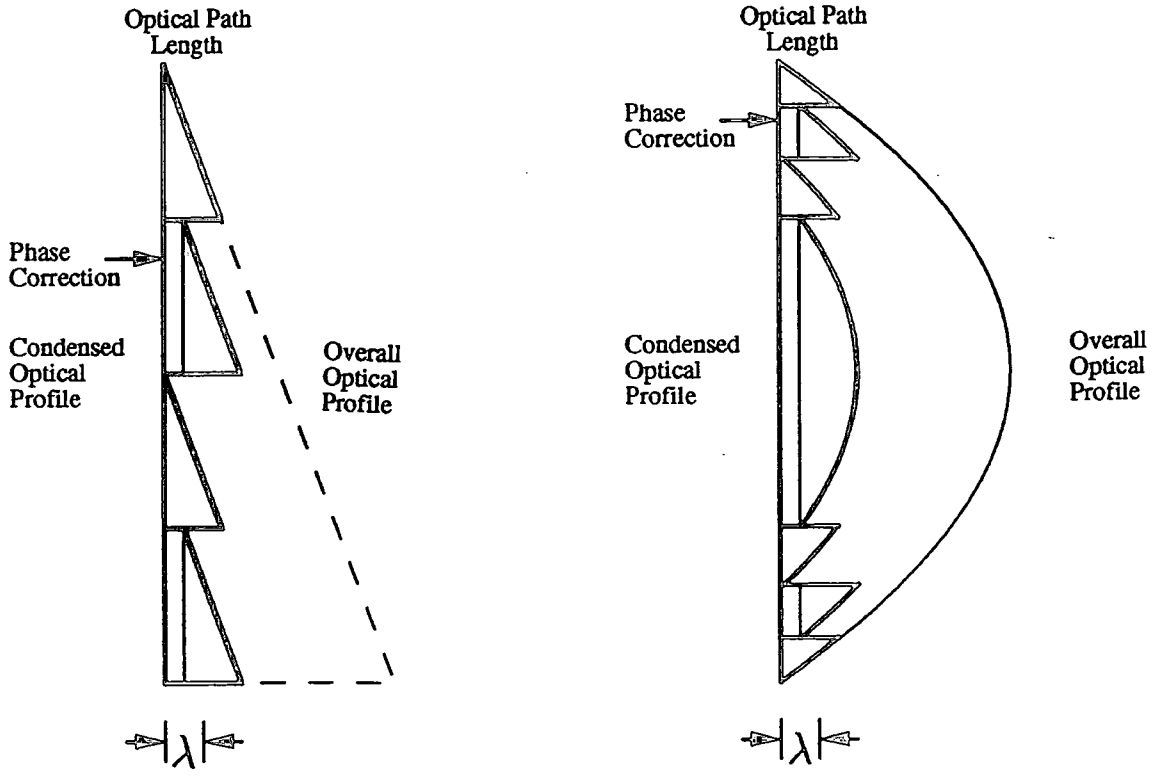

Figure 5.6: Phase Corrected Prism and Lens

In order to avoid this disruptive diffraction about the zone boundaries and allow for the constructive interference of the blazed zones into the intermediate deflection angle or focus, a phase correction is required for each zone (figure 5.6). This phase correction is made in such a way as to ensure that the optical path change between consecutive zones is a whole number of wavelengths, consequently a continuous phase surface is constructed, making the zone boundaries 'transparent' to the incident light. In this manner a continuous range of phase surfaces can be produced, providing a continuous range of prism pitches or focal lengths.

In the case of the phase corrected, condensed prism, the optical path structure becomes (figure 5.6a);

$$\varrho(x) = x\tan\varphi - i\lambda \tag{5.20}$$

where i is an arbitrary integer, the complex amplitude becomes;

$$u_0(x) = \exp(jk(x\tan\varphi - i\lambda)) = \exp(jkx\tan\varphi) \tag{5.21}$$

hence the intensity distribution is given by;

$$I = \left(\frac{\sin(kl(\sin\vartheta - \tan\varphi)/2)}{k(\sin\vartheta - \tan\varphi)/2}\right)^2 \left(\frac{\sin(Nkl(\sin\vartheta - \tan\varphi)/2)}{\sin(kl(\sin\vartheta - \tan\varphi)/2)}\right)^2 \tag{5.22}$$

in which the *comb* function diffraction orders move with the $sinc^2$ function, and only a single deflection angles produced;

$$\sin\vartheta = \tan\varphi$$

where φ is continuously variable.

Similarly, the condensed lens with phase correction has an optical path given by (figure 5.6b);

$$\varrho(r) = (r - z)\frac{\upsilon z}{\lambda f} - i\lambda \tag{5.23}$$

the complex amplitude becomes;

$$u_0 = \exp\left(jk\left((r - z)\frac{\upsilon z}{\lambda f} - i\lambda\right)\right) = \exp\left(jk(r - z)\frac{\upsilon z}{\lambda f}\right) \tag{5.24}$$

and the intensity distribution is given by;

$$I = \left(2\pi a\frac{f}{z}\right)^2 \left(\frac{\sin(k\lambda(f/z - \upsilon/\lambda)/2)}{k(f/z - \upsilon/\lambda)/2}\right)^2 \left(\frac{\sin(Nk\lambda(f/z - \upsilon/\lambda)/2)}{\sin(k\lambda(f/z - \upsilon/\lambda)/2)}\right)^2 \tag{5.25}$$

again the diffraction orders of the *comb* function move with the $sinc^2$ function and a single focus is produced at;

$$z = \frac{f\lambda}{\upsilon} \tag{5.26}$$

where υ is continuously variable.

In order to facilitate this phase correction, a clearance of one wavelength is required, this reduces the maximum optical path depth a diffractive/refractive device can obtain in this continuous manner by one wavelength. The full refractive power state can still be obtained as a discrete state, if desired. The addressing for such devices is complicated, as the voltages for each zone must be individually determined and addressed.

The ideas in this section have been considered exclusively in terms of a prism or a lens. They can be extended to any general refractive object, or any piece-wise continuous phase surface arrived at through either Fraunhofer or Fresnel diffraction considerations. They have also been included in a British Patent [3].

5.5 Chromatic Aberration

It has been shown that the diffractive devices exhibit a high degree of chromatic aberration; the deflection angle of the diffraction orders being proportional to the illuminating wavelength (equation (4.2)), and the focal length being inversely proportional (equation (4.6)). The variation of the wavelength across the visible spectrum was found to be ~30% (equation (4.1)). Refractive devices suffer from chromatic aberration, due to the dispersive properties of the liquid crystal, again causing the deflection angle and focal length to shift with wavelength (~30% for E44 across the visible spectrum (equation (4.8))).

In the case of diffractive/refractive devices, the zone structure will cause diffraction of the illuminating light. This diffraction structure will have the same wavelength dependence as the diffractive devices, hence the same chromatic aberration. The refractive, blazing elements will also disperse with wavelength, but in the opposite direction to the dispersion caused by diffraction, exaggerating the phase discontinuities at the zone boundaries, promoting diffraction into all orders.

Unless these sources of chromatic aberration are compensated for, the operation of these devices is limited to monochromatic applications.

5.6 Cascading Devices

A cascaded device constructed of diffractive/refractive devices would overcome the problems of cascading binary Fresnel lenses (section 4.7). The single state devices could be combined to produce the desired 2^3 focal lengths, without the large loss in intensity and the production of extra foci. The multiple state devices would provide an even greater range of foci, as the different orders of focus are selected on each lens. Combinations of the continuously variable devices could produce some very flexible composite devices. For example, two prisms could produce two-dimensional beam translation, which could in turn be combined with a variable focus lens, providing three degrees of freedom for the position of the focus.

5.7 Summary

In Chapter 4 diffractive devices were found to be inefficient, scattering light into several diffraction orders and limited in the voltage controllability to switching the devices on and off. The refractive devices were limited by the maximum optical path the device could achieve, $\Delta n\, d$. The voltage controllability of refractive devices is very flexible, allowing for the continuous variation of prism pitch or focal length and the very high efficiency.

By combining these two approaches the high efficiency and voltage control flexibility of refractive devices can be combined with the higher optical power of diffractive devices. The refractive power can be improved by including only the fractional wavelength changes in optical path required to produce the desired emerging wavefront, allowing a thin liquid crystal film to mimic the effect of an optically thick, solid, refractive device. The efficiency of the diffractive devices can be improved by blazing the structure to deflect all the incident light into one diffraction order. These two approaches can be seen to produce identical diffractive/refractive structures, with high efficiency and high refractive power.

By scaling the optical path structures by an integer, a series of discrete prism pitches or focal lengths can be obtained from the same structure. This was shown to be equivalent to increasing the height of the blazing to select higher diffraction orders. By reversing the direction of the blazing, negative versions of the devices could be produced.

It was shown that continuously variable versions of the devices can be obtained by including an optical path variation to each region of the device to provide a phase correction. The cascading of these devices could provide very flexible composite devices.

Diffractive/refractive devices suffer chromatic aberration from both its diffractive and refractive properties, consequently these liquid crystal devices are restricted to monochromatic applications.

5.8 References

[1] R. S. Longhurst. *Geometrical and Physical Optics.* 3rd edition, Longman (1973).

[2] P. F. Brinkley and S. T. Kowel. 'Liquid Crystal Adaptive Lens: Operation and Aberration' *SPIE Proc.* 1773 (1992) 449-457.

[3] M. G. Clark, M. C. K. Wiltshire, A. Purvis and N. J. Powell. 'Tapered - Electrode LC Prism.', *British Patent* No. 9 305 143.1 (1992).

Chapter 6

Addressing Diffractive/Refractive Devices

6.1 Introduction

In Chapter 5 the required optical path surfaces for the implementation of diffractive/refractive devices have been discussed without any consideration given to how the voltage distributions are applied to obtain these surfaces. This chapter will summarize the ideas developed during the research project concerning the voltage addressing employed to obtain the required optical structures.

The voltages are applied through the etched ITO electrodes, the minimum feature size that these electrodes can be produced to is found to be limited. In the devices discussed in Chapter 4 three addressing techniques have been described, these will be summarized. The optical path surfaces required in the diffractive/refractive devices are piece-wise continuous, in addition some of the required structures are two-dimensional in form, the problems associated with obtaining such optical surfaces will be discussed in turn. The possible use of pixelated devices and reflective, double passage devices will be mentioned and a comment made about the application of switching speed enhancing techniques to these devices.

6.2 Electrode Resolution

The electrode structure is etched into the ITO layer using a wet etching technique (section 4.2). This technique is limited in the resolution of the electrode structure that can be reliably etched to the scale of $\sim 2\frac{1}{2}\mu$m. Marginal improvements on this

technique may be made by the successive refinement of each stage, but the limit of this technique is close to being reached, and sub-micron etching is seen to be well beyond this limit [1]. Moving to plasma etching is made difficult by the nature of the chemicals needed to etch ITO [2].

This is an important design limitation to the resolution of the electrodes and gaps that can be implemented. There are other, more dominant factors when the resolution of the liquid crystal phase surface is considered, these will be discussed in Chapter 7.

6.3 Existing Addressing

Monolithic electrodes are the simplest form of electrode, requiring no etching. They have been used in the implementation of low refractive prisms [3]. This structure is limited to linear voltages drops. The complete phase response of the liquid crystal to applied voltage is non-linear (figure 4.7), consequently the phase surface produced by a monolithic electrode will reflect this non-linearity, unless operation is restricted to the approximately linear region. There is also the potential problem of the liquid crystal being heated by the heat dissipated from the conducting electrode. These problems become more pronounced the narrower the electrode size.

A two-dimensional, binary diffractive structure [4] can be implemented using a single etched electrode, with a connecting areas bridging the gaps in the structure, ensuring the applied voltage is carried to all regions of the electrode. Such an electrode structure is limited to applying one voltage to the whole device, and having a single fixed diffraction structure.

A one-dimensional, phase surface can be implemented using a series of strip electrodes, each with an independent applied voltage. The application of an independent voltage to each electrode can become problematic as the size of the electrodes is reduced and the number increased. For example, a 5mm device, with wet etching limited electrodes, requires 1000 individual applied voltages. This addressing approach has been used to implement adaptive lenses [5, 6, 7].

6.4 Piece-Wise Continuous Optical Path Structures

In order to achieve the piece-wise continuous optical path required to implement the diffraction/refractive devices, a piece-wise continuous voltage distribution needs to be applied which is continuous within each zone and discontinuous at the zone boundaries. Four possible electrode structures will now be considered.

6.4.1 Strip Electrode Elements

Strip electrodes could potentially be used to providing a sampling of the required phase surface. In order to obtain a good approximation of the required phase surface, the size of the electrodes and the inter-electrode gaps need to be very small, approaching the wet etching limit. This is because the detail and spatial variation in the optical path of the diffractive/refractive structures is much greater than the smoothly varying, continuous refractive structures.

The electrodes can be placed as close together as manufacturing, connectivity and cost considerations will allow, providing a straightforward one-dimensional spatial sampling of any condensed refractive structure. This device would be extremely flexible as no regard is made to the zone-boundaries, so a variety of diffractive/refractive device profiles may be applied. The resolution and fidelity of the phase surface produced is limited by the size of one electrode and gap ($\sim 5\mu$m). This may be improved by the use of buried electrodes (section 6.5.1).

The use of strip electrodes represents the upper limit to the addressing flexibility and resolution that can be achieved with discrete electrodes. However, the intensive demands on the generation and connectivity of the applied voltages may make reaching this limit impractical.

6.4.2 Monolithic Elements

A continuous, current carrying electrode can be employed to provide the continuous voltage distribution for each zone. By their very nature, the zones are expected to be very narrow, with respect to the direction of optical path change, hence voltage

Figure 6.1: Voltage Distribution on a Monolithic Element

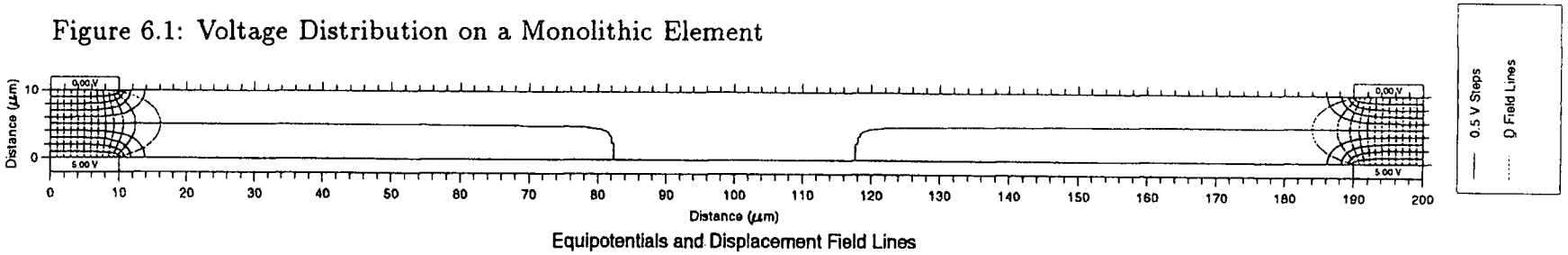

Figure 6.2: Two Resistance Conducting Electrode

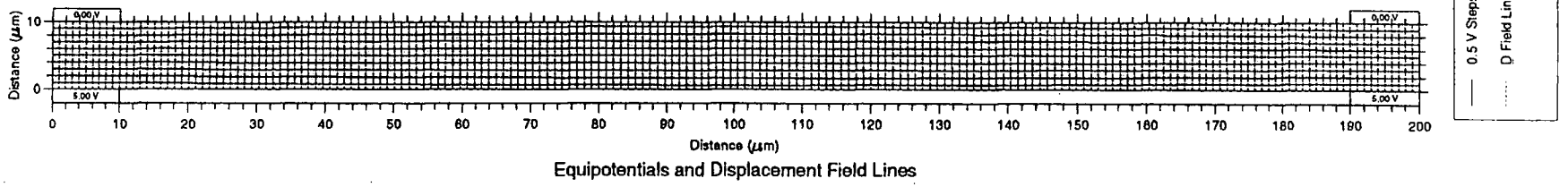

It is important to note that the figures 6.1 & 6.2 represent the potential distribution in the plane of the electrode. All other figures of this type, presented in this thesis, represent the potential distribution in a plane perpendicular to the electrodes.

change, and also very long, carrying the same voltage profile along the whole length of the device or the whole circumference of a circular symmetric device. This leads to two very serious problems in the use of continuous current carrying electrode elements.

Firstly, the voltage profile is required to be uniform throughout the whole length of the zone, applying the appropriate voltages at the corners of a long electrode will not produce this. The majority of the current will flow at the edges of the electrode, leaving the voltages in the middle of the electrode to flatten out to the mid voltage value (figure 6.1). To maintain the same voltage profile along the zone, the applied voltage to either side of the zone must be constant along the full length of the zone. This could be achieved using two values of resistance in the electrode; low resistance electrodes carrying the applied voltages to either side of the high resistance electrode, across which the current is conducted and the voltage dropped (figure 6.2). The fabrication of electrodes with such different resistances may be difficult while ensuring that the low resistance electrodes are relatively transparent and the high resistance electrodes are conductive enough to behave as conductors.

Secondly, the resistance of the electrodes is given by;

$$\mathcal{R} = \frac{\sigma l}{L} \tag{6.1}$$

where σ is the sheet resistance of the electrode layer, l is the length of the zone across which the voltage is dropped, and L is the length of the zone along which the voltage profile is maintained. Due to the geometry of the zones this resistance will be very low. Consequently, there is a grave problem of heat dissipation, from conduction across the electrode, potentially overheating the cell. In order to reduce this heating the sheet resistance must be extremely high, again this may push the resistance into a region where it no longer behaves as a conductor.

In addition, the optical path response of the liquid crystal to the applied voltage (figure 4.7) is non-linear, which will be reflected in the optical path profile produced by these electrode structures. The narrowness of the zones will emphasise this non-linearity. In general, the optical path profile of each zone is set by the voltage response of the liquid crystal, the only control that can be made over this is in the selection of which part of the curve is being used. For example if low voltages are used the steeper part of the curve may be used exploiting the approximately

linear form of the curve in this region. Unfortunately the refractive index response to voltage is concave, which is inappropriate for the approximation of the convex profiles required for the implementation of a positive lens (figure 5.2b).

The use of continuous, conductive plates between electrodes has recently been proposed for refractive devices [8], to provide a linear interpolation voltage in the inter-electrode gaps. As the voltages of adjacent electrodes are expected to be similar in refractive devices, the power loss and subsequent heating is expected to be less of a problem.

6.4.3 Electro-Static Elements

Both problems encountered using a monolithic element could be avoided by the removal of the conducting electrode altogether, leaving the voltage to drop electrostatically between the two voltage supply electrodes. The resulting optical path profile is far from straightforward to obtain, but two general observations may be made. The voltage drop will be greater at the edge of the electrode with the higher voltage, which will act to counter the curvature of the voltage response, possibly providing the required convex curved profiles to approximate the positive lens's blazed elements. If the voltage on both the supply electrodes are greater than that on the earth-plate, as will be required in a phase corrected element (section 5.4), there will be a drop in the potential between these two electrodes, generating a hump in the optical path profile (figure 6.3), which would be inappropriate for the required optical path profiles. Again very little control can be exerted over the resulting profiles. One method which could be employed to shape the profile is the insertion of electrodes of intermediate voltage. This approach would be similar to the strip electrode implementation, mentioned above.

6.4.4 Combed Current Carrying Elements

The problem of obtaining the required optical path profile for a blazed element of a diffractive/refractive device can be decomposed into two related problems. The first is obtaining the appropriate voltage distribution to produce the required optical path profile. The second is to transport this voltage distribution faithfully along the

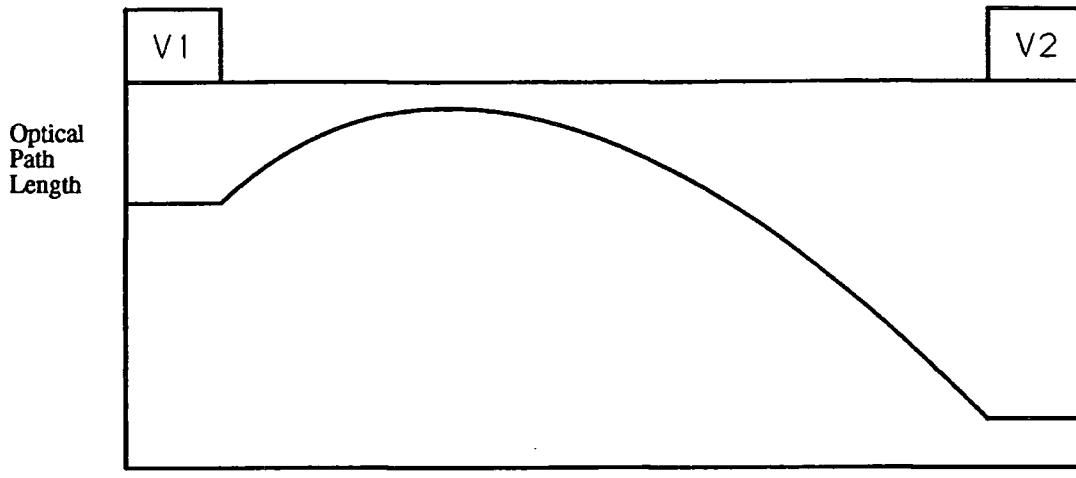

Figure 6.3: Hump in an Electro-Static Electrode Element

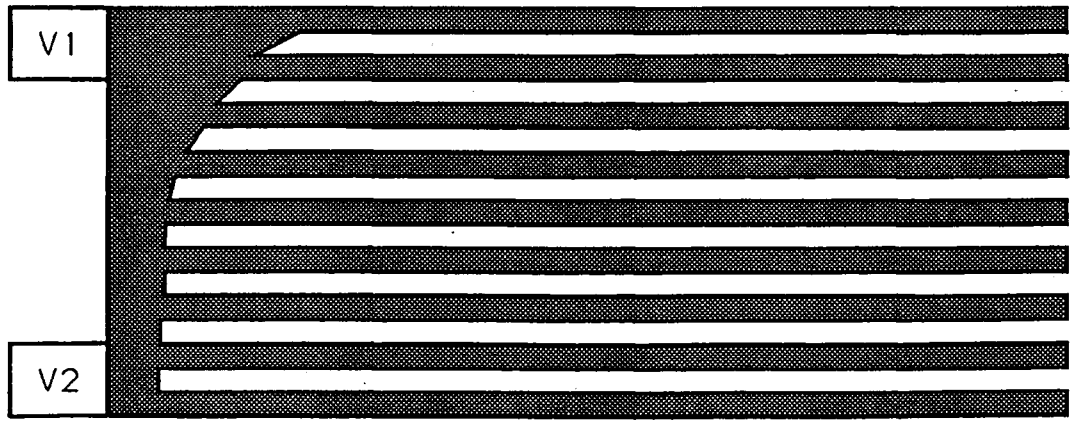

Figure 6.4: Combed, Charge Carrying Electrode

whole length of the zone.

Dealing with the second part first, the most reliable method of transporting the required voltage distribution is through a series of discrete electrodes in the same manner as the strip electrode structure. The use of a continuous conducting zone element runs into three problems;

- maintaining the voltage throughout the full length of the zone,
- the low resistance due to the geometry of the element causing heating of the cell,
- the voltage profile being determined by the uniform resistance of the conducting element.

The voltage profiles, in the cases of the monolithic and electro-static elements, were set by the behaviour of the systems involved, there being no scope for designing in the required profiles. In the case of the strip electrodes, the voltage profile is determined off the device, providing more flexibility but requiring more intensive addressing and connectivity to the device.

By splitting the electrode into two parts, each part of the voltage profile problem can be addressed separately. A narrow conducting strip can be constructed, across which the supply voltages to either side of the blazed element are conducted. The voltage distribution across the strip can be designed into the conductor by varying its width and hence the variation in resistance across the strip. Strip electrodes then take their supply from points along the conducting strip and transport a sampling of the resulting profile along the full length of the zone (figure 6.4). Consequently, the required optical path profile can be achieved by the application of just two voltages across each zone. This greatly reduces the connectivity problem found in the strip electrode approach. The geometry of the conducting strip has a great advantage over the monolithic conducting elements, taking the form of a thin taper whose narrow end can be as small as conveniently etched, hence providing a much greater resistance, reducing any potential of heating problems. The minimum track width must large enough to take the expected current density without burning out like a fuse [9].

The geometry of the conductive strip can be designed to produce the appropriate voltage profiles in order to obtain the required optical profiles. Applying Ohm's Law to a small drop in voltage δV across a sliver of the conductive strip of width $w(x)$ and length δx the relationship between the voltage distribution and the electrodes' geometry can be found;

$$dV = \frac{\Delta V \sigma}{\mathcal{R}_T w(x)} dx \tag{6.2}$$

where σ is the sheet resistance of the electrode, ΔV the potential drop across the conducting strip, and $\mathcal{R}_T$ the total resistance of the strip. Since the electrode geometry is fixed then the resulting, normalized voltage profile $V_0(x)$ is also fixed, though it may be scaled by adjusting the potential drop across the strip or arbitrarily shifted relative to earth by a relative voltage V_C;

$$V(x) = \Delta V . V_0(x) + V_C \tag{6.3}$$

The liquid crystal optical path length response to voltage (figure 4.7) can be approximated by;

$$\varrho(V) \approx \begin{cases} \varrho_{off} & 0 \leq V < V_{th} \\ -\varrho_{grad} V + \varrho_{int} & V_{th} \leq V < V_l \\ \frac{C}{V-B} & V_l \leq V \end{cases} \tag{6.4}$$

which is split into three regions; an off-state, an approximately linear region, and a reciprocal response region.

The optical profiles that are required to produce the continuously variable diffractive/refractive devices are of the form;

$$\varrho(x) = \Delta\varrho . \varrho_0(x) + \varrho_C \tag{6.5}$$

consisting of a designed, normalized optical profile $\varrho_0(x)$ which can be arbitrarily scaled by a factor $\Delta\varrho$ and displaced by an independent phase correction ϱ_C.

Initially, the design of the conducting strip for operation in the reciprocal response region was considered. It was found, however, that the required arbitrary scaling and phase correction of the optical profile could not be achieved in this region. There was no direct relationship between the variation in optical profiles that could be produced in this region and the required optical profiles.

Subsequently, the approximately linear region was found to produce the required optical profiles. Using the relationship between the voltage and electrode geometry,

equation (6.2), the required form of the conducting strip for a general optical profile can be found;

$$w(x) = -\frac{\Delta V_0 \sigma \varrho_{grad}}{\mathcal{R}_T p_0'(x)} \tag{6.6}$$

where p_0' is the first spatial derivative of the required, normalized optical profile $\varrho_0(x)$ which is produced by a potential drop of ΔV_0. The optical profiles of a condensed prism, equation (5.5), or a condensed lens, equation (5.3), can be implemented in this way. The resulting optical profile can be expressed in terms of the designed profile;

$$\varrho(x) \approx \frac{\Delta V}{\Delta V_0}\varrho_0(x) - \varrho_{grad} V_C + \varrho_{int} \tag{6.7}$$

with the required scalability provided by ΔV and independent phase correction provided by V_C, both emerging naturally from the linear relationship. The optical path shift can be obtained by either: the independent adjustment of the supply voltages to each zone, or application of the same voltages across the electrodes of all the zones with an independent earth voltage supplied to each zone, whichever is most convenient. The performance of devices designed in this way depend on the strength of the linear approximation of the optical path response.

The electrode structure and design considerations described in this section have been made the subject of a British Patent [10]

6.5 Two-Dimensional Structures

The addressing methods above are applicable to obtaining one-dimensional optical path profiles, as the appropriate voltages can be connected via one of the edges of the electrode structure. Some of the devices that may be implemented require a two-dimensional optical path structure, for example a spherical lens, here the required electrode structure is circularly symmetric. This creates a problem applying voltages to the annular electrodes, which are closed from contact from the outer edges of the device by the outer electrodes. In the case of a binary, diffractive Fresnel zone-plate lens, only one voltage is applied to a series of concentric ring electrodes. This is achieved by leaving a line running through one of the diameters of the zone structure which is left unetched (figure 6.5), providing an electrical contact to all the zones. More than one voltage cannot be applied through this electrode structure.

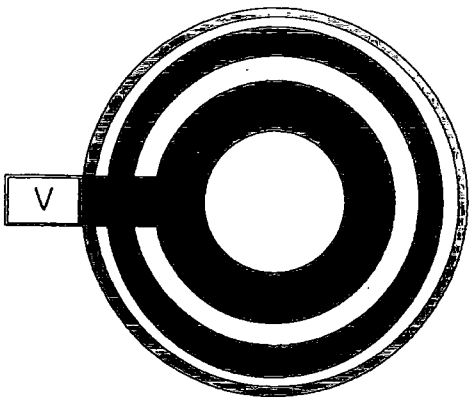

Figure 6.5: Binary Zone-Plate Electrode Structure

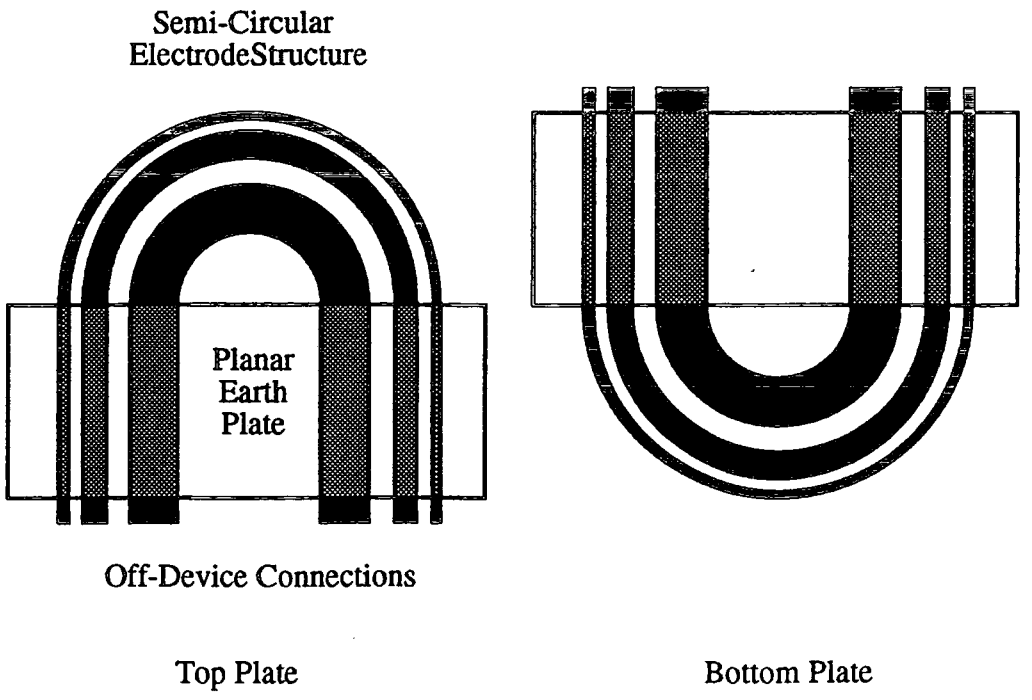

Figure 6.6: Full Lens Electrode Structure Using Earth Masking

6.5.1 Buried Electrodes and Inter-Electrode Gaps

It is possible to bury an ITO electrode [1]. An electrode structure could be wet etched, then a resistive layer deposited and an ITO layer deposited and etched, this could be repeated, building up layers of electrodes.

An incidental application to this burying of electrodes is to address the problem of inter-electrode gaps. Concern has been expressed about the presence of the gaps between the electrodes, in which the required optical profile may not be maintained, such problems arise in refractive devices and diffractive/refractive devices which use strip electrode structures to carry the applied voltages. The operation of these devices rely on the liquid crystal gap taking the optical path of the surrounding electrodes. The opposite problem occurs with binary diffractive devices, where the inter-electrode gaps are expected to take the off-state. A spreading of the on-state from the surrounding electrodes into the gap would prove detrimental to the devices performance. Both these problems are discussed in more detail in Chapter 7. A possible solution to these problems could be achieved by the burying of an electrode structure which fills in all the inter-electrode gaps, the required voltages can be supplied to the gaps via these buried electrodes, leaving no region of the device unaddressed. This will have the additional effect of ensuring that any amplitude loss, due to the transmission of light through the ITO, will be constant throughout the device.

6.5.2 Earth-Masking

The problem, which has not yet been addressed is that the concentric circular form of the zone structure is geometrically closed to connections from outside. One way of opening up this structure is considering half a lens, all the required connections could be made along the now exposed diameter. This far more open structure allows for each zone to take an individual set of voltages, as required for the continuously variable diffractive/refractive structures.

The advantage of this open structure can be exploited for a full lens by designing a half lens, with the connections running from the diameter, across the other half of the lens and off the device. This electrode can then be buried under a planar

electrode which covers the connections but leaves the half lens electrode structure exposed. A second electrode of the same design, rotated so that the planar electrode corresponds with the exposed half lens electrode structure, provides the opposite plate. In this way a full lens, with full connectivity can be achieved (figure 6.6), with the flexibility to implement a continuously variable diffractive/refractive device.

If current carrying electrodes are used, the conductive strips should be placed as close to the points where the voltages are supplied to avoid any voltage drop along long supply electrodes.

6.5.3 Cascading Devices

Spherical Lens

An alternative approach is to simply cascade devices, as Kowel cascaded two cylindrical lenses [6] to approximate a spherical lens. The optical path of a spherical diffractive/refractive lens, equation (5.3), is approximated by the sum of two crossed cylindrical lenses;

$$\varrho(x,y) = 2n\lambda - \sqrt{f^2+x^2} - \sqrt{f^2+y^2} + 2f^2$$

using a parametric substitution for x and y;

$$\begin{aligned} x &= R\cos\beta \\ y &= R\sin\beta \end{aligned}$$

the circular symmetry of this approximation can be tested. The greatest extremes will occur when $\beta = 0$ and $\beta = \pi/4$. It can be shown in this manner that the relative error is given by;

$$\epsilon \sim \left(\frac{R}{2f}\right)^4$$

for an $f/10$ lens $\epsilon \sim 0.4 \times 10^{-4}\%$ which is negligible. The 1-2mm separation of the lenses by the retaining glass can be corrected by shifting the respective focal lengths by $\pm$1-$\frac{1}{2}$mm to compensate.

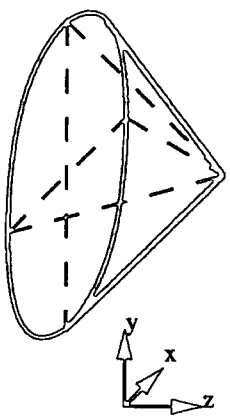

a) Lens

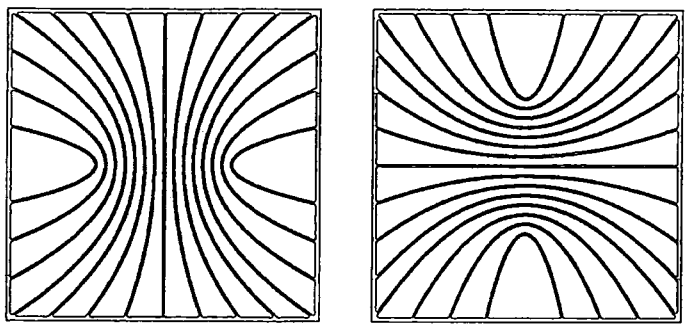

b) Zone Structure

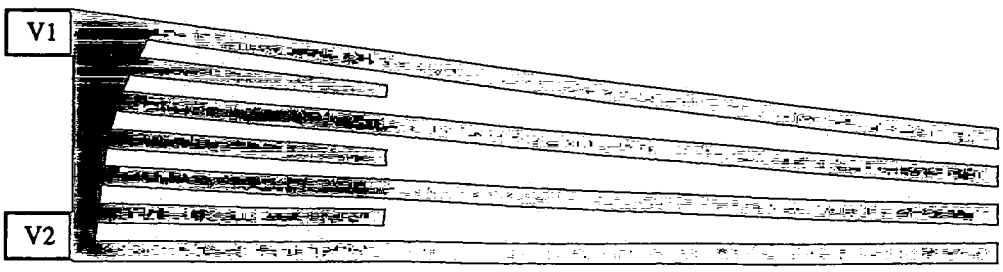

c) Electrode Strucure

Figure 6.7: Conical Lens

It appears that the spherical lens was a fortuitous example, but the same approach may be applied to other devices. Consider a conical lens, a lens whose cross-section is of two back to back prisms and is circularly symmetric (figure 6.7a), so taking the shape of a cone. Such a device is expected to produce a line of focused light along the optical axis for a finite length [11].

Cascading two orthogonally aligned cells with two back to back condensed prisms on each would not produce the required circular symmetric optical path structure;

$$\varrho(R) = AR$$

However, circular symmetric can be achieved if the two component optical profiles were of the form;

$$\begin{aligned} \varrho_1(R,\beta) &= AR\cos^2\beta \\ \varrho_2(R,\beta) &= AR\sin^2\beta \end{aligned}$$

in cylindrical coordinates, one being a $\pi/2$ rotation of the other.

Even though the resulting structures are not as straight forward as the cylindrical lens, the important feature is that the structures are open with plenty of scope of connection at the edges (figure 6.7b), unlike the circular symmetric structure of a single device implementation of a conical lens. The broader regions of the zones may be spanned by wider electrodes, or more electrodes which peter out as the zone becomes narrower (figure 6.7c). It may be possible to construct many complicated and closed structures by cascading several contributing devices, with electrode structures open to edge connections, which add together to provide the required optical structure.

6.6 Pixelated and Reflective Double Passage Devices

The resolution required to accurately reproduce the piece-wise continuous optical path surfaces will make the addressing of a device very intensive. Pixelated devices do not take advantage of the spatial coherence expected in the required optical path surfaces which has shown to be useful in reducing the required number of input

voltages to dedicated electrode structures. The cascading of a variety of dedicated devices may prove to be a more practical alternative to a general pixelated device, taking advantage of the spatial coherence. More sophisticated addressing techniques than the direct addressing so far discussed may be applied to these dedicated structures.

Some of the addressing problems and the ITO electrode resolution limit may be relieved by mounting the devices on a reflective medium, with the electrical connections mounted on or behind, for example liquid crystal devices could be laid on a chip [12], or a drilled PCB [9]. The devices would be reflective instead of transmissive, with light passing through the liquid crystal film twice, effectively doubling the optical path depth available.

6.7 Switching Speeds

Using the transient nematic effect (section 4.10.1), thick cells can be used to achieve faster switching times between phases of large multiples of π. Regarding diffractive/refractive devices, if a significant amount of optical response of the cell is being used very few regions of the cell will be in the required highly activated stated to make effective use of the effect. In order to make use of the effect thick cells would be required, and only the highest part of the voltage response curve could be exploited. The consequences of this would be;

- inefficient use of the available optical path of the cell,
- the operation in the reciprocal part of the voltage response curve with the associated problems of producing the required optical path surface (section 6.4.4),
- the increased effects of fringing fields due to the cell thickness (Chapter 7), which will have detrimental effects on the resulting optical phase structure.

An additional complication in the switching of diffractive/refractive devices is that the optical path lengths switched between will be different throughout the device, even throughout each zone. It is likely that the times required for the extremes of the zone to reach the required optical path length will be different,

and different for each zone. This will prove to be an major complication to any addressing technique employed to enhance switching speeds.

6.8 Summary

The required optical path surfaces for the implementation of diffractive/refractive devices are implemented through the application of applied voltages throughout the cell. The voltages are applied through the etched ITO electrodes, which are limited to a minimum feature size of $\sim 2\frac{1}{2}\mu$m by the wet etching technique. This provides a limit to the resolution of any electrode structure that may be used.

The optical path surfaces required for the implementation of diffractive/refractive devices are piece-wise continuous and two-dimensional structures in some cases. The piece-wise continuous zone structures could be applied through combed current carrying electrode structures, requiring only two or three independent applied voltages to each zone. To allow for the voltage scalability and independent phase correction required to produce continuous variation of the diffractive/refractive devices, it was found to be necessary to restrict the operation of these devices to the low voltage, approximate-linear region of the optical path response curve. The two-dimensional optical structures can either be achieved by the use of planar earth plates to mask the connections to the centre of the device, or by cascading devices with electrode structures open to connection at the edges whose combined effect is to produce the required two-dimensional optical structure.

The discussion presented here has presumed that the liquid crystal driven by these electrode structures of varying complication will behave as characterized by an essentially, one-dimensional electrode configuration. The possibility that this may not be the case will be dealt with in Chapter 7.

6.9 References

[1] M. C. K. Wiltshire. *Private Communication,* GEC-Marconi, Hirst Research Centre.

[2] D. Wood. *Private Communication,* Uni. of Durham.

[3] G. D. Love. *The use of liquid crystal adaptive optics devices in astronomy.* PhD Thesis, Uni. of Durham (1992).

[4] G. Williams. *Electrically Controllable Liquid Crystal Fresnel Lenses.* PhD Thesis, Uni. of Durham (1991).

[5] S. T. Kowel, D. S. Clevery and P. G. Kornreich. 'Focusing by electrical modulation of refraction in a liquid crystal cell', *Appl. Opt.,* 23, 2 (1984) 278-289.

[6] S. T. Kowel, P. G. Kornreich and A Nouhi. 'Adaptive Spherical Lens', *Appl. Opt.,* 23, 16 (1984) 2774-2777.

[7] P. F. Brinkley, S. T. Kowel and C, Chu. 'Liquid crystal adaptive lens: beam translation and field meshing', *Appl. Opt.,* 27, 21 (1984) 4578-4586.

[8] W. Chan, L. Ning, S. T. Kowel and P. F. Brinkley. 'Liquid Crystal Adaptive Lens: Aberration Correction' *SPIE Proc.* 1773 (1992) 468-475.

[9] A. Purvis. *Private Communication,* Uni. of Durham.

[10] M. G. Clark, M. C. K. Wiltshire, A. Purvis and N. J. Powell. 'Tapered - Electrode LC Prism.', *British Patent* No. 9 305 143.1 (1992).

[11] L. C. Laycock. *Private Communication,* GEC-Marconi, Hirst Research Centre.

[12] K.M. Johnson, D. J. McKnight and Ian Underwood. 'Smart Spatial Light Modulators Using Liquid Crystals On Silicon', *IEEE J. Quantum Electronics,* 29, 2 (1993) 699-714.

Chapter 7

Fringing Fields and Edge Effects

7.1 Introduction

So far the response of a liquid crystal cell's optical path to an applied voltage has been considered in terms of the response under the majority of the electrode, away from the effect of edges. This is essentially a one-dimensional situation which has successfully been numerically modelled by D.W. Berreman [1, 2]. From such a model a theoretical optical path or refractive index response curve can be obtained of the form figure 4.7. Direct measurements of the electro-optical Freedricksz transition have frequently been made and empirical response curves produced, it is used as a standard technique for determining material constants [3, 4, 5, 6].

An important consideration for the devices discussed in this thesis is the optical response of liquid crystals to applied electric fields, specifically in the region around the edges of the electrodes. In diffractive devices a sharp transition is required, and in refractive devices the optical path of the inter-electrode gap is required to be indistinguishable from the optical path of the surrounding electrodes.

The behaviour of the liquid crystal in the edge region is governed by the behaviour of the electric fields there. Under the electrodes, the electric field is uniform and perpendicular to the electrodes and can be approximated as a one-dimensional system, the fields are not confined at the edges of the electrodes but bow out into the inter-electrode gaps, partly activating some of the liquid crystal there (figure 7.1). These intruding fields are known as fringing fields, or transverse fields, due to their lateral component, the smoothing out of the optical path in the inter-electrode gap

Figure 7.1: Fringing Fields Intrusion into the Inter-Electrode Gap

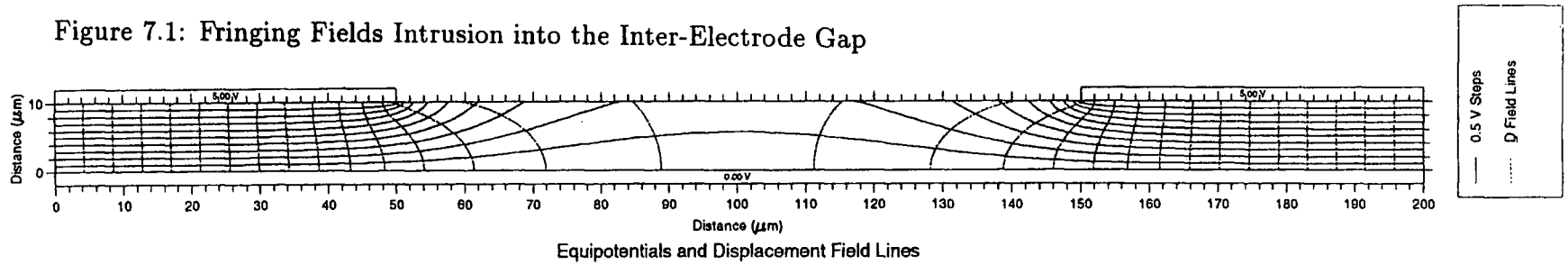

Figure 7.2: Weak Meshing

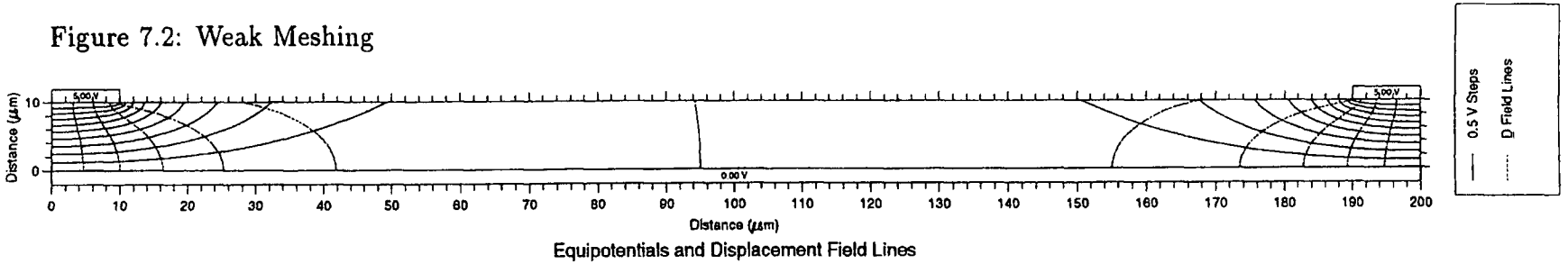

Figure 7.3: Strong Meshing

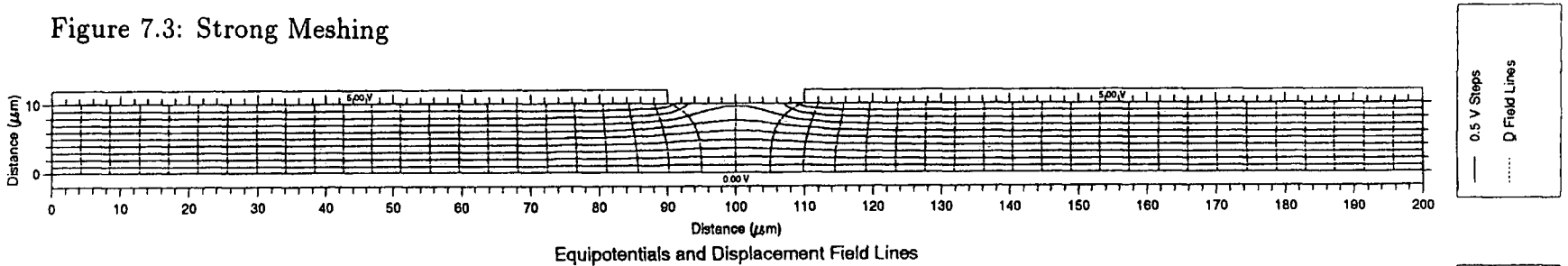

Figure 7.4: Reducing the Intrusion of Fringing Fields using an Etched Earth-Plate

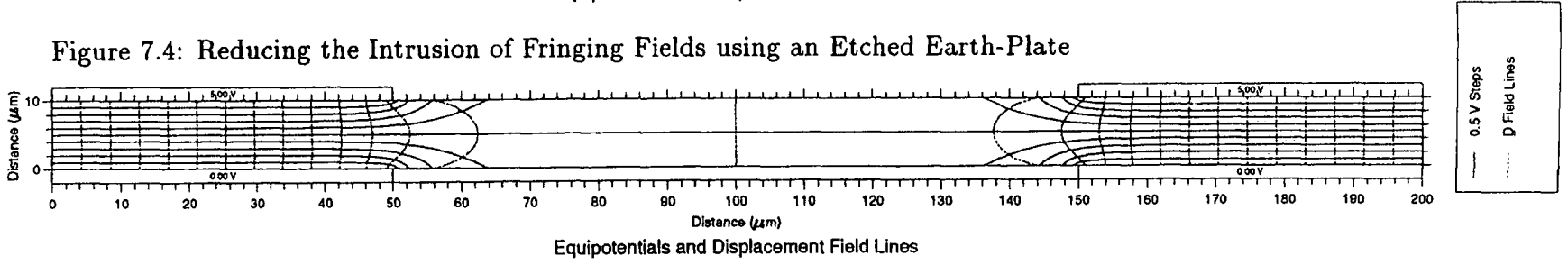

due to these fields is called meshing. The degree of this intrusion and the activation of liquid crystal in the gap are very important design considerations for liquid crystal optical devices.

The critical factor in the determining the extent of fringing fields is the ratio of the inter-electrode gap size and the liquid crystal film thickness, g/d. From electro-static considerations, it is expected that weak meshing occurs when $g/d \gg 1$ (figure 7.2), and strong meshing when $g/d \ll 1$ (figure 7.3). It is important to note that these plots include the off-state dielectric anisotropy, effectively expanding the horizontal direction of the solution by four from the isotropic case (see section 10.2.1). This is fortunate when considering the operation of diffractive and refractive devices;

- diffractive devices can be achieved in relatively thin liquid crystal films, allowing for sharp transitions due to weak meshing,
- refractive devices require relatively thick liquid crystal films in order to obtain larger optical path lengths, allowing for strong meshing to smooth out the optical path in the inter-electrode gap.

Effective limits to electrode sizes required for either meshing régime need to be found to establish design limits for potential liquid crystal devices.

7.2 Diffractive Devices

It has been shown that the minimum size of the inter-electrode gap that can produce a distinct off-state provides an important design limit for the diffractive devices that can be implemented in liquid crystal. The f-number of a binary Fresnel zone-plate lens being limited by equation (4.7) and the broadest grating diffraction pattern determined by equation (4.2). The effect of fringing fields on the liquid crystal provide this limit and needs to be determined in order to establish the range of diffractive devices which can be implemented as liquid crystal cells. The fringing fields also affect how sharp these transitions are, hence how well the produced optical surfaces match the ones required, and so the optical performance of the device.

From purely electro-static considerations variations on the electrode structures that supply the applied voltages can be used to reduce the extent of the fringing

Figure 7.5: Fringing Fields of Cell with Half the Film Thickness

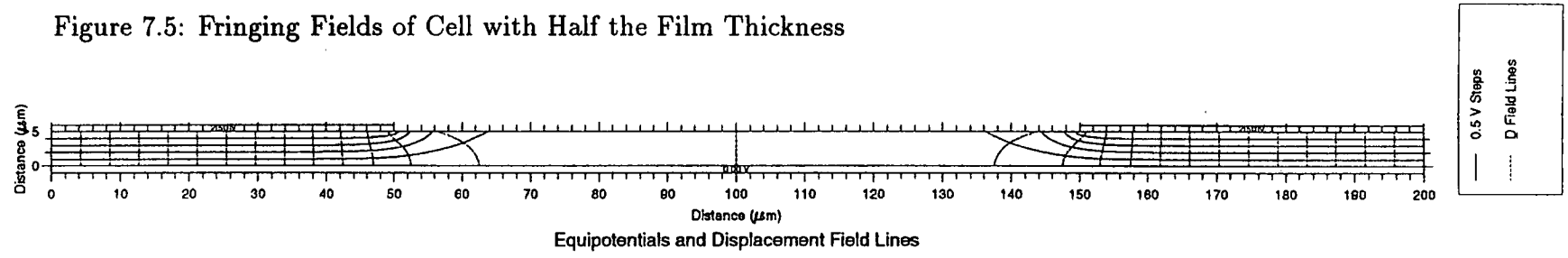

Figure 7.6: Reducing the Intrusion of Fringing Fields using Buried Electrodes

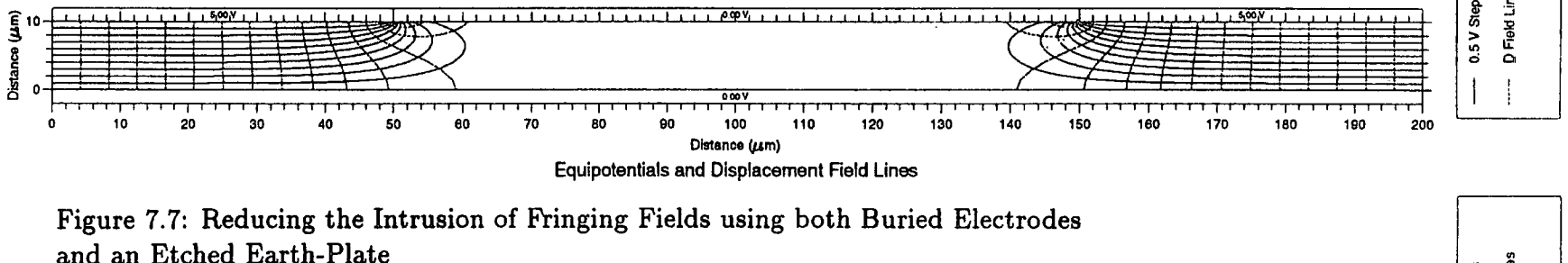

Figure 7.7: Reducing the Intrusion of Fringing Fields using both Buried Electrodes and an Etched Earth-Plate

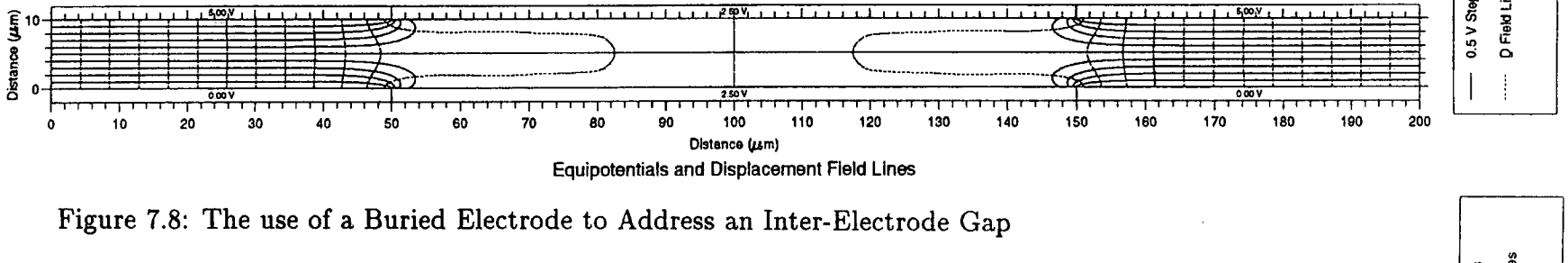

Figure 7.8: The use of a Buried Electrode to Address an Inter-Electrode Gap

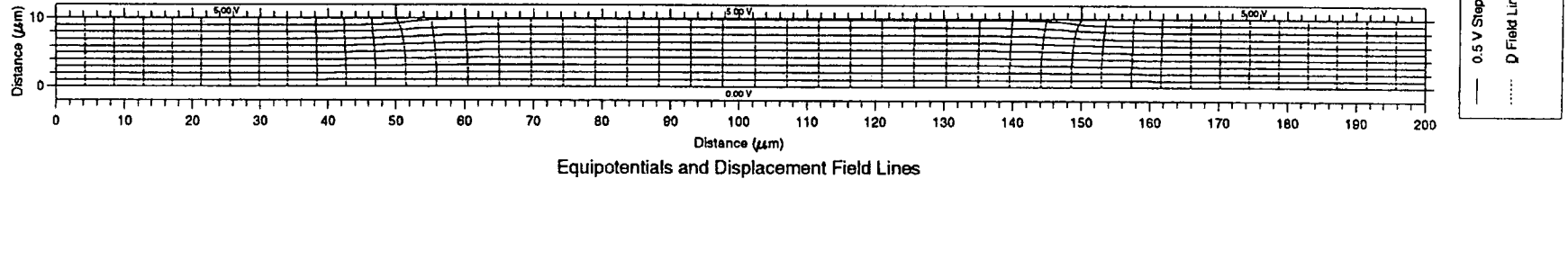

fields. By etching the earth-plate to have an identical structure to the electrode plate the g/d ratio can be effectively doubled (figure 7.4). The fringing fields in a planar electrode structure spread out from the edges of the electrodes reaching their broadest at the planar electrode (figure 7.2). In etching a defined structure into the earth-plate the fringing fields bow out from both the electrode and earth-plate, reaching their maximum spread at the centre of the film, assuming an isotropic dielectric system. This system is equivalent to two planar earth-plate structures of half the film thickness placed back to back (figure 7.5), hence the g/d ratio is effectively doubled. This discussion assumes that the dielectric properties of liquid crystals are isotropic, which of course is not true, it does however illustrate the possible advantage of etching the earth-plate.

A buried electrode structure could be used to supply a zero voltage to the inter-electrode gaps (section 6.5.1), also reducing the intrusion of fringing fields (figure 7.6). A combination of buried electrodes and an etched earth-plate could be potentially used providing further improvements (figure 7.7). The effects of these variations need to be quantified in order to find the design limitations in each case. The resulting optical profiles of each structure would be useful to determine optical efficiency and performance of the resulting devices.

The importance of fringing fields in the performance of a binary Fresnel lens has clearly been demonstrated [7, 8]. An $f/10$ lens of 0.2m focal length at 500nm wavelength, diameter 20mm, with 5μm minimum feature size and 3.5μm cell thickness, was fabricated with circular symmetric zones. The spot intensity was measured with the aperture size of the lens used, the ideal linear relationship was observed up to a 9mm aperture, the contributions of regions beyond this leveled off. Switching between the phases of π and 2π was observed, a modulation depth of 76% was observed at a 9mm aperture and approaching full modulation at 2.5mm. Microscopic measurements indicated an inter-electrode gap reduction of 3.9μm for a phase of π, corresponding to 15.5%, 34% and 78% reductions of the off zones at 2.5mm, 9mm and 20mm diameters respectively. This was reflected in the spot sizes of 1.32×, 3.3× and 5.8× the diffraction limit at the three diameters. There is clearly a trade off between the optical performance of the device and the diffractive power exploited, governed by the presence of fringing fields.

7.3 Refractive Devices

In refractive devices the optical path of the inter-electrode gap is required to be indistinguishable from the optical path of the surrounding electrodes. The value of g/d when this is the case provides the maximum size of the gaps that can be used. The effects of an electrode structure, not operating in the strong meshing régime can clearly be seen as diffraction about the electrodes in the presented results [9, 10, 11]. The use of a buried electrode structure (section 6.5.1) may however relieve this limit (figure 7.8), relaxing the resolution requirements of the electrode to that of providing a good approximation of the optical path surface. The use of continuous, conductive plates in the inter-electrodes has also been proposed [12], to provide a linear interpolation of the voltage.

7.4 Diffractive/Refractive Devices

The optical surfaces required of the diffractive/refractive devices contain features common to both diffractive and refractive devices. The sharp transitions at the zone boundaries when the optical path is discontinuous are similar to the sharp transitions required in the diffractive devices. Hence, the intrusion of fringing fields across zone boundaries, which would have the effect of smoothing out the transitions, should be kept low, suggesting operation in the $g/d \gg 1$ régime.

The continuous optical path profile within the zones is similar to the optical path of refractive devices. An important difference being that large changes in optical path are required across each zone as opposed to being spread across the whole device. In order to provide a good approximation of these rapidly changing optical surfaces a much higher electrode resolution is required. Using a combed current carrying electrode (section 6.4.4) to produce these surfaces a stepped approximation of the required voltage distribution with inter-electrode gaps is provided (figure 7.9). Consequently, a periodic distortion of the required optical profile is expected, the distortions coinciding with the positions of the inter-electrode gaps (figure 7.10). This would cause scattering of light into diffraction orders appropriate to a grating of the same period, impairing the performance of the device. Concern about these distortions in refractive devices have been independently expressed [12, 13].

This situation could be improved by the burying of a second combed current carrying electrode to fill in the inter-electrode gaps (figure 7.11). The resulting optical profile is expected to be a stepped approximation of the required profile (figure 7.12). The steps corresponding to the electrodes, the transitions between the steps being smoothed by the presense of fringing fields between adjacent electrodes. The resolution of the electrode structure is doubled, there being twice as many electrodes present, and the distortions from the required optical surface will be reduced. Consequently, less light will be scattered into diffraction orders of twice the deflection angle compared to the single combed electrode structure.

It would be advantageous if the fringing fields were large enough to smooth out the periodic distortions of the inter-electrode gaps, or the transitions between electrodes, reproducing a good approximation of the required optical profile, without being too large and swamping any of the profile structure. This suggests operation in the $g/d \gg 1$ or $e/d \gg 1$ régime, where e is the electrode width. This is at variance with the requirement of the sharp transitions required at the zone boundaries. A compromise between these two operating requirements needs to be found.

The limit of refractive power that can be achieved in diffractive/refractive devices is limited by the largest gradient of the optical profile that can be achieved across a zone. The optical profile and zone transition produced at this maximum gradient should still be of sufficient quality to avoid serious degradation of the optical performance of the device. This refractive power limit determines the maximum prism pitch that can be implemented;

$$\varphi \leq \arctan\left(\left[\frac{d\varrho(x)}{dx}\right]_{MAX}\right) \tag{7.1}$$

and the f-number of the lenses that can be produced are limited by the gradient required in the outer most zone;

$$\frac{f}{2R} \geq \frac{1}{2}\left(\left[\frac{d\varrho(x)}{dx}\right]_{MAX}\right)^{-1} \tag{7.2}$$

These limits are dependent on the interaction between the applied voltages with the director distribution and the optical surface produced.

Figure 7.9: The Potential Distribution under a Combed Current Carrying Electrode

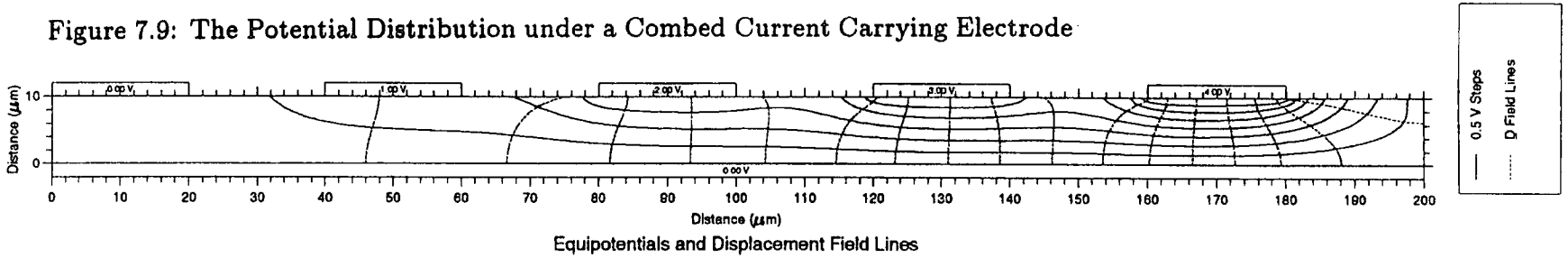

Figure 7.11: The Potential Distribution under a Combed Current Carrying Electrode with a Second Buried Combed Current Carrying Electrode

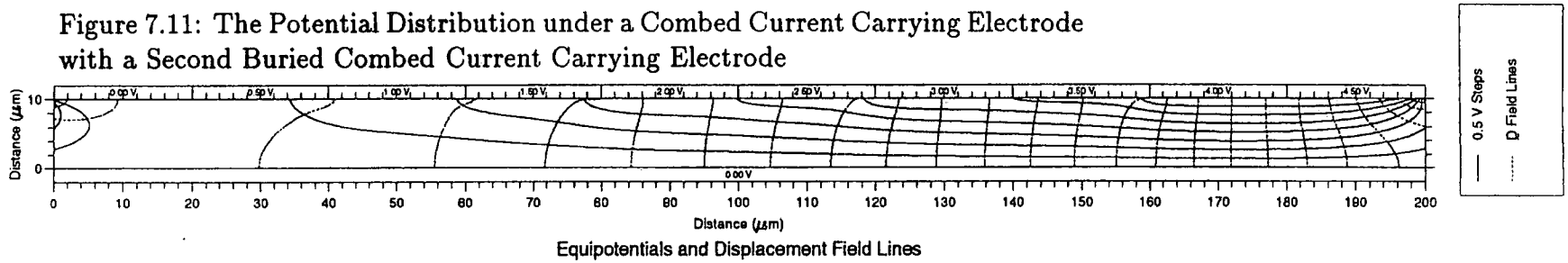

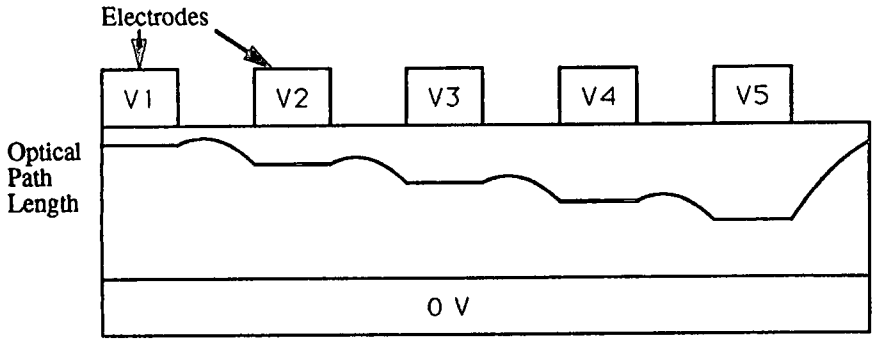

Figure 7.10: The Optical Profile produced by a Combed Current Carrying Electrode

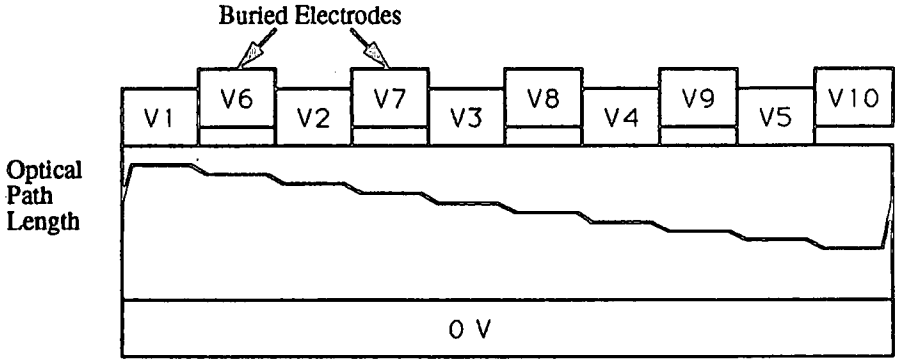

Figure 7.12: The Optical Profile produced by a Combed Current Carrying Electrode with a Second Buried Combed Current Carrying Electrode

The addressing of these diffractive/refractive devices was discussed in Chapter 6 assuming the essentially one-dimensional optical path response (figure 4.7). It can be seen however that the one-dimensional assumptions, which hold under large electrodes, no longer apply to the combed current carrying electrodes. This is especially true in cases where the fringing fields smooth out the steps of the electrode structure and the optical profile is steep (figure 7.11 & 7.12). There are lateral components to the fields throughout the device, consequently some of the assumptions made when considering the design of the electrodes may not hold.

7.5 An Electro-Static Model

A purely electro-static model of two electrodes and a planar earth-plate submerged in an isotropic dielectric medium (figure 7.3), has been reported [11]. It was used to determine the meshing limit for electrodes in a refractive, adaptive liquid crystal lens (section 4.6.2). The voltage profiles between the two electrodes, for varying g/d geometries, were obtained and related linearly to the refractive index change for low voltages [4].

This approach is only an approximation as liquid crystals have a strong dielectric anisotropy, and the relationship between the voltage and refactive index assumes an approximately one-dimensional system. For the purposes this model is employed, finding the strong meshing régime, this approach is acceptable. The stronger the meshing the closer the system approximates to a one-dimensional form.

7.6 A Full Model

An electro-static model is useful for thinking about the distribution of the fringing fields, as the examples in this section illustrate (figures 7.1–7.12). The results of the models cannot be taken as a true representation of the system. Liquid crystals have strong dielectric anisotropy, which will affect the field and potential distributions of the system. The director orientation, and hence the orientation of the extraordinary dielectric, throughout the cell is determined by the fields in the cell, which in turn are affected by the director distribution. As can be seen in figures 7.1–7.12, in many case the fields have strong lateral components, deviating enormously from the

one-dimensional structure previously solved by D. W. Berreman.

The forms of the optical profiles produced by these two-dimensional structures are important in determining the range and limitations of the devices which can be implemented as liquid crystal devices. The optical profiles can be further used in predicting the performance of these devices, submitting them as the phase screens for Fresnel and Fraunhofer diffraction programs. A two-dimensional model of these systems would prove to be a very useful design tool for the development of liquid crystal optical devices.

In order to obtain the optical profile of a two-dimensional structure both the potential and director distributions throughout the system need to be found. The required distributions are the distributions which minimize the electrical Gibbs free energy of the system (equation (2.11)). It is the development of such a model which the rest of this thesis is concerned with.

7.7 Summary

The minimum inter-electrode gap in which a satisfactory off state can be achieved limits the optical power of the diffractive devices that can be implemented. The broadest grating diffraction pattern being given by equation (4.2) and the f-number of a Fresnel lens being limited by equation (4.7). The maximum inter-electrode gap in which the optical path is indistinguishable from the surrounding electrodes is an important consideration in the design of electrode structures in refractive devices. The steepest gradient of the optical path that can be achieved in a diffractive/refractive device limits the refractive power that can be implemented, the maximum prism pitch being given by equation (7.1) and the f-number of the lens limited by equation (7.2).

The optical performance of these devices depends on how well the required optical path structures are reproduced in the liquid crystal. The diffractive devices require sharp transitions between the on and off regions, the refractive devices are required to be smooth and continuous, and the diffractive/refractive devices require sharp transitions at the zone boundaries, and steep, smooth and continuous profiles within the zones. If the optical profiles of these devices could be predicted, they could then

be used to assess the optical performance of any device and provide an opportunity for testing and improving the design of the electrode structures.

These limits and optical profiles are determined by the interaction of the applied voltages with the elastic liquid crystal continuum. This interaction has been modelled successfully numerically for one-dimensional systems by D. W. Berreman. The systems considered here are however far from one-dimensional, the applied fields having significant lateral components in the critical regions. Due to the strong dielectric anisotropy of liquid crystal the potential and field distributions through the system and the director distribution are strongly interdependent. In order to obtain these limits and optical profiles, it is necessary to find the director distribution which minimizes the electrical Gibbs free energy of the system (equation (2.11)). It is the development of such a model which the rest of this thesis is concerned.

7.8 References

[1] D. W. Berreman. *J. Opt. Soc. Am.*, 63 (1973) 1374.

[2] D. W. Berreman. 'Numerical modelling of twisted nematic devices', *Phil. Trans. R. Soc. Lond.*, A309 (1983) 203-216.

[3] L. M. Blinov. *Electro-optical and magneto-optical properties of liquid crystals.* Wiley (1983).

[4] P. G. deGennes. *The properties of Liquid Crystals.* Clarendon Press, Oxford (1974).

[5] S. Chandraskhar. *Liquid Crystals.* Cambridge Press, Oxford (1977).

[6] W. M. de Jeu. *Physical Properties of Liquid Crystalline Materials.* Gordon and Breach (1980).

[7] G. Williams. *Electrically Controllable Liquid Crystal Fresnel Lenses.* PhD Thesis, Uni. of Durham (1991).

[8] G. Williams, A. Purvis and M. C. K. Wiltshire. 'Design Criteria and Fringing Field effects on the performance of LC Fresnel Lenses', *Applied Optics and Opto-Electronics Digest, Nottingham,* (1990) 225.

[9] S. T. Kowel, D. S. Clevery and P. G. Kornreich. 'Focusing by electrical modulation of refraction in a liquid crystal cell', *Appl. Opt.*, 23, 2 (1984) 278-289.

[10] S. T. Kowel, P. G. Kornreich and A Nouhi. 'Adaptive Spherical Lens', *Appl. Opt.*, 23, 16 (1984) 2774-2777.

[11] P. F. Brinkley, S. T. Kowel and C, Chu. 'Liquid crystal adaptive lens: beam translation and field meshing', *Appl. Opt.*, 27, 21 (1984) 4578-4586.

[12] W. Chan, L. Ning, S. T. Kowel and P. F. Brinkley. 'Liquid Crystal Adaptive Lens: Aberation Correction' *SPIE Proc.* 1773 (1992) 468-475.

[13] P. F. Brinkley and S. T. Kowel. 'Liquid Crystal Adaptive Lens: Operation and Aberation' *SPIE Proc.* 1773 (1992) 449-457.

Chapter 8

The Modelling of Nematic Liquid Crystal using the Finite Element Method

8.1 Introduction

In Chapter 7, we saw that in order to predict the optical performance of the proposed liquid crystal devices it was necessary to construct a model which describes the director orientation, throughout two-dimensional sections of the devices. In Chapter 2, it was shown that the director orientation taken at equilibrium must minimize the *electrical Gibbs free energy*, equation (2.11), of the system. The *variational finite element method*, described in Chapter 3, was used to solve problems of this form and will be employed here.

The work presented here is an initial attempt to use the finite element method to solve this problem, in order to explore the validity of this approach as well as to obtain some initial results. The elastic energy equation is known to be very non-linear and difficult to solve, it was expected that any attempt to solve it may become very involved. The finite element method is very well established and has been developed to a great level of sophistication for a wide range of applications. With these points in mind, the most simple and direct approach was taken to avoid any unnecessary complications, the scope of the problems addressed was also restricted for this reason. Once the validity of the approach is established and the potential pitfalls better understood, the scope of the problem can be broadened and more sophisticated techniques incorporated in later developments of the model. Some of these possible developments are discussed in Chapter 12.

This chapter will detail the formularization of the electrical Gibbs free energy in a variational finite element form. The general features and choices that form this formularization are presented. The problem is partitioned into two parts; an electro-static part and an elastic part. Details of the formularization of each part are presented in turn, followed by their combination into a two-step iterative solution. There are several levels of approximation that may be used in the developed model, three specific sets of approximation were developed, these will be outlined in turn. The effect of the second order energy term on the formularization is discussed. The error-estimator and adaptive mesh refinement strategy are described.

8.2 General Formularization

In the course of moving from a general approach to a problem to a specific model, decisions have to be made which restrict the generality of the approach. This section will outline some of the decisions taken, with their underlying reasons, in the development of the model presented in this thesis.

8.2.1 Two-Dimensional Sections

The model will be restricted to two-dimensional sections through regions of the device. Strictly, this assumes that the physical system is invariant perpendicular to the two-dimensional plane considered. More generally, two-dimensional results will hold for systems that vary gradually enough in the perpendicular direction that they can be locally considered invariant. For example, a radial section through the outer regions of a circular symmetric electrode structure could be successfully modelled by a two-dimensional system. These two-dimensional sections should be sufficient to describe the majority of the functional regions of the liquid crystal devices proposed in this thesis. A full three-dimensional model can be developed in a similar manner, but such a model would be computationally much more demanding.

The x-axis is defined to be parallel to the glass substrate, the y-axis perpendicular to this substrate and the system is assumed to be invariant in the z-direction (figure 8.1).

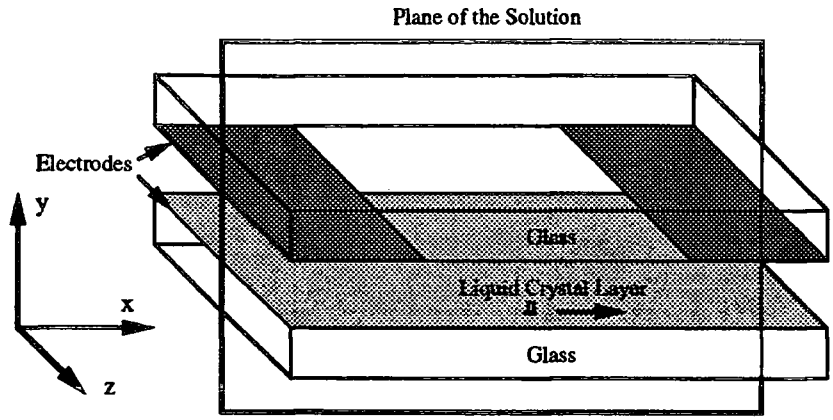

Figure 8.1: Definition of the Global Reference Frame

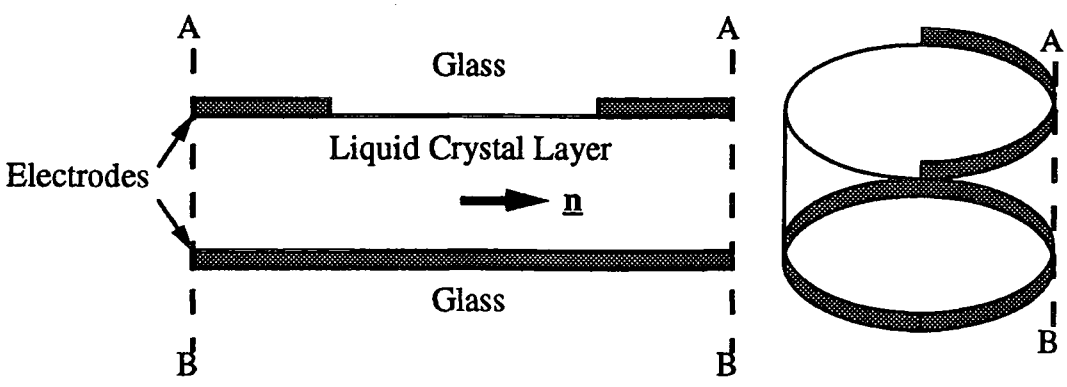

Figure 8.2: Modelling a Periodic Structure by connecting one edge of the Periodic Structure to the other.

8.2.2 The Finite Elements

The elements used, introduced in section 3.2.2, are the simplest adaptive elements for a two-dimensional problem; linear triangular elements. The variation of the dependent variable across the element is given by equation (3.9);

$$\hat{\psi}(x,y) = \alpha_0 + \alpha_1 x + \alpha_2 y$$

This is a *complete* polynomial for systems to be solved, that is it is capable of approximating all the derivatives of the dependent variable, required to construct the functional. This is an important condition for the choice of an element shape function for a successful finite element formularization. This choice was made to avoid any unnecessary complications which the use of more sophisticated elements may incur. The linear form is also consistent with the linear form of the small local, elementary distortions, equation (2.7), used in the development of Frank's equation in Chapter 2.

The geometry of the linear triangular elements was chosen with simplicity in mind. The two-dimensional plane is divided up into an irregular rectangular mesh, each rectangle is sub-divided into two right-angled triangles (figure 3.1), which form the finite elements. The trial function can be simply expressed as equation (3.10);

$$\hat{\psi}(x,y) = \left[\begin{array}{ccc} \frac{1}{3} - \frac{x}{b} - \frac{y}{c}, & \frac{1}{3} + \frac{x}{b}, & \frac{1}{3} + \frac{y}{c} \end{array} \right] \left[\begin{array}{c} \bar{\psi}_1 \\ \bar{\psi}_2 \\ \bar{\psi}_3 \end{array} \right]$$

where b & c are the x & y dimensions of the element respectively, x & y being measured locally from the centroid of the triangle.

8.2.3 The Periodic Boundary

Many of the electrode structures proposed in this thesis are periodic in form, the size of the period being constant or varying gradually. This property can be exploited to reduce the solution area from an entire slice through a device to a single period of the repeated structure. The effects of fringing fields are expected to be very localized, so the influence of a gradual change of scale of the periodic structure and the effect of the termination of the periodic structure are expected to be negligible to a 'typical' period or zone.

In order to realize a periodic structure, whilst only modelling a single period of it, the space at one boundary of the period is made consecutive with the space at the other boundary. This can be viewed as wrapping the period around a cylinder (figure 8.2). This procedure has important consequences on the node numbering of the elements, which will be discussed in Chapter 9.

8.2.4 In-Planar Rotation

In Chapter 2, the representation of the director orientation in the global reference frame by two angles of rotation, θ & ϕ, the tilt and orientation of the director respectively (figure 2.4), was introduced. To completely describe the system, the director orientation needs to be found in terms of these two angular distributions, throughout the whole system. It was considered expedient to initially restrict the problem to a single angular distribution, greatly reducing and simplifying the task of formularization. This restriction can be achieved by restricting the problems that will be considered to those in which the boundary director is perpendicular to the z-axis. As the system is invariant in the z-direction there will be no field components in this direction to cause rotation of the director out of the xy-plane. Consequently, the director rotation will be confined to this plane and the director can be described by a single angle, ϕ (figure 8.3). The extension of the solution to the full two angle description will be considered in Chapter 12.

8.2.5 Partitioning the Problem

Restricting the problem to one angular distribution leaves two unknown dependent variables required to completely describe the system; the angular distribution and the potential distribution. The approach used in the model presented here is to partition the problem into two independent parts; an electro-static part in which the potential distribution is solved independently, with a given angular distribution, and an elastic part in which the angular distribution is solved independently with a given potential distribution. Taken together they form a two step iterative solution. Initially, neither the potential nor the angular distributions are known. Given an arbitrary angular distribution a rough approximation of the potential distribution can be obtained. Using this rough approximation, an approximation of the angular

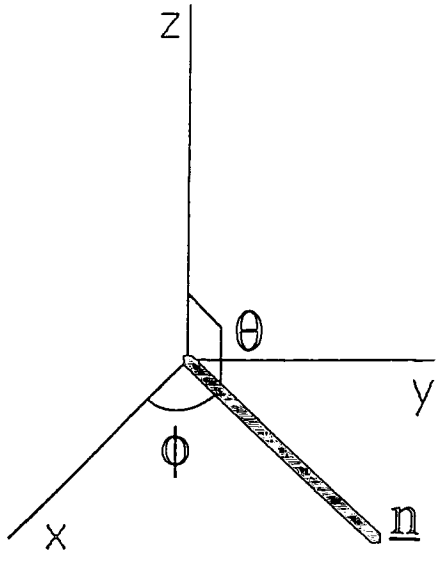

Figure 8.3: In-Planar Rotation described by a Single Angle

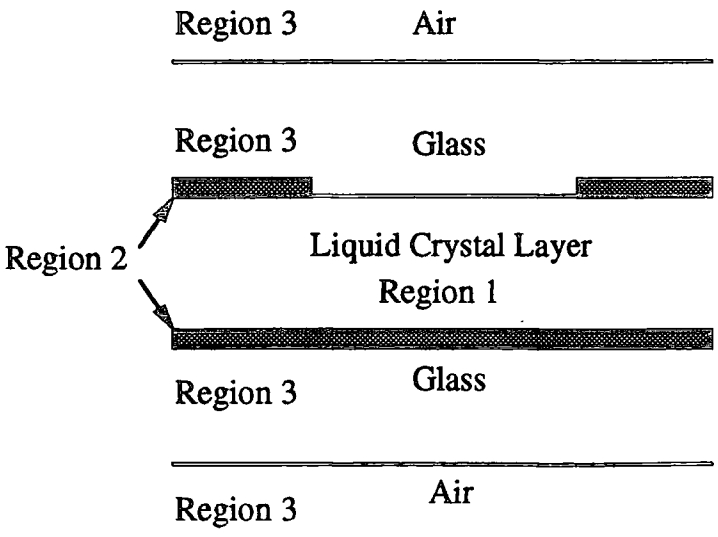

Figure 8.4: The Three Regions of the Electro-Static Systems

distribution can be obtained. This can in turn be used to obtain a better approximation of the potential distribution, and so on. This process can be repeated, with each approximation being used as the basis of a better approximation, until an acceptable approximate solution is converged to.

An alternative approach would be to solve the angular and potential distributions in a single step. It will be seen, in section 8.5, that the iterative feedback of approximate solutions will still be required. The single step approach will be discussed further in Chapter 12.

The choice of partitioning the model into two steps arose partly out of the evolution of the project. The observation that the finite element method could be employed to solve the electro-statics of the system occurred before the realization that it could also be extended to solving the angular distribution. Consequently, a purely electro-static model was developed on the presumption of a two-step iterative solution. Once the use of the finite element method was decided upon for the angular distribution, the partitioned two-step approach was continued for the following reasons:

- Having progressed part way along the two-step route, it was considered that the most direct course to achieving a solution was to continue on this course.
- It was realized that an iterative solution would still be required whichever approach was taken.
- The two partitioned models were expected to be simpler in form than the single step model.
- It had been observed, developing the electro-static model, that the upper limit to the size of the matrix that could be solved was problematically small. The single step solution, having doubled the number of dependent variables, would require a matrix with four-fold the number of matrix elements for a system with the same number of nodes, hence exacerbating the problem.

The formularization of each part will now be presented in turn.

8.3 Electro-Static Formularization

8.3.1 Minimizing the Electro-Static Energy Equation

The potential distribution of an electro-static system can be found by minimizing the electro-static energy equation. The liquid crystal system is distinguished from other electro-static systems by the anisotropic dielectric property of the liquid crystal and the arbitrarily variable director orientation throughout the system.

Recalling from Chapter 2, the electro-static energy is given by (equation (2.4));

$$\chi_e = \int_{\mathcal{D}} \frac{1}{2} \mathbb{D} \cdot \mathbb{E} d\mathcal{D}$$

where $\mathcal{D}$ is the domain of the problem, $\mathbb{E}$ is the electric field and $\mathbb{D}$ is the displacement field. The symbol χ_e will be used to indicate the electro-static energy solved with respect to the potential distribution. The fields are related to the electrical potential V via (equation (2.1));

$$\begin{aligned} \mathbb{D} &= \varepsilon \boldsymbol{\varepsilon}_r \mathbb{E} \\ \mathbb{E} &= -\nabla V \end{aligned}$$

where

$$\nabla = \begin{bmatrix} \partial/\partial x \\ \partial/\partial y \\ \partial/\partial z \end{bmatrix}$$

in Cartesian co-ordinates, ε is the permittivity of free space and $\boldsymbol{\varepsilon}_r$ is the relative permittivity tensor. The relative permittivity tensor $\boldsymbol{\varepsilon}_r$ can be related to the relative permittivity tensor $\boldsymbol{\varepsilon}_l$, in a local reference frame parallel to the principle axis of the liquid crystal, by the rotational matrix, $\mathbb{R}(\theta, \phi)$, which relates the two reference frames (equation (2.3));

$$\boldsymbol{\varepsilon}_r = \mathbb{R}^T(\theta, \phi)\, \boldsymbol{\varepsilon}_l\, \mathbb{R}(\theta, \phi)$$

where θ and ϕ represent the tilt and orientation of the liquid crystal (figure 2.4). The local relative permittivity tensor is given by (equation (2.2));

$$\boldsymbol{\varepsilon}_l = \begin{bmatrix} \varepsilon_o & 0 & 0 \\ 0 & \varepsilon_o & 0 \\ 0 & 0 & \varepsilon_e \end{bmatrix}$$

where ε_o and ε_e are the ordinary and extraordinary relative permittivities, respectively.

The rotational matrix, $\mathbb{R}(\theta,\phi)$,can be constructed from the successive tilt and orientation rotation matrices;

$$\begin{aligned}\mathbb{R}(\theta,\phi) &= \begin{bmatrix}\cos\theta & 0 & -\sin\theta\\ 0 & 1 & 0\\ \sin\theta & 0 & \cos\theta\end{bmatrix}\begin{bmatrix}\cos\phi & \sin\phi & 0\\ -\sin\phi & \cos\phi & 0\\ 0 & 0 & 1\end{bmatrix}\\ &= \begin{bmatrix}\cos\theta\cos\phi & \cos\theta\sin\phi & -\sin\theta\\ -\sin\phi & \cos\phi & 0\\ \sin\theta\cos\phi & \sin\theta\sin\phi & \cos\theta\end{bmatrix}\end{aligned} \tag{8.1}$$

this is simplified by restricting the problem to in-planar rotation ($\theta = \pi/2$);

$$\begin{aligned}\mathbb{R}(\pi/2,\phi) &= \begin{bmatrix}0 & 0 & -1\\ 0 & 1 & 0\\ 1 & 0 & 0\end{bmatrix}\begin{bmatrix}\cos\phi & \sin\phi & 0\\ -\sin\phi & \cos\phi & 0\\ 0 & 0 & 1\end{bmatrix}\\ &= \begin{bmatrix}0 & 0 & -1\\ -\sin\phi & \cos\phi & 0\\ \cos\phi & \sin\phi & 0\end{bmatrix}\end{aligned} \tag{8.2}$$

Recalling the finite element procedure, described in Chapter 3, the system is divided into finite elements and the finite element approximation of the dependent variable is applied across each element;

$$\hat{V} = \mathbf{N}\bar{\mathbf{V}}$$

The electro-static energy contribution for each element can be expressed in matrix form;

$$\chi_e^e = \frac{\varepsilon}{2}\int_{\mathcal{D}_e}(\nabla\mathbf{N}\bar{\mathbf{V}})^T\boldsymbol{\varepsilon}_r(\nabla\mathbf{N}\bar{\mathbf{V}})d\mathcal{D} \tag{8.3}$$

where $\mathcal{D}_e$ is the domain of the element, which is clearly quadratic in terms of $\bar{\mathbf{V}}$, hence the first derivatives of the energy form a set of linear equations;

$$\frac{\partial\chi_e^e}{\partial\bar{\mathbf{V}}} = \varepsilon\int_{\mathcal{D}_e}(\nabla\mathbf{N})^T\boldsymbol{\varepsilon}_r(\nabla\mathbf{N})\bar{\mathbf{V}}d\mathcal{D} \tag{8.4}$$

The contributions of each element can then be added into a set of linear equations that describe the system and then be solved.

For simplicity, the orientation of the director within each element will be approximated by a constant orientation, ϕ_c, which is the average orientation of the element, or the orientation at the centroid of the element. Consequently, the rotational matrix, $\mathbf{R}$, is constant across the element, simplifying the integration over the element. The validity of this approximation will be considered in section 8.6.

The linear triangular shape function used to describe the potential variation across the element is;

$$\hat{V}(x,y) = \left[\frac{1}{3} - \frac{x}{b} - \frac{y}{c}, \quad \frac{1}{3} + \frac{x}{b}, \quad \frac{1}{3} + \frac{y}{c} \right] \begin{bmatrix} \bar{V}_1 \\ \bar{V}_2 \\ \bar{V}_3 \end{bmatrix} \tag{8.5}$$

where b & c are the x & y dimensions of the element respectively, x & y being measured locally from the centroid of the triangle. This has constant first derivatives within the element;

$$\nabla \mathbf{N} = \begin{bmatrix} -\frac{1}{b} & \frac{1}{b} & 0 \\ -\frac{1}{c} & 0 & \frac{1}{c} \\ 0 & 0 & 0 \end{bmatrix} \tag{8.6}$$

These two considerations leave the terms of the integral independent of the spatial variables, consequently the integral over the element becomes simply the area of the element;

$$\int_{\mathcal{D}_e} d\mathcal{D} = \Delta = bc/2 \tag{8.7}$$

hence,

$$\frac{\partial \chi_e^e}{\partial \bar{\mathbf{V}}} = \varepsilon \Delta (\nabla \mathbf{N})^T \boldsymbol{\varepsilon}_r (\nabla \mathbf{N}) \bar{\mathbf{V}} \tag{8.8}$$

Substituting in the various terms it can be shown that the contribution from each element to the minimization equations is given by;

$$\begin{bmatrix} \partial \chi_e^e / \partial \bar{V}_1 \\ \partial \chi_e^e / \partial \bar{V}_2 \\ \partial \chi_e^e / \partial \bar{V}_3 \end{bmatrix} =$$

$$\frac{\varepsilon}{4\Delta} \begin{bmatrix} c^2 \varepsilon_{11} + b^2 \varepsilon_{22} + 2bc\varepsilon_{12} & -c^2 \varepsilon_{11} - bc\varepsilon_{12} & -b^2 \varepsilon_{22} - bc\varepsilon_{12} \\ -c^2 \varepsilon_{11} - bc\varepsilon_{12} & c^2 \varepsilon_{11} & bc\varepsilon_{12} \\ -b^2 \varepsilon_{22} - bc\varepsilon_{12} & bc\varepsilon_{12} & b^2 \varepsilon_{22} \end{bmatrix} \begin{bmatrix} \bar{V}_1 \\ \bar{V}_2 \\ \bar{V}_3 \end{bmatrix} \tag{8.9}$$

where

$$\begin{aligned} \boldsymbol{\varepsilon}_r &= \begin{bmatrix} \varepsilon_{11} & \varepsilon_{12} & \varepsilon_{13} \\ \varepsilon_{21} & \varepsilon_{22} & \varepsilon_{23} \\ \varepsilon_{31} & \varepsilon_{32} & \varepsilon_{33} \end{bmatrix} \\ &= \begin{bmatrix} \varepsilon_o \sin^2 \phi_c + \varepsilon_e \cos^2 \phi_c & (\varepsilon_e - \varepsilon_o) \cos \phi_c \sin \phi_c & 0 \\ (\varepsilon_e - \varepsilon_o) \cos \phi_c \sin \phi_c & \varepsilon_o \cos^2 \phi_c + \varepsilon_e \sin^2 \phi_c & 0 \\ 0 & 0 & \varepsilon_o \end{bmatrix} \end{aligned} \tag{8.10}$$

This provides a finite element approximation for the contribution of each element to the minimization of the electro-static energy of the system, in terms of the potential distribution. The contribution from each element can be added in turn to the set of equations describing the whole system, which can then be solved.

8.3.2 Boundary Conditions

A description of the electro-statics of the liquid crystal region has been given, now consideration will be made of the boundary conditions. These fall into three groups;

- the periodic boundary, as described in section 8.2.3,
- the electrodes, which form internal regions of prescribed voltage,
- the far boundary, for a complete description of an electro-static system the form of the potential distribution as it spreads to infinity is required.

Electrodes

The electrodes in the systems considered are held at constant voltages by external power supplies. These voltages can be inserted into the finite element description of the system as prescribed nodal values and treated as described in section 3.2.4.

The Far Boundary Condition

An open electro-static structure requires the potential distribution, as it spreads out to infinity, in order to provide a complete description of the system. It is impractical to include infinite distances in a finite element model, requiring either an infinite number of elements or elements of infinite length. In electro-static problems it is assumed that there are no fields infinitely far from the system, which can be represented by;

$$\frac{\partial V}{\partial y} \to 0 \quad \text{as} \quad y \to \pm\infty \tag{8.11}$$

In order to make an appropriate approximation of this condition in the finite element model, the electro-static system will be considered in terms of Fourier decomposition [1, section 11.3], [2, section 7.5].

The electro-static systems that will be considered can be split into three regions (figure 8.4):

1. The liquid crystal region, which is treated as an anisotropic dielectric with arbitrarily variable orientation throughout.
2. The electrodes, which form internal regions of prescribed voltage.
3. The rest of the system, including the glass slide and air reaching to infinity.

The potential distribution in this third region is only of interest because it affects the potential distribution in the liquid crystal region and so needs to be correctly evaluated.

As there is no free charge in the third region the potential distribution must satisfy Laplace's equation;

$$\frac{\partial^2 V}{\partial x^2} + \frac{\partial^2 V}{\partial y^2} = 0$$

this can be solved by separating the dependent variable in terms of the spatial co-ordinates of the system; $V(x,y) = X(x)Y(y)$. Substituting into Laplace's Equation and dividing through by XY, gives;

$$\frac{1}{X}\frac{\partial^2 X}{\partial x^2} + \frac{1}{Y}\frac{\partial^2 Y}{\partial y^2} = 0$$

Since the two terms are independent and add to zero, each term must be related to a constant;

$$-\frac{1}{X}\frac{\partial^2 X}{\partial x^2} = \frac{1}{Y}\frac{\partial^2 Y}{\partial y^2} = a$$

To solve this, consistent with the periodic boundary condition in the x-direction a must be positive, $a = k^2$. A general solution for X can be constructed as a Fourier series;

$$X = \sum_n A_n e^{ik_n x}$$

where

$$k_n = \frac{2\pi n}{L_x}$$

L_x being the length of the period. The potential distribution is then described by;

$$V = \sum_n Y_n(y) e^{ik_n x}$$

where Y_n is the amplitude of the nth harmonic, for which an expression can be found by substitution into the Laplace's equation;

$$\frac{\partial^2 Y_n}{\partial y^2} - k_n^2 Y_n = 0$$

which has the solution;

$$Y_n = C_n e^{k_n y} + D_n e^{-k_n y}$$

To be consistent with the infinite boundary condition, $C_n = 0$.

As can be seen, the potential distribution can be described by a Fourier Series in the x-direction and a related decay series in the y-direction;

$$V = \sum_n B_n e^{ik_n x} e^{-k_n y}$$

The size of the Fourier terms are heavily attenuated by the decay term at significant distances from the electrode structure. For example, the slowest decay term, $n = 1$, attenuates its oscillatory component to $\sim 0.2\%$ of its value, the length of one period from the electrode system. Consequently, a good approximation to the finite boundary condition would be to allow the natural boundary condition;

$$\frac{\partial V}{\partial y} = 0$$

to occur at an appropriately large distance from the electrode structure for the Fourier components to have decayed below any significance.

The initial mesh used in the far boundary region is based on a $\log 10$ scale, in order to provide a richer density of elements closer to the electrode region and relatively few near the far boundary, where the potential distribution is expected to be flat. The same electro-static formularization holds in this region as in the liquid crystal region, with the appropriate choice of dielectric; $\varepsilon_o = \varepsilon_e = \varepsilon_d$. Several layers of isotropic, or even anisotropic, dielectric can be modelled in this region by modifying the relative permittivity of the elements appropriately.

8.4 Elastic Formularization

The potential distribution was solved using only the electro-static energy equation, the angular distribution, however, requires both the elastic and electrical energy terms, since it appears as a dependent variable in both. The formularization of each term will be dealt with in turn.

8.4.1 The Elastic Term

Recalling the elastic energy equation (equation (2.10));

$$f_K = \frac{1}{2}\left[K_{11}\left(\nabla \cdot \mathbf{n}\right)^2 + K_{22}\left(\mathbf{n} \cdot \nabla \times \mathbf{n}\right)^2 + K_{33}\left(\mathbf{n} \times \nabla \times \mathbf{n}\right)^2\right]$$

where $\mathbf{n}$ is the director and K_{11}, K_{22} and K_{33} are the splay, twist and bend elastic constants, respectively, it can be seen that the twist and bend terms are expressed in terms of the fourth power of the director. This is far from *quadratic-linear* form required to obtain a set of linear equations, as described in Chapter 3. The elastic energy density equation, expressed in terms of elementary distortions (equation (2.9));

$$f_K = \frac{1}{2}\left[K_{11}\left(\frac{\partial n_\iota}{\partial \iota} + \frac{\partial n_\kappa}{\partial \kappa}\right)^2 + K_{22}\left(\frac{\partial n_\iota}{\partial \kappa} - \frac{\partial n_\kappa}{\partial \iota}\right)^2 + K_{33}\left(\frac{\partial n_\iota}{\partial \lambda} + \frac{\partial n_\kappa}{\partial \lambda}\right)^2\right]$$

is however of more promising form. This represents the energy density in a local reference frame $(\bar{0}, \iota, \kappa, \lambda)$ located with the λ-axis parallel to the director $\mathbf{n}$ at the local origin $\bar{0}$, in terms of elementary distortions from the director at $\bar{0}$. Exploiting the division of the system into finite elements, this localized energy density can be applied to each element. This does however presume prior knowledge to the average director in each element.

The director is defined as a unit vector which is orientated parallel to the direction of the principle axis of the molecule. A local co-ordinate system which follows the director can be defined; $(\bar{0}, \mu, \nu, o)$. The director in this co-ordinate system is simply;

$$\mathbf{n}(\bar{0}, \mu, \nu, o) = \begin{bmatrix} n_\mu \\ n_\nu \\ n_o \end{bmatrix} = \begin{bmatrix} 0 \\ 0 \\ 1 \end{bmatrix} \tag{8.12}$$

The director in the local reference frame $(\bar{0}, \iota, \kappa, \lambda)$, based on the centroid director orientation of each element is required for the elastic energy density equation. The angle between the director and the global reference frame, ϕ, can be split into two parts;

$$\phi(x, y) = \phi_c + \phi_v(x, y) \tag{8.13}$$

where ϕ_c is the centroid director orientation, and ϕ_v represents the spatial variation of the director from ϕ_c. The director can then be expressed in terms of successive rotations between the $(\bar{0}, \iota, \kappa, \lambda)$ and $(\bar{0}, \mu, \nu, o)$ reference frames, via the globally aligned reference frame $(\bar{0}, x, y, z)$;

$$\mathbf{n}(\bar{0}, \iota, \kappa, \lambda) = \mathbb{R}(\theta_c, \phi_c)\mathbf{n}(\bar{0}, x, y, z) = \mathbb{R}(\theta_c, \phi_c)\mathbb{R}^T(\theta, \phi)\mathbf{n}(\bar{0}, \mu, \nu, o) \tag{8.14}$$

where $\mathbb{R}(\theta_c, \phi_c)$ and $\mathbb{R}(\theta, \phi)$ are defined above. Setting $\theta_c = \theta = \pi/2$;

$$\begin{aligned}\begin{bmatrix} n_\iota \\ n_\kappa \\ n_\lambda \end{bmatrix} &= \begin{bmatrix} 0 & 0 & -1 \\ -\sin\phi_c & \cos\phi_c & 0 \\ \cos\phi_c & \sin\phi_c & 0 \end{bmatrix} \begin{bmatrix} 0 & -\sin\phi & \cos\phi \\ 0 & \cos\phi & \sin\phi \\ -1 & 0 & 0 \end{bmatrix} \begin{bmatrix} 0 \\ 0 \\ 1 \end{bmatrix} \\ &= \begin{bmatrix} 1 & 0 & 0 \\ 0 & \cos\phi_v & \sin\phi_v \\ 0 & -\sin\phi_v & \cos\phi_v \end{bmatrix} \begin{bmatrix} 0 \\ 0 \\ 1 \end{bmatrix} = \begin{bmatrix} 0 \\ \sin\phi_v \\ \cos\phi_v \end{bmatrix} \end{aligned} \tag{8.15}$$

It is also necessary to express the partial derivatives of the local reference frame $(\bar{0}, \iota, \kappa, \lambda)$ in terms of the globally aligned reference frame $(\bar{0}, x, y, z)$;

$$\begin{bmatrix} \partial/\partial\iota \\ \partial/\partial\kappa \\ \partial/\partial\lambda \end{bmatrix} = \begin{bmatrix} \partial x/\partial\iota & \partial y/\partial\iota & \partial z/\partial\iota \\ \partial x/\partial\kappa & \partial y/\partial\kappa & \partial z/\partial\kappa \\ \partial x/\partial\lambda & \partial y/\partial\lambda & \partial z/\partial\lambda \end{bmatrix} \begin{bmatrix} \partial/\partial x \\ \partial/\partial y \\ \partial/\partial z \end{bmatrix} = \mathbb{R}(\theta_c, \phi_c) \begin{bmatrix} \partial/\partial x \\ \partial/\partial y \\ \partial/\partial z \end{bmatrix} \tag{8.16}$$

Substituting in the expressions for the director and the partial derivatives, setting $\theta_c = \pi/2$ and noting also that the system is invariant in the z-direction, the local elastic energy density becomes;

$$\begin{aligned} f_K^e &= \frac{K_{11}}{2}\left(-\sin\phi_c \frac{\partial \sin\phi_v}{\partial x} + \cos\phi_c \frac{\partial \sin\phi_v}{\partial y}\right)^2 \\ &+ \frac{K_{33}}{2}\left(\cos\phi_c \frac{\partial \sin\phi_v}{\partial x} + \sin\phi_c \frac{\partial \sin\phi_v}{\partial y}\right)^2 \end{aligned} \tag{8.17}$$

As a consequence of restricting the director motion to within the plane the twist term disappears, leaving a purely splay and bend system.

8.4.2 The Electrical Term

It has been shown that the electrical energy is given by equation (8.3). Using the shape function and the potential values from the electro-static solution with the expression for ε_r, equation (8.10), in terms of the complete director orientation, ϕ, it can be rewritten as;

$$\begin{aligned} F_e^e &= \frac{\varepsilon}{2}\int_{\mathcal{D}_e} \Big\{\alpha_1^2(\varepsilon_o \sin^2\phi + \varepsilon_e \cos^2\phi) \\ &+ 2\alpha_1\alpha_2(\varepsilon_e - \varepsilon_o)\cos\phi\sin\phi \\ &+ \alpha_2^2(\varepsilon_o \cos^2\phi + \varepsilon_e \sin^2\phi)\Big\}\, d\mathcal{D} \end{aligned} \tag{8.18}$$

where

$$\alpha_1 = \frac{\bar{V}_2 - \bar{V}_1}{b}, \qquad \alpha_2 = \frac{\bar{V}_3 - \bar{V}_1}{c}$$

The symbol F_e will be used to indicate the electro-static energy being expressed for the director orientation model.

8.4.3 The Finite Element Approximation

As can be seen, the energy expressions are in terms of sinusoidal functions of the dependent variable, ϕ, which is clearly not the quadratic-linear form required to obtain a set of linear equations. There is also the presumption in using the localized energy density equation, that the average director orientation in each element is known. In order to circumvent these problems the dependent variables can be split into two parts;

$$\phi(x,y) = \phi_o(x,y) + \delta\phi(x,y) \tag{8.19}$$

where ϕ_o is a constant large angle part, which represents a given approximation of the angular distribution and $\delta\phi$ is a small variation from the pre-set angles, which is solved for, as a refinement of the approximation. By applying small angle approximations to the angular functions, the small angle variations can be expressed in quadratic-linear terms;

$$\sin\phi \approx \left(1 - \frac{\delta\phi^2}{2}\right)\sin\phi_o + \delta\phi\cos\phi_o \tag{8.20}$$

$$\cos\phi \approx \left(1 - \frac{\delta\phi^2}{2}\right)\cos\phi_o - \delta\phi\sin\phi_o \tag{8.21}$$

Substituting these expressions into the energy densities, small angle approximations can be generated in terms of polynomials of the dependent variables. Terms that combine to form higher than quadratic functions of the variables can be ignored as negligible compared with the quadratic-linear terms, noting that variables represent small angles. The quadratic-linear approximation of the energy of the system can then be minimized by solving the resulting set of linear equations, as described in Chapter 3. In this way the non-linear expression can be represented by a set of linear equations which are a local, small angle approximation to the system.

The angular distribution is approximated as a linear function over the triangular finite elements;

$$\hat{\phi} = (\beta_0 + \gamma_0) + (\beta_1 + \gamma_1)x + (\beta_2 + \gamma_2)y \tag{8.22}$$

where β represents the constant, pre-set angular distribution terms and γ terms of the small angle variations from it. The triangular elements are right-angular and

the shape function given by;

$$\hat{\phi}(x,y) = \left[\begin{array}{ccc} \frac{1}{3} - \frac{x}{b} - \frac{y}{c}, & \frac{1}{3} + \frac{x}{b}, & \frac{1}{3} + \frac{y}{c} \end{array} \right] \left[\begin{array}{c} \bar{\phi}_{o1} + \delta\bar{\phi}_1 \\ \bar{\phi}_{o2} + \delta\bar{\phi}_2 \\ \bar{\phi}_{o3} + \delta\bar{\phi}_3 \end{array} \right] \tag{8.23}$$

The energy minimization may be solved in terms of either the overall angular distribution, $\hat{\phi}$, or the variation from the pre-set angular distribution, $\delta\hat{\phi}$.

Initially, the angular distribution will be completely unknown. Consequently, the initial pre-set angles will be quite arbitrary. By successive refinements of the pre-set angles, a better approximation of the angular distribution can be obtained, and consequently a closer description of the system. This can be repeated until the corrective refinements become negligibly small and the system converges to an acceptable solution.

8.4.4 Boundary Conditions

The boundary condition in the x-direction is periodic and has been described in section 8.2.3. The boundary condition the y-direction is simply the pre-tilt angle of the liquid crystal at the substrate interface, described in section 4.2.1, typically 1-2°. This can be applied as a prescribed boundary condition, setting the nodal values at the substrate boundary to the appropriate value, or the variation of the angle to zero, depending on whether $\hat{\phi}$ or $\delta\hat{\phi}$ is being solved for. These nodal values can be treated as described in section 3.2.4.

8.5 The Iterative Model

In section 8.2.5, we saw that by partitioning the problem into two dependent solutions for the potential and angular distributions, the interdependence of the two distributions required that the partitioned model be iterative. Successive refinements of the approximate distributions being used to inform the next approximation. The electro-static model, described in section 8.3, can produce an approximation of the potential distribution given an approximate angular distribution. Due to the non-linearities of the elastic model, described in section 8.4, an initial approximation of the angular distribution, as well as the potential distribution, is required to pro-

duce a solution. The model is a localized, small angle approximation of the system, which provides a refinement to the angular distribution. By the iterative refinement of the angular approximation, the model can converge to an acceptable approximate solution.

Initially, the angular distribution is not known. Consequently, the initial approximation of the model is likely to be very poor. The partitioning of the problem also means that the relationship between the changes in the potential and angular distributions are not explicitly accounted for in either of the two calculation steps. This may be detrimental to the convergence rate of the model to an acceptable solution. With knowledge of successive estimates and refinements of the angular distribution, techniques could be employed to accelerate the search for a good approximation and the subsequent convergence of the model. Successive refinements could either be extrapolated or interpolated, for example. This will be discussed further in Chapter 10.

8.6 Degrees of Approximation

Whether the energy is minimized with respect to the overall angular distribution, $\hat{\phi}$, or the variation from the pre-set angular distribution, $\delta\hat{\phi}$, and the choice of which terms of the angular distribution function, $\hat{\phi}$, are included in the small angle approximation, give rise to various degrees of approximation. It is these degrees of approximation that will now be considered.

Initially, following the stated intention of taking the simplest and most direct approach, the broadest approximations were taken. This was found not to converge, the reason for this will be dealt with in section 8.7, but it was suspected at the time that the fault lay in some of the approximations used. Consequently, a model was developed which took the least amount of approximations possible. Far from solving the problem, more complications were found. Once these problems had been addressed a third model, which was a compromise between the first two, was developed.

The three levels of approximation used can be summarized by;

- solving in terms of the total angular distribution, $\hat{\phi}$, and including the pre-set variation of the director within each element in the small angle approximations,
- solving in terms of the variation from the pre-set angular distribution, $\delta\hat{\phi}$, and excluding the pre-set variation of the director within the element from the small angle approximations,
- solving in terms of the variation from the pre-set angular distribution, $\delta\hat{\phi}$, and including the pre-set variation of the director within the element in the small angle approximations.

Each of these three levels of approximation will be dealt with in turn.

8.6.1 The Simplest Approximation

The Elastic Term

In order to solve for the total angular distribution, it was necessary to group the pre-set spatial variation within the element and the small variation terms together;

$$\hat{\phi} = \phi_c + \delta\phi_c + \omega_1 x + \omega_2 y \tag{8.24}$$

The small angle approximations can be applied to the ω terms, which represent the spatial variation of the director across the element. Applying this to the director, it becomes;

$$\begin{bmatrix} n_\iota \\ n_\kappa \\ n_\lambda \end{bmatrix} = \begin{bmatrix} 0 \\ \omega_1 x + \omega_2 y \\ 1 \end{bmatrix} \tag{8.25}$$

ignoring second order terms. This is clearly a pared back version of the director description, equation (2.7), used in the development of Frank's equation. Applying this to the elastic energy density expression;

$$f_K^e = \frac{K_{11}}{2}\left(-\omega_1 \sin\phi_c + \omega_2 \cos\phi_c\right)^2 + \frac{K_{33}}{2}\left(\omega_1 \cos\phi_c + \omega_2 \sin\phi_c\right)^2 \tag{8.26}$$

it is clear that since the ω terms represent the unknowns of the problem and every term contains a second order ω, the average director orientation must be treated

as a constant and not allowed to vary. This is a consequence of solving for the whole angular distribution and not taking advantage of the knowledge of the pre-set spatial variation of the director within the element. The implication in the model is that the variation of the average director orientation, $\delta\phi_c$, is not accounted for in the form of the elastic constants.

The energy density for each element is spatially independent, hence simplifying the integration over the element, to obtain the energy contribution of the element, F_K^e. Substituting in the function parameters in terms of the nodal values;

$$\begin{aligned} \omega_1 &= \frac{\bar{\phi}_2 - \bar{\phi}_1}{b} \\ \omega_2 &= \frac{\bar{\phi}_3 - \bar{\phi}_1}{c} \end{aligned}$$

it can be shown that the elementary contribution to the energy minimization of the elastic term is given by;

$$\begin{bmatrix} \partial F_K^e/\partial\bar{\phi}_1 \\ \partial F_K^e/\partial\bar{\phi}_2 \\ \partial F_K^e/\partial\bar{\phi}_3 \end{bmatrix} =$$

$$\frac{1}{4\Delta}\begin{bmatrix} c^2 A_{11} + b^2 A_{22} + 2bc A_{12} & -c^2 A_{11} - bc A_{12} & -b^2 A_{22} - bc A_{12} \\ -c^2 A_{11} - bc A_{12} & c^2 A_{11} & bc A_{12} \\ -b^2 A_{22} - bc A_{12} & bc A_{12} & b^2 A_{22} \end{bmatrix}\begin{bmatrix} \bar{\phi}_1 \\ \bar{\phi}_2 \\ \bar{\phi}_3 \end{bmatrix} \tag{8.27}$$

where

$$\begin{aligned} A_{11} &= K_{11}\sin^2\phi_c + K_{33}\cos^2\phi_c \\ A_{12} &= (K_{33} - K_{11})\cos\phi_c \sin\phi_c \\ A_{22} &= K_{11}\cos^2\phi_c + K_{33}\sin^2\phi_c \end{aligned} \tag{8.28}$$

This is very similar in form to the electro-static model equations (8.9 & 8.10), which is not unexpected as both the electro-static and elastic systems are anisotropic physical systems, being described mathematically as energy minimizations.

Applying the small angle approximations, equations (8.20 & 8.21), gives;

$$\begin{aligned} f_e^e &= \frac{\varepsilon}{2}\Big\{\Big[\alpha_1^2(\varepsilon_o \sin^2\phi_o + \varepsilon_e \cos^2\phi_o) \\ &+ 2\alpha_1\alpha_2(\varepsilon_e - \varepsilon_o)\cos\phi_o \sin\phi_o \\ &+ \alpha_2^2(\varepsilon_o \cos^2\phi_o + \varepsilon_e \sin^2\phi_o)\Big] \\ &+ \delta\phi\,(\varepsilon_e - \varepsilon_o)\left[\left(\alpha_2^2 - \alpha_1^2\right)\sin 2\phi_o + 2\alpha_1\alpha_2 \cos 2\phi_o\right] \\ &+ \delta\phi^2\,(\varepsilon_e - \varepsilon_o)\left[\left(\alpha_2^2 - \alpha_1^2\right)\cos 2\phi_o + 2\alpha_1\alpha_2 \sin 2\phi_o\right]\Big\} \end{aligned} \tag{8.29}$$

This is consistent of a Taylor's expansion of the electrical energy density;

$$f_e\,(\phi_o + \delta\phi) = f_e\,(\phi_o) + \frac{\partial f_e\,(\phi_o)}{\partial\phi}\cdot\delta\phi + \frac{\partial^2 f_e\,(\phi_o)}{\partial\phi^2}\cdot\frac{\delta\phi^2}{2} + \cdots$$

If the $\delta\phi^2/2$ is omitted from the small angle approximations, equations (8.20 & 8.21), the $\delta\phi^2$ of f_e becomes;

$$\alpha_1^2(\varepsilon_o \cos^2\phi_o + \varepsilon_e \sin^2\phi_o) - 2\alpha_1\alpha_2(\varepsilon_e - \varepsilon_o)\cos\phi_o \sin\phi_o + \alpha_2^2(\varepsilon_o \sin^2\phi_o + \varepsilon_e \cos^2\phi_o)$$

which is inconsistent with the Taylor's expansion. This illustrates the importance of the $\delta\phi^2/2$ term in the small angle approximation. This inappropriate term was used in early developments of the model. In the higher order elastic terms below, the $\delta\phi^2/2$ term also makes a significant difference.

The simplest form of the electrical term is developed by including all but the average, pre-set orientation, ϕ_c, in the small angle approximation;

$$\begin{aligned} \phi_o &= \phi_c \\ \delta\phi &= \delta\phi_c + \omega_1 x + \omega_2 y \end{aligned}$$

where

$$\delta\phi_c = \frac{\left(\bar{\phi}_1 + \bar{\phi}_2 + \bar{\phi}_3\right) - \left(\bar{\phi}_{o1} + \bar{\phi}_{o2} + \bar{\phi}_{o3}\right)}{3}$$

Consequently, the terms in the square brackets of equation (8.29), are spatial invariant, simplifying the integration of the energy density. The integrals of the spatially variant parts being given by;

$$\begin{aligned} \int_{\mathcal{D}_e} d\mathcal{D} &= \Delta \\ \int_{\mathcal{D}_e} \delta\phi d\mathcal{D} &= \Delta\delta\phi_c \\ \int_{\mathcal{D}_e} \delta\phi^2 d\mathcal{D} &= \Delta\left(\delta\phi_c^2 + \frac{1}{36}\left\{\left(\bar{\phi}_2 - \bar{\phi}_1\right)^2 + \left(\bar{\phi}_3 - \bar{\phi}_1\right)^2 + \left(\bar{\phi}_3 - \bar{\phi}_2\right)^2\right\}\right) \end{aligned}$$

The element contribution to the energy minimization is then given by;

$$\begin{bmatrix} \partial F_e^e/\partial\bar{\phi}_1 \\ \partial F_e^e/\partial\bar{\phi}_2 \\ \partial F_e^e/\partial\bar{\phi}_3 \end{bmatrix} = \frac{\varepsilon\Delta}{6}\begin{bmatrix} 2E_2 & E_2 & E_2 \\ E_2 & 2E_2 & E_2 \\ E_2 & E_2 & 2E_2 \end{bmatrix}\begin{bmatrix} \bar{\phi}_1 \\ \bar{\phi}_2 \\ \bar{\phi}_3 \end{bmatrix} + \frac{\varepsilon\Delta}{6}\begin{bmatrix} E_1 - \phi_c E_2 \\ E_1 - \phi_c E_2 \\ E_1 - \phi_c E_2 \end{bmatrix} \tag{8.30}$$

where the E terms are from the electrical density equation;

$$f_e = \frac{\varepsilon}{2}\left\{E_0 + \delta\phi E_1 + \delta\phi^2 E_2\right\}$$

This electrical contribution is subtracted from the elastic contribution, noting the definition of the electrical Gibbs free energy, given in Appendix A.

8.6.2 The Richest Approximation

The simplest form of the model was the first to be encoded, it was however, found not to converge. It was suspected that this was because of some of the approximations used, this prompted the development of a model which took the smallest possible number of approximations. The perceived faults with the simplest model were;

- the variation of the average director orientation in each element was neglected in the elastic term,
- the spatial, pre-set variation of the director within each element was not expected to decrease as the solution converged, consequently the small angle approximations which include these terms were not expected to improve with the iterative refinement.

Consequently, a refined model was developed which;

- solved the problem in terms of the variation from the pre-set angles, $\delta\hat{\phi}$, to allow for the variation of the average director to be accounted for,
- only allowed the inclusion of the variable terms, $\delta\hat{\phi}$, in the small angle approximation, the pre-set spatial variation being treated as a large angle.

Applying these stricter approximations to the director;

$$\begin{bmatrix} n_\iota \\ n_\kappa \\ n_\lambda \end{bmatrix} = \begin{bmatrix} 0 \\ \sin\hat{\beta} + \hat{\gamma}\cos\hat{\beta} \\ \cos\hat{\beta} - \hat{\gamma}\sin\hat{\beta} \end{bmatrix} \tag{8.31}$$

ignoring square terms, where

$$\begin{aligned} \hat{\beta} &= \beta_1 x + \beta_2 y \\ \hat{\gamma} &= \gamma_1 x + \gamma_2 y \end{aligned}$$

hence,

$$\begin{aligned} \frac{\partial n_\kappa}{\partial x} &= \beta_1\left(\cos\hat{\beta} - \hat{\gamma}\sin\hat{\beta}\right) - \gamma_1\cos\hat{\beta} \\ \frac{\partial n_\kappa}{\partial y} &= \beta_2\left(\cos\hat{\beta} - \hat{\gamma}\sin\hat{\beta}\right) - \gamma_2\cos\hat{\beta} \end{aligned}$$

The average director orientation can include a variable component; $\hat{\phi_c} = \phi_c + \delta\phi_c$, which can be applied to the element elastic energy density, equation (8.17), which becomes;

$$\begin{aligned} f_K^\varepsilon &= \{2\delta\phi_c[(K_{11}-K_{33})(\beta_1\sin\phi_c - \beta_2\cos\phi_c)(\beta_1\cos\phi_c + \beta_2\sin\phi_c)] \\ &+ 2\gamma_2[-K_{11}(\beta_1\sin\phi_c - \beta_2\cos\phi_c)\cos\phi_c + K_{33}(\beta_1\cos\phi_c + \beta_2\sin\phi_c)\sin\phi_c] \\ &+ 2\gamma_1[-K_{11}(\beta_1\sin\phi_c - \beta_2\cos\phi_c)\sin\phi_c + K_{33}(\beta_1\cos\phi_c + \beta_2\sin\phi_c)\cos\phi_c] \\ &+ \delta\phi_c^2[K_{11}(\beta_1\cos\phi_c + \beta_2\sin\phi_c)^2 + K_{33}(\beta_1\sin\phi_c - \beta_2\cos\phi_c)^2] \\ &+ 2\delta\phi_c\gamma_2[-(K_{11}-K_{33})((\beta_1\cos\phi_c + \beta_2\sin\phi_c)\cos\phi_c - (\beta_1\sin\phi_c - \beta_2\cos\phi_c)\sin\phi_c)] \\ &+ 2\delta\phi_c\gamma_1[(K_{11}-K_{33})((\beta_1\cos\phi_c + \beta_2\sin\phi_c)\sin\phi_c + (\beta_1\sin\phi_c - \beta_2\cos\phi_c)\cos\phi_c)] \\ &+ 2\gamma_2^2[K_{11}\cos^2\phi_c + K_{33}\sin^2\phi_c] \\ &+ 2\gamma_1\gamma_2[(K_{33}-K_{11})\cos\phi_c\sin\phi_c] \\ &+ 2\gamma_1^2[K_{11}\sin^2\phi_c + K_{33}\cos^2\phi_c]\}\cos^2\hat{\beta} \\ &+ \{2[-K_{11}(\beta_1\sin\phi_c - \beta_2\cos\phi_c)^2 - K_{33}(\beta_1\cos\phi_c + \beta_2\sin\phi_c)^2] \\ &+ 2\delta\phi_c[2(K_{11}-K_{33})(\beta_1\sin\phi_c - \beta_2\cos\phi_c)(\beta_1\cos\phi_c + \beta_2\sin\phi_c)] \\ &+ 2\gamma_2[K_{11}(\beta_1\sin\phi_c - \beta_2\cos\phi_c)\cos\phi_c - K_{33}(\beta_1\cos\phi_c + \beta_2\sin\phi_c)\sin\phi_c] \\ &+ 2\gamma_1[-K_{11}(\beta_1\sin\phi_c - \beta_2\cos\phi_c)\sin\phi_c + K_{33}(\beta_1\cos\phi_c + \beta_2\sin\phi_c)\cos\phi_c]\}\hat{\gamma}\cos\hat{\beta}\sin\hat{\beta} \\ &+ \{[K_{11}(\beta_1\sin\phi_c - \beta_2\cos\phi_c)^2 + K_{33}(\beta_1\cos\phi_c + \beta_2\sin\phi_c)^2]\}\hat{\gamma}^2\sin^2\hat{\beta} \end{aligned} \tag{8.32}$$

The γ_1^2, $2\gamma_1\gamma_2$ & γ_2^2 terms correspond with the A_{11}, A_{12} & A_{22} terms, equation (8.29), of the simplest formularization. The $\delta\phi_c$ & $\delta\phi_c^2$ terms represent the effect of the variation of the average director. The $\delta\phi_c^2$ requires the square terms of the small angle approximations, equations (8.20 & 8.21), in a similar way as the E_2 term of

the electrical term, equation (8.29). The γ_1 & γ_2 arise out of the split between the pre-set spatial variation and the variation from the pre-set angles. The $\hat{\gamma}$ & $\hat{\gamma}^2$ terms arise from the large angle form of $\hat{\beta}$ in the sinusoidal functions.

The Electrical Term

The electrical equation is of the same form as equation (8.29), but with a different division of terms;

$$\begin{aligned} \hat{\phi}_o &= \phi_c + \beta_1 x + \beta_2 y \\ \delta\hat{\phi} &= \delta\phi_c + \gamma_1 x + \gamma_2 y \end{aligned}$$

Integration of the Energy Density Expression

The energy density expression has the following spatially variant terms; $\cos^2\hat{\beta}$, $\hat{\gamma}\cos\hat{\beta}\sin\hat{\beta}$ & $\hat{\gamma}^2\sin^2\hat{\beta}$ in the elastic term and 1, $\delta\hat{\phi}$ & $\delta\hat{\phi}^2$ combined with $\cos^2\hat{\phi}_o$, $\cos\hat{\phi}_o\sin\hat{\phi}_o$ & $\sin^2\hat{\phi}_o$ in the electrical term. These terms clearly complicate the integration of the energy density term over the element. Consider the integration by parts of the functions; u, a polynomial up to second order with respect to the spatial coordinates, and v, a sinusoidal function of the spatial coordinates. The complete expansion of

$$\int\int_{\mathcal{D}_e} u\frac{d^2v}{dx\,dy}dx\,dy$$

given in Appendix D, produces 4 terms if u is constant, 12 terms if u is linear, and 24 terms if u is quadratic, with respect to the spatial variables. It is important to note that the functions $\hat{\gamma}$ and $\delta\hat{\phi}$ which are represented by u are in terms of the unknown variables, consequently, each derivative of u at each of the four sets of limits of the integration, will produce a different form of contribution to the k-element matrix.

A further complication to the integration is possibility that the variation of pre-set director orientations between pairs of nodes may be zero or non-zero. This has a great influence on the integration results, for example;

$$\int\cos\hat{\beta}dx = \left[\frac{\sin\hat{\beta}}{\beta_2}\right] \qquad \beta_2 \neq 0 \quad \bar{\phi}_{o1} \neq \bar{\phi}_{o2}$$

$$\int\cos\hat{\beta}dx = \left[x\cos\hat{\beta}\right] \qquad \beta_2 = 0 \quad \bar{\phi}_{o1} = \bar{\phi}_{o2}$$

this consideration applies to every pair of nodal values, consequently there are five possible forms of the resulting integration:

1. $\bar{\phi}_{o1} \neq \bar{\phi}_{o2}$, $\bar{\phi}_{o1} \neq \bar{\phi}_{o3}$, $\bar{\phi}_{o2} \neq \bar{\phi}_{o3}$
2. $\bar{\phi}_{o1} = \bar{\phi}_{o2}$, $\bar{\phi}_{o1} \neq \bar{\phi}_{o3}$, $\bar{\phi}_{o2} \neq \bar{\phi}_{o3}$
3. $\bar{\phi}_{o1} \neq \bar{\phi}_{o2}$, $\bar{\phi}_{o1} = \bar{\phi}_{o3}$, $\bar{\phi}_{o2} \neq \bar{\phi}_{o3}$
4. $\bar{\phi}_{o1} \neq \bar{\phi}_{o2}$, $\bar{\phi}_{o1} \neq \bar{\phi}_{o3}$, $\bar{\phi}_{o2} = \bar{\phi}_{o3}$
5. $\bar{\phi}_{o1} = \bar{\phi}_{o2} = \bar{\phi}_{o3}$,

A full developement of these terms is provided in Appendix D.

Switching between Integration Cases

The development of the richest approximation is clearly complicated by the large number of integration terms and the provision of the five possible integration cases for each element. In order to successfully implement the model it was found that the criteria used to select the appropriate integration case was critical. Consider the integration of $\cos \hat{\phi}_o$ over an element using the results in Appendix D, if the element is flat, $\bar{\phi}_{o1} = \bar{\phi}_{o2} = \bar{\phi}_{o3} = \phi_c$, case 5;

$$\int_{\mathcal{D}_e} \cos^2 \hat{\phi}_o d\mathcal{D} = \triangle \cos^2 \phi_c$$

if there is a slight shift in the nodal values;

$$\begin{aligned} \bar{\phi}_{o1} &= \phi_c - \Delta\phi \\ \bar{\phi}_{o2} &= \phi_c + \Delta\phi \\ \bar{\phi}_{o1} &= \phi_c \end{aligned}$$

then the results of case 1 are required;

$$\begin{aligned} \int_{\mathcal{D}_e} \cos^2 \hat{\phi}_o d\mathcal{D} &= \triangle \left(\frac{6\phi_3^2 - (3 + 3\cos 2\phi_3)}{12(\phi_3 - \phi_2)(\phi_2 - \phi_1)} \right) \\ &- \triangle \left(\frac{6\phi_2^2 - (3 + 3\cos 2\phi_2)}{12(\phi_3 - \phi_2)(\phi_2 - \phi_1)} \right) \\ &- \triangle \left(\frac{6\phi_3^2 - (3 + 3\cos 2\phi_3)}{12(\phi_3 - \phi_1)(\phi_2 - \phi_1)} \right) \\ &+ \triangle \left(\frac{6\phi_1^2 - (3 + 3\cos 2\phi_1)}{12(\phi_3 - \phi_1)(\phi_2 - \phi_1)} \right) \end{aligned}$$

using the small angle expansions;

$$\begin{aligned}\cos 2\Delta\phi &\approx 1 - 2\Delta\phi^2 + \frac{2}{3}\Delta\phi^4 \\ \sin 2\Delta\phi &\approx 2\Delta\phi - \frac{4}{3}\Delta\phi^3\end{aligned}$$

it can be shown that the integral reduces to;

$$\int_{\mathcal{D}_e} \cos^2\hat{\phi}_o d\mathcal{D} \approx \Delta\left\{\cos^2\phi_c - \frac{\Delta\phi^2}{6}\cos 2\phi_c\right\}$$

with all but the $\Delta\phi^2$ terms and higher subtracting exactly. As a consequence of this subtraction, the calculation is very susceptible to noise associated with rounding or truncation errors. The calculation is conducted in FORTRAN DOUBLE PRECISION numbers, which have ~ 15 decimal places of precision. Consider the evaluation of the integral where $\Delta\phi$ is of the order 10^{-N}. As part of the construction of the terms which make up the integral result, constant terms are combined with terms which can be constructed from a power series of $\Delta\phi$. When the terms are combined, all terms with up to $\Delta\phi^2$ are subtracted exactly, consequently the resulting term is only accurate up to the $15 + \log 10|\Delta\phi^2| = 15 - 2N$ decimal places. If $N > 8$ then the resulting number is swamped completely by the rounding or truncation noise of the calculation and the result will be erroneous. The $\Delta\phi^2$ term represents the result that would be obtained if the calculation was made assuming the element was flat, case 5. The $\Delta\phi^4$ term carries the first variation from the flat case, consequently it is only worth while calculating integral in the non-flat case if this first variation is distinguishable from the noise. This consideration gives the general expression;

$$N < \frac{D}{O} \tag{8.33}$$

for the criteria of using a non-flat case, where N is given by the order of the variation of the angles; $\Delta\phi \sim 10^{-N}$, D is the number of significant figures of the calculation ($\sim$ 15), and O is the first order of the spatial variation term which produces a variation from the flat case.

More generally, the angular functions can be expressed as double angles, the spatially variant part, $\hat{\beta}$, split from the average orientation, ϕ_c, and a small angle expansion applied to the spatially variant terms;

$$\cos^2\hat{\phi}_o = \frac{1}{2} + \left(\frac{1}{2} - \hat{\beta}^2\right)\cos 2\phi_c - \hat{\beta}\sin 2\phi_c$$

$$
\begin{aligned}
\sin^2\hat{\phi}_o &= \frac{1}{2} - \left(\frac{1}{2} - \hat{\beta}^2\right)\cos 2\phi_c + \hat{\beta}\sin 2\phi_c \\
\sin\hat{\phi}_o\cos\hat{\phi}_o &= \left(\frac{1}{2} - \hat{\beta}^2\right)\sin 2\phi_c + \hat{\beta}\cos 2\phi_c \\
\cos^2\hat{\beta} &= 1 - \hat{\beta}^2 \\
\sin^2\hat{\beta} &= \hat{\beta}^2 \\
\sin\hat{\beta}\cos\hat{\beta} &= \hat{\beta}
\end{aligned}
$$

The integrals of the spatially variant parts are given by;

$$
\begin{aligned}
\int_{\mathcal{D}_e} d\mathcal{D} &= \Delta \\
\int_{\mathcal{D}_e} \hat{\beta} d\mathcal{D} &= 0 \\
\int_{\mathcal{D}_e} \hat{\beta}^2 d\mathcal{D} &= \frac{\Delta}{36}\left(\left(\bar{\phi}_{o2} - \bar{\phi}_{o1}\right)^2 + \left(\bar{\phi}_{o3} - \bar{\phi}_{o1}\right)^2 + \left(\bar{\phi}_{o3} - \bar{\phi}_{o2}\right)^2\right) \qquad (8.34)
\end{aligned}
$$

Clearly, the first significant deviation from the flat is the $\hat{\beta}^2$ term. Substituting the variations of the above example calculation gives;

$$\int_{\mathcal{D}_e} \hat{\beta}^2 d\mathcal{D} = \frac{\Delta\,\Delta\phi^2}{6}$$

agreeing with the resulting approximation.

In the above calculation, the first deviation from the flat case was given by the $O = 4$ term, therefore $N < 4$, which is appropriate for situations where $u = 1$ and only the first level of the integration terms are used. In cases where u is linear or quadratic in form, higher level integral results are required to construct the terms. It was observed from the integration results, Appendix D, the highest common denominators are in terms of $\Delta\phi^3$ and $\Delta\phi^4$ for linear and quadratic u, respectively. Noting that the first variation from the flat is expected to be carried by terms multiples of $\Delta\phi^2$ higher, it is expected that $N < 3$ and $N < 2$ will be suitable criteria for linear and quadratic u, respectively.

By selecting a non-flat integration result when $\Delta\phi > 10^{-4}, 10^{-3}, 10^{-2}$, depending on the order of u, the smoothest transition between integration results is achieved. It must be noted that the noise levels, near the change over level, are approaching the threshold value of $\Delta\phi^2$ in the integral result, which is not insignificant considering the precision the rest of the calculation is conducted at. There is also a discontinuous change in integration results of the size of the threshold $\Delta\phi^2$, for results of elements

on either side of the threshold level. These considerations suggest that a significant level of noise and discontinuity in results is present in the calculation, which is potential detrimental to the accuracy and stability of the results. Instability, is observed in the convergence of this model.

8.6.3 The Compromise Approximation

In trying to improve the approximation of the model the required integration of the complicated spatial functions brought about several undesirable consequences; large rounding or truncation errors, discontinuities in the integration results for small changes in angle and high computational overheads. All these consequences arose from the treatment of the pre-set spatial variation of the director within the element as a large angle term. A third model was developed with the pre-set spatial variation included in the small angle approximation, but maintaining the split between the pre-set angles and the variation from them, hence solving the problem with respect to the variation from the pre-set angles, $\delta\hat{\phi}$.

The Elastic Term

The director is approximated by;

$$\begin{bmatrix} n_\iota \\ n_\kappa \\ n_\lambda \end{bmatrix} = \begin{bmatrix} 0 \\ (\beta_1 + \gamma_1)\, x + (\beta_2 + \gamma_2)\, y \\ 1 \end{bmatrix} \tag{8.35}$$

Consequently, the elastic energy density becomes identical with equation (8.32), but with $\cos\hat{\beta} = 1$ and $\sin\hat{\beta} = 0$. This contains many of the extra terms of the richest approximation, without the spatial sinusoidal terms.

The Electrical Term

The electrical term is of the same form as equation (8.29), but with the division of terms;

$$\begin{aligned} \phi_o &= \phi_c \\ \delta\phi &= \delta\phi_c + (\beta_1 + \gamma_1)\, x + (\beta_2 + \gamma_2)\, y \end{aligned}$$

This compromise approximation requires that the spatial variation of the director across each element is small enough to be included in the small angle approximation, without degrading the accuracy of the model significantly. It was noted in the previous section that the first variation from the flat approximation of the integral results is given by equation (8.34). This consideration can be included in the adaptive mesh refinement strategy, ensuring that the elements are reduced to a size where the approximation is valid. This will be dealt with in section 8.8. The electro-static model, section 8.3, also used this approximation to simplify the integration of the energy density over the element.

8.7 The Second Order Electrical Energy Term

In order to understand the failure of the models, discussed in the previous section, to converge, it is instructive to simplify the system. If the anisotropy of the elastic constants is neglected, $K_{11} = K_{22} = K_{33} = K$, then an 'isotropic' approximation of Frank's equation results;

$$f_K = \frac{K}{2}(\nabla.\mathbf{n})^2 \tag{8.36}$$

It has previously been shown that the form of the electrical energy term is a second order Taylor's expansion of the the electrical energy density;

$$f_e = E + E'\delta\mathbf{n} + E''\frac{\delta\mathbf{n}^2}{2} \tag{8.37}$$

Assuming straightforward integration of the terms, the energy minimization can be expressed as;

$$\frac{\partial f_K}{\partial \mathbf{n}} - \frac{\partial f_e}{\partial \mathbf{n}} = 0 \tag{8.38}$$

Solving this with respect to the director distribution, $\mathbf{n} = \mathbf{n}_o + \delta\mathbf{n}$;

$$\mathbf{n} = \frac{E' + \mathbf{n}_o E''}{K\nabla^2 - E''} \tag{8.39}$$

the resulting director distribution is given by the driving electrical term, scaled by the elastic term. The second order electrical term, E'', as well as contributing to the electrical term, also modifies the elastic term, acting as a negative elastic contribution.

Solving with respect to the changes in director distribution;

$$\delta \mathbb{m} = \frac{E' - K\nabla^2 \mathbb{m}_o}{K\nabla^2 - E''} \tag{8.40}$$

the change in director being given by the balancing of the electrical driving force and the elastic restoring force produced by the pre-set director distribution, $\mathbb{m}_o$. Clearly, when these two forces are balanced there is no change in the director distribution. Again, this is scaled by the elastic term, modified by the second order electrical term.

This provides a very good description of the system at low voltages, at higher voltages, however, problems arise. Consider the case when the second order electrical term cancels exactly the elastic term; $E'' = K\nabla^2$, infinite director orientations or changes in director orientation result, which are clearly erroneous and physically meaningless. At larger voltages; $E'' > K\nabla^2$, director distributions which are orientated against the applied field, or changes in director orientation away from the equilibrium of the forces, result. In this case the model is being pushed away from the required solution director distribution, due to the detrimental influence of the second order electrical term on the denominator. It was found that the threshold at which the influence of the second order term became detrimental to the model corresponded with the threshold voltage of the cell, equation (2.13). Consequently the second order term was dropped from the model. This reduced the description of the model, but ensured its stability and its eventual convergence. Whether or not the second order term should remain in the numerator, corresponding to the constant terms, v_p, of a finite element formularization, equation (3.14), is an open question.

8.8 Error Estimation and Adaptive Mesh Refinement

The error of the finite element approximation, the estimation of this error, and the use of this error estimation in an adaptive mesh refinement strategy to optimally redesign the mesh in order to achieve a required accuracy, have been discussed in Chapter 3. The application of these ideas to the specific formularization presented in this chapter will now be considered.

8.8.1 Mesh Refinement

The elements used in this formularization are the simplest possible; linear triangular elements based on a rectangular mesh, (figure 3.1). The simplest method of adjusting the element sizes is to modify the dimensions of the rectangular mesh's rows and columns. This strategy can be incorporated without reformularizing the system. The efficiency of such an approach depends on whether the errors of the system resolve into the rectangular components of the global reference frame. As described in Chapter 3, the errors of the finite element approximation are related to the curvature of the underlying solution. The geometry of the system is conveniently rectangular. In the y-direction the liquid crystal is most susceptible to alignment with the field at the centre of the cell, most of the curvature is expected to occur at the edges, where the electrical realignment pulls against the fixed boundary orientation. The curvature in the x-direction is caused by the transverse electric fields, which are expected to be localized about the edges of the electrodes. These two considerations bode well for this rectangularly resolved refinement strategy.

8.8.2 Error Norms

The error norms used are based on the L_2 norm of the first derivatives of the dependent variables along the rectangular coordinate system;

$$\begin{aligned} |\epsilon_x|^2 &= \int_{\mathcal{D}_e} \left(\psi_x^* - \hat{\psi}_x\right)^2 d\mathcal{D} \\ |\epsilon_y|^2 &= \int_{\mathcal{D}_e} \left(\psi_y^* - \hat{\psi}_y\right)^2 d\mathcal{D} \end{aligned}$$

In the linear, finite element approximation, the gradients are constant and the projected gradients, linear;

$$\begin{aligned} \psi_x^* &= \bar{\psi}_x + \bar{\psi}_{xx}\delta^x + \bar{\psi}_{xy}\delta^y \\ \psi_y^* &= \bar{\psi}_y + \bar{\psi}_{yx}\delta^x + \bar{\psi}_{yy}\delta^y \end{aligned}$$

using notation $\delta^x = x - \bar{x}$, $\delta^y = y - \bar{y}$ and $\bar{\psi} = \psi(\bar{x}, \bar{y})$, $\bar{\psi}_x = \partial\psi(\bar{x}, \bar{y})/\partial x$, *etc.*, where $(\bar{x}, \bar{y})$ is the mid-point of the element side which the derivative is tangential to. As can be seen $\bar{\psi}_{xx}$ & $\bar{\psi}_{xy}$ represent the error contributions of the x derivative in the x & y directions, respectively. Similarly, $\bar{\psi}_{yx}$ & $\bar{\psi}_{yy}$ represent the error contributions of the y derivative in the x & y directions, respectively. Errors in the x-direction

can be reduced by scaling the size of the columns, b, independently to the size of the rows, c, which can be altered to reduce the errors in the x-direction. Consequently, the error norms are split into the x and y contributions;

$$\begin{array}{rcccl} |\epsilon_{xx}|_e^2 & = & \int_{\mathcal{D}_e} \left(\bar{\psi}_{xx}\delta^x\right)^2 d\mathcal{D} & = & \frac{\triangle}{18}\bar{\psi}_{xx}^2 b^2 \\ |\epsilon_{xy}|_e^2 & = & \int_{\mathcal{D}_e} \left(\bar{\psi}_{xy}\delta^y\right)^2 d\mathcal{D} & = & \frac{\triangle}{18}\bar{\psi}_{xy}^2 c^2 \\ |\epsilon_{yx}|_e^2 & = & \int_{\mathcal{D}_e} \left(\bar{\psi}_{yx}\delta^x\right)^2 d\mathcal{D} & = & \frac{\triangle}{18}\bar{\psi}_{yx}^2 b^2 \\ |\epsilon_{yy}|_e^2 & = & \int_{\mathcal{D}_e} \left(\bar{\psi}_{yy}\delta^y\right)^2 d\mathcal{D} & = & \frac{\triangle}{18}\bar{\psi}_{yy}^2 c^2 \end{array} \tag{8.41}$$

In addition to the finite element approximations there is the integration approximation that the angular functions can be considered constant across the element, with respect to the integration, section 8.6.3. The error associated with this approximation will also be resolved into rectangular components;

$$\begin{array}{rcccl} |\epsilon_{\beta_2}|_e & = & \int_{\mathcal{D}_e} (\beta_2 x)^2 d\mathcal{D} & = & \frac{\triangle}{18}\beta_2^2 b^2 \\ |\epsilon_{\beta_3}|_e & = & \int_{\mathcal{D}_e} (\beta_3 y)^2 d\mathcal{D} & = & \frac{\triangle}{18}\beta_3^2 c^2 \end{array} \tag{8.42}$$

these error terms are relative to the approximation;

$$\int_{\mathcal{D}_e} \cos^2\hat{\beta} d\mathcal{D} \approx \triangle$$

8.8.3 Error Estimation

The first derivatives of the finite element approximation are given by;

$$\begin{aligned} \hat{\psi}_x &= \frac{\bar{\psi}_2 - \bar{\psi}_1}{b} \\ \hat{\psi}_y &= \frac{\bar{\psi}_3 - \bar{\psi}_1}{c} \end{aligned}$$

which are constant over the element. Pairs of elements, which share the side along which the gradient is evaluated share the same gradient (figure 8.5). It has been shown, in Chapter 3 and Appendix C, that these gradients are exceptionally accurate at the mid-sides of the elements that they are tangential to. These gradients form the basis of the projected, derivative functions, ψ_x^* & ψ_y^*. The nodal values of the projected gradients can be obtained by interpolating the elements values from adjacent sides (figure 8.6);

$$\begin{aligned} \psi^*_{x(i)} &= \frac{\hat{\psi}_{x(i-1)}b_{i-1} + \hat{\psi}_{x(i)}b_i}{b_{i-1} + b_i} \\ \psi^*_{y(j)} &= \frac{\hat{\psi}_{y(j-1)}c_{j-1} + \hat{\psi}_{y(j)}c_j}{c_{j-1} + c_j} \end{aligned}$$

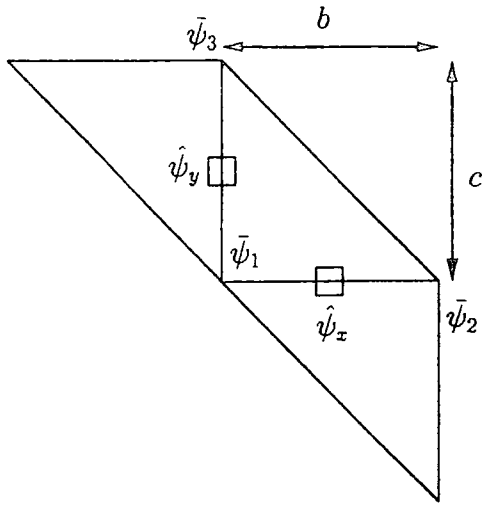

Figure 8.5: Adjacent Elements

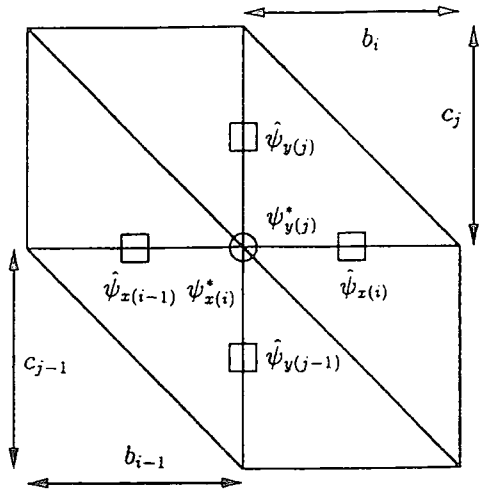

Figure 8.6: Interpolation of Derivatives

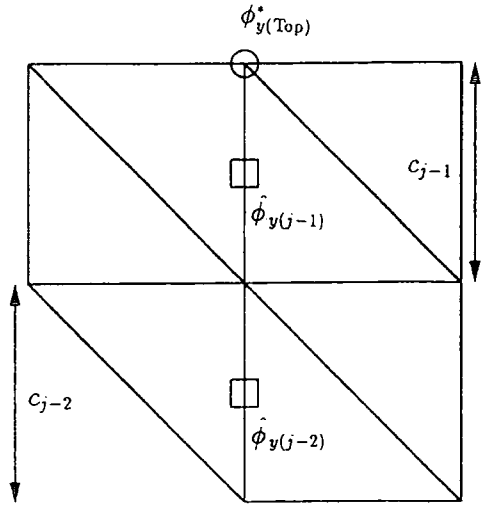

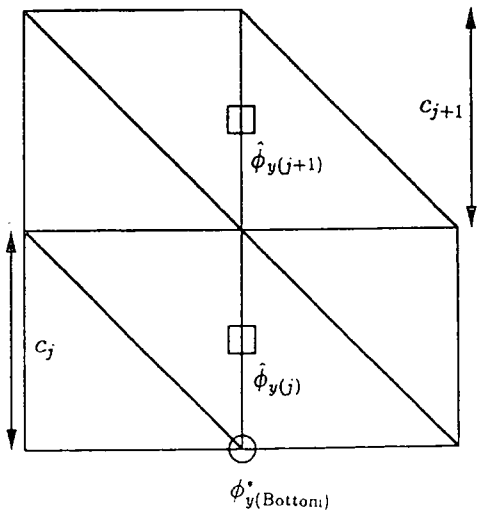

Figure 8.7: Extrapolation of Derivatives

where b_i is the x-dimension of the ith column and c_j is the y-dimension of the jth row. There are, however, regions in the system where this interpolation is inappropriate, these cases will be dealt with in turn.

The y-gradient of the angular function at either of the liquid crystal/substrate interfaces cannot be found be interpolation, but may be obtained by extrapolation from the bulk of the liquid crystal (figure 8.7);

$$\phi^{\circ}_{y(\text{Top})} = \frac{\hat{\phi}_{y(j-1)}(2c_{j-1} + c_{j-2}) - \hat{\phi}_{y(j-2)}c_{j-1}}{c_{j-2} + c_{j-1}}$$

$$\phi^{\circ}_{y(\text{Bottom})} = \frac{\hat{\phi}_{y(j)}(2c_j + c_{j+1}) - \hat{\phi}_{y(j+1)}c_j}{c_j + c_{j+1}}$$

There are no boundaries in the x-direction as the solution area 'wraps round' to form a periodic section.

In the electro-static system, the edge of the region occurs at the far boundary. Extrapolation was found to be inappropriate in this case, since the boundary elements where found to have derivatives, normal to the boundary, very close to zero. This corresponds to the far boundary condition for the normal electric field at infinity, consequently it was considered more appropriate to assign the element values to the nodes on the far boundary.

The electrodes form internal boundaries in the system. The fields inside the electrodes are expected to be zero, screened from the fields outside by surface charge at the interfaces (figure 8.8). The electric fields, and hence the gradients of the potential function, crossing these interfaces are consequently discontinuous. These discontinuities are physical consequences of the system and are not due to the finite element approximation error, it would be inappropriate to allow them to influence the error calculation. Consequently, the bulk of the electrodes are removed from the calculation. The value of the fields normal to the electrode interface, for nodes lying on the interface, are found by extrapolation from outside the electrode, in a similar way to the angular derivatives at the boundary. Special consideration has to be taken at the corners of the electrode (figure 8.9). The field normal to one of the electrode sides passes a charge surface at the corner, consequently the field is discontinuous at the corner node. The node then has two possible values for the field, depending on which side of the charge surface it is being considered. Both these gradients are calculated, by extrapolation from either side, and used appropriately

in the error calculation.

In addition to the free electric charge of the electrode interfaces, there also exists bound electric charge at the dielectric interfaces. This has the effect of making the fields crossing these interfaces discontinuous. It is known, however, that the normal displacement field and the tangential electric field to a dielectric interface are continuous [3, p 316]. The rectangular geometry of the system ensures that all the dielectric interfaces are in the x-direction. Consequently, the discontinuities in field due to the bound surface charge at the dielectric interfaces can be neglected by conducting all the derivative projection in terms of the electric field for the x-derivative, and the displacement field for the y-derivative. The curvature in the potential function due to the continuous director distribution, and hence dielectric properties, throughout the liquid crystal region, is of prime importance in assessing the finite element approximation. Therefore, no account of the changes of these dielectric properties should be made in the evaluation of the curvature in the liquid crystal region. The y component of the field is scaled by the ordinary relative permittivity, ε_o, to provide an appropriate approximation for the displacement field normal to the liquid crystal/substrate interface, assuming a small angle of boundary tilt. The displacement fields are converted back to electric fields or gradients, when the curvature within each element is evaluated.

The local interpolation/extrapolation approach of obtaining the projected derivative functions is very direct and computationally cheap, making it ideal for an error estimator that may be used several times during a solution. One consequence of this method is that the mid-side value of the projected derivative no longer coincides with the finite element value. A refinement of the error estimator may be made by including this shift;

$$
\begin{aligned}
|\epsilon_{xx}|_e^2 &= \Delta\left(\tfrac{1}{2}\left(\bar{\psi}^*_{x(2)} + \bar{\psi}^*_{x(1)}\right) - \hat{\psi}_x\right)^2 + \tfrac{\Delta}{18}\bar{\psi}^2_{xx}b^2 \\
|\epsilon_{xy}|_e^2 &= \Delta\left(\tfrac{1}{2}\left(\bar{\psi}^*_{x(3)} + \bar{\psi}^*_{x(1)}\right) - \hat{\psi}_x\right)^2 + \tfrac{\Delta}{18}\bar{\psi}^2_{xy}c^2 \\
|\epsilon_{yx}|_e^2 &= \Delta\left(\tfrac{1}{2}\left(\bar{\psi}^*_{y(2)} + \bar{\psi}^*_{y(1)}\right) - \hat{\psi}_y\right)^2 + \tfrac{\Delta}{18}\bar{\psi}^2_{yx}b^2 \\
|\epsilon_{yy}|_e^2 &= \Delta\left(\tfrac{1}{2}\left(\bar{\psi}^*_{y(3)} + \bar{\psi}^*_{y(1)}\right) - \hat{\psi}_y\right)^2 + \tfrac{\Delta}{18}\bar{\psi}^2_{yy}c^2
\end{aligned}
$$

where $\bar{\psi}^*_{x(i)}$ represents the value of ψ^*_x at node i of the element (figure 3.1). This refinement has not been incorporated.

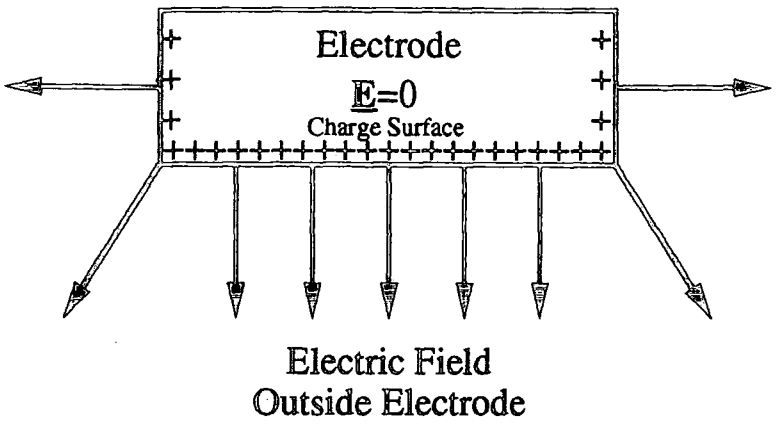

Figure 8.8: Charge Surface at Electrode

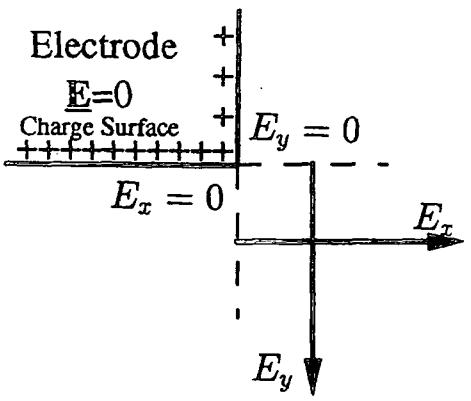

Figure 8.9: Charge Surface at Corner of Electrode

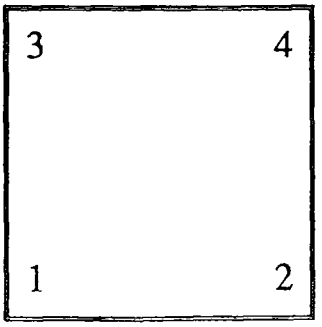

Figure 8.10: Rectangular Mesh Element

The curvature can be expressed in terms of the projected derivative functions;

$$\begin{aligned}
\bar{\psi}_{xx} &= \tfrac{1}{b}(\bar{\psi}^*_{x(2)} - \bar{\psi}^*_{x(1)}) \\
\bar{\psi}_{xy} &= \tfrac{1}{c}(\bar{\psi}^*_{x(3)} - \bar{\psi}^*_{x(1)}) \\
\bar{\psi}_{yx} &= \tfrac{1}{b}(\bar{\psi}^*_{y(2)} - \bar{\psi}^*_{y(1)}) \\
\bar{\psi}_{yy} &= \tfrac{1}{c}(\bar{\psi}^*_{y(3)} - \bar{\psi}^*_{y(1)})
\end{aligned}$$

The error is evaluated for each rectangular mesh element (figure 8.10) as the sum of the squares of the error in the two component triangular elements, and can be shown to be given by;

$$\begin{aligned}
|\epsilon_{xx}|^2_{\text{rect.}} &= \tfrac{\Delta}{18}\left\{(\bar{\psi}^*_{x(4)} - \bar{\psi}^*_{x(3)})^2 + (\bar{\psi}^*_{x(2)} - \bar{\psi}^*_{x(1)})^2\right\} \\
|\epsilon_{xy}|^2_{\text{rect.}} &= \tfrac{\Delta}{18}\left\{(\bar{\psi}^*_{x(4)} - \bar{\psi}^*_{x(2)})^2 + (\bar{\psi}^*_{x(3)} - \bar{\psi}^*_{x(1)})^2\right\} \\
|\epsilon_{yx}|^2_{\text{rect.}} &= \tfrac{\Delta}{18}\left\{(\bar{\psi}^*_{y(4)} - \bar{\psi}^*_{y(3)})^2 + (\bar{\psi}^*_{y(2)} - \bar{\psi}^*_{y(1)})^2\right\} \\
|\epsilon_{yy}|^2_{\text{rect.}} &= \tfrac{\Delta}{18}\left\{(\bar{\psi}^*_{y(4)} - \bar{\psi}^*_{y(2)})^2 + (\bar{\psi}^*_{y(3)} - \bar{\psi}^*_{y(1)})^2\right\}
\end{aligned} \tag{8.43}$$

Similarly, the error associated with the integral approximation is given, for the rectangular element, by;

$$\begin{aligned}
|\epsilon_{\beta_2}|_{\text{rect.}} &= \tfrac{\Delta}{18}\left\{(\bar{\phi}_{(4)} - \bar{\phi}_{(3)})^2 + (\bar{\phi}_{(2)} - \bar{\phi}_{(1)})^2\right\} \\
|\epsilon_{\beta_3}|_{\text{rect.}} &= \tfrac{\Delta}{18}\left\{(\bar{\phi}_{(4)} - \bar{\phi}_{(2)})^2 + (\bar{\phi}_{(3)} - \bar{\phi}_{(1)})^2\right\}
\end{aligned} \tag{8.44}$$

The global errors can be found by the sum of the squares of the rectangular element error terms.

8.8.4 Adaptive Mesh Refinement

The error components; $|\epsilon_{xx}|$, $|\epsilon_{yx}|$, & $|\epsilon_{\beta_2}|$, are improved by refinement of the column parameter, b, and components; $|\epsilon_{xy}|$, $|\epsilon_{yy}|$, & $|\epsilon_{\beta_3}|$, are improved by refinement of the row parameter, c. The refinement parameters, equations (3.42 & 3.45), are constructed for each component of error, within each rectangular element. The appropriate values; $a = 1$ & $n = 1$ were found to produce unstable meshes, a value of $n = 2$ was adopted, to provide a gradual approach to the optimal mesh over several refinements, which improved the stability.

The rectangular based mesh is very rigid and any refinement must be made for an entire row or column. In order to determine the mesh refinement the largest refinement parameter, from the appropriate components of error, were found for each row and column, and the new mesh dimensions calculated using equation (3.43).

It was noted in Chapter 3, that the error refinement parameter was incorrect and a more appropriate parameter, ξ_c, given by equation (3.48), was presented. In order to correctly apply the improved refinement parameter it must be noted that the refinement consists of two one-dimensional refinements, the area of the elements is reduced in only one dimension with each refinement, hence $d = 1$ should be used. The resulting parameter is given by;

$$\xi_c = \frac{(|\epsilon|_e^2 N|\epsilon|)^{\frac{1}{3}}}{\eta|\psi'|} \tag{8.45}$$

where η is the required relative error and N is the number of elements. This corrected refinement parameter has not yet been implemented.

An additional measure was taken to improve the stability of the mesh, to avoid over-depletion the increase in size of any row or column was limited to 10%, by restricting the value of the refinement parameter, $\xi \geq 0.9$.

The problem area consists of rectangular subdomains, whose boundaries should correspond to a row or column of mesh nodes. These boundaries include the liquid crystal, electrode and dielectric interfaces. Consequently, the number of new rows and columns in each sub-section is rounded up and the dimensions appropriately scaled.

Provision was made for the use of enriched refinement about singularities, using $n = \lambda$, the singularity strength, in equation (3.45). It was assumed that the electrode corners would be potential singularities. The result was a large increase in the number of elements required with each remeshing, without any corresponding improvement in the resulting accuracy. This provision was subsequently omitted from the refinement strategy.

From Chapter 3, there are two criteria for determining whether a mesh of required accuracy has been achieved;

- the global criteria, that the total error is below the required accuracy,
- the local criteria, that the error is evenly distributed across the rows and columns of the mesh.

Both these criteria were initially used however, it was subsequently found that when

the local criteria was fulfilled the accuracy was twice that required. The reason for this is not clear, there may be an erroneous factor in the error calculations. At high accuracies, ~5%, the mesh was well behaved. Larger problems, however, could not be solved at these consequently accuracies due to memory restrictions, accuracies of ~10–15% were used. At the lower accuracies the mesh was less well behaved and prone to oscillation, it was found necessary to relax the mesh requirements to the global criteria alone.

It was was suspected that the imperfections in the mesh refinement strategy arose from the following sources:

- The underlying non-linearity of the system,
- The low accuracies worked at fell below the level that the approximations would be self-correcting in successive iterations.
- The imperfections in the adaptive mesh refinement strategy.

Further work is required to improve its performance.

8.9 Summary

The general formularization of the model has been described, simplicity and directness of approach were important considerations in its development. The key features of the formalization are;

- the restriction of the problem to two-dimensional sections,
- the use of linear triangular elements based on a rectangular mesh,
- the periodic boundary condition,
- the restriction of the model to one angle of rotation,
- the partition of the problem into an electro-static part and an elastic part.

The electro-static part of the problem was described as the minimization of the electro-static energy with a continuously variable director orientation throughout the

liquid crystal layer. The electrodes were described as internal regions of prescribed voltage. The description of the far boundary was described as a natural boundary condition at a large distance from the solution area.

The elastic formularization was described by an elastic term, the local form of Frank's equation, and an electrical term, a Taylor's expansion of the electrostatic energy, with respect to the angular variable. Small angle approximations were applied to the function in order to solve the angular distribution for a local, linear approximation of the system. The director orientation at the boundaries was prescribed.

These two parts were combined to form an iterative two step model. Successive iterations improved the approximation of the potential and angular distributions throughout the system, hence improving the localized approximations of the system equations.

Three levels of approximation were used to describe the elastic system, these can be summarized;

- solving in terms of the total angular distribution, $\hat{\phi}$, and including the pre-set variation of the director within each element in the small angle approximations,
- solving in terms of the variation from the pre-set angular distribution, $\delta\hat{\phi}$, and excluding the pre-set variation of the director within the element from the small angle approximations,
- solving in terms of the variation from the pre-set angular distribution, $\delta\hat{\phi}$, and including the pre-set variation of the director within the element in the small angle approximations.

It was suspected that the first approximation was too simple as it did not account for the variation of the average director orientation within each element or the large angle effects of the spatial variation of the director across the element. The second approximation was found to introduce; large rounding or truncation errors, discontinuities in the integration results for small changes in angle, and high computational overheads. The third approximation, a compromise between the previous approximations was developed, in which small angle approximations were applied in order

to simplify the integration results.

Consideration of the second order term in the electro-static Taylor's expansion showed it to be detrimental to the convergence of the model, it was consequently removed.

The triangular elements are based on a rectangular mesh, the most direct method of modifying the element sizes was found to be adjusting the row and column dimensions of the mesh. The error estimation and adaptive mesh refinement used was described, and a note made of possible improvements. The error associated with the small angle approximation used for the integration results of both the electro-static and elastic parts of the model, was also incorporated into the adaptive mesh refinement strategy, to ensure the associated error was kept within exceptable limits.

The implementation of this formalization on a computer will be discussed in the next chapter.

8.10 References

[1] P. Lorrain and D. R. Corson. *Electromagnetic Fields and Waves.* 2nd edition, Freeman (1970).

[2] R. P. Feynman, R. B. Leighton and M. L. Sands. *The Feynman Lectures on Physics.* vol. 2 (1964).

[3] W. J. Duffin. *Electricity and Magnetism.* 3rd edition, McGraw-Hill (1980).

Chapter 9

Computer Implementation of the Model

9.1 Introduction

In Chapter 8, the variational finite element formularization of the electrical Gibbs free energy of a liquid crystal device was described. This Chapter will discuss the implementation of this formalization in FORTRAN 77.

The maximum run-time memory was found to be a major restriction to the size of the problems solved, in terms of the number of nodes and elements, hence rows and columns of the system mesh. The memory assignment in FORTRAN is inflexible, for example array sizes are declared as constants of the program. In order to simplify memory handling, whilst attempting to make optimal use of the available memory, the program was split up into discrete sub-programs, controlled by a *script*. This has the advantage of allowing independent memory structures for each sub-program. Data is transferred between the sub-programs via sequential, binary files, for speed and efficient storage.

The form of the controlling *script* will be described and the form of the sub-programs summarized. The major programming considerations will be discussed. The representation of the results will then be described.

9.2 Program Structures

9.2.1 The *Script*

The program was split into modular subprograms, which were run from a *script* which controls the flow of the programs. The *script* is listed and its flow described in Appendix E.1.

Initially, the input file is read and the information transformed and written out in an appropriate form, as binary files, for the rest of the programs.

The main body of the *script* is a loop which is terminated only when the final solution has been found. Within there are several decisions made, according to the point in the procedure the model is at, these are controlled by two variables; *res*, the stage of the result, and *mesh*, a flag which is set if a new mesh is required. The stages of convergence, indicated by *res* are;

4 Initial iteration, set *mesh*.

3 Converging to a solution, clear *mesh*.

2 Remeshing, solution has been reached, set *mesh*.

1 Converging to a final solution, mesh criteria have been satisfied, clear *mesh*.

0 Final solution, exit loop.

The convergence of the solution and the refinement of the mesh have been kept separate. Each of these stages has the potential of being unstable, combining them would undermine the stability of each part and complicate the convergence strategies developed.

The initial mesh is coarse and linearly spaced within each subdomain, the far boundary region being described by a logarithmically spaced mesh. The solution is allowed to converge for this coarse mesh (stage **3**). The convergence criteria is that the maximum change in angle of the iteration has fallen below a certain limit ($\sim 10^{-3}$ radians). Once this has been achieved the mesh is redesigned using the

adaptive mesh refinement strategy described in Chapters 3 & 8 (stage 2). If the change in angle rises above a threshold, the remeshing is stopped and the solution is allowed to converge again (return to stage 3). Once the mesh criteria has been fulfilled, and the reconvergence limit has not been triggered, the solution is allowed to converge for a final time (stage 1) and then the final solution has been found (stage 0).

Provision was made for the solution to be found at several mesh accuracies during solution seeking. The idea was to allow the majority of the solution seeking to be conducted on a coarse, inaccurate mesh and then the final refinements made on the final, high accuracy mesh, hence reducing the computational time of the early stages of the convergence. This is implicitly achieved, since the optimal mesh is converged to through several sub-optimal meshes. The explicit use of low accuracy meshes was found to impractical due to their unstability.

The programs can be summarized;

int	Initializes data files from the input file.
msh	Constructs mesh and interpolates angular distribution.
lp1	Solves electro-static potential.
fr(k/1/2)	Solves director orientation.
fem	Finite element skeleton program, used for **lp1** & **fr(k/1/2)**.
co1	Applies convergence strategies.
er3	Error estimator and adaptive mesh refinement.

The structure of these programs are given in section 9.2.3.

9.2.2 File Structures

All the files were stored as binary, sequential files, with the exception of the `input` and `Aim` files which are ASCII. The input file completely defines the problem to solved in a simple and short form. The values are stored as DOUBLE PRECISION or INTEGERS as appropriate. The file formats are given in Appendix E.2 and can be summarized;

Input	Input file.
Aim	Aims and control information.
LC	Liquid crystal data.
SUB	Subdomain data.
PE	Electrode data.
DIS	Dielectric data.
XY	Row and column dimensions for current mesh.
XYO	Row and column dimensions for old mesh.
PHI	Orientation distribution for current iteration.
DPHI	Change in orientation distribution for current iteration.
PHIO	Orientation distribution for last iteration.
DPHIO	Change in orientation distribution for last iteration.
PHIB	Orientation distribution of buckled iteration.
DPHIB	Change in orientation distribution of buckled iteration.
NODLP	Node numbering for electro-static part.
NODFR	Node numbering for elastic part.
BCLP	Prescribed boundary values for electro-static part.
BCFR(K/1)	Prescribed boundary values for elastic part.
BCFRK	For simplest approximation, the boundary angles.
BCFR1	For other approximations, zero change in angle.

9.2.3 Sub-Programs

The functionality of the sub-programs will now be described.

int: INITIALIZATION

- Read *input* file.
- Convert to SI units.
- Find subdomains in x & y and relate electrode and dielectric interface positions.
- Assign initial mesh, linear divisions in subdomains, except far boundary which is logarithmic in the y-direction.
- Output; Aim, LC, PE, SUB, DIS, XY, XYO, PHI.

msh: MESH CONSTRUCTION

- Input; PE, SUB, XY, XYO, PHI.
- Linear interpolation of angular distribution from the old mesh to the new mesh.
- Node numbering; creates an array of numbers which can be indexed by the x and y indices in the mesh, and contains the position system matrix.
  - Flag prescribed nodes with negative index to array containing prescribed values.
  - Number nodes in order they appear in system matrix, ensuring minimum bandwidth of system matrix.
- Output; NODLP, NODFR, BCLP, BCFRK, BCFR1, PHI.

fem: FINITE ELEMENT METHOD SKELETON

- Input; LC, *DATA, NOD, BC.*
- Assemble system matrix, $\mathbf{k}_{sys}$.

  For each row;
  Set *Row Data.*
  For each upper and lower triangular element in row;
  Obtain node numbers.
  Set *Element Data.*
  Set *Element Matrix*, $\mathbf{k}_{ele}$.
  Add the contribution of the element matrix to the system matrix, accounting for the prescribed node elimination.

- Factorize and solve system matrix.
- Input; *NOD, BC.*
- *Post processing.*
- Output *results.*

Programs:	lp1	frk	fr1	fr2
DATA	PHI XY DIS SUB	PHI XY V		
NOD	NODLP	NODFR		
BC	BCLP	BCFRK	BCFR1	
Row Data	$\varepsilon_o\ \varepsilon_e\ c$	c		
Element Data	$\phi_{o1}\ \phi_{o2}\ \phi_{o3}\ b$	$\phi_{o1}\ \phi_{o2}\ \phi_{o3}\ V_1\ V_2\ V_3\ b$		
Element Matrix As section	8.3	8.6.1	8.6.2	8.6.3
Post Processing		$\delta\phi = \phi - \phi_o$		
Results	V	DPHI		

Table 9.1: Variations on the General Finite Element Method

To avoid repetitive code, a general skeleton finite element program was written in which the specific variations of each model could be slotted in on compilation. These variations are indicated with *italics* and summarized in table 9.1.

er3: Error Estimation and Adaptive Mesh Refinement

- Input; LC, AIM, SUB, DIS, PE, XY.
- Input; V, NODLP.
- Find E_x & D_y for elements then nodes.
- Find errors of potential distribution.
- Find maximum errors of rows and columns.
- Input; PHI, DPHI.
- Find ϕ_x & ϕ_y for elements then nodes.
- Find errors due to orientation distribution.
- Find maximum errors of rows and columns.
- Restrict growth of elements.
- Scale errors to ensure whole number of elements in each subdomain.

- Check for memory overflows.
- Find new mesh dimensions.
- Output; AIM, SUB, XYO, XY.
- Set *res* value.

col: CONVERGENCE CONTROL

- Input; XY, AIM, PHI, DPHI, PHIO, DPHIO, PHIB, DPHIB.
- Find position of maximum change in angle.
- Apply convergence control strategies.
- Output; AIM, PHI, PHIO, DPHIO, PHIB, DPHIB.
- Set *res* value.

9.3 Programming Considerations

9.3.1 Subdomains

In order to accurately define the positions of the liquid crystal, dielectric and electrode interfaces it is necessary for these interfaces to be defined by element boundaries. This allows the physical properties to be constant within the elements and to change discontinuously across the element boundaries. The rectangular geometry of the physical system can be incorporated into the rectangular mesh by defining subdomains in x and y, whose boundaries correspond to the physical boundaries, (figure 9.1). These form a fixed mesh geometry, within which the numbers and dimensions of the rows and columns are free to change.

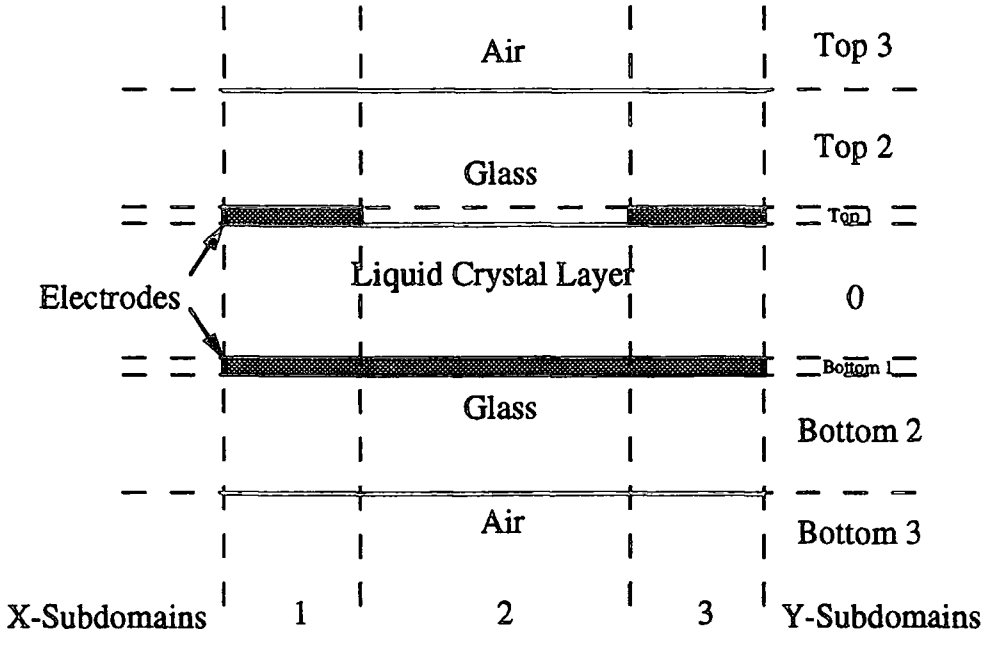

Figure 9.1: Division of the Problem into Subdomains

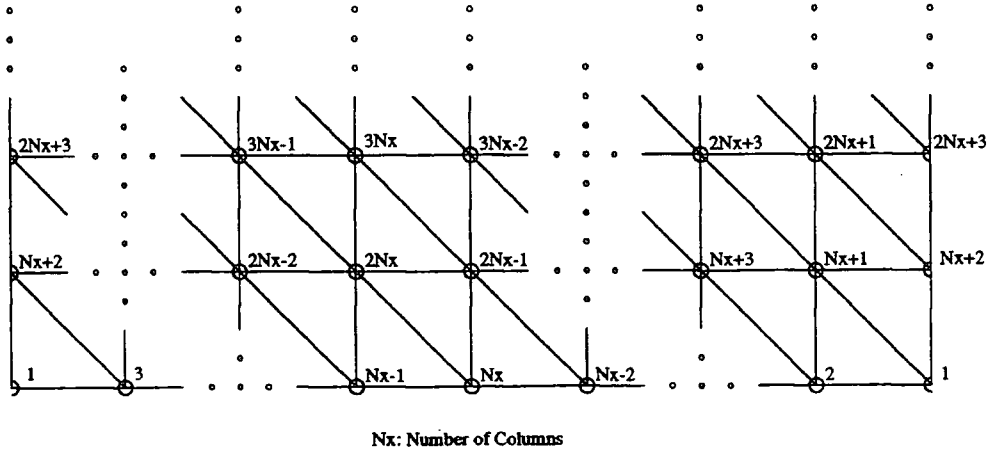

Figure 9.2: Node Numbering Strategy

9.3.2 Mesh Generation

The mesh is defined by the dimensions of the rows and columns from which it is made up. The nodes of the mesh can either be described by their x and y indices or by the order they occur in the system matrix. In order to relate these two types of indexing a two-dimensional array is constructed which can be accessed using the x and y indices, and contains the system matrix index. There are two important considerations in the construction of this node numbering array; accounting for the elimination of the prescribed nodes and ensuring that the band width of the resulting system matrix is at a minimum.

Elimination of Nodes

The nodes which occupy the electrodes of the electro-static model and the boundary liquid crystal of the elastic model have prescribed values, and are eliminated from the system matrix as described in section 3.2.4. These nodes are flagged in the node numbering array by a negative index which refers to an array containing the prescribed values.

Node Numbering

The system matrix is banded, as described in Chapter 3, since only the bandwidth of the matrix need be stored in the run-time memory or be included in the matrix calculation, it is advantageous to ensure that the bandwidth used is the minimum bandwidth possible. The mesh used in this model has a periodic boundary condition which is implemented by making the nodes at one boundary common to the nodes at the other. The node numbering strategy used to achieve the minimum bandwidth for a mesh of this type was found by observation. It is illustrated in figure 9.2 and has the following features:

- From the starting point of each row the nodes are numbered alternatively to the left and right of the starting point.

- The order of the node numbering; left then right or right then left, alternates between rows.
- The position of the starting point, on higher rows, is alternately shifted one node to the left or directly above the starting point of the previous row.
- Numbering is suspended over prescribed nodes.

The resulting system matrix has a bandwidth of $2N_x + 3$, for a mesh with N_x columns.

9.3.3 Factorizing and Solving the System Matrix

The numerical routines used are from the NAG FORTRAN routine library [1, 2, 3].

FACTORIZING: F01LBF

The system matrix $\mathbb{k}_{sys}$ is factorized into a lower unit triangular matrix $\mathbb{L}$ and a singular upper triangular matrix $\mathbb{U}$; $\mathbb{k}_{sys} = \mathbb{LU}$ via Gaussian elimination. Partial pivoting with row exchange is used to ensure numerical stability.

The major memory requirments for this program are an array of integers containing the pivotal information, of length equal to the number of nodes, the system matrix of size; bandwidth by number of nodes, this contains the upper matrix on the return of the function, and the lower triangular matrix of size; half bandwidth by the number of nodes.

SOLVING: F04LDF

This solves $\mathbb{k}_{sys}\bar{\psi} = \mathbb{b}$, where $\mathbb{k}_{sys}$ has been factorized by the above routine. $\mathbb{b}$ is subject to the same procedure used to reduce $\mathbb{k}_{sys}$ to upper triangular form. This gives matrix $\mathbb{c} = \mathbb{L}^{-1}\mathbb{P}^T\mathbb{b}$ and the upper triangular system $\mathbb{U}\bar{\psi} = \mathbb{c}$ is then solved by backwards substitution to give $\bar{\psi}$.

In addition to the arrays required from the factorizing routine, the array $\mathbb{b}$ is required, size; number of nodes, the results $\bar{\psi}$ are stored here on return from the function.

9.3.4 Memory Considerations

The run-time memory was found to be the biggest limiting factor in the size of the problems and the accuracy that they could be solved to. Splitting the program into sub-programs has the advantage of allowing independent memory structures for each of the sub-programs. Also only a proportion of the total code is stored in the run-time memory at one time.

The memory structures used in FORTRAN are very inflexible, arrays are declared with static dimensions, and stored in COMMON BLOCKS. As a consequence, the maximum limits of the mesh, the number of rows, columns and nodes, are set in advance. In certain situations COMMON BLOCKS can be reused to store different arrays as information becomes redundant during the program. It is necessary to keep the lengths of COMMON BLOCKS constant throughout a program, consequently the various lengths of the different arrays must be compensated for. *Junk* files were used at the end of COMMON BLOCKS to collect any spare elements. The two memory critical programs were found to be fem and er3.

fem: MEMORY STRUCTURE

To allow for greater flexibility in the of use of the major arrays using fem, they are declared as one dimensional arrays, close to the largest possible size. This allows for the storage of broad banded matrices with few nodes and narrow banded matrices with many nodes, upto the memory limitations of machine, without any adjustment of the array parameters and consequent recompilation of the programs. Indexing algebra was required to relate the two-dimensional system matrix to the one-dimensional storage array. The form the array is stored in is compressed, exploiting the banded form, hence further index algebra was required to compensate.

The data used to construct the system matrix is stored in the space later to be used for the lower triangular matrix. The node numbering was stored in the space later to be used for the pivotal, factorizing information. The node numbering is required for the reorganizing of the results into the $x - y$ mesh, and reintroducing the prescribed nodal values to the results, hence they require reloading after the solution is found. The NAG routines also reuse memory locations, as described in the previous section. This approach ensures the optimal use of the memory.

er3: Memory Structure

Memory was also found to be a problem with sub-program er3, when compiled with the maximum array sizes that could be solve in fem. To reduce this problem the calculations of the errors due to the potential and orientational distributions are calculated separately, and the memory space reused, only the maximum errors of the rows and columns being retained. This measure was not found to be sufficient by itself, it was also necessary to store the error components in the element and nodal gradient values from which they were calculated. To avoid overwriting gradient values that were still required to calculate the errors, it was necessary to temporarily store the errors for the row being calculated, before overwriting the gradient arrays. The dimensions of the new mesh were stored in the space where the distributions were stored.

At this stage of the model, when a new mesh is being designed, there is the possibility that the required mesh breaks the memory limits of the program. If one of the minor limits is broken, for example the number of rows or columns, it is still possible that the solution can be salvaged. The program is exited with a message indicating the size of the new limit which the programs should be complied with. The solution can be resummed from this point, with the modified programs. The size of the system matrix is however very close to the maximum possible on the machine, extending its size would not be productive. Provision was made such that if this critical limit was breached, the element refinement parameters were scaled to produce the largest mesh that could be solved in the memory limit. This enabled the best possible solution within the memory limitations to be achieved on the machine, though below the required accuracy.

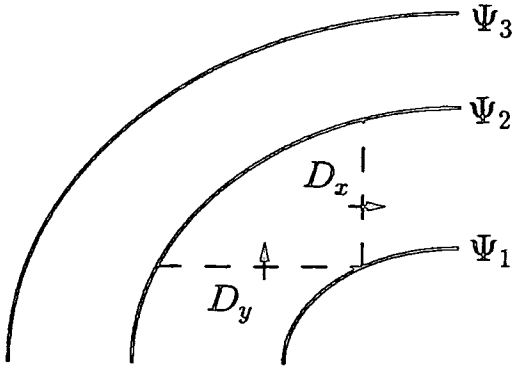

Figure 9.3: Displacement Field Lines

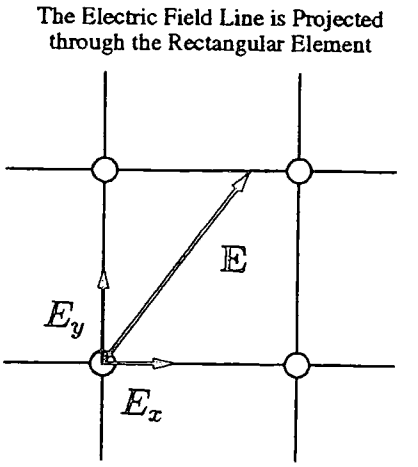

Figure 9.4: Electric Field Lines

9.3.5 Generation of Integration Results

The integration results required for the richest approximation, section 8.6.2, given in Appendix D, are quiet expansive and are required to be found for each element for each iteration. This represents a very high computational overhead, and potentially a very large program. In order to reduce these problems, extensive use of the recurring terms, common factors and forms of expression, and patterns evident in the results, were made. The calculations were reduced to recursive build of series, look-up arrays, loops with index calculation, and indirect addressing, the complexity of which it is beyond the scope of this thesis.

9.3.6 Generation of the Contributions to the Element Matrix

Both the richest and the compromise approximations contain many terms which are combinations of $\delta\phi_c$, γ_1, γ_2, $\hat{\gamma}$ and $\delta\hat{\phi}$, each combination producing a unique contribution form to the element matrix. These contribution terms were generated from;

$$c_{ij} = \frac{1}{2}(a_i b_j + b_i a_j)$$

where **c** is the contribution of the combination of **a** and **b**. Again, indirect addressing through look-up tables was used to reduce the storage required for the matrices.

9.4 Result Presentation

The results are presented within a schematic of the electrode system that was modelled.

9.4.1 Potential and Orientation Distributions

The distribution of the electrical potential throughout the system was contoured, displaying lines of equi-potential.

9.4.2 Displacement Field Lines

From the potential distribution the displacement field can be calculated. The displacement field can be depicted by displacement field lines which show the direction of the displacement field, and whose density indicate its strength. In order to draw these lines a displacement field potential function, Ψ, is required which can be contoured to produce the field lines. The differential form of the displacement field line potential is given by;

$$d\Psi = \frac{\partial \Psi}{\partial x} dx + \frac{\partial \Psi}{\partial y} dy \tag{9.1}$$

The line $\Psi = \text{CONSTANT}$, hence $d\Psi = 0$, represents a field line.

Consider the x and y components of displacement field between two displacement field lines (figure 9.3). The quantity of the y-component of the displacement field crossed in travelling in the x-direction between the two lines must be equal to the quantity of the x-component in the y-direction, hence;

$$D_y dx - D_x dy = 0 \tag{9.2}$$

The relationship between the displacement field and its field line potential can be seen by comparing equations (9.1) and (9.2), giving;

$$\begin{aligned} \frac{\partial \Psi}{\partial x} &= D_y \\ \frac{\partial \Psi}{\partial y} &= -D_x \end{aligned} \tag{9.3}$$

The displacement field line potential function can then be found by integrating the displacement field crossed from a point (x_0, y_0), which is defined as the zero potential value;

$$\Psi(x,y) = \int_{(x_0,y_0)}^{(x,y)} \mathbb{D}.d\mathbb{r} \tag{9.4}$$

The rectangular form of the system makes the x and y components of the field convenient;

$$\begin{aligned} \Psi(x,y) &= \int_{(x_0,y_0)}^{(x,y_0)} D_y dx - \int_{(x,y_0)}^{(x,y)} D_x dy \\ \Psi(x,y) &= -\int_{(x_0,y_0)}^{(x_0,y)} D_x dy + \int_{(x_0,y)}^{(x,y)} D_y dx \end{aligned} \tag{9.5}$$

It was found that by chosing the integration path which avoided the electrode corners, integrating along a planar electrode, or else the centre of the cell, then integrating in the y-direction, reduces the error in the calculation and produces better displacement field lines. The curvature of the field and hence the errors in its approximation are expected to be higher near the electrode corners. There is usually a great deal of element depletion in the x-direction under the electrodes, where the solution is almost constant in the x-direction. The displacement field line calculation can be erroneous in this region. Subdividing this region up into smaller elements improves the calculation.

This approach of displacement field line calculation implies that the displacement field is continuous in the region considered. This continuity requirement can be expressed by Maxwell's first law, in a system with zero charge;

$$\nabla.\mathbb{D} = 0 \tag{9.6}$$

$$\frac{\partial D_x}{\partial x} + \frac{\partial D_y}{\partial y} = 0 \tag{9.7}$$

which is the equation that the electro-static model solves. Only at the electrode corners, where the field x-component of the displacement crosses a charge surface is the continuity compromised, but the effect of these regions can be reduced by the appropriate choice of integration path. Substituting the potential functions into the continuity equation shows it is satisfied;

$$\frac{\partial}{\partial x}\left(-\frac{\partial \Psi}{\partial y}\right) + \frac{\partial}{\partial y}\left(\frac{\partial \Psi}{\partial x}\right) = 0$$

9.4.3 Electrical Field Lines

The approach used to generate the displacement field lines can not be used for the electric field lines, as the continuity requirement is broken, due to the continuously variable, anisotropic properties of liquid crystal. The continuously variable director orientation has the effect of introducing a continuum of bound charge into the liquid crystal region, continuously modifying the electric field. As a consequence, a set of field lines which reflects both the field strength and the direction of the electric field cannot be constructed. A set of lines which show the direction of the electric field can, however, be constructed.

A potential distribution whose contours produce the fields lines is again needed. The approach taken was to initially integrate the field in the x-direction along the centre of the cell, or in the y-direction in the quarter and three quarters positions, whichever the majority of the field lines were expected to cross. This provides a set of reference potential values, which are a little bit arbitrary, but produce reasonable looking field line spacing. The direction of the electric fields at the nodes of the rows or columns adjacent to the rows or columns that the potential values have been assigned are found from the components of electric field. A hypothetical field line is then projected from the node, through a rectangular element, to the point where it leaves the element (figure 9.4). If the potential value is known for the nodes that surround the element side the field line leaves the element, a linear interpolation of the potential values is made from nodes to the field line and attributed to the node from which it was projected. This is based on the principle that the field lines are lines of equal potential. Two passes, in opposite directions, are made of this linear projection, interpolation routine, to account for field which do not pass straight back into the previous row or column. A third pass is made to account for field lines that pass over the edge of the calculated region, these are assigned the value of an adjacent known to ensure a featureless region is created.

9.4.4 Mesh Points

The positions of the nodes are marked as points.

9.4.5 Normalized Optical Profile

The effective refractive index, n_{eff} for every column of nodes is calculated using equation (2.6) and normalized in the following manner;

$$n_{normalized} = \frac{n_{eff} - n_o}{n_e - n_o} \tag{9.8}$$

where n_o and n_e ordinary and extraordinary refractive indices, respectively.

9.4.6 Integration

The integration routine D01GAF from the NAG FORTRAN routine library [1, 4] was used for the displacement field lines, electric field lines and effective refractive index calculations.

9.5 Summary

The structures of the script, files and sub-programs used in implementing the model have been summarized. The major programming considerations have been discussed, including the design and node numbering of the mesh and the memory limitations. The presentation of the results has been described, particularly the methods employed to depict the displacement and electric field lines.

9.6 References

[1] *NAG Fortran Library Routine Document-Mark 15.* (1991).

[2] J. H. Wilkinson and C. Reinsch. *Handbook for Automatic Computation, (Vol. II, Linear Algebra).* Springer-Verlag, (1972).

[3] Z. Bothe. 'Bounds for Rounding Errors in the Gaussian Eliminator for Band Systems.' *J. INST. MATH. Appl.,* 16 (1975) 133-142.

[4] P. E. Gill and G. F. Miller. 'An algorithm for the Integration of Unequally Spaced Data.' *Comput. J.,* 15 (1972) 80-83.

Chapter 10

The Model's Performance

10.1 Introduction

The variational finite element formularization of the electrical Gibbs free energy in liquid crystal devices was described in Chapter 8 and the major programming considerations discussed in Chapter 9. The performance of this model will now be considered for one and two-dimensional problems in turn. The performance will be considered in terms of the model's convergence to a solution, how well it compares with Berreman's model [1, 2] and the consistency results with variations on the form of the model and systems solved.

10.2 One-Dimensional Problems

This sub-set of problems has already been solved by D. W. Berreman [1, 2]. The problems are completely defined by the liquid crystal material properties, the thickness of the cell and the potential drop across the cell. The convergence strategies developed for the one-dimensional problems will be described. The phase-voltage profiles will then be compared to the results produced by the Berreman model.

10.2.1 Convergence Strategies

The following strategies were developed through trial and error on a series of one-dimensional problems. The intention was to develop a series of strategies that did not make many presumptions on the relationship between the calculated variation

and the true variation from the pre-set to the solution angular distribution. The resulting strategies should be both simple and robust, hence applicable to a wide variety of situations, especially when extending the model to two-dimensions.

Maximum Angular Variation

The convergence criteria is that the maximum angular variation falls below a certain limit. The convergence strategies will concentrate on the maximum change of angle in the distribution, since it represents the region where the most correction is likely to be needed. If the maximum variation in angle, $\delta\phi_{\max}$, is considered as a function of the pre-set angle at that point, ϕ_o, while the maximum variation is centred about a specific point, it can be expressed as a Taylor's expansion about the solution orientation, ϕ_s;

$$\delta\phi_{\max}(\phi_o) = \delta\phi_{\max}(\phi_s) + \frac{\partial\left(\delta\phi_{\max}(\phi_s)\right)}{\partial\phi}(\phi_s - \phi_o) + O\left((\phi_s - \phi_o)^2\right) \qquad (10.1)$$

This is an approximation as the angular variation distribution, $\delta\phi$, is dependent on the entire pre-set angular distribution, $\phi_o(i,j)$, which is modified with each iteration. The maximum angular variation acts as an indication of the convergence of the whole distribution. It is an implicit assumption of the model that once the solution angular distribution has been found there will be no angular variation from it, hence $\delta\phi_{\max}(\phi_s) = 0$. When the angular distribution approaches the solution distribution, it is reasonable to assume that the linear term of the Taylor's expansion dominates the form of $\delta\phi_{\max}(\phi_o)$, since $(\phi_s - \phi_o)$ approaches zero. The gradient of the linear term will have a great affect on the convergence of the model, if the model is left to converge naturally, this effect is summarized;

	$\mathcal{A}$	< 0	The model moves away from the solution, no convergence.
	$\mathcal{A}$	$= 0$	The model does not move, no convergence.
$0 <$	$\mathcal{A}$	$\ll 1$	Gradual convergence, approaching solution from one side.
$0 \ll$	$\mathcal{A}$	< 1	Rapid convergence, approaching solution from one side.
	$\mathcal{A}$	$= 1$	One step to solution.
$1 <$	$\mathcal{A}$	$\ll 2$	Rapid convergence, oscillation about solution.
$1 \ll$	$\mathcal{A}$	< 2	Gradual convergence, oscillation about solution.
	$\mathcal{A}$	$= 2$	Fixed oscillations about solution, no convergence.
$2 <$	$\mathcal{A}$		Runaway oscillations, no convergence.

where $\mathcal{A} = \partial(\delta\phi_{\max}(\phi_s))/\partial\phi$.

Clearly, if the first case is possible, $\mathcal{A} < 0$, then solution seeking would be very difficult, since the direction of the calculated variation of angle could not be relied upon. It is assumed that this case does not occur.

Proportional Step

In the region where the linear term is dominant, a linear interpolation or extrapolation of the pre-set angles and their variations could be used to accelerate the convergence of the model. An estimate of the gradient of convergence can be obtained from consecutive iterations of the model;

$$\mathcal{A} \sim \frac{1}{\mathcal{C}} = -\frac{\delta\phi'_{\max} - \delta\phi_{\max}}{\phi'_o - \phi_o} \tag{10.2}$$

where ϕ_o & $\delta\phi_{\max}$ are the pre-set angle and the variation from the pre-set angle, respectively, at the position of maximum angular variation in the current iteration, and ϕ'_o & $\delta\phi'_{\max}$ are the same quantities at the same point of the previous iteration. It is presummed that the position of the maximum angular variation has not moved. The estimated gradient can then be used to interpolate or extrapolate the pre-set angles for the next iteration;

$$\phi_n(i,j) = \phi_o(i,j) + \mathcal{C}\delta\phi(i,j) \tag{10.3}$$

where $\phi_n(i,j)$, $\phi_o(i,j)$ & $\delta\phi(i,j)$ are the new pre-set angles, old pre-set angles and the variation from the old pre-set angle, respectively, for the node (i,j) in the column and row indexing. This is referred to as a *proportional* step.

It was found that scaling the angular variation, based on the interpolation or extrapolation of the maximum variation was more reliable than attempts to interpolate or extrapolate the whole distribution. It was found to be preferable to always step from the current iteration, instead of choosing between the current and previous iteration, based on which had the smaller maximum variation. This ensured that the angular distribution was always progressing, and any local minima which were advantageous for the maximum variation, but not necessarily for the entire distribution, were avoided. Consequently, the convergence would not be derailed by any unfortunate decisions, based on the crude criteria used in the convergence strategies.

Free Step

On the first iteration, there is no previous iteration to interpolate or extrapolate from, so a *free* step is taken, that is a step where $\mathcal{C} = 1$. Also, when the position of the maximum variation of the angular distribution moves it is inappropriate to use a *proportional* step, so again a *free* step is taken.

Changing Maxima

The changing of the column and row indices was not considered an appropriate criteria to determine whether the position of the maximum angular variation has changed. It does not allow for the slight shifting of the maximum position over neighbouring nodes or angular variation distributions which have more than one peak of approximately equal significance which the maxima can shift between. The criteria adopted was to compare the angular variation at the two maxima positions, the maxima position of the current and previous iterations, in the current and previous angular variation distributions. If they differ by more than 10%, then they are considered to belong to the different maximas;

$$\left| \frac{\delta\phi_{\max} - \delta\phi_{\max'}}{\delta\phi_{\max} + \delta\phi_{\max'}} \right| > 0.5 \tag{10.4}$$

$$\left| \frac{\delta\phi'_{\max} - \delta\phi'_{\max'}}{\delta\phi'_{\max} + \delta\phi'_{\max'}} \right| > 0.5 \tag{10.5}$$

where $\delta\phi_{\max}$ & $\delta\phi_{\max'}$ are the angular variations of the current iteration, at the maxima positions of the current and previous iterations, respectively, and $\delta\phi'_{\max}$ & $\delta\phi'_{\max'}$ are the angular variations of the previous iteration, at the maxima positions of the current and previous iterations.

Scaling the Free Step

If the gradient of $\delta\phi_{\max}$ is steep, then a *free* step may cause a significant shift away from the solution. To avoid this, if a *free* step overshoots the solution and the size of $\delta\phi_{\max}$ has not reduced by 20%;

$$\frac{\delta\phi_{\max}}{\delta\phi'_{\max'}} < -0.8 \tag{10.6}$$

then the scaling factor used in the subsequent interpolation of the pre-set angles is used for future *free* steps.

Form of Maximum Angular Variation

The previous ideas have been developed presumming that the model is in a predominately linear region with respect to the maximum angular variation. It was considered instructive to view the form of $\delta\phi_{\max}(\phi_o)$. In order to achieve this a four row mesh was constructed for a variety of voltages. This mesh has three free nodes, the central node and two nodes at the quarter and three quarters positions, which due to the symmetry of the system are equivalent. The first iteration was made and the values of the angular variation distribution stored. The following iterations were generated by scaling the results from the first iteration such that the central pre-set angle is set from 1° to 90° in 1°steps and the resulting angular variations plotted in figures F.1.1 & F.1.2.

It is clear from these results that there are regions where *proportional* stepping would be advantageous, but also regions where it would be disastrous; the regions of positive gradient and the 'crowns' of the curves. The initial variations, form the first iteration are small, <1°, not strongly reflecting the true variation from the solution. The angular variations appeared to be scaled by the pre-set angle for the high voltage curves at low pre-set angles. It would take many iterations to start from the off-state and to naturally converge to a solution, or even step to a region where *proportional* stepping would be appropriate.

Controlled Step

It is important to identify whether it is appropriate to make a *proportional* step, the criteria used is whether the maximum angular variation has decreased by more than 20% between iterations;

$$|\delta\phi_{\max}| < 0.8\,|\delta\phi'_{\max'}| \tag{10.7}$$

In order to accelerate the convergence of the model to the region where *proportional* stepping can be used *controlled* steps are taken. The angular variation is scaled such that the maximum angular variation is a power of 3°;

$$C = \frac{3^{Nc}}{\delta\phi_{\max}} \cdot \frac{\pi}{180} \tag{10.8}$$

The power is chosen such that on the first *control* step it is the minimum power that produces a step greater than the *free* step. It is then incremented with each control step, until a maximum value, $N_C(\max) = 1$, has been reached or the step size no longer needs controlling.

Summary of Control Strategies

If first iteration: *free* step.
If position of maxima changed, equations (10.4) & (10.5): *free* step.
If converging, equation (10.7):
  If last iteration was *controlled*: *free* step.
  Else: *proportional* step.
Else if maximum variation still in same direction: *controlled* step.
Else: *proportional* step.
  If last iteration was a *free* step: assign *proportional* step factor to *free* step factor.

These strategies are very crude but do produce accelerated convergence of the results without making too many presumptions, hence prove to be robust in varying situations. Clearly, the effectiveness of these strategies could be investigated in order to developement them further and improve the convergence of the model.

10.2.2 Phase-Voltage Profiles

Once the solution has been obtained for a one-dimensional problem, the potential and orientational distributions through the cell are known and can be plotted. The orientation distribution of the director can then be used to calculate the normalized effective refractive index of the cell. The solution for a single cell at several different applied voltages can be found and the relationship between the effective refractive index and applied voltage observed. A series of plots of this kind are presented in Appendix F.1.

Berreman Statistics

D. W. Berreman [1, 2] has provided a method for solving these one dimensional problems. The results of his method (figure F.1.3) [3] have been provided for comparison with the results produced by the finite element method (figures F.1.4 to F.1.9).

The elastic constants of liquid crystal E44 were not known at the time of the comparison, consequently the elastic constants of a related liquid crystal E7 were used in conjunction with the dielectric permittivities of E44. Since the purpose of the calculation was the comparison of the two numerical methods, the correct elastic constants are of no significance.

An uniformly spaced, 60 node Berreman solution was compared with the three levels of approximation of the elastic model with both an uniformly spaced 41 node mesh (figures F.1.4 to F.1.6) and an adaptive mesh of 1% accuracy (figures F.1.7 to F.1.9). The resulting profiles compare very well with the Berreman results, the largest deviations being observed at 10V in the fixed mesh solutions and the simplest approximation, **fr0** (synonymous with **frk** of Chapter 9) in the adaptive mesh. These discrepancies being of the order of 1%. The results from the richest and compromise approximations with the adaptive mesh are indistinguishable from the Berreman results. This comparison validates the results of the finite element model for one-dimensional problems, and provides strong evidence for its validity in two-dimensions.

Fixed and Adaptive Meshes

Comparing the fixed mesh results with the adaptive mesh, the adaptive mesh clearly provides an improved accuracy in the solution, though at great computational expense. This assumes that the Berreman results are very accurate, the convergence of the higher accuracy finite element meshes to the same curve seem to imply this.

Due to the underlying non-linearity of the orientational distributions, the linear elements do not describe them efficiently, a large number of elements are required to follow the curvature of the results. Only in the saturation region of the high voltage results is there any significant depletion of elements. Higher order elements, for example quadratic elements, could be used to approximate the angular distribution more efficiently, requiring far fewer elements for the same accuracy. Note that the distributions are drawn with straight lines between the nodes to provide a fair representation of the linear, finite element approximation.

Approximations of Elastic Model

Looking at the three approximations of the elastic part used, with the adaptive mesh the simplest approximation is still slightly adrift from the others, suggesting that the approximations used do cause an inaccuracy in the results. This inaccuracy is of the order of 2% at the 2V region of the curve. This variation is not present in the richest and compromise approximations, which are indistinguishable from each other, therefore the compromise approximation is acceptable and can be used instead of the more computational expensive richest approximation.

Cell Thickness

All the previous results are generated for a cell thickness of 10 μm, a further result was generated for a cell thickness of 2 μm (figure F.1.10). The results generated are identical to those of the 10 μm cell, illustrating both the independence of solution to cell thickness and the consequent voltage dependence of the device, as described in section 2.4.2.

Elastic Constants

The splay and bend elastic constants, K_{11} & K_{33} [4], for E44 were obtained from the threshold voltage and capacitance-voltage curves of an electric field induced Freedricksz transition experiment. The twist elastic constant, K_{22} [5], was obtained from a light scattering experiment, this constant plays no part in the calculation but is quoted for completeness.

The major difference in the elastic constants is that the bend constant is much greater for E44, consequently the bend distortions are expected to be much 'stiffer', requiring more energy. The bend distortions are dominant in the activated regions of the liquid crystal, whereas the splay distortions are expected to be dominant near the threshold voltage. The threshold voltage itself is only dependent on the splay elastic constant, as was shown in equation (2.13);

$$V_{th} = \sqrt{\frac{\pi^2 K_{11}}{\varepsilon(\varepsilon_e - \varepsilon_o)}}$$

Consequently, using the correct E44 data, the threshold voltage is not expected to be affected, but the activation curve is expected to be slightly less rapid. This is borne out by the results (figure F.1.11).

Mesh Accuracies

The number of elements required to obtain a 1% accuracy mesh is prohibitively high for two-dimensional systems, consequently lower accuracy meshes will have to be used. Meshes of accuracies; 5% & 2.5% have also been calculated (figures F.1.12 & F.1.13). Despite the understandable rougher linear approximations of the orientation distribution, the resulting phase-voltage profiles are indistinguishable from the 1% mesh, with the exception of the 10V point of the 5% mesh. The robustness of the phase-voltage profile is promising for the use of coarser meshes.

Dispersion

The normalized phase profile, given by equations (2.6) & (9.8), are dependent on the refractive indices of the liquid crystal, consequently it will be effected by the dispersion of the refractive indices across the visible spectrum. The change in birefringence is scaled out by the normalization, but there are still the remaining effect on the form of the profile. The normalized phase-voltage profiles for the extreme wavelengths of the visible spectrum have been plotted (figure F.1.14), showing a variation of <2%, which is negligible.

Voltage Distributions

Throughout the plots the voltage distribution through the cell have been presented, illustrating the variation in electric field throughout the cell. These variations are caused by the variation in dielectric properties of the liquid crystal at differing orientations. It is known that the y-component of displacement field is constant throughout a one-dimensional cell [6, page 111], this arises out of the continuity of the displacement field in a system with no free charge. The consequent variation of the electric field can be seen, larger fields being dropped near the boundaries, ensuring $D_y = \varepsilon_{yy} E_y$, since $E_x = E_z = 0$ for a one-dimensional system.

Linear Operating Region

In Chapter 6, great importance was attached to the approximately linear region of the phase-voltage profile. The linearity of this region can now be examined. A straight line of form (equation (6.4));

$$\varrho(V) \approx -\varrho_{grad} V + \varrho_{int} \qquad V_{th} \leq V \leq V_l$$

with the parameters $\varrho_{int} = 1.507 \pm 0.008$ and $\varrho_{grad} = 0.601 \pm 0.006$ was fitted using a regression package, with a regression co-efficient of 98.4%, for a voltage range 0.9–1.6V (figure F.1.15). This provides an acceptable, linear operating region over 40% of the liquid crystal birefringence.

10.3 Two-Dimensional Problems

A simple electrode structure with a 100μm period, 50μm gap, and an applied voltage of 2V was used as the sample two-dimensional system.

10.3.1 Convergence Strategies

BUCKLING

The two-dimensional problem was found to reach a state in which an excessive number of iterations was required to make any reduction in the maximum angular variation. The application of the one-dimensional convergence strategies improved the rate of convergence for the system to reach this state and also appeared to make some improvement once this state had been achieved. The unvarying maximum angular variation had the effect of triggering the *controlled* step mechanism. This operated until the *controlled* steps disturbed the angular distribution such that a larger angular variation was produced elsewhere in the system, triggering a change of maxima. Once these other distortions where dealt with the system settled down to the original angular variation distribution, with only a marginal improvement, if any, in the size of the maximum variation.

Observation of the convergence strategies showed that they were behaving as expected and the appropriate decision was being made on each iteration. The persistence of an underlying form in the angular variation suggested that the system had been trapped into a *buckled* distribution, that is the angular distribution is energetically favourable for the majority of the system, but not for a localized, *buckled* region. The *controlled* steps disturb the system as they attempt to 'straighten out' the *buckled* region. The changing of maxima and the subsequent focusing on the convergence strategies on the new maxima, cause the system to settle back into the *buckled* state before it has been 'straightened out'.

In order to try and force the system out of this *buckled* state an additional strategy was added to the convergence strategies. The criteria of a *buckled* distribution employed was the maximum angular variation changing by less than 2% between iterations. Once a *buckled* distribution was detected the current pre-set angular

distribution, ϕ_o, and angular variation distribution, $\delta\phi$, where stored as *buckled* distributions $\phi_o^{\mathcal{B}}$ & $\delta\phi^{\mathcal{B}}$. On subsequent iterations a *unbuckling* step is taken, this is very similar to the *controlled* step. The *buckled* angular variation distribution is amplified such that the maximum angular variation is scaled to be a power of 3°, and added to the pre-set angular distribution of the current iteration;

$$\phi_n(i,j) = \phi_o(i,j) + \mathcal{B}\delta\phi^{\mathcal{B}}(i,j) \tag{10.9}$$

where

$$\mathcal{B} = \frac{3^{N_{\mathcal{B}}}}{\delta\phi^{\mathcal{B}}_{\max}} \cdot \frac{\pi}{180} \tag{10.10}$$

the power, $N_{\mathcal{B}}$, is treated in the same manner as the *controlled* step power, N_C. This *unbuckling* step is taken in conjunction with the other convergence strategies. The *unbuckling* steps are only stopped when the direction of the angular variation, at the position of the *buckled* maximum angular variation, has reversed. This indicates that either the *buckle* has been forced out of the angular distribution or that the disturbance of the rest of the distribution has swamped the *buckled* region. In either case it is appropriate to allow the normal convergence strategies to settle the system down. The persistent application of the *unbuckling* steps is expected to cause a great deal of disruption to the rest of the distribution, the continued application of the other convergence strategies attempts to keep these disruptions under control.

The application of this *unbuckling* strategy allows a solution to eventually be found, though the number of iterations and consequently the computational time required is still very high.

The Evolution of the System to a Solution

Figure F.2.1 presents eight iterations during the convergence of the system to a solution. Initially, the dominant effects on the angular distribution are the transverse fields at the edges of the electrodes. The fields in the vicinity of the electrode corners are the strongest in the system, consequently they begin the change in orientation of the director. The fields at each corner have opposite lateral components. The fields on the left-hand side of the gap are predominantly leftwards and upwards, towards the electrode corner. The fields on the right-hand side of the gap are predominantly rightwards and upwards, again towards the electrode corner.

It is important to note that even before the first iteration the system is asymmetrical, despite the apparent symmetry of the electrode structure. This is due to the boundary pre-tilt, 1° upwards and rightwards in this case, which provides a preferential direction for the activation orientation of the director. The pre-tilt is in favour of the activating fields on the right side of the gap and against those on the left side. This preference can already be seen in the marginally larger activation of the right-hand region, but overall the effects of each edge are almost even, with an approximately 60/40 domination of areas to the right-hand side region.

By the 5th iteration, the activation of the edges has progressed, the 60/40 ratio of areas is maintained. The activation of the edges has extended from the locality of the electrode corners and spread across the full depth of the cell.

In the 10th iteration the 60/40 region is still entrenched and the activation of the two regions has progressed. The activation region of the right-hand edge has spread out under the electrode and appears to be much more dominant. The boundary between the two regions, at the 10μm position, is now beginning to look very taut, with a rapid change from a positive rotation to a negatively rotation.

The coarse, initial mesh finally reaches a converged state at the 114th iteration. This represents a large commitment of processing time even with a coarse mesh. The left-hand boundary between the two regions has been pushed right up to the electrode edge, leaving a 75/25 ratio of areas. The orientation of the negatively rotated region has been significantly reduced.

Remeshing now takes place, concentrating columns in the regions about the electrode edges and depleting the columns under the electrode, where the solution is almost invariant in the x-direction. Rows are concentrated at the liquid crystal boundaries. This pattern of refinement was anticipated in section 8.8.1. The resulting angular distribution is a significantly smoothed version of the last iteration of the coarse mesh.

The form of the controlling *script* allows for at least two remeshes at the remeshing stage. The first remeshing occurs after the system has converged and is based on a further iteration of the old mesh. As the solution has already converged it is very unlikely that there will be a large enough angular variation to trigger the need

for a reconvergence. This allows a second iteration to be taken, based on the new mesh, and a second remeshing takes place. The change between the old mesh and the first remeshing is often enough to trigger reconvergence. A second mesh has by this time been designed and is subsequently used. This provides an opportunity for the tempered adaptive mesh refinement strategies to converge to an optimal mesh. The first of these meshes is illustrated in the first iteration of the intermediate and final meshes, and the mesh used for the convergence illustrated in the last iteration of the intermediate and final meshes.

The intermediate mesh converges after 36 iterations, by which time the negatively orientated region has been completely eradicated from the system. The only indication of lateral fields at the left edge being a narrow region at the boundary, in the gap, where the director orientation is slightly less than the boundary pre-tilt, flattened by the predominantly horizontal field in that region. The angular distribution is essentially the form of the final solution, obtained after remeshing and an additional 8 iterations.

This convergence case-study illustrates the importance of a good mesh, the initial mesh converged to a state which is clearly not a rough approximation of the solution, but a trapped state.

Relating the evolution of the angular distribution to the difficulties in ensuring that the system converges, it can be seen that the suggested *buckled* region can be related to the left-hand boundary between the positively and negatively orientated regions, which is extremely taut. This boundary is gradually pushed rightwards over 150 iterations and many evocations of the *unbuckling* routine.

One-Dimensional Preprocessing

Now that the major obstacle to convergence has been identified, the question arises; can it be avoided in order to achieve rapid convergence?

The problem is the development of a negatively orientated region at the initial stages of convergence, which gives rise to the *buckled* region. The eradication of the negatively orientated region takes up many iterations. Avoiding the development

of this negatively orientated region would be advantageous to convergence. The emphasis of the preferential activation orientation at the outset could be employed.

The approach taken is to initially solve the one-dimensional system, describing the majority of the electrode region, and using the resulting orientation distribution as the initial pre-set distribution. In this manner the region is initially positively rotated, avoiding the development of any negatively rotated region.

Figure F.2.2 shows the evolution of the model to a solution with this one-dimensional preprocessing. In the first iteration, the orientation in the gap has been reduced significantly compared to the orientation under the electrodes. The second iteration produces an orientation distribution identical by observation to the first iteration. It is possible that there has been an erroneous over-writing of the results file. It is important to note that since the potential distribution is based on the pre-set angles the potential distribution is appropriate for the angular distribution of the previous iteration. Hence, the potential distribution of the first distribution is based on the initial pre-set angles, the second on the results of the first iteration and the third on the results of the second iteration. Consequently, if the orientational distributions of the first and second iterations are identical, the potential distributions of the second and third iterations should also be identical, this is not the case.

By the third iteration, the orientation in the gap has been reduced even further, the broad features of this distribution can be seen to already approximate the final solution. The initial mesh converges in 12 iterations, less than a tenth the number of iterations of the model without the one-dimensional preprocessing. In this time the left-hand edge has tightened up and the right-hand edge has loosened. This is a natural progression from the more symmetrical form of iteration 3 to the final solution.

As in the previous example, the remeshing concentrates columns around the electrode edges, depletes columns under the majority of the electrode and concentrates rows close to the liquid crystal boundary. The resulting orientation distribution is again a smoothed version of the last iteration of the initial mesh.

The intermediate mesh converges in 13 iterations, a third the number required without the preprocessing. The resulting distribution is very similar to the final solution, which is obtained after a further remeshing and an additional 10 iterations.

The final solutions and meshes from the models with and without the preprocessing compared extremely well. The use of the preprocessing produces a great reduction in computational time.

Comparing the converged distributions of the initial mesh to the intermediate and final meshes, it is clear that the coarse mesh produces solutions significantly different from the eventual solution. This situation may be improved by using a finer initial mesh, at the cost of making the earlier stages of convergence more expensive. Choosing the optimal grade of the initial mesh requires further consideration.

10.3.2 The Form of the Solution

The Director Distribution

In discussing the evolution of the system to a solution, it was observed that the system is intrinsically asymmetrical due to the boundary pre-tilt of the liquid crystal, which provides a preferential direction of orientation when activated. It is not surprising to find that the final solution is also asymmetrical. The majority of the liquid crystal is rotated in the preferential orientation direction when activated. The lateral components of the fields at the edges of the electrodes are in opposite directions.

The fields on the left-hand side of the gap are in a direction against the preferential rotation of the activated region, consequently the fields in this region drives the liquid crystal off, causing a rapid transition between the on and off regions. The liquid crystal in the region just under the electrode on the left-hand side of the gap is slightly more activated than the liquid crystal under the majority of the electrode, this can be seen as a slight bulge in the contours at the 15-20μm position. The fields in this region are of comparable strength to the fields under the electrode but are slanted slightly more to the left, hence pulling the activated liquid crystal a little further round. When this tilt to the field becomes more pronounced, it has

the reverse effect of driving the liquid crystal off. This results in a relatively sharp transition region.

The fields on the right-hand side of the gap are in the direction of the preferential rotation. Under the edge of the electrode the fields are begin to slant more rightwards and the strength begins to diminish. Both these considerations reduce the orientation of the activated liquid crystal in this region. Moving into the gap, the displacement field lines become more slanted and their strength reduced, hence the director orientation gradually diminishes. As the fields are still present and in an appropriate direction for activating the liquid crystal, there is a residual activation of the liquid crystal up to 50μm into the gap. This transition region is very gradual.

The Potential Distribution

Observing the form of the electrical energy density of the dielectrically anisotropic liquid crystal, equation (2.12);

$$f_e = \frac{\varepsilon}{2}\left\{\varepsilon_o\left(\frac{\partial V}{\partial \iota}\right)^2 + \varepsilon_o\left(\frac{\partial V}{\partial \kappa}\right)^2 + \varepsilon_e\left(\frac{\partial V}{\partial \lambda}\right)^2\right\}$$

This can be expressed in the same form as an isotropic dielectric media by scaling the λ-direction, such that $\lambda' = \lambda\sqrt{\varepsilon_o/\varepsilon_e}$, giving;

$$f_e = \frac{\varepsilon}{2}\left\{\varepsilon_o\left(\frac{\partial V}{\partial \iota}\right)^2 + \varepsilon_o\left(\frac{\partial V}{\partial \kappa}\right)^2 + \varepsilon_o\left(\frac{\partial V}{\partial \lambda'}\right)^2\right\}$$

Consequently, the potential distribution is expected to vary relatively slowly in the direction of the director. This was seen in the one-dimensional systems, the potential drop in the centre of the activated cells was much more gradual than at the edges of the cell.

The effect of the director distribution on the potential distribution can be clearly seen by comparing the first iterations of the convergence with and without an one-dimensional preprocessor. Without the preprocessor the initial director orientation is tilted 1° to the boundary, effectively compressing the system in the x-direction. Consequently the potential distribution changes slowly in this direction. With the preprocessor the initial director distribution is predominantly at >60° to the boundary, especially in the centre of the cell. Consequently, the equivalent isotropic

electro-static system would have a much greater aspect ratio than the system without the preprocessing and also be skewed in the direction of the director. This is reflected in the resulting director distribution which changes much more rapidly in the x-direction and exhibits appropriate asymmetry, distorting the distribution to aligment with the director.

In the final potential distribution, the effects of the changes in director distribution can be clearly seen. The potential distribution in the vicinity of the electrodes changes very rapidly, where the liquid crystal is activated. Further out in the gap the liquid crystal is less activated and the changes in the potential distribution become more gradual. Compare these two regions to the initial distributions, with and without a preprocessor respectively. The asymmetry in the potential distribution reflects both the skewing of the electro-static system by the director and the asymmetry present in the director distribution. These asymmetries are also evident in the displacement field lines, which are 'displaced' towards alignment with the director.

10.3.3 Elastic Approximations with Fixed and Adaptive Mesh

Fixed and Adaptive Meshes

For the three approximations of the elastic model a fixed mesh, with 60 uniformly spaced rows in the liquid crystal region, and 60 columns, 20 uniformly spaced columns in each sub-domain, was compared to a 5% accuracy adaptive mesh.

The normalized phase response of the fixed mesh has very distinct linear approximations, especially in the left-hand transition region. The adaptive mesh concentrates the columns about the electrode edges and the rows about the liquid crystal boundaries. As previously observed the linear elements are very inefficient at approximating the underlying non-linear orientation distribution and higher order elements, such as quadratic elements, would be preferable. The results of the adaptive mesh are smoother and the transition regions are marginally sharper, providing a significant improvement on the fixed mesh. This is true of all the elastic approximations.

The discrepancy between the simplest approximation and the richest and compromise approximations, which is present in the one dimensional results is very evident in the orientational distribution and the normalized phase, especially in the activated region. This again suggests that there is a significant difference in the approximations taken. This discrepancy is equally present in both the fixed and adaptive meshes.

The compromise and richest approximations compared extremely well, the only deviations in the fine detail of the orientation distribution in the gap, which does not effect the normalized phase profile. The convergence of the richest approximation was less stable, and the tolerance of the convergence thresholds was relaxed. It is not clear which approximation produces the more accurate results, which are practically indistinguishable, the compromise approximation, however, is preferred for reasons previously discussed and is used solely for the remainder of the results.

10.3.4 The Far Boundary Condition

The invariance of the solution with the position of the far boundary was conceived as an appropriate test for the validity of the model. This test exposed the erroneous use of a flawed error estimator during the development of the model. The flawed error estimator can be summarized;

$$\begin{aligned}
|\epsilon_{xx}|^2_{\text{rect.}} &= \frac{\Delta b^2}{8}\left(\bar{\psi}^*_{x(4)} - \bar{\psi}^*_{x(3)} + \bar{\psi}^*_{x(2)} - \bar{\psi}^*_{x(1)}\right) \\
|\epsilon_{xy}|^2_{\text{rect.}} &= \frac{\Delta c^2}{8}\left(\bar{\psi}^*_{x(4)} - \bar{\psi}^*_{x(2)} + \bar{\psi}^*_{x(3)} - \bar{\psi}^*_{x(1)}\right) \\
|\epsilon_{yx}|^2_{\text{rect.}} &= \frac{\Delta b^2}{8}\left(\bar{\psi}^*_{y(4)} - \bar{\psi}^*_{y(3)} + \bar{\psi}^*_{y(2)} - \bar{\psi}^*_{y(1)}\right) \\
|\epsilon_{yy}|^2_{\text{rect.}} &= \frac{\Delta c^2}{8}\left(\bar{\psi}^*_{y(4)} - \bar{\psi}^*_{y(2)} + \bar{\psi}^*_{y(3)} - \bar{\psi}^*_{y(1)}\right)
\end{aligned} \tag{10.11}$$

which is compared with the function norm;

$$|\psi|^2_{\text{rect.}} = \frac{\Delta}{16}\left(\psi_{(1)} + \psi_{(2)} + \psi_{(3)} + \psi_{(4)}\right)^2 \tag{10.12}$$

This can be compared to the error estimator eventually used, equation (8.43), there are common features, but the flawed estimator does not have the same theoretical underpinning.

The results of the flawed error estimator with various positions of the far boundary are presented in figure F.2.9. The first example, with the far boundary at 10μm, is very different from the previously considered solutions. This is not unexpected since 10μm is far shorter than the expected decay length of the electric field, which is about the length of a period (section 8.3.2). The 100μm and the 1mm examples are closer to the form expected. As the far boundary is moved further away from the solution area the orientation distribution becomes progressively more symmetrical and the liquid crystal in the gap more activated. The 10m and 100m results appear to be in reverse order in this progression.

The variation of the solution with the position of the far boundary indicates something is wrong with the model. To observe what was happening in the far boundary region a section of the potential distribution was taken from the centre of the electrode to the far boundary. This is plotted on a linear scale for the first 150μm (figure F.2.10) and a logarithmic scale for the whole region (figure F.2.11). The expected form of the fundamental decay is indicated on the plots.

The 10μm case clearly has the decay accelerated to the boundary, distorting the potential distribution in the solution region. The general form of the solutions approximate the general decay form. The number of linear elements that approximate the decay form is, however, progressively reduced with increasing distance to the far boundary, especially in the critical first 150μm. This can clearly be seen as a failing of the adaptive mesh refinement strategy.

The results for the corrected error estimator are presented in figure F.2.9. The form of the 10μm solution is identical to the form in the previous results, the error being the position of the far boundary. For the remaining cases the solutions remain very consistent, with a variation of 1° in the gap of the 100m case.

Comparing the meshes of the old and new estimators, the new estimator is much more demanding, requiring significantly greater concentrations of rows and columns in the critical regions.

In the mid-electrode sections of potential distribution, the decay forms and the mesh on which they are approximated are very consistent for the first 150μm (figure F.2.13), with the exception of the 10μm case and a slight variation in the 100m

case. The decay beyond this to the far boundary (figure F.2.14), is flat, with the exceptions of the last row in the potential distribution of cases 10m and 100m. It was suspected that the variation in the last element arose from the truncation errors in the calculation of the elements, due to the disproportionality of their dimensions.

This series of results emphasis the importance of the far boundary region and the correct formularization of adaptive mesh refinement strategy. A far boundary of 1mm, the dimension of the glass enclosure, is used throughout the rest of the results.

10.3.5 Truncation Error

In order to investigate the cause and effect of truncation errors in disproportionality sized elements, a simplified system was constructed. A 100μm wide, one-dimensional, earthed, planar electrode in vacuum, with a far boundary at various distances, was constructed from 16 uniform rectangular elements. The results are presented in figure F.2.15.

It can be shown that the triangular element matrix contribution for a homogeneous, isotropic electro-static system reduces to;

$$\mathbf{k}_{\text{ele}} = \begin{bmatrix} \frac{1}{b^2} + \frac{1}{c^2} & -\frac{1}{b^2} & -\frac{1}{c^2} \\ -\frac{1}{b^2} & \frac{1}{b^2} & 0 \\ -\frac{1}{c^2} & 0 & \frac{1}{c^2} \end{bmatrix} \tag{10.13}$$

where b & c are the x & y dimensions of the element, respectively.

Combining the upper and lower triangular elements to form the 2 node, one-dimensional rectangular element (figure 10.1), gives;

$$\mathbf{k}_{\text{rect}} = \begin{bmatrix} 2(\frac{1}{b^2} + \frac{1}{c^2} - \frac{1}{b^2}) & -2(\frac{1}{c^2}) \\ -2(\frac{1}{c^2}) & 2(\frac{1}{b^2} + \frac{1}{c^2} - \frac{1}{b^2}) \end{bmatrix} \tag{10.14}$$

It is at this stage that the truncation errors may occur. If the dimensions of the element are disproportionate, $b \ll c$, then the subtraction, $\frac{1}{b^2} + \frac{1}{c^2} - \frac{1}{b^2}$, may incur an error, ϵ_t;

$$\frac{1}{b^2} + \frac{1}{c^2} - \frac{1}{b^2} \approx \frac{1}{c^2}(1 \pm \epsilon_t) \tag{10.15}$$

hence,

$$\mathbf{k}_{\text{rect}} = \frac{2}{c^2} \begin{bmatrix} 1 \pm \epsilon_t & -1 \\ -1 & 1 \pm \epsilon_t \end{bmatrix} \tag{10.16}$$

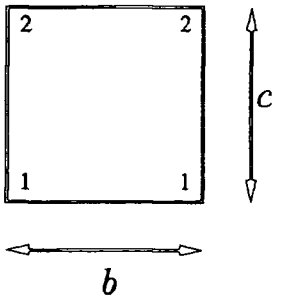

Figure 10.1: One-Dimensional Rectangular Mesh Element

The system equations can be expressed;

$$\begin{bmatrix} V_{\text{app}} \\ 0 \\ 0 \\ \vdots \\ 0 \\ 0 \\ 0 \end{bmatrix} = \begin{bmatrix} 2(1\pm\epsilon_t) & -1 & 0 & \cdots & 0 & 0 & 0 \\ -1 & 2(1\pm\epsilon_t) & -1 & \cdots & 0 & 0 & 0 \\ 0 & -1 & 2(1\pm\epsilon_t) & \cdots & 0 & 0 & 0 \\ \vdots & \vdots & \vdots & \ddots & \vdots & \vdots & \vdots \\ 0 & 0 & 0 & \cdots & 2(1\pm\epsilon_t) & -1 & 0 \\ 0 & 0 & 0 & \cdots & -1 & 2(1\pm\epsilon_t) & -1 \\ 0 & 0 & 0 & \cdots & 0 & -1 & (1\pm\epsilon_t) \end{bmatrix} \begin{bmatrix} V_n \\ V_{n-1} \\ V_{n-2} \\ \vdots \\ V_2 \\ V_1 \\ V_0 \end{bmatrix} \tag{10.17}$$

where the prescribed node, $V_{n+1} = V_{\text{app}}$, has been eliminated and node 0 represents the far boundary. The nodes are numbered in reverse for convenience.

If the error is zero the nodes take the value of the applied voltage throughout the system. If there is a finite error then it can be proved by induction that the potential distribution takes the form;

$$V_i = (1 \pm i^2\epsilon_t)V_0 \tag{10.18}$$

in terms of the potential at the far boundary.

From the bottom rows of the matrix;

$$\begin{aligned} V_1 &= (1\pm\epsilon_t)V_0 \\ V_2 &= 2(1\pm\epsilon_t)^2V_0 - V_0 \\ &\approx (1\pm 4\epsilon_t)V_0 \end{aligned}$$

dropping higher order ϵ_t terms. From the matrix the voltage at the ith node is given by;

$$V_i = 2(1\pm\epsilon_t)V_{i-1} - V_{i-2}$$

Assuming that the relationship given in equation (10.18) is true for V_{i-1} & V_{i-2};

$$V_i = 2(1\pm\epsilon_t)(1\pm(i-1)^2\epsilon_t)V_0 - (1\pm(i-2)^2\epsilon_t)V_0$$

$$\approx \quad (1 \pm i^2 \epsilon_t) V_0$$

The size of this error for FORTRAN DOUBLE PRECISION numbers is given by; $|\epsilon_t| \leq 10^{2N_t - 16}$ where the ratio of the element sizes is given by $\frac{c}{b} = 10^{N_t}$.

This quadratic relationship of the potential distribution, based on the truncation error, can clearly be seen in the 10mm to 10km results, with the associated linear displacement field. The distribution of the potential and normal displacement fields for the 10μm to 1mm cases are at the digitization level of the calculation, this can be seen by the points falling on discrete, uniformly spaced values. It can be seen that the truncation error only becomes significant for greatly elongated elements, this is consistent with the errors observed in figure F.2.14.

10.3.6 Symmetry

In order to test the self-consistency and indexing of the model a series of symmetrical tests were conducted. Figure F.2.16 is a reproduction of the results previously observed, figure F.2.17 is a rotation of the same system, which produces a rotated angular and potential distributions. Figure F.2.18 is a system with two points of rotational symmetry in the centre of the cell; in the centre of the electrode and the centre of the gap, these symmetries are reflected in the results. Figure F.2.19 is a similar system to figure F.2.16 with the boundary pre-tilt reversed, the solution is appropriately reversed. These results also demonstrate that the asymmetry of the results is entirely due to the asymmetry of the physical system and not the asymmetry of the mesh, caused by the sub-division of the rectangular elements.

10.4 Summary

A series of convergence strategies have been developed for the one-dimensional systems, based on the scaling of the maximum angular variation distribution, according to the behaviour of the maximum angular variation of consecutive iterations. These strategies were very crude, making very few assumptions about the underlying form of the converging solution, to ensure the robustness of the strategies when applied to a wide variety of problems.

Results from D. W. Berreman's one-dimensional model [2] were compared to three elastic, finite element approximations with fixed and adaptive meshes. The richest and compromise approximations with adaptive meshes were indistinguishable from the Berreman results. The adaptive mesh was found to produce improved results compared to the fixed mesh, it was also observed that linear elements are very inefficient at approximating the non-linear solutions. The solutions were found to be independent of cell thickness, demonstrating that the devices are voltage driven. Comparisons of the 5%, 2.5% and 1% accuracy meshes showed that the model produced good results even at lower accuracies. The dispersion of the refractive index across the visible spectrum was shown to have only a marginal effect on the normalized phase profile. The potential distribution was discussed and the linear operating region of the phase-voltage profile characterized.

The one-dimensional convergence strategies were applied to a two-dimensional problem. There appeared to be a persistent *buckled* region, which required an additional strategy to force the *buckle* out. Once a solution had been obtained the evolution of the system to the solution was observed and the *buckle* related to the development of a negatively orientated region which subsequently required flattening out. One-dimensional preprocessing was employed to provided a positively rotated starting condition, preventing the development of the negatively rotated region and hence vastly improving the convergence rate of the system.

The form of the solution was described, the asymmetry arising principally from the boundary pre-tilt.

For two-dimensional systems the solutions of the three elastic approximations with fixed and adaptive meshes were compared. The adaptive mesh was found to provide a smoother more accurate solution. The simplest approximation deviated noticeably from the richest and compromise approximations, suggesting an inaccurate approximation. The richest approximation was observed to be less stable in its convergence.

The expected invariance of the solution with the position of the far boundary was used to expose a flawed error estimator and the consistency of a corrected error estimator was demonstrated. It was observed that the far boundary was required to be far enough for the full decay of the potential distribution and that the ex-

amples with extremely elongated elements produced significant truncation errors into the solution. The development of truncation errors was illustrated with a one-dimensional example and it was noted that the elements were required to be very disproportionate to for the development of truncation errors.

A series of symmetrically related problems were also presented.

A model of the director orientation in a two-dimensional electrode structure has been demonstrated to reproduce the results of a previously existing one-dimensional numerical methods. Accelerated convergence can be achieved with a series of unsophisticated convergence strategies. The two-dimensional results are consistent with the physical considerations of the system, the one-dimensional results and a series of self-consistency examples. This model will be employed to investigate a variety of two-dimensional electrode structures in Chapter 11.

10.5 References

[1] D. W. Berreman. *J. Opt. Soc. Am.*, 63 (1973) 1374.

[2] D. W. Berreman. 'Numerical modelling of twisted nematic devices', *Phil. Trans. R. Soc. Lond.*, A309 (1983) 203-216.

[3] M. C. K. Wiltshire. *Unpublished Data,* GEC-Marconi, Hirst Research Centre.

[4] M. J. Bradshaw and E. P. Raynes. *Unpublished Data,* DRA. *Kindly forwarded by* M. S. Bancroft.

[5] Richard Hall. *Light Scattering in Nematic Liquid Crystals.* PhD Thesis, University of Lancaster (1992).

[6] L. M. Blinov. *Electro-optical and magneto-optical properties of liquid crystals.* Wiley (1983).

Chapter 11

Results

11.1 Introduction

A model which describes the director distribution in a liquid crystal cell has been developed and its performance observed. This model will now be employed to observe the effects of various electrode structures on the optical profile of liquid crystal cells, in order to explore some of the issues which arose in Chapter 7. The majority of the results concentrate on the problem of obtaining a sharp transition region in binary diffractive devices. This problem is used to explore the behaviour of a liquid crystal device in a variety of situations and to provide some insight for diffractive/refractive structures, which also require sharp transition regions. Some example electrode structures for refractive and diffractive/refractive devices are also examined, as well as the possibility of electrode structures which drive off the liquid crystal. Some observations are made about the effect of the initial conditions on the final solution.

11.2 Binary Diffractive Structures

In Chapter 7, it was observed that the ideal optical profile of binary diffractive devices required a sharp transition between the on and off regions. Several electrode structures where suggested for the improvement of the transition regions. In order to examine the performance of these electrode structures a series of experiments spanning the nine applied voltages and nine electrode geometries were run. Only three geometries are presented for each structure, the full set of results are available

separately [1]. The equipotential lines are chosen to be in steps of one fifth of the applied voltage, to simplify the comparison of potential distributions of various applied voltages.

The systems considered are simplified by ignoring the material properties of the layers spun onto the glass. The electrodes are considered as 0.02μm thick layers touching the liquid crystal layer, flush with the glass interface or buried 1μm. The results are based on a 10μm cell, but the electrode geometries may be scaled for any cell thickness, d.

11.2.1 Improving the Transition Region

Simple Electrode Structures

The electrode used in the previously constructed devices simply have the designed off regions etched from the electrode, similar to the structures examined in Chapter 10, the results are presented in figures G.1.1. As discussed in Chapter 10, the lateral components of the field at the electrode edges are in opposite directions. The fields at the left-hand edge are against the activation of the liquid crystal and the fields at the right-hand edge are in the direction appropriate for activation. The gradual diminishing and tilting of the field from the right-hand electrode edge into the gap allows a gradually diminishing of the director orientation, providing a gradual transition region.

Again as described in Chapter 10, the activation of the liquid crystal in the vicinity of the electrode has the effect of increasing the rate of change of the potential distribution in the x-direction. As the applied voltage increases the activation orientation also increases, as was seen in the one-dimensional results. This has a significant effect on the compression of the potential distribution in the vicinity of the right-hand edge, which in turn has the effect of compressing the transition region.

If there were no change in the dielectric properties of the system with varying applied voltages, then the expected potential distribution would be identical in form, with scaled potential values. It is expected that the intrusion of the activated liquid crystal into the gap, for increasing applied voltages, would increase significantly,

since the potential drops equivalent to the threshold voltage would occur further into the gap.

The compression of the potential distribution at high voltages counteracts the increase in applied voltage, resulting in only a marginal increase in the transition region of the right-hand edge into the gap. The compression of the potential distribution is most pronounced at the edges of the electrode, sharpening the transition region in the vicinity, also reducing significantly the intrusion of the transition region under the electrode. As the transition region trails into the gap the potential compression is less pronounced and the form of the transition region is a gradual decay, approximately $3 \times d$ in length where d is the cell thickness.

The effects of the fields on the director distribution on the left-hand edge are very different. In the gap, the fields are in the direction counter to the preferential rotation of the liquid crystal, consequently there is a region of negative rotation. At low applied voltages this is the dominant feature of the left-hand edge and can be seen as a slight 'bulge' in the optical profile, immediately after the transition region. The transition region undercuts the electrode at low voltages, since the fields creating the negatively orientated region dominate over the fields under the electrode. The low activation orientations of both regions allow a smooth and gradual transition between the two regions. The narrowest electrodes are undercut completely by the low voltage transition regions.

The effect of the compression of the potential distribution at higher voltages is to produce strong fields immediately below the electrode edge, which tilt leftwards in comparison to the fields under the majority of the electrode. This produces a region where the director is pulled round to a higher activation orientation in the vicinity of the edge. This can be seen in the director distribution and as a bulge developing on the electrode side of the transition region in the optical profiles.

As the applied voltage increases this region of greater orientation becomes more dominant, marginalizing the negatively orientated region and pushing the transition region out from under the electrode and into the gap. At higher voltages the director is pulled round beyond 90° and begins to tilt back on itself. This has the effect of producing an indentation instead of a bulge in the optical profile, since the over-rotation increases the effective refractive index in this region. The rapid transition

between the positively and negatively orientated regions provides a taut transition at the left-hand edge, approximately $0.6 \times d$ in length.

The geometries chosen have a constant period of 200μm and the dimensions of the electrode and the gap are varied dependently. For a complete examination of the geometry the dimensions of electrode and gap should be varied independently, increasing the dimensions of the parameter space of the investigation. It was presummed, however, that the effect of a large electrode is to isolate the effects of the edges from interfering through the electrode region. The system under the centre of the electrode regions is one-dimensional in form, i.e. invariant in the x-direction, consequently the length of this region can be altered without affecting the form of the edges. This presumption is borne out by the results, only the edges of the narrowest electrode, at low applied voltages, interfere across the electrode. Even in these cases the edges are similar in form to the edges of the wider electrode geometries.

The isolation of the edges in the electrode region is not expected to extend to the gap. For very large gaps there is expected to be a degree of independence, but for narrower gaps the potential distributions from each edge will begin to interfere, decreasing the change of potential distribution in the gap. Consequently, the transition regions extend further into the gap forming slightly more gradual decays in the effective refractive index. This effect is minor but can be detected by comparing the right-hand edges of the $18 \times d$ and $10 \times d$ gap size geometries.

The narrowing of the gap has a much more significant effect on the left-hand edge due to the proximity of the right-hand transition region. This has the effect of squeezing out the negatively orientated region between the two positively orientated regions of the edges. This is more noticeable at higher applied voltages partly due the left-hand transition region extending further into the gap, reducing the distance between the two transition regions. Since it is the presense of the negatively orientated regions which create relatively sharp transition regions, their reduction has the effect of producing much more gradual transitions. This is much more significant at high voltages, especially where the negatively orientated region has been eradicated.

The narrowest gaps, $2 \times d$ gap size, are swamped with the fields from both edges. The greater change of the potential distribution in the x-direction of activated,

higher voltage cells can be clearly seen. The transition regions overlap in the gap and a fully off region is not realized. The transition regions begin to overlap in the $\sim 8 \times d$ gap geometries for the 5V examples.

Etched Earth Plate

In Chapter 7 it was suggested that etching the earth-plate into the gap would reduce the intrusion of the fringing fields in the gap and hence the intrusion of the transition regions. The resulting electrode structures have rotational symmetry about the centre of the electrode region and the centre of the gap, half-way through the cell. Consequently, the resulting distributions (figures G.1.2) are expected to reflect this symmetry.

Comparing the potential distributions to the previous, simple electrode structure (figures G.1.1), it can be seen that the top left and bottom right edge regions are similar in form to the left-hand edge of the simple electrode structure and the bottom left and top right edge regions are similar to the right-hand edge. Under the electrodes the influence of the left-hand potential distribution extends to the third contour, further into the gap this contour follows the right-hand form of the potential distribution. As expected the intrusion of the fields into the gap is greatly reduced.

The potential distribution of the top left and bottom right edge regions has the same increased orientation, but localized to just greater than half the depth of the cell and consequently not as strongly developed. The negatively orientated region is not present, consequently the sharp transition form of the left-hand edge is not reproduced. The form of the transition region of the director distribution in the gap is of the same form as the right-hand gap, but intruding half the distance, $\sim 1.5 \times d$.

The transition regions take the form of a combination of the left and right-hand edges in the optical profiles. The increased orientation of the left-hand edge excludes the intrusion of the transition region from under the electrode at high applied voltages, but does not push it out into the gap. The form of the gap side of the transition region is of the form of the right-hand simple electrode edge, but of half the length. The absence of the negatively orientated region and its sharpening

effect on the transition regions cause them to be approximately three times as long as the left-hand region of the simple electrode structure. This variation has only been partially successful.

The proximity of the electrodes on the potential distribution, in the $10 \times d$ gap size geometries, is still present but less marked than in the simple electrode structure. The proximity of the transition regions increases the activation in the gap, again this is less marked than in the simple electrode structure due to the more localized forms of the director distributions in the edge regions. This increase in activation is undetectable in the optical profiles.

The fields and transition regions overlap in the $2 \times d$ gap geometries, but again not to the same extent as in the simple electrode structure. The transition regions of the 5V cases begin to overlap at $\sim 5 \times d$ gap size.

Guard Plate

In Chapter 7 it was also suggested that a buried guard plate in the gap would exclude the fringing fields from the gap. The resulting edges are expected to be isolated by guard plate and asymmetrical in form, narrower but similar in form to the simple electrode structure. This is borne out by the results (figures G.1.3).

The potential distributions are similar to the those of the simple electrode structure (figures G.1.1). The guard plate confines the potential distribution to the edge of the electrode. The contours appear to be pulled back on themselves to disappear between the electrode and the guard plate. At high voltages this produces strong fields localized about the edge next to the guard plate, which are appropriately orientated for activating the liquid crystal in the opposite sense as the majority of the fields associated with each edge. Narrow regions of partly activated liquid crystal result, which provide sharpened transition regions as the director rapidly changes between positive and negative orientations. The right-hand transition region compares well to the etched earth plate transition regions, slightly sharper in the gap but without the increased orientation excluding the transition region from the under the electrode. The overall transition region is approximately the same length $\sim 1.5 \times d$. The left-hand edge has three distinct regions, a negative region sand-

wiched between the increased orientated, positive region under the electrode and the shallow positive region adjacent to the guard plate. The positive guard plate region stops the left-hand edge being pushed out into the gap as it was in the simple electrode structure, confining the transition region to the edge. The result is an extremely sharp transition region, $\sim 0.4 \times d$ length, centred on the electrode edge, very close to the ideal step function.

The $10 \times d$ gap geometries demonstrate the isolation of the edges by the guard plate.

In the $2 \times d$ gap geometries, at high voltages the interaction of the potential distributions of each edge have been greatly reduced. The director transition regions, however, overlap and the left-hand, positive guard plate region appears to be squeezed out by the surrounding negative regions of the left-hand edge and the right-hand guard plate region. The left-hand negative region is also reduced, to a very small region at the electrode edge, by the proximity of the positively orientated edge regions of both edges. Consequently, the sharpness of the left-hand edge is greatly reduced, but the intrusion of the transition regions into the gap is less than the intrusion in the previous two electrode structures. The 5V transition regions begin to overlap at gap sizes of $\sim 3 \times d$.

Etched Earth Plate and Guard Plate

In Chapter 7 the idea of combining the symmetry of the etched earth plate, halving the spread of the fields into the gap, and the isolated edges of the guard plate electrode structure was suggested.

The resulting potential distributions (figures G.1.4) are similar in form to those of the etched earth plate structure (figures G.1.2) with the pulling back of the contours at the edges associated with the guard plate structure (figures G.1.3). The director distributions are a narrower form of those of the etched earth plate structure, with approximately two thirds of the intrusion length and no reversely orientated regions which where associated with the guard plate structure. The optical profiles are also of the form of those of the etched earth plate with transition regions of two thirds the size, $\sim 1 \times d$.

In the $2 \times d$ gap geometries, there is a greater isolation of the potential distributions, even at lower voltages. The director distributions overlap causing a slight increase in the activation of the liquid crystal in the gap which is again undetectable in the optical profiles. Again, the 5V transition regions begin to overlap at gap sizes of $\sim 3 \times d$.

This electrode structure has been only partially successful, as in the etched earth plate structure, the extremely sharp edges of the left-hand edge are lost.

Staggered Etched Earth Plate and Guard Plate

This electrode structure was designed as an attempt to obtain two transition regions with the form of the left-hand transition region of the guard plate electrode structure on both sides of the gap. The resulting electrode structures have the earth plates buried by 1μm and is rotational symmetric about the centre points of the electrode and guard plate regions. Consequently, the electrode structure reproduces the structure of the left-hand guard plate at right-hand of the gap, the earth plate and the guard plate exchanging roles. The structure is repeated with the role of the guard and earth plates exchanged with the electrode plates to a complete period of the electrode structure containing two electrode regions and two gaps.

The resulting orientation (figures G.1.5) under the electrode is found to be against the boundary pre-tilt, producing two transitions regions of the form of the right-hand transition region of the guard plate structure (figures G.1.3). Comparing the director distributions of the left-hand and right-hand transition regions of the guard plate structure, it is clear that the right-hand distribution is energetically more favourable since it only contains one transition between regions of opposite orientation, whereas the left-hand edge contains two such transitions. The preference for two right-hand transition regions must be great enough to overcome the preference of the electrode region to rotate in the direction of the boundary pre-tilt, which is normally energetically favourable. This electrode structure fails provide the required sharp transitions.

The potential distribution of the narrowest electrodes, $2 \times d$ electrode geometry, is undercut by the intrusion of the right-hand formed distributions on both sides. Consequently, the electrode region does not reach full activation.

In the $2 \times d$ gap geometries, the potential distributions begin to interfere across the gap. The positively orientated regions, associate with the guard remain present in the top left and bottom right of the gap Their presense may be mutually supportive against erosion by the negatively orientated regions of the majority of the edges. The continued presense of these regions maintains the sharpness of the transition region which in other electrode structure is eroded by the overlap of the director distributions.

11.2.2 Ensuring Positive Rotation

Variations on the previous electrode structures were explored in an attempt to create a positively orientated solution with transition regions of the same form as the left-hand of the guard plate structure (figures G.1.3).

Increasing Boundary Pre-Tilt

It was thought that by increasing the boundary pre-tilt that the energetic preference of the a positively orientated solution may be restored. The result (figures G.1.6) is simply to decrease the effective refractive index of the off-state, the solution remains negatively rotated.

Broken Electrode

Breaking the electrode in half and adjusting the voltages to provide fields in the centre of the electrode which are in the direction appropriate for the positive orientation of the director may promote a positive orientated solution. The result (figures G.1.7) is a negatively orientated solution in which the director in the vicinity of the break is orientated <-90°, to align with the fields at the break. This produces an increase in effective refractive index around the break.

Broken Guard Plate

It was observed that the symmetrically etched earth plate and guard plate electrode structure (figures G.1.4) produced a positively orientated solution without the sharp edges of the left-hand edge in guard plate structure (figures G.1.3). An attempt was made to modify this electrode structure to make the transition regions resemble the left-hand guard plate electrode structure. This was achieved by breaking the guard plates into three. The potential of the central guard plate remains the same, but the outer guard plates were adjusted to progressively resemble the left-hand guard plate electrodes.

The changes in the guard plate potentials is in steps of 0.25V. Note the fractional voltages, .75V and .25V, are rounded up in the plots (figures G.1.8) to .8V and .3V.

The edges can be seen to progressively sharpen as the voltages are modified. The edges are softened by the interaction of the potential distributions of the edge region with the minor potential distributions caused by the break in the guard plates. This marginalizes the negatively orientated regions of the transition regions.

Broken and Shifted Guard Plate I

A simplified form of the previous electrode structure can be constructed with the guard plate broken into two (figures G.1.9). This has the advantage of being constructed from less electrodes and the break is further away from the edges reducing any interaction between them. This produces the required left-hand guard plate transition regions at both sides of the gap. Unfortunately, at the centre of the gap, the break in the guard plates causes a slightly activated region.

The fields produced by the break have four distinct regions; the bottom left and top right, which promote positive orientation and the top left and bottom right, which promote negative orientation. The positive orientation is dominant spreading to the centre of the layer and producing the activated region.

The dominance of the positively orientated region can be reduced by shifting the break in the guard plates relative to each other in such a way as to tilt the majority

of the field to promote negative orientation. A series of results (figures G.1.9) with increasing relative shift have been constructed. At a relative shift of 2μm, the positive and negative activating fields are of approximately equal dominance and at 3μm the negative fields begin to dominate, this produces approximately the least disruption of the unactivated region.

It is puzzling that this electrode structure can produce a positively orientated solution with sharp edges and the staggered guard plate solution fails. Compare the narrow electrode structures of the staggered guard plate structure (figures G.1.5) to that of the broken and shifted guard plate (figures G.1.9). They are very closely related, if the shift in the break was increased to 20μm the electrode structure would be identical. The example with a 16μm shift has potential and director distributions associated with the break resembling the distributions in the staggered guard plate structure. The relationship between these structures requires further investigation.

11.2.3 Narrow Electrode Structures

Broken and Shifted Guard Plate II

The broken guard plate structure (figures G.1.10) can be seen to consistently produce the sharp edges of the left-hand guard plate structure (figures G.1.3) at both edges with the cost of some distortion in the unactivated region. Unfortunately, the presence of the director distribution distortions associated with the break in the guard plate means that the potential distributions begin to interfere at much broader gaps, $\sim 6 \times d$. The $4 \times d$ gap geometries have similar smoothed edges of the $2 \times d$ guard plate geometries, since the proximity of the positively orientated region of the break begins to suppress the negatively orientated region of the edges, which softens the transition region.

In the $2 \times d$ gap geometries, the potential distribution of the break interferes with the potential distribution of the edges. The positively orientated region of break combines with the positive region of the edges and the proximity of the positive regions of the two edges squeezes the negative region of the break . The resulting optical profile is very distorted from the ideal sharp transition form.

Broken and Shifted Guard Plate III

Changing the size of the relative shift in the guard plate breaks (figures G.1.11), was expected to increase the dominance of the negative orientated regions in the gap. This does occur but fails to restore the stepped form of the transition regions.

Staggered Guard Plates with Narrow Gaps

It was observed that the proximity of the minority positively orientated regions in the narrow gaps of the staggered guard plate structure (figures G.1.5) maintained their presense. It was considered that the positive edges for the same structure may also be mutually supportive in a positive solution of a similar electrode structure with narrow gaps (figures G.1.12).

Structures with a gap of $< 2 \times d$ were found to produce a positively orientated solution with a relatively sharp transition regions and a slightly activated central region. As the gap narrows the activation in the centre increases and the gap loses its rectangular form.

In the example with the gap of $2 \times d$, the right-hand edge collapses to a negatively orientated region, with a sharp transition between the negatively orientated edge and the positively orientated electrode region. This appears to be the same form as the *buckled* region observed in Chapter 10 and is probably not a realistic solution.

An attempt was made to reduce the activation of the liquid crystal in the gap by reversing the sign of the potential on the second electrode, this produces horizontal 'driving off' fields in the gap. Both these edges collapse to negative orientated regions, indicating that there is probably no positively orientated solution for this structure.

The success of these narrow structures in producing positively orientated solutions seems to rely on the proximity of the positive regions to reduce the negative region. The wider $2 \times d$ geometry is not stable. The positive guard plate regions seem to have been combined with the positive edge region.

To ensure that the size of the electrodes do not effect the narrow gap solutions some examples are repeated with narrow electrodes (figures G.1.13). For the majority of the results there is no change in the solution, as expected the electrode region isolates the edges. Only in the negatively orientated results do the edges undercut the electrode reducing the orientation under the electrode. There is the additional effect, the positively oriented solutions of the staggered guard plate structures with narrow gaps (figures G.1.12) are no longer produced.

11.3 Refractive Structures

As suggested in Chapter 7 the change in optical profile in the inter-electrode gap can be reduced by reducing the size of the gap (figures G.2.1) or by inserting a buried electrode (figures G.2.2). The narrower the gap or the closer the buried electrode is to the liquid crystal layer the better the resulting optical profile. The applied voltage of the buried electrode may be modified to compensate for its displacement from the liquid crystal layer.

11.4 Diffractive/Refractive Structures

The cell thickness required for diffractive/refractive devices is much greater than that for binary diffractive devices. At least one wavelength of optical path length change is required for the optical profile. An additional wavelength is required to provide the phase correction. If the combed electrode structure is being used, then the cell operates in the approximately linear region of the optical path response, hence only half the total optical path change of the cell is used. Consequently, a total optical path change of at least four wavelengths is required, hence a minimum cell thickness of $\sim 10\mu$m (@ 589.6nm).

The transition between the zones is required to be sharp like the transition between the on and off regions in the binary diffractive devices. It was observed in the binary diffractive electrode structures (figures G.1) that the sharpest edges were produced at high voltages by the guard plate electrode structure (figures G.1.3) in

the transition from on to off in the left to right direction. Unfortunately, the edges at lower voltages (1–2V), consistent with the approximately linear region, produce longer transition regions, due to absence of the x-direction compression of the potential distribution present and the lower tension between the regions of oppositely orientated activation. Some variation from these structures will be required in order to produce a sharp transition at lower operating voltages. The favourable direction of the transition is a useful observation for the design of the transition region electrode structures, transitions in the opposite direction may be constructed from rotated forms of a successful electrode structure. With respect to the transition region it is advantageous for the thinnest cell possible to be used, $\sim 10\mu$m in this case, since the transition regions scale with the cell thickness.

The optical profile in the zone is required to be smooth, continuous and relatively steep. As discussed in Chapter 6, the voltages used to achieve this profile will be applied through a series of discrete electrodes. It was seen from the refractive results (figures G.2) that distortion of the optical profile due to the inter-electrode gap can be reduced by narrowing the gap or the inclusion of buried electrodes. Since the minimum cell thickness is $\sim 10\mu$m it is expected that the minimum sized electrodes, $\sim 2.5\mu$m, will produce a good approximation of the required continuous optical profile, the electrode geometry being well within the meshing régime.

In Chapter 7 it was observed that the refractive power of these devices is limited by the maximum gradient of the optical profile equations (7.1 & 7.2). Since both the optical path change and the optical profile scale with cell thickness, the gradient is independent of cell thickness. The maximum optical profile gradient that can successfully be implemented is clearly an important factor.

It was also suggested in Chapter 7 that narrow electrode structures, dominated by fringing fields, may behave very differently than expected from predictions based on the one-dimensional model.

Variations on the simple zone structures have been presented in order to explore the following issues:

- Can sharp transitions be achieved?
- Do the voltage profiles, based on the one-dimensional behaviour of the cell

produce the expected optical profiles, especially for relatively narrow zones?

- What gradient optical profiles can be produced?
- Can the required continuous voltage profiles be successfully approximated by a series of discrete electrodes, such as the combed electrode structure?

Initially, a $4 \times d$ linear ramp structure, spanning the approximately linear operating region (0.9V–1.8V) was examined. It was surrounded by two $4 \times d$ electrodes with constant voltages of 0.9V and 1.8V, which isolated it from any fringing fields associated with the transition between zones (figure G.3.1a). The fields produced are relatively slowly varying, but contain lateral components due to the spatially varying applied voltage. The majority of the resulting profile has the expected linear form with the extreme ends slightly flattened.

The intrusion of the transition region for a similar linear ramp electrode in a $4 \times d$ periodic structure reduces the extent of the linear profile to approximately half of the period (figure G.3.1b), due to the long transition regions associated with low voltages. The transition region intrudes most under the high voltage end of the ramp structure.

It was observed that the sharpest edge was produced by the left hand edge of the guard plate structure at high voltages. In order to reproduce this sharp transition two electrodes were buried in the vicinity of the transition (figure G.3.1c). As in the guard plate structure (figure G.1.3) there is a region of increased activation, adjacent to a negatively orientated region associated with a left hand edge, and a positively orientated region associated with the guard plate. The negatively orientated region is greatly reduced by the activation of the majority of the zone and the positively orientated guard plate region is reduced by the size of the guard plate. In addition, the 1.8V end of the ramp electrode behaves as a right hand guard plate to the 5V electrode, 'pinching' the top of the activated region so it resembles a pear shape as it pulls the adjacent region into an off orientation. The resulting optical profile has increased activation at the high voltage end and an initial sharp transition. The low activation side of the transition region is smoothed and intrudes into low activation region of the zone.

It was considered that the activation of the low voltage end of the ramp could be improved by putting a negative voltage on the guard plate (figure G.3.1d-i). This has the effect of increasing the negative region of the transition region, which displaces and destroys the region of high activation, eroding the high voltage end of the zone. The low voltage end of the ramp electrode behaves as a left hand guard plate to the negative electrode, producing localized negatively and positively orientated regions. The optical profile at the low voltage end of the zone is improved at the detriment of the profile at the high voltage end.

A variation on this structure is to use the low voltage end of the ramp structure as the guard plate to the high voltage electrode and to insert an additional electrode in the earth plate directly below the high voltage electrode (figure G.3.2). The earth plate behaves a guard plate, producing a negatively orientated region which reduces the intrusion of the transition region into the low voltage side of the zone. The presense of these electrodes distorts the linear region of the zone, but the optical profile still approximates a ramp.

As the zone is narrowed the profile steepens and the transition region, which remains approximately the same length, erodes proportionally more of the low activation of the zone. The form of the high activation end of the zone remains constant until extremely narrow zone geometries are reached.

It was suspected that the form of the discrete electrodes was the dominant factor in the resulting profiles. This can be seen by comparison to a similar electrode structure without the linear ramp electrode (figure G.3.3). The resulting optical profiles are very similar, again the transition region erodes the low activation end of the zone, reducing the steepness and the overall change in optical path across the zone.

Clearly, the interaction of the potential and director distributions in these narrow electrode structures is very involved and not easily predictable. With trail and error the ideal optical profiles for both narrow, diffractive structures and steep diffractive/refractive zones may be constructed from a collection of discrete electrodes. The forms of these structures and the limit of their effectiveness require further investigation. Broader electrode structures may be designed using combed electrode approximations of the required continuous voltage profiles with discrete electrodes

supporting the transition regions.

Figure G.3.4 illustrates that a continuous profile can be constructed from narrow discrete electrodes, such as in the combed electrode structure.

The steepest profile observed in these results (figure G.3.3h) has a gradient of $\sim$ 0.16. If such a slope could be controllably implemented with arbitrary scalability and independent phase correction, then a prism with a maximum deflection angle of $\sim 9°$ and a lens with a minimum f-number of ~ 3.125 could be constructed. Again, the optimal form and the effectiveness of these structures require further investigation.

11.5 Driving Off Electrode Structures

In Chapter 4 the possibility of driving off the liquid crystal with lateral fields was suggested for improving the relaxation time. Three electrode structures are presented (figure G.4), illustrating the equilibrium distributions of the structures. The residual activation in the vicinity of the electrode edges was successfully reduced in the successive structures. This model provides no information on the affect on the relaxation time that these structures may have.

11.6 The Effects of the Initial Conditions

During the presentation of the results the issue of the predominantly positively and negatively orientated results arose. There also appeared a couple of results which contained *buckled* regions, specifically the second and third examples of the staggered guard plate with narrow gaps (figures G.1.12). An attempt will now be made to deal with these issues.

There is a potential danger with minimization methods that the system may settle into a local minima instead of finding the global minima, which is normally considered the solution. Initial conditions in the vicinity of a local minima may cause the system to become trapped in the local minima, consequently the initial conditions can be critical to the outcome of the model. In Chapter 10 it was shown how one-dimensional preprocessing could be used to provide different initial condi-

tions in order to improve the rate of convergence. With the use of one-dimensional preprocessing there are three possible initial conditions:

- The off-state; the director distribution is prescribed by the boundary pre-tilt throughout the system.
- The positive on-state; the one-dimensional solution to the electrode region is used as the initial director distribution throughout the system.
- The negative on-state; the one-dimensional solution that would be obtained if the activation was against the boundary pre-tilt. This is in effect a local minima of the one-dimensional system. The one-dimensional solution with reversed sign for all but the boundary director is used to approximate this state.

As described the one-dimensional solution has two minima with positively and negatively orientated director distributions. In this situation the positively orientated distribution is the solution, being clearly energetically favourable, there are 2° of energetically unfavourably orientated liquid crystal near the boundary in the negatively orientated distribution. It is also intuitively the expected form of the director distribution.

In Chapter 10 it was seen that the use of the off-state and positive on-state as the initial conditions for the simple electrode structure both produced positively orientated results. If the negative on-state was used as the initial conditions it is expected that negatively orientated distribution would result, approximately a mirror image of the positively orientated results, which is clearly not the true solution. For other electrode systems the case is not so clear cut. This is especially true for the structures with staggered or broken guard plates. Two forms of the staggered guard plate and one of the broken guard plate have been presented with each of the three initial conditions (figures G.5).

In the case of the staggered structures both the off-state and the negative on-state initial conditions produced negatively orientated results. The positive on-state produces a negatively orientated solution in the vicinity of the edges and a positive orientated region under the majority of the electrode. The transition

between these two regions takes the form of a *buckled* region. Clearly, the solution has developed from a positive form, but only a negative distribution was found to be stable for the edge regions. Due to the uniformity of the electrode region the transition between the positive solution and the negative solution became trapped while traversing the electrode region. Globally, the completely negatively orientated solution is favourable, containing no *buckled* regions. These results suggest that not even a local minima exists for a positively orientated solution in the staggered guard plate structure.

The results of the broken guard plate are slightly different. The positive on-state initial condition produces the positively orientated results with the sharp edges associated with the left-hand edge of the guard plate structure. The negative on-state produces a negatively orientated solution with two smooth edges associated with the right-hand edges of the guard plate structure. The off-state initial condition produces a solution similar to the positive on-state solution of the staggered electrode structure. The edges have collapsed to a negatively orientated distribution, the electrode is in a positively orientated state and there are *buckled* regions between the two.

Comparing the positive and negative solutions, the negative solution is clearly energetically favourable, each edge containing the transition between only two regions and not three as the positive solution does. Even though the negative solution is energetically the global minimum it is not obvious that a real liquid crystal cell would reach this state. Since the cell is predominantly driven by the electrodes in towards the positive solution it is possible that this local minima is the one the cell reaches. Extending this idea to the staggered electrode structure, it is not clear how the negatively orientated distribution is arrived at from a positively driven cell if this is indeed the final solution. The dynamics of the cell need to be considered to resolve these issues.

Comparing the staggered and guard plate structures, the similarity of these structures has already been commented on, but there is a significant enough difference to allow a local positive solution to be formed by the broken guard plate but not the staggered guard plate. The only difference is the presence of the break in the guard plate and the associated director distribution. The presence of a significant

positively orientated region, due to the break, may subdue the negative region at the edges and consequently support the positively orientated edge region. In the narrow gapped staggered electrode structure (figures G.1.12), the extreme proximity of the positively orientated regions of the opposite edge reduce the negatively orientated region, allowing a positive solution to form. In the shifted and broken guard plate (figures G.1.9), when the relative shift in the breaks is 16μm the negative region associated with the break appears to be increasing in significance, there also appears to be a slight increase in the orientation of the negative region associated with the edges. A further increase in the strength of the negative region may cause the positive edge to collapse as the local energy minima is undermined.

There are clearly some very important unresolved issues concerning the validity and interpretation of the results produced by this model.

11.7 Summary

A variety of possible electrode structures for the binary, diffractive devices have been compared and descriptions of the optical profiles presented. The sharpest transition regions were found to be produced by the left-hand edge of the guard plate structure. A staggered guard plate structure, which has the electrode structure of the left-hand guard plate on both sides of the gap, resulted in a negatively orientated distribution with two edges of the form of the right-hand edge of the guard plate structure. Variations on this structure were explored in order to create a positively oriented solution with sharp edges. A structure with a broken guard plate was found to be successful. Due to the overlapping of the director distribution of the edges with the director distribution produced by the break in the guard plate, the edges were found to be blunted for geometries of $< 6 \times d$ gap.

The effects of narrowing the gap of a simple electrode structure and a buried electrode were illustrated for refractive devices.

Variations of a linear optical profile zone for a diffractive/refractive device were presented, demonstrating that the major components for the implementation of diffractive/refractive devices are possible. It was illustrated that for broad zones, $> 3 \times d$ period, the optical profile follows the expected form for the majority of the

electrode, but are eroded by the transition between adjacent zones. The insertion of discrete electrodes can help to improve the transition regions, but the ideal form of the electrode structure is not obvious. For narrower zones the optical path does not compress as expected and the form of the discrete electrodes becomes dominant. A combed electrode structure was shown to be capable of producing a smooth and continuous optical profile.

The effects of the initial conditions on the final results were discussed, local minima and trapped solutions were described. Whether or not the global minima represents a realist solution remains an open question requiring the dynamics of the system to be considered.

11.8 References

[1] N. J. Powell. *Collection of Results for Binary Diffractive Devices.* (unpublished).

Chapter 12

Conclusions and Further Work

12.1 Introduction

Nematic liquid crystal devices have been successfully employed as electronic displays. The application of nematic liquid crystals may be extended to voltage controlled optical devices which exploit the voltage modification of the electrical Freedrichsz transition described in Chapter 2.

Two approaches may be employed to implement an optical device in a liquid crystal cell:

- A diffractive phase structure can be produced by activating regions of different phase, incident light then diffracts about this structure. The resulting devices are expected to be inefficient, diffracting light into many diffraction orders and inflexible, the optical structure being defined by the fixed electrode structure.
- The optical path may be varied spatially across the device to mimic the optical path profile of a solid, refractive device, for example a lens or a prism. The resulting devices are expected to be very efficient and flexible, but due to the limited change in optical path length that can be obtained in a liquid crystal film the devices will have low refractive powers.

These approaches were presented in Chapter 4.

It was suggested in Chapter 5 that by combining these approaches efficient and flexible devices could be obtained with higher refractive powers. Blazed diffractive structures which deflect all the incident light into the required diffraction order have improved efficiencies. This is equivalent to mimicing the optical profile of a refractive device by only reproducing the fractional wavelength changes in optical path length. Consequently, higher refractive powers can be obtain from a medium with a small change in optical path length. The optical characteristics of these devices can be adjusted by scaling the optical profiles and providing a correction to each zone which ensures that the transition between adjacent zones is an integer number of wavelengths, hence producing a continuous optical profile.

The continuous optical profiles within each zone require a continuous applied voltage profile. In Chapter 6 it was suggested that the continuous optical profile required within each zone could be approximated by a combed electrode structure. The required voltage profile is obtained by dropping the applied voltages across a shaped conductive strip. This strip forms the back of the comb structure from which teeth electrodes carry the voltages along the whole length of the zone. A second buried comb structure may be used to address the regions which fall between the teeth of the first combed electrode. The combed structure has the advantages of;

- only requiring two externally applied voltages,
- only conducting across a narrow strip, reducing any heat dissipation,
- providing the possibility of designing the required voltage profiles into the geometry of the conducting strip.

It was found that in order to produce an optical profile which could be arbitrarily scaled and have an independent phase correction it was necessary to restrict the design and operation of the electrode to the approximately linear region of the optical path response curve. Two-dimensional optical structures can either be achieved by the use of planar earth plates to mask the connections to the centre of the device or by cascading devices, with electrode structures open to connection at the edges, whose combined effect is to produce the required two-dimensional optical structures.

The use of the optical path response curve to design the combed electrode structure assumes that the response under these spatially varying electrode structures

will be consistent with the response from an essentially one-dimensional electrode. In Chapter 7 it was observed that the presence of fringing fields, fields with a significant lateral component, would invalidate this assumption. These fields are present at the edges of the electrodes in binary diffractive devices, causing the partial activation of liquid crystal in the off-region. Various electrode structures were suggested to reduce and confine the effects of these fringing fields. In refractive devices the fringing fields advantageously smooth out the optical profile in the inter-electrode gap. The presence of fringing fields in the diffractive/refractive devices would be useful to smooth out the stepped approximation of the ideal profile, but detrimental to the sharp transitions required at the zone boundaries. In electrode structures with rapidly changing profiles the fringing fields are expected to dominate and the predictions based on the one-dimensional optical path response are no longer valid.

In order to predict the optical profiles of these devices a model was constructed which describes the director orientation throughout a two-dimensional electrode structure. The *variational finite element method*, described in Chapter 3, was used to minimize the *electrical Gibbs free energy*, presented in Chapter 2, of a liquid crystal cell, in order to find the equilibrium director orientation. The formularization of this model was presented in Chapter 8 and its computer implementation in Chapter 9. The performance of this model was presented in Chapter 10, in which the one-dimensional results reproduced the results of Berreman's one-dimensional model and the two-dimensional results appeared self-consistent in a variety of situations.

The model was then employed to observe the effects of various electrode structures on the optical profile of liquid crystal cells. The majority of the results concentrated on binary diffractive devices, some example electrode structures for refractive and diffractive/refractive devices were also examined. Some observations were made about the effect of the initial conditions on the final solution. The implications of these results on the design of further liquid crystal optical devices will now be discussed and suggestions for further work presented.

Electrode Structure	Transition Regions		Minimum
	Left Hand	Right Hand	Feature Size
Simple	$\sim 0.6 \times d$	$\sim 3.0 \times d$	$\sim 8 \times d$
Etched Earth Plate	$\sim 1.5 \times d$	$\sim 1.5 \times d$	$\sim 5 \times d$
Guard Plate	$\sim 0.4 \times d$	$\sim 1.5 \times d$	$\sim 3 \times d$
Etched Earth Plate & Guard Plate	$\sim 1.0 \times d$	$\sim 1.0 \times d$	$\sim 3 \times d$
Staggered Guard Plate	$\sim 1.5 \times d$	$\sim 1.5 \times d$	$\sim 3 \times d$
Broken and Shifted Guard Plate	$\sim 0.4 \times d$	$\sim 0.4 \times d$	$\sim 6 \times d$

Table 12.1: Summary of Binary Diffractive Results at 5V

12.2 Conclusions

12.2.1 Binary Diffractive Devices

Table 12.1 summarises the key features of the binary diffractive electrode structures. The extent of the transition regions represents the amount of distortion from the ideal stepped form of the optical profiles, it is advantageous that these are made as small as possible. The minimum feature size determines the maximum diffractive power that the devices can exhibit while still just approximating the required phase contrast between the off and on regions. The maximum first order diffraction angle in terms of the minimum feature size was given in equation (4.2) and the minimum f-number of a Fresnel zone plate was given in equation (4.7). To find the optical performance of these profiles, in order to find the minimum feature size which produces a required efficiency, it is necessary to apply them to a numerical Fraunhofer or Fresnel diffraction program.

The sharpest transition regions are produced at higher voltages with electrode structures containing guard plates. The compression of the potential distribution in the x-direction for highly activated regions reduces the intrusion of the transition region under the electrode and also reduces the spreading of the activating fields into the gap. The guard plate confines the fringing fields and hence the transition regions to the vicinity of the electrode, isolating the effects of edges from each other across the gap. The guard plate also produces fields which activate the liquid crystal in the opposite direction to the majority of the transition region, causing a taut transition between the regions of opposing activation.

In addition to providing the sharpest transitions, higher voltages also produce the greatest change in optical path between the on and off regions. Consequently, the required π phase change can be achieved with thin cells operating at high voltages. Since the geometry of the optical profile scales with the cell thickness, d, it is advantageous to use the thinnest cells possible. If thicker cells are required, for example to exploit the transient nematic effect (section 4.10.1), it is still advantageous to use the thinnest cell possible, since the scaling of the geometry will be the determining factor in the extent of the fringing fields.

Take for example of a 1.25μm cell, theoretically a π shift can be obtain with an applied voltage ~5V (@ 589.6nm). If an electrode structure similar to the broken guard plate (figures G.1.10) is used, then the transition regions are confined to $0.4 \times d$, hence 0.5μm. Since the centre of these transition regions coincide with the edge of the electrode no correction of the electrode positions is required. The presence of the break in this electrode structure distorts the optical profile in the gap, this can be reduced for large gaps by making several breaks of smaller voltage changes, ensuring that the breaks do not interact with the edges, i.e. are further than $3 \times d$ away. The presence of the break also limits the diffractive power that can be achieved by this electrode structure, the first diffraction order is limited to 2.3° and the minimum f-number lens is limited to ~ 13.

This investigation of various electrode structures has not been exhaustive, it is possible that some improvement may be made with further variations.

The implementation of binary diffractive devices with an electrode structure has been superseded by the method proposed by Patel [1], described in section 4.8, in which the alternate zones are implemented by orthogonally aligned boundary orientations. This has the clear advantage of operating on unpolarized light. In addition it is implemented by a planar electrode, hence there are no fringing fields and associated distortions of the optical profile and the limits of wet etching become irrelevant. The results, however, still provide an insight into the behaviour of the liquid crystal in a variety of situations.

12.2.2 Refractive Devices

The continuously, slowly varying optical profiles required for refractive devices appear to be achievable using narrow electrodes and supporting buried electrodes addressing the inter-electrode gap.

12.2.3 Diffractive/Refractive Devices

The required piece-wise continuous optical profiles with sharp zone transitions appear to be implementable using the combed electrode structure. The minimum size of the electrodes which can be used to construct the combed structure, compared to the minimum cell thickness required, puts the operation of the device well into the meshing régime. Consequently, smooth profiles are produced which do not have the distortions of the stepped approximation anticipated in Chapter 7, hence the potential scattering of light into diffraction orders of the steps will not occur. A single comb structure has been shown to produce a linear ramp (Figure G.3.4) without requiring a second buried comb to address the inter-electrode gaps.

The sharp transitions require additional discrete electrodes of relatively high voltages at the zone boundaries. The optimal form of these transitional electrodes and the voltages required for the full range of transitions expected in the operation of a continuously variable diffractive/refractive devices needs a great deal of further investigation.

The steepest optical profiles occur in the narrowest zones, in which the effects of the transition electrodes dominate over the combed electrode structure. These zones can effectively be addressed with a series of discrete electrodes, omitting the combed electrode structure completely. Again, the optimal forms of these zones and the applied voltages required to produce the range of optical profiles needs further investigation, as does the maximum refractive power that can be successfully achieved.

From the results presented, the implementation of high efficiency, continuously variable diffractive/refractive devices, with relatively high refractive powers, does seem possible.

12.3 Further Work

The results in Chapter 11 represent only a small portion of the possible electrode structures that could be employed for the implementation of diffractive and diffractive/refractive devices. Consequently, there is a great deal of scope for the improvement and characterization of the optical profiles through both trial and error, and the systematic exploration of variations on electrode structures. In order to determine the optical performance of these profiles it is necessary to find the Fresnel and Fraunhofer diffraction patterns they produce.

Aside from the employment of the existing model to develop electrode structures appropriate for the implementation of diffractive/refractive devices, there are further developments that can be made to the model. These developments will now be outlined.

12.3.1 Increasing the Maximum Size of the System Matrix

The size of the system matrix is a limiting factor to the accuracy and size of the problems that can be solved by the model. This limit also excludes the possibility of solving more than one variable in each step of the model, as discussed in section 8.2.5. Consequently, the bottle-neck caused by this limit requires solving before further developments to this model can be made.

The limit is due to the maximum run-time memory available on the machine used. Short of changing the computer this factor can not be changed. It is, however, possible to circumvent this limit by developing matrix factorizing and solving algorithms which do not require the full matrix to be stored in memory. For example, the system matrix could be progressively decomposed as it is constructed element by element, the data for the construction of the system matrix and the decomposed results being progressively read from and stored in file-space, reducing the demands on run-time memory. An in-house algorithm could also make full use of the expected symmetry, bandwidth and regular structure, due to the regular mesh topology, of the sparse system matrix, in order to optimize the use of memory and processor time.

12.3.2 The Finite Elements

In Chapter 10 it was observed that the non-linear form of the solutions was very inefficiently described by linear elements. The use of elements described by higher order polynomials would improve the efficiency of the model, reducing the number of nodes required to obtain the same accuracy.

The use of triangular elements in a rectangular mesh also represents an inefficiency of the model. Rectangular elements are more flexible, hence provide a better approximation than the equivalent triangular element of the same polynomial order. Triangular elements could be used to produce more flexible meshes. The movement to either rectangular elements or triangular based meshes would improve the efficiency of the resulting model. The rectangular elements are more consistent with the orthogonally resolved error estimation and adaptive mesh strategy used. The flexibility of the rectangular mesh can be increased by the use of quadrilateral elements.

It was observed that the error estimator and adaptive mesh strategy required fine tuning. The use of higher order elements or elements of different geometries would require that they are completely reformulated.

12.3.3 Extra-Planar Rotation

As described in section 8.2.4, the model was restricted to in-planar rotation, with one angle of rotational freedom. A full description of the possible combinations of boundary orientations to the electrode structure requires formularization in terms of both the tilt and orientation of the director. The local variation of the director with respect to small angle, spatial variations of tilt and orientation, $\hat{\theta}_v$ and $\hat{\phi}_v$ respectively, becomes;

$$\begin{bmatrix} n_\iota \\ n_\kappa \\ n_\lambda \end{bmatrix} = \begin{bmatrix} \hat{\theta}_v \\ \hat{\phi}_v \sin\hat{\theta} \\ 1 \end{bmatrix} \tag{12.1}$$

where $\hat{\theta}$ is the resulting overall tilt. The resulting formularization will be very involved, complicated by the combination of tilt and orientation terms in the n_κ term. The angular variables may be solved separately in a partitioned three step model,

or in one single step. Partitioning the problem would simplify the formularization at the expense of excluding the interaction terms between the two variables. It is expected that a single step formularization would exhibit superior convergence.

12.3.4 A Single Step Model

The model developed, partitioned the solution of the electrical potential and the change in director orientation into two separate steps, as described in section 8.2.5. In this partitioned form, the solution of the director distribution takes no account of the effect the change in director will have on the potential distribution. This change in potential distribution clearly has consequences on the director distribution that minimizes the system, which again are not accounted for in either step of the model. The absence of these interaction terms from the model reduces the validity of each iteration.

A single step solution which includes these interaction terms, or at least a linear approximation of them, is expected to produce much more informed approximations in each iteration and consequently have improved convergence. In this way the interactions between the three variables; tilt, orientation and electrical potential can be accounted for. Unfortunately, the terms of the electro-static energy, equation 8.3, are quadratic with respect to the electrical potential, the inclusion of the variation of angle would make the energy expression higher than the required *quadratic-linear* form. This problem can be overcome by splitting the potential variable into a constant pre-set potential, $\hat{V}_0$, and a variable change in potential, $\delta\hat{V}$;

$$\hat{V}(x,y) = \hat{V}_0(x,y) + \delta\hat{V}(x,y) \tag{12.2}$$

in the same way as the angular terms were.

The pre-set potential can be calculated with a static, initial director orientation, prior to the solving of the director distribution. This electro-static pre-processing may be used as an opportunity to construct a mesh which fulfills the required solution accuracy, with respect to the initial potential distribution. The initial director distribution may in turn be based on one-dimensional pre-processing, which may also involve the remeshing in order to obtain the required accuracy for the initial director distribution. The use of a more informed initial mesh is expected to reduce

the number of iterations required by avoiding the director distributions distorted by a coarse or badly designed initial mesh.

12.3.5 A Dynamical Model

In Chapter 11, the issue of whether the director distribution representing the global or local minimum of the system, represented the behaviour of a real device, arose. The local minimum director distribution is closer to the initial director distribution and appears intuitively a more appropriate distribution. This lead to the idea of considering the dynamics of the system. Following the evolution of the system from an unactivated state to its final activated state would shed some light on this issue. A dynamical model would also be of use in exploring issues connected to switching speeds of two-dimensional electrode structures. The formularization of a dynamical model is much more involved than the minimizing of the overall energy used in the static model.

In order to create a dynamic model, the elastic and motor couple per unit volume $\mathcal{M}$ needs to be equated with the resistive couple per unit volume $\mathcal{Q}$ [2], where;

$$\mathcal{M} + \mathcal{Q} = 0 \tag{12.3}$$

at any time. The elastic and motor couple per unit volume is given by;

$$\mathcal{M}_\theta = \frac{\delta g}{\delta \theta} \tag{12.4}$$

$$\mathcal{M}_\phi = \frac{\delta g}{\delta \phi} \tag{12.5}$$

which can be obtained by applying *variational calculus* (Appendix B.2) to the Gibbs free energy of the system, g. It must be noted that the generality of two angular variables and two-dimensions needs to be maintained throughout. The resistive couple per unit volume due to the rotational viscosity, γ_1, is given by;

$$\mathcal{Q}_\theta = \frac{d\theta}{dt} \tag{12.6}$$

$$\mathcal{Q}_\phi = \frac{d\phi}{dt} \tag{12.7}$$

This ignores any 'backflow' effects, the movement of the centres of gravity of the liquid crystal. The resulting equations are second order differentials, to which the

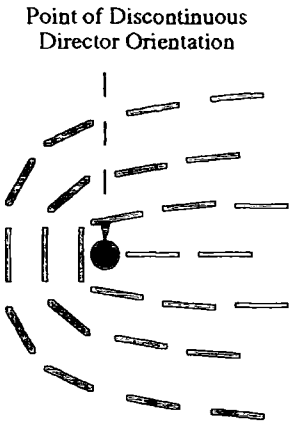

Figure 12.1: Disclination

Garlerkin, residual formulation, described in Chapter 3, can be applied with the small angle approximations, described in Chapter 8. The result will be a finite element model which is a small angle, linear approximation describing the rate of change of the director distribution. The results from this model can be used for a short time step in which the linear approximations are assumed to hold. This formularization is expected to have many similarities to the equivalent static formularization with the small variation in angle being replaced by the rate of change of director, scaled by the viscosity.

12.3.6 Disclinations

Throughout this thesis liquid crystals have been considered to behave in terms of an elastic continuum. This is not always true, *disclinations* may occur, that is lines of discontinuous director orientation. For example, figure 12.1 illustrates a line, perpendicular to the page, in which the director orientation can not be expressed as a single orientation, everywhere else the director is continuous. It is possible that the high voltage electrode structures, which have adjacent regions of oppositely orientated director, will collapse into a disclination, if it is energetically favourable. Whether disclinations do occur and can be modelled using a finite element model requires further consideration.

12.3.7 Light Transmission

The transmission of light through the liquid crystal film has been treated very simply in this thesis. In order to obtain a complete picture of the effect of the liquid crystal film on the emerging light, it may be necessary to use a more sophisticated description. For example, a description which includes the wave guiding effects of the director may be required to describe the effects of director distributions which are distorted out of the plane of polarization.

12.3.8 Observing the Optical Profile

In order to confirm the predictions of the model, an experiment which directly measures the optical profile through a liquid crystal cell would be useful. Light polarized and analysised at 45° to the boundary director orientation can be used to measure the difference in optical path length between the active and passive polarizations of the cell, $n_{\text{eff}}d$ and $n_o d$, respectively. To capture the form of the optical profile before the emerging light is diffracted about the optical structure presented by the liquid crystal, it is necessary to re-image the emerging light, from through the containing glass, with a magnifying microscope objective. The image can then be captured by scanning a photo-multiplier tube or some other form of photo-detector across the image.

12.4 Summary

The further development of the proposed diffractive/refractive devices depends on whether the appropriate optical profiles can be obtained with practical electrode structure. The preliminary results presented here appear promising in this respect. There also requires the identification of an application area which matches their switching speeds and resulting optical performance.

The preliminary model presented in this thesis opens up the possibility of exploring the optical performance of liquid crystal devices, constructed from a wide variety of electrode structures without the incurred cost and delay of manufacture. This provides a suitable test-bed for exploring the possibility of constructing novel

optical devices, such as the diffractive/refractive prism and lens presented.

Whilst there is a wide variety of problems which can be studied with the presented model, there is also a great deal of scope for improving its performance and extending the range of problems which can be addressed. These improvements can be summarized;

- increasing the size and accuracy of the problems which can be addressed,
- using finite elements described by higher order polynomials,
- including extra-planar rotation
- using a single step formularization,
- developing a dynamics model.

Each of these represent a major development of the model, there still remain some important issues concerning the model, namely;

- whether the global or local minima are more representative of the equilibrium state of a real device,
- whether disclinations occur and can they be modelled,
- whether the results produced by the model provide a good representation of the behaviour of a real device,

which require a great deal of further investigation.

12.5 References

[1] J. S. Patel and K. Rastani. 'Electrically controlled polarization-independent liquid-crystal Fresnel lens array', *Opt. Lett.*, 16, 7 (1991) 523-534.

[2] G. Labranie and J. Robert. 'Transient behaviour of the electrically controlled birefringence in a nematic liquid crystal', *J. Appl. Phys.*, 44 (11), (1973) 4869-74.

Appendix A

The Electrical Gibbs Free Energy

A.1 Thermodynamical Systems

A.1.1 Extensive and Intensive Parameters

In thermodynamics the *internal energy* U of a system is given as a function of its *extensive* parameters, x_i;

$$U = U(x_i) \tag{A.1}$$

these are the macroscopic properties of the system, such as entropy S or volume $\mathcal{V}$ and are dependent on the extent of the system considered. For example, if two identical systems are combined the extensive properties of the the composite system are double those of the individual systems. If a proportion, a, of the system is taken the portion has extensive properties that are the same proportion, a, of the extensive properties of the original system.

Intensive properties of the system may be inferred from the effects of the changes of the extensive properties on the internal energy;

$$\left.\frac{\partial U}{\partial x_i}\right|_{x^0_{1,\ldots,n}} = X_i \tag{A.2}$$

where $x^0_{1,\ldots,n}$ form a specified set of extensive values. Temperature T and pressure P are the intensive parameters relating to entropy and volume;

$$\left.\frac{\partial U}{\partial S}\right|_{x^0_{1,\ldots,n}} = T$$

$$-\left.\frac{\partial U}{\partial \mathcal{V}}\right|_{x^0_{1,\ldots,n}} = P$$

Intensive properties are invariant to the proportion of the system considered, for example similar systems with the same intensive properties may be combined or divided without effecting the intensive properties.

A.1.2 Partial Legrendre Transformations

A general variation of the energy can be expressed in terms of variations of the extensive variables;

$$dU = \sum X_i dx_i \tag{A.3}$$

It is often desirable to examine the change of energy with respect to the intensive parameters, for example temperature can be measured and controlled in an experimental situation, the same is not true of entropy. In order to achieve this the energy needs to be re-expressed in terms of one or more of its intensive parameters. By constructing a new energy term;

$$U[X_k] = U - X_k x_k \tag{A.4}$$

which is the *partial Legrendre transformation* of U, the extensive variable x_k has been replaced by the intensive variable X_k as the independent variable. This can be seen when considering the variation of $U[X_k]$ with respect to X_k;

$$\frac{\partial U}{\partial X_k} = x_k \tag{A.5}$$

In this way the internal energy $U(S, \mathcal{V})$ may be transformed to an energy G, in which temperature and pressure are made the independent variables by two partial Legrendre transformations;

$$G \equiv U[T, P] = U - TS + P\mathcal{V} \tag{A.6}$$

this is known as the *Gibbs free energy.*

A.2 Electro-Static Systems

These ideas can be extended to electro-static systems, the relative electrical potential V being the intensive parameter relating to the extensive charge Q of the system. Consider two identical parallel plate capacitors, when combined there is twice the charge on the plates which are still at the same potential difference.

The internal energy of an electro-static system has an additional electro-static energy, U_e;

$$U = U_0 + U_e \tag{A.7}$$

where U_0 represent other contributions, which is a function of charge, Q. This is appropriate for systems which are electrically isolated, or the charge is controlled. In systems where the potentials of the system is controlled by external supplies a partial Legrendre transformation is required to make V the independent variable;

$$G_e \equiv U[V] = U - QV \tag{A.8}$$

this is known as the *electrical Gibbs free energy.*

In a system constructed of N conductors with charge q_i and at potential v_i, the QV term becomes the sum of the products of each charge and potential;

$$QV = \sum_{i=1}^{N} q_i v_i = 2U_e \tag{A.9}$$

which represents twice the electro-static energy of that system. Hence the electrical Gibbs free energy can be written;

$$G_e = U_o - U_e \tag{A.10}$$

A.3 References

[1] R. N. Thurston and D. W. Berreman. 'Equilibrium and stability of liquid-crystal configurations in an electric field', *J. Appl. Phys.*, 52(1), (1981) 508-9.

[2] H.D. Callan. *Thermodynamics and an introduction to Thermostatistics.* 2nd edition, Wiley (1985).

[3] G. N. Lewis and M. Randal. *Thermodynamics.* McGraw-Hill (1961).

[4] W. J. Duffin. *Electricity and Magnetism.* 3rd edition, McGraw-Hill (1980).

Appendix B

Variational Calculus

B.1 The Extremum of a Function

The condition for a function $f(x_i)$ with n independent variables x_j $(j = 1, \ldots, n)$ to be stationary at a point $X^0 = (x_1^0, \ldots, x_n^0)$ is that the first variation of the function δf with respect to arbitrary variations δx_i must vanish;

$$\delta f = \sum_{j=1}^{n} \left. \frac{\partial f(x_i)}{\partial x_j} \right|_{X^0} \delta x_j = \sum_{j=1}^{n} \frac{\partial f(X^0)}{\partial x_j} \delta x_j = 0 \tag{B.1}$$

The variations δx_j are arbitrary, so may be chosen such that all but one is zero, for example the variation of independent variable x_k;

$$\delta x_j = 0 \quad j \neq k \tag{B.2}$$

Equation (B.1) reduces to;

$$\delta f = \frac{\partial f(X^0)}{\partial x_k} \delta x_k = 0 \tag{B.3}$$

for an arbitrary δx_k, hence;

$$\frac{\partial f(X^0)}{\partial x_k} = 0 \tag{B.4}$$

Since the independent variable x_k was chosen arbitrarily, the result must be true for all x_k. The condition for $f(x_i)$ to be stationary at point X^0 reduces to a system of simultaneous equations;

$$\frac{\partial f(X^0)}{\partial x_i} = 0 \tag{B.5}$$

B.2 The Extremum of a Functional

Consider a field with m dependent variables, $\psi_i(x_j)$ $(i = 1, \ldots, m)$, and n independent variables, which is described by a *Lagrangian density*, $\mathcal{L}(x_j, \psi_i, \partial\psi_i/\partial x_j)$, often relating to an energy density in a physical system, and integral;

$$\chi = \int_{\mathcal{D}} \mathcal{L}\left(x_j, \psi_i, \frac{\partial \psi_i}{\partial x_j}\right) d\mathcal{D} \tag{B.6}$$

over the domain $\mathcal{D}$. The field equations corresponding to the Lagrangian density can be found by considering the condition required for the integral, or functional, to be stationary for arbitrary variations of the dependent variables;

$$\psi_i(x_j) \rightarrow \psi_i(x_j) + \epsilon\eta_i(x_j) \tag{B.7}$$

where $\eta_i(x_j)$ are a set of linearly independent functions of x_j which vanish over the boundary surface $\mathcal{S}$.

A variation in χ is given by;

$$\delta\chi = \int_{\mathcal{D}} \mathcal{L}\left(x_j,\ \psi_i + \epsilon\eta_i,\ \frac{\partial \psi_i}{\partial x_j} + \epsilon\frac{\partial \eta_i}{\partial x_j}\right) d\mathcal{D} - \int_{\mathcal{D}} \mathcal{L}\left(x_j, \psi_i, \frac{\partial \psi_i}{\partial x_j}\right) d\mathcal{D} \tag{B.8}$$

which may be written to the first order of ϵ;

$$\delta\chi = \epsilon \int_{\mathcal{D}} \sum_{i=1}^{m} \left\{ \frac{\partial \mathcal{L}}{\partial \psi_i}\eta_i + \sum_{j=1}^{n} \frac{\partial \mathcal{L}}{\partial(\partial\psi_i/\partial x_j)} \frac{\partial \eta_i}{\partial x_j} \right\} d\mathcal{D} \tag{B.9}$$

Using a general form of Green's Theorem (section B.4) the second series of terms may be re-expressed;

$$\begin{aligned} \int_{\mathcal{D}} \sum_{j=1}^{n} \frac{\partial \mathcal{L}}{\partial(\partial\psi_i/\partial x_j)} \frac{\partial \eta_i}{\partial x_j} d\mathcal{D} &= \int_{\mathcal{S}} \eta_i \sum_{j=1}^{n} \frac{\partial \mathcal{L}}{\partial(\partial\psi_i/\partial x_j)} s_j d\mathcal{S} \\ &- \int_{\mathcal{D}} \eta_i \sum_{j=1}^{n} \frac{\partial}{\partial x_j} \frac{\partial \mathcal{L}}{\partial(\partial\psi_i/\partial x_j)} d\mathcal{D} \end{aligned} \tag{B.10}$$

where s_j are the directional cosines of the outward normal to the surface $\mathcal{S}$ at any point. Since η_i vanishes at the surface $\mathcal{S}$ the variation of χ can be rewritten;

$$\delta\chi = \epsilon \int_{\mathcal{D}} \sum_{i=1}^{m} \eta_i \left\{ \frac{\partial \mathcal{L}}{\partial \psi_i} - \sum_{j=1}^{n} \frac{\partial}{\partial x_j} \frac{\partial \mathcal{L}}{\partial(\partial\psi_i/\partial x_j)} \right\} d\mathcal{D} \tag{B.11}$$

If the functional χ is stationary then its first variation is zero; $\delta\chi = 0$. As the variations $\eta_i(x_j)$ are arbitrary they may be chosen to vary for only one of the dependent variables $\psi_k(x_j)$;

$$\eta_i(x_j) = 0 \quad i \neq k \tag{B.12}$$

such an arbitrary variation may be made for each variable $\psi_i(x_j)$, consequently equation (B.11) reduces to m simultaneous equations;

$$\frac{\partial \mathcal{L}}{\partial \psi_i} = \sum_{j=1}^{n} \frac{\partial}{\partial x_j} \frac{\partial \mathcal{L}}{\partial(\partial \psi_i / \partial x_j)} \quad i = 1, \ldots, m \tag{B.13}$$

These are the *Euler-Lagrange* equations which correspond to the Lagrangian density $\mathcal{L}$ and provide the field equations of the system.

From this argument it is clear that the function $\psi_i(x_j)$ which satisfy the field equations (B.13) also make the functional $\chi(\psi_i)$, equation (B.6), stationary. This is the underlying principle of the variational finite element method (section 3.2.1).

B.3 The Application of Variational Calculus to Electro-Statics

The relationship between the Lagrange energy density and the Euler-Lagrange equations has been shown (section B.2). This relationship will now be illustrated with a physical example; relating the electro-static energy density of an isotropic dielectric and Maxwell's first law.

The electro-static energy density of an anisotropic dielectric, in a local co-ordinate system $(\bar{0}, \iota, \kappa, \lambda)$ parallel to the principle axis of the dielectric, is given by;

$$\mathcal{L}_e = \frac{1}{2}\mathbf{D} \cdot \mathbf{E} = \frac{\varepsilon}{2}\left\{\varepsilon_\iota \left(\frac{\partial V}{\partial \iota}\right)^2 + \varepsilon_\kappa \left(\frac{\partial V}{\partial \kappa}\right)^2 + \varepsilon_\lambda \left(\frac{\partial V}{\partial \lambda}\right)^2\right\} \tag{B.14}$$

where $\mathbf{D}$ is the displacement field, $\mathbf{E}$ is the electric field and V the electric potential. The fields are related to the electric potential via;

$$\mathbf{E} = -\nabla V \tag{B.15}$$

$$\mathbf{D} = -\varepsilon \boldsymbol{\varepsilon}_l \nabla V \tag{B.16}$$

where ε is the permittivity of free space and $\boldsymbol{\varepsilon}_l$ is the relative permittivity tensor, given by;

$$\boldsymbol{\varepsilon}_l = \begin{bmatrix} \varepsilon_\iota & 0 & 0 \\ 0 & \varepsilon_\kappa & 0 \\ 0 & 0 & \varepsilon_\lambda \end{bmatrix} \tag{B.17}$$

Substituting the electro-static equation into the Euler-Lagrange equations;

$$\frac{\partial}{\partial \iota}\left(\frac{\partial \mathcal{L}_e}{\partial(\partial V/\partial \iota)}\right) + \frac{\partial}{\partial \kappa}\left(\frac{\partial \mathcal{L}_e}{\partial(\partial V/\partial \kappa)}\right) + \frac{\partial}{\partial \lambda}\left(\frac{\partial \mathcal{L}_e}{\partial(\partial V/\partial \lambda)}\right) = \frac{\partial \mathcal{L}_e}{\partial V} \tag{B.18}$$

$$\varepsilon\left\{\frac{\partial}{\partial\iota}\left(\varepsilon_\iota\left(\frac{\partial V}{\partial\iota}\right)\right)+\frac{\partial}{\partial\kappa}\left(\varepsilon_\kappa\left(\frac{\partial V}{\partial\kappa}\right)\right)+\frac{\partial}{\partial\lambda}\left(\varepsilon_\lambda\left(\frac{\partial V}{\partial\lambda}\right)\right)\right\}=0 \tag{B.19}$$

$$\varepsilon\nabla^T\boldsymbol{\epsilon}_l\nabla V = 0 \tag{B.20}$$

$$\nabla.\mathbb{D} = 0 \tag{B.21}$$

gives directly Maxwell's first law, the electro-static field equation.

B.4 The Generalized Form of Green's Theorem

The general form of Green's theorem was used in the development of the Euler-Lagrange equations from the Lagrange density (section B.2). The general form is given by;

$$\int_{\mathcal{D}} f\frac{\partial g}{\partial x_k}d\mathcal{D}=\int_{\mathcal{S}} fg\ s_k d\mathcal{S}-\int_{\mathcal{D}}\frac{\partial f}{\partial x_k}g d\mathcal{D} \tag{B.22}$$

where f and g are functions of the independent variables x_j which are continuous and have continuous first order partial derivatives $\partial f/\partial x_i$ and $\partial g/\partial x_i$ over domain $\mathcal{D}$.

If $\mathcal{D}$ is a special domain which is bound by a piece-wise smooth *orientable*[1] surface $\mathcal{S}$ and has the property that any straight line parallel to any co-ordinate axis and intersecting $\mathcal{D}$ has at most one segment (or single point) in common with $\mathcal{D}$. This implies $\mathcal{D}$ can be represented in the form;

$$a(x_j)\le x_k\le b(x_j)\quad j\neq k \tag{B.23}$$

where $(x_j)\ j\neq k$ varies in the orthogonal projection of $\mathcal{D}'$ of $\mathcal{D}$ in the x_k =*constant* plane (figure B.1). Clearly $x_k=a(x_j)$ represents the 'bottom' surface $\mathcal{S}_1$ of $\mathcal{S}$ and $x_k=b(x_j)$ represents the 'top' surface $\mathcal{S}_2$ of $\mathcal{S}$, the portion $\mathcal{S}_3$ may degenerate into a curve separating the 'top' and 'bottom' surfaces.

Consider first the integral of a single function in domain $\mathcal{D}$;

$$\begin{aligned}\int_{\mathcal{D}}\frac{\partial g(x_j,x_k)}{\partial x_k}d\mathcal{D} &= \int_{\mathcal{D}'}\left[\int_a^b\frac{\partial g(x_j,x_k)}{\partial x_k}dx_k\right]d\mathcal{D}'\\ &= \int_{\mathcal{D}'} g\left[x_j,b\right]d\mathcal{D}'-\int_{\mathcal{D}'} g\left[x_j,a\right]d\mathcal{D}'\end{aligned}$$

[1] An orientable surface is one whose positive normal direction cannot be reversed by traversing the surface, a counter example is a Möbius strip.

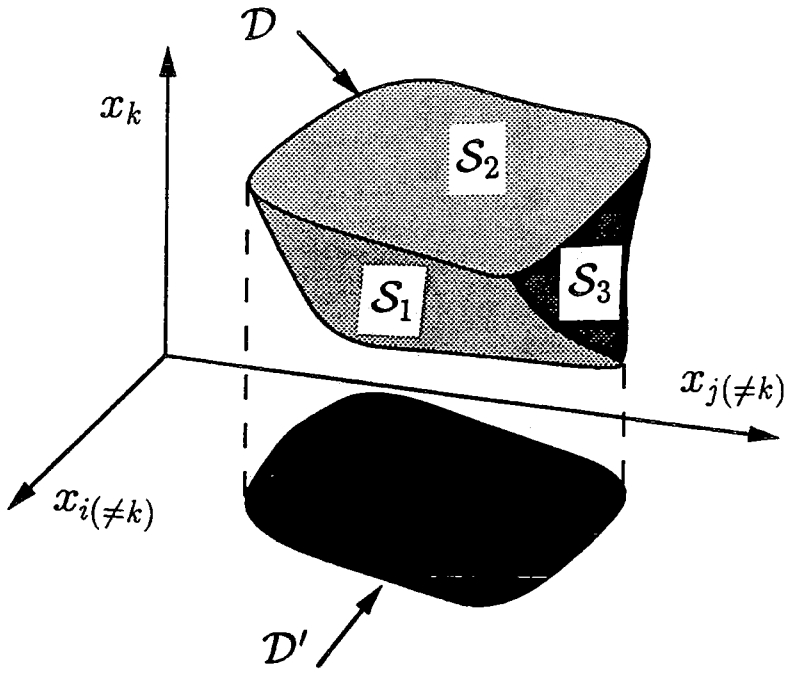

Figure B.1: Orthoganal Projection $\mathcal{D}'$ of Special Domain $\mathcal{D}$ onto x_k =*constant* Plane

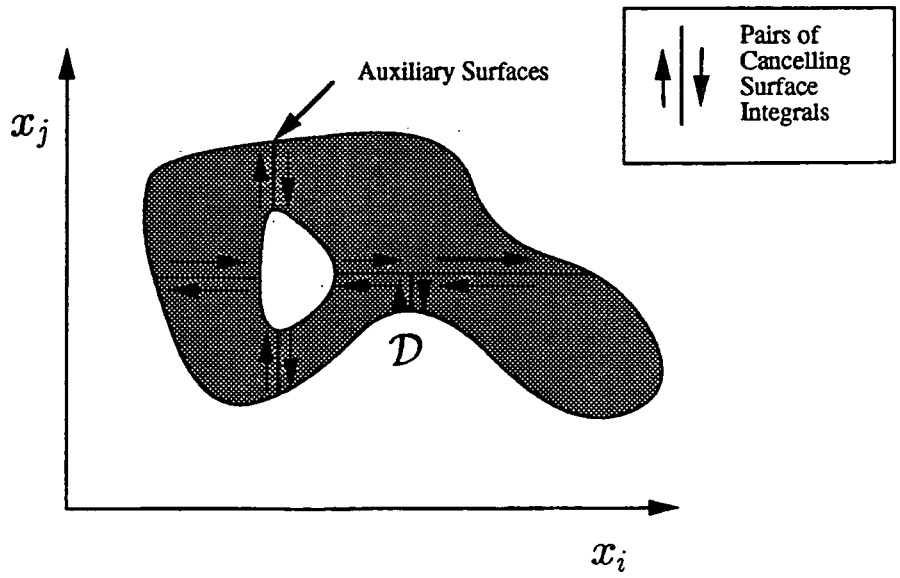

Figure B.2: Subdivisions of General Domain into Special Domains

This can be expressed in terms of surface integrals of the 'top' $\mathcal{S}_2$ and 'bottom' $\mathcal{S}_1$ surfaces, which in turn can be expressed as the integral over the whole surface $\mathcal{S}$, as contributions from regions such as $\mathcal{S}_3$, normal to the x_k =*constant* plane, are zero;

$$\int_{\mathcal{D}} \frac{\partial g(x_j, x_k)}{\partial x_k} d\mathcal{D} = \int_{\mathcal{S}_1} g s_k d\mathcal{S}_1 + \int_{\mathcal{S}_2} g s_k d\mathcal{S}_2 = \int_{\mathcal{S}} g s_k d\mathcal{S} \qquad \text{(B.24)}$$

This relationship is true for special domains described above. For any domain which can be subdivided into finitely many special domains by auxiliary surfaces, the same result can be obtained by adding the results of each part separately (figure B.2). The surface integrals over the auxiliary surfaces cancel in pairs, and the sum of the remaining surface integrals is the surface over the whole boundary $\mathcal{S}$ of domain $\mathcal{D}$. The volume integrals over parts of $\mathcal{D}$ add up to the volume integral over the whole domain $\mathcal{D}$.

Consider integration by parts, again over a special domain;

$$\int_{\mathcal{D}} f \frac{\partial g}{\partial x_k} d\mathcal{D} = \int_{\mathcal{D}'} [fg]_a^b \, d\mathcal{D}' - \int_{\mathcal{D}} \frac{\partial f}{\partial x_k} g d\mathcal{D} \qquad \text{(B.25)}$$

and following the argument that obtained equation (B.24), equation (B.22), a general form of Green's theorem is arrived at;

$$\int_{\mathcal{D}} f \frac{\partial g}{\partial x_k} d\mathcal{D} = \int_{\mathcal{S}} f g s_k d\mathcal{S} - \int_{\mathcal{D}} \frac{\partial f}{\partial x_k} g d\mathcal{D}$$

Again this relationship is true for a special domain, and can be extended to a general domain which can be subdivided into special domains. The result holds true for any choice of independent variable x_k.

B.5 References

[1] D. H. Norrie and G. de Vries. *An Introduction to Finite Element Analysis.* Academic Press (1978).

[2] D. H. Norrie and G. de Vries. *The Finite Element Method.* Academic Press (1973).

[3] B. L. Moiseiwitsch. *Variational Principles.* Wiley (1966).

[4] E. Kreyszig. *Advanced Engineering Mathematics.* 5th edition, Wiley (1983).

[5] W. J. Duffin. *Electricity and Magnetism.* 3rd edition, McGraw-Hill (1980).

Appendix C

Superconvergence in Linear Triangular Elements: A Taylor Series Analysis

The tangential derivatives at the mid-sides of linear triangular elements are believed to be exceptionally accurate with higher convergence rates than at any other position in the element, that is they are *superconvergent* at these points. This is demonstrated using Taylor series expansions, following reference [1].

The finite element approximation of the solution is of the form;

$$\hat{\psi} = \sum_{k=1}^{s} \mathrm{N}_k(x_j)\bar{\psi}_k \tag{C.1}$$

a Lagrangian interpolation over the element of the nodal values of the function $\bar{\psi}_k$ over the s nodes ($k = 1, \ldots, s$), where $\mathrm{N}_k(x_j)$ is the shape function, dependent on m independent variables, x_j ($j = 1, \ldots, m$).

An approximation of the first derivatives of ψ can be given by the derivatives of equation (C.1);

$$\frac{\partial \hat{\psi}}{\partial x_j} = \sum_{k=1}^{s} \frac{\partial \mathrm{N}_k}{\partial x_j}\bar{\psi}_k \tag{C.2}$$

for two-dimensions;

$$\frac{\partial \hat{\psi}}{\partial x} = \sum_{k=1}^{s} \mathrm{N}_k^x \bar{\psi}_k \tag{C.3}$$

$$\frac{\partial \hat{\psi}}{\partial y} = \sum_{k=1}^{s} \mathrm{N}_k^y \bar{\psi}_k \tag{C.4}$$

where N_k^x and N_k^y are the first derivatives of the shape function with respect to x and y respectively.

The exact solution can be expressed as a Taylor expansion about point $(\bar{x}, \bar{y})$, using the notation; $\delta^x = x - \bar{x}$, $\delta^y = y - \bar{y}$ and $\bar{\psi} = \psi(\bar{x}, \bar{y})$, $\bar{\psi}_x = \partial\psi(\bar{x}, \bar{y})/\partial x$, *etc.*;

$$\psi_k = \psi(x_k, y_k) = \bar{\psi} + \bar{\psi}_x\delta_k^x + \bar{\psi}_y\delta_k^y + \frac{1}{2}\bar{\psi}_{xx}(\delta_k^x)^2 + \frac{1}{2}\bar{\psi}_{yy}(\delta_k^y)^2 + \bar{\psi}_{xy}\delta_k^x\delta_k^y + \dots \quad \text{(C.5)}$$

This expansion can be applied to equation (C.3);

$$\begin{aligned}\sum_{k=1}^{s} \mathrm{N}_k^x\psi_k &= \left(\sum_{k=1}^{s} \mathrm{N}_k^x\right)\bar{\psi} + \left(\sum_{k=1}^{s} \mathrm{N}_k^x\delta_k^x\right)\bar{\psi}_x + \left(\sum_{k=1}^{s} \mathrm{N}_k^x\delta_k^y\right)\bar{\psi}_y \\ &+ \frac{1}{2}\left(\sum_{k=1}^{s} \mathrm{N}_k^x(\delta_k^x)^2\right)\bar{\psi}_{xx} + \frac{1}{2}\left(\sum_{k=1}^{s} \mathrm{N}_k^x(\delta_k^y)^2\right)\bar{\psi}_{yy} \\ &+ \left(\sum_{k=1}^{s} \mathrm{N}_k^x\delta_k^x\delta_k^y\right)\bar{\psi}_{xy} + \dots \end{aligned} \quad \text{(C.6)}$$

a similar expresion can be constructed for equation (C.4).

The shape function is a *complete* linear iterpolation function, hence it can interpolate the functions, 1, x & y exactly;

$$\sum_{k=1}^{s} \mathrm{N}_k = 1, \qquad \sum_{k=1}^{s} x_k\mathrm{N}_k = x, \qquad \sum_{k=1}^{s} y_k\mathrm{N}_k = y \quad \text{(C.7)}$$

hence by taking the first derivatives of these functions with respect to x and y;

$$\sum_{k=1}^{s} \mathrm{N}_k^x = 0, \qquad \sum_{k=1}^{s} x_k\mathrm{N}_k^x = 1, \qquad \sum_{k=1}^{s} y_k\mathrm{N}_k^x = 0 \quad \text{(C.8)}$$

$$\sum_{k=1}^{s} \mathrm{N}_k^y = 0, \qquad \sum_{k=1}^{s} x_k\mathrm{N}_k^y = 0, \qquad \sum_{k=1}^{s} y_k\mathrm{N}_k^y = 1 \quad \text{(C.9)}$$

Substituting equations C.8 into equation C.6 and rearranging;

$$\begin{aligned}\bar{\psi}_x &= \sum_{k=1}^{s} \mathrm{N}_k^x\psi_k \\ &- \frac{1}{2}\left(\sum_{k=1}^{s} \mathrm{N}_k^x(\delta_k^x)^2\right)\bar{\psi}_{xx} - \frac{1}{2}\left(\sum_{k=1}^{s} \mathrm{N}_k^x(\delta_k^y)^2\right)\bar{\psi}_{yy} - \left(\sum_{k=1}^{s} \mathrm{N}_k^x\delta_k^x\delta_k^y\right)\bar{\psi}_{xy} \\ &+ O(\delta^2)\end{aligned} \quad \text{(C.10)}$$

where δ is the maximum element dimension. The expansion for $\bar{\psi}_y$ is of identical form with N_k^y replacing N_k^x.

It can be seen from equation (C.10) that $\sum_{k=1}^{s} \mathrm{N}_k^x\psi_k$ is an order $O(\delta)$ approximation of $\bar{\psi}_x$, except at points $(\bar{x}, \bar{y})$ where the first order terms are zero. These

points can be found by finding the positions when the coefficients of $\bar{\psi}_{xx}$, $\bar{\psi}_{xy}$ & $\bar{\psi}_{yy}$ are zero. These conditions imply;

$$\bar{x} = \frac{1}{2}\sum_{k=1}^{s} x_k^2 \mathbb{N}_k^x, \qquad \bar{y} = \sum_{k=1}^{s} x_k y_k \mathbb{N}_k^x, \qquad \sum_{k=1}^{s} y_k^2 \mathbb{N}_k^x = 0 \tag{C.11}$$

The last condition only holds if one side of the element is parallel to the y-axis. Satisfying the first two conditions, it is found that $\hat{\psi}_x$ is an $O(\delta^2)$ approximation of ψ_x at the midpoint of this side. Similarly, $\hat{\psi}_y$ can be shown to be an $O(\delta^2)$ approximation of ψ_y at the midpoint of the side of the element parallel to the x-axis.

Applying these results to the shape function used in this thesis (section 3.2.2, figure 3.1);

$$\mathbb{N} = \left[\tfrac{1}{3} - \tfrac{x}{b} - \tfrac{y}{c}, \;\; \tfrac{1}{3} + \tfrac{x}{b}, \;\; \tfrac{1}{3} + \tfrac{y}{c} \right] \tag{C.12}$$

where b & c are respectively the x & y dimensions of the element, x & y being measured locally from the centroid of the triangle, exceptional accuracies can be found at the points $(b/6, -c/3)$ & $(-b/3, c/6)$, for ψ_x & ψ_y respectively. These are the midpoints of the sides at which the derivatives are tangential.

C.1 References

[1] R. J. MacKinnon and G. F. Carey. 'Superconvergent Derivatives: A Taylor Series Analysis', *Int. Numer. Meth. Engrg.*, 28 (1989) 489-509.

Appendix D

Integration over Element for Richest Approximation

In order to integrate the energy density function for the richest approximation of the elastic model, section 8.6.2, it is necessary to integrate functions of the form;

$$\int\int_{\mathcal{D}_e} u\frac{d^2v}{dx\,dy}dx\,dy \tag{D.1}$$

where u is a polynomial up to second order with respect to the spatial coordinates and v is a sinusoidal function of the spatial coordinates. These results need generating for the five possible forms of angular variation across the element;

1. $\bar{\phi}_{o1} \neq \bar{\phi}_{o2}$, $\bar{\phi}_{o1} \neq \bar{\phi}_{o3}$, $\bar{\phi}_{o2} \neq \bar{\phi}_{o3}$
2. $\bar{\phi}_{o1} = \bar{\phi}_{o2}$, $\bar{\phi}_{o1} \neq \bar{\phi}_{o3}$, $\bar{\phi}_{o2} \neq \bar{\phi}_{o3}$
3. $\bar{\phi}_{o1} \neq \bar{\phi}_{o2}$, $\bar{\phi}_{o1} = \bar{\phi}_{o3}$, $\bar{\phi}_{o2} \neq \bar{\phi}_{o3}$
4. $\bar{\phi}_{o1} \neq \bar{\phi}_{o2}$, $\bar{\phi}_{o1} \neq \bar{\phi}_{o3}$, $\bar{\phi}_{o2} = \bar{\phi}_{o3}$
5. $\bar{\phi}_{o1} = \bar{\phi}_{o2} = \bar{\phi}_{o3}$,

The integral, equation D.1, can be evaluted either with respect to x then y or y then x, producing slightly different algebraic terms, which combine to form the same overall result. Form A is given by;

$$\int_{yl}^{yu}\left(\int_{xl}^{xu} u\frac{d^2v}{dx\,dy}dx\right)dy \tag{D.2}$$

where

$$\begin{array}{lllll} xu & = & \frac{b}{3} - \frac{b}{c}y & xl & = & -\frac{b}{3} \\ yu & = & \frac{2c}{3} & yl & = & -\frac{c}{3} \end{array}$$

and form B is given by;

$$\int_{xl}^{xu}\left(\int_{yl}^{yu} u\frac{d^2v}{dx\,dy}dy\right)dx \tag{D.3}$$

where

$$\begin{array}{rclrcl} yu &=& \frac{c}{3}-\frac{c}{b}y & yl &=& -\frac{c}{3} \\ xu &=& \frac{2b}{3} & xl &=& -\frac{b}{3} \end{array}$$

These are integrated by parts until the polynomial term is differentiated out of existence. To ensure that the algebraic forms of cases 2 and 3 are similar, form B will be used to evaluate case 2 and form A for all other cases. These forms were chosen to keep the algebra as simple as possible.

Table D.1 summarize the form u and its derivatives, where $\bar{\gamma}_i = \delta\bar{\phi}_i - \delta\phi_c$.

Tables D.2 to D.6 summarize the integral results of $d^2v/dx\,dy$, for each of the five cases. These results were generated on an analytical algebra package, *Mathematica*. The tables provide the results for the $\hat{\phi}_o$ terms, the $\hat{\beta}$ terms can be obtained by substituting $\bar{\phi}_{oi} - \phi_c$ for all the $\bar{\phi}_{oi}$ terms in the numerators. The o subscript and the *bar* have been dropped for brevity.

It was noted that the spatial co-efficients, b and c, representing the dimensions of the triangular element, cancel when the u and v terms are combined, leaving a factor, $\Delta = bc/2$, representing the area of the triangle. These co-efficients and factor are omitted from the following tables.

Limits	xu		xl	
	yu	yl	yu	yl
	Form A			
$\hat{\gamma}$	$\bar{\gamma}_3$	$\bar{\gamma}_2$	$\bar{\gamma}_3$	$\bar{\gamma}_1$
$d\hat{\gamma}/dy$	$\delta\phi_3 - \delta\phi_2$		$\delta\phi_3 - \delta\phi_1$	
$d\hat{\gamma}/dx$	$\delta\phi_2 - \delta\phi_1$			
$\hat{\gamma}^2$	$\bar{\gamma}_3^2$	$\bar{\gamma}_2^2$	$\bar{\gamma}_3^2$	$\bar{\gamma}_1^2$
$d\hat{\gamma}^2/dy$	$2\bar{\gamma}_3(\delta\phi_3 - \delta\phi_2)$	$2\bar{\gamma}_2(\delta\phi_3 - \delta\phi_2)$	$2\bar{\gamma}_3(\delta\phi_3 - \delta\phi_1)$	$2\bar{\gamma}_1(\delta\phi_3 - \delta\phi_1)$
$d\hat{\gamma}^2/dx$	$2\bar{\gamma}_3(\delta\phi_2 - \delta\phi_1)$	$2\bar{\gamma}_2(\delta\phi_2 - \delta\phi_1)$	$2\bar{\gamma}_3(\delta\phi_2 - \delta\phi_1)$	$2\bar{\gamma}_1(\delta\phi_2 - \delta\phi_1)$
$d^2\hat{\gamma}^2/dy^2$	$2(\delta\phi_3 - \delta\phi_2)^2$		$2(\delta\phi_3 - \delta\phi_1)^2$	
$d^2\hat{\gamma}^2/dx\,dy$	$2(\delta\phi_3 - \delta\phi_2)(\delta\phi_2 - \delta\phi_1)$		$2(\delta\phi_3 - \delta\phi_1)(\delta\phi_2 - \delta\phi_1)$	
$d^2\hat{\gamma}^2/dx^2$	$2(\delta\phi_2 - \delta\phi_1)^2$			
$\hat{\delta\phi}$	$\bar{\delta\phi}_3$	$\bar{\delta\phi}_2$	$\bar{\delta\phi}_3$	$\bar{\delta\phi}_1$
$d\hat{\delta\phi}/dy$	$\bar{\delta\phi}_3 - \bar{\delta\phi}_2$		$\bar{\delta\phi}_3 - \bar{\delta\phi}_1$	
$d\hat{\delta\phi}/dx$	$\bar{\delta\phi}_2 - \bar{\delta\phi}_1$			
$\hat{\delta\phi}^2$	$\bar{\delta\phi}_3^2$	$\bar{\delta\phi}_2^2$	$\bar{\delta\phi}_3^2$	$\bar{\delta\phi}_1^2$
$d\hat{\delta\phi}^2/dy$	$2\bar{\delta\phi}_3(\bar{\delta\phi}_3 - \bar{\delta\phi}_2)$	$2\bar{\delta\phi}_2(\bar{\delta\phi}_3 - \bar{\delta\phi}_2)$	$2\bar{\delta\phi}_3(\bar{\delta\phi}_3 - \bar{\delta\phi}_1)$	$2\bar{\delta\phi}_1(\bar{\delta\phi}_3 - \bar{\delta\phi}_1)$
$d\hat{\delta\phi}^2/dx$	$2\bar{\delta\phi}_3(\bar{\delta\phi}_2 - \bar{\delta\phi}_1)$	$2\bar{\delta\phi}_2(\bar{\delta\phi}_2 - \bar{\delta\phi}_1)$	$2\bar{\delta\phi}_3(\bar{\delta\phi}_2 - \bar{\delta\phi}_1)$	$2\bar{\delta\phi}_1(\bar{\delta\phi}_2 - \bar{\delta\phi}_1)$
$d^2\hat{\delta\phi}^2/dy^2$	$2(\bar{\delta\phi}_3 - \bar{\delta\phi}_2)^2$		$2(\bar{\delta\phi}_3 - \bar{\delta\phi}_1)^2$	
$d^2\hat{\delta\phi}^2/dx\,dy$	$2(\bar{\delta\phi}_3 - \bar{\delta\phi}_2)(\bar{\delta\phi}_2 - \bar{\delta\phi}_1)$		$2(\bar{\delta\phi}_3 - \bar{\delta\phi}_1)(\bar{\delta\phi}_2 - \bar{\delta\phi}_1)$	
$d^2\hat{\delta\phi}^2/dx^2$	$2(\bar{\delta\phi}_2 - \bar{\delta\phi}_1)^2$			
	Form B			
$\hat{\gamma}$	$\bar{\gamma}_2$	$\bar{\gamma}_3$	$\bar{\gamma}_2$	$\bar{\gamma}_1$
$d\hat{\gamma}/dx$	$\delta\phi_2 - \delta\phi_3$		$\delta\phi_2 - \delta\phi_1$	
$d\hat{\gamma}/dy$	$\delta\phi_3 - \delta\phi_1$			
$\hat{\gamma}^2$	$\bar{\gamma}_2^2$	$\bar{\gamma}_3^2$	$\bar{\gamma}_2^2$	$\bar{\gamma}_1^2$
$d\hat{\gamma}^2/dx$	$2\bar{\gamma}_2(\delta\phi_2 - \delta\phi_3)$	$2\bar{\gamma}_3(\delta\phi_2 - \delta\phi_3)$	$2\bar{\gamma}_2(\delta\phi_2 - \delta\phi_1)$	$2\bar{\gamma}_1(\delta\phi_2 - \delta\phi_1)$
$d\hat{\gamma}^2/dy$	$2\bar{\gamma}_2(\delta\phi_3 - \delta\phi_1)$	$2\bar{\gamma}_3(\delta\phi_3 - \delta\phi_1)$	$2\bar{\gamma}_2(\delta\phi_3 - \delta\phi_1)$	$2\bar{\gamma}_1(\delta\phi_3 - \delta\phi_1)$
$d^2\hat{\gamma}^2/dx^2$	$2(\delta\phi_2 - \delta\phi_3)^2$		$2(\delta\phi_2 - \delta\phi_1)^2$	
$d^2\hat{\gamma}^2/dx\,dy$	$2(\delta\phi_2 - \delta\phi_3)(\delta\phi_3 - \delta\phi_1)$		$2(\delta\phi_2 - \delta\phi_1)(\delta\phi_3 - \delta\phi_1)$	
$d^2\hat{\gamma}^2/dy^2$	$2(\delta\phi_3 - \delta\phi_1)^2$			
$\hat{\delta\phi}$	$\bar{\delta\phi}_2$	$\bar{\delta\phi}_3$	$\bar{\delta\phi}_2$	$\bar{\delta\phi}_1$
$d\hat{\delta\phi}/dx$	$\bar{\delta\phi}_2 - \bar{\delta\phi}_3$		$\bar{\delta\phi}_2 - \bar{\delta\phi}_1$	
$d\hat{\delta\phi}/dy$	$\bar{\delta\phi}_3 - \bar{\delta\phi}_1$			
$\hat{\delta\phi}^2$	$\bar{\delta\phi}_2^2$	$\bar{\delta\phi}_3^2$	$\bar{\delta\phi}_2^2$	$\bar{\delta\phi}_1^2$
$d\hat{\delta\phi}^2/dx$	$2\bar{\delta\phi}_2(\bar{\delta\phi}_2 - \bar{\delta\phi}_3)$	$2\bar{\delta\phi}_3(\bar{\delta\phi}_2 - \bar{\delta\phi}_3)$	$2\bar{\delta\phi}_2(\bar{\delta\phi}_2 - \bar{\delta\phi}_1)$	$2\bar{\delta\phi}_1(\bar{\delta\phi}_2 - \bar{\delta\phi}_1)$
$d\hat{\delta\phi}^2/dy$	$2\bar{\delta\phi}_2(\bar{\delta\phi}_3 - \bar{\delta\phi}_1)$	$2\bar{\delta\phi}_3(\bar{\delta\phi}_3 - \bar{\delta\phi}_1)$	$2\bar{\delta\phi}_2(\bar{\delta\phi}_3 - \bar{\delta\phi}_1)$	$2\bar{\delta\phi}_1(\bar{\delta\phi}_3 - \bar{\delta\phi}_1)$
$d^2\hat{\delta\phi}^2/dx^2$	$2(\bar{\delta\phi}_2 - \bar{\delta\phi}_3)^2$		$2(\bar{\delta\phi}_2 - \bar{\delta\phi}_1)^2$	
$d^2\hat{\delta\phi}^2/dx\,dy$	$2(\bar{\delta\phi}_2 - \bar{\delta\phi}_3)(\bar{\delta\phi}_3 - \bar{\delta\phi}_1)$		$2(\bar{\delta\phi}_2 - \bar{\delta\phi}_1)(\bar{\delta\phi}_3 - \bar{\delta\phi}_1)$	
$d^2\hat{\delta\phi}^2/dy^2$	$2(\bar{\delta\phi}_3 - \bar{\delta\phi}_1)^2$			

Table D.1: Differentiation Results

$\frac{d^2v}{dx\,dy}$		$\cos^2\hat{\phi}_o$	$\cos\hat{\phi}_o \sin\hat{\phi}_o$	$\sin^2\hat{\phi}_o$
Integral	Limits			
v	$xu\ yu$	$\frac{6\phi_3^2-(3+3\cos 2\phi_3)}{12(\phi_3-\phi_2)(\phi_2-\phi_1)}$	$\frac{-(6\phi_3+3\sin 2\phi_3)}{12(\phi_3-\phi_2)(\phi_2-\phi_1)}$	$\frac{6\phi_3^2+(3+3\cos 2\phi_3)}{12(\phi_3-\phi_2)(\phi_2-\phi_1)}$
	$xu\ yl$	$\frac{6\phi_2^2-(3+3\cos 2\phi_2)}{12(\phi_3-\phi_2)(\phi_2-\phi_1)}$	$\frac{-(6\phi_2+3\sin 2\phi_2)}{12(\phi_3-\phi_2)(\phi_2-\phi_1)}$	$\frac{6\phi_2^2+(3+3\cos 2\phi_2)}{12(\phi_3-\phi_2)(\phi_2-\phi_1)}$
	$xl\ yu$	$\frac{6\phi_3^2-(3+3\cos 2\phi_3)}{12(\phi_3-\phi_1)(\phi_2-\phi_1)}$	$\frac{-(6\phi_3+3\sin 2\phi_3)}{12(\phi_3-\phi_1)(\phi_2-\phi_1)}$	$\frac{6\phi_3^2+(3+3\cos 2\phi_3)}{12(\phi_3-\phi_1)(\phi_2-\phi_1)}$
	$xl\ yl$	$\frac{6\phi_1^2-(3+3\cos 2\phi_1)}{12(\phi_3-\phi_1)(\phi_2-\phi_1)}$	$\frac{-(6\phi_1+3\sin 2\phi_1)}{12(\phi_3-\phi_1)(\phi_2-\phi_1)}$	$\frac{6\phi_1^2+(3+3\cos 2\phi_1)}{12(\phi_3-\phi_1)(\phi_2-\phi_1)}$
$\int v dy$	$xu\ yu$	$\frac{4\phi_3^3-(6\phi_3+3\sin 2\phi_3)}{24(\phi_3-\phi_2)^2(\phi_2-\phi_1)}$	$\frac{-(6\phi_3^2-(3+3\cos 2\phi_3))}{24(\phi_3-\phi_2)^2(\phi_2-\phi_1)}$	$\frac{4\phi_3^3+(6\phi_3+3\sin 2\phi_3)}{24(\phi_3-\phi_2)^2(\phi_2-\phi_1)}$
	$xu\ yl$	$\frac{4\phi_2^3-(6\phi_2+3\sin 2\phi_2)}{24(\phi_3-\phi_2)^2(\phi_2-\phi_1)}$	$\frac{-(6\phi_2^2-(3+3\cos 2\phi_2))}{24(\phi_3-\phi_2)^2(\phi_2-\phi_1)}$	$\frac{4\phi_2^3+(6\phi_2+3\sin 2\phi_2)}{24(\phi_3-\phi_2)^2(\phi_2-\phi_1)}$
	$xl\ yu$	$\frac{4\phi_3^3-(6\phi_3+3\sin 2\phi_3)}{24(\phi_3-\phi_1)^2(\phi_2-\phi_1)}$	$\frac{-(6\phi_3^2-(3+3\cos 2\phi_3))}{24(\phi_3-\phi_1)^2(\phi_2-\phi_1)}$	$\frac{4\phi_3^3+(6\phi_3+3\sin 2\phi_3)}{24(\phi_3-\phi_1)^2(\phi_2-\phi_1)}$
	$xl\ yl$	$\frac{4\phi_1^3-(6\phi_1+3\sin 2\phi_1)}{24(\phi_3-\phi_1)^2(\phi_2-\phi_1)}$	$\frac{-(6\phi_1^2-(3+3\cos 2\phi_1))}{24(\phi_3-\phi_1)^2(\phi_2-\phi_1)}$	$\frac{4\phi_1^3+(6\phi_1+3\sin 2\phi_1)}{24(\phi_3-\phi_1)^2(\phi_2-\phi_1)}$
$\int v dx$	$xu\ yu$	$\frac{4\phi_3^3-(6\phi_3+3\sin 2\phi_3)}{24(\phi_3-\phi_2)(\phi_2-\phi_1)^2}$	$\frac{-(6\phi_3^2-(3+3\cos 2\phi_3))}{24(\phi_3-\phi_2)(\phi_2-\phi_1)^2}$	$\frac{4\phi_3^3+(6\phi_3+3\sin 2\phi_3)}{24(\phi_3-\phi_2)(\phi_2-\phi_1)^2}$
	$xu\ yl$	$\frac{4\phi_2^3-(6\phi_2+3\sin 2\phi_2)}{24(\phi_3-\phi_2)(\phi_2-\phi_1)^2}$	$\frac{-(6\phi_2^2-(3+3\cos 2\phi_2))}{24(\phi_3-\phi_2)(\phi_2-\phi_1)^2}$	$\frac{4\phi_2^3+(6\phi_2+3\sin 2\phi_2)}{24(\phi_3-\phi_2)(\phi_2-\phi_1)^2}$
	$xl\ yu$	$\frac{4\phi_3^3-(6\phi_3+3\sin 2\phi_3)}{24(\phi_3-\phi_1)(\phi_2-\phi_1)^2}$	$\frac{-(6\phi_3^2-(3+3\cos 2\phi_3))}{24(\phi_3-\phi_1)(\phi_2-\phi_1)^2}$	$\frac{4\phi_3^3+(6\phi_3+3\sin 2\phi_3)}{24(\phi_3-\phi_1)(\phi_2-\phi_1)^2}$
	$xl\ yl$	$\frac{4\phi_1^3-(6\phi_1+3\sin 2\phi_1)}{24(\phi_3-\phi_1)(\phi_2-\phi_1)^2}$	$\frac{-(6\phi_1^2-(3+3\cos 2\phi_1))}{24(\phi_3-\phi_1)(\phi_2-\phi_1)^2}$	$\frac{4\phi_1^3+(6\phi_1+3\sin 2\phi_1)}{24(\phi_3-\phi_1)(\phi_2-\phi_1)^2}$
$\int v dy^2$	$xu\ yu$	$\frac{2\phi_3^4-(6\phi_3^2-(3+3\cos 2\phi_3))}{48(\phi_3-\phi_2)^3(\phi_2-\phi_1)}$	$\frac{-(4\phi_3^3-(6\phi_3+3\sin 2\phi_3))}{48(\phi_3-\phi_2)^3(\phi_2-\phi_1)}$	$\frac{2\phi_3^4+(6\phi_3^2-(3+3\cos 2\phi_3))}{48(\phi_3-\phi_2)^3(\phi_2-\phi_1)}$
	$xu\ yl$	$\frac{2\phi_2^4-(6\phi_2^2-(3+3\cos 2\phi_2))}{48(\phi_3-\phi_2)^3(\phi_2-\phi_1)}$	$\frac{-(4\phi_2^3-(6\phi_2+3\sin 2\phi_2))}{48(\phi_3-\phi_2)^3(\phi_2-\phi_1)}$	$\frac{2\phi_2^4+(6\phi_2^2-(3+3\cos 2\phi_2))}{48(\phi_3-\phi_2)^3(\phi_2-\phi_1)}$
	$xl\ yu$	$\frac{2\phi_3^4-(6\phi_3^2-(3+3\cos 2\phi_3))}{48(\phi_3-\phi_1)^3(\phi_2-\phi_1)}$	$\frac{-(4\phi_3^3-(6\phi_3+3\sin 2\phi_3))}{48(\phi_3-\phi_1)^3(\phi_2-\phi_1)}$	$\frac{2\phi_3^4+(6\phi_3^2-(3+3\cos 2\phi_3))}{48(\phi_3-\phi_1)^3(\phi_2-\phi_1)}$
	$xl\ yl$	$\frac{2\phi_1^4-(6\phi_1^2-(3+3\cos 2\phi_1))}{48(\phi_3-\phi_1)^3(\phi_2-\phi_1)}$	$\frac{-(4\phi_1^3-(6\phi_1+3\sin 2\phi_1))}{48(\phi_3-\phi_1)^3(\phi_2-\phi_1)}$	$\frac{2\phi_1^4+(6\phi_1^2-(3+3\cos 2\phi_1))}{48(\phi_3-\phi_1)^3(\phi_2-\phi_1)}$
$\int v dx\,dy$	$xu\ yu$	$\frac{2\phi_3^4-(6\phi_3^2-(3+3\cos 2\phi_3))}{48(\phi_3-\phi_2)^2(\phi_2-\phi_1)^2}$	$\frac{-(4\phi_3^3-(6\phi_3+3\sin 2\phi_3))}{48(\phi_3-\phi_2)^2(\phi_2-\phi_1)^2}$	$\frac{2\phi_3^4+(6\phi_3^2-(3+3\cos 2\phi_3))}{48(\phi_3-\phi_2)^2(\phi_2-\phi_1)^2}$
	$xu\ yl$	$\frac{2\phi_2^4-(6\phi_2^2-(3+3\cos 2\phi_2))}{48(\phi_3-\phi_2)^2(\phi_2-\phi_1)^2}$	$\frac{-(4\phi_2^3-(6\phi_2+3\sin 2\phi_2))}{48(\phi_3-\phi_2)^2(\phi_2-\phi_1)^2}$	$\frac{2\phi_2^4+(6\phi_2^2-(3+3\cos 2\phi_2))}{48(\phi_3-\phi_2)^2(\phi_2-\phi_1)^2}$
	$xl\ yu$	$\frac{2\phi_3^4-(6\phi_3^2-(3+3\cos 2\phi_3))}{48(\phi_3-\phi_1)^2(\phi_2-\phi_1)^2}$	$\frac{-(4\phi_3^3-(6\phi_3+3\sin 2\phi_3))}{48(\phi_3-\phi_1)^2(\phi_2-\phi_1)^2}$	$\frac{2\phi_3^4+(6\phi_3^2-(3+3\cos 2\phi_3))}{48(\phi_3-\phi_1)^2(\phi_2-\phi_1)^2}$
	$xl\ yl$	$\frac{2\phi_1^4-(6\phi_1^2-(3+3\cos 2\phi_1))}{48(\phi_3-\phi_1)^2(\phi_2-\phi_1)^2}$	$\frac{-(4\phi_1^3-(6\phi_1+3\sin 2\phi_1))}{48(\phi_3-\phi_1)^2(\phi_2-\phi_1)^2}$	$\frac{2\phi_1^4+(6\phi_1^2-(3+3\cos 2\phi_1))}{48(\phi_3-\phi_1)^2(\phi_2-\phi_1)^2}$
$\int v dx^2$	$xu\ yu$	$\frac{2\phi_3^4-(6\phi_3^2-(3+3\cos 2\phi_3))}{48(\phi_3-\phi_2)(\phi_2-\phi_1)^3}$	$\frac{-(4\phi_3^3-(6\phi_3+3\sin 2\phi_3))}{48(\phi_3-\phi_2)(\phi_2-\phi_1)^3}$	$\frac{2\phi_3^4+(6\phi_3^2-(3+3\cos 2\phi_3))}{48(\phi_3-\phi_2)(\phi_2-\phi_1)^3}$
	$xu\ yl$	$\frac{2\phi_2^4-(6\phi_2^2-(3+3\cos 2\phi_2))}{48(\phi_3-\phi_2)(\phi_2-\phi_1)^3}$	$\frac{-(4\phi_2^3-(6\phi_2+3\sin 2\phi_2))}{48(\phi_3-\phi_2)(\phi_2-\phi_1)^3}$	$\frac{2\phi_2^4+(6\phi_2^2-(3+3\cos 2\phi_2))}{48(\phi_3-\phi_2)(\phi_2-\phi_1)^3}$
	$xl\ yu$	$\frac{2\phi_3^4-(6\phi_3^2-(3+3\cos 2\phi_3))}{48(\phi_3-\phi_1)(\phi_2-\phi_1)^3}$	$\frac{-(4\phi_3^3-(6\phi_3+3\sin 2\phi_3))}{48(\phi_3-\phi_1)(\phi_2-\phi_1)^3}$	$\frac{2\phi_3^4+(6\phi_3^2-(3+3\cos 2\phi_3))}{48(\phi_3-\phi_1)(\phi_2-\phi_1)^3}$
	$xl\ yl$	$\frac{2\phi_1^4-(6\phi_1^2-(3+3\cos 2\phi_1))}{48(\phi_3-\phi_1)(\phi_2-\phi_1)^3}$	$\frac{-(4\phi_1^3-(6\phi_1+3\sin 2\phi_1))}{48(\phi_3-\phi_1)(\phi_2-\phi_1)^3}$	$\frac{2\phi_1^4+(6\phi_1^2-(3+3\cos 2\phi_1))}{48(\phi_3-\phi_1)(\phi_2-\phi_1)^3}$

Table D.2: Integration Results: Case 1

$\frac{d^2v}{dx\,dy}$ Integral	Limits	$\cos^2\hat{\phi}_o$	$\cos\hat{\phi}_o \sin\hat{\phi}_o$	$\sin^2\hat{\phi}_o$
v	$xu\ yu$	$\frac{-(6\phi_1^2-(3+3\cos 2\phi_1))}{12(\phi_3-\phi_1)^2}$	$\frac{6\phi_1+3\sin 2\phi_1}{12(\phi_3-\phi_1)^2}$	$\frac{-(6\phi_1^2+(3+3\cos 2\phi_1))}{12(\phi_3-\phi_1)^2}$
	$xu\ yl$	$\frac{2(6\phi_1+3\sin 2\phi_1)}{18(\phi_3-\phi_1)}$	$\frac{-2(3+3\cos 2\phi_1)}{18(\phi_3-\phi_1)}$	$\frac{2(6\phi_1-3\sin 2\phi_1)}{18(\phi_3-\phi_1)}$
	$xl\ yu$	$\frac{-(6\phi_3^2-(3+3\cos 2\phi_3))}{12(\phi_3-\phi_1)^2}$	$\frac{6\phi_3+3\sin 2\phi_3}{12(\phi_3-\phi_1)^2}$	$\frac{-(6\phi_3^2+(3+3\cos 2\phi_3))}{12(\phi_3-\phi_1)^2}$
	$xl\ yl$	$\frac{-(6\phi_1+3\sin 2\phi_1)}{18(\phi_3-\phi_1)}$	$\frac{3+3\cos 2\phi_1}{18(\phi_3-\phi_1)}$	$\frac{-(6\phi_1-3\sin 2\phi_1)}{18(\phi_3-\phi_1)}$
$\int v\,dx$	$xu\ yu$	$\frac{4\phi_1^3-(6\phi_1+3\sin 2\phi_1)}{24(\phi_3-\phi_1)^3}$	$\frac{-(6\phi_1^2-(3+3\cos 2\phi_1))}{24(\phi_3-\phi_1)^3}$	$\frac{4\phi_1^3+(6\phi_1+3\sin 2\phi_1)}{24(\phi_3-\phi_1)^3}$
	$xu\ yl$	$\frac{4(6\phi_1+3\sin 2\phi_1)}{108(\phi_3-\phi_1)}$	$\frac{-4(3+3\cos 2\phi_1)}{108(\phi_3-\phi_1)}$	$\frac{4(6\phi_1-3\sin 2\phi_1)}{108(\phi_3-\phi_1)}$
	$xl\ yu$	$\frac{4\phi_3^3-(6\phi_3+3\sin 2\phi_3)}{24(\phi_3-\phi_1)^3}$	$\frac{-(6\phi_3^2-(3+3\cos 2\phi_3))}{24(\phi_3-\phi_1)^3}$	$\frac{4\phi_3^3+(6\phi_3+3\sin 2\phi_3)}{24(\phi_3-\phi_1)^3}$
	$xl\ yl$	$\frac{6\phi_1+3\sin 2\phi_1}{108(\phi_3-\phi_1)}$	$\frac{-(3+3\cos 2\phi_1)}{108(\phi_3-\phi_1)}$	$\frac{6\phi_1-3\sin 2\phi_1}{108(\phi_3-\phi_1)}$
$\int v\,dy$	$xu\ yu$	$\frac{-(4\phi_1^3-(6\phi_1+3\sin 2\phi_1))}{24(\phi_3-\phi_1)^3}$	$\frac{6\phi_1^2-(3+3\cos 2\phi_1)}{24(\phi_3-\phi_1)^3}$	$\frac{-(4\phi_1^3+(6\phi_1+3\sin 2\phi_1))}{24(\phi_3-\phi_1)^3}$
	$xu\ yl$	$\frac{2(6\phi_1^2-(3+3\cos 2\phi_1))}{36(\phi_3-\phi_1)^2}$	$\frac{-2(6\phi_1+3\sin 2\phi_1)}{36(\phi_3-\phi_1)^2}$	$\frac{2(6\phi_1^2+(3+3\cos 2\phi_1))}{36(\phi_3-\phi_1)^2}$
	$xl\ yu$	$\frac{-(4\phi_3^3-(6\phi_3+3\sin 2\phi_3))}{24(\phi_3-\phi_1)^3}$	$\frac{6\phi_3^2-(3+3\cos 2\phi_3)}{24(\phi_3-\phi_1)^3}$	$\frac{-(4\phi_3^3+(6\phi_3+3\sin 2\phi_3))}{24(\phi_3-\phi_1)^3}$
	$xl\ yl$	$\frac{-(6\phi_1^2-(3+3\cos 2\phi_1))}{36(\phi_3-\phi_1)^2}$	$\frac{6\phi_1+3\sin 2\phi_1}{36(\phi_3-\phi_1)^2}$	$\frac{-(6\phi_1^2+(3+3\cos 2\phi_1))}{36(\phi_3-\phi_1)^2}$
$\int v\,dx^2$	$xu\ yu$	$\frac{-2\phi_1^4+(6\phi_1^2-(3+3\cos 2\phi_1))}{48(\phi_3-\phi_1)^4}$	$\frac{4\phi_1^3-(6\phi_1+3\sin 2\phi_1)}{48(\phi_3-\phi_1)^4}$	$\frac{-2\phi_1^4-(6\phi_1^2-(3+3\cos 2\phi_1))}{48(\phi_3-\phi_1)^4}$
	$xu\ yl$	$\frac{8(6\phi_1+3\sin 2\phi_1)}{972(\phi_3-\phi_1)}$	$\frac{-8(3+3\cos 2\phi_1)}{972(\phi_3-\phi_1)}$	$\frac{8(6\phi_1-3\sin 2\phi_1)}{972(\phi_3-\phi_1)}$
	$xl\ yu$	$\frac{-2\phi_3^4+(6\phi_3^2-(3+3\cos 2\phi_3))}{48(\phi_3-\phi_1)^4}$	$\frac{4\phi_3^3-(6\phi_3+3\sin 2\phi_3)}{48(\phi_3-\phi_1)^4}$	$\frac{-2\phi_3^4-(6\phi_3^2-(3+3\cos 2\phi_3))}{48(\phi_3-\phi_1)^4}$
	$xl\ yl$	$\frac{-(6\phi_1+3\sin 2\phi_1)}{972(\phi_3-\phi_1)}$	$\frac{3+3\cos 2\phi_1}{972(\phi_3-\phi_1)}$	$\frac{-(6\phi_1-3\sin 2\phi_1)}{972(\phi_3-\phi_1)}$
$\int v\,dx\,dy$	$xu\ yu$	$\frac{2\phi_1^4-(6\phi_1^2-(3+3\cos 2\phi_1))}{48(\phi_3-\phi_1)^4}$	$\frac{-4\phi_1^3+(6\phi_1+3\sin 2\phi_1)}{48(\phi_3-\phi_1)^4}$	$\frac{2\phi_1^4+(6\phi_1^2-(3+3\cos 2\phi_1))}{48(\phi_3-\phi_1)^4}$
	$xu\ yl$	$\frac{4(6\phi_1^2-(3+3\cos 2\phi_1))}{216(\phi_3-\phi_1)^2}$	$\frac{-4(6\phi_1+3\sin 2\phi_1)}{216(\phi_3-\phi_1)^2}$	$\frac{4(6\phi_1^2+(3+3\cos 2\phi_1))}{216(\phi_3-\phi_1)^2}$
	$xl\ yu$	$\frac{2\phi_3^4-(6\phi_3^2-(3+3\cos 2\phi_3))}{48(\phi_3-\phi_1)^4}$	$\frac{-4\phi_3^3+(6\phi_3+3\sin 2\phi_3)}{48(\phi_3-\phi_1)^4}$	$\frac{2\phi_3^4+(6\phi_3^2-(3+3\cos 2\phi_3))}{48(\phi_3-\phi_1)^4}$
	$xl\ yl$	$\frac{6\phi_1^2-(3+3\cos 2\phi_1)}{216(\phi_3-\phi_1)^2}$	$\frac{-(6\phi_1+3\sin 2\phi_1)}{216(\phi_3-\phi_1)^2}$	$\frac{6\phi_1^2+(3+3\cos 2\phi_1)}{216(\phi_3-\phi_1)^2}$
$\int v\,dy^2$	$xu\ yu$	$\frac{-2\phi_1^4+(6\phi_1^2-(3+3\cos 2\phi_1))}{48(\phi_3-\phi_1)^4}$	$\frac{4\phi_1^3-(6\phi_1+3\sin 2\phi_1)}{48(\phi_3-\phi_1)^4}$	$\frac{-2\phi_1^4-(6\phi_1^2-(3+3\cos 2\phi_1))}{48(\phi_3-\phi_1)^4}$
	$xu\ yl$	$\frac{2(4\phi_1^3-(6\phi_1+3\sin 2\phi_1))}{72(\phi_3-\phi_1)^3}$	$\frac{-2(6\phi_1^2-(3+3\cos 2\phi_1))}{72(\phi_3-\phi_1)^3}$	$\frac{2(4\phi_1^3+(6\phi_1+3\sin 2\phi_1))}{72(\phi_3-\phi_1)^3}$
	$xl\ yu$	$\frac{-2\phi_3^4+(6\phi_3^2-(3+3\cos 2\phi_3))}{48(\phi_3-\phi_1)^4}$	$\frac{4\phi_3^3-(6\phi_3+3\sin 2\phi_3)}{48(\phi_3-\phi_1)^4}$	$\frac{-2\phi_3^4-(6\phi_3^2-(3+3\cos 2\phi_3))}{48(\phi_3-\phi_1)^4}$
	$xl\ yl$	$\frac{-(4\phi_1^3-(6\phi_1+3\sin 2\phi_1))}{72(\phi_3-\phi_1)^3}$	$\frac{6\phi_1^2-(3+3\cos 2\phi_1)}{72(\phi_3-\phi_1)^3}$	$\frac{-(4\phi_1^3+(6\phi_1+3\sin 2\phi_1))}{72(\phi_3-\phi_1)^3}$

Table D.3: Integration Results: Case 2

$\frac{d^2v}{dx\,dy}$		$\cos^2\phi_o$	$\cos\phi_o \sin\phi_o$	$\sin^2\phi_o$
Integral	Limits			
v	$xu\ yu$	$\frac{-(6\phi_1^2-(3+3\cos 2\phi_1))}{12(\phi_2-\phi_1)^2}$	$\frac{6\phi_1+3\sin 2\phi_1}{12(\phi_2-\phi_1)^2}$	$\frac{-(6\phi_1^2+(3+3\cos 2\phi_1))}{12(\phi_2-\phi_1)^2}$
	$xu\ yl$	$\frac{-(6\phi_2^2-(3+3\cos 2\phi_2))}{12(\phi_2-\phi_1)^2}$	$\frac{6\phi_2+3\sin 2\phi_2}{12(\phi_2-\phi_1)^2}$	$\frac{-(6\phi_2^2+(3+3\cos 2\phi_2))}{12(\phi_2-\phi_1)^2}$
	$xl\ yu$	$\frac{2(6\phi_1+3\sin 2\phi_1)}{18(\phi_2-\phi_1)}$	$\frac{-2(3+3\cos 2\phi_1)}{18(\phi_2-\phi_1)}$	$\frac{2(6\phi_1-3\sin 2\phi_1)}{18(\phi_2-\phi_1)}$
	$xl\ yl$	$\frac{-(6\phi_1+3\sin 2\phi_1)}{18(\phi_2-\phi_1)}$	$\frac{3+3\cos 2\phi_1}{18(\phi_2-\phi_1)}$	$\frac{-(6\phi_1-3\sin 2\phi_1)}{18(\phi_2-\phi_1)}$
$\int v dy$	$xu\ yu$	$\frac{4\phi_1^3-(6\phi_1+3\sin 2\phi_1)}{24(\phi_2-\phi_1)^3}$	$\frac{-(6\phi_1^2-(3+3\cos 2\phi_1))}{24(\phi_2-\phi_1)^3}$	$\frac{4\phi_1^3+(6\phi_1+3\sin 2\phi_1)}{24(\phi_2-\phi_1)^3}$
	$xu\ yl$	$\frac{4\phi_2^3-(6\phi_2+3\sin 2\phi_2)}{24(\phi_2-\phi_1)^3}$	$\frac{-(6\phi_2^2-(3+3\cos 2\phi_2))}{24(\phi_2-\phi_1)^3}$	$\frac{4\phi_2^3+(6\phi_2+3\sin 2\phi_2)}{24(\phi_2-\phi_1)^3}$
	$xl\ yu$	$\frac{4(6\phi_1+3\sin 2\phi_1)}{108(\phi_2-\phi_1)}$	$\frac{-4(3+3\cos 2\phi_1)}{108(\phi_2-\phi_1)}$	$\frac{4(6\phi_1-3\sin 2\phi_1)}{108(\phi_2-\phi_1)}$
	$xl\ yl$	$\frac{6\phi_1+3\sin 2\phi_1}{108(\phi_2-\phi_1)}$	$\frac{-(3+3\cos 2\phi_1)}{108(\phi_2-\phi_1)}$	$\frac{6\phi_1-3\sin 2\phi_1}{108(\phi_2-\phi_1)}$
$\int v dx$	$xu\ yu$	$\frac{-(4\phi_1^3-(6\phi_1+3\sin 2\phi_1))}{24(\phi_2-\phi_1)^3}$	$\frac{6\phi_1^2-(3+3\cos 2\phi_1)}{24(\phi_2-\phi_1)^3}$	$\frac{-(4\phi_1^3+(6\phi_1+3\sin 2\phi_1))}{24(\phi_2-\phi_1)^3}$
	$xu\ yl$	$\frac{-(4\phi_2^3-(6\phi_2+3\sin 2\phi_2))}{24(\phi_2-\phi_1)^3}$	$\frac{6\phi_2^2-(3+3\cos 2\phi_2)}{24(\phi_2-\phi_1)^3}$	$\frac{-(4\phi_2^3+(6\phi_2+3\sin 2\phi_2))}{24(\phi_2-\phi_1)^3}$
	$xl\ yu$	$\frac{2(6\phi_1^2-(3+3\cos 2\phi_1))}{36(\phi_2-\phi_1)^2}$	$\frac{-2(6\phi_1+3\sin 2\phi_1)}{36(\phi_2-\phi_1)^2}$	$\frac{2(6\phi_1^2+(3+3\cos 2\phi_1))}{36(\phi_2-\phi_1)^2}$
	$xl\ yl$	$\frac{-(6\phi_1^2-(3+3\cos 2\phi_1))}{36(\phi_2-\phi_1)^2}$	$\frac{6\phi_1+3\sin 2\phi_1}{36(\phi_2-\phi_1)^2}$	$\frac{-(6\phi_1^2+(3+3\cos 2\phi_1))}{36(\phi_2-\phi_1)^2}$
$\int v dy^2$	$xu\ yu$	$\frac{-2\phi_1^4+(6\phi_1^2-(3+3\cos 2\phi_1))}{48(\phi_2-\phi_1)^4}$	$\frac{4\phi_1^3-(6\phi_1+3\sin 2\phi_1)}{48(\phi_2-\phi_1)^4}$	$\frac{-2\phi_1^4-(6\phi_1^2-(3+3\cos 2\phi_1))}{48(\phi_2-\phi_1)^4}$
	$xu\ yl$	$\frac{-2\phi_2^4+(6\phi_2^2-(3+3\cos 2\phi_2))}{48(\phi_2-\phi_1)^4}$	$\frac{4\phi_2^3-(6\phi_2+3\sin 2\phi_2)}{48(\phi_2-\phi_1)^4}$	$\frac{-2\phi_2^4-(6\phi_2^2-(3+3\cos 2\phi_2))}{48(\phi_2-\phi_1)^4}$
	$xl\ yu$	$\frac{8(6\phi_1+3\sin 2\phi_1)}{972(\phi_2-\phi_1)}$	$\frac{-8(3+3\cos 2\phi_1)}{972(\phi_2-\phi_1)}$	$\frac{8(6\phi_1-3\sin 2\phi_1)}{972(\phi_2-\phi_1)}$
	$xl\ yl$	$\frac{-(6\phi_1+3\sin 2\phi_1)}{972(\phi_2-\phi_1)}$	$\frac{3+3\cos 2\phi_1}{972(\phi_2-\phi_1)}$	$\frac{-(6\phi_1-3\sin 2\phi_1)}{972(\phi_2-\phi_1)}$
$\int v dx\,dy$	$xu\ yu$	$\frac{2\phi_1^4-(6\phi_1^2-(3+3\cos 2\phi_1))}{48(\phi_2-\phi_1)^4}$	$\frac{-4\phi_1^3+(6\phi_1+3\sin 2\phi_1)}{48(\phi_2-\phi_1)^4}$	$\frac{2\phi_1^4+(6\phi_1^2-(3+3\cos 2\phi_1))}{48(\phi_2-\phi_1)^4}$
	$xu\ yl$	$\frac{2\phi_2^4-(6\phi_2^2-(3+3\cos 2\phi_2))}{48(\phi_2-\phi_1)^4}$	$\frac{-4\phi_2^3+(6\phi_2+3\sin 2\phi_2)}{48(\phi_2-\phi_1)^4}$	$\frac{2\phi_2^4+(6\phi_2^2-(3+3\cos 2\phi_2))}{48(\phi_2-\phi_1)^4}$
	$xl\ yu$	$\frac{4(6\phi_1^2-(3+3\cos 2\phi_1))}{216(\phi_2-\phi_1)^2}$	$\frac{-4(6\phi_1+3\sin 2\phi_1)}{216(\phi_2-\phi_1)^2}$	$\frac{4(6\phi_1^2+(3+3\cos 2\phi_1))}{216(\phi_2-\phi_1)^2}$
	$xl\ yl$	$\frac{6\phi_1^2-(3+3\cos 2\phi_1)}{216(\phi_2-\phi_1)^2}$	$\frac{-(6\phi_1+3\sin 2\phi_1)}{216(\phi_2-\phi_1)^2}$	$\frac{6\phi_1^2+(3+3\cos 2\phi_1)}{216(\phi_2-\phi_1)^2}$
$\int v dx^2$	$xu\ yu$	$\frac{-2\phi_1^4+(6\phi_1^2-(3+3\cos 2\phi_1))}{48(\phi_2-\phi_1)^4}$	$\frac{4\phi_1^3-(6\phi_1+3\sin 2\phi_1)}{48(\phi_2-\phi_1)^4}$	$\frac{-2\phi_1^4-(6\phi_1^2-(3+3\cos 2\phi_1))}{48(\phi_2-\phi_1)^4}$
	$xu\ yl$	$\frac{-2\phi_2^4+(6\phi_2^2-(3+3\cos 2\phi_2))}{48(\phi_2-\phi_1)^4}$	$\frac{4\phi_2^3-(6\phi_2+3\sin 2\phi_2)}{48(\phi_2-\phi_1)^4}$	$\frac{-2\phi_2^4-(6\phi_2^2-(3+3\cos 2\phi_2))}{48(\phi_2-\phi_1)^4}$
	$xl\ yu$	$\frac{2(4\phi_1^3-(6\phi_1+3\sin 2\phi_1))}{72(\phi_2-\phi_1)^3}$	$\frac{-2(6\phi_1^2-(3+3\cos 2\phi_1))}{72(\phi_2-\phi_1)^3}$	$\frac{2(4\phi_1^3+(6\phi_1+3\sin 2\phi_1))}{72(\phi_2-\phi_1)^3}$
	$xl\ yl$	$\frac{-(4\phi_1^3-(6\phi_1+3\sin 2\phi_1))}{72(\phi_2-\phi_1)^3}$	$\frac{6\phi_1^2-(3+3\cos 2\phi_1)}{72(\phi_2-\phi_1)^3}$	$\frac{-(4\phi_1^3+(6\phi_1+3\sin 2\phi_1))}{72(\phi_2-\phi_1)^3}$

Table D.4: Integration Results: Case 3

$\frac{d^2v}{dx\,dy}$		$\cos^2\vec{\phi}_o$	$\cos\vec{\phi}_o \sin\vec{\phi}_o$	$\sin^2\vec{\phi}_o$
Integral	Limits			
v	$xu\ yu$	$\frac{2(6\phi_2+3\sin 2\phi_2)}{18(\phi_2-\phi_1)}$	$\frac{-2(3+3\cos 2\phi_2)}{18(\phi_2-\phi_1)}$	$\frac{2(6\phi_2-3\sin 2\phi_2)}{18(\phi_2-\phi_1)}$
	$xu\ yl$	$\frac{-(6\phi_2+3\sin 2\phi_2)}{18(\phi_2-\phi_1)}$	$\frac{3+3\cos 2\phi_2}{18(\phi_2-\phi_1)}$	$\frac{-(6\phi_2-3\sin 2\phi_2)}{18(\phi_2-\phi_1)}$
	$xl\ yu$	$\frac{6\phi_2^2-(3+3\cos 2\phi_2)}{12(\phi_2-\phi_1)^2}$	$\frac{-(6\phi_2+3\sin 2\phi_2)}{12(\phi_2-\phi_1)^2}$	$\frac{6\phi_2^2+(3+3\cos 2\phi_2)}{12(\phi_2-\phi_1)^2}$
	$xl\ yl$	$\frac{6\phi_1^2-(3+3\cos 2\phi_1)}{12(\phi_2-\phi_1)^2}$	$\frac{-(6\phi_1+3\sin 2\phi_1)}{12(\phi_2-\phi_1)^2}$	$\frac{6\phi_1^2+(3+3\cos 2\phi_1)}{12(\phi_2-\phi_1)^2}$
$\int v dy$	$xu\ yu$	$\frac{4(6\phi_2+3\sin 2\phi_2)}{108(\phi_2-\phi_1)}$	$\frac{-4(3+3\cos 2\phi_2)}{108(\phi_2-\phi_1)}$	$\frac{4(6\phi_2-3\sin 2\phi_2)}{108(\phi_2-\phi_1)}$
	$xu\ yl$	$\frac{6\phi_2+3\sin 2\phi_2}{108(\phi_2-\phi_1)}$	$\frac{-(3+3\cos 2\phi_2)}{108(\phi_2-\phi_1)}$	$\frac{6\phi_2-3\sin 2\phi_2}{108(\phi_2-\phi_1)}$
	$xl\ yu$	$\frac{4\phi_2^3-(6\phi_2+3\sin 2\phi_2)}{24(\phi_2-\phi_1)^3}$	$\frac{-(6\phi_2^2-(3+3\cos 2\phi_2))}{24(\phi_2-\phi_1)^3}$	$\frac{4\phi_2^3+(6\phi_2+3\sin 2\phi_2)}{24(\phi_2-\phi_1)^3}$
	$xl\ yl$	$\frac{4\phi_1^3-(6\phi_1+3\sin 2\phi_1)}{24(\phi_2-\phi_1)^3}$	$\frac{-(6\phi_1^2-(3+3\cos 2\phi_1))}{24(\phi_2-\phi_1)^3}$	$\frac{4\phi_1^3+(6\phi_1+3\sin 2\phi_1)}{24(\phi_2-\phi_1)^3}$
$\int v dx$	$xu\ yu$	$\frac{2(6\phi_2^2-(3+3\cos 2\phi_2))}{36(\phi_2-\phi_1)^2}$	$\frac{-2(6\phi_2+3\sin 2\phi_2)}{36(\phi_2-\phi_1)^2}$	$\frac{2(6\phi_2^2+(3+3\cos 2\phi_2))}{36(\phi_2-\phi_1)^2}$
	$xu\ yl$	$\frac{-(6\phi_2^2-(3+3\cos 2\phi_2))}{36(\phi_2-\phi_1)^2}$	$\frac{6\phi_2+3\sin 2\phi_2}{36(\phi_2-\phi_1)^2}$	$\frac{-(6\phi_2^2+(3+3\cos 2\phi_2))}{36(\phi_2-\phi_1)^2}$
	$xl\ yu$	$\frac{4\phi_2^3-(6\phi_2+3\sin 2\phi_2)}{24(\phi_2-\phi_1)^3}$	$\frac{-(6\phi_2^2-(3+3\cos 2\phi_2))}{24(\phi_2-\phi_1)^3}$	$\frac{4\phi_2^3+(6\phi_2+3\sin 2\phi_2)}{24(\phi_2-\phi_1)^3}$
	$xl\ yl$	$\frac{4\phi_1^3-(6\phi_1+3\sin 2\phi_1)}{24(\phi_2-\phi_1)^3}$	$\frac{-(6\phi_1^2-(3+3\cos 2\phi_1))}{24(\phi_2-\phi_1)^3}$	$\frac{4\phi_1^3+(6\phi_1+3\sin 2\phi_1)}{24(\phi_2-\phi_1)^3}$
$\int v dy^2$	$xu\ yu$	$\frac{8(6\phi_2+3\sin 2\phi_2)}{972(\phi_2-\phi_1)}$	$\frac{-8(3+3\cos 2\phi_2)}{972(\phi_2-\phi_1)}$	$\frac{8(6\phi_2-3\sin 2\phi_2)}{972(\phi_2-\phi_1)}$
	$xu\ yl$	$\frac{-(6\phi_2+3\sin 2\phi_2)}{972(\phi_2-\phi_1)}$	$\frac{3+3\cos 2\phi_2}{972(\phi_2-\phi_1)}$	$\frac{-(6\phi_2-3\sin 2\phi_2)}{972(\phi_2-\phi_1)}$
	$xl\ yu$	$\frac{2\phi_2^4-(6\phi_2^2-(3+3\cos 2\phi_2))}{48(\phi_2-\phi_1)^4}$	$\frac{-(4\phi_2^3-(6\phi_2+3\sin 2\phi_2))}{48(\phi_2-\phi_1)^4}$	$\frac{2\phi_2^4+(6\phi_2^2-(3+3\cos 2\phi_2))}{48(\phi_2-\phi_1)^4}$
	$xl\ yl$	$\frac{2\phi_1^4-(6\phi_1^2-(3+3\cos 2\phi_1))}{48(\phi_2-\phi_1)^4}$	$\frac{-(4\phi_1^3-(6\phi_1+3\sin 2\phi_1))}{48(\phi_2-\phi_1)^4}$	$\frac{2\phi_1^4+(6\phi_1^2-(3+3\cos 2\phi_1))}{48(\phi_2-\phi_1)^4}$
$\int v dx\,dy$	$xu\ yu$	$\frac{4(6\phi_2^2-(3+3\cos 2\phi_2))}{216(\phi_2-\phi_1)^2}$	$\frac{-4(6\phi_2+3\sin 2\phi_2)}{216(\phi_2-\phi_1)^2}$	$\frac{4(6\phi_2^2+(3+3\cos 2\phi_2))}{216(\phi_2-\phi_1)^2}$
	$xu\ yl$	$\frac{6\phi_2^2-(3+3\cos 2\phi_2)}{216(\phi_2-\phi_1)^2}$	$\frac{-(6\phi_2+3\sin 2\phi_2)}{216(\phi_2-\phi_1)^2}$	$\frac{6\phi_2^2+(3+3\cos 2\phi_2)}{216(\phi_2-\phi_1)^2}$
	$xl\ yu$	$\frac{2\phi_2^4-(6\phi_2^2-(3+3\cos 2\phi_2))}{48(\phi_2-\phi_1)^4}$	$\frac{-(4\phi_2^3-(6\phi_2+3\sin 2\phi_2))}{48(\phi_2-\phi_1)^4}$	$\frac{2\phi_2^4+(6\phi_2^2-(3+3\cos 2\phi_2))}{48(\phi_2-\phi_1)^4}$
	$xl\ yl$	$\frac{2\phi_1^4-(6\phi_1^2-(3+3\cos 2\phi_1))}{48(\phi_2-\phi_1)^4}$	$\frac{-(4\phi_1^3-(6\phi_1+3\sin 2\phi_1))}{48(\phi_2-\phi_1)^4}$	$\frac{2\phi_1^4+(6\phi_1^2-(3+3\cos 2\phi_1))}{48(\phi_2-\phi_1)^4}$
$\int v dx^2$	$xu\ yu$	$\frac{2(4\phi_2^3-(6\phi_2+3\sin 2\phi_2))}{72(\phi_2-\phi_1)^3}$	$\frac{-2(6\phi_2^2-(3+3\cos 2\phi_2))}{72(\phi_2-\phi_1)^3}$	$\frac{2(4\phi_2^3+(6\phi_2+3\sin 2\phi_2))}{72(\phi_2-\phi_1)^3}$
	$xu\ yl$	$\frac{-(4\phi_2^3-(6\phi_2+3\sin 2\phi_2))}{72(\phi_2-\phi_1)^3}$	$\frac{6\phi_2^2-(3+3\cos 2\phi_2)}{72(\phi_2-\phi_1)^3}$	$\frac{-(4\phi_2^3+(6\phi_2+3\sin 2\phi_2))}{72(\phi_2-\phi_1)^3}$
	$xl\ yu$	$\frac{2\phi_2^4-(6\phi_2^2-(3+3\cos 2\phi_2))}{48(\phi_2-\phi_1)^4}$	$\frac{-(4\phi_2^3-(6\phi_2+3\sin 2\phi_2))}{48(\phi_2-\phi_1)^4}$	$\frac{2\phi_2^4+(6\phi_2^2-(3+3\cos 2\phi_2))}{48(\phi_2-\phi_1)^4}$
	$xl\ yl$	$\frac{2\phi_1^4-(6\phi_1^2-(3+3\cos 2\phi_1))}{48(\phi_2-\phi_1)^4}$	$\frac{-(4\phi_1^3-(6\phi_1+3\sin 2\phi_1))}{48(\phi_2-\phi_1)^4}$	$\frac{2\phi_1^4+(6\phi_1^2-(3+3\cos 2\phi_1))}{48(\phi_2-\phi_1)^4}$

Table D.5: Integration Results: Case 4

$\frac{d^2v}{dx\,dy}$		1 (as the terms $\cos^2\hat{\phi}_o$, $\cos\hat{\phi}_o \sin\hat{\phi}_o$ & $\sin^2\hat{\phi}_o$ are constant)
Integral	Limits	
v	$xu\ yu$	$0/9$
	$xu\ yl$	$-3/9$
	$xl\ yu$	$-4/9$
	$xl\ yl$	$2/9$
$\int v dy$	$xu\ yu$	$4/81$
	$xu\ yl$	$4/81$
	$xl\ yu$	$-12/81$
	$xl\ yl$	$-3/81$
$\int v dx$	$xu\ yu$	$2/81$
	$xu\ yl$	$-7/81$
	$xl\ yu$	$6/81$
	$xl\ yl$	$-3/81$
$\int v dy^2$	$xu\ yu$	$16/972$
	$xu\ yl$	$-5/972$
	$xl\ yu$	$-32/972$
	$xl\ yl$	$4/972$
$\int v dx\,dy$	$xu\ yu$	$8/972$
	$xu\ yl$	$11/972$
	$xl\ yu$	$24/972$
	$xl\ yl$	$6/972$
$\int v dx^2$	$xu\ yu$	$0/972$
	$xu\ yl$	$-15/972$
	$xl\ yu$	$-8/972$
	$xl\ yl$	$4/972$

Table D.6: Integration Results: Case 5

Appendix E

Program Structures

E.1 The *Script*

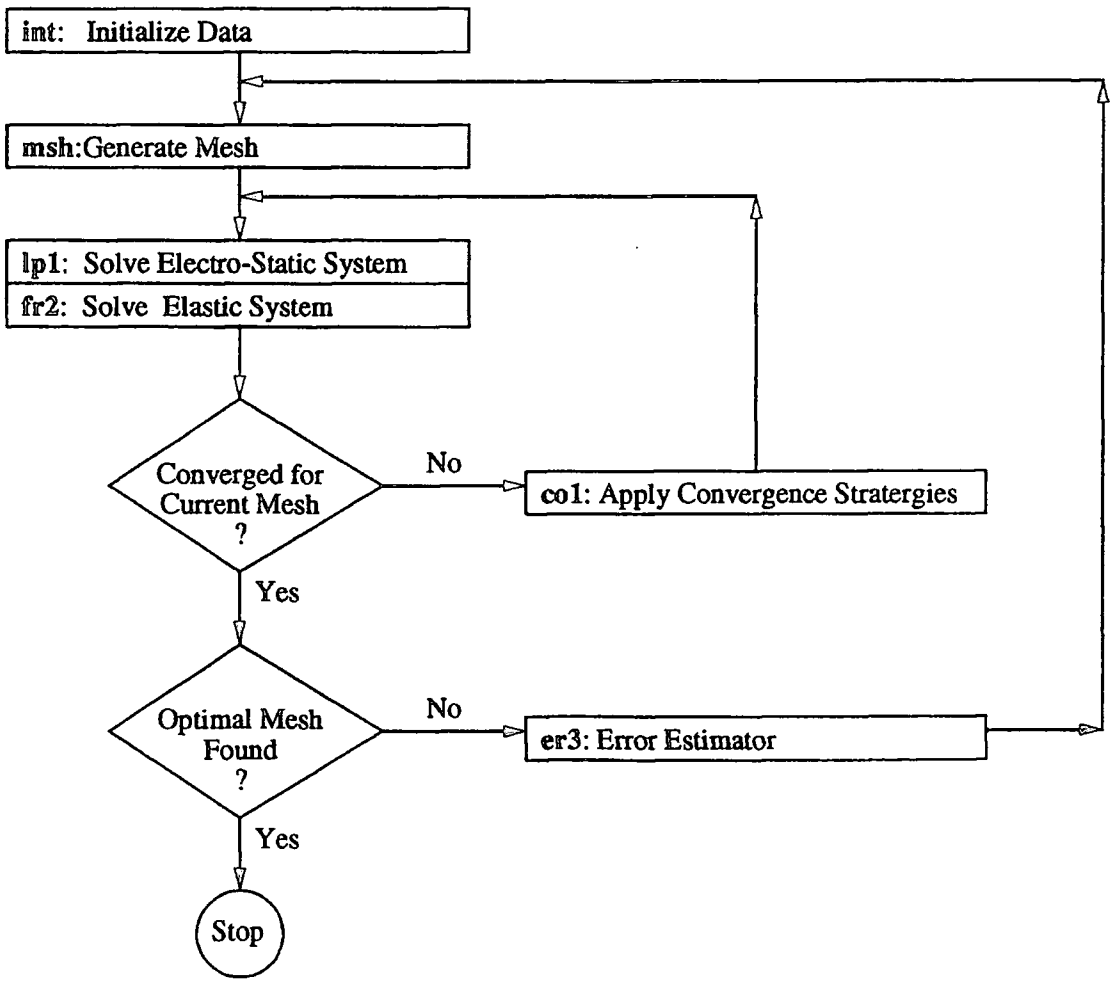

Figure E.1: Structure of the *Script*

E.1.1 Listing of the *Script*

```
#!/bin/sh
home=/users/des3njp
cd $home/temp
for i
do
  mkdir $home/results/$i
  cp $home/input/$i ftn04
  res=4
  mesh=1
  if test $res = 4
  then
    int || ( echo 'int failure' && false ) || exit
  fi
  until [ $res = 0 ]
  do
    if test $mesh = 1
    then
      mesh=0
      msh || ( echo 'msh failure' && false ) || exit
    fi
    lp1 || ( echo 'lp1 failure' && false ) || exit
    fr2 || ( echo 'fr2 failure' && false ) || exit
    cp $home/data/PHI $home/results/$i
    cp $home/data/V   $home/results/$i
    cp $home/data/XY  $home/results/$i
    if test $res = 2
    then
      mesh=1
      er3
      res=$?
    else
      mesh=0
      co1
      res=$?
    fi
    echo "res: $res"
    test $res -ge 5 && echo 'res out of bounds' && exit
  done
  echo "Done $i"
  cp $home/data/PHI $home/results/$i
  cp $home/data/V   $home/results/$i
  cp $home/data/XY  $home/results/$i
done
echo 'fini'
exit
```

E.2 File Structures

E.2.1 Input File

The input file is completely defines the problem to solved in the simple and short form. All distances are given in microns.

Length of Period (μm).
Thickness of Liquid Crystal Layer (μm).

Number of Electrodes at Bottom of Cell.
Number of Electrodes at Top of Cell.
For each Electrode:
    Position it begins in x-direction (μm),
    Position it ends in x-direction (μm),
    Distance it begins from Liquid Crystal Layer in y-direction (μm),
    Distance it ends from Liquid Crystal Layer in y-direction (μm),
    Voltage at Left of Electrode,
    Voltage at Right of Electrode,
    Code for variation of voltage along the Electrode
    (0: Linear, no others coded).
Type of Liquid Crystal.
ε_o ε_e Ordinary and Extraordinary Relative Permittivities,
n_o n_e λ Ordinary and Extraordinary Refractive Indices,
at Wavelength (nm),
K_{11} K_{22} K_{33} Splay, Twist and Bend Elastic constants (pN),
θ_B ϕ_B Boundary Tilt and Orientation at Bottom Boundary,
θ_T ϕ_T Boundary Tilt and Orientation at Top Boundary.
Number of Dielectric Layers at Bottom of Cell.
Number of Dielectric Layers at Top of Cell.
For each Dielectric Layer:
    Name of Substance,
    Thickness of Layer (μm),
    Relative Permittivity.

E.2.2 Aim: Aims and Control Information

Accuracy Index,
Number of Accuracies,
res value,
Scaling factor for free step.

List of Accuracies.

Iteration Number,
Controlled step size as a power of 3^c, ie 3^N degrees,
Maximum Power,
Minimum Power,
Buckle Flag.

E.2.3 LC: Liquid Crystal Data

ε_o ε_e K_{11} K_{22} K_{33}

E.2.4 SUB: Subdomain Data

Number of Subdomains in the x-direction,
Number of Subdomains in the y-direction, below the Liquid Crystal Layer,
Number of Subdomains in the y-direction, above the Liquid Crystal Layer.

x-dimensions of the Subdomains.
y-dimensions of the Subdomains.
Number of columns in x Subdomains.
Number of rows in y Subdomains.

E.2.5 NOD(LP/FR): Node Numbering

Separate meshes for the electro-static and elastic parts of the model are required, as the electro-static part must include the far boundary regions.

```
For each row of the mesh, starting from the bottom:
The node number, listed from left to right.
```

Negative numbers represent prescribed values, which are stored in prescribed boundary condition file, the number providing an index.

E.2.6 BC(LP/FR1/FRK): Prescribed Boundary Conditions

```
Prescribed Boundary Value, indexed as negative node number.
```

E.2.7 PE: Electrode Data

```
Number of Electrodes at Bottom of Cell,
Number of Electrodes at Top    of Cell.

For each Electrode:
    Position it begins in x-direction,
    Position it ends   in x-direction,
    Distance it begins from Liquid Crystal Layer in y-direction,
    Distance it ends   from Liquid Crystal Layer in y-direction,
    Voltage at Left    of Electrode,
    Voltage at Right   of Electrode,
    Code for variation of voltage along the Electrode
    Number of x Subdomain Electrode begins
    Number of x Subdomain Electrode ends
    Number of y Subdomain Electrode begins
    Number of y Subdomain Electrode ends
```

E.2.8 DIS: Dielectric Data

```
Number of Dielectric Layers at Bottom of Cell,
Number of Dielectric Layers at Top    of Cell.

Relative Permittivity of each Layer.
Number of y Subdomain each Layer ends.
```

E.2.9 XY(O): Row and Column Dimensions

Two files of type are produces; XY, the dimensions of the current mesh, and XYO the dimensions of the old mesh.

```
Number of columns,
Number of Rows in Liquid Crystal Layer,
Number of Rows below Liquid Crystal Layer,
Number of Rows above Liquid Crystal Layer.

Dimensions of Columns.
Dimensions of Rows in Liquid Crystal Layer,
Dimensions of Rows below and above Liquid Crystal Layer.
```

E.2.10 (D)PHI(O/B) & V: Orientation and Potential Distributions

Several distribution files are required; PHI for the pre-set angular distribution $\bar{\phi}$ and DPHI for the variation from this $\delta\bar{\phi}$. Copies from previous iterations PHIO, DPHIO, PHIB, & DPHIB are kept for the convergence strategies. The potential distribution, V, includes the far boundary regions.

```
For each row of the mesh, starting from the bottom:
The value at each node, listed from left to right.
```

Appendix F

Performance Results

F.1 One-Dimensional Results

F.1.1 Angular Variation versus Pre-Set Orientation for Central Node

F.1.2 Angular Variation versus Pre-Set Orientation for Quarter Node

Plot of Change in Orientation versus Pre-Set Orientation
For a 1-D Cell at Various Applied Voltages
Central Node
FRI: NY = 4
Cell Thickness: 10.0μm

Liquid Crystal: E_{44}

Bottom				Top
θ = 90.0°	e_o = 5.2	e_o = 22.0		θ = 90.0°
ϕ = 1.00°	K_{11} = 11.1	K_{22} = 6.3	K_{33} = 17.1	ϕ = 1.00°

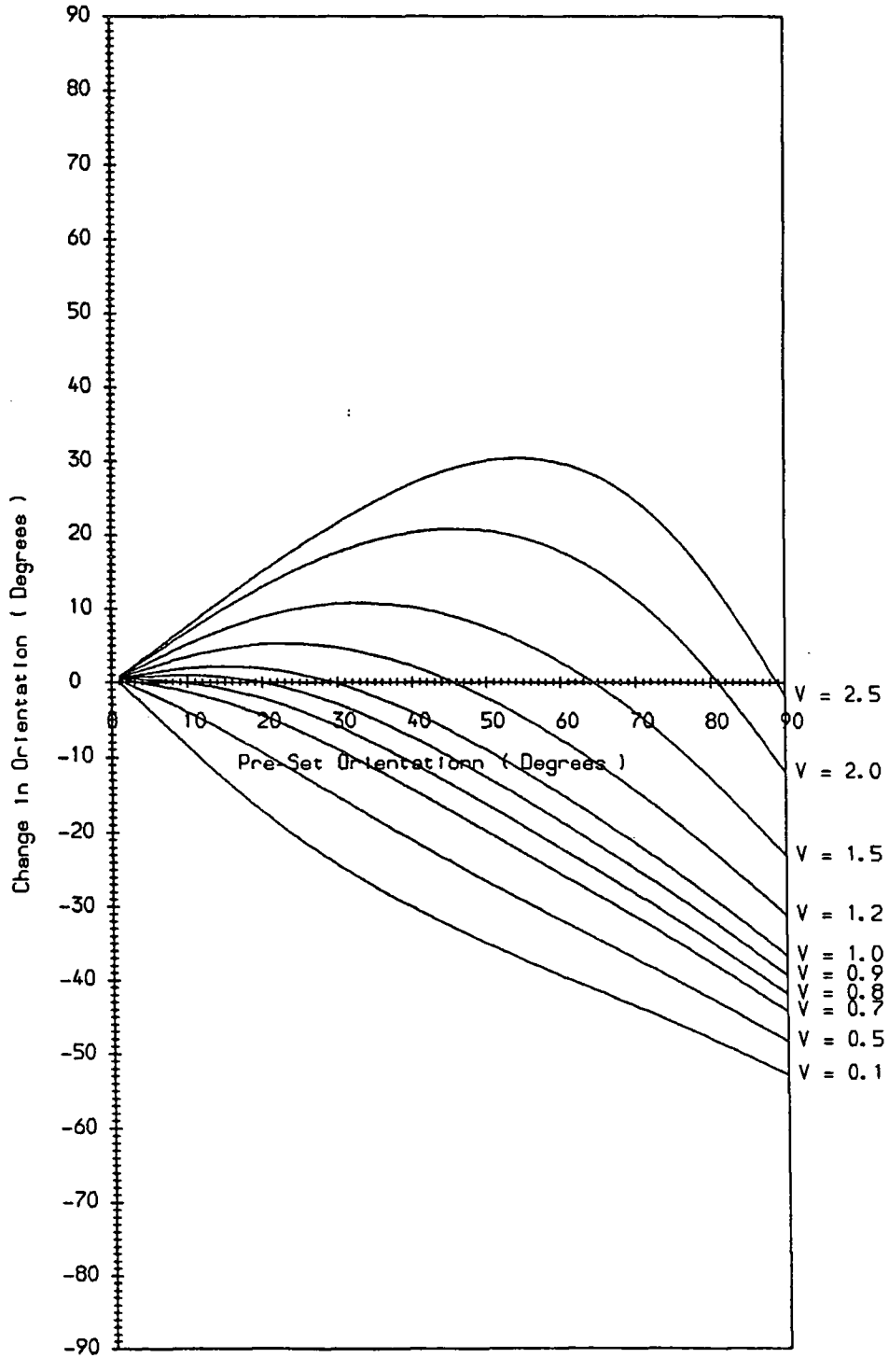

Plot of Change in Orientation versus Pre-Set Orientation
For a 1-D Cell at Various Applied Voltages
Quarter Node

FR1: NY = 4

Cell Thickness: 10.0μm

Liquid Crystal: E_{44}

Bottom				Top
θ = 90.0°	ϵ_o = 5.2	ϵ_o = 22.0		θ = 90.0°
φ = 1.00°	K_{11} = 11.1	K_{22} = 6.3	K_{33} = 17.1	φ = 1.00°

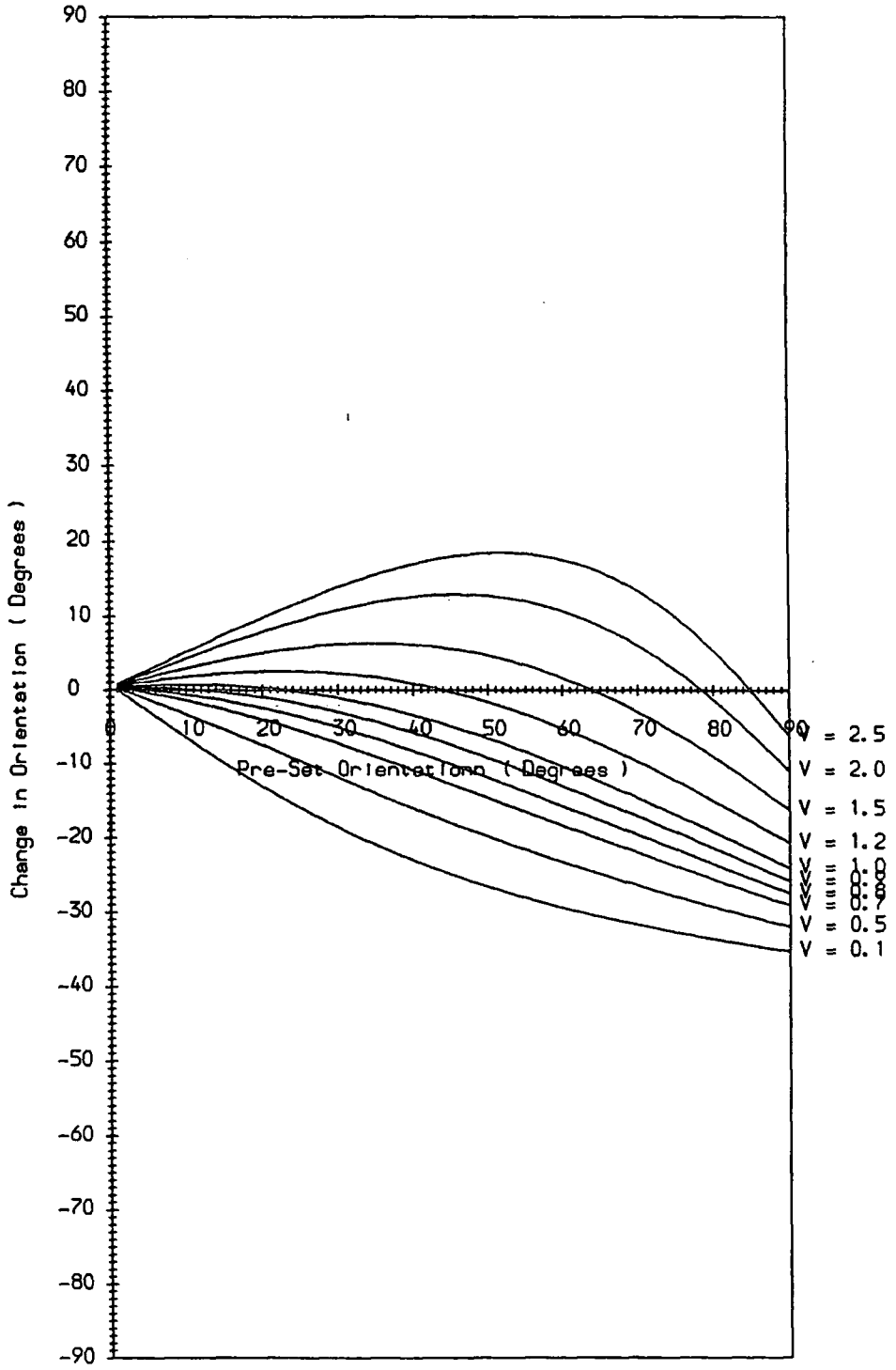

F.1.3 Berreman Statistic

F.1.4 Simplest Approximation with Fixed Mesh

F.1.5 Richest Approximation with Fixed Mesh

F.1.6 Compromise Approximation with Fixed Mesh

F.1.7 Simplest Approximation with Adaptive Mesh

F.1.8 Richest Approximation with Adaptive Mesh

F.1.9 Compromise Approximation with Adaptive Mesh

F.1.10 Two Micron Thick Cell

F.1.11 The Correct Elastic Constants for E44

F.1.12 5% Accuracy Mesh

F.1.13 2.5% Accuracy Mesh

F.1.14 1% Accuracy Mesh, showing the effects of Dispersion

F.1.15 Linear Operating Region

Berreman Statistics

Liquid Crystal: E44 ε_o= 5.2 ε_e= 22.0 K_{11}= 11.1 K_{22}= 6.3 K_{33}= 17.1 φ_b= 1°

Cell Thickness = 10.0μm

Plot of Liquid Crystal Orientation through a Cell
For Various Applied Voltages

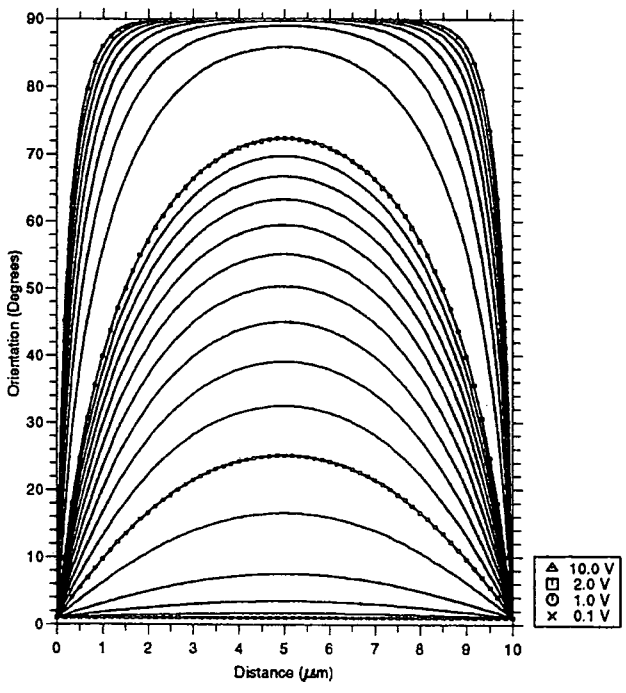

Plot of Phase against Voltage of a Liquid Crystal Cell

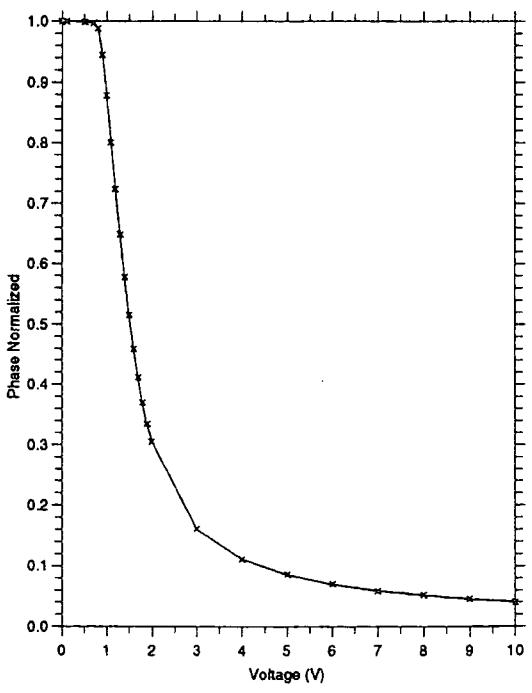

Finite Element Program: fr0 with a Fixed Mesh

Liquid Crystal: E44 ε_o= 5.2 ε_e= 22.0 K_{11}= 11.1 K_{22}= 6.3 K_{33}= 17.1 φ_b= 1°

Cell Thickness = 10.0μm

Plot of Voltage through a Nematic Liquid Crystal Cell
For Various Applied Voltages

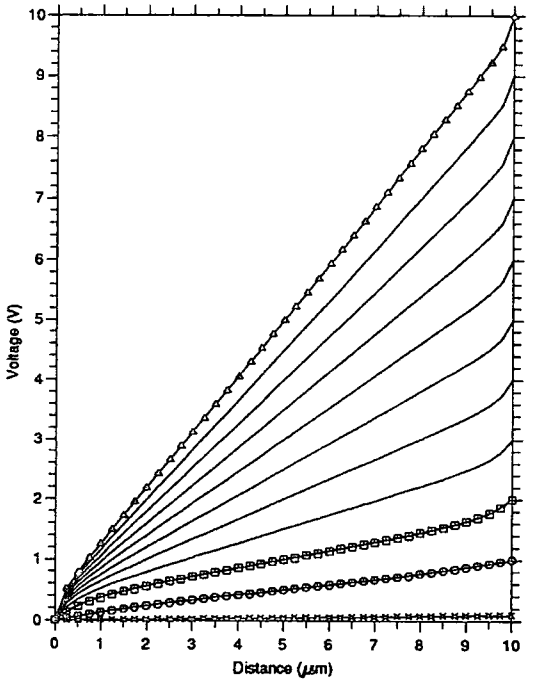

Plot of Normalized Voltage through a Nematic Liquid Crystal Cell
For Various Applied Voltages

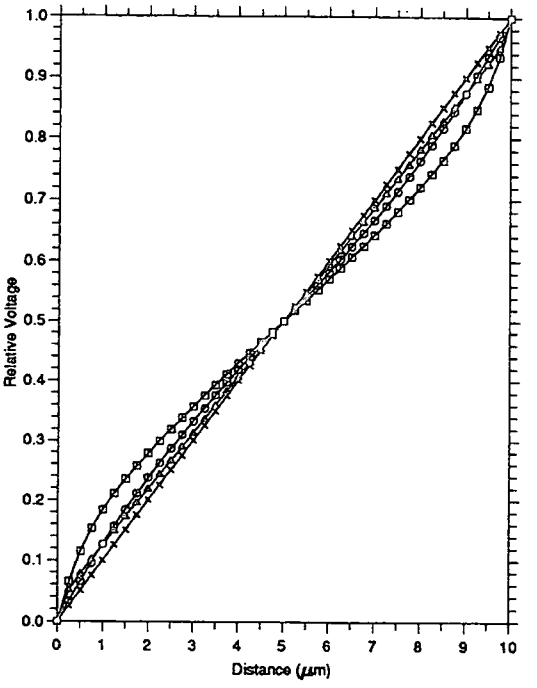

Plot of Liquid Crystal Orientation through a Cell
For Various Applied Voltages

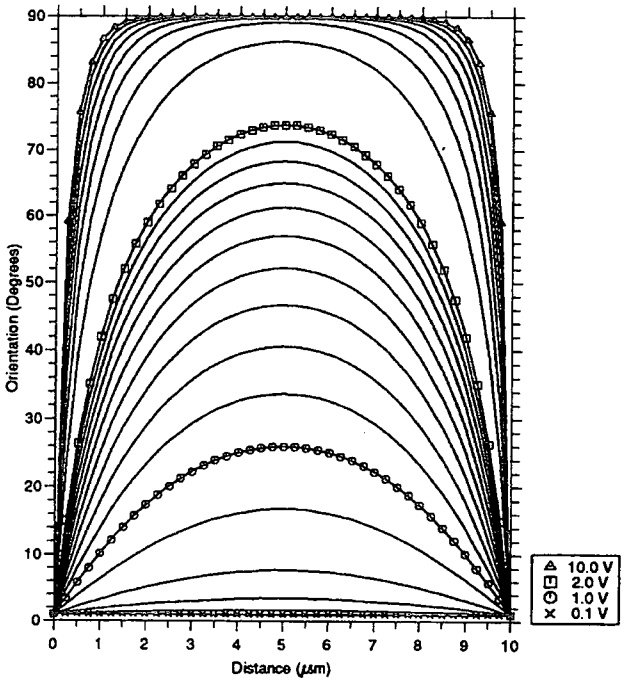

Plot of Phase against Voltage of a Liquid Crystal Cell

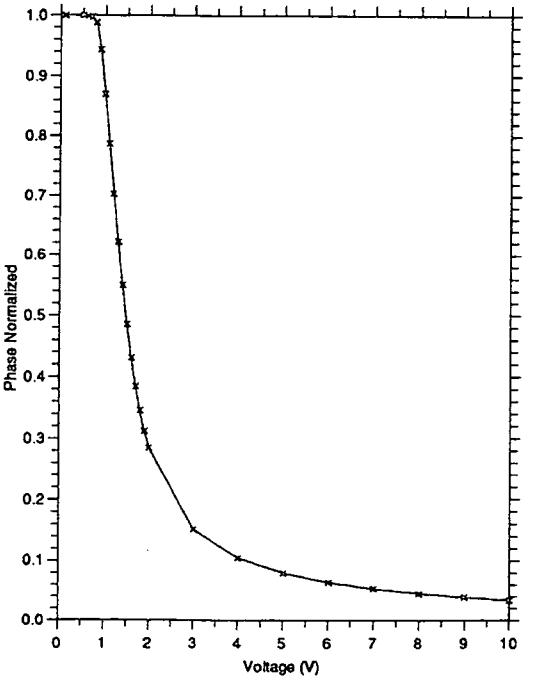

Finite Element Program: fr1 with a Fixed Mesh

Liquid Crystal: E44 ε_o= 5.2 ε_e= 22.0 K_{11}= 11.1 K_{22}= 6.3 K_{33}= 17.1 φ_b= 1°

Cell Thickness = 10.0μm

Plot of Voltage through a Nematic Liquid Crystal Cell
For Various Applied Voltages

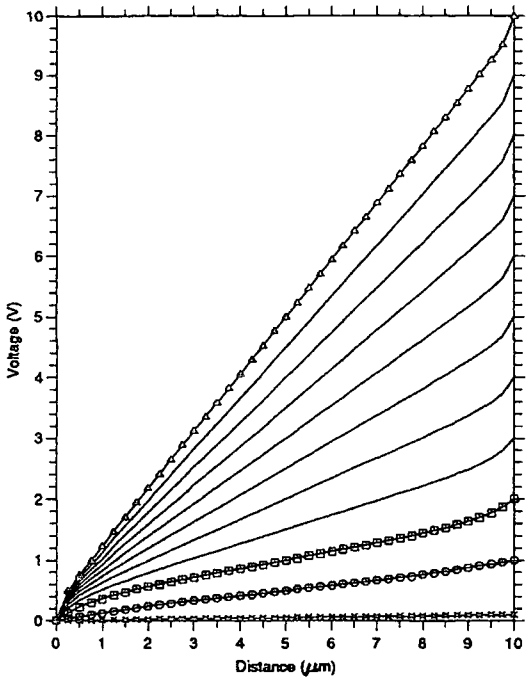

Plot of Normalized Voltage through a Nematic Liquid Crystal Cell
For Various Applied Voltages

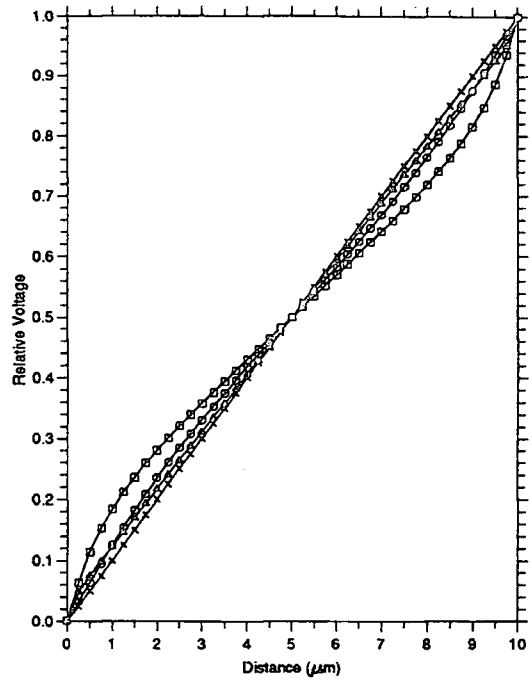

Plot of Liquid Crystal Orientation through a Cell
For Various Applied Voltages

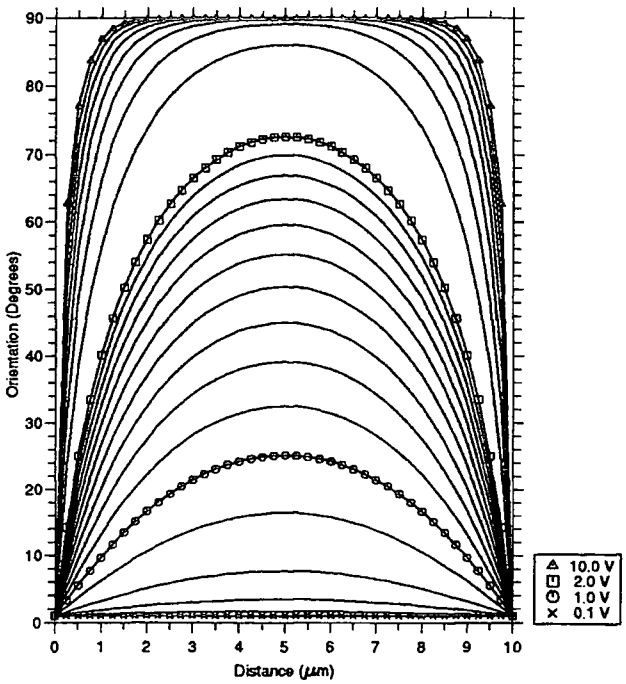

Plot of Phase against Voltage of a Liquid Crystal Cell

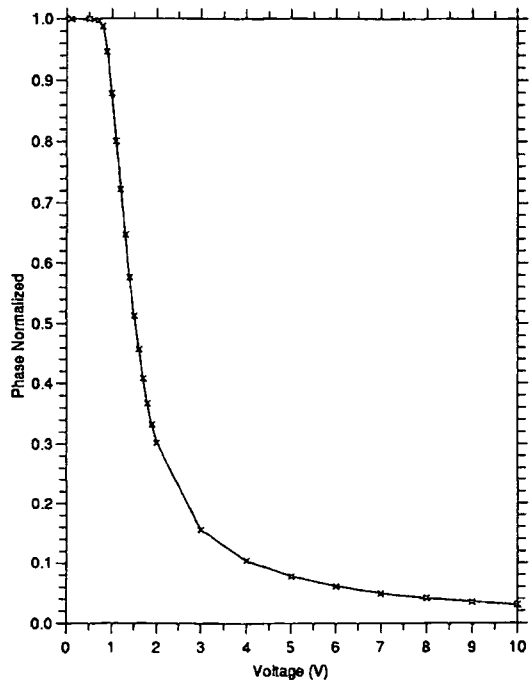

Finite Element Program: fr2 with a Fixed Mesh

Liquid Crystal: E44 ε_o= 5.2 ε_e= 22.0 K_{11}= 11.1 K_{22}= 6.3 K_{33}= 17.1 φ_b= 1°

Cell Thickness = 10.0μm

Plot of Voltage through a Nematic Liquid Crystal Cell
For Various Applied Voltages

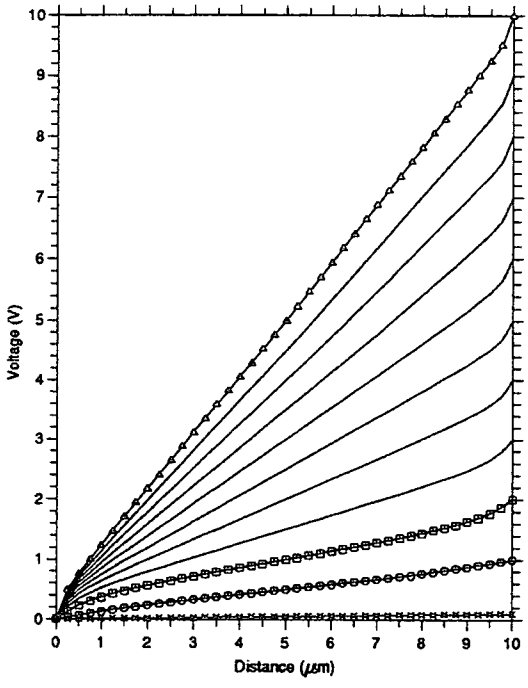

Plot of Normalized Voltage through a Nematic Liquid Crystal Cell
For Various Applied Voltages

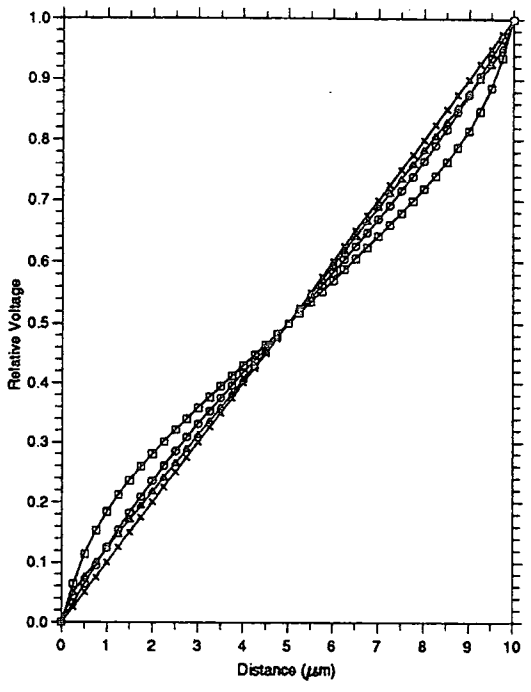

Plot of Liquid Crystal Orientation through a Cell
For Various Applied Voltages

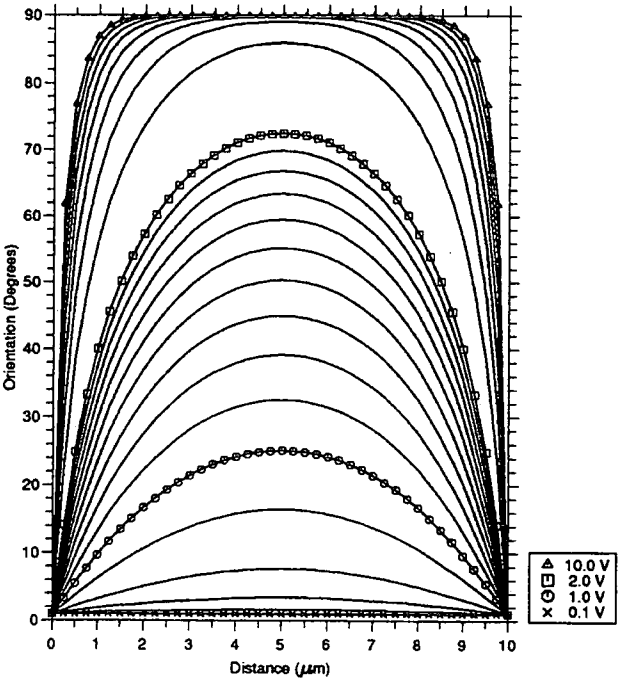

Plot of Phase against Voltage of a Liquid Crystal Cell

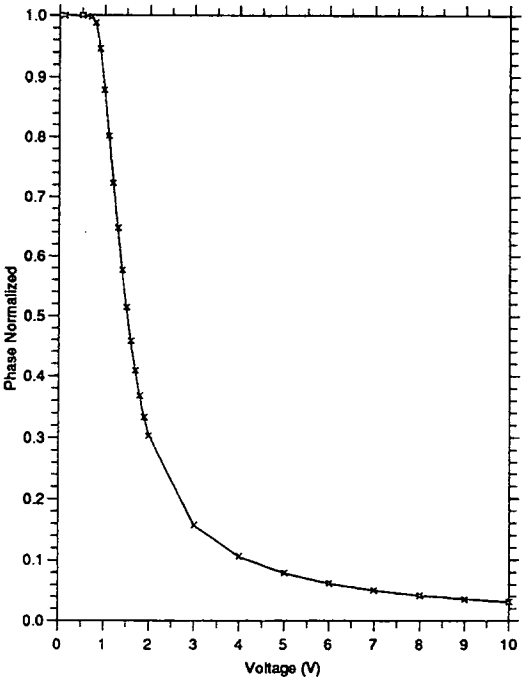

Finite Element Program: fr0 with an Adaptive Mesh

Liquid Crystal: E44 ε_o= 5.2 ε_e= 22.0 K_{11}= 11.1 K_{22}= 6.3 K_{33}= 17.1 φ_b= 1°

Cell Thickness = 10.0μm

Plot of Voltage through a Nematic Liquid Crystal Cell
For Various Applied Voltages

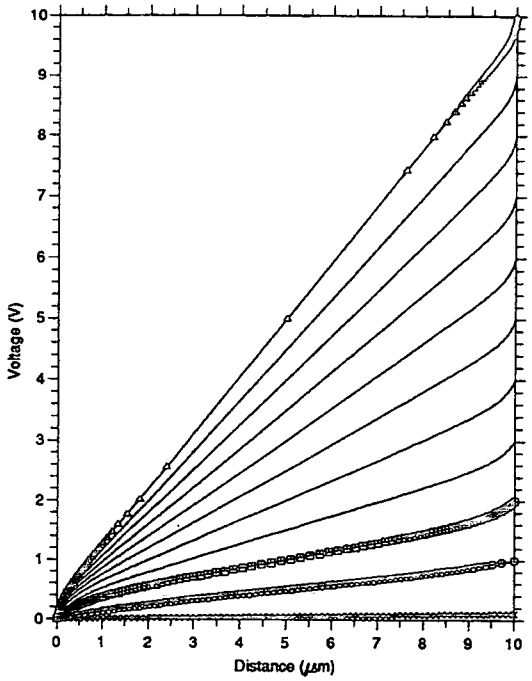

Plot of Normalized Voltage through a Nematic Liquid Crystal Cell
For Various Applied Voltages

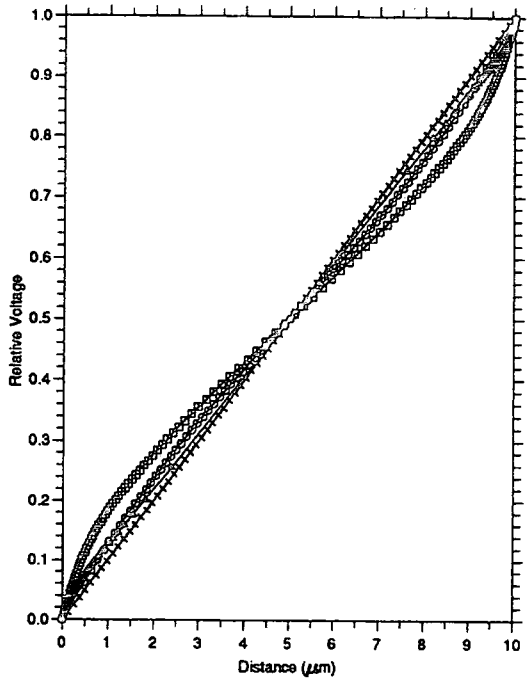

Plot of Liquid Crystal Orientation through a Cell
For Various Applied Voltages

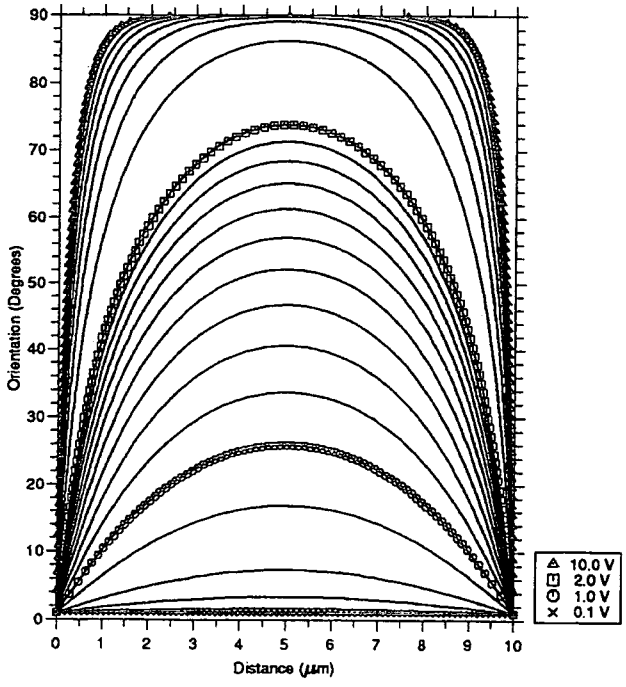

Plot of Phase against Voltage of a Liquid Crystal Cell

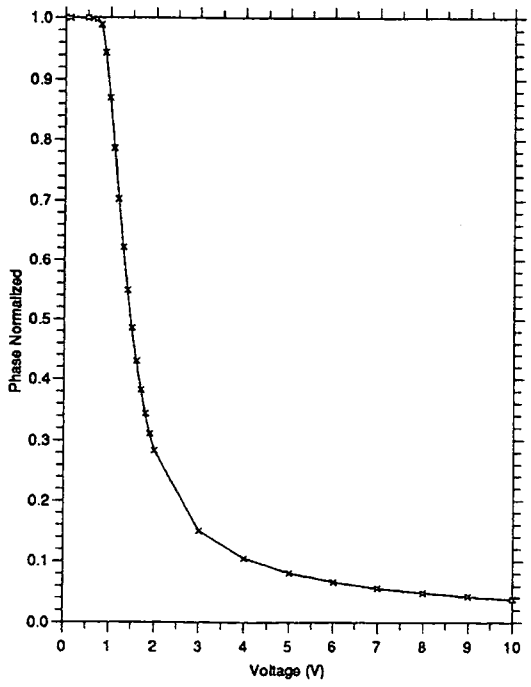

Finite Element Program: fr1 with an Adaptive Mesh

Liquid Crystal: E44 ε_o= 5.2 ε_e= 22.0 K_{11}= 11.1 K_{22}= 6.3 K_{33}= 17.1 φ_b= 1°

Cell Thickness = 10.0μm

Plot of Voltage through a Nematic Liquid Crystal Cell
For Various Applied Voltages

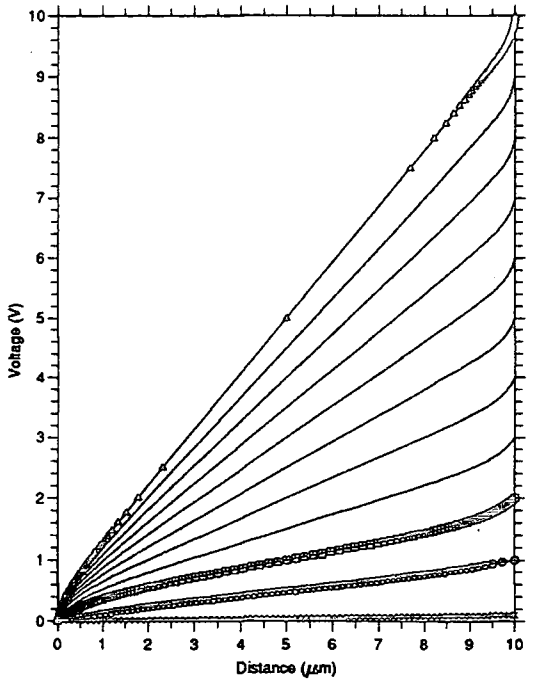

Plot of Normalized Voltage through a Nematic Liquid Crystal Cell
For Various Applied Voltages

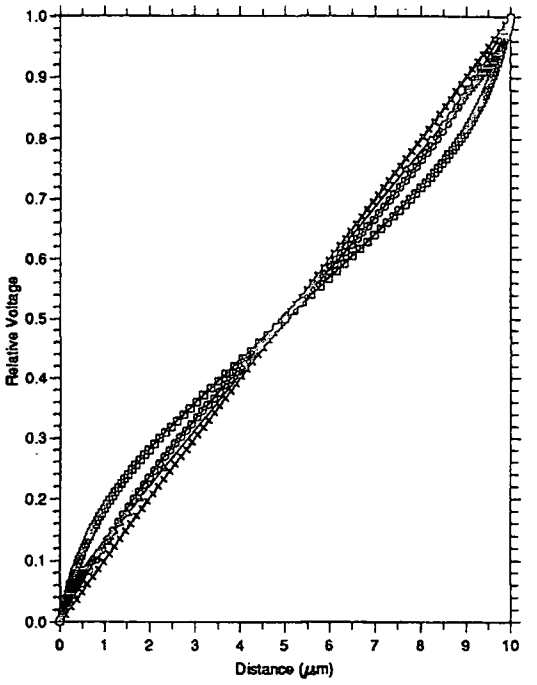

Plot of Liquid Crystal Orientation through a Cell
For Various Applied Voltages

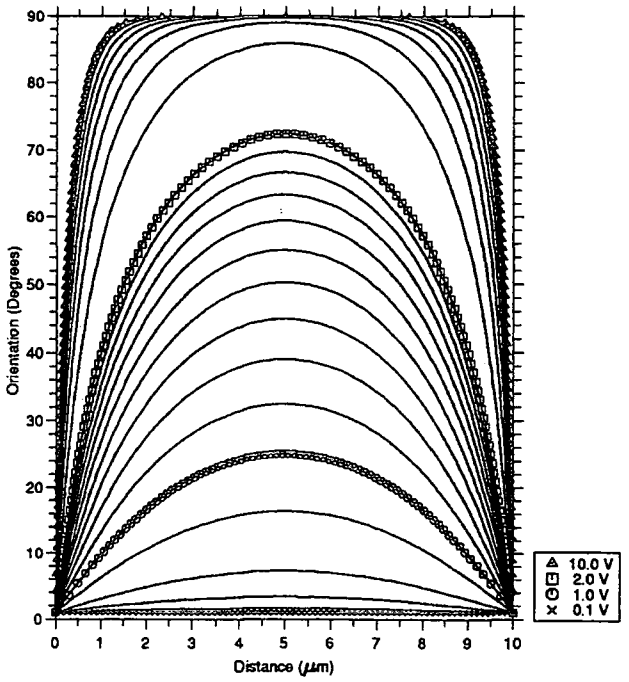

Plot of Phase against Voltage of a Liquid Crystal Cell

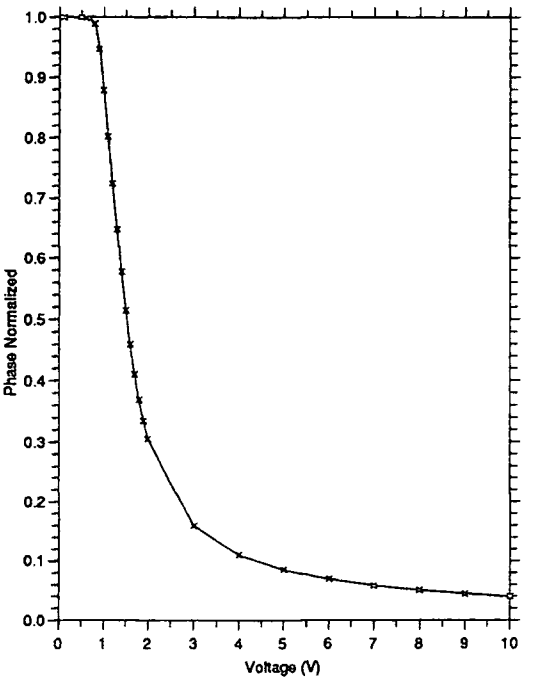

Finite Element Program: fr2 with an Adaptive Mesh

Liquid Crystal: E44 ε_o= 5.2 ε_e= 22.0 K_{11}= 11.1 K_{22}= 6.3 K_{33}= 17.1 φ_b= 1°

Cell Thickness = 10.0μm

Plot of Voltage through a Nematic Liquid Crystal Cell
For Various Applied Voltages

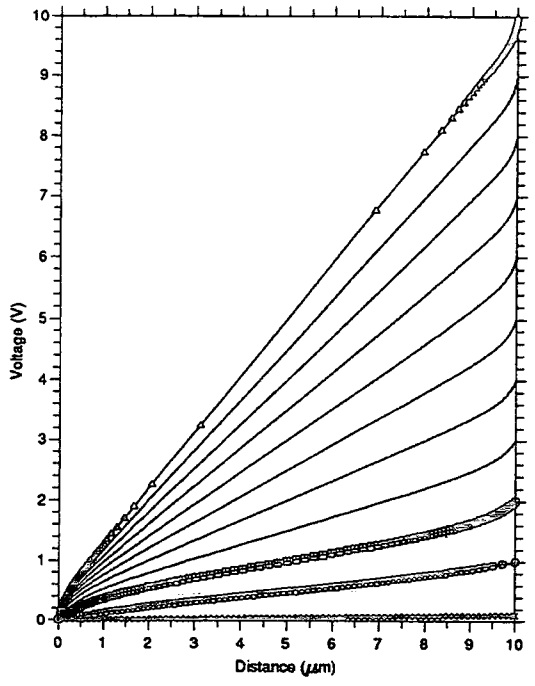

Plot of Normalized Voltage through a Nematic Liquid Crystal Cell
For Various Applied Voltages

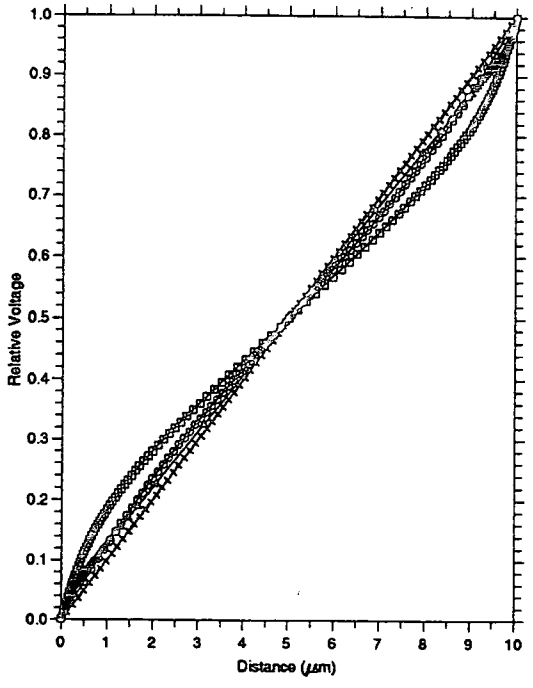

Plot of Liquid Crystal Orientation through a Cell
For Various Applied Voltages

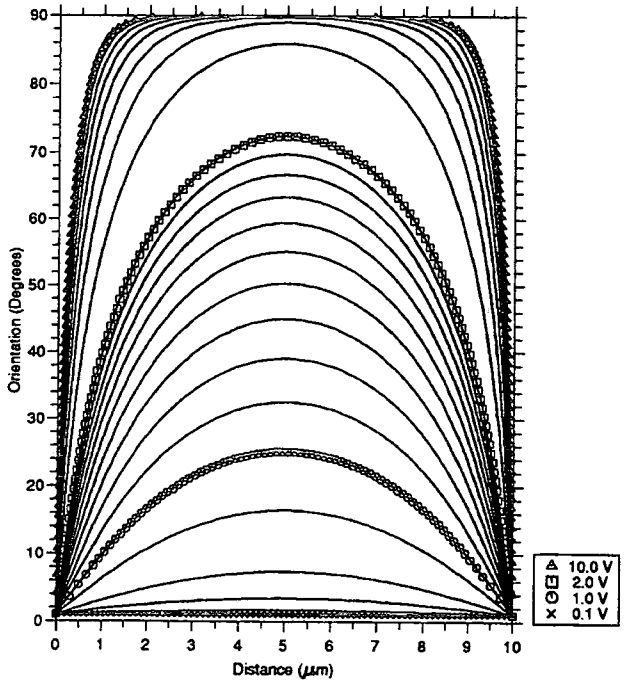

Plot of Phase against Voltage of a Liquid Crystal Cell

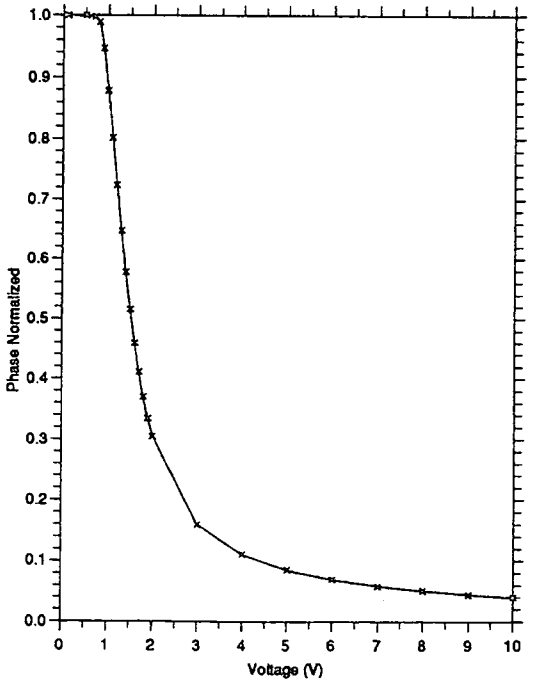

Finite Element Program: fr2 with an Adaptive Mesh

Liquid Crystal: E44 ε_o= 5.2 ε_e= 22.0 K_{11}= 11.1 K_{22}= 6.3 K_{33}= 17.1 φ_b= 1°

Cell Thickness = 2.0μm

Plot of Voltage through a Nematic Liquid Crystal Cell
For Various Applied Voltages

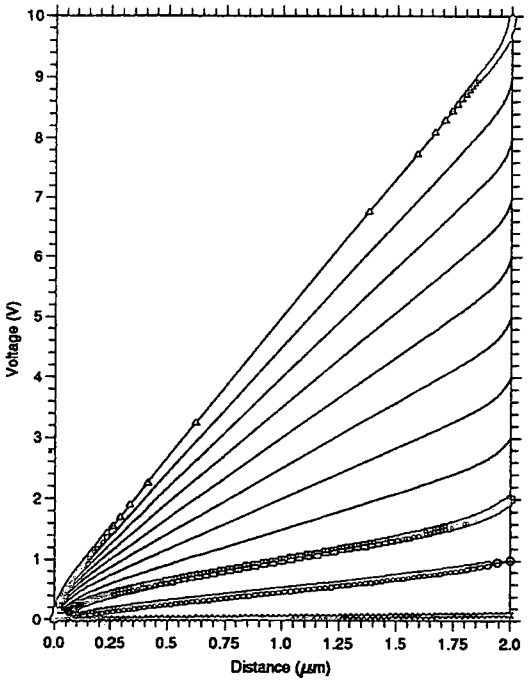

Plot of Normalized Voltage through a Nematic Liquid Crystal Cell
For Various Applied Voltages

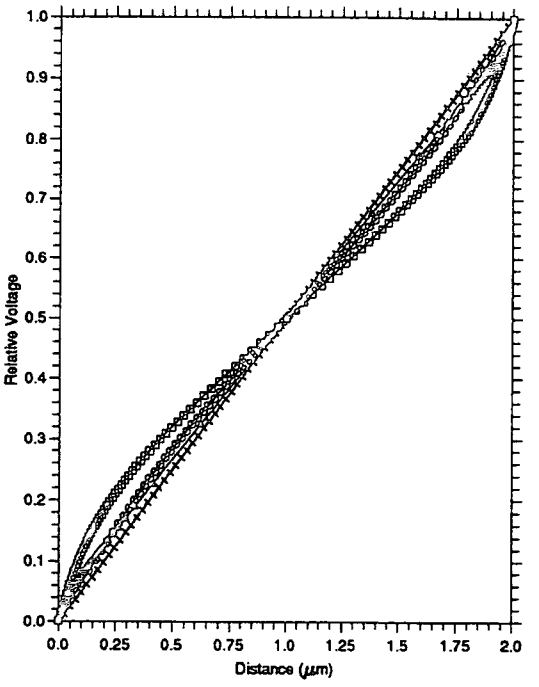

Plot of Liquid Crystal Orientation through a Cell
For Various Applied Voltages

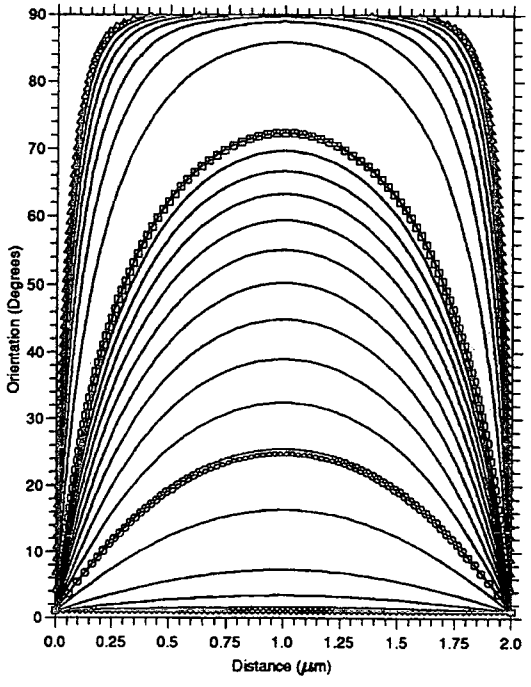

Plot of Phase against Voltage of a Liquid Crystal Cell

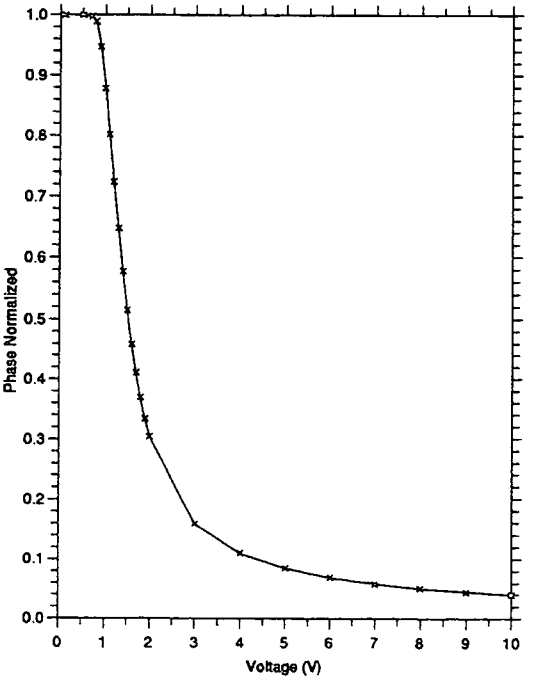

Finite Element Program: fr2 with an Adaptive Mesh

Liquid Crystal: E44 ε_o= 5.2 ε_e= 22.0 K_{11}= 11.6 K_{22}= 7.7 K_{33}= 27.5 φ_b= 1°

Cell Thickness = 10.0μm

Plot of Voltage through a Nematic Liquid Crystal Cell
For Various Applied Voltages

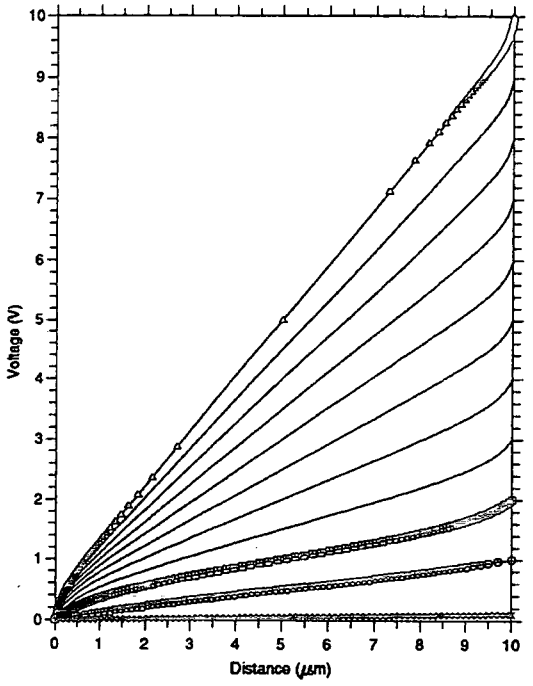

Plot of Normalized Voltage through a Nematic Liquid Crystal Cell
For Various Applied Voltages

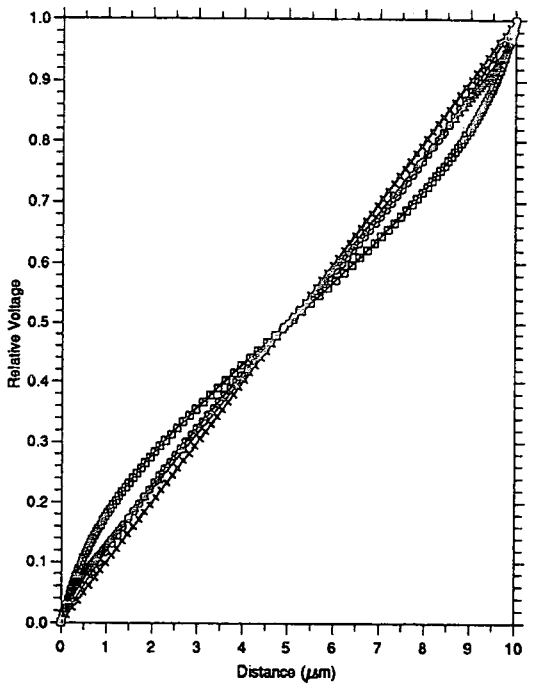

Plot of Liquid Crystal Orientation through a Cell
For Various Applied Voltages

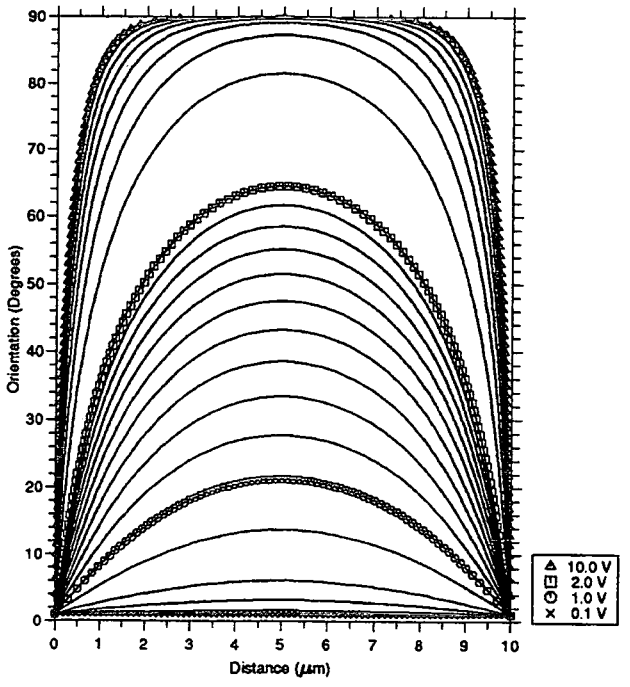

Plot of Phase against Voltage of a Liquid Crystal Cell

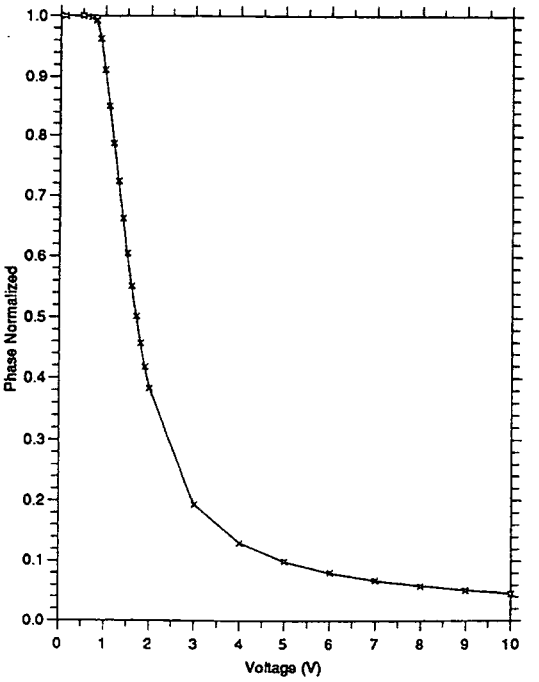

Mesh Accuracy of 5%

Liquid Crystal: E44 ε_o= 5.2 ε_e= 22.0 K_{11}= 11.6 K_{22}= 7.7 K_{33}= 27.5 φ_b= 1°

Cell Thickness = 10.0μm

Plot of Voltage through a Nematic Liquid Crystal Cell
For Various Applied Voltages

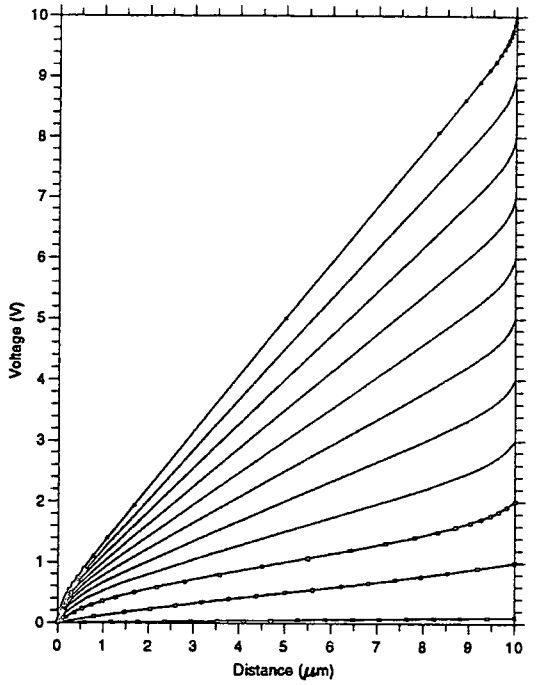

Plot of Normalized Voltage through a Nematic Liquid Crystal Cell
For Various Applied Voltages

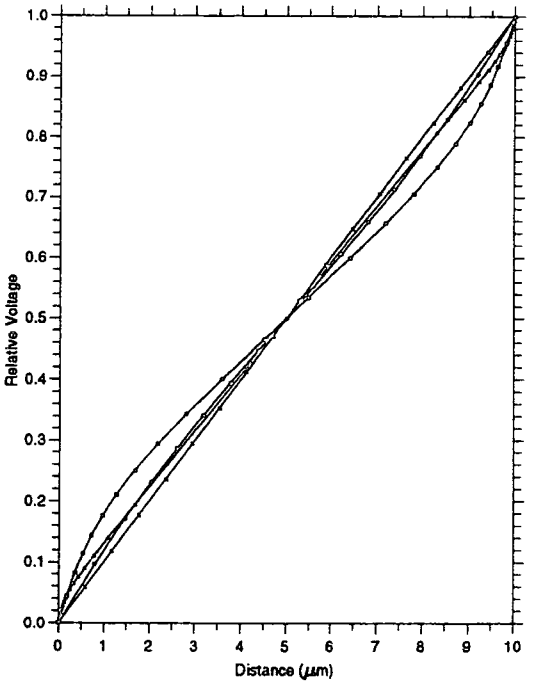

Plot of Liquid Crystal Orientation through a Cell
For Various Applied Voltages

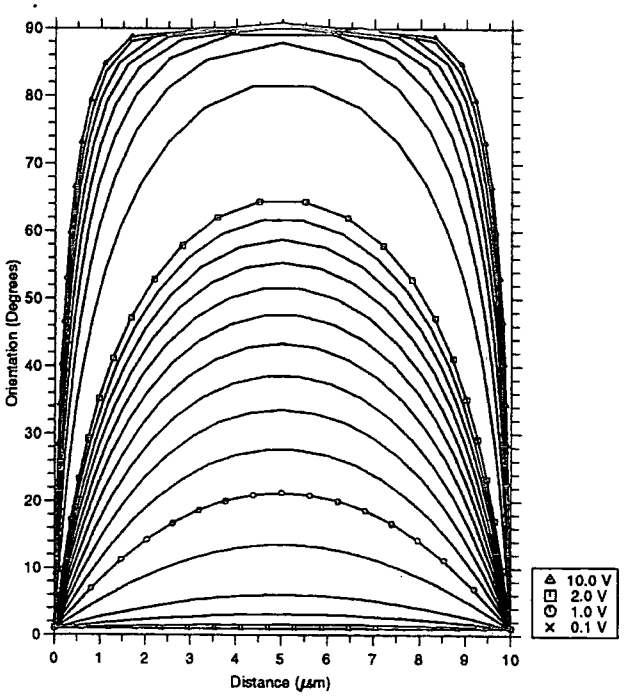

Plot of Phase against Voltage of a Liquid Crystal Cell

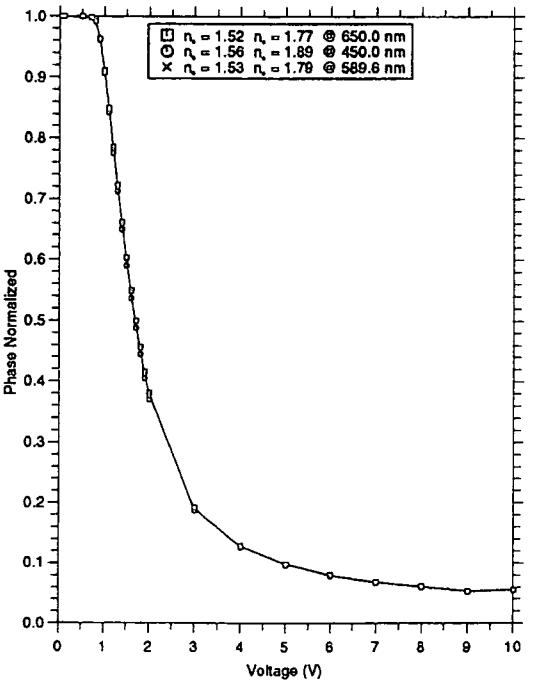

Mesh Accuracy of 2.5%

Liquid Crystal: E44 ε_o= 5.2 ε_e= 22.0 K_{11}= 11.6 K_{22}= 7.7 K_{33}= 27.5 φ_b= 1°

Cell Thickness = 10.0μm

Plot of Voltage through a Nematic Liquid Crystal Cell
For Various Applied Voltages

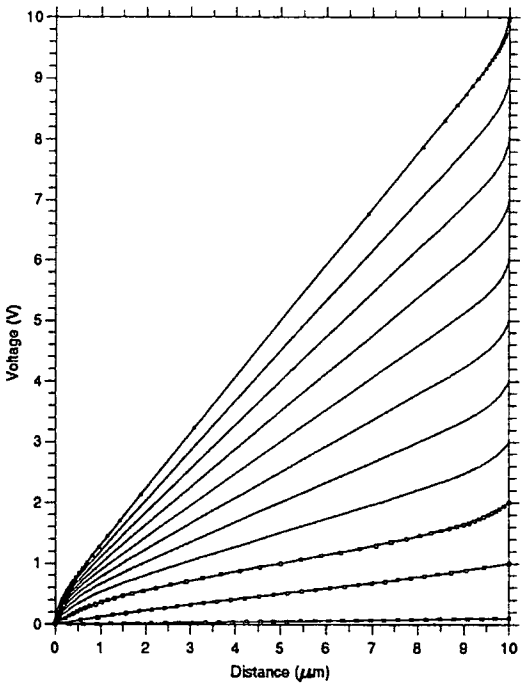

Plot of Normalized Voltage through a Nematic Liquid Crystal Cell
For Various Applied Voltages

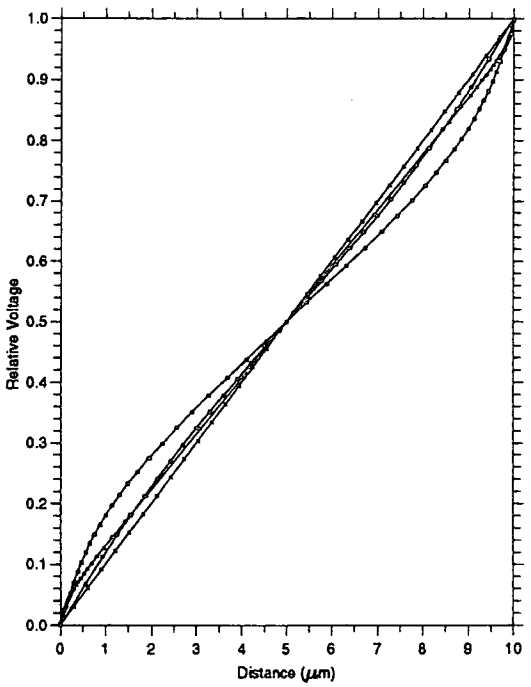

Plot of Liquid Crystal Orientation through a Cell
For Various Applied Voltages

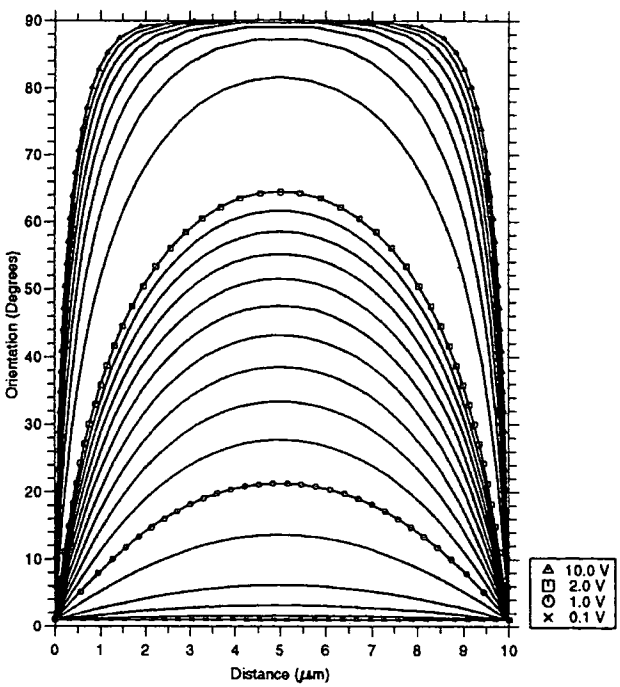

Plot of Phase against Voltage of a Liquid Crystal Cell

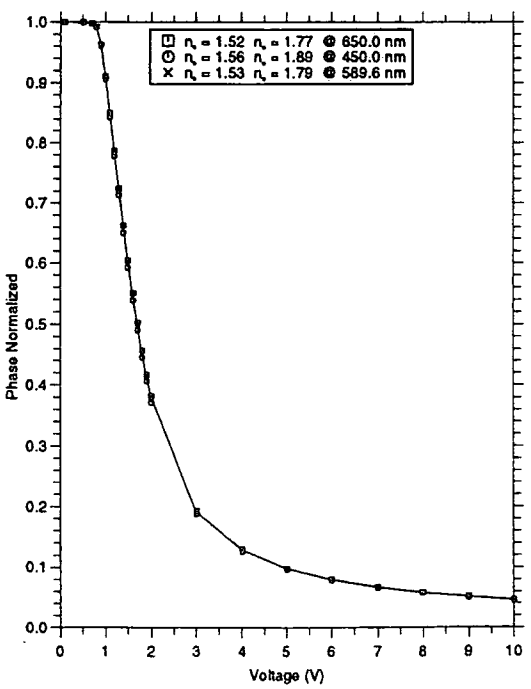

The Effect of Dispersion on the Phase Profile

Liquid Crystal: E44 ε_o= 5.2 ε_e= 22.0 K_{11}= 11.6 K_{22}= 7.7 K_{33}= 27.5 φ_b= 1°

Cell Thickness = 10.0μm

Plot of Voltage through a Nematic Liquid Crystal Cell
For Various Applied Voltages

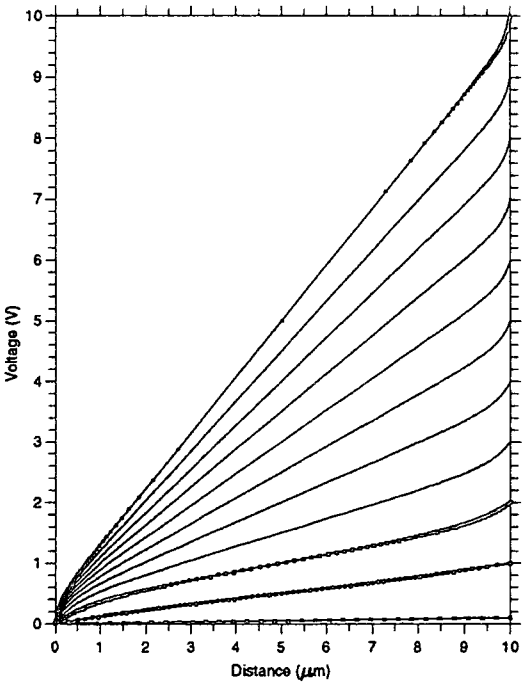

Plot of Normalized Voltage through a Nematic Liquid Crystal Cell
For Various Applied Voltages

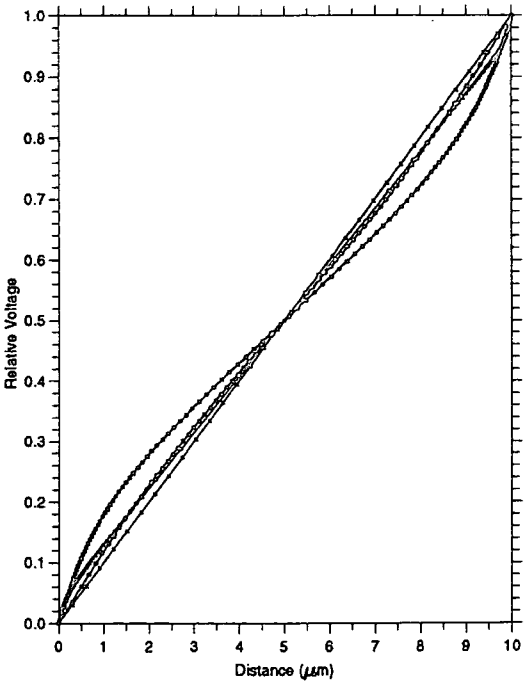

Plot of Liquid Crystal Orientation through a Cell
For Various Applied Voltages

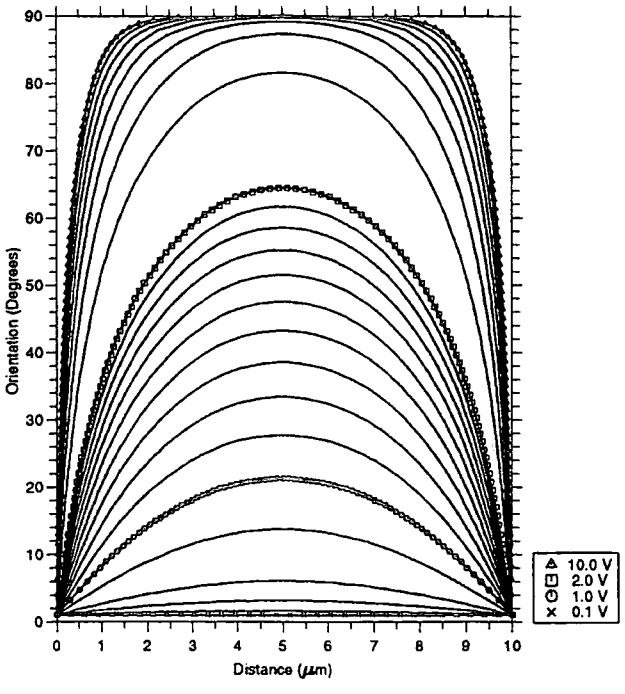

Plot of Phase against Voltage of a Liquid Crystal Cell

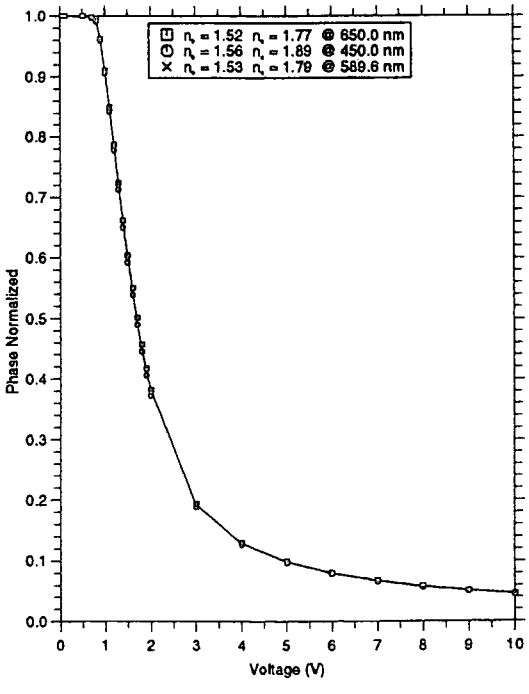

Linear Operating Region

Plot of Phase against Voltage of a Liquid Crystal Cell

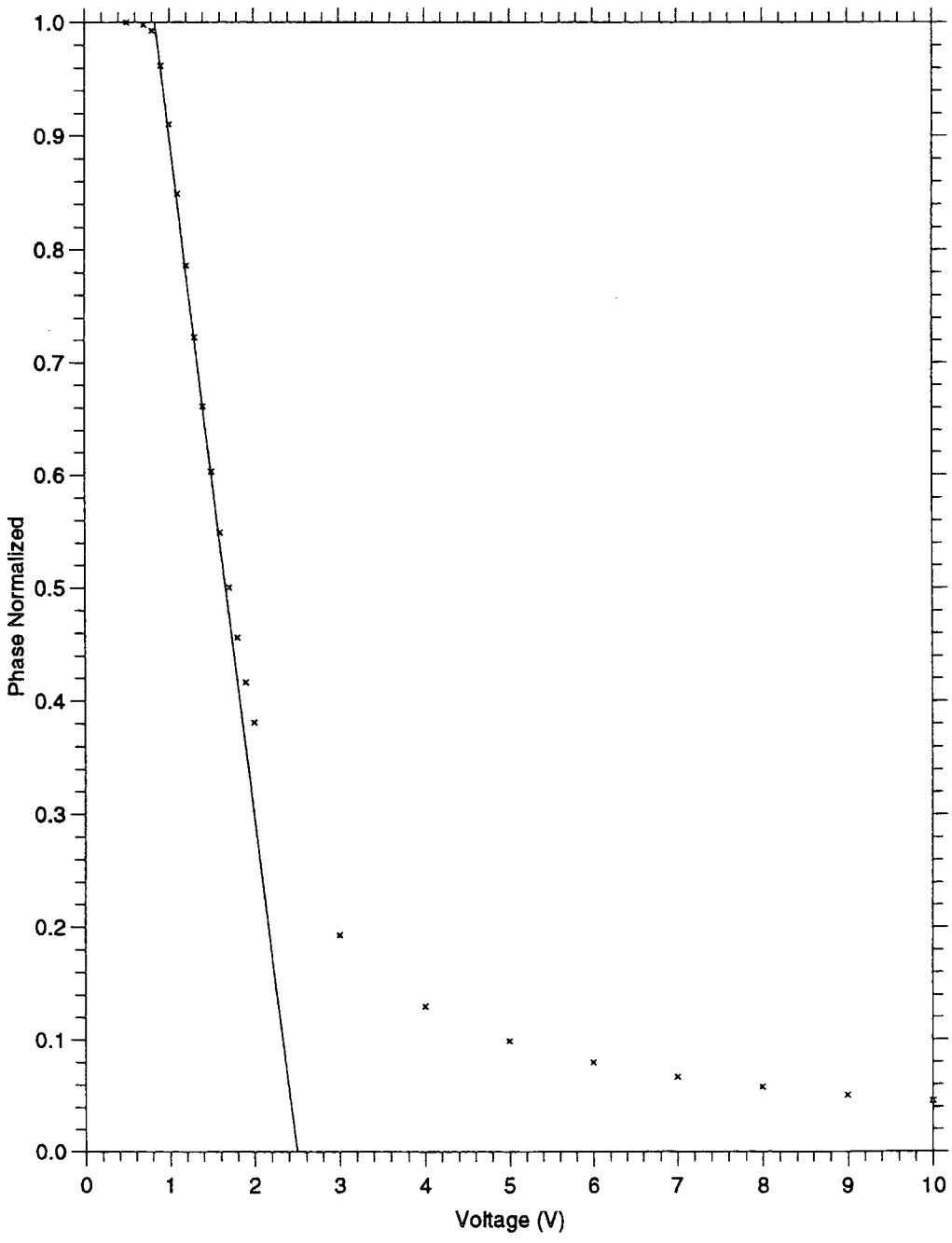

F.2 Two-Dimensional Results

F.2.1 Stages of Convergence without Preprocessing

F.2.2 Stages of Convergence with Preprocessing

F.2.3 Simplest Approximation with Fixed Mesh

F.2.4 Richest Approximation with Fixed Mesh

F.2.5 Compromise Approximation with Fixed Mesh

F.2.6 Simplest Approximation with Adaptive Mesh

F.2.7 Richest Approximation with Adaptive Mesh

F.2.8 Compromise Approximation with Adaptive Mesh

Potential Distribution and Electric Field for a Periodic Liquid Crystal E44 Cell

at Various Stages of Convergence

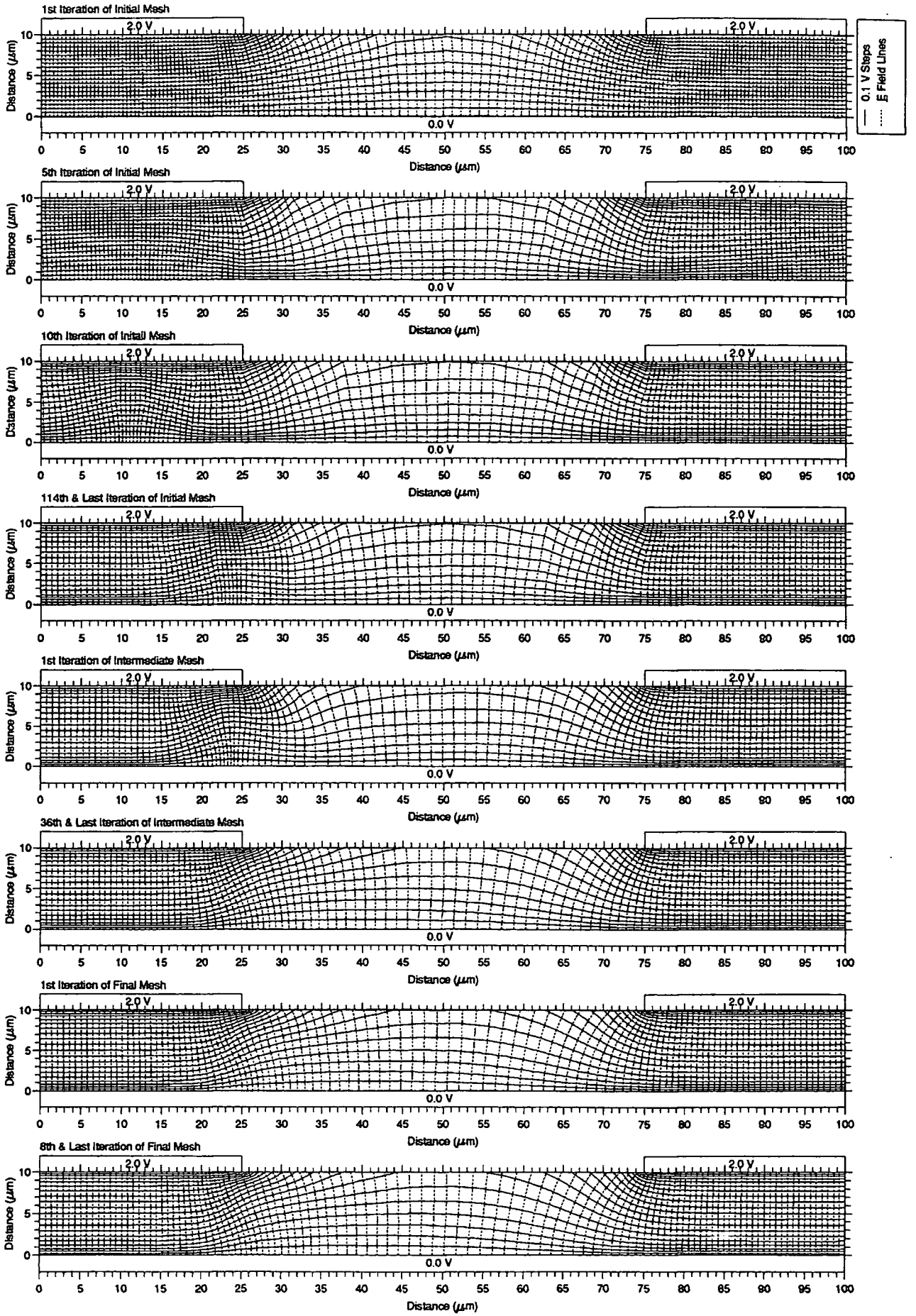

Potential Distribution and Displacement Field for a Periodic Liquid Crystal E44 Cell

at Various Stages of Convergence

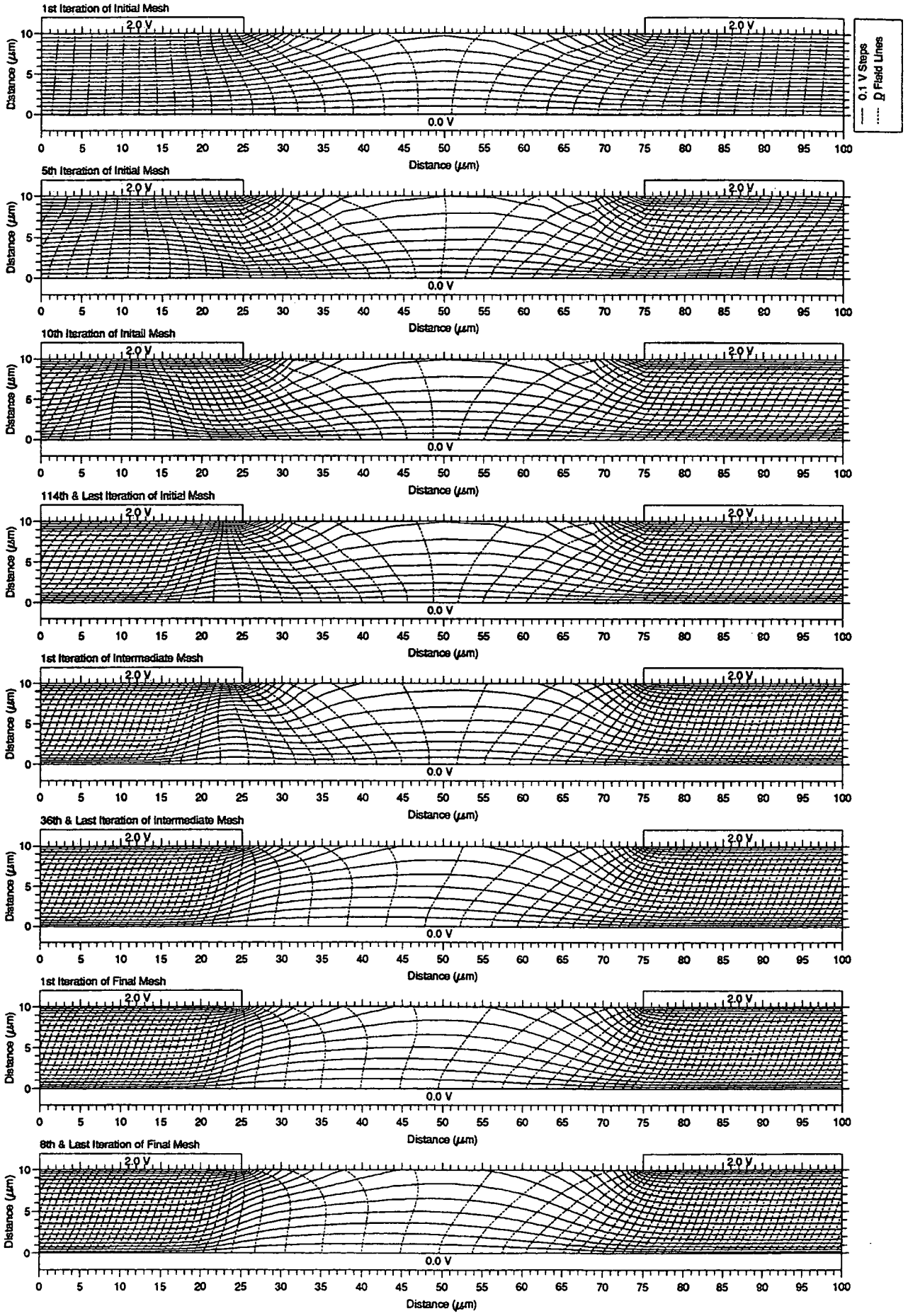

Director Orientation Distribution for a Periodic Liquid Crystal E44 Cell

at Various Stages of Convergence

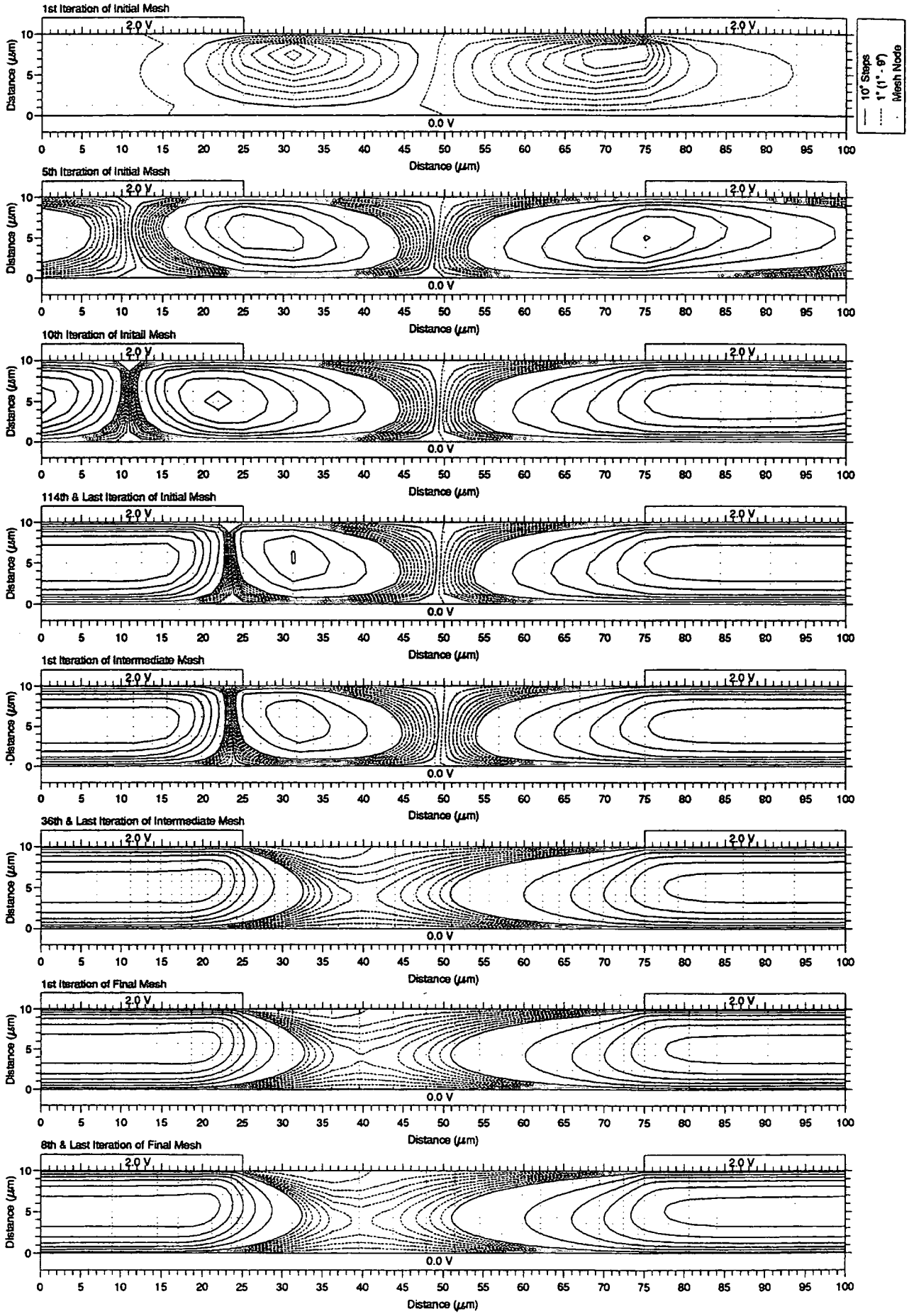

Normalised Phase Distribution for a Periodic Liquid Crystal E44 Cell

at Various Stages of Convergence

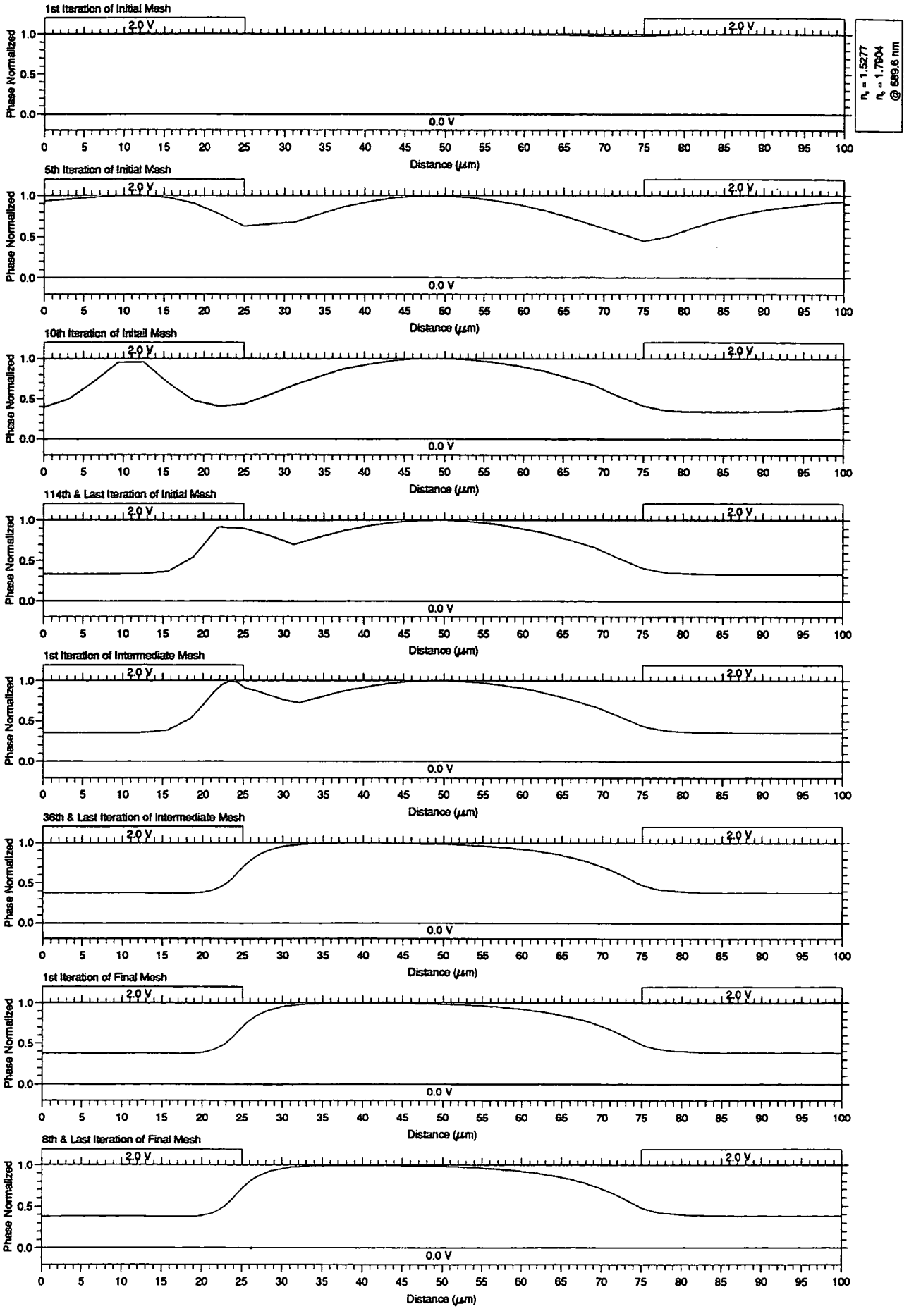

Potential Distribution and Electric Field for a Periodic Liquid Crystal E44 Cell

at Various Stages of Convergence

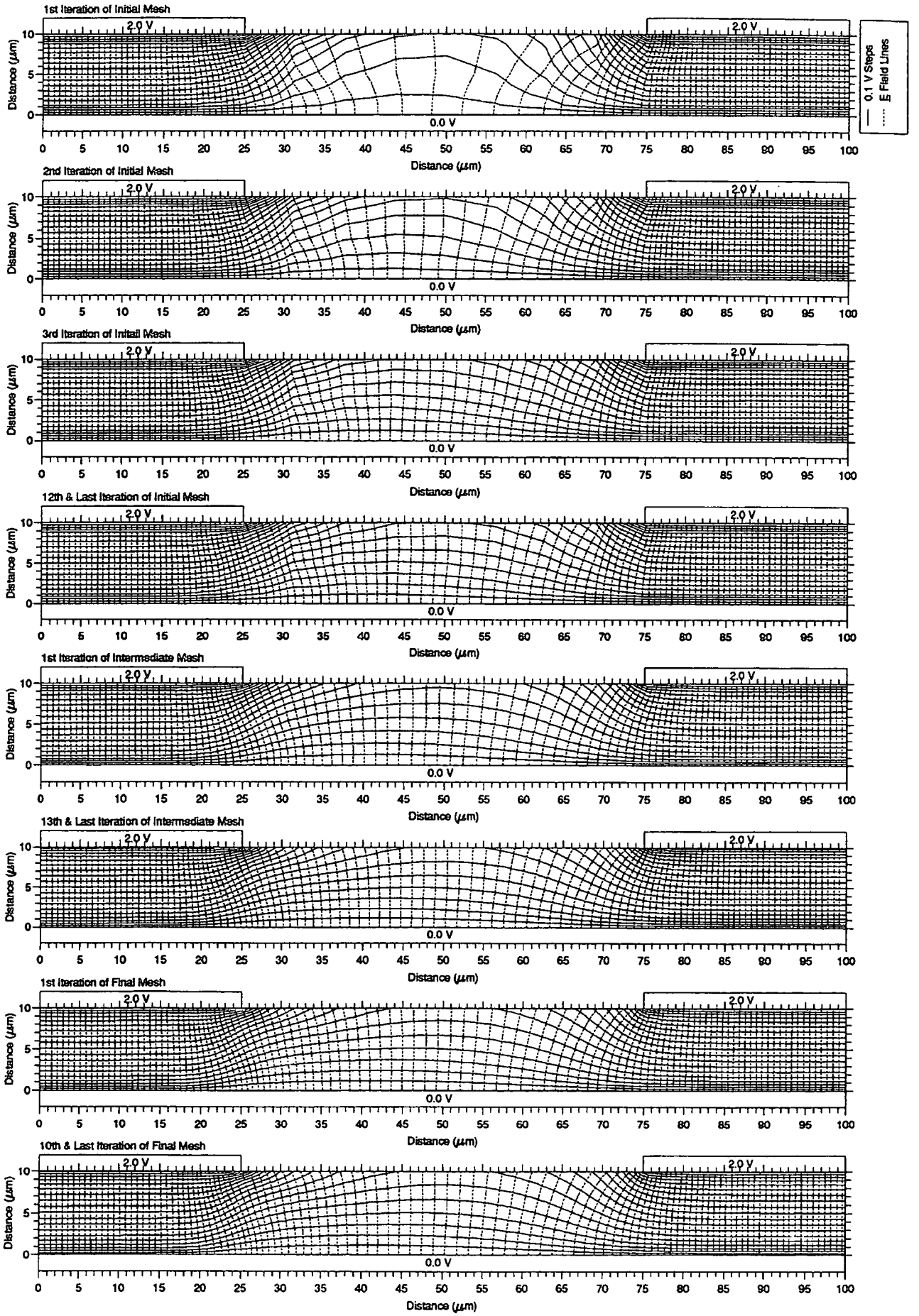

Potential Distribution and Displacement Field for a Periodic Liquid Crystal E44 Cell

at Various Stages of Convergence

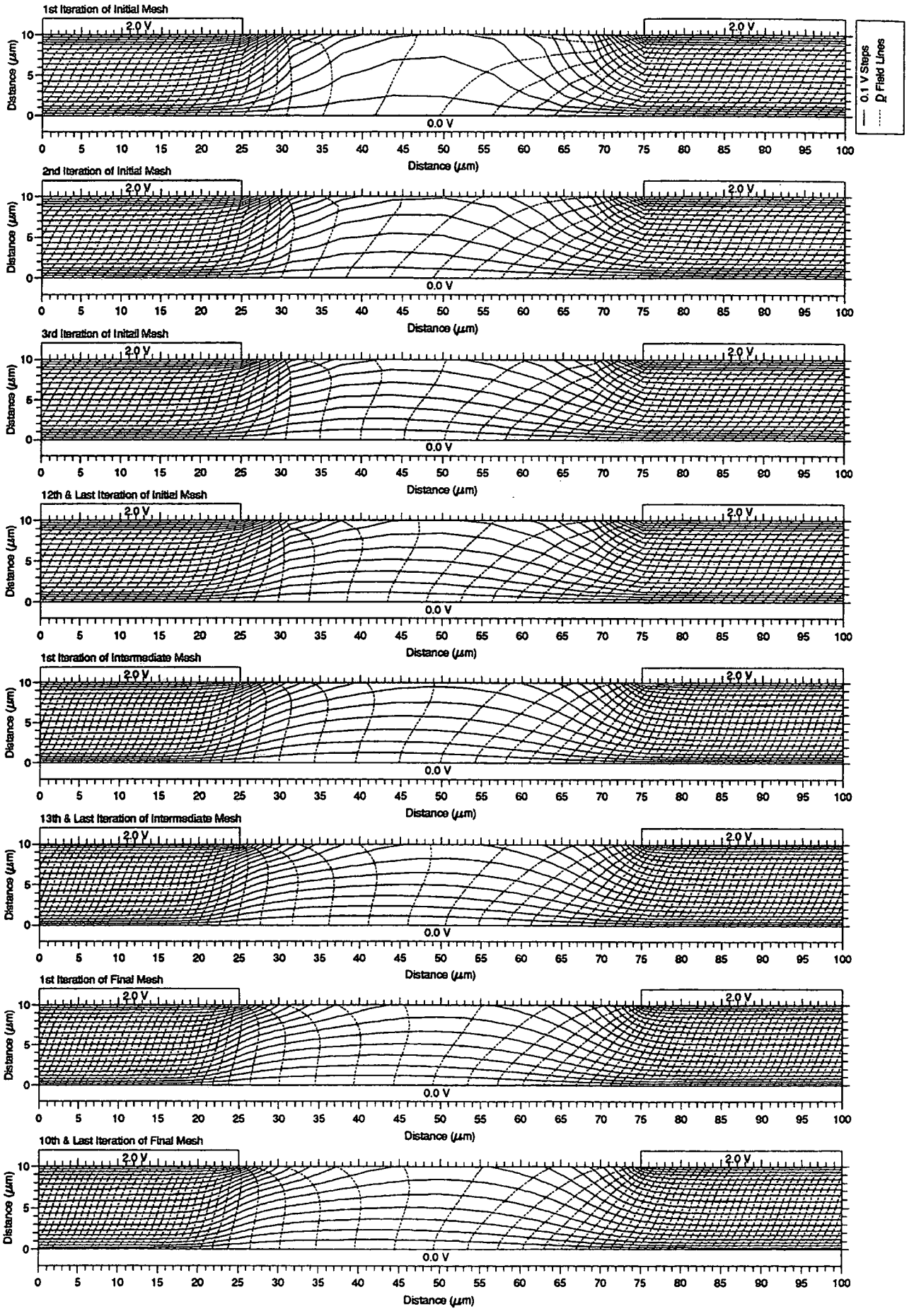

Director Orientation Distribution for a Periodic Liquid Crystal E44 Cell

at Various Stages of Convergence

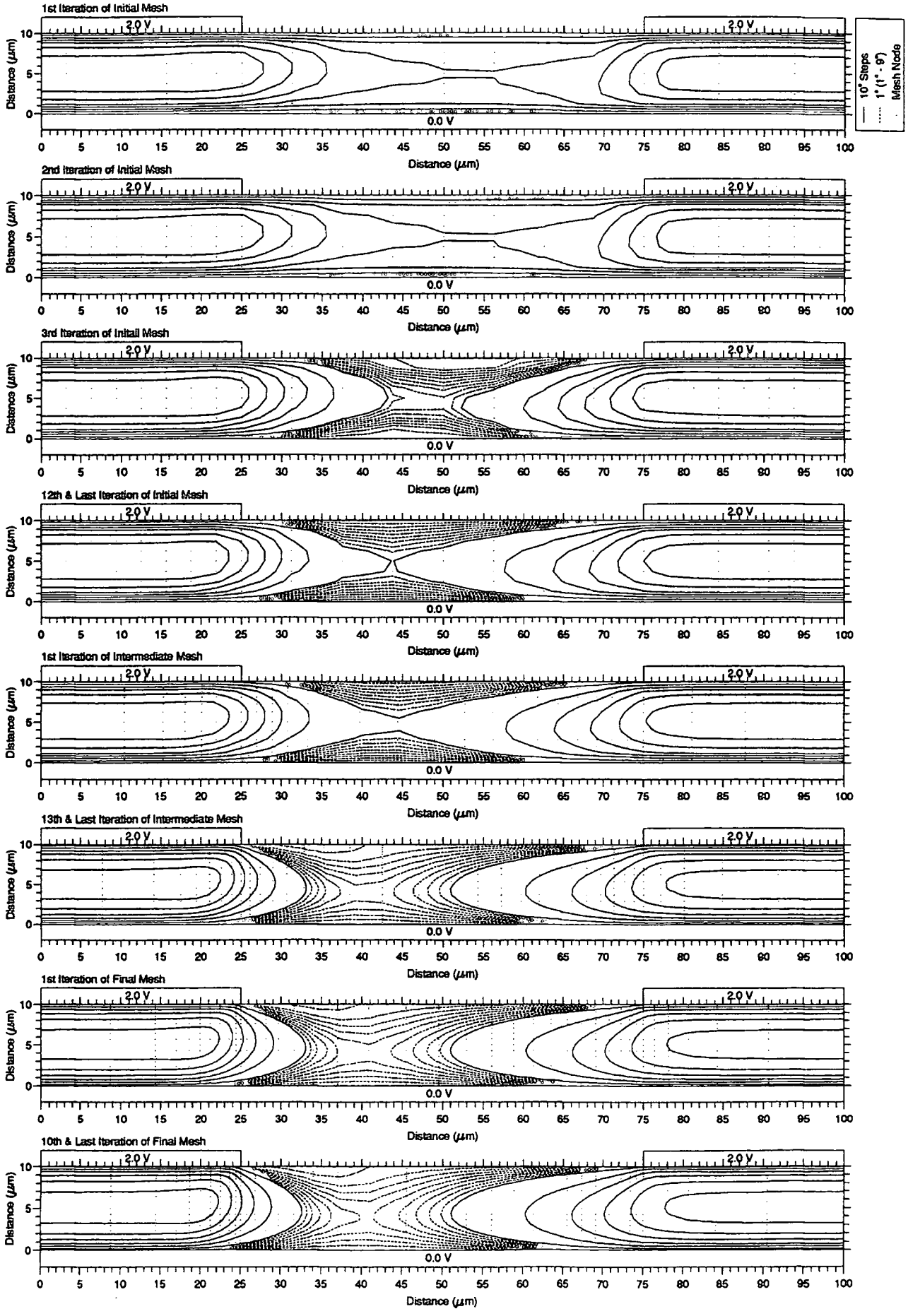

Normalised Phase Distribution for a Periodic Liquid Crystal E44 Cell

at Various Stages of Convergence

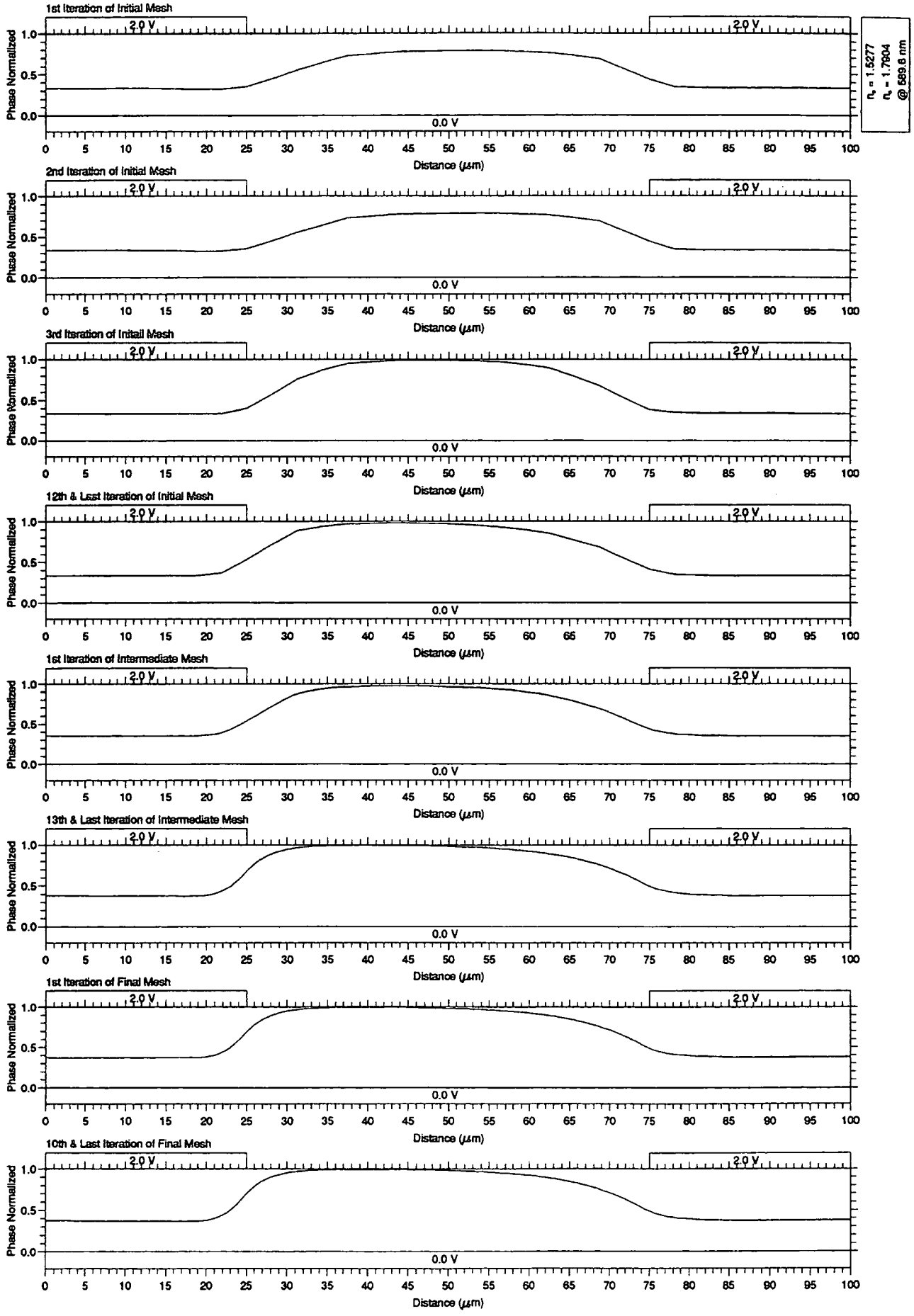

Liquid Crystal: E44 Finite Element Program: fr0 with a Fixed Mesh

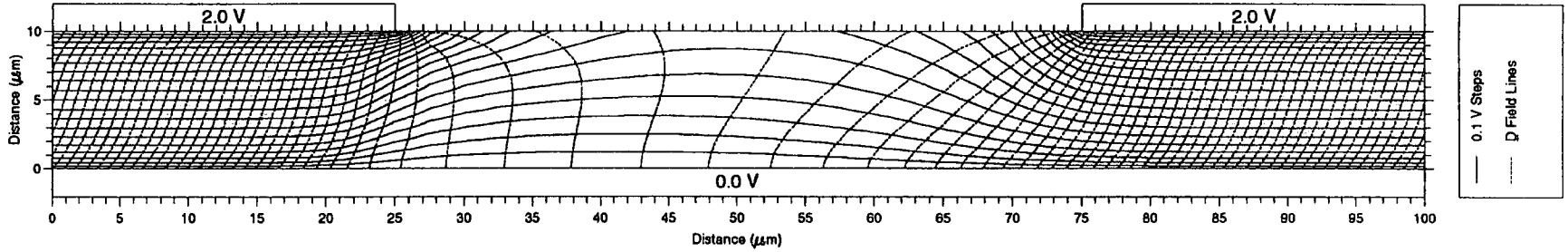

Equipotentials and Displacement Field Lines

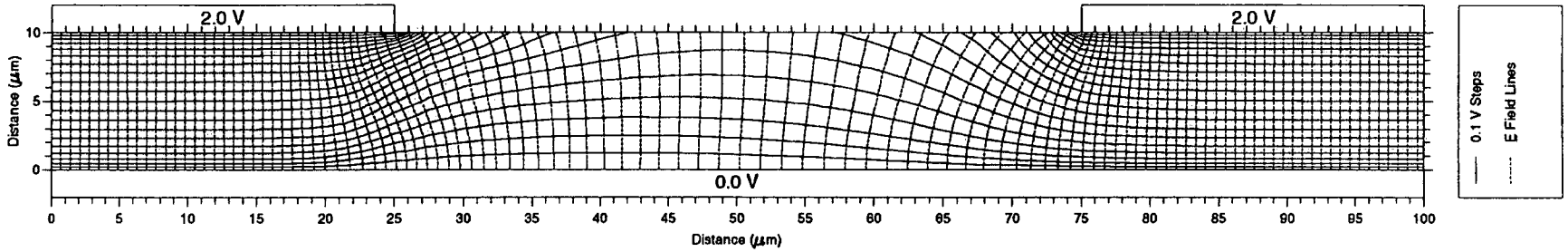

Equipotentials and Electric Field Lines

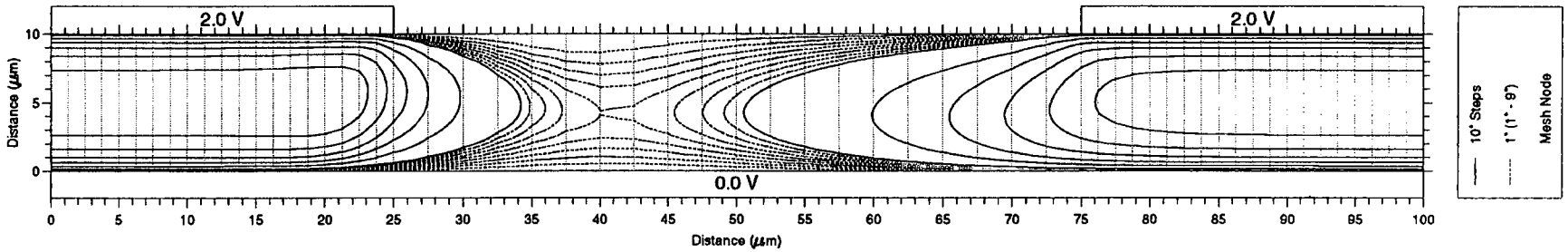

Director Orientation

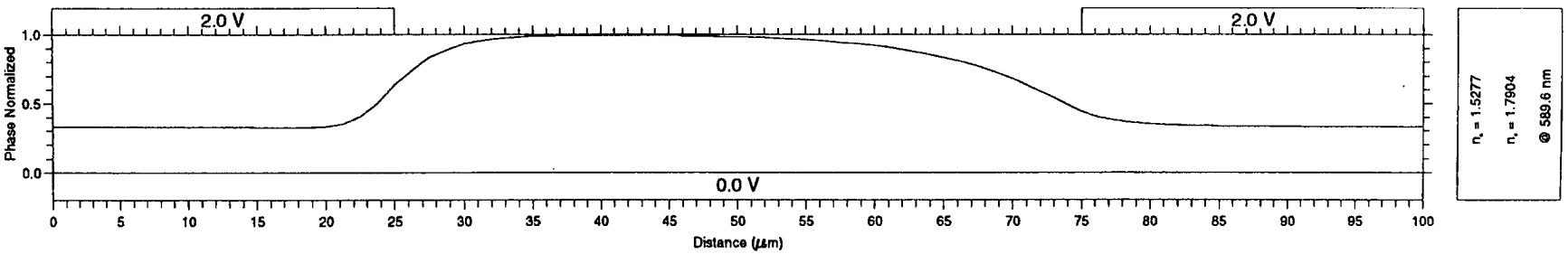

Normalized Phase Response

Liquid Crystal: E44 Finite Element Program: fr1 with a Fixed Mesh

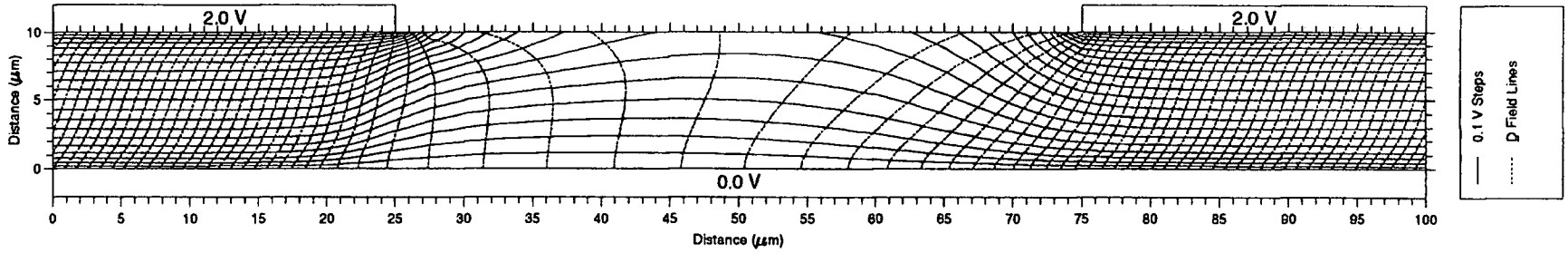

Equipotentials and Displacement Field Lines

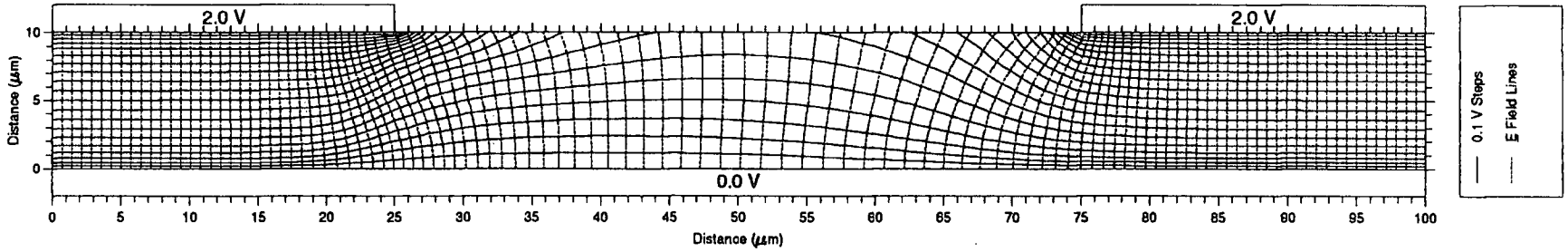

Equipotentials and Electric Field Lines

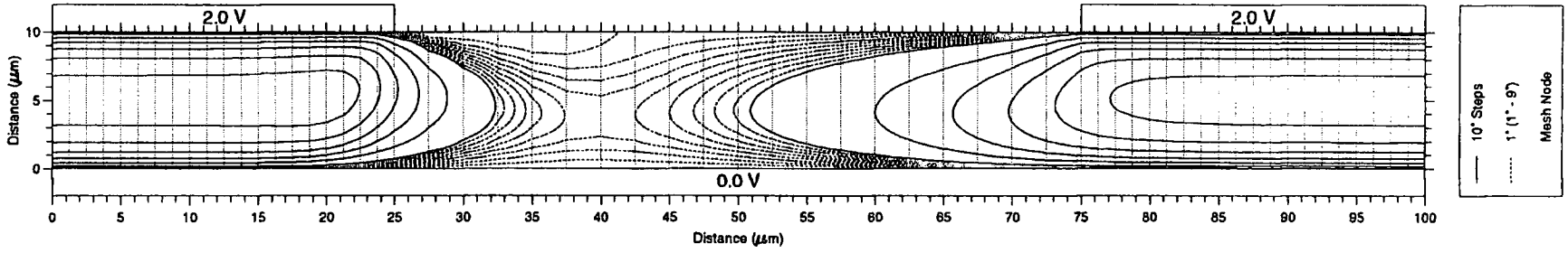

Director Orientation

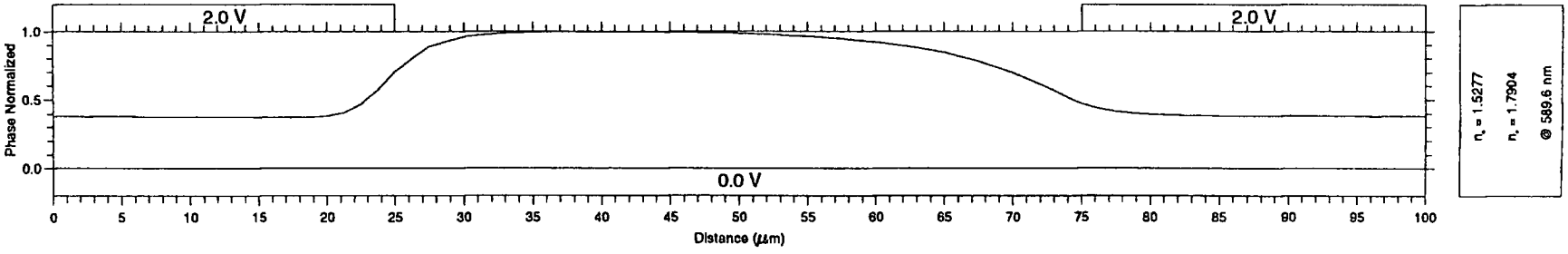

Normalized Phase Response

Liquid Crystal: E44 Finite Element Program: fr2 with a Fixed Mesh

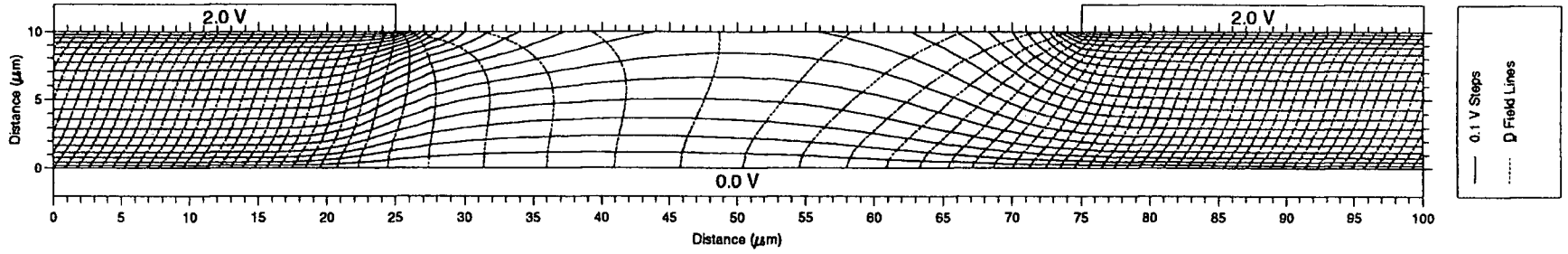

Equipotentials and Displacement Field Lines

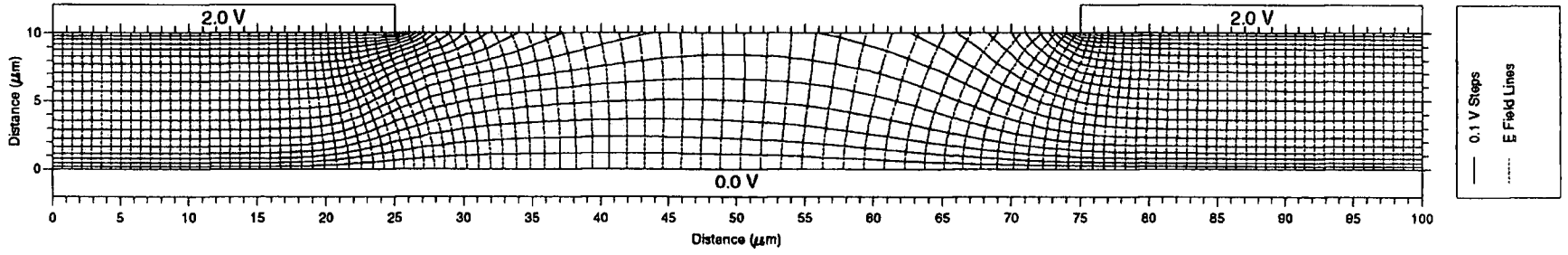

Equipotentials and Electric Field Lines

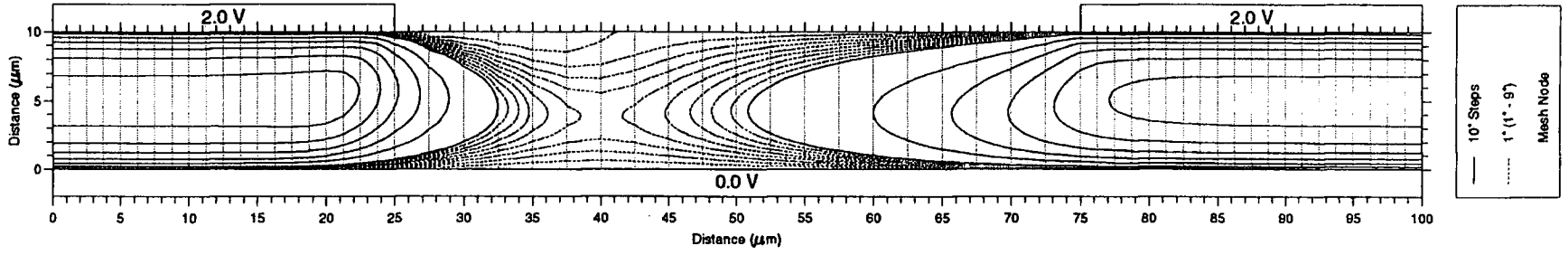

Director Orientation

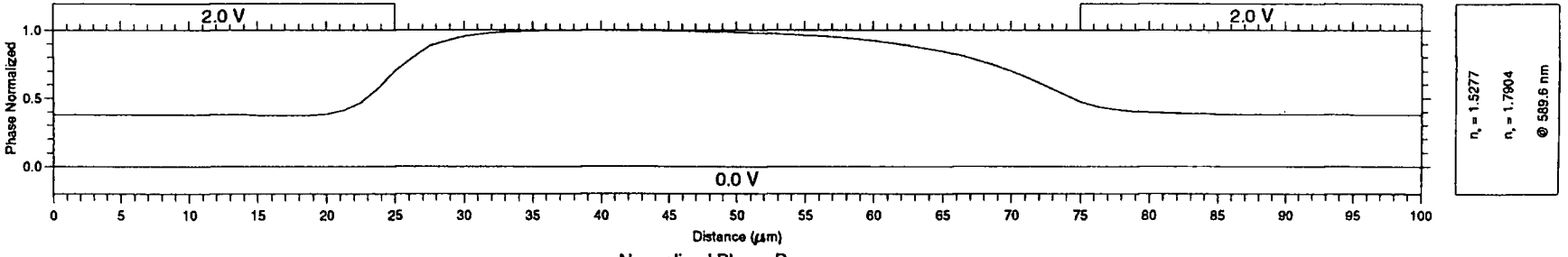

Normalized Phase Response

Liquid Crystal: E44 Finite Element Program: fr0 with an Adaptive Mesh

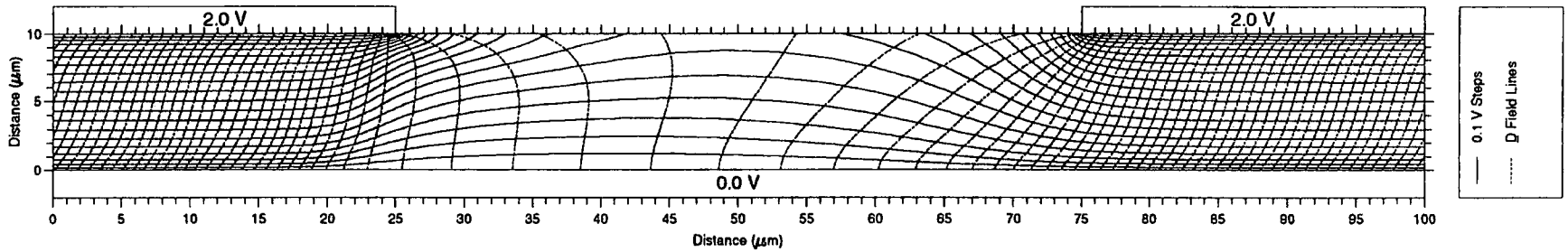

Equipotentials and Displacement Field Lines

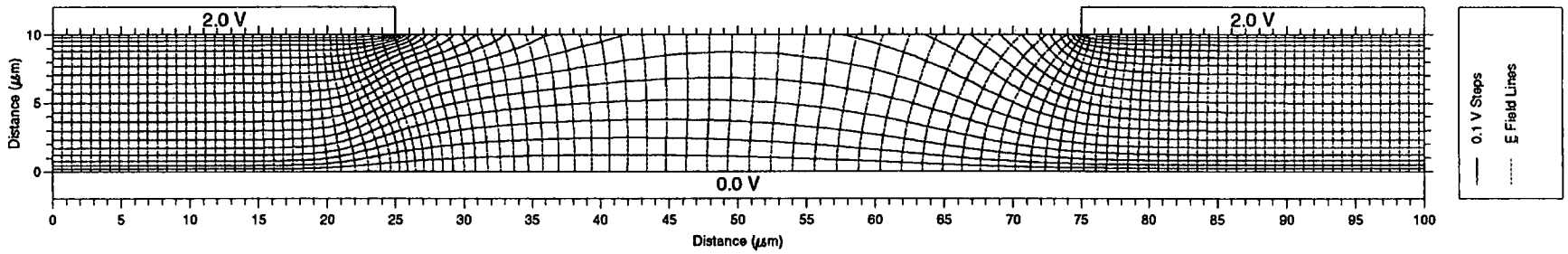

Equipotentials and Electric Field Lines

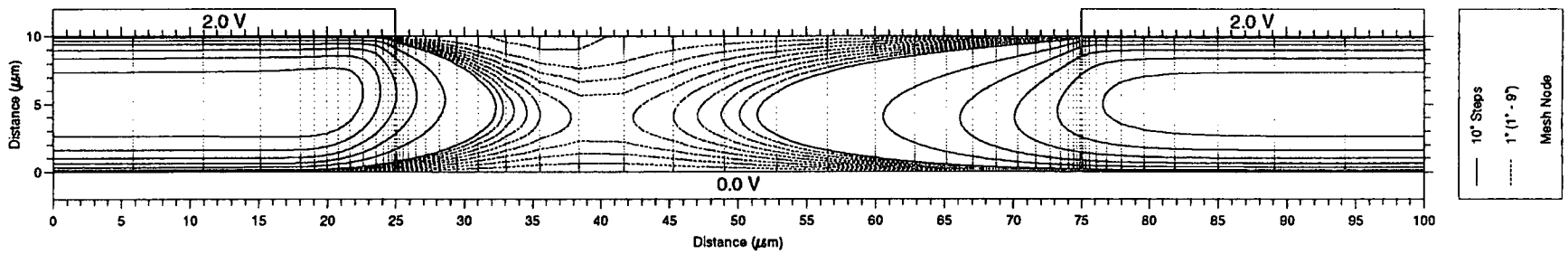

Director Orientation

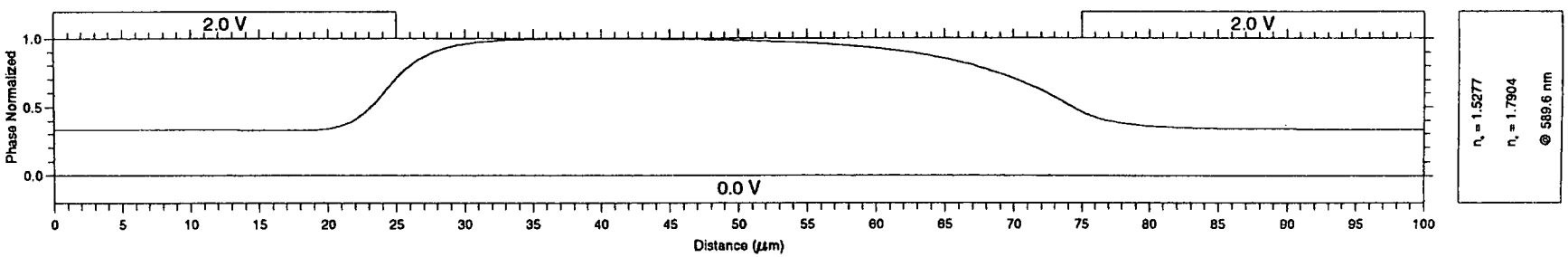

Normalized Phase Response

Liquid Crystal: E44 Finite Element Program: fr1 with an Adaptive Mesh

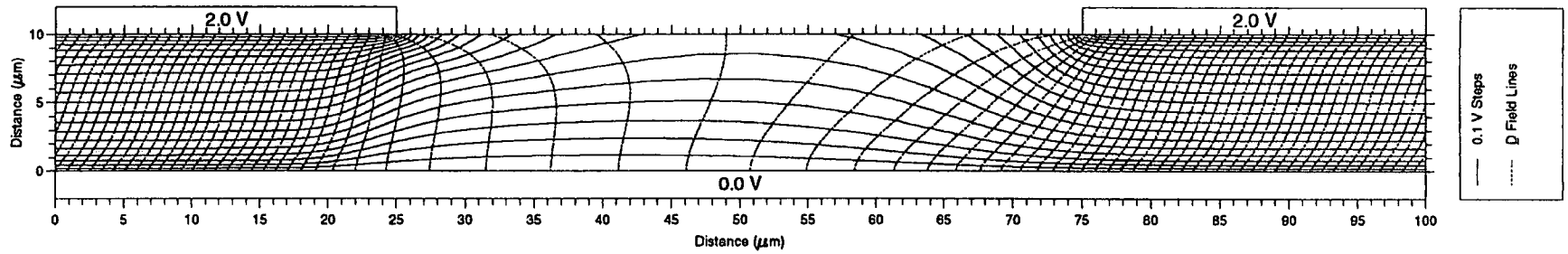

Equipotentials and Displacement Field Lines

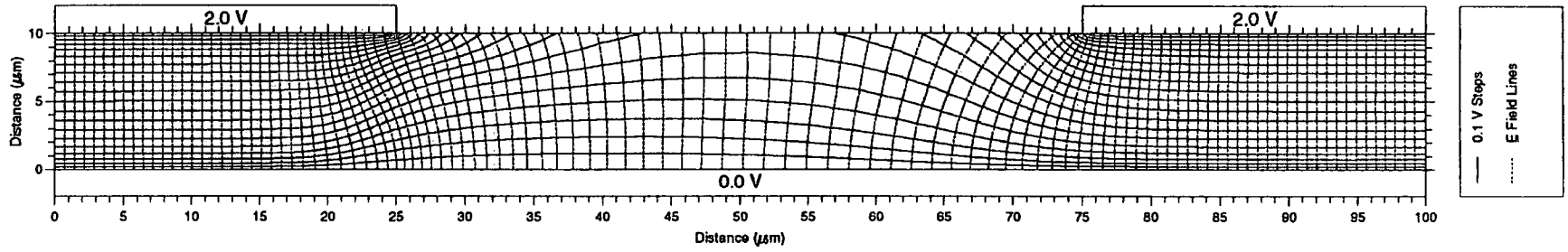

Equipotentials and Electric Field Lines

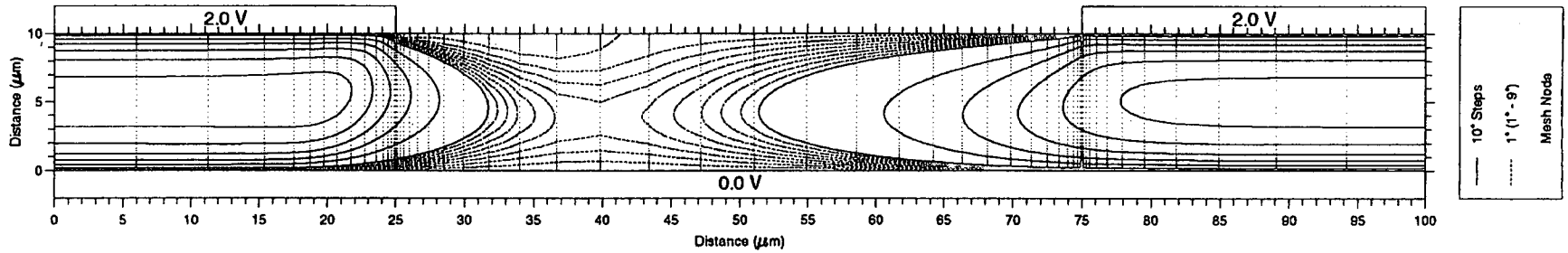

Director Orientation

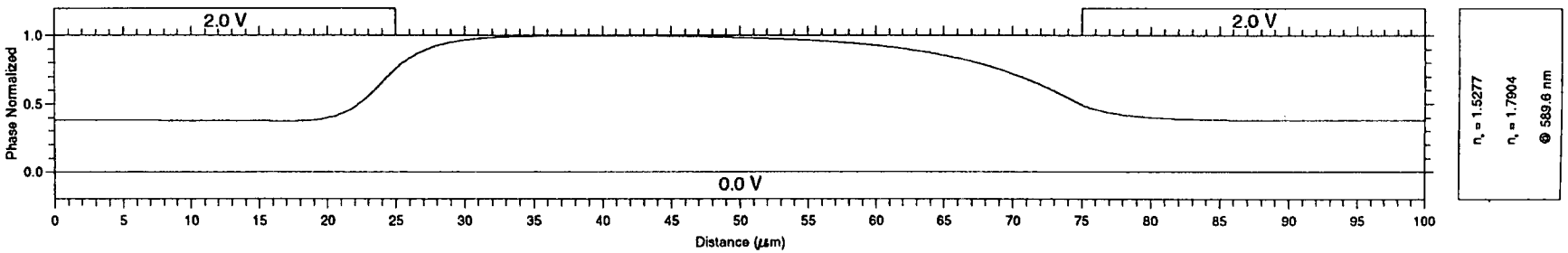

Normalized Phase Response

Liquid Crystal: E44 Finite Element Program: fr2 with an Adaptive Mesh

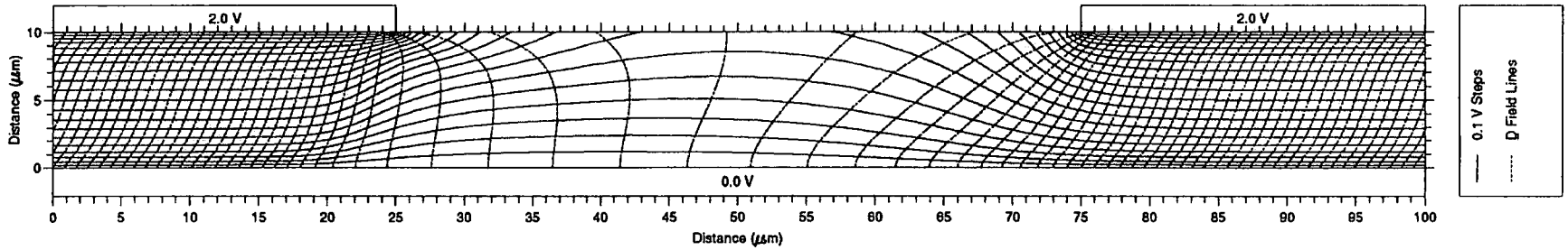

Equipotentials and Displacement Field Lines

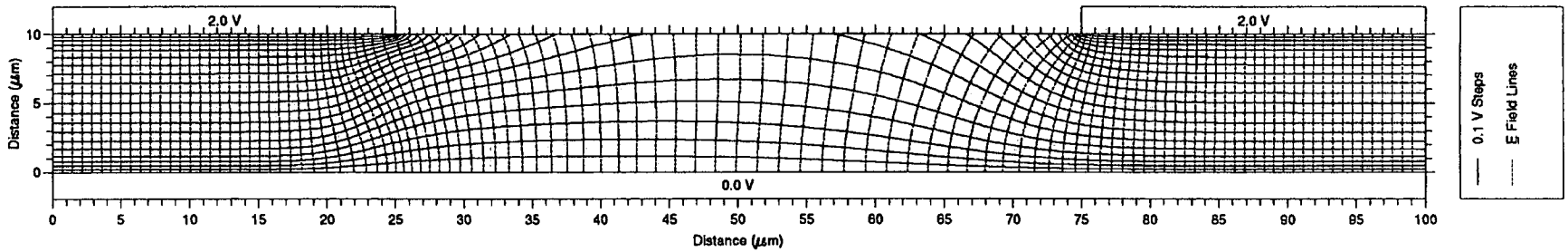

Equipotentials and Electric Field Lines

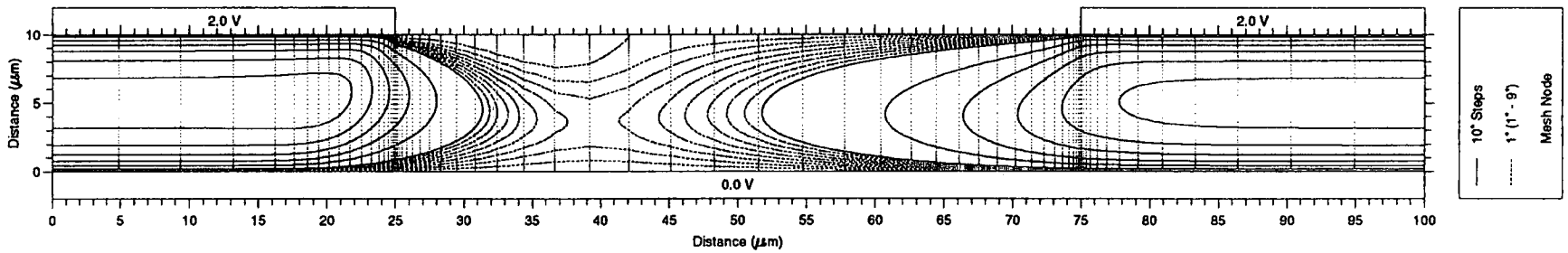

Director Orientation

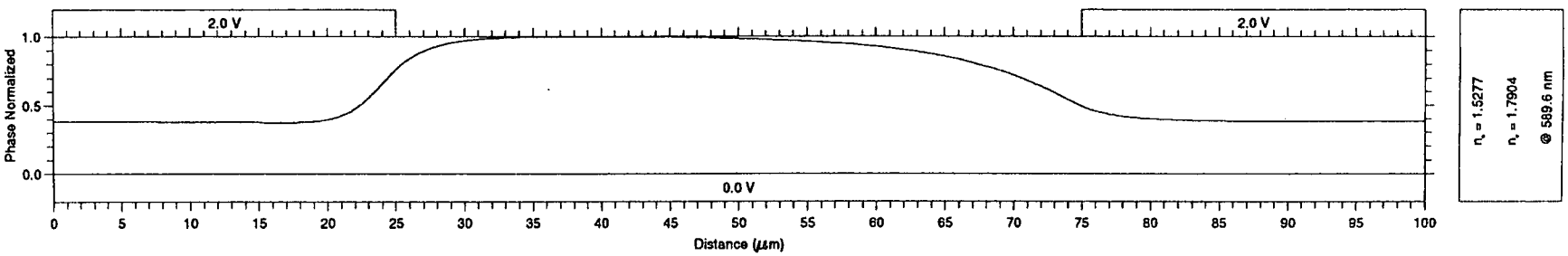

Normalized Phase Response

Potential Distribution and Electric Field for a Periodic Liquid Crystal E44 Cell

from a far boundary at various distances with an Adaptive Mesh

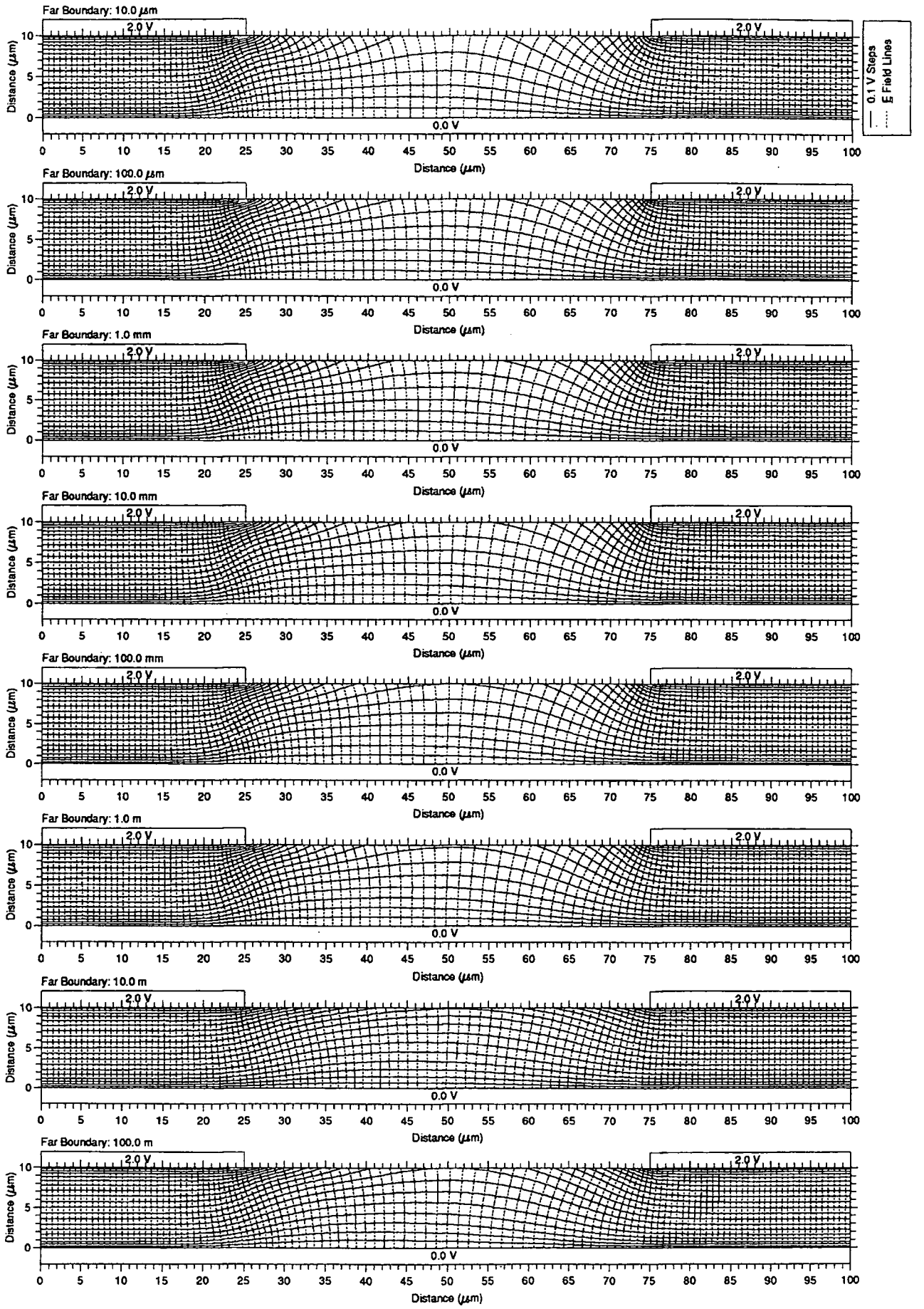

Potential Distribution and Displacement Field for a Periodic Liquid Crystal E44 Cell

from a far boundary at various distances with an Adaptive Mesh

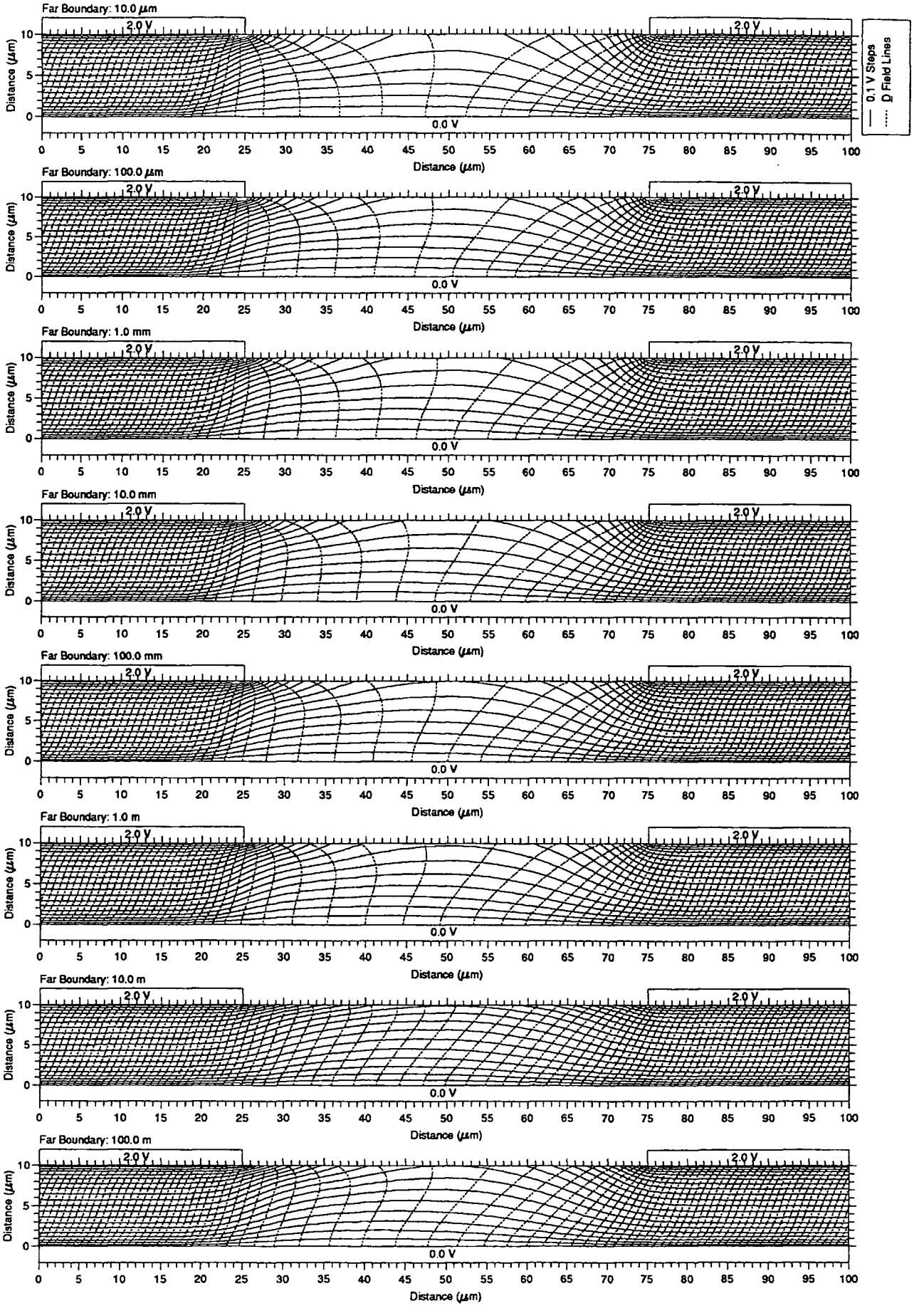

Director Orientation Distribution for a Periodic Liquid Crystal E44 Cell

from a far boundary at various distances with an Adaptive Mesh

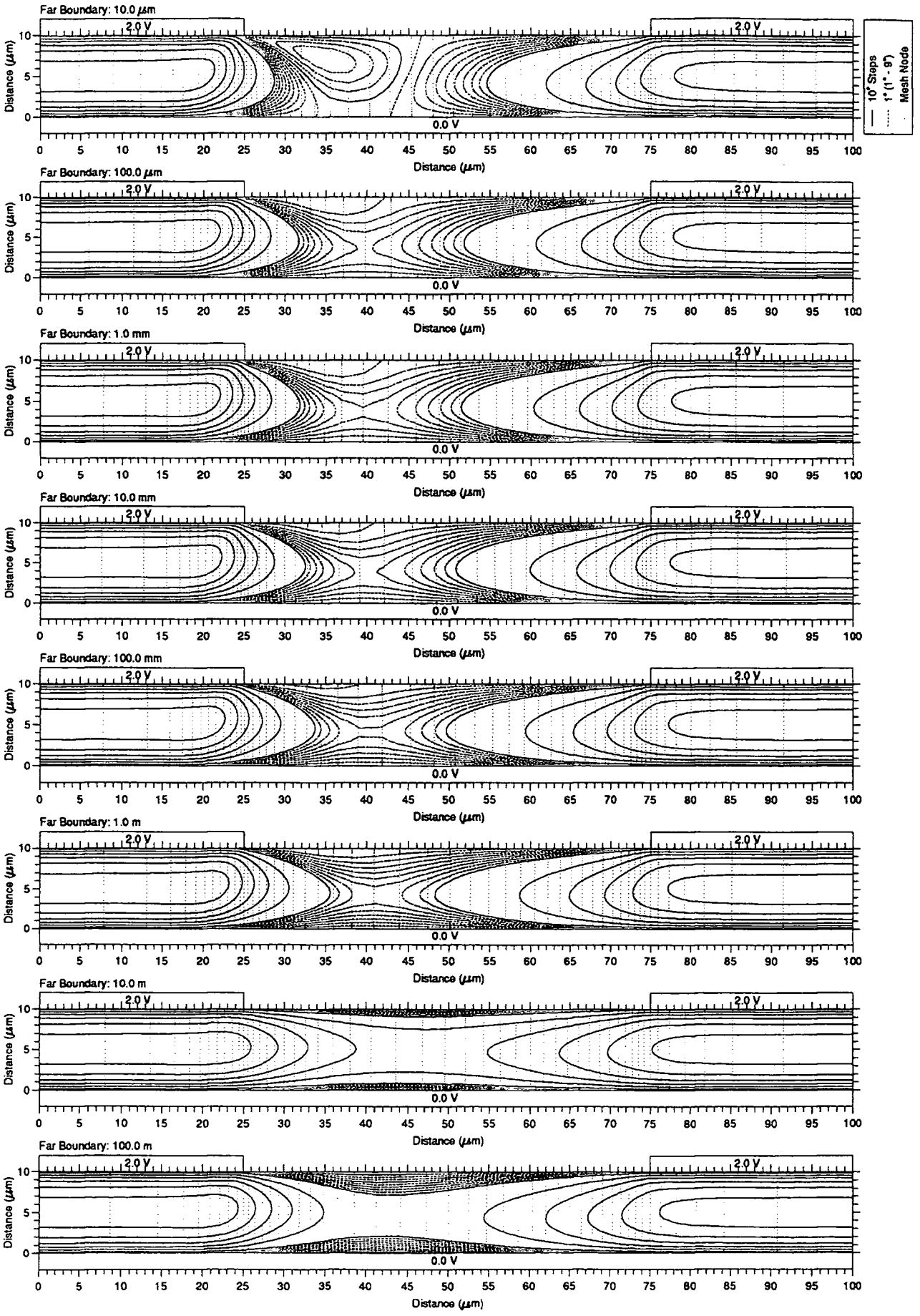

Normalised Phase Distribution for a Periodic Liquid Crystal E44 Cell

from a far boundary at various distances with an Adaptive Mesh

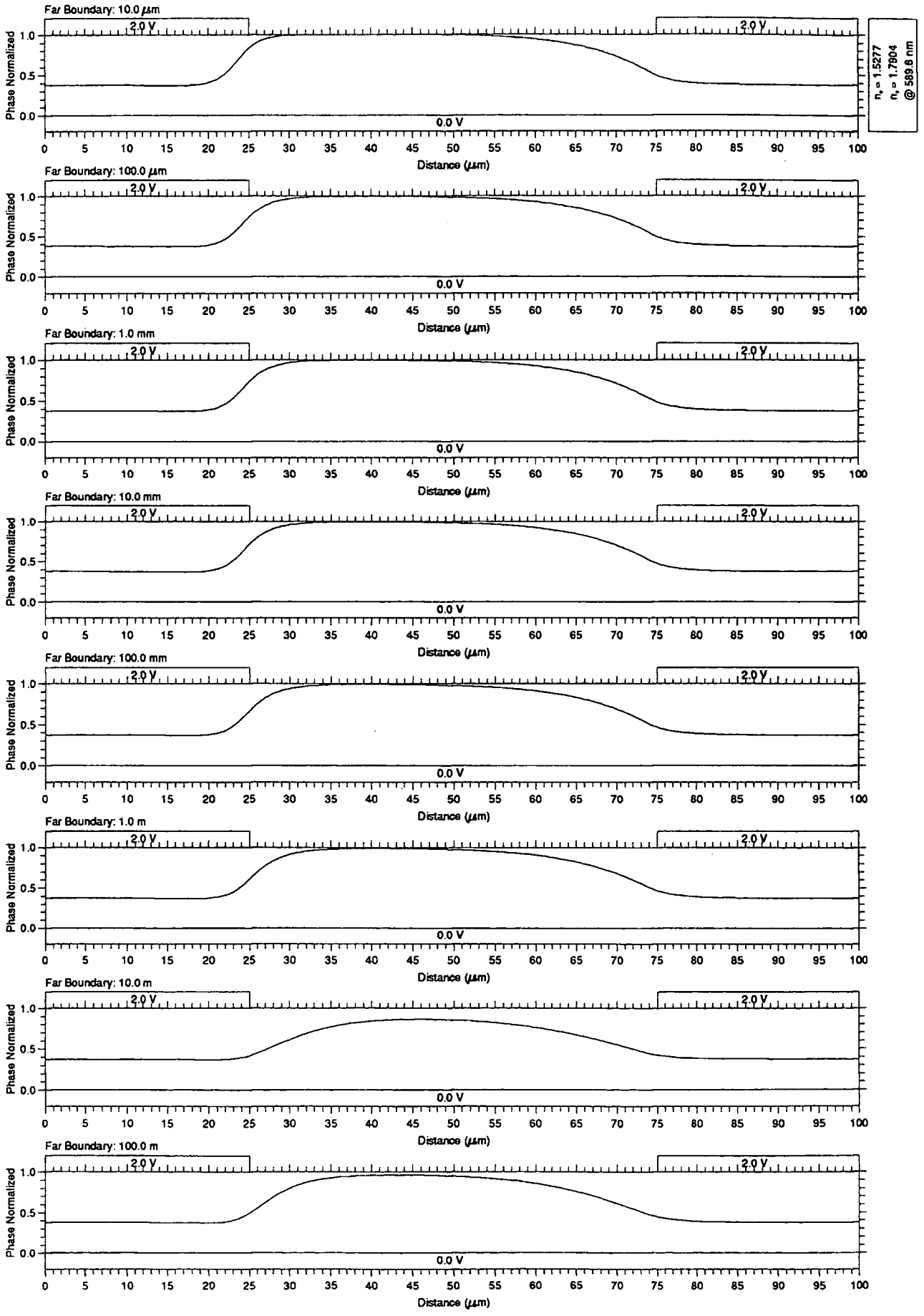

Plots of Potential and Normal Displacement Field for a Periodic Liquid Crystal E44 Cell

from a Neuman far boundary at various distances with an Adaptive Mesh

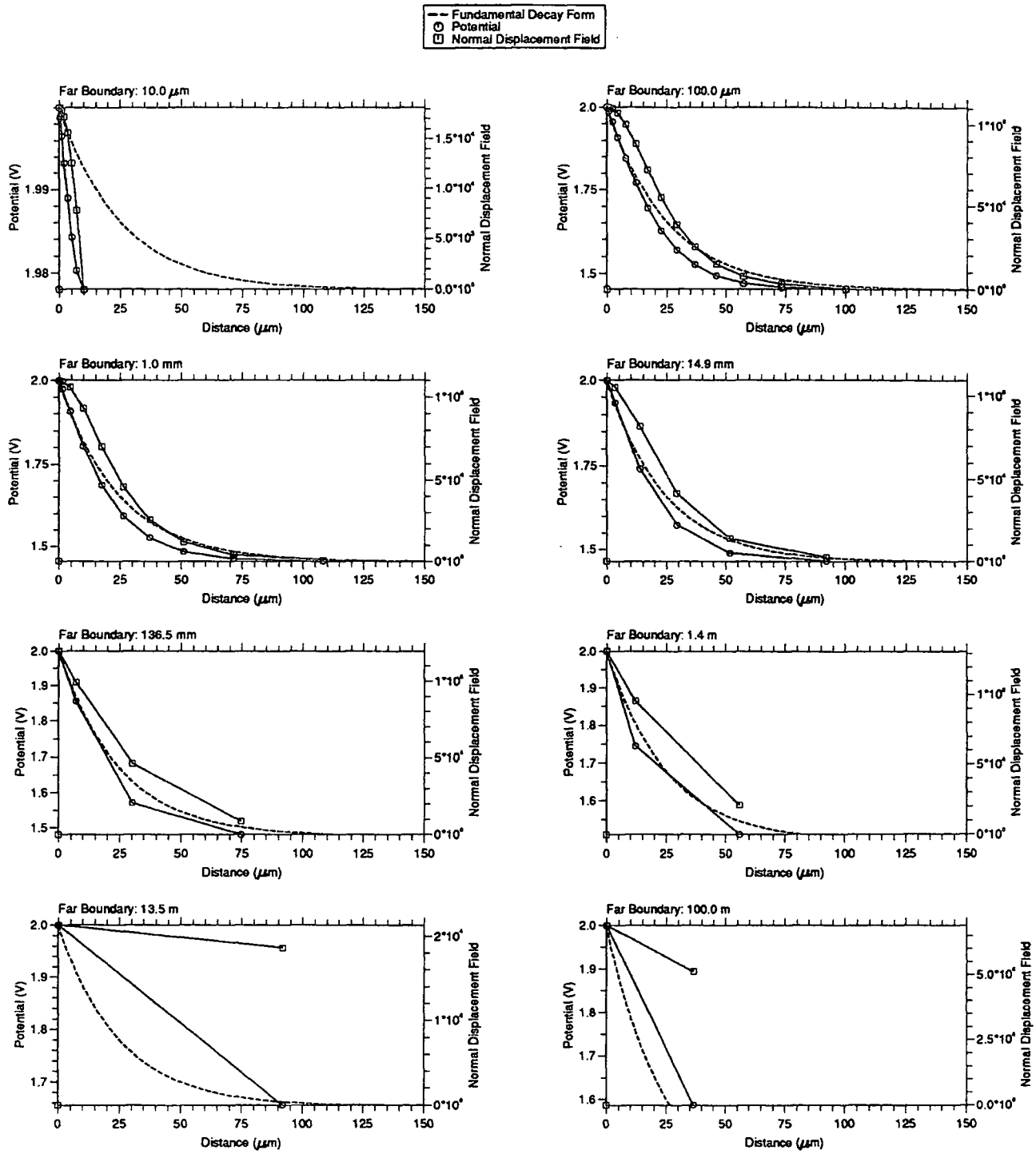

Plots of Potential and Normal Displacement Field for a Periodic Liquid Crystal E44 Cell

from a Neuman far boundary at various distances with an Adaptive Mesh

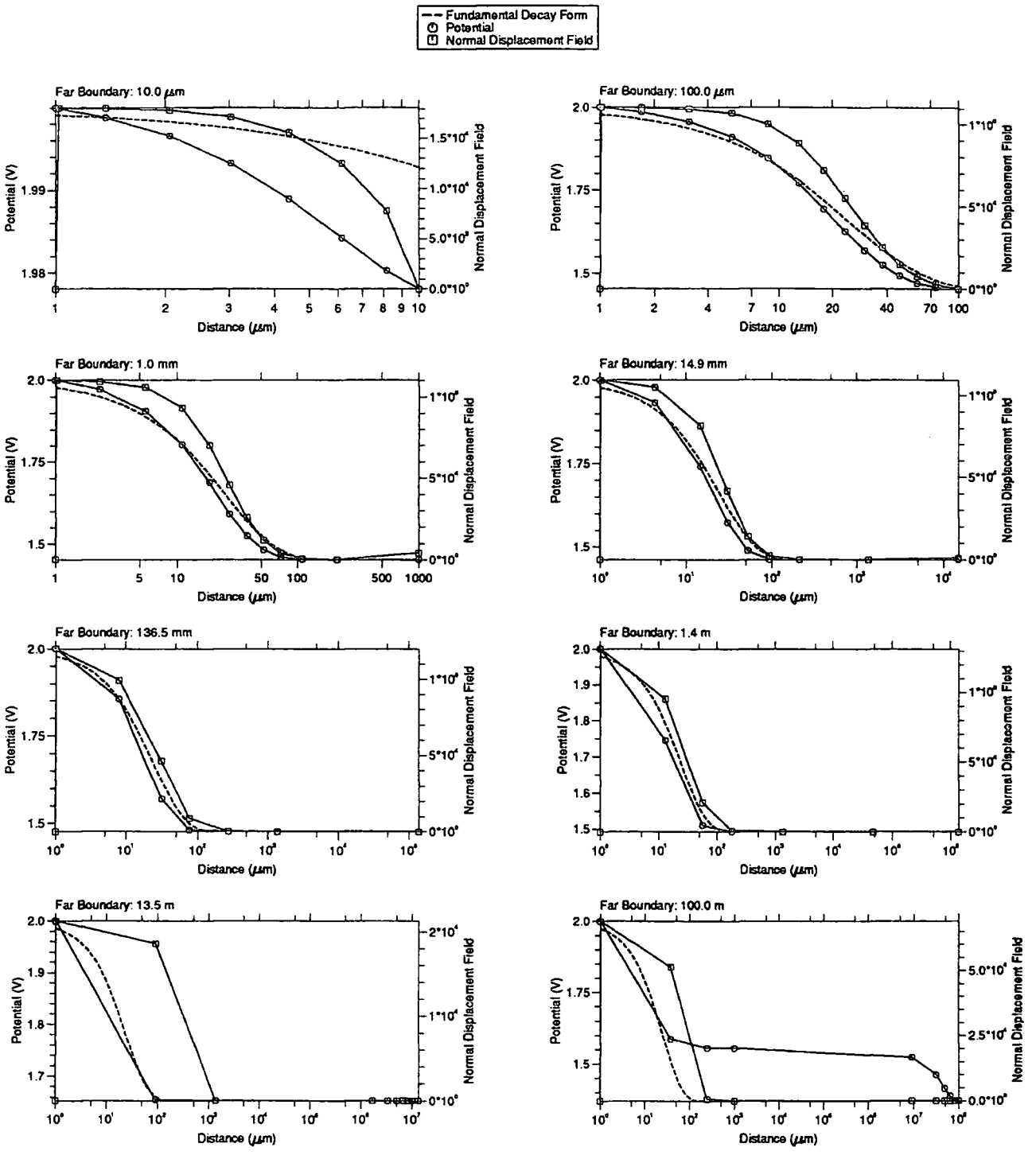

Potential Distribution and Electric Field for a Periodic Liquid Crystal E44 Cell

from a far boundary at various distances with Adaptive Mesh II

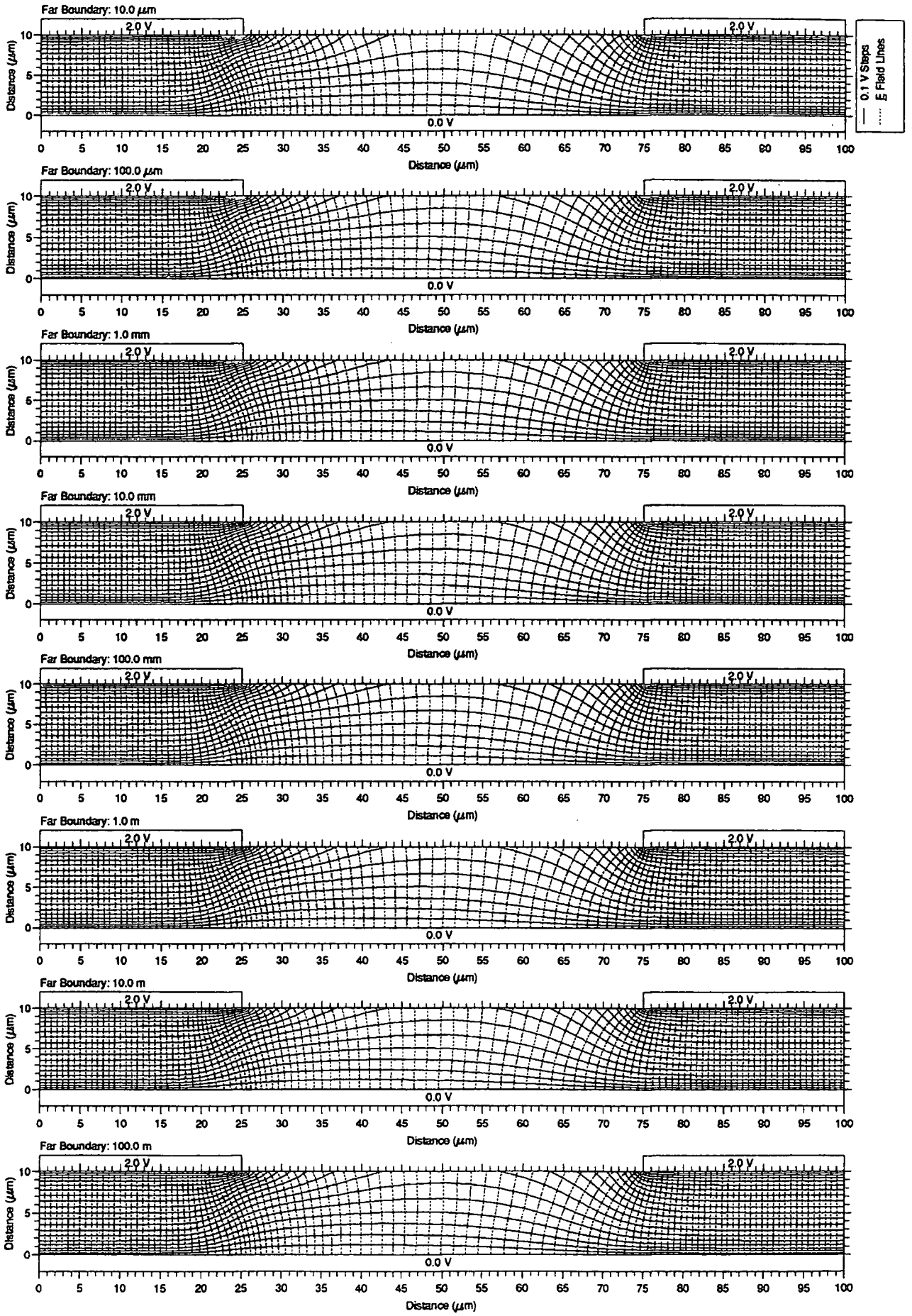

Potential Distribution and Displacement Field for a Periodic Liquid Crystal E44 Cell

from a far boundary at various distances with Adaptive Mesh II

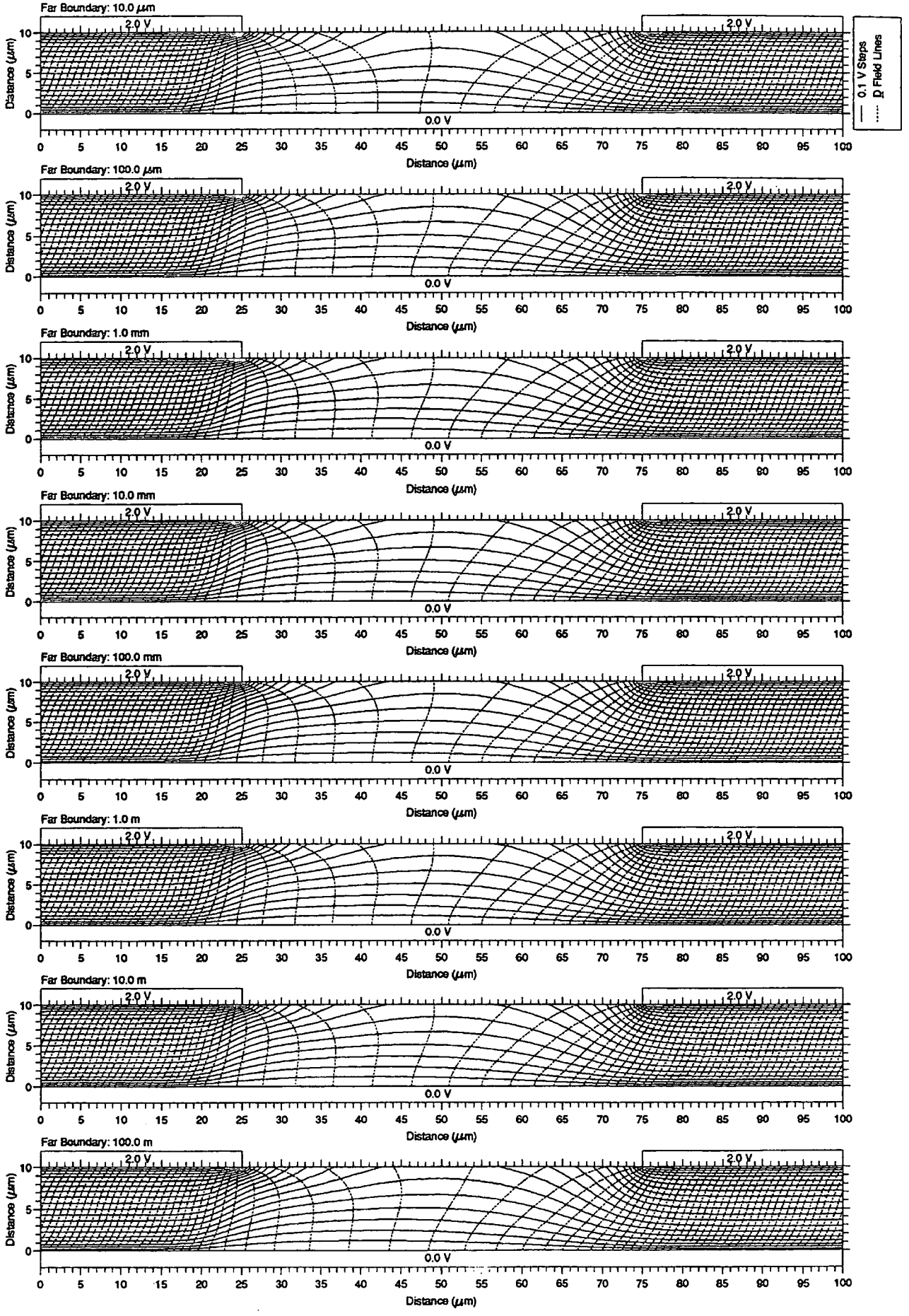

Director Orientation Distribution for a Periodic Liquid Crystal E44 Cell

from a far boundary at various distances with Adaptive Mesh II

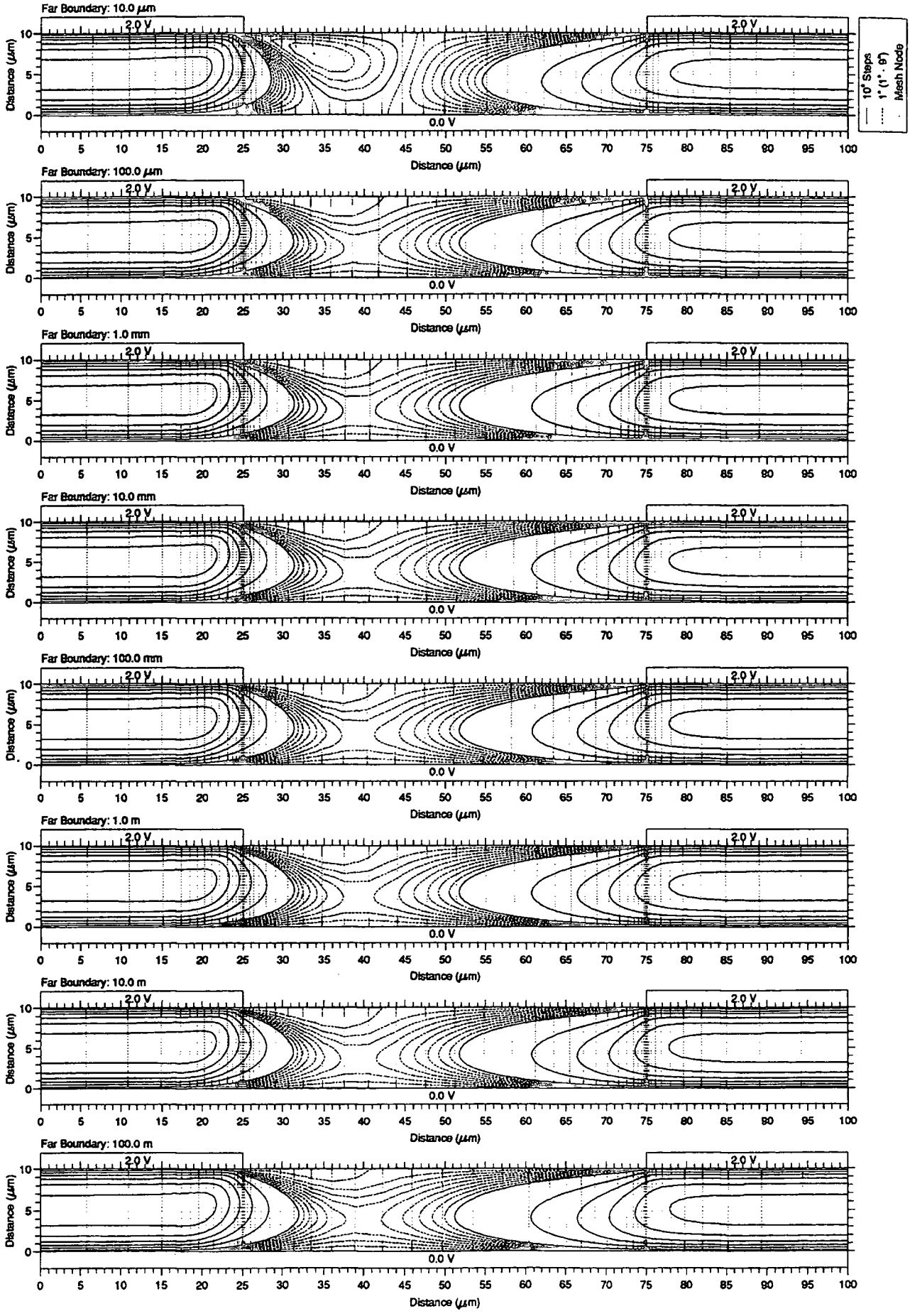

Normalised Phase Distribution for a Periodic Liquid Crystal E44 Cell

from a far boundary at various distances with Adaptive Mesh II

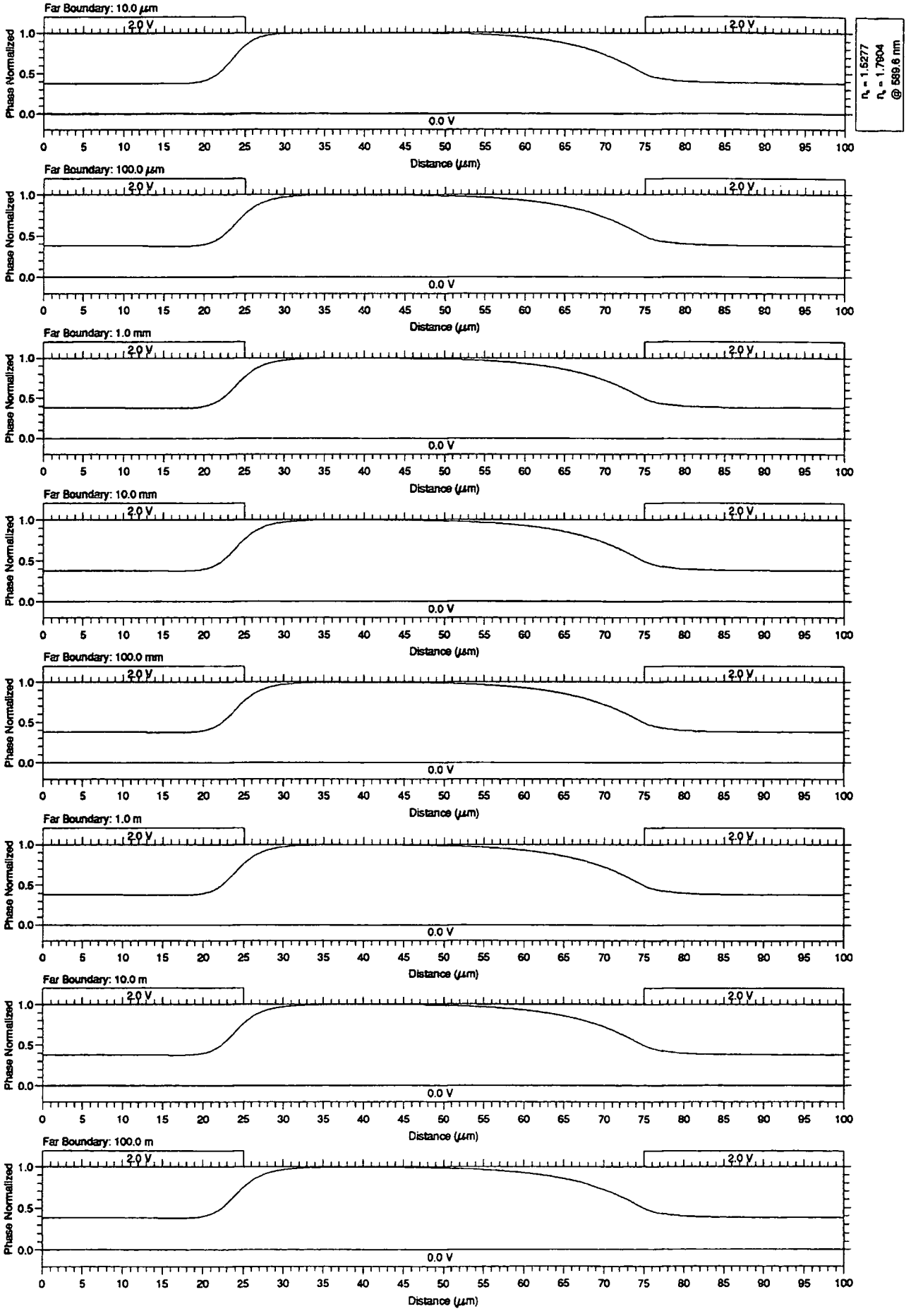

Plots of Potential and Normal Displacement Field for a Periodic Liquid Crystal E44 Cell

from a Neuman far boundary at various distances with Adaptive Mesh II

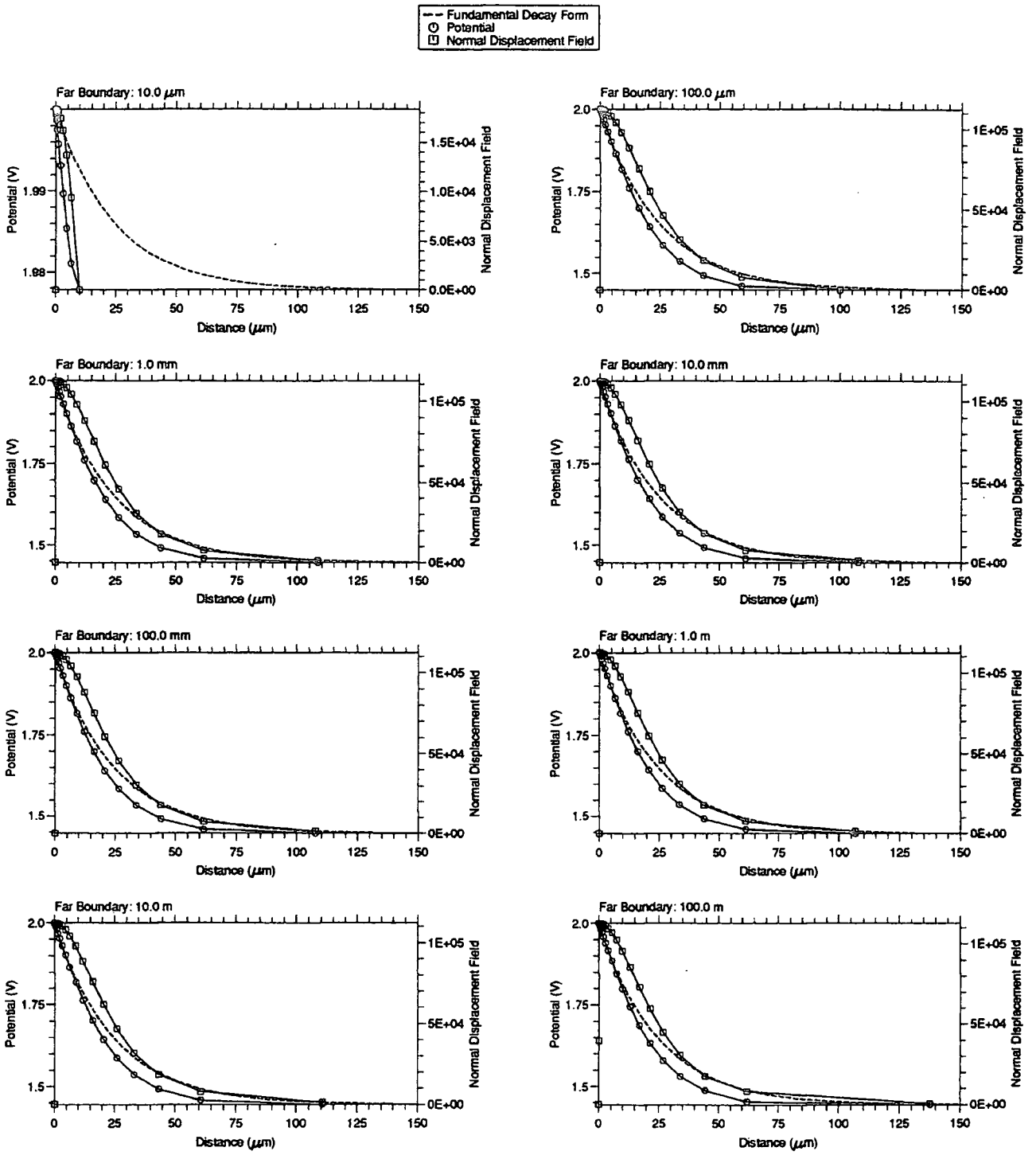

Plots of Potential and Normal Displacement Field for a Periodic Liquid Crystal E44 Cell

from a Neuman far boundary at various distances with Adaptive Mesh II

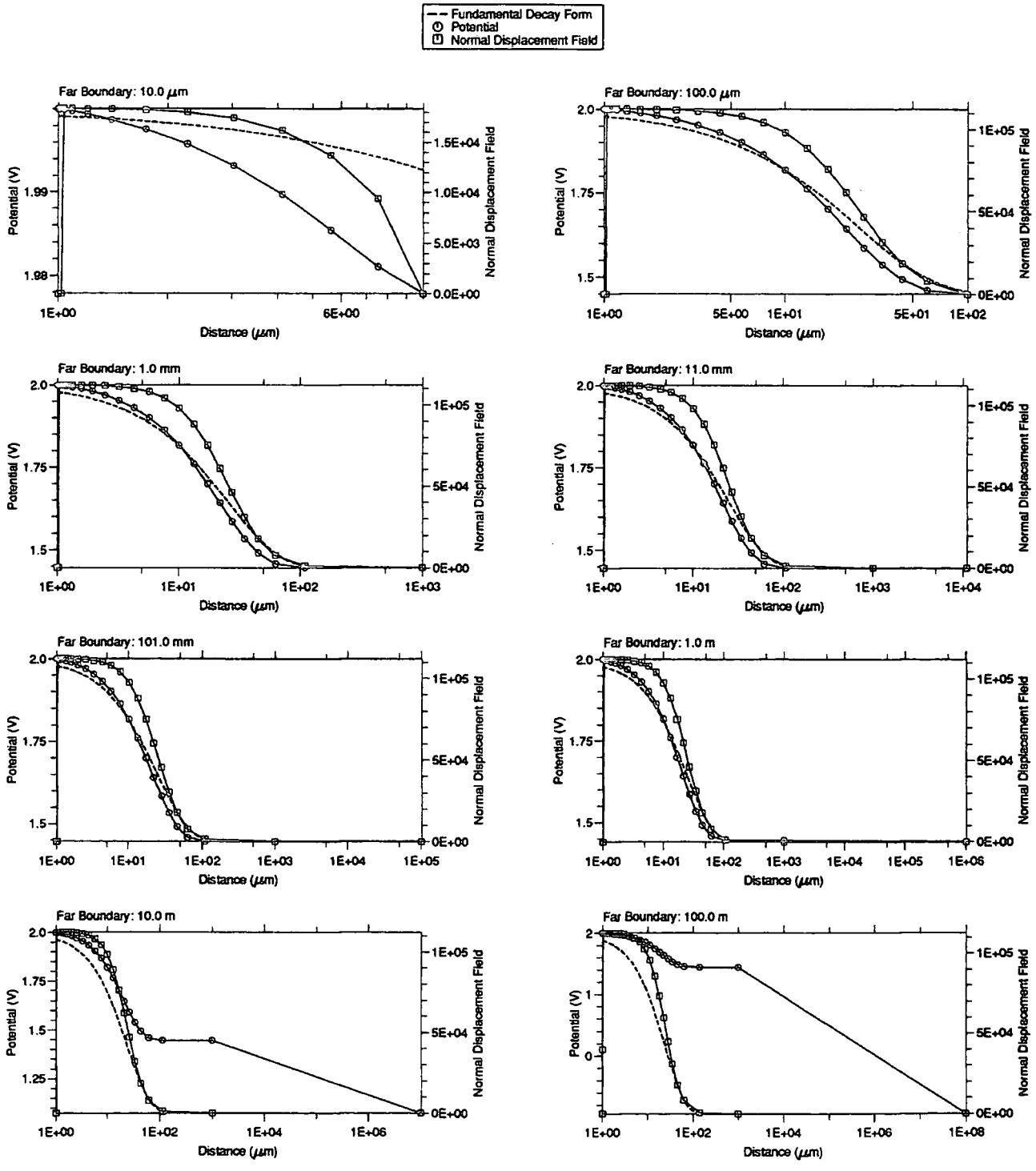

Plots of Potential and Normal Displacement Field for a Planar Electrode in Air

from a Neuman far boundary at various distances with a Linear Mesh

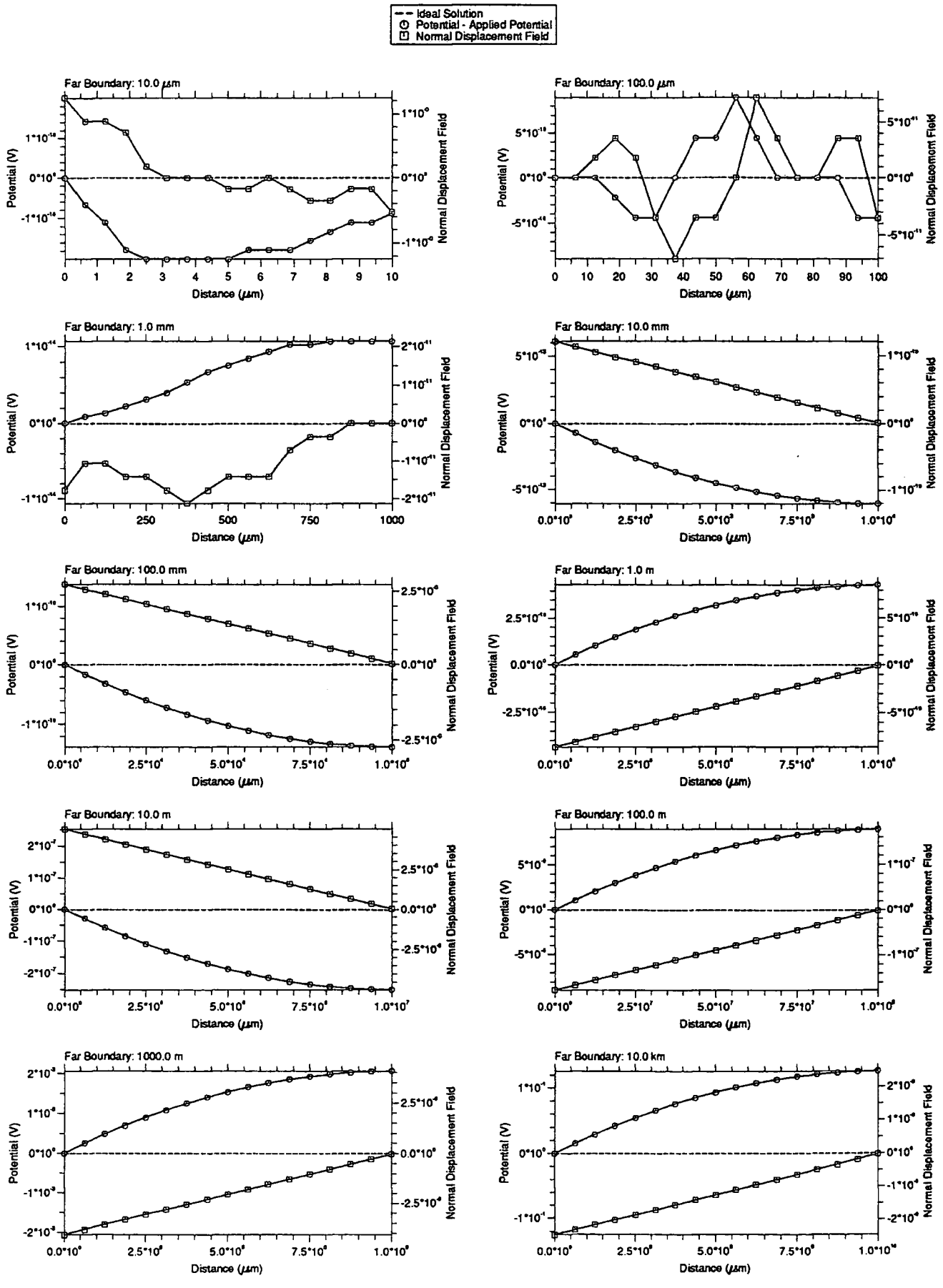

Liquid Crystal: E44 Symmetry Test: 1

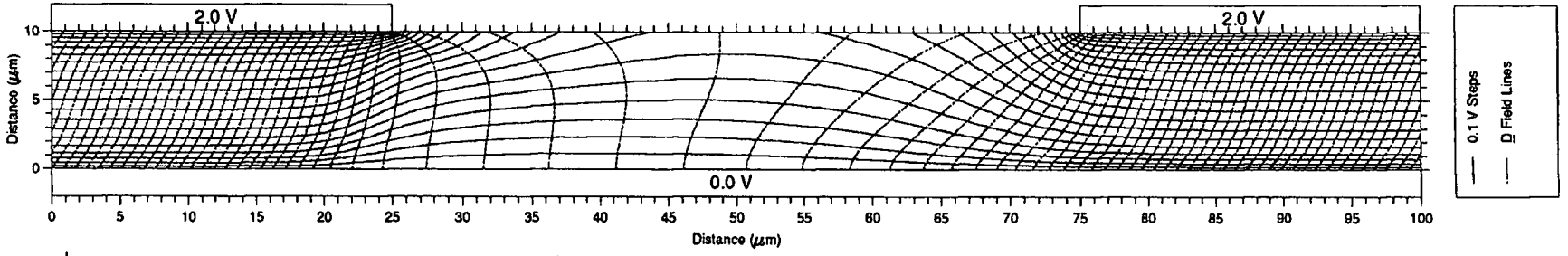

Equipotentials and Displacement Field Lines

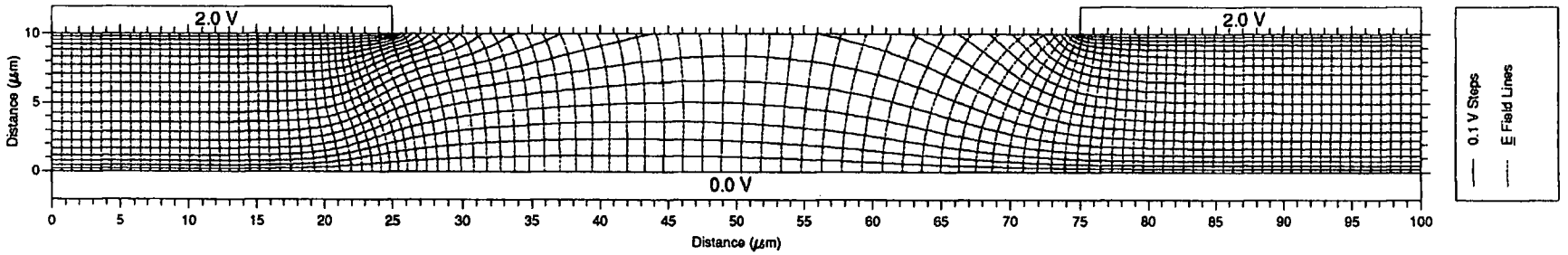

Equipotentials and Electric Field Lines

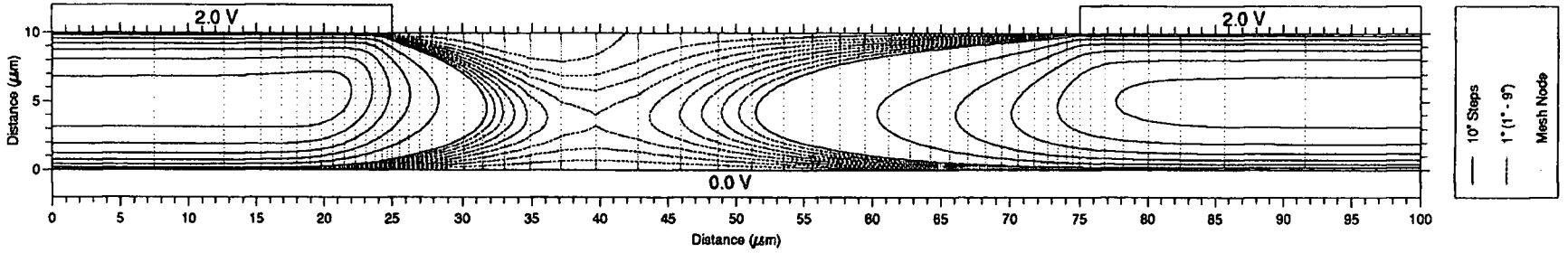

Director Orientation

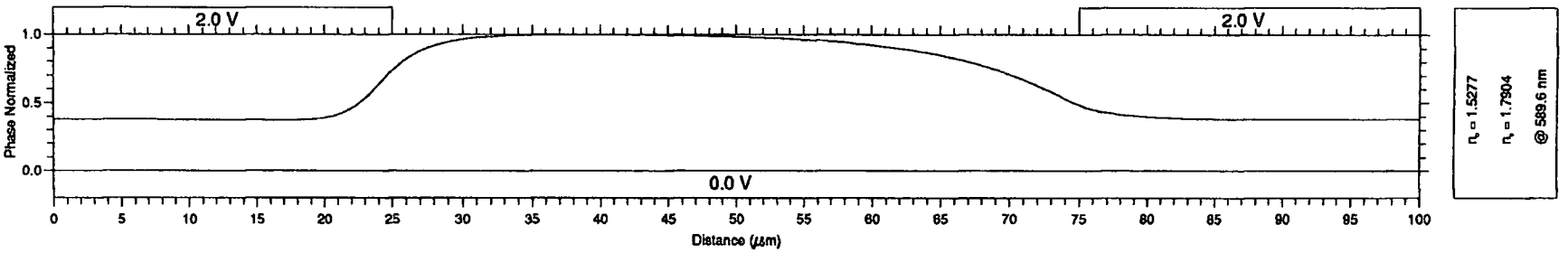

Normalized Phase Response

Liquid Crystal: E44 Symmetry Test: 2

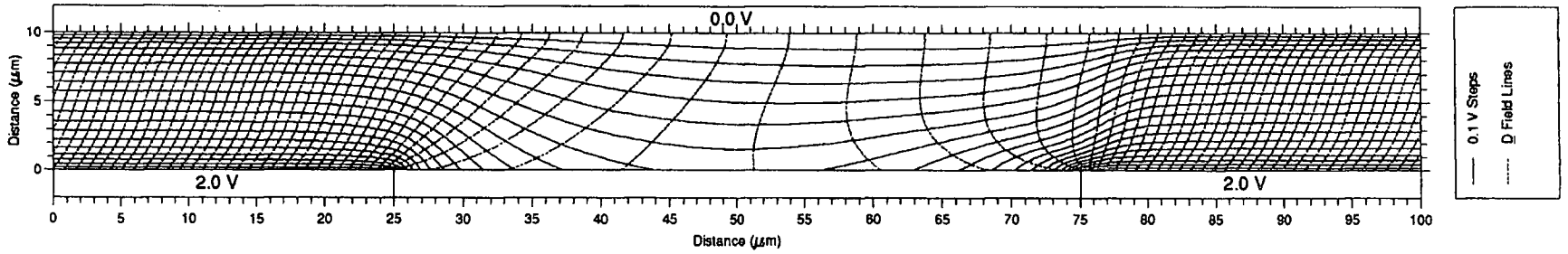

Equipotentials and Displacement Field Lines

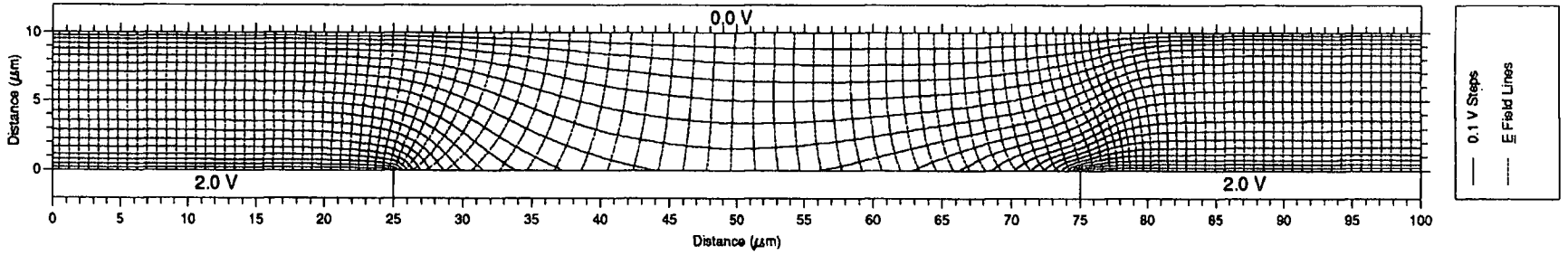

Equipotentials and Electric Field Lines

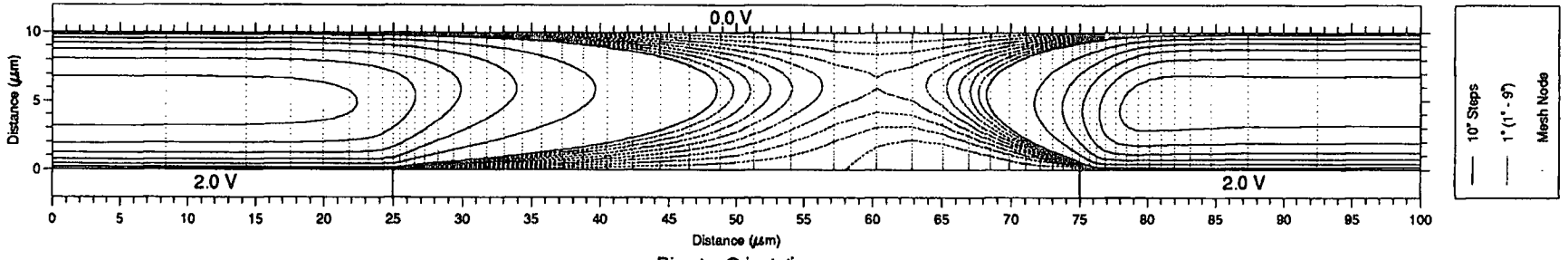

Director Orientation

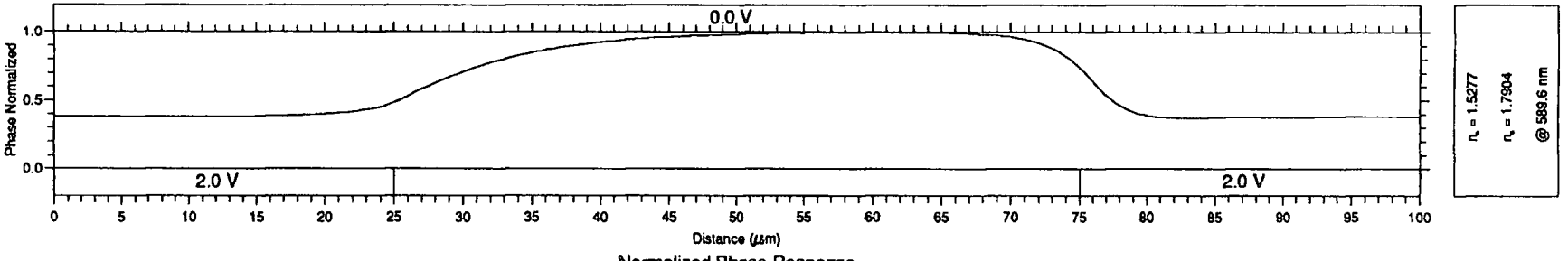

Normalized Phase Response

Liquid Crystal: E44 Symmetry Test: 3

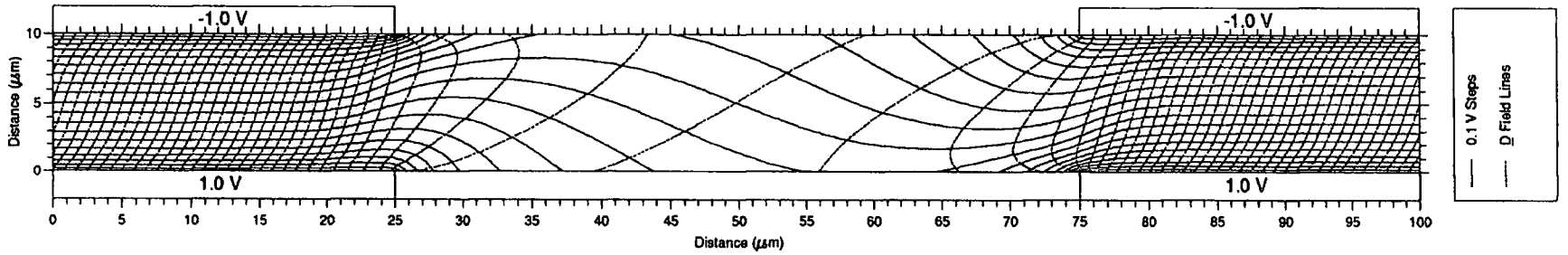

Equipotentials and Displacement Field Lines

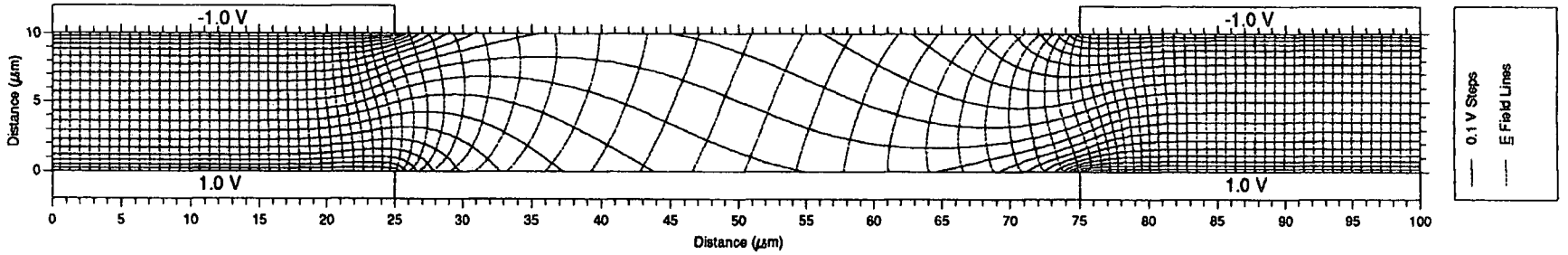

Equipotentials and Electric Field Lines

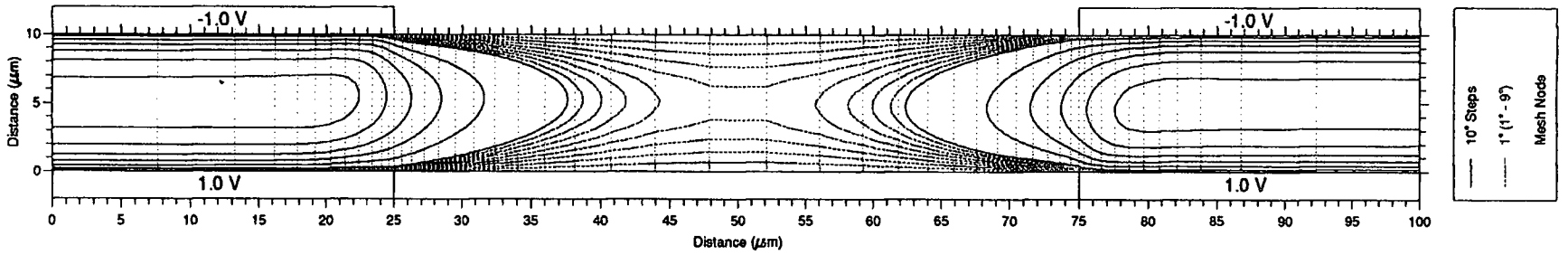

Director Orientation

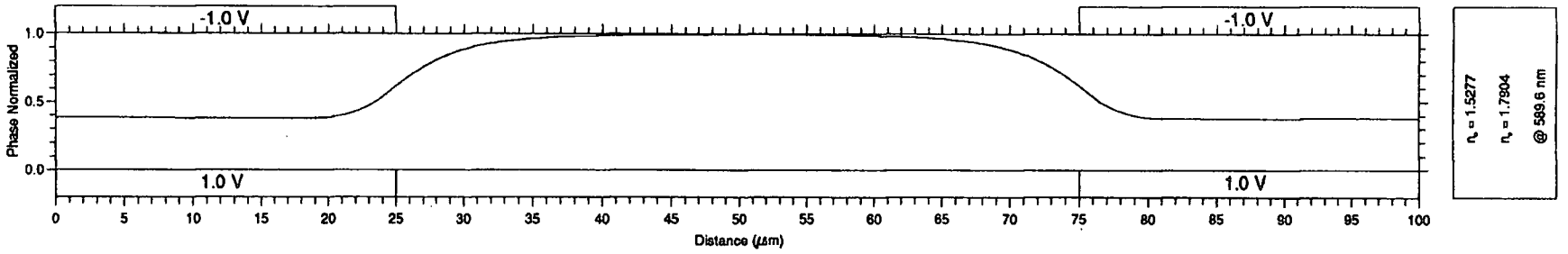

Normalized Phase Response

Liquid Crystal: E44 Symmetry Test: 4

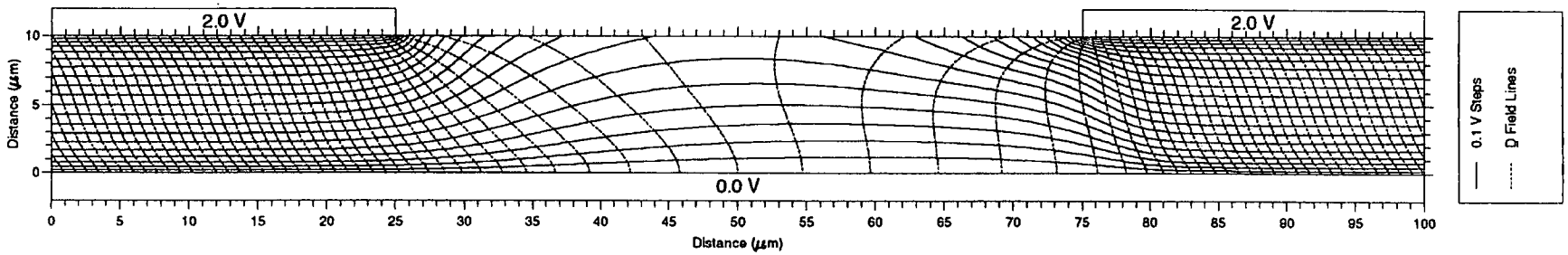

Equipotentials and Displacement Field Lines

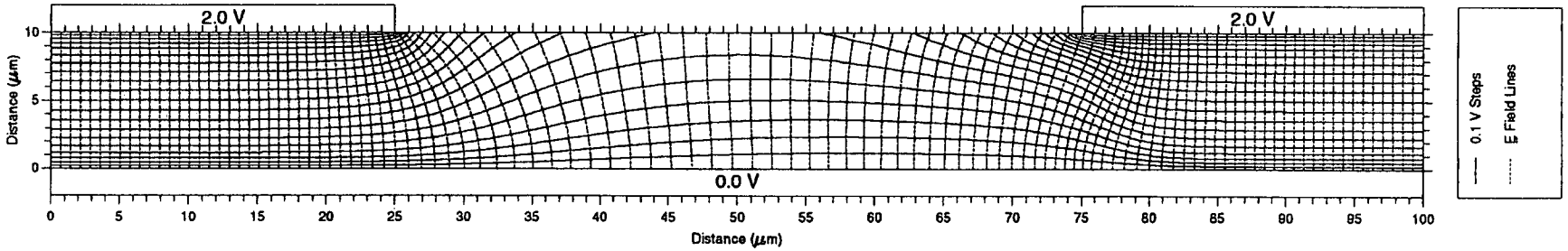

Equipotentials and Electric Field Lines

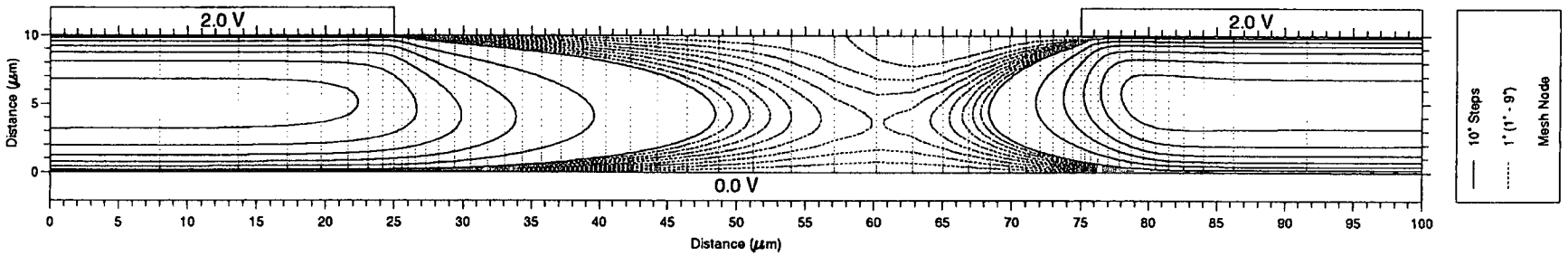

Director Orientation

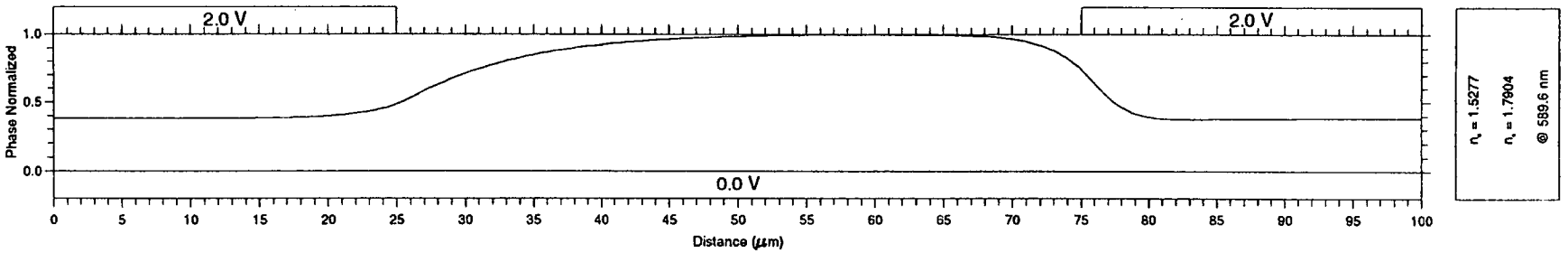

Normalized Phase Response

Appendix G

Result Plots

G.1 Binary Diffractive Structures

G.1.1 Simple Electrode Structure

Normalised Phase Distribution for a Periodic Liquid Crystal E44 Cell

Experiment for the Characterization of Edge Effects

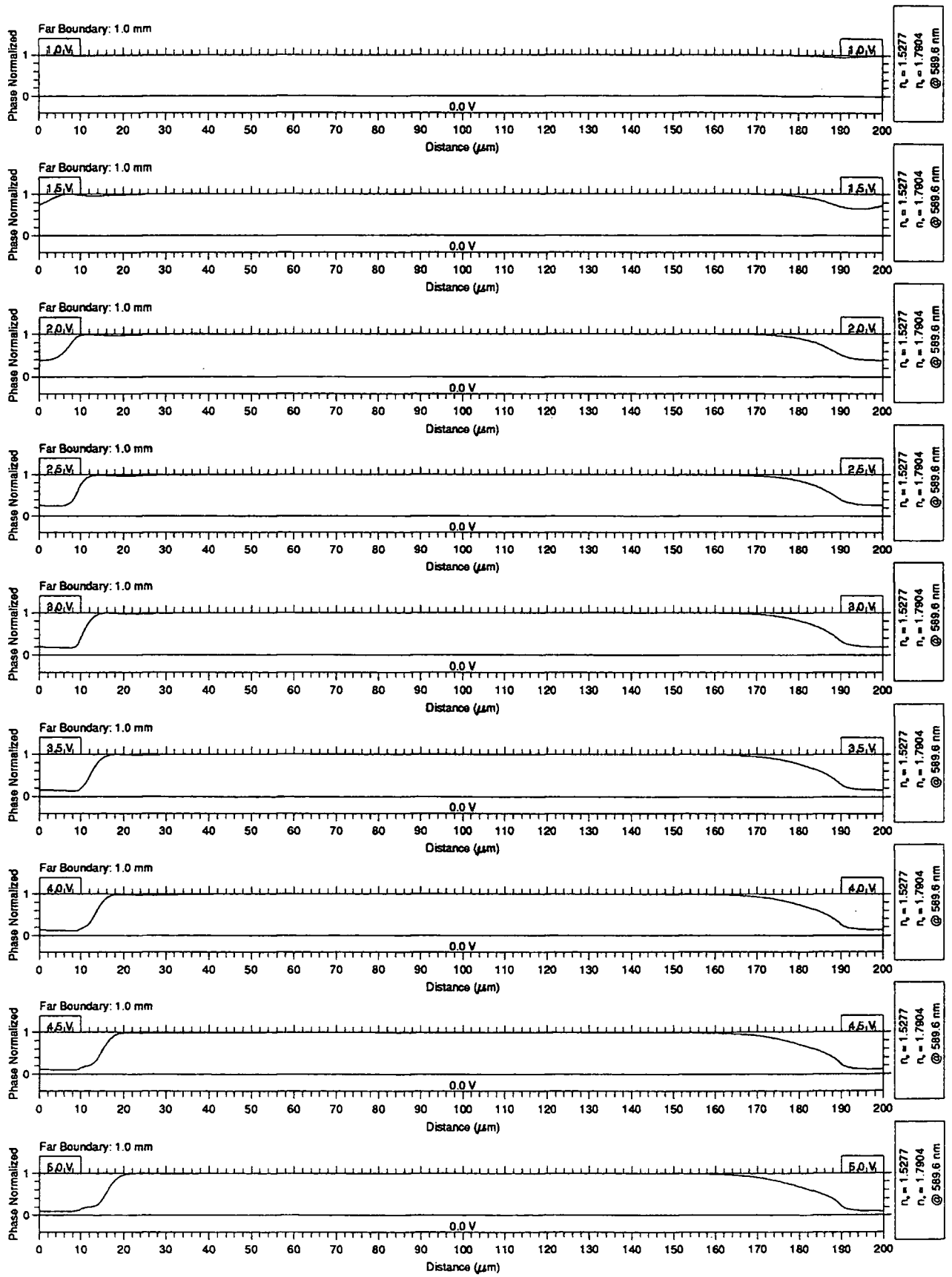

Normalised Phase Distribution for a Periodic Liquid Crystal E44 Cell

Experiment for the Characterization of Edge Effects

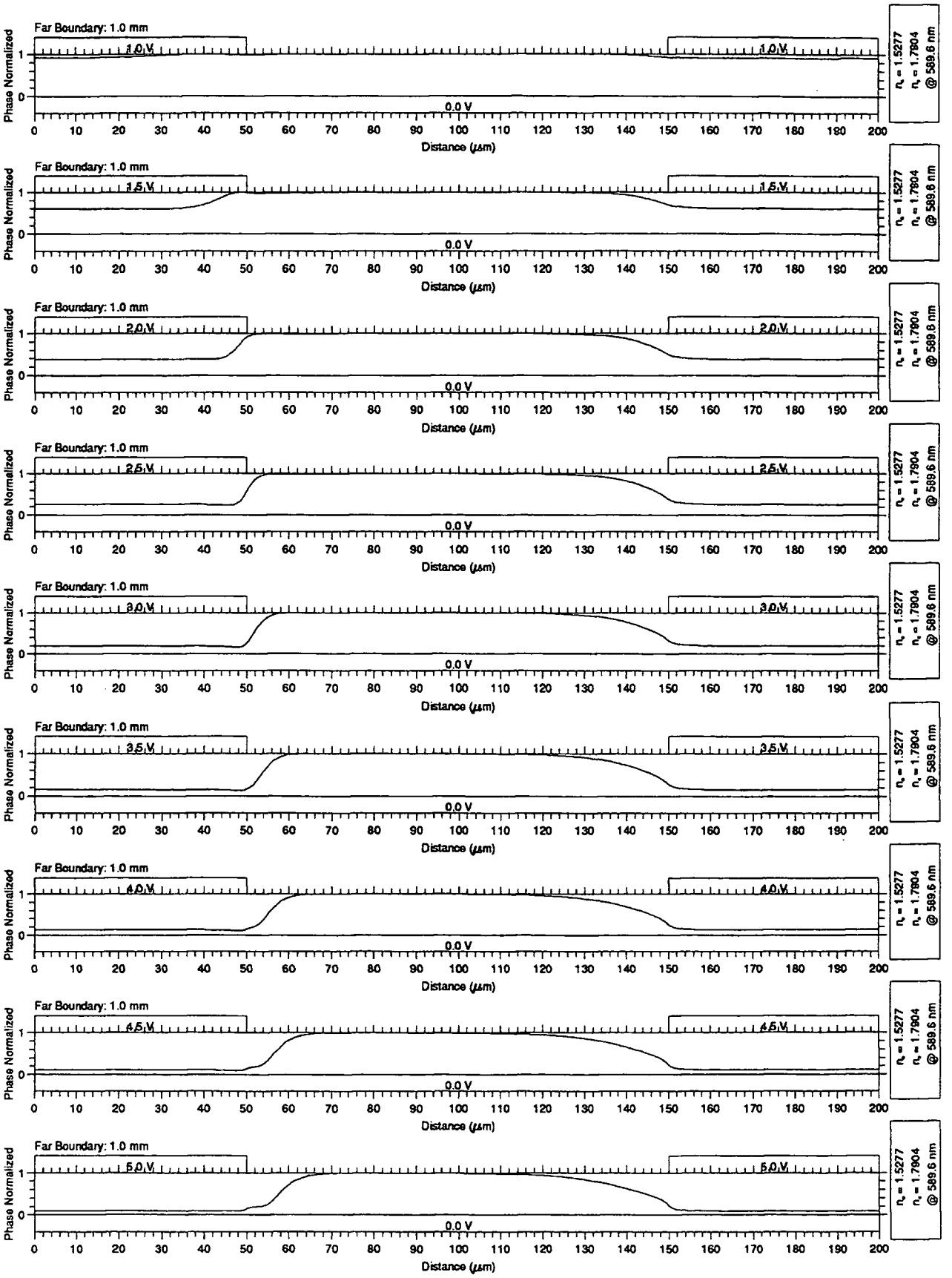

Normalised Phase Distribution for a Periodic Liquid Crystal E44 Cell

Experiment for the Characterization of Edge Effects

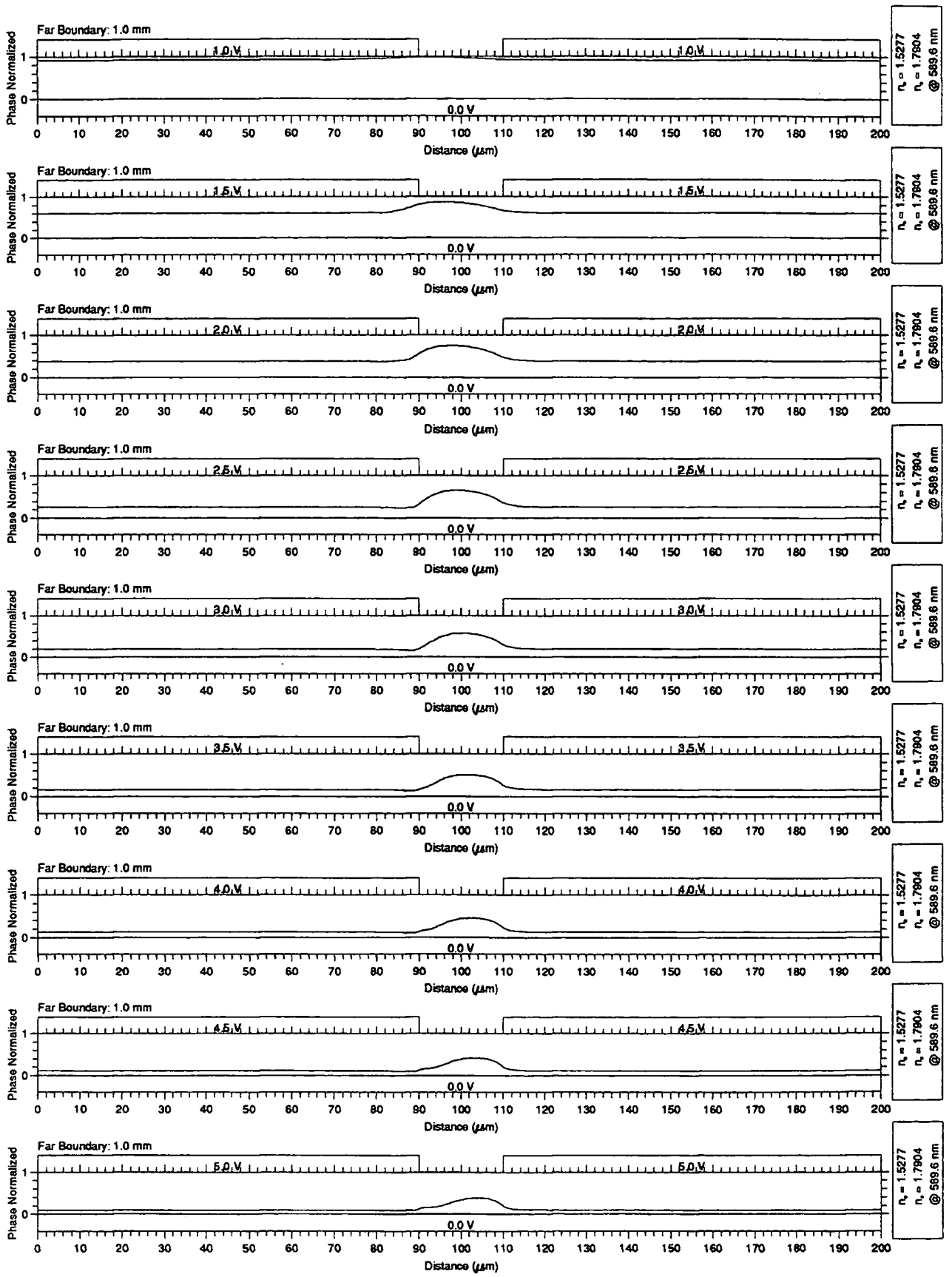

Director Orientation Distribution for a Periodic Liquid Crystal E44 Cell

Experiment for the Characterization of Edge Effects

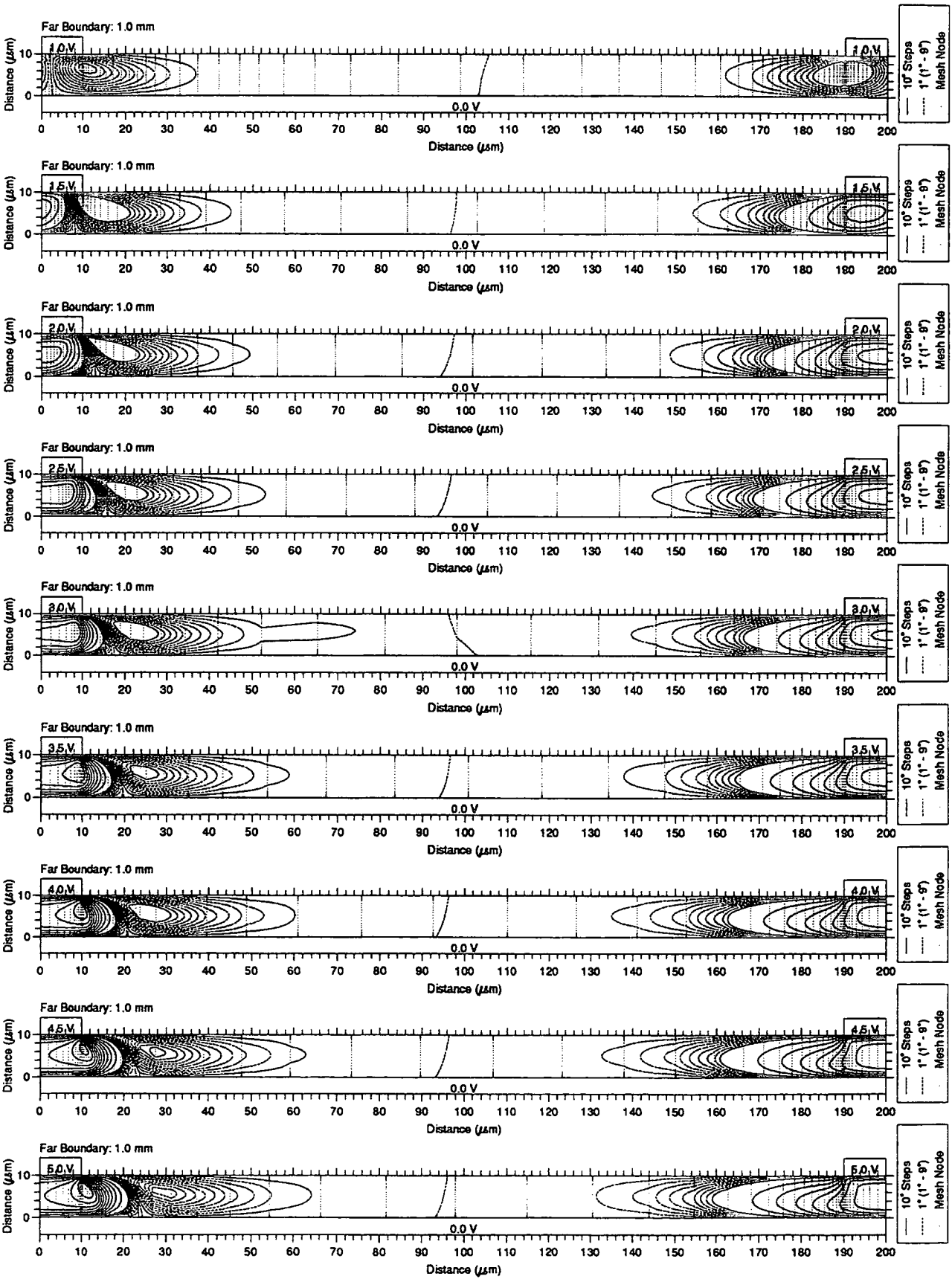

Director Orientation Distribution for a Periodic Liquid Crystal E44 Cell

Experiment for the Characterization of Edge Effects

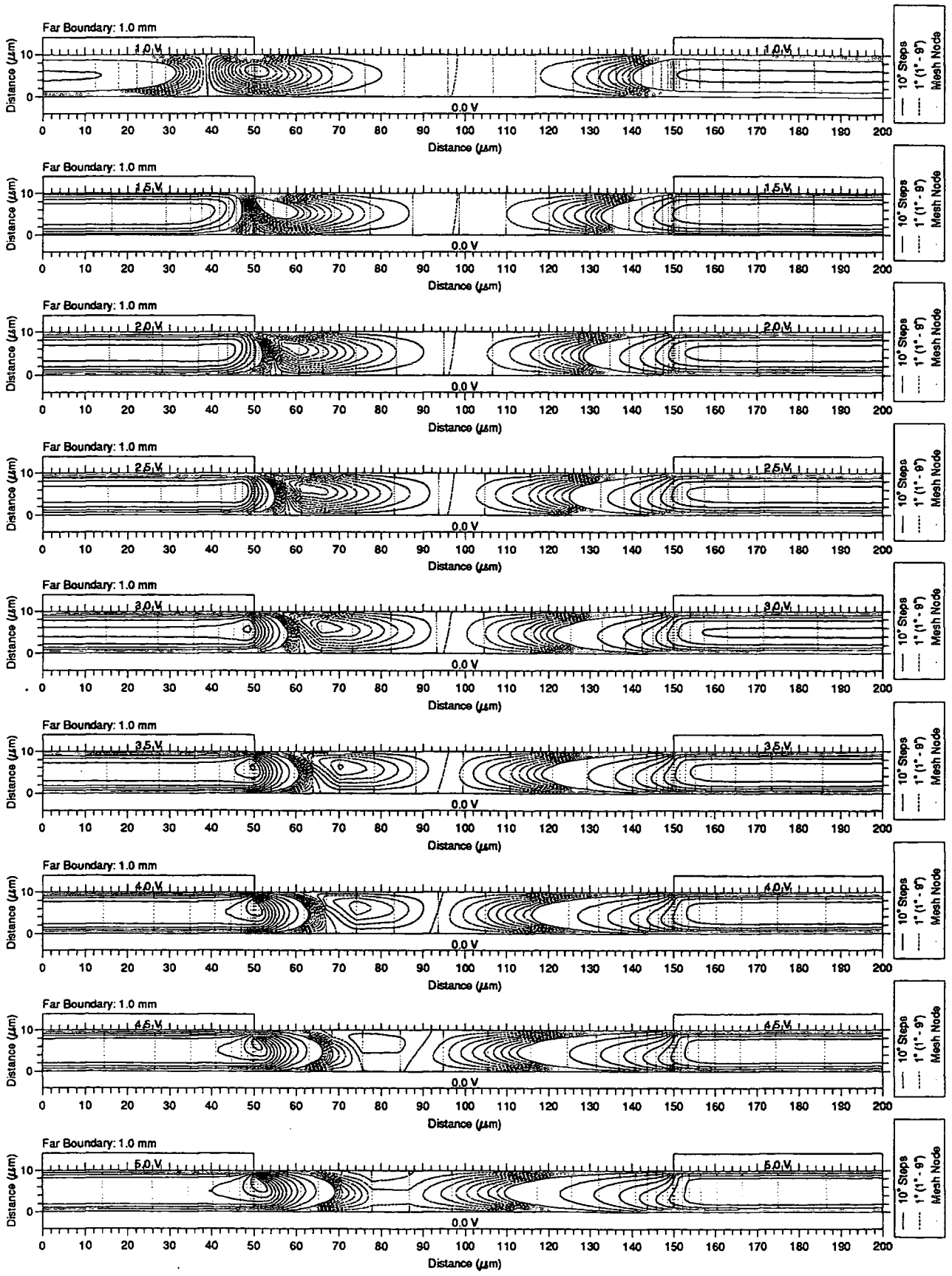

Director Orientation Distribution for a Periodic Liquid Crystal E44 Cell

Experiment for the Characterization of Edge Effects

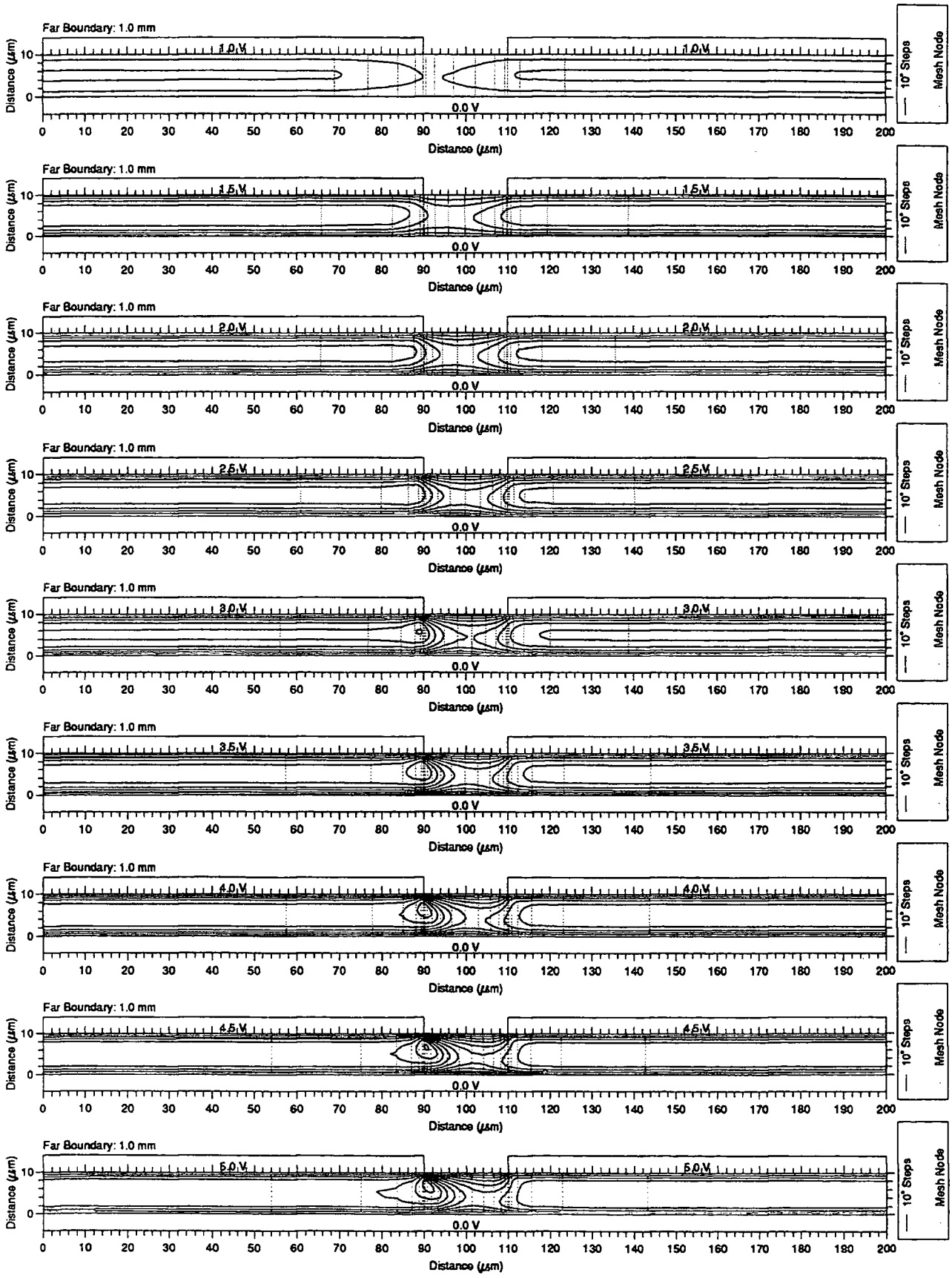

Potential Distribution and Displacement Field for a Periodic Liquid Crystal E44 Cell

Experiment for the Characterization of Edge Effects

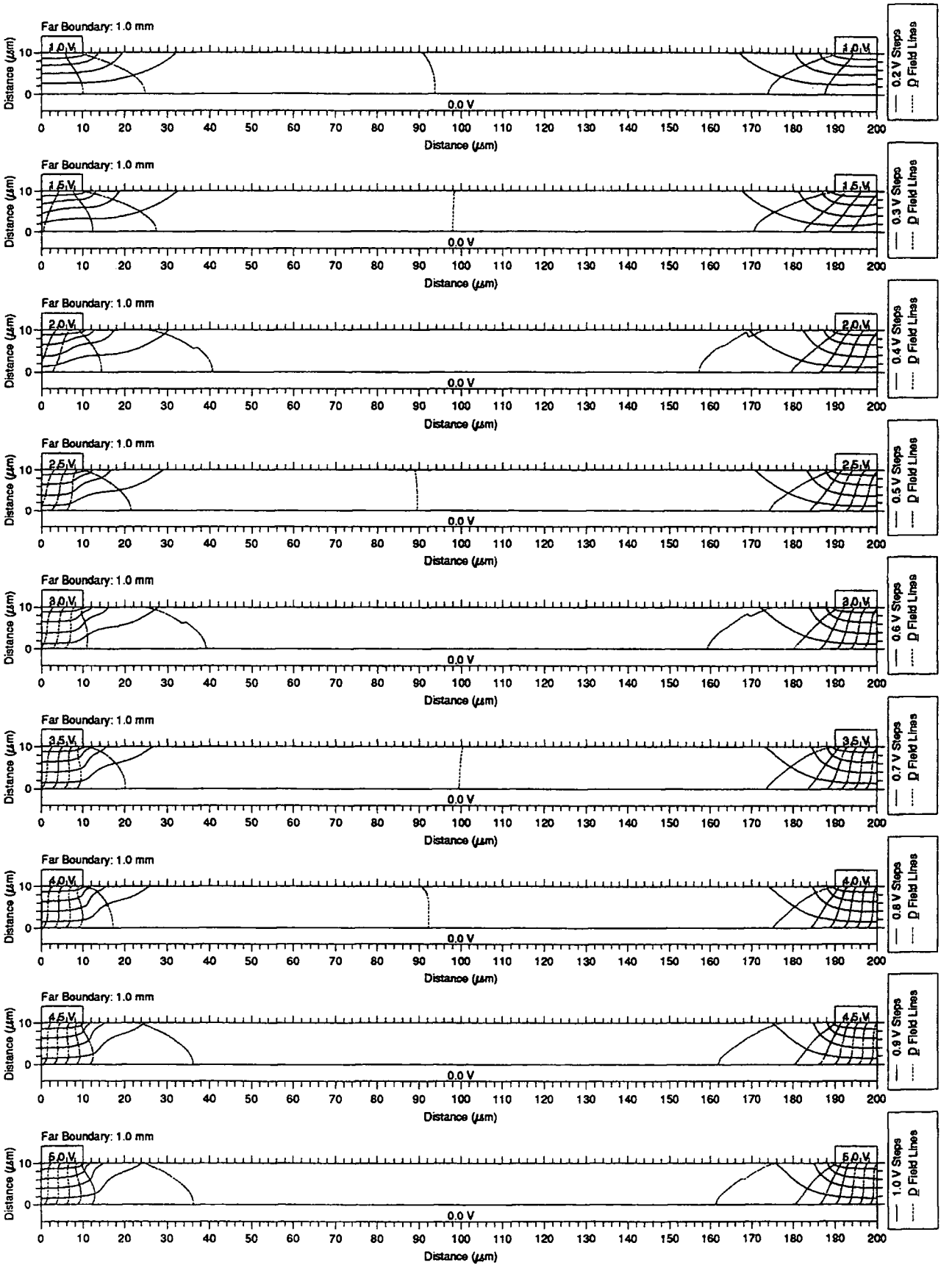

Potential Distribution and Displacement Field for a Periodic Liquid Crystal E44 Cell

Experiment for the Characterization of Edge Effects

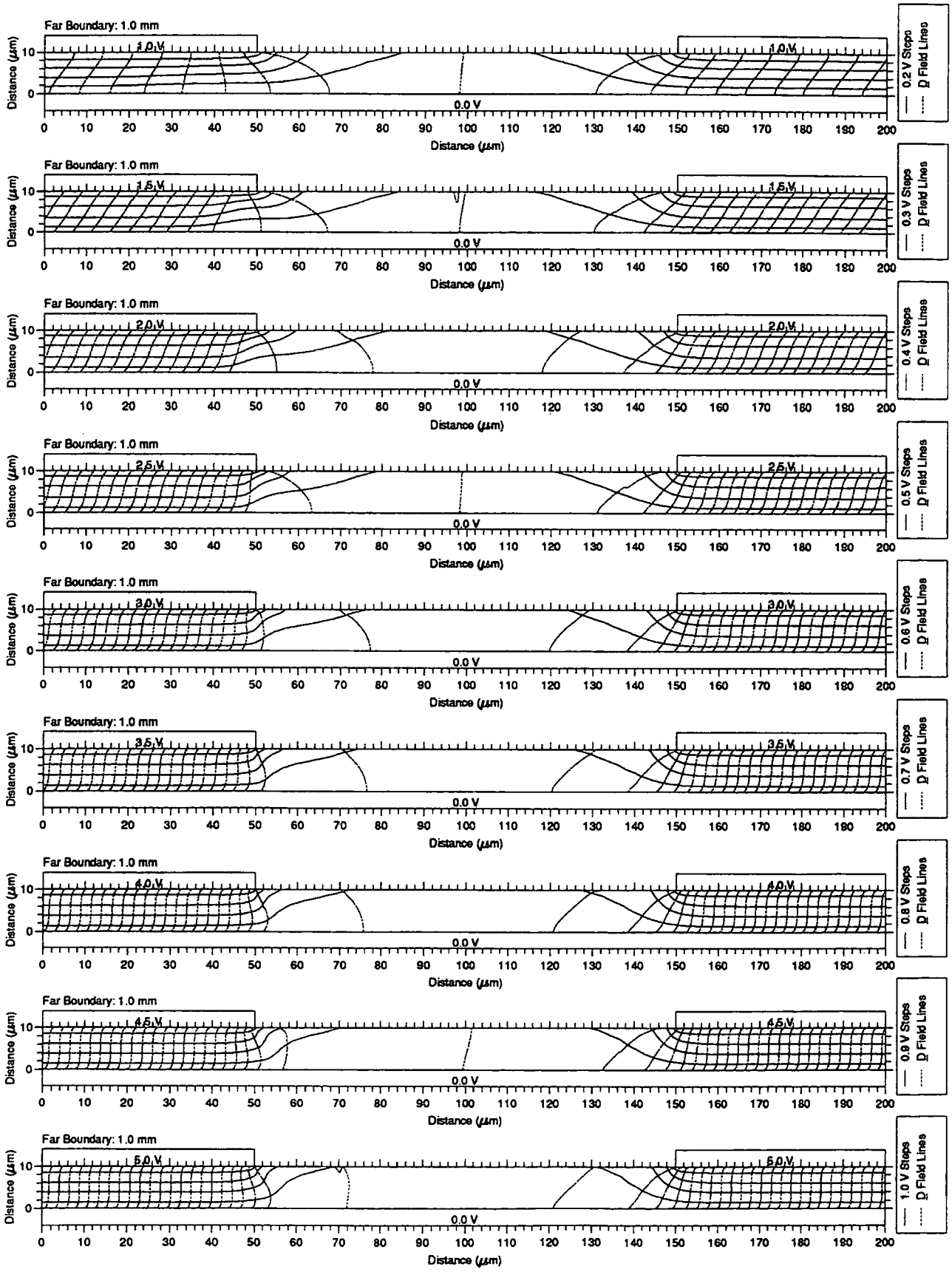

Potential Distribution and Displacement Field for a Periodic Liquid Crystal E44 Cell

Experiment for the Characterization of Edge Effects

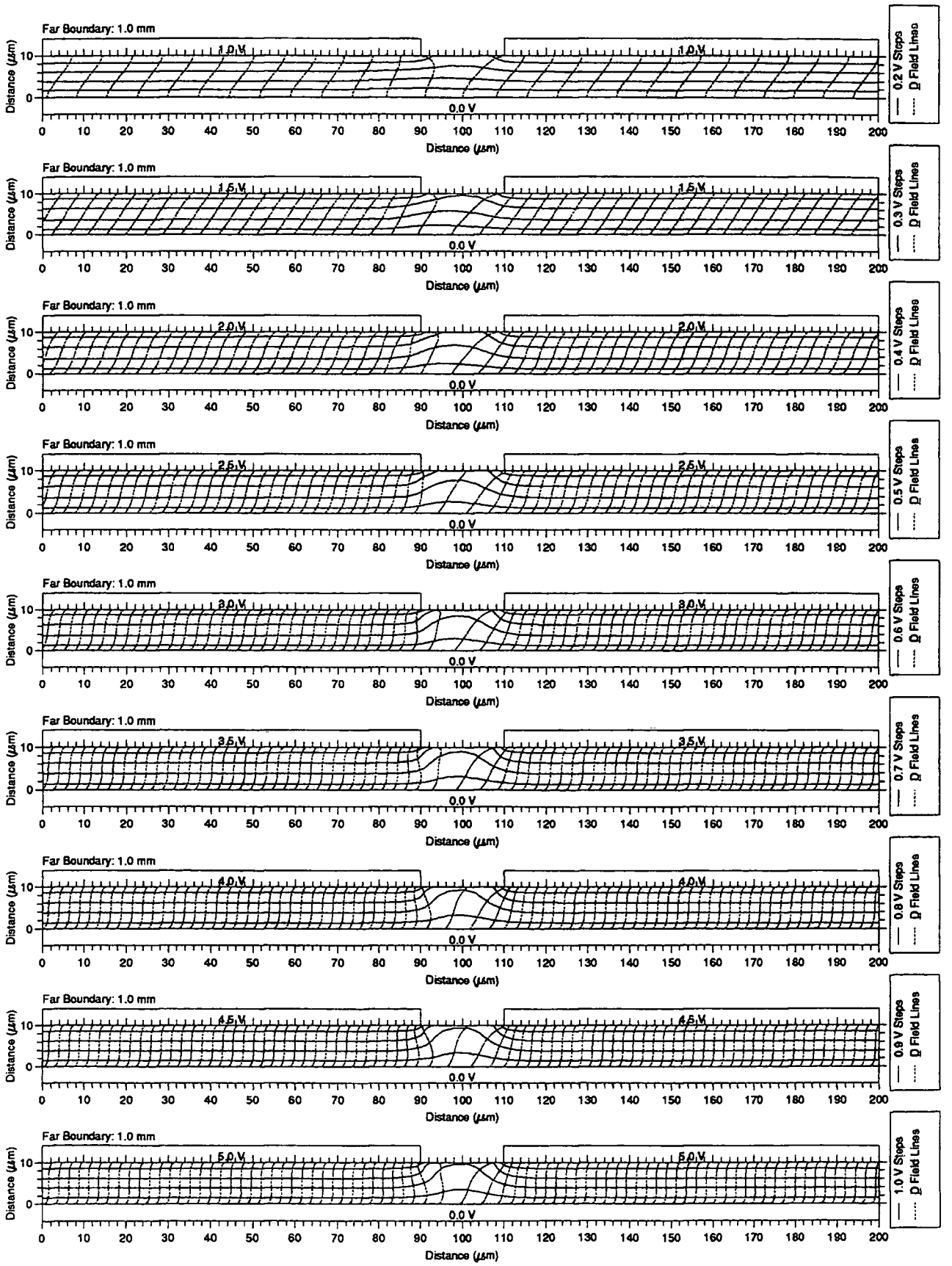

G.1.2 Etched Earth Plate

Normalised Phase Distribution for a Periodic Liquid Crystal E44 Cell

Experiment for the Characterization of Edge Effects

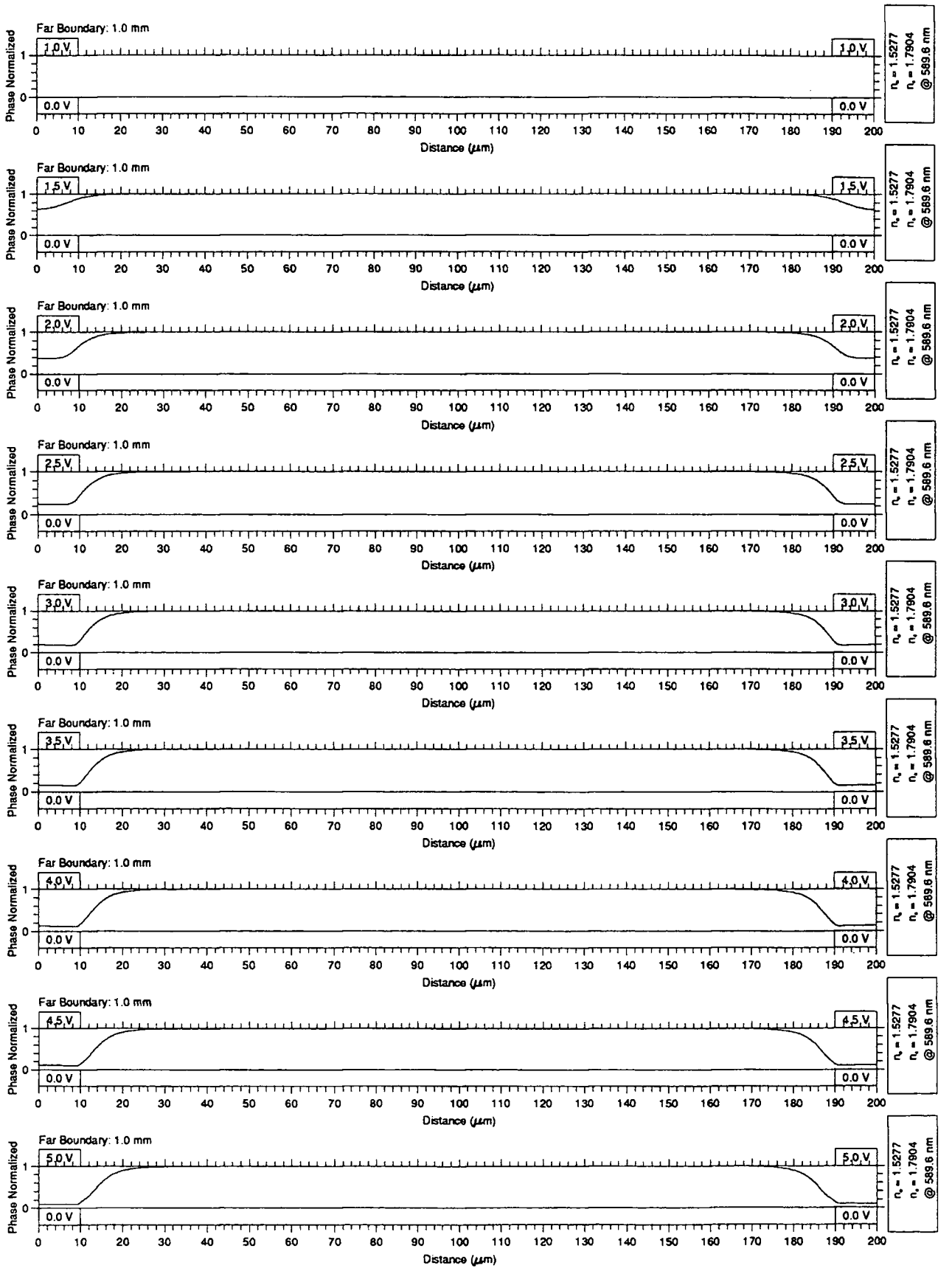

Normalised Phase Distribution for a Periodic Liquid Crystal E44 Cell

Experiment for the Characterization of Edge Effects

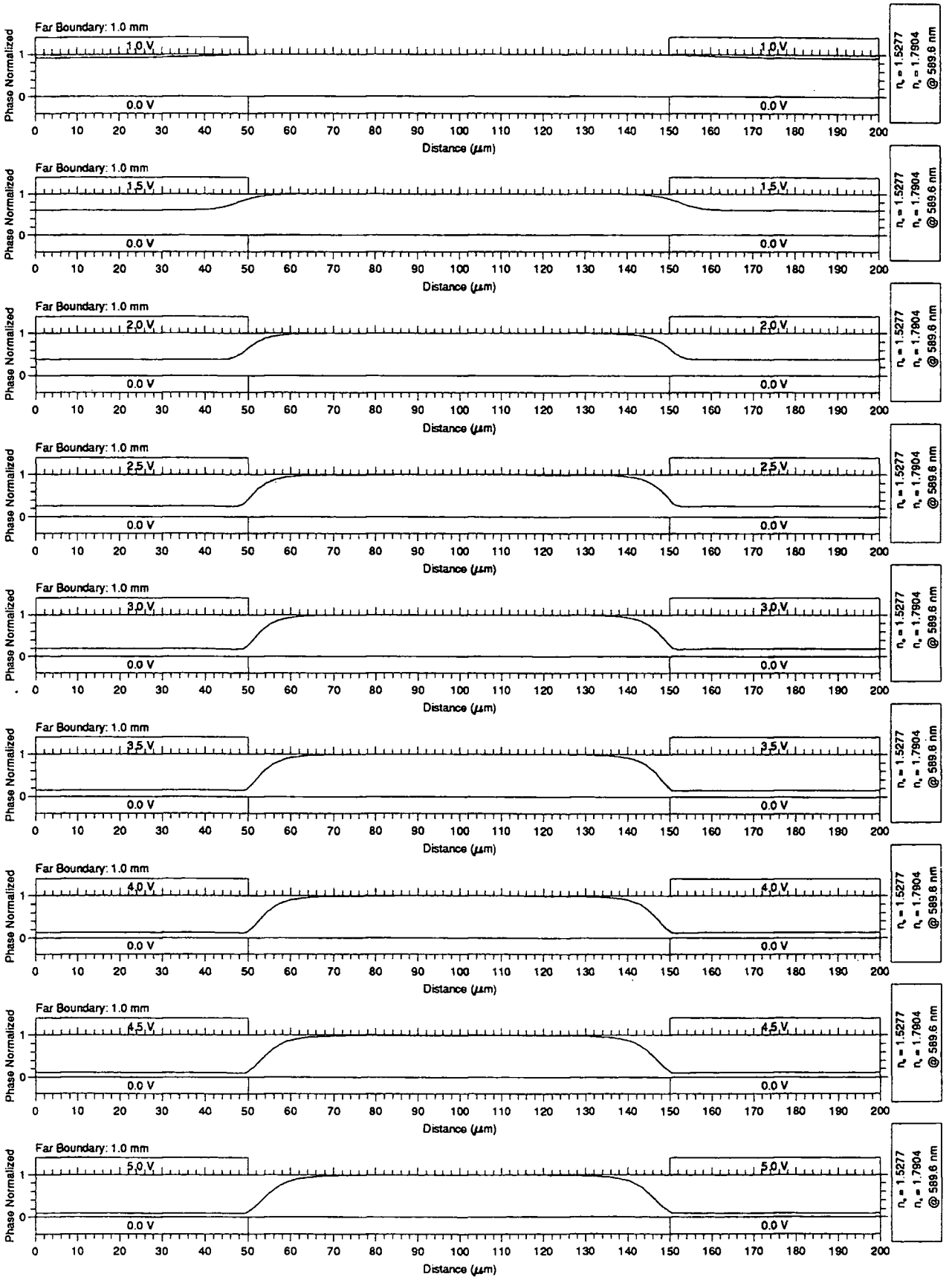

Normalised Phase Distribution for a Periodic Liquid Crystal E44 Cell

Experiment for the Characterization of Edge Effects

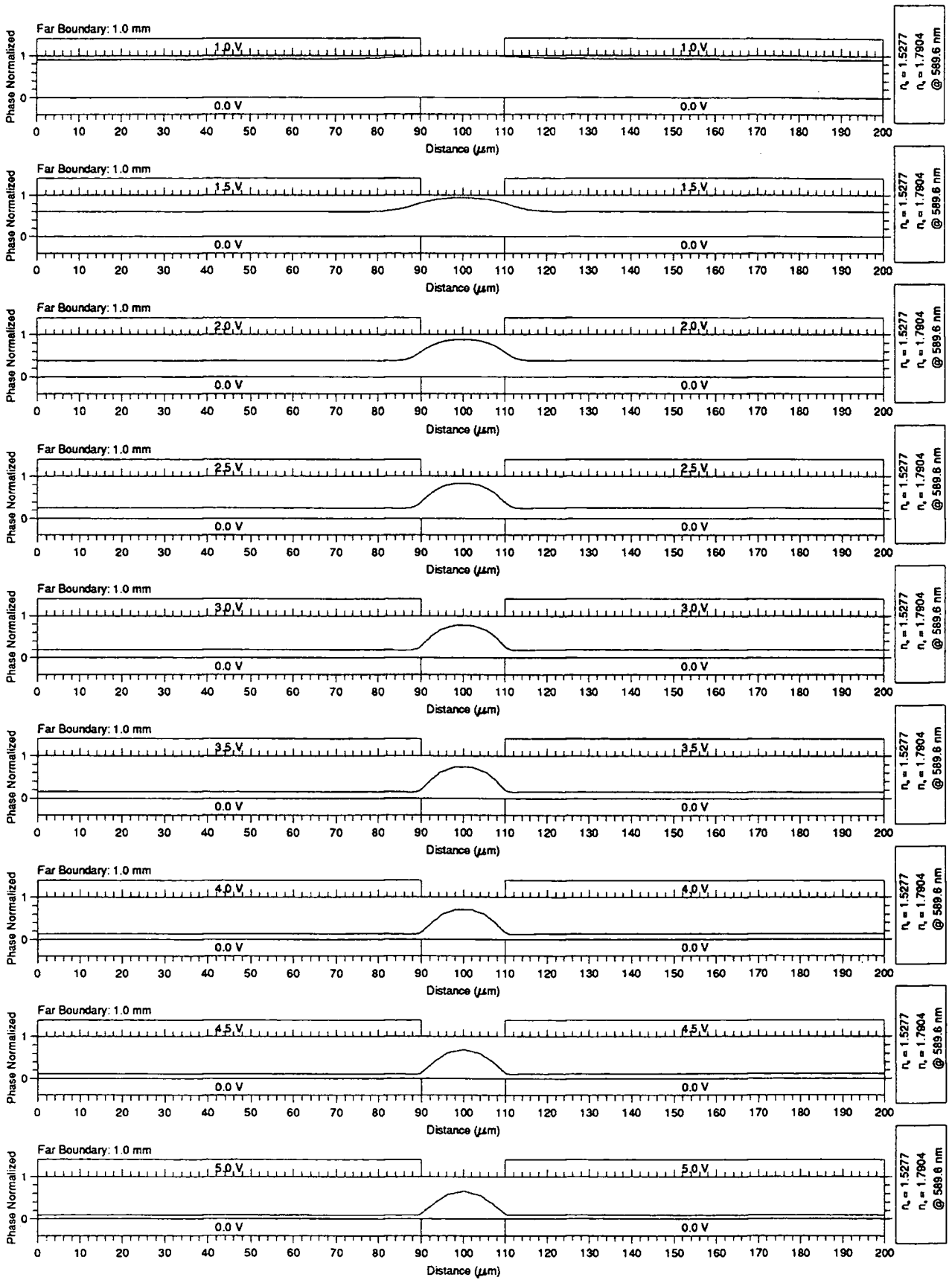

Director Orientation Distribution for a Periodic Liquid Crystal E44 Cell

Experiment for the Characterization of Edge Effects

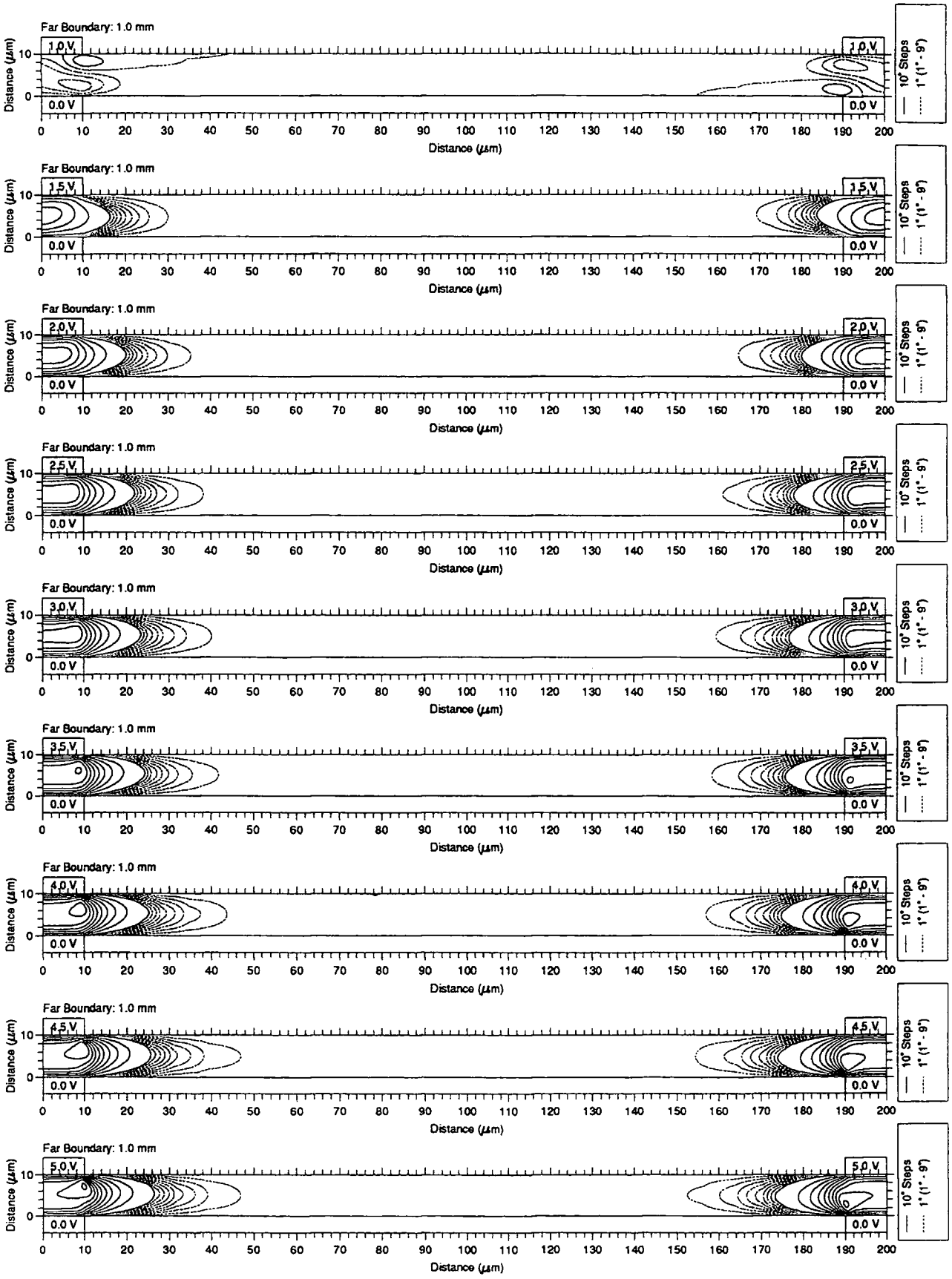

Director Orientation Distribution for a Periodic Liquid Crystal E44 Cell

Experiment for the Characterization of Edge Effects

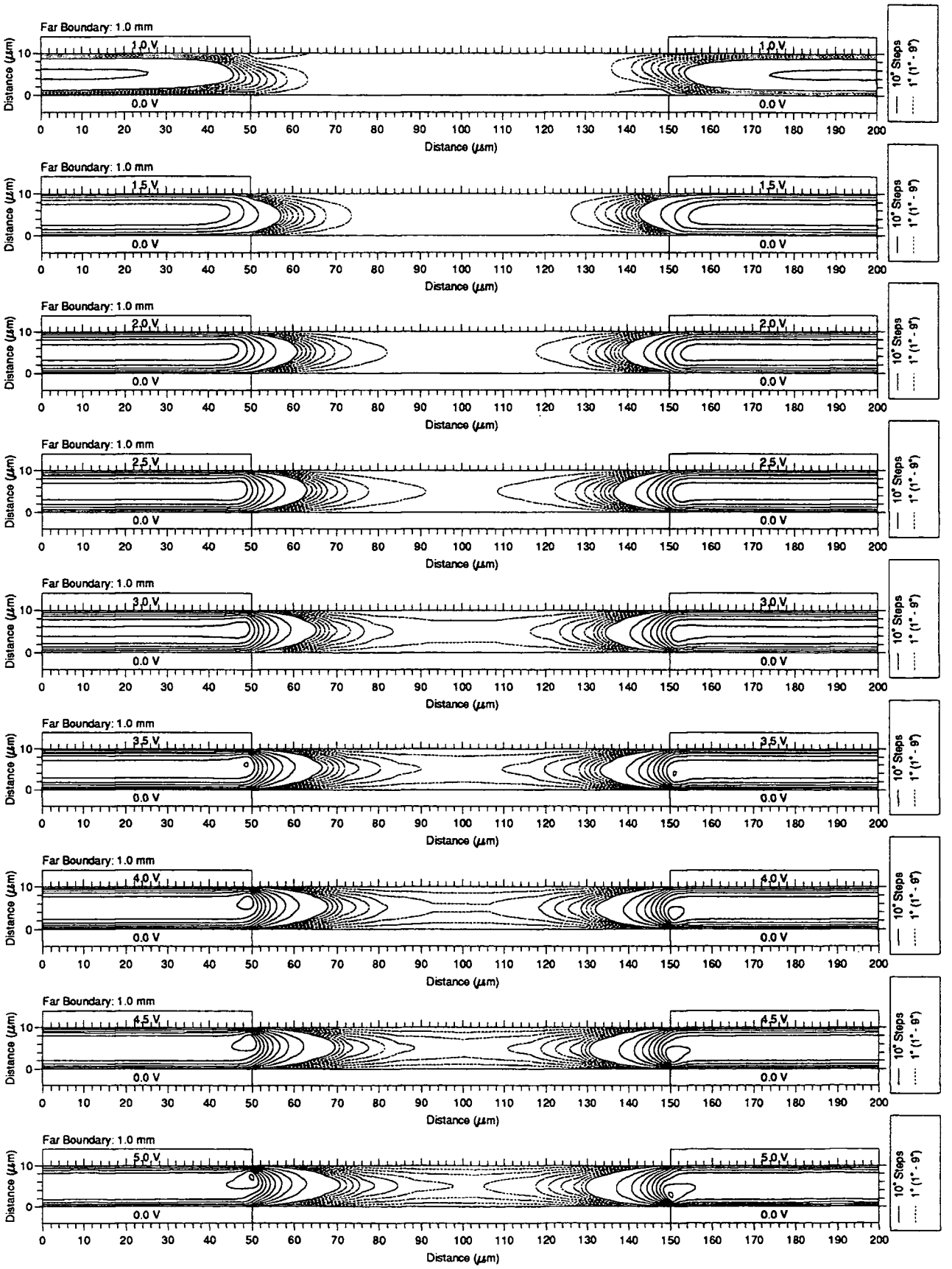

Director Orientation Distribution for a Periodic Liquid Crystal E44 Cell

Experiment for the Characterization of Edge Effects

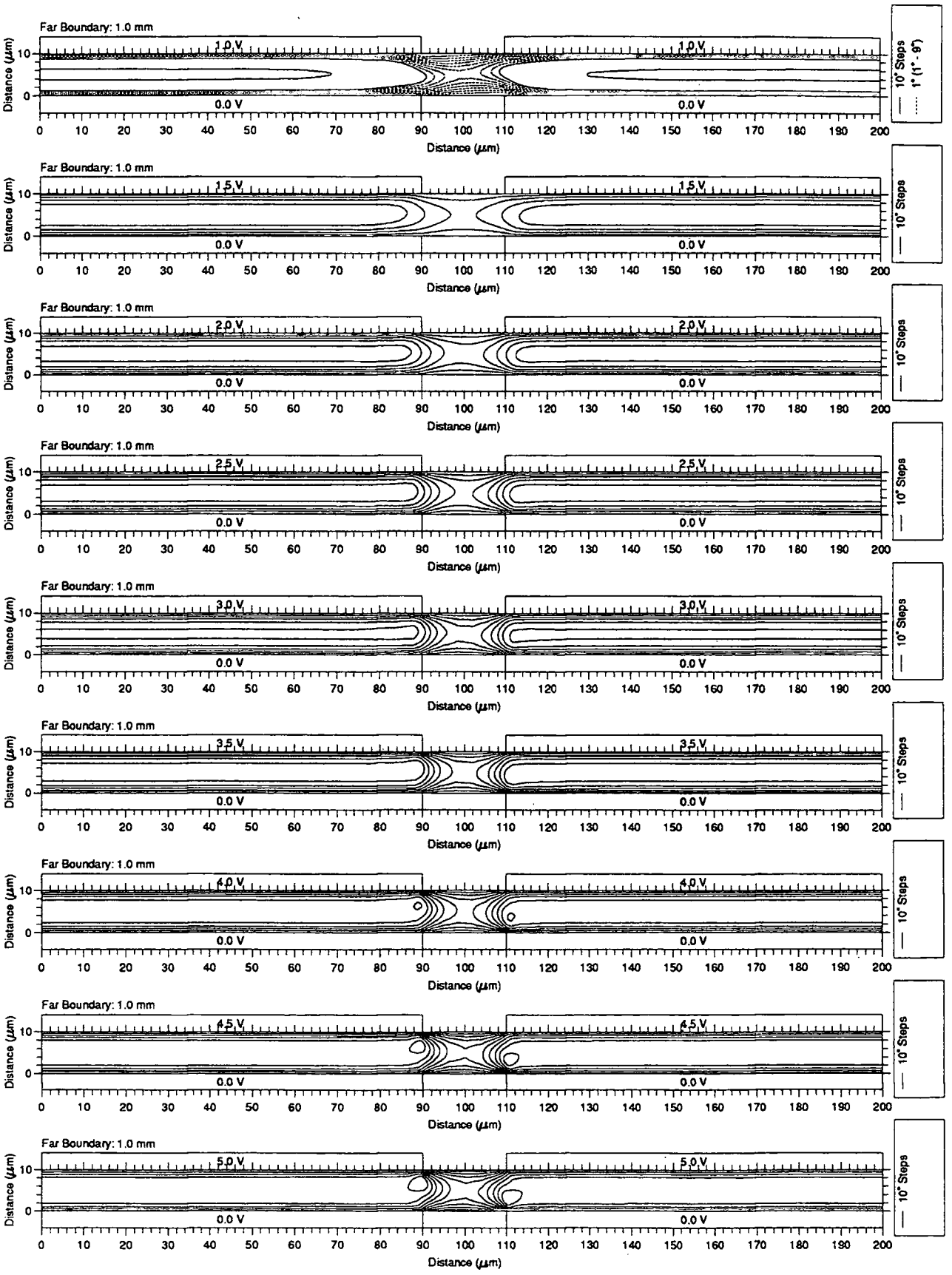

Potential Distribution and Displacement Field for a Periodic Liquid Crystal E44 Cell

Experiment for the Characterization of Edge Effects

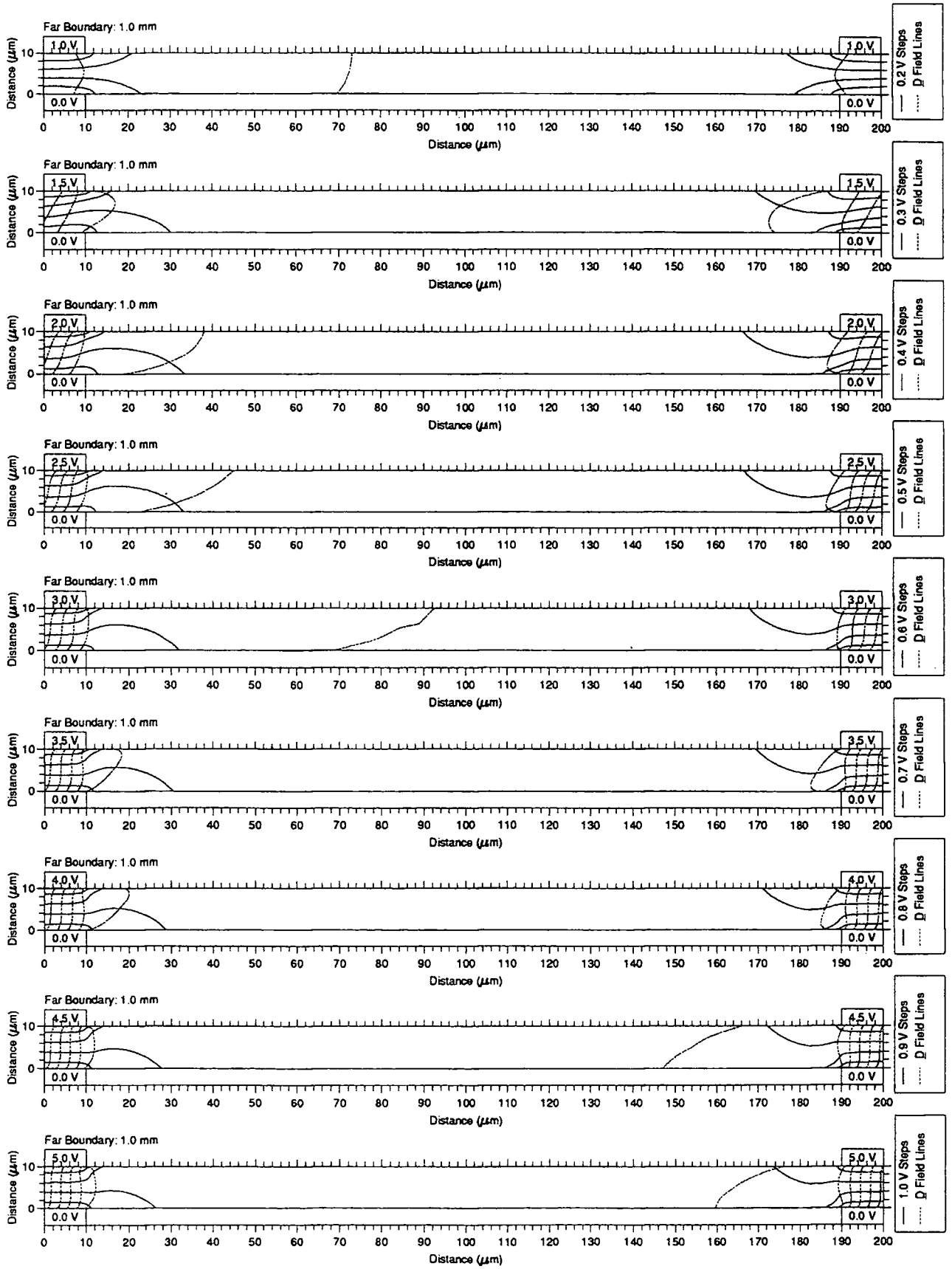

Potential Distribution and Displacement Field for a Periodic Liquid Crystal E44 Cell

Experiment for the Characterization of Edge Effects

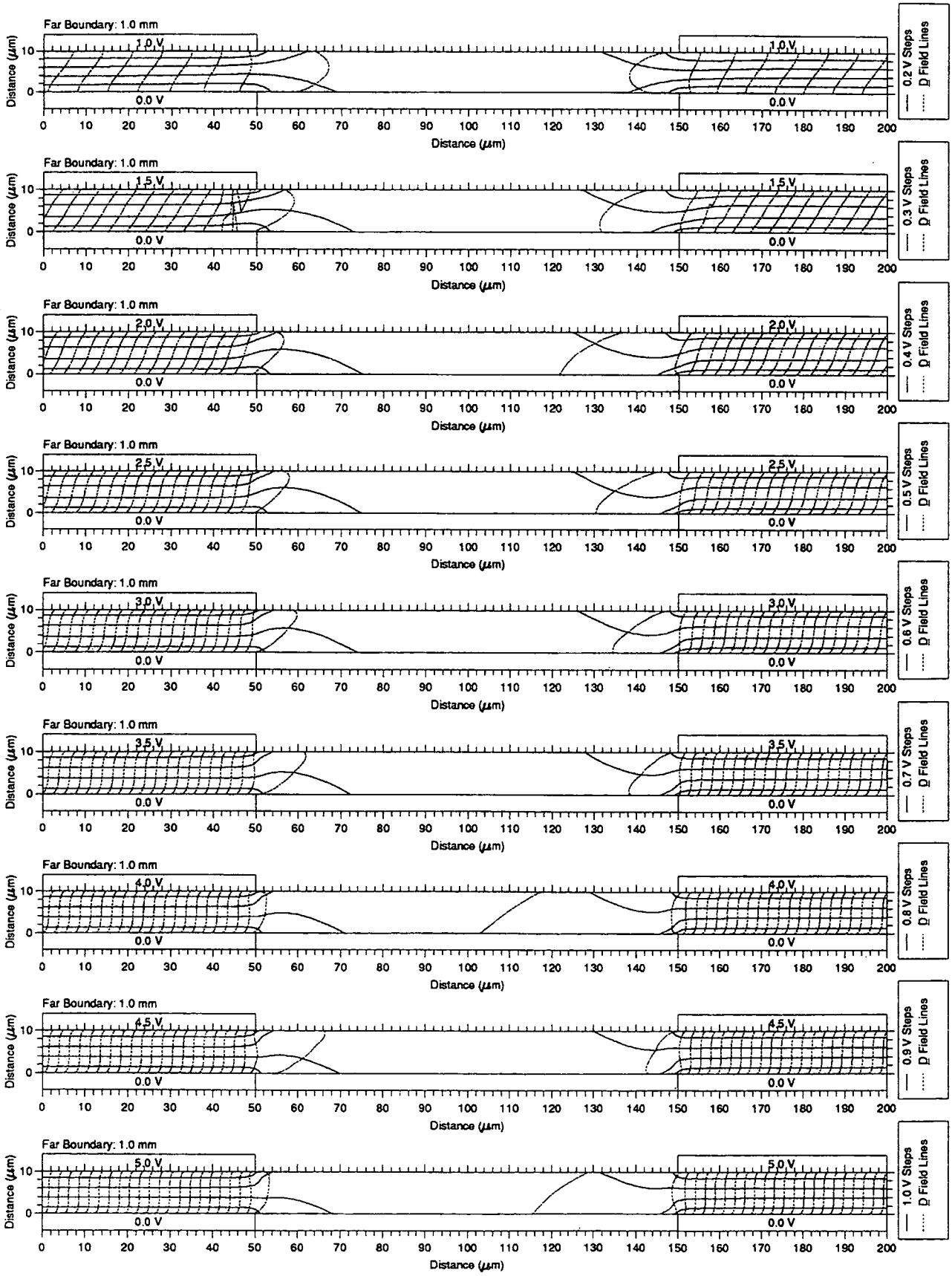

Potential Distribution and Displacement Field for a Periodic Liquid Crystal E44 Cell

Experiment for the Characterization of Edge Effects

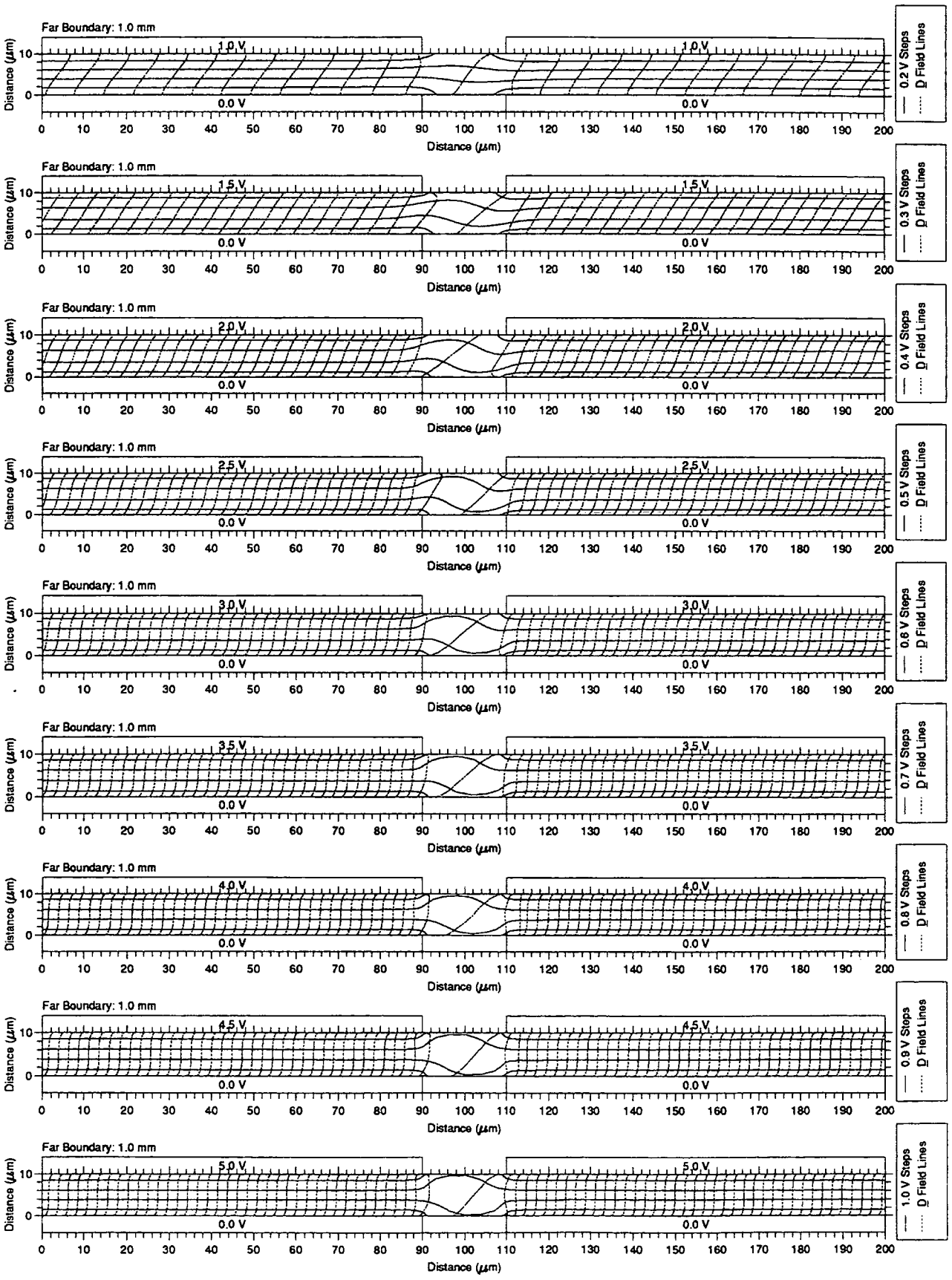

G.1.3 Guard Plate

Normalised Phase Distribution for a Periodic Liquid Crystal E44 Cell

Experiment with Guard Plate

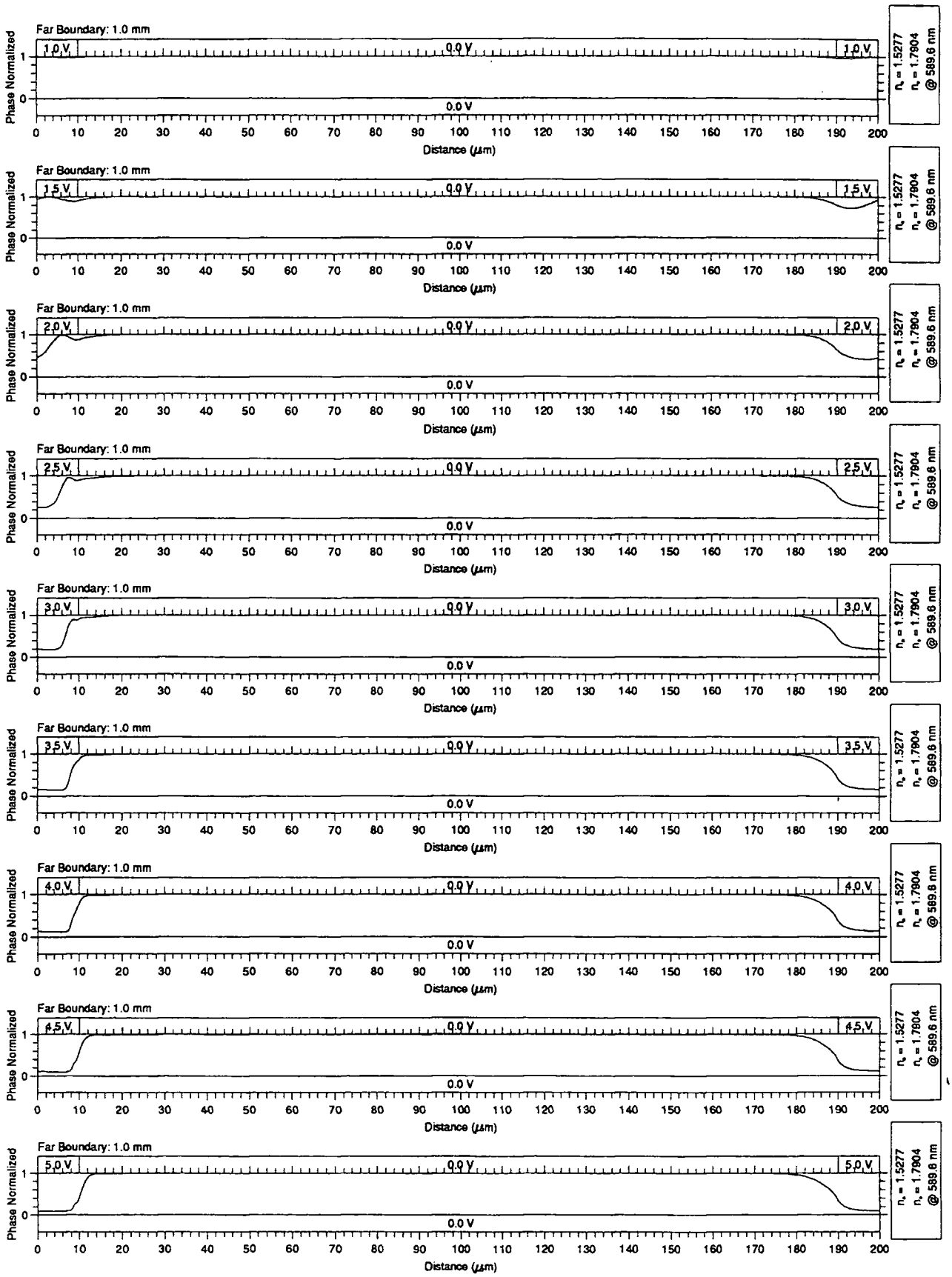

Normalised Phase Distribution for a Periodic Liquid Crystal E44 Cell

Experiment with Guard Plate

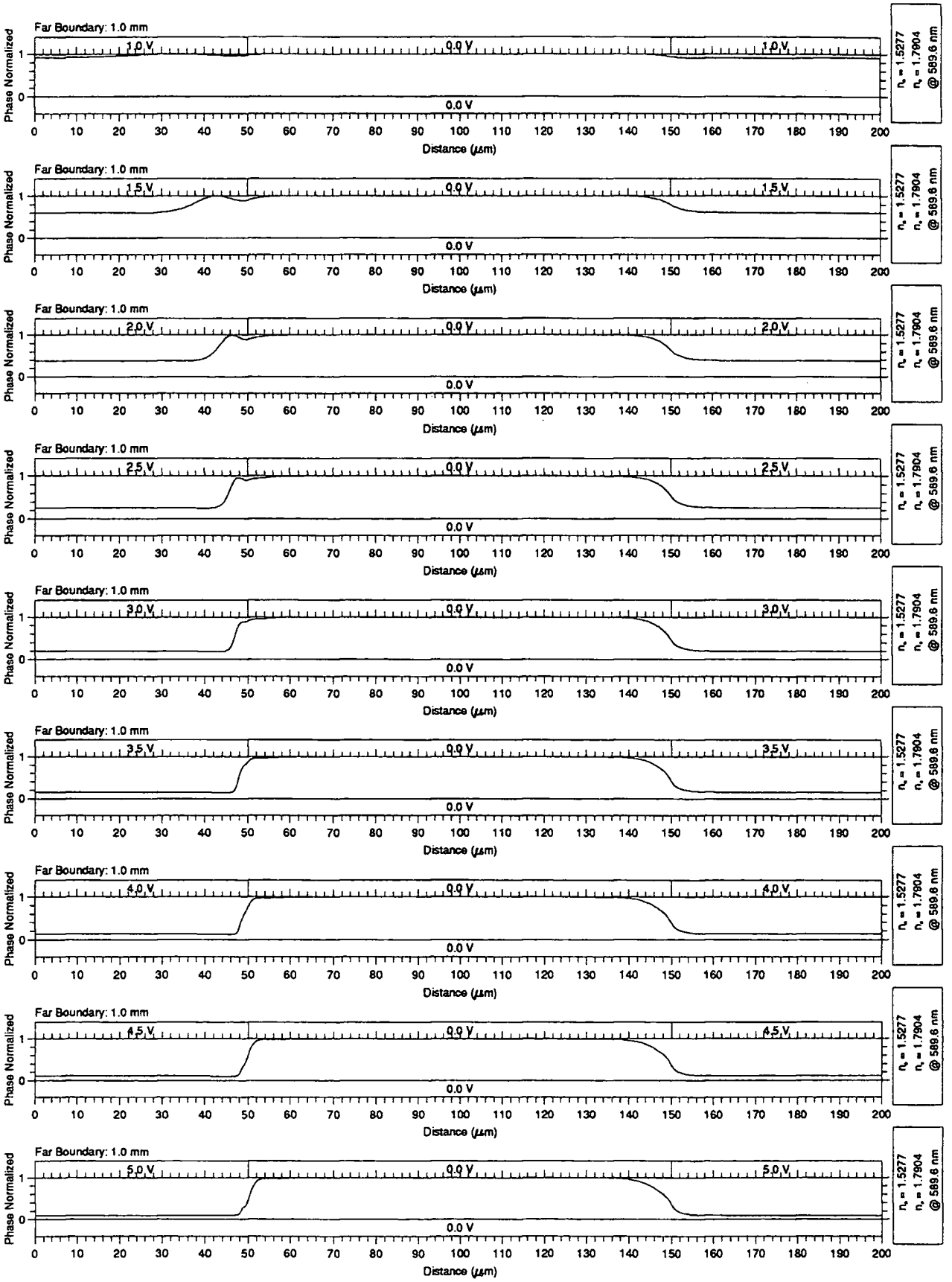

Normalised Phase Distribution for a Periodic Liquid Crystal E44 Cell

Experiment with Guard Plate

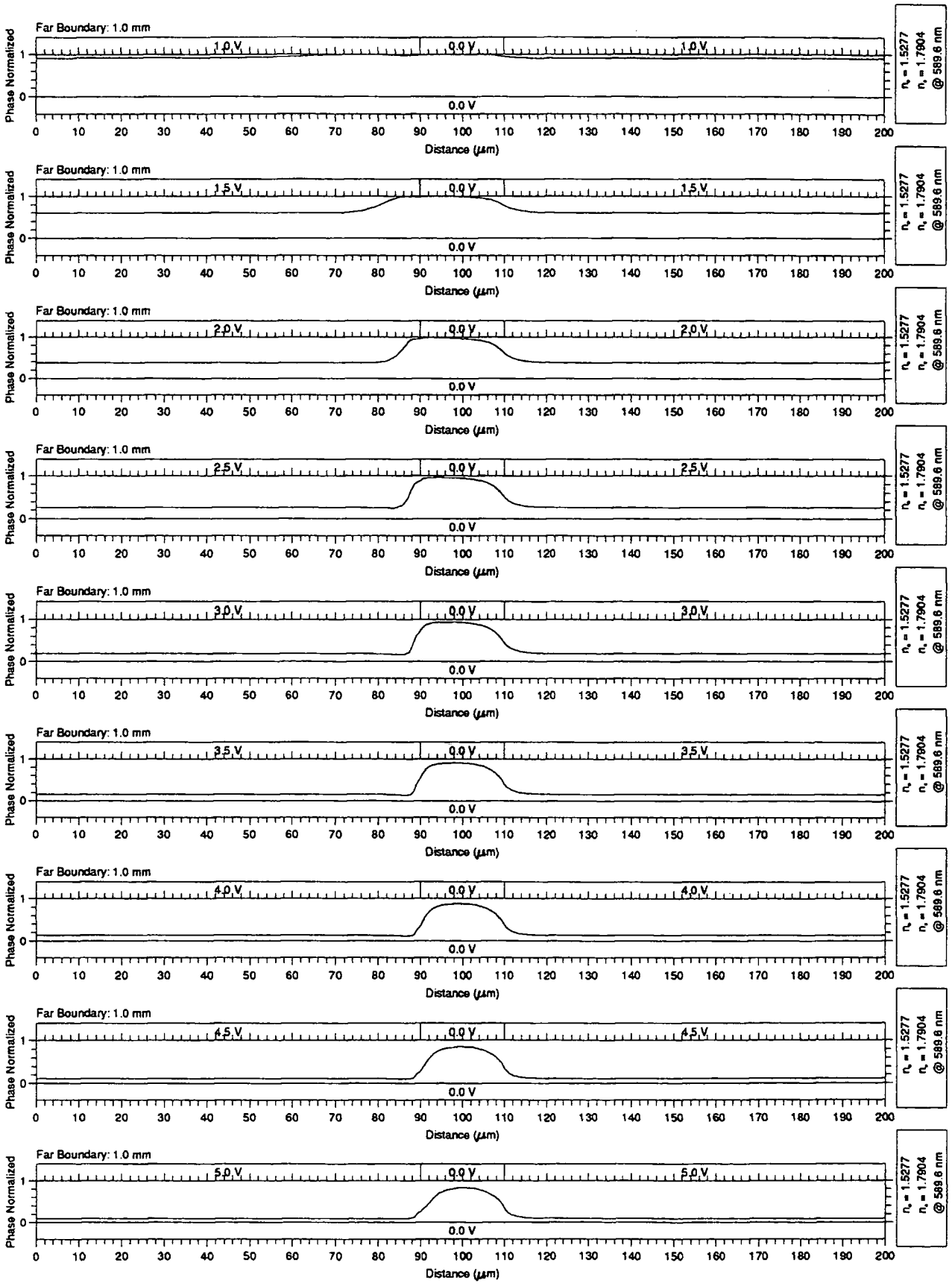

Director Orientation Distribution for a Periodic Liquid Crystal E44 Cell

Experiment with Guard Plate

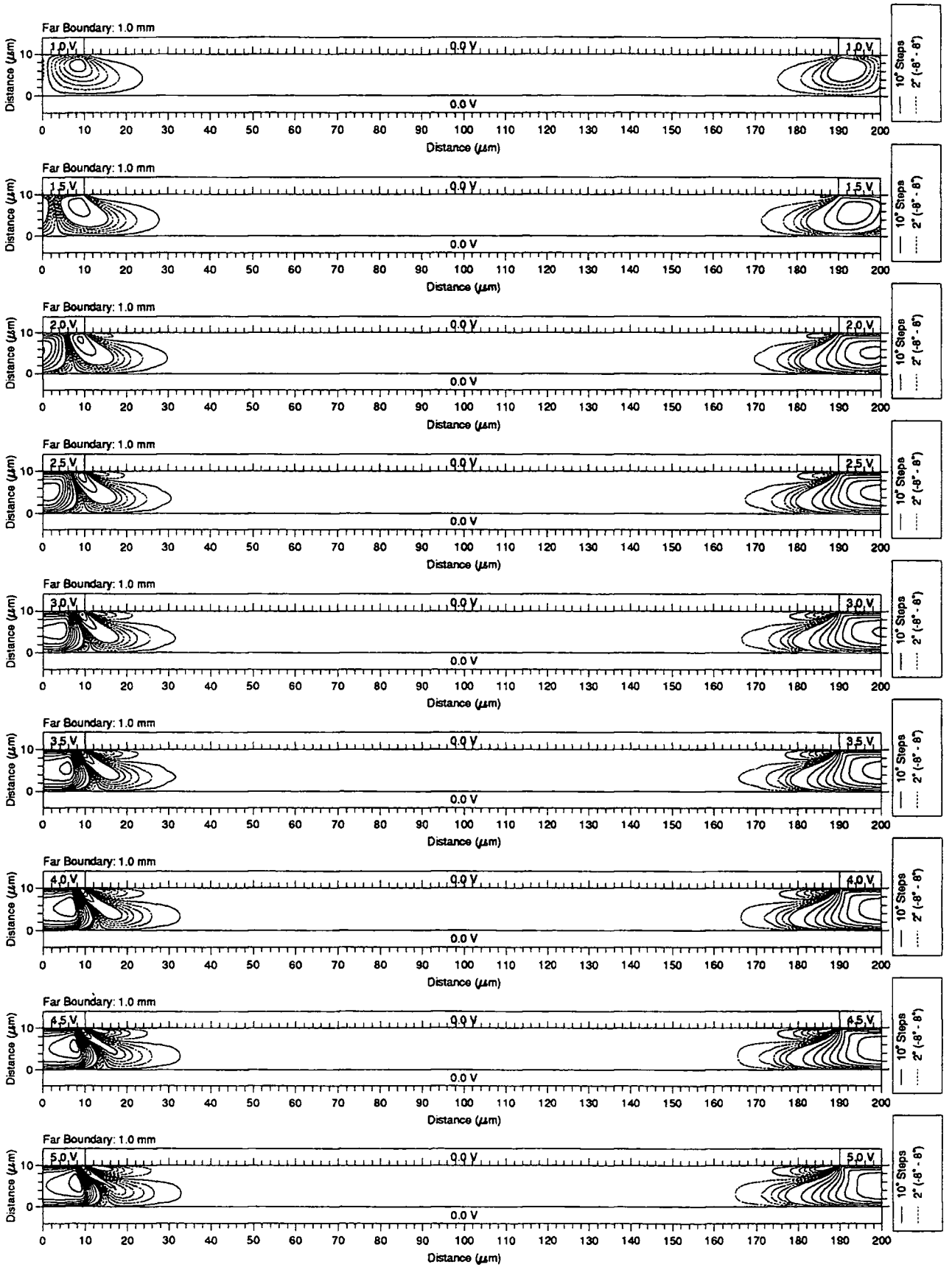

Director Orientation Distribution for a Periodic Liquid Crystal E44 Cell

Experiment with Guard Plate

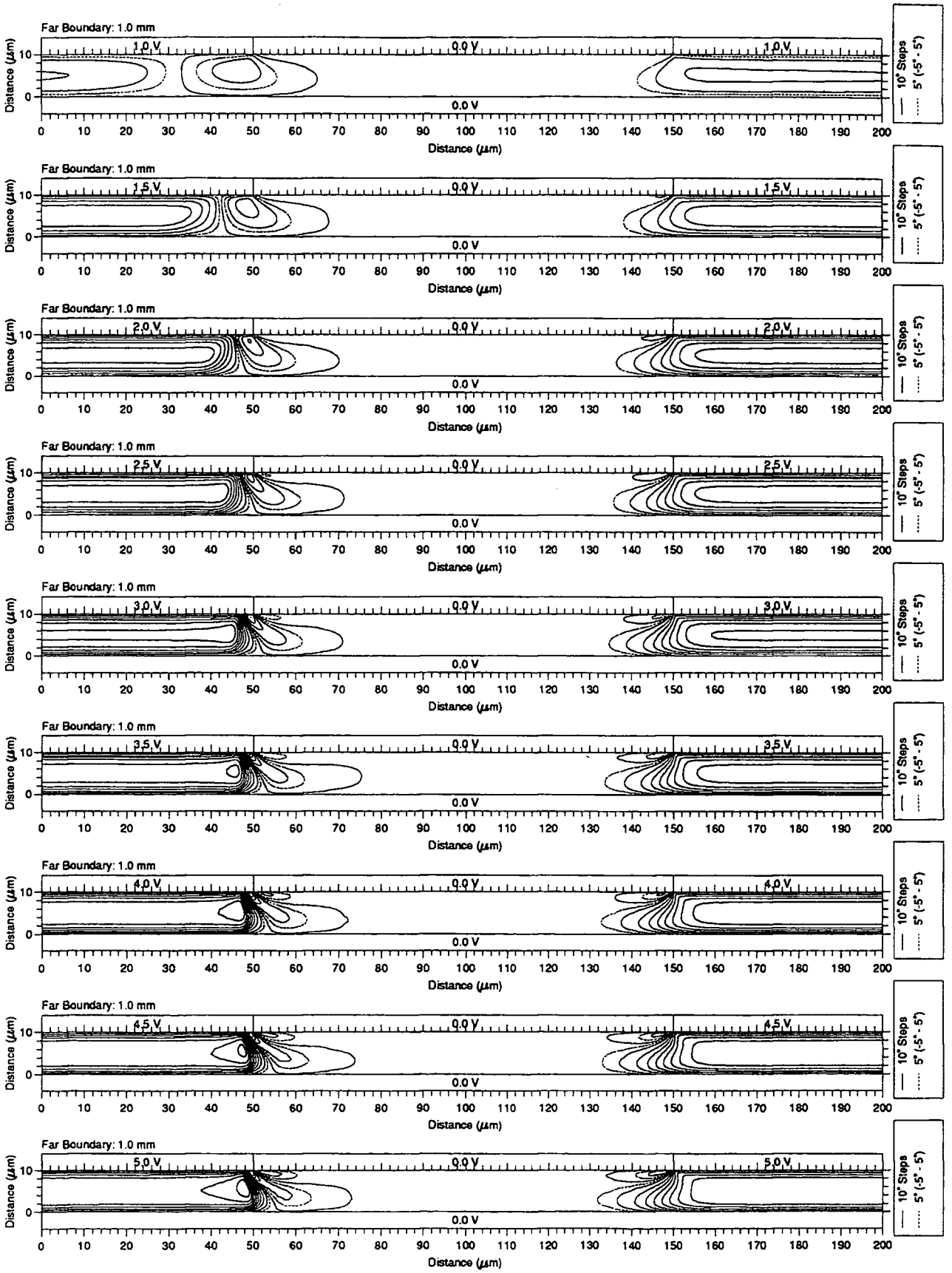

Director Orientation Distribution for a Periodic Liquid Crystal E44 Cell

Experiment with Guard Plate

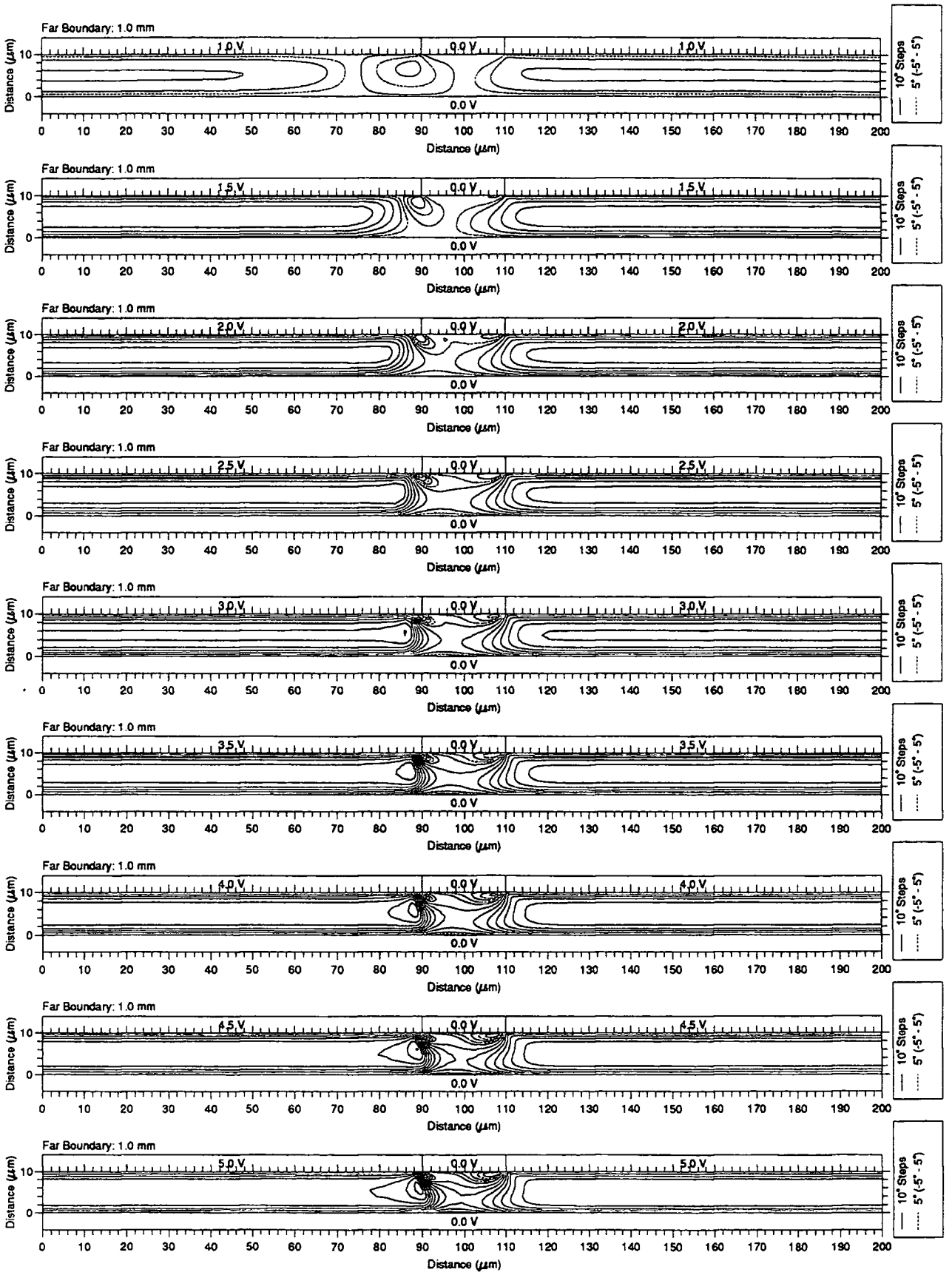

Potential Distribution and Displacement Field for a Periodic Liquid Crystal E44 Cell

Experiment with Guard Plate

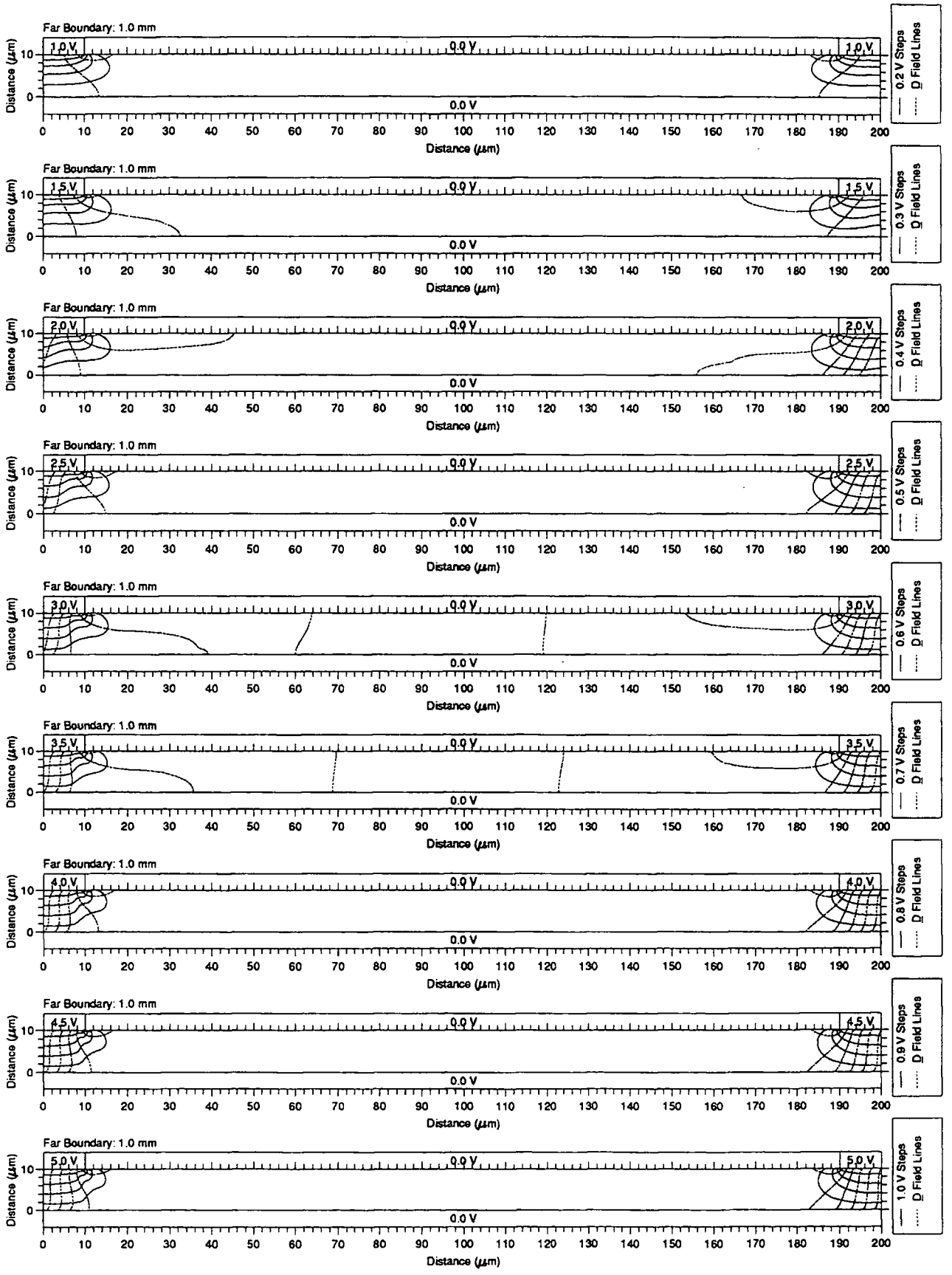

Potential Distribution and Displacement Field for a Periodic Liquid Crystal E44 Cell

Experiment with Guard Plate

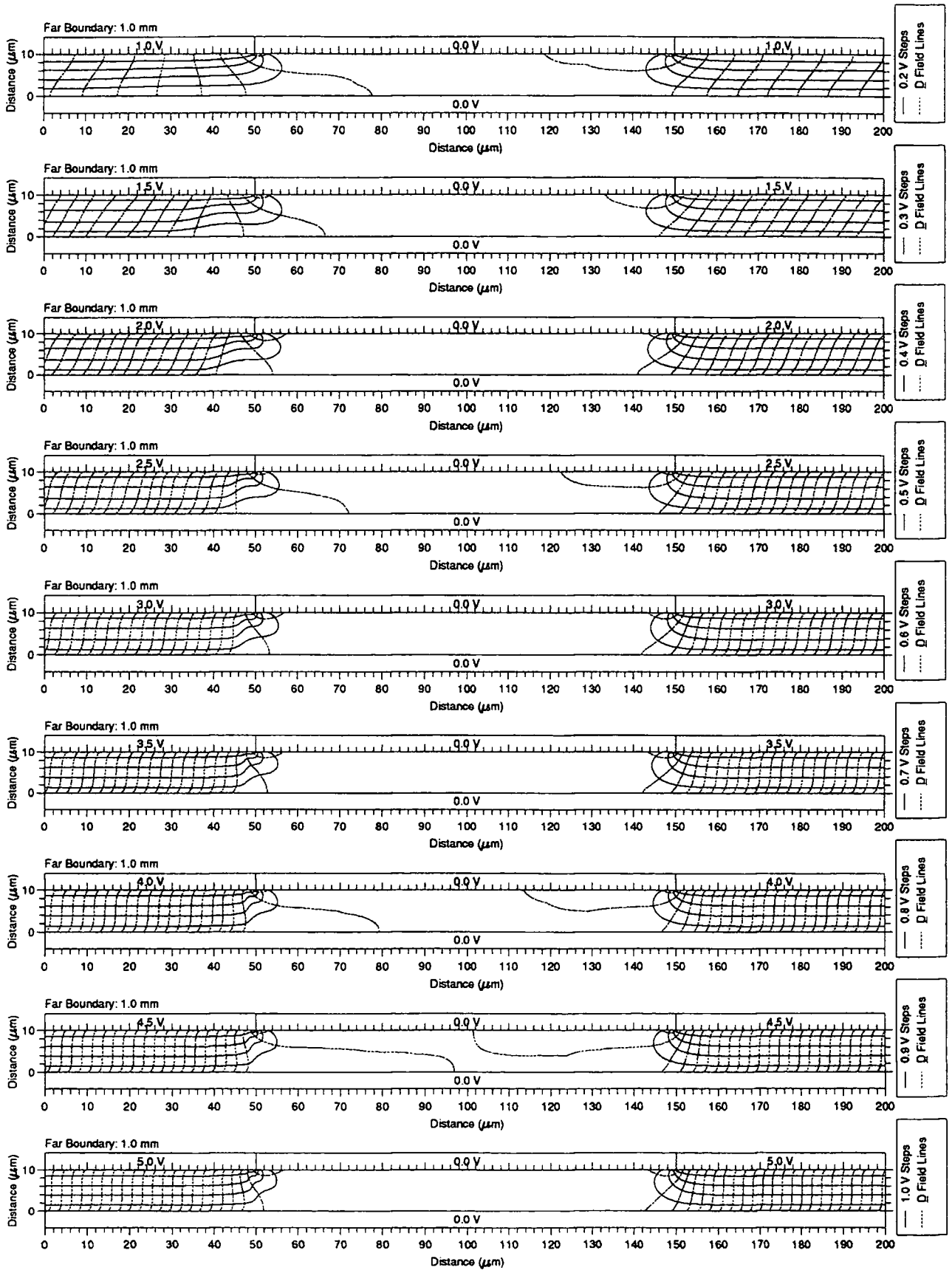

Potential Distribution and Displacement Field for a Periodic Liquid Crystal E44 Cell

Experiment with Guard Plate

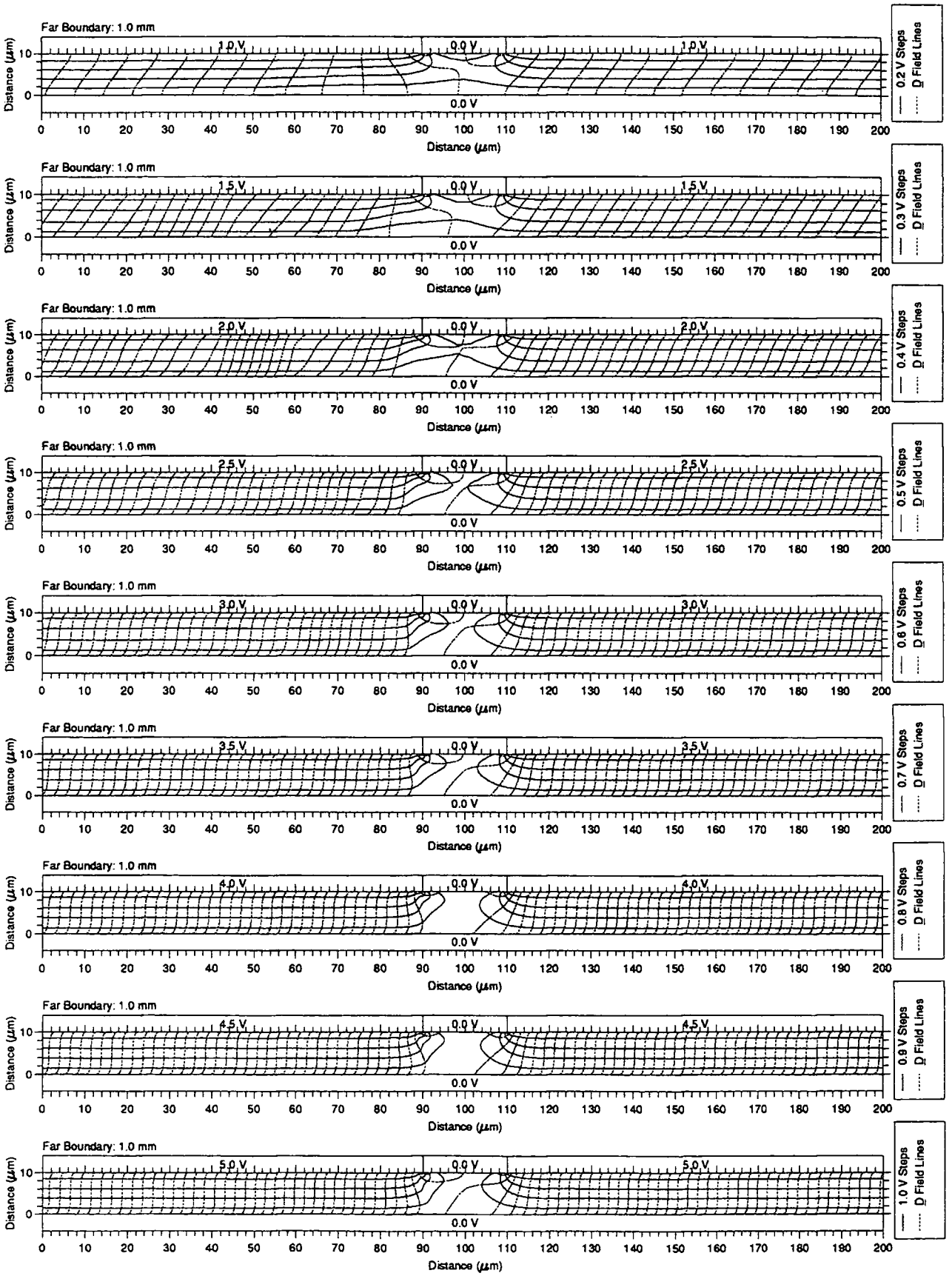

G.1.4 Etched Earth Plate and Guard Plate

Normalised Phase Distribution for a Periodic Liquid Crystal E44 Cell

Experiment with Etched Earth Plate and Guard Plates

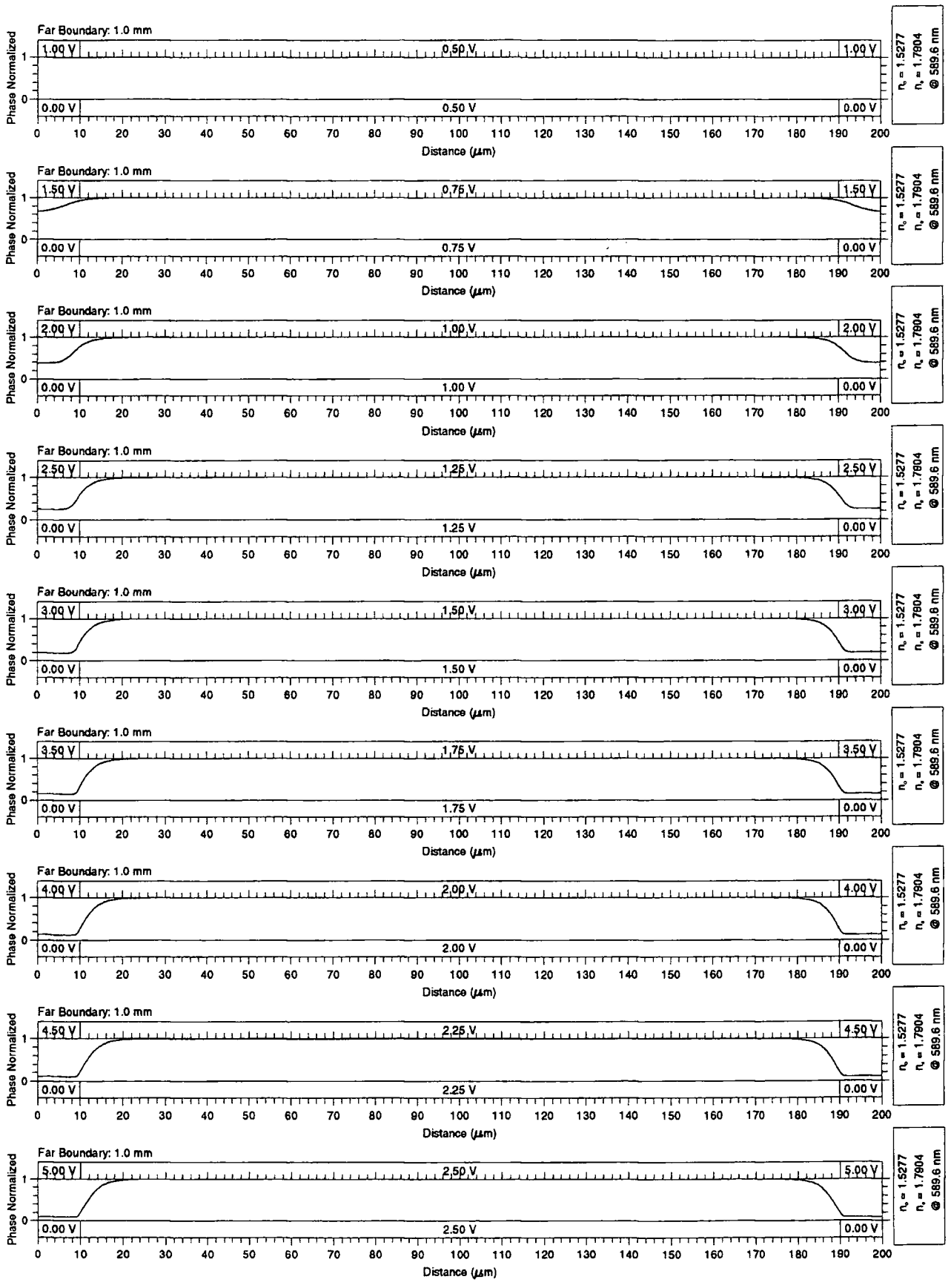

Normalised Phase Distribution for a Periodic Liquid Crystal E44 Cell

Experiment with Etched Earth Plate and Guard Plates

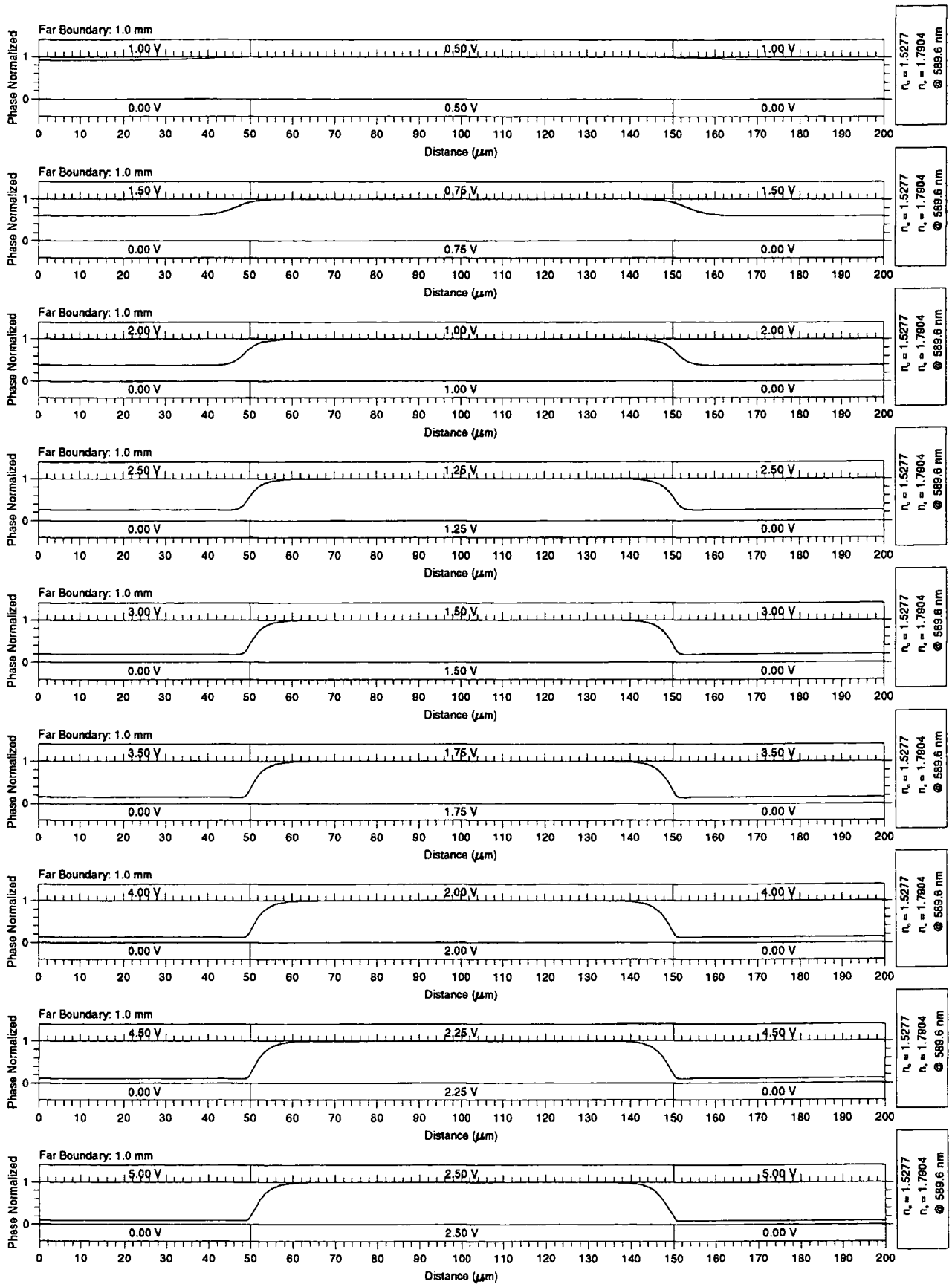

Normalised Phase Distribution for a Periodic Liquid Crystal E44 Cell

Experiment with Etched Earth Plate and Guard Plates

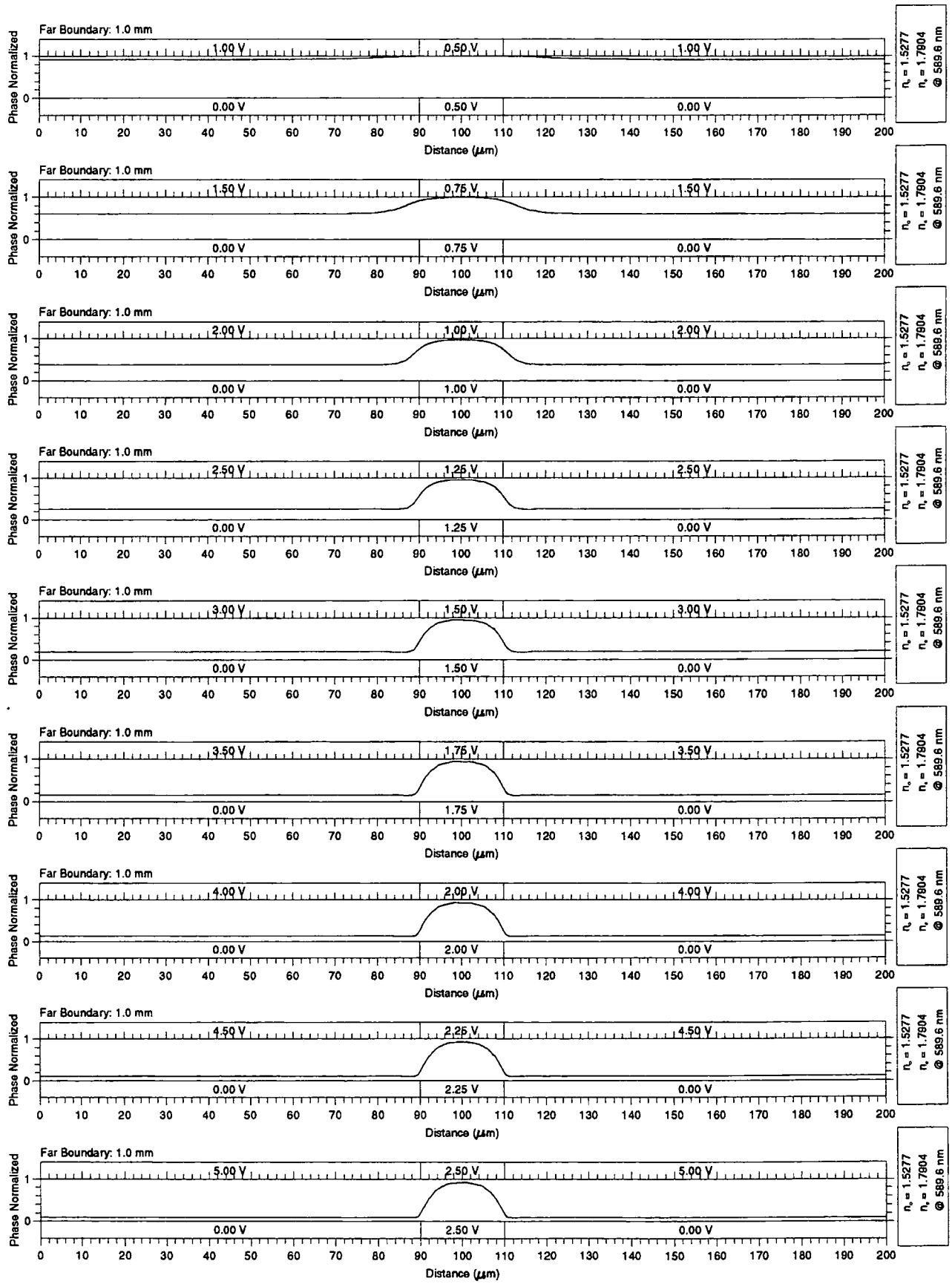

Director Orientation Distribution for a Periodic Liquid Crystal E44 Cell

Experiment with Etched Earth Plate and Guard Plates

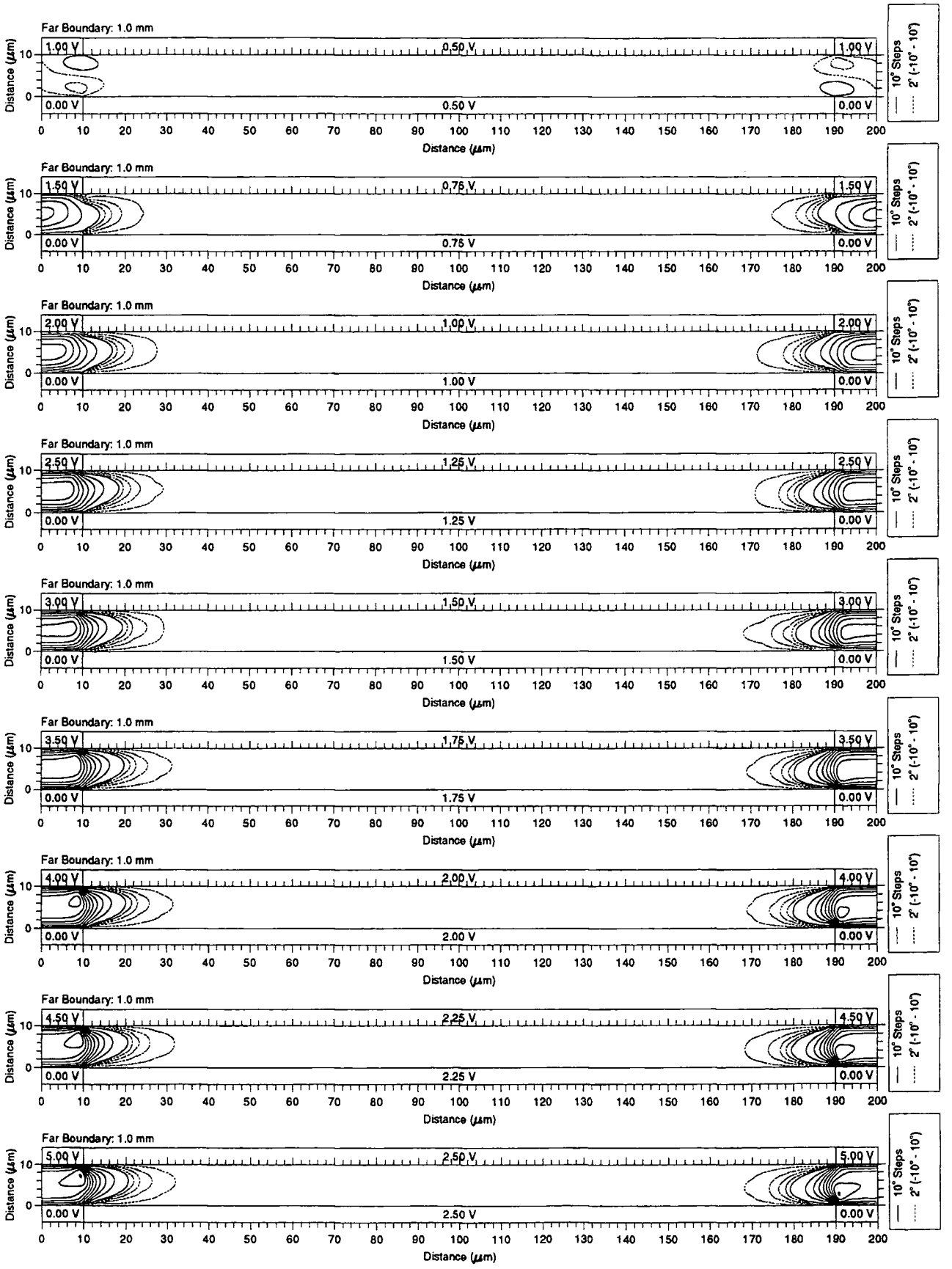

Director Orientation Distribution for a Periodic Liquid Crystal E44 Cell

Experiment with Etched Earth Plate and Guard Plates

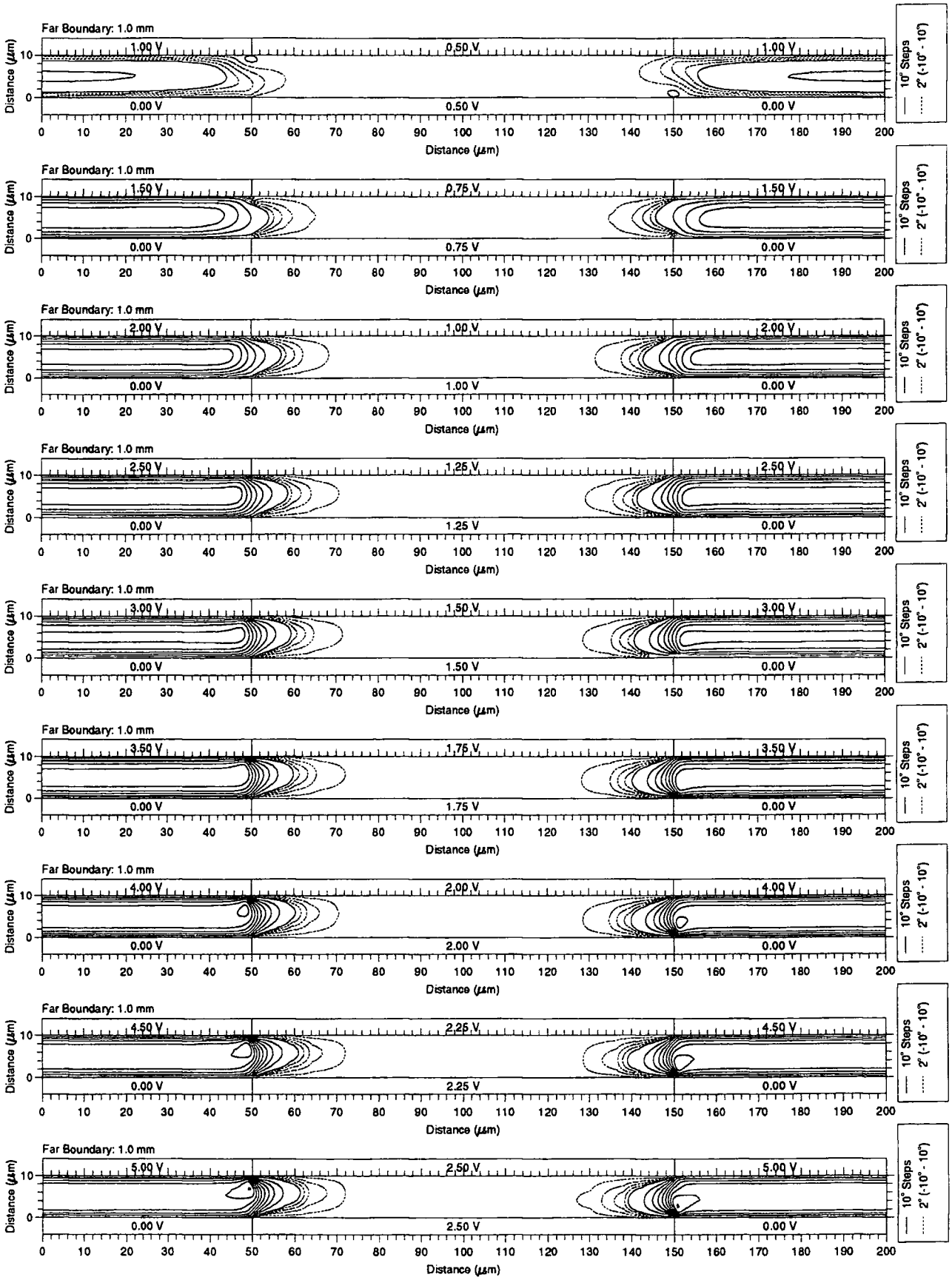

Director Orientation Distribution for a Periodic Liquid Crystal E44 Cell

Experiment with Etched Earth Plate and Guard Plates

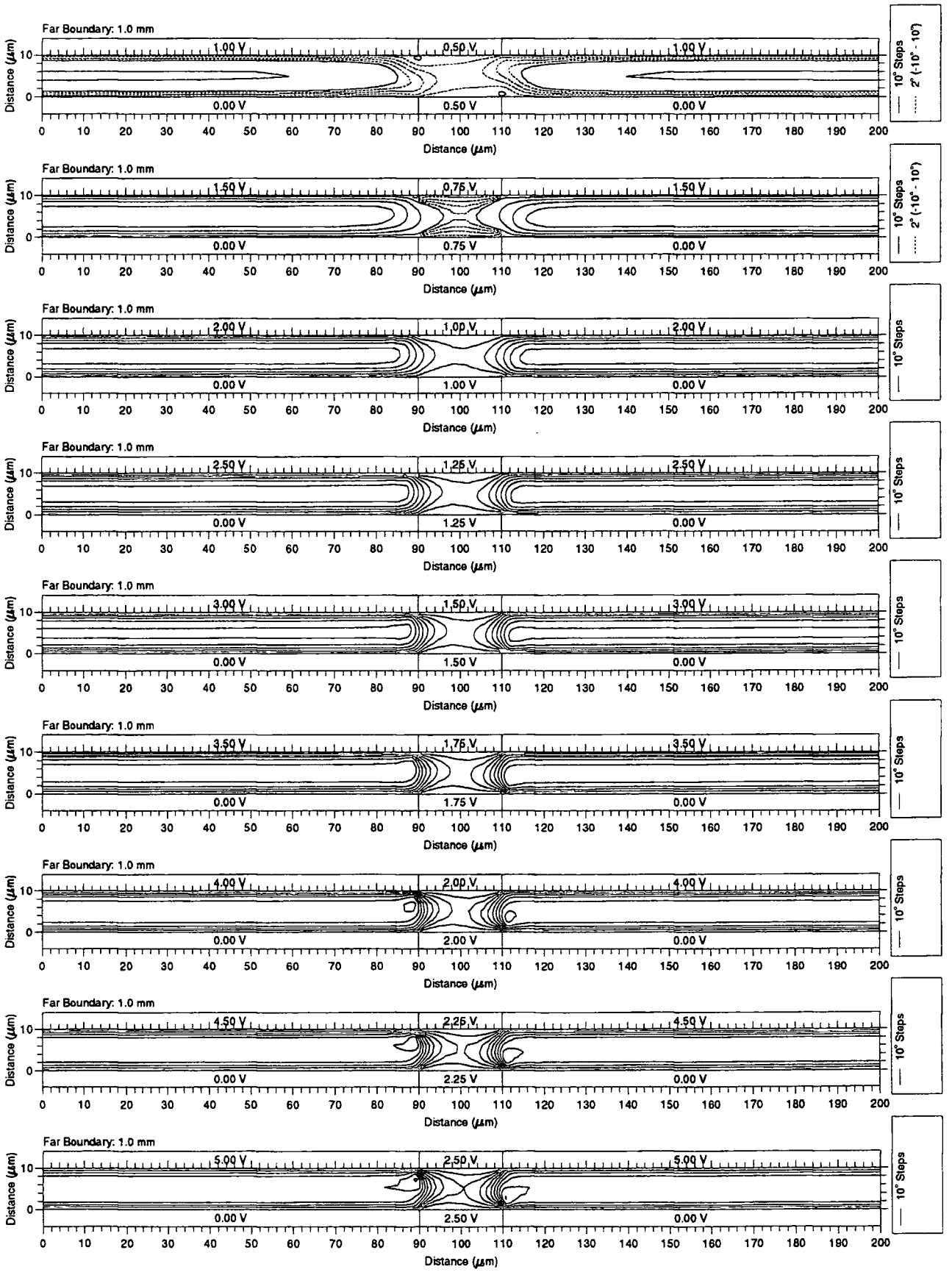

Potential Distribution and Displacement Field for a Periodic Liquid Crystal E44 Cell

Experiment with Etched Earth Plate and Guard Plates

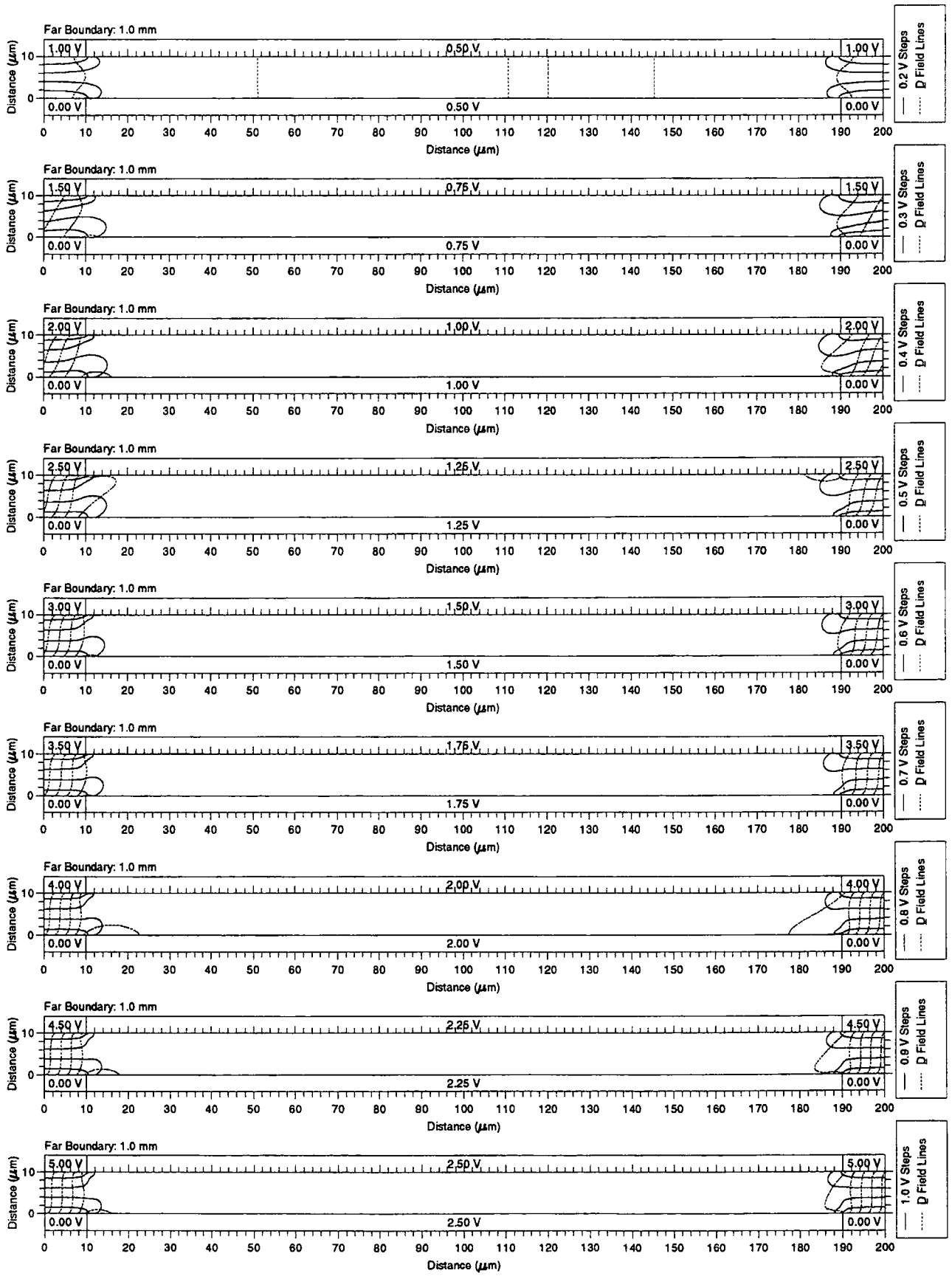

Potential Distribution and Displacement Field for a Periodic Liquid Crystal E44 Cell

Experiment with Etched Earth Plate and Guard Plates

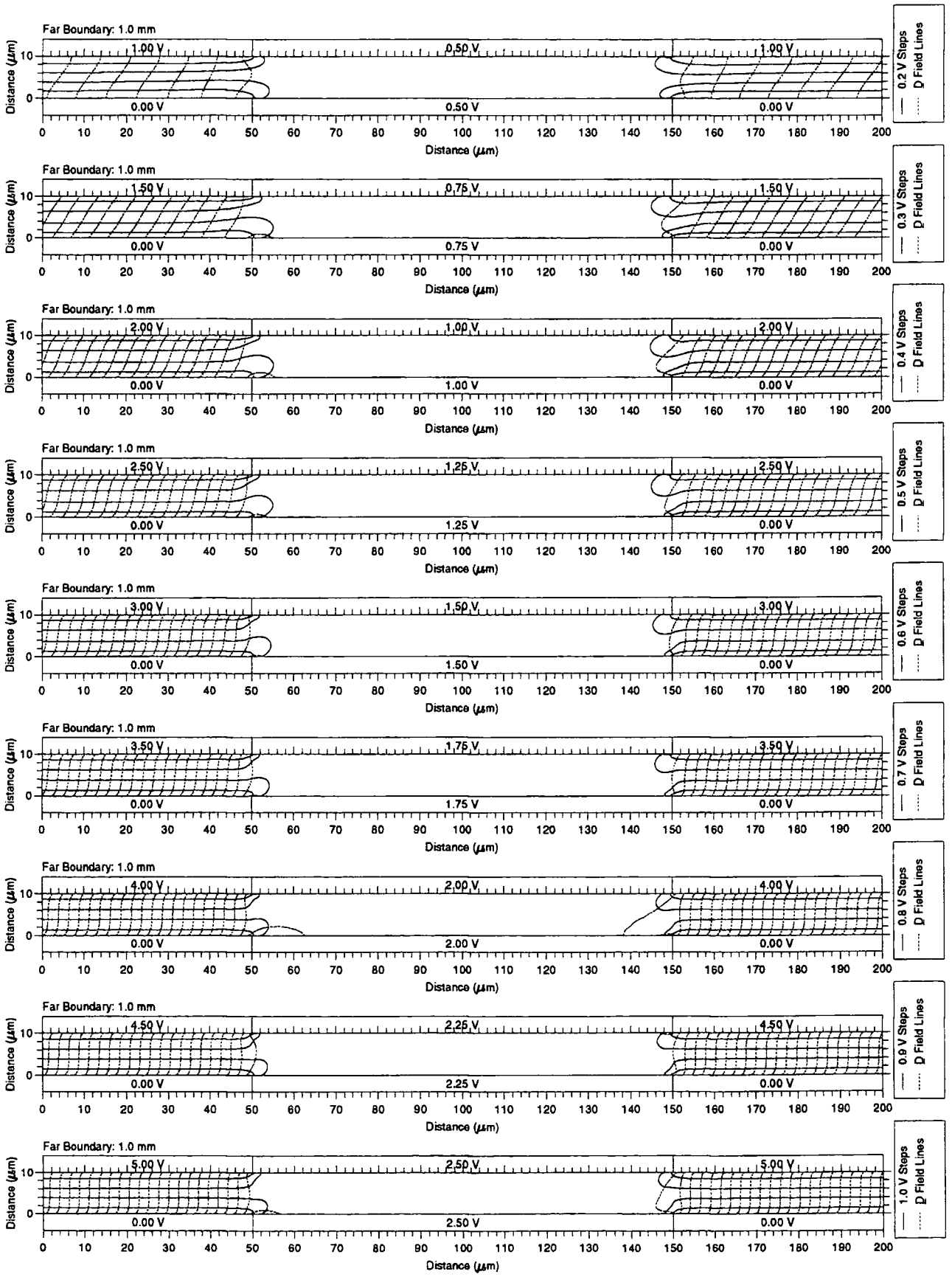

Potential Distribution and Displacement Field for a Periodic Liquid Crystal E44 Cell

Experiment with Etched Earth Plate and Guard Plates

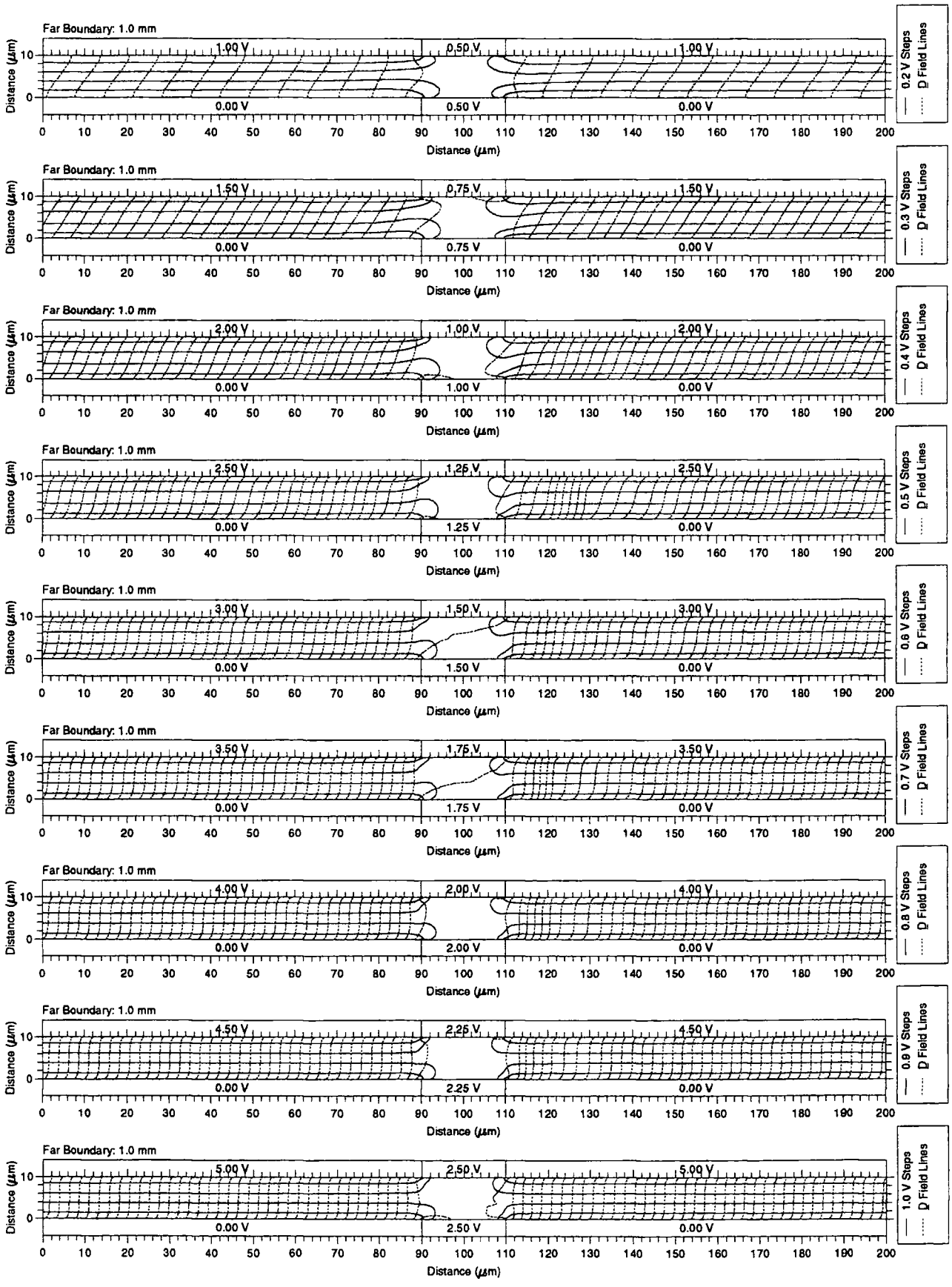

G.1.5 Staggered Guard Plate

Normalised Phase Distribution for a Periodic Liquid Crystal E44 Cell

Staggered Etched Earth Plate and Guard Plates

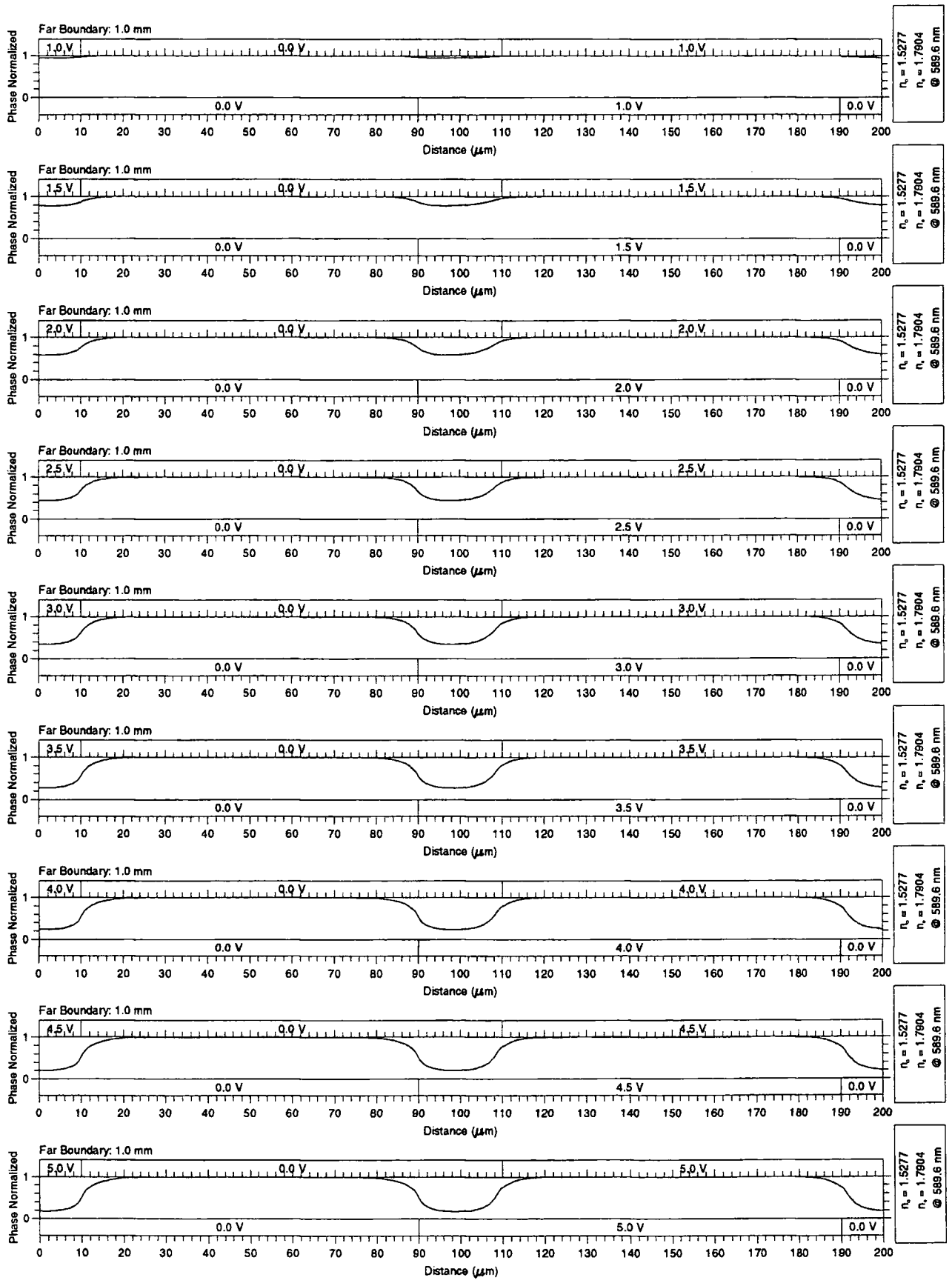

Normalised Phase Distribution for a Periodic Liquid Crystal E44 Cell

Staggered Etched Earth Plate and Guard Plates

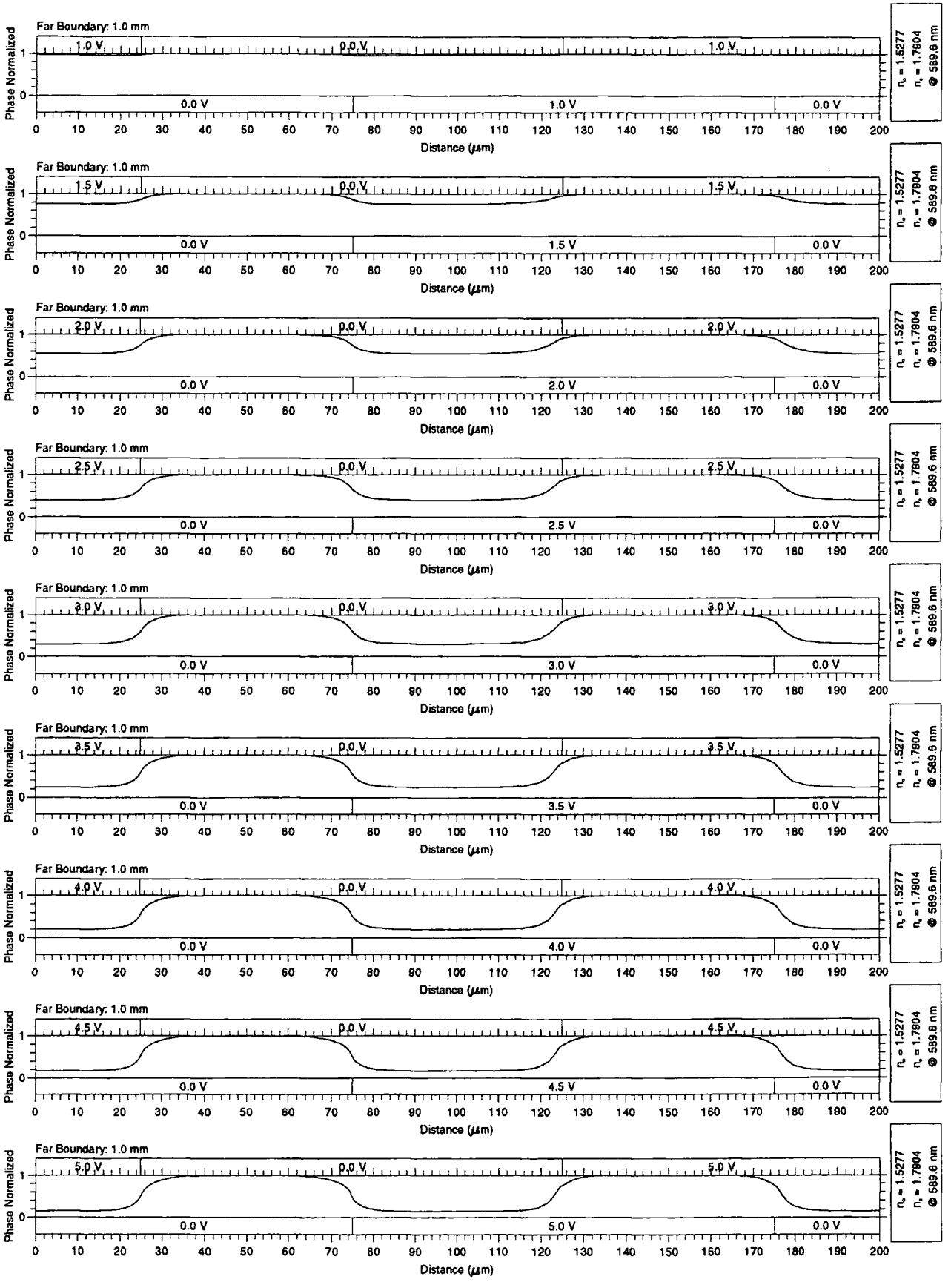

Normalised Phase Distribution for a Periodic Liquid Crystal E44 Cell

Staggered Etched Earth Plate and Guard Plates

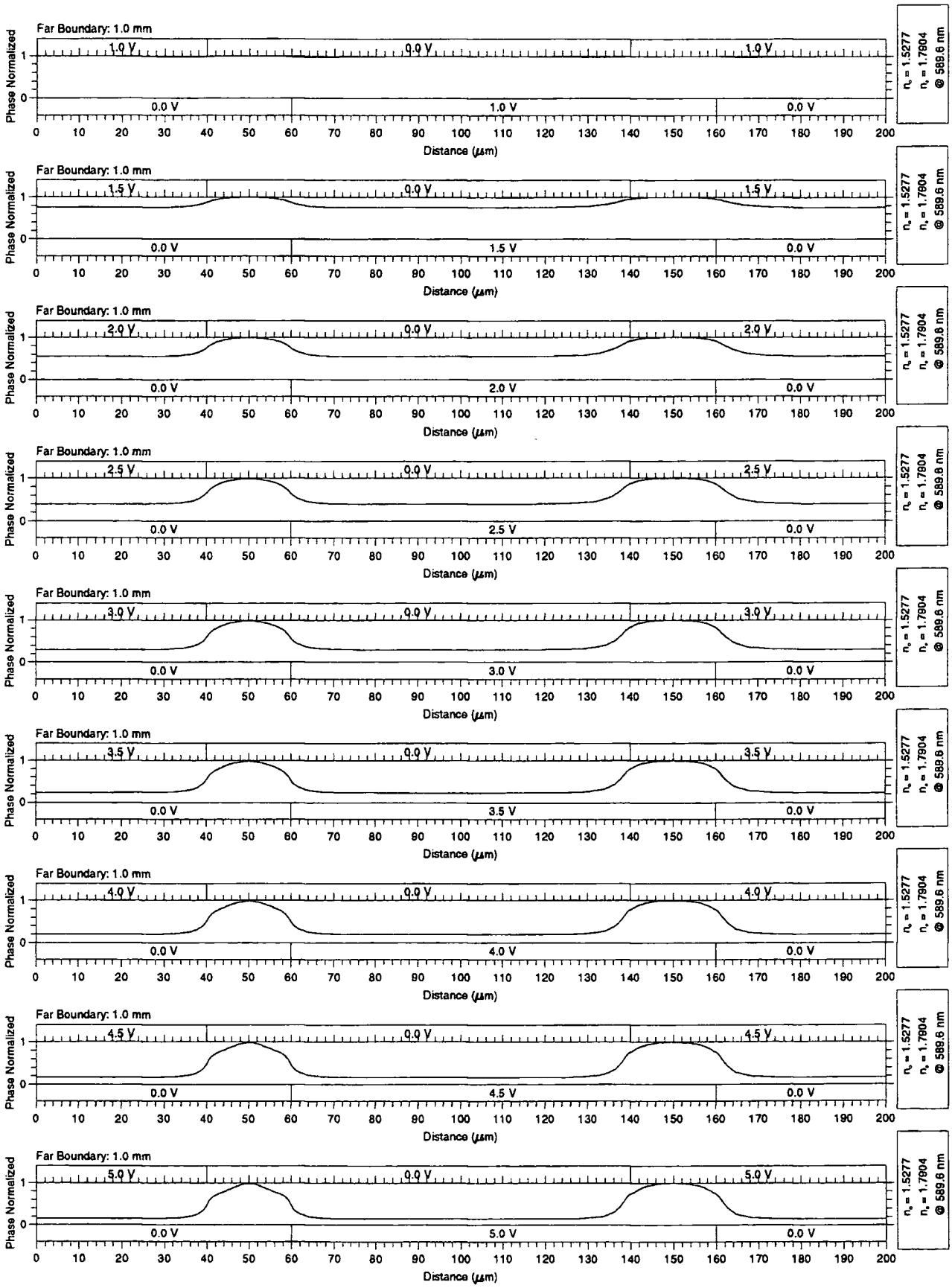

Director Orientation Distribution for a Periodic Liquid Crystal E44 Cell

Staggered Etched Earth Plate and Guard Plates

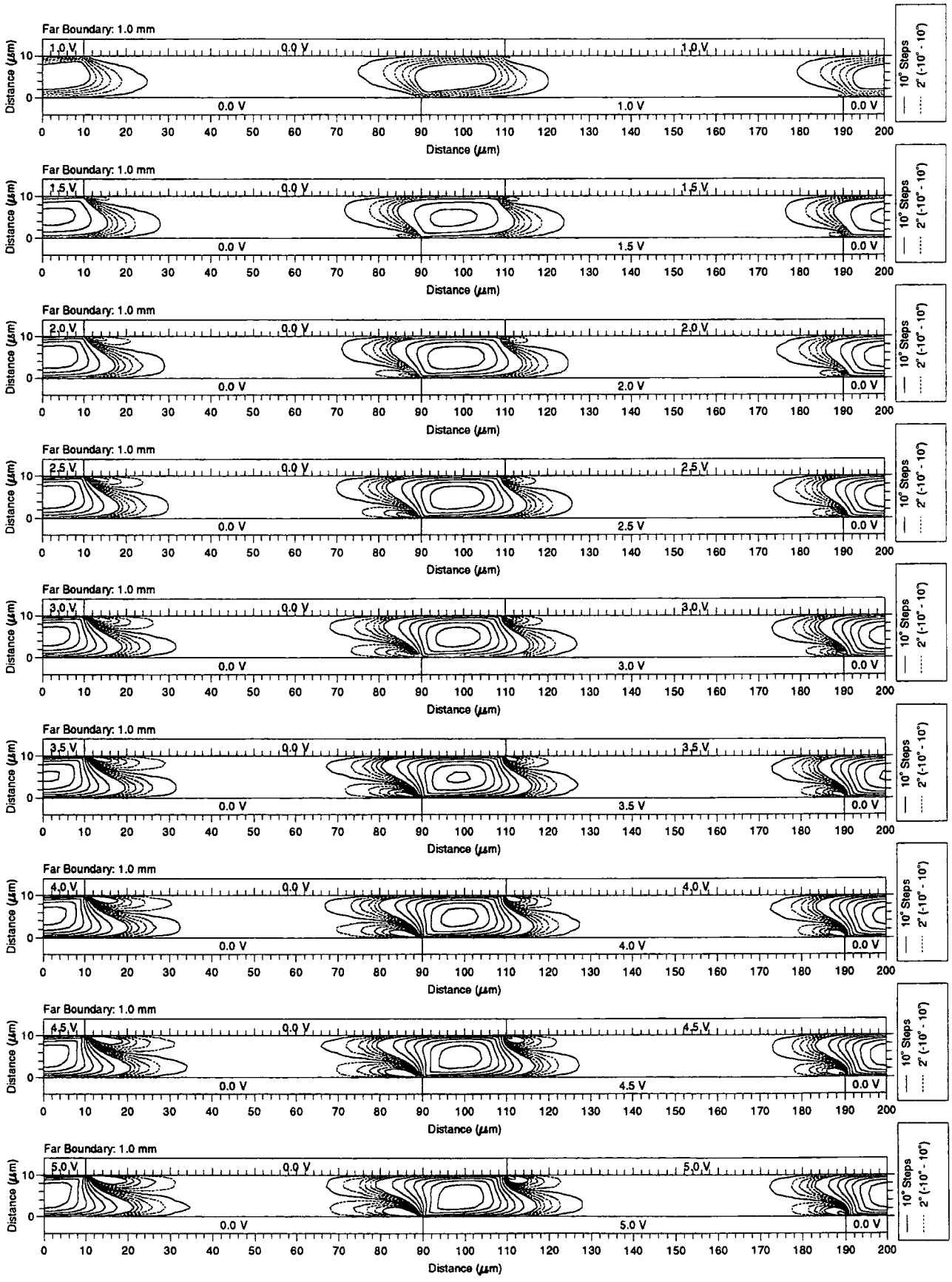

Director Orientation Distribution for a Periodic Liquid Crystal E44 Cell

Staggered Etched Earth Plate and Guard Plates

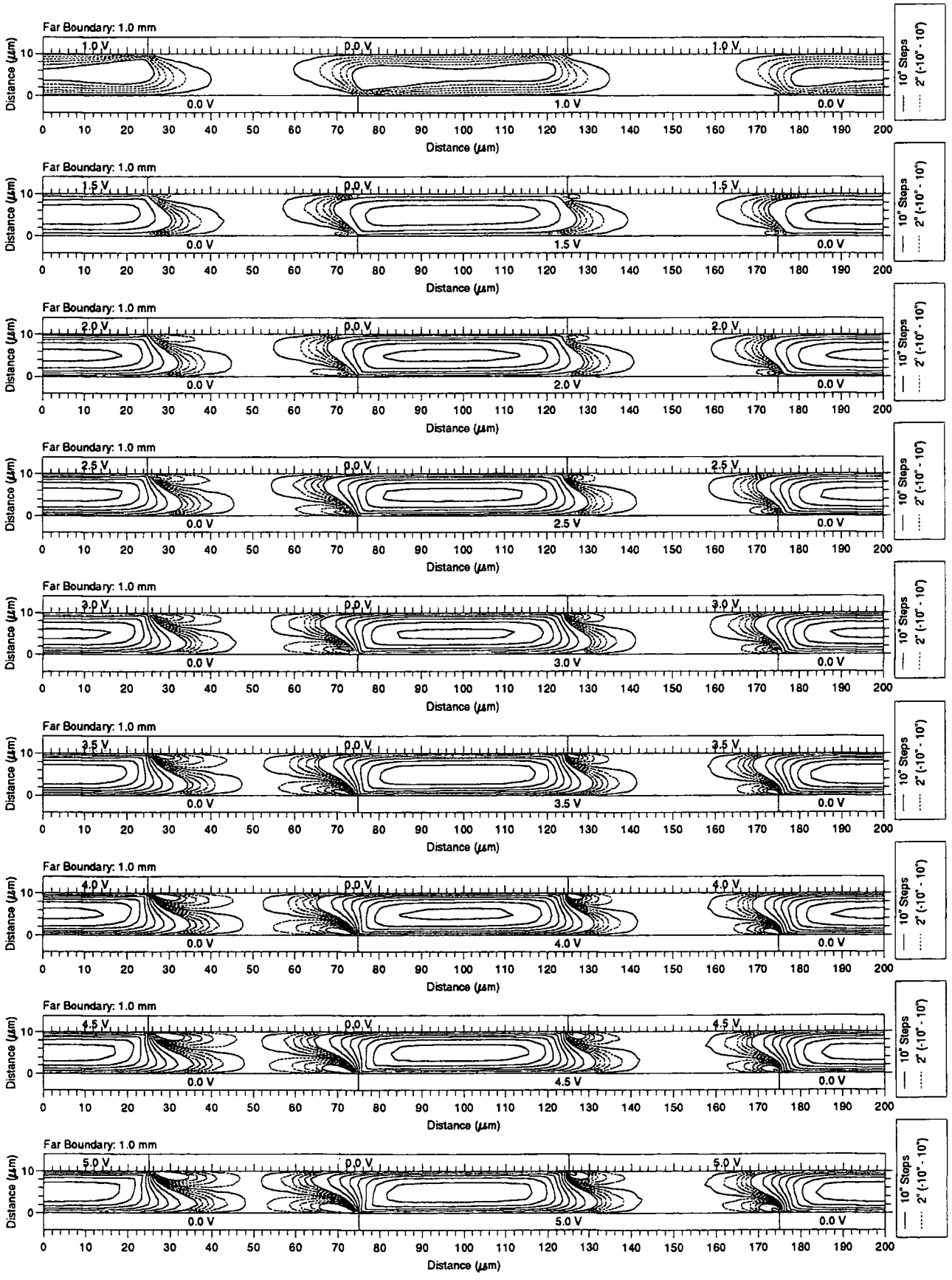

Director Orientation Distribution for a Periodic Liquid Crystal E44 Cell

Staggered Etched Earth Plate and Guard Plates

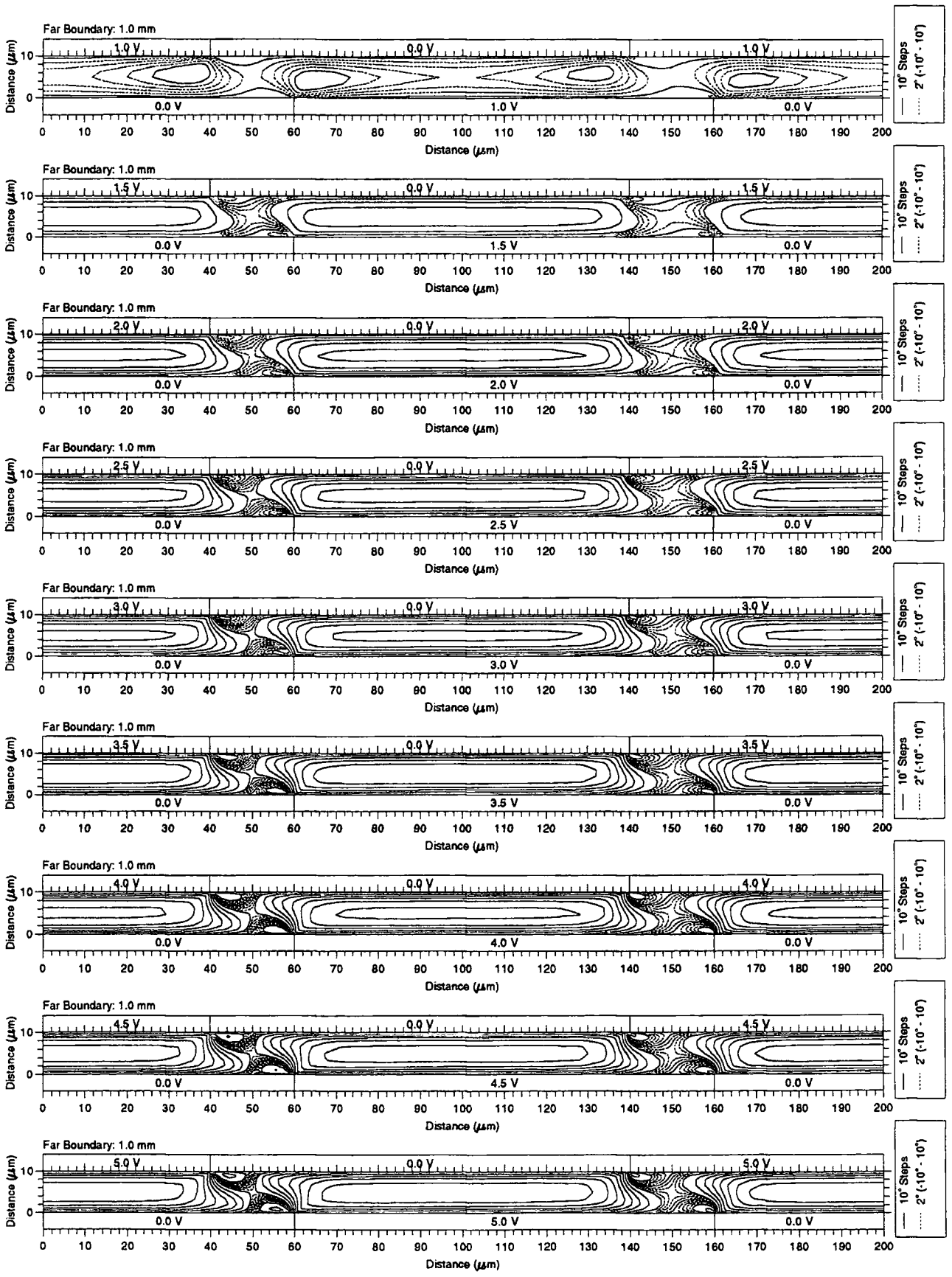

Potential Distribution and Displacement Field for a Periodic Liquid Crystal E44 Cell

Staggered Etched Earth Plate and Guard Plates

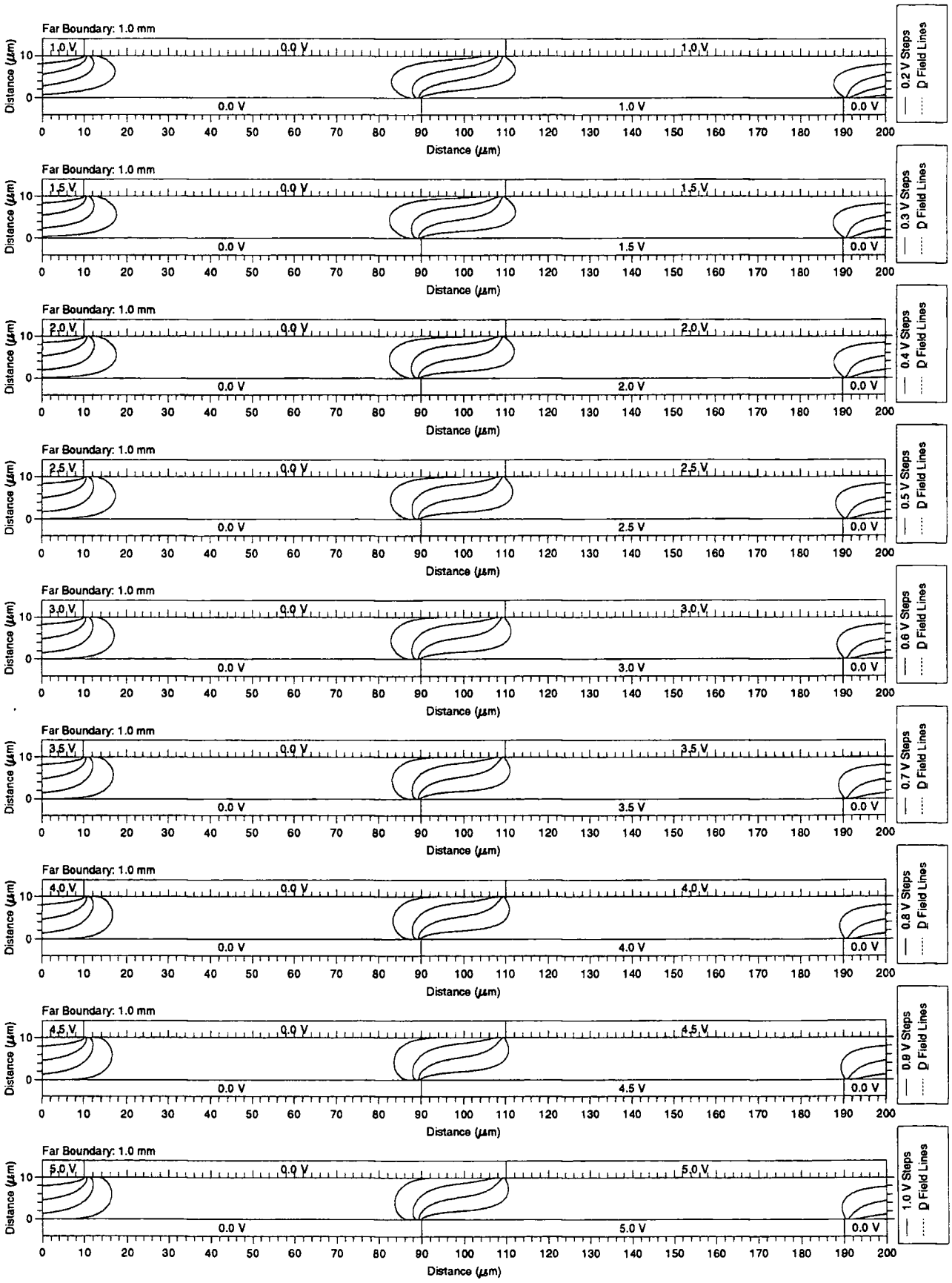

Potential Distribution and Displacement Field for a Periodic Liquid Crystal E44 Cell

Staggered Etched Earth Plate and Guard Plates

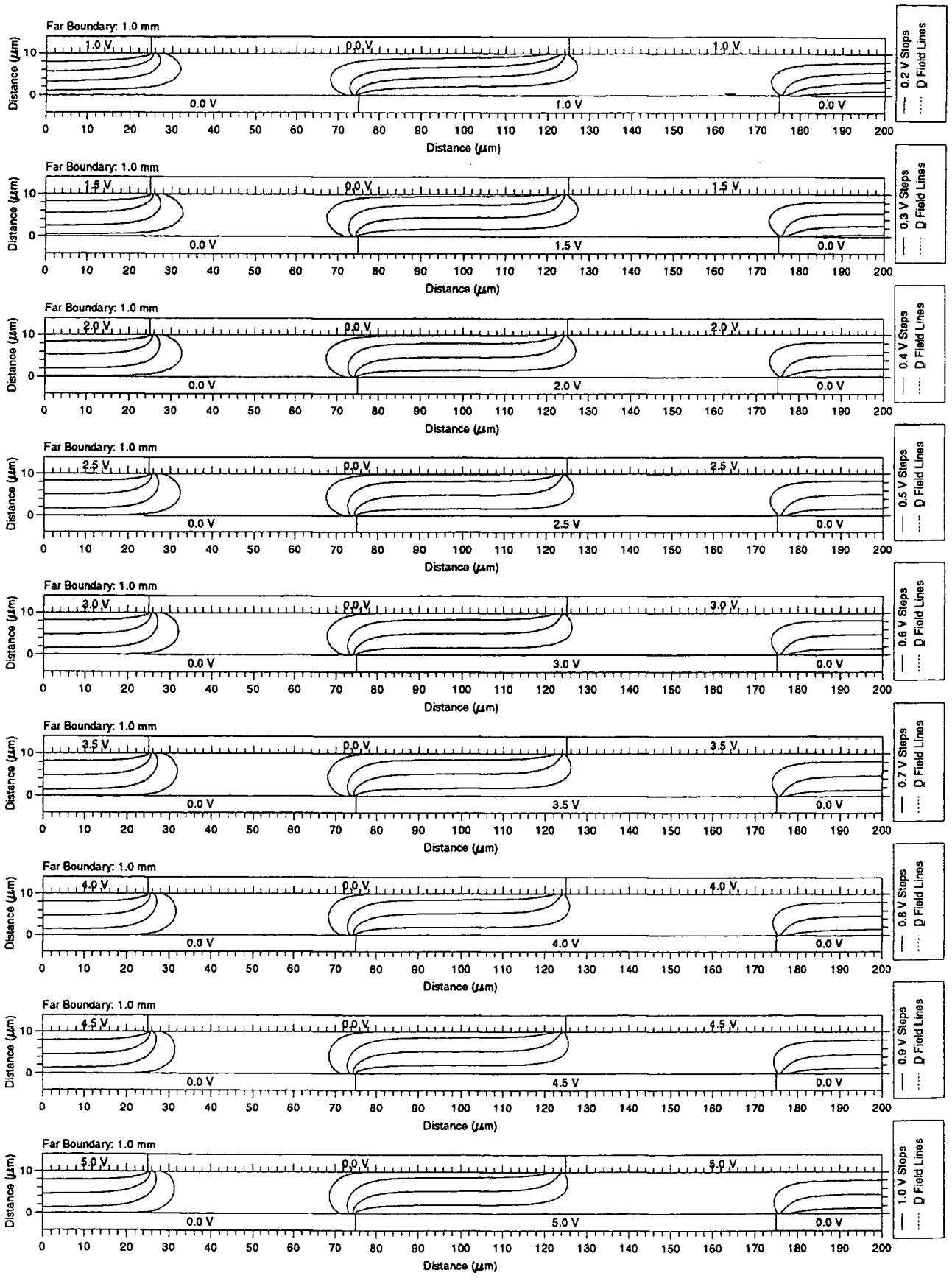

Potential Distribution and Displacement Field for a Periodic Liquid Crystal E44 Cell

Staggered Etched Earth Plate and Guard Plates

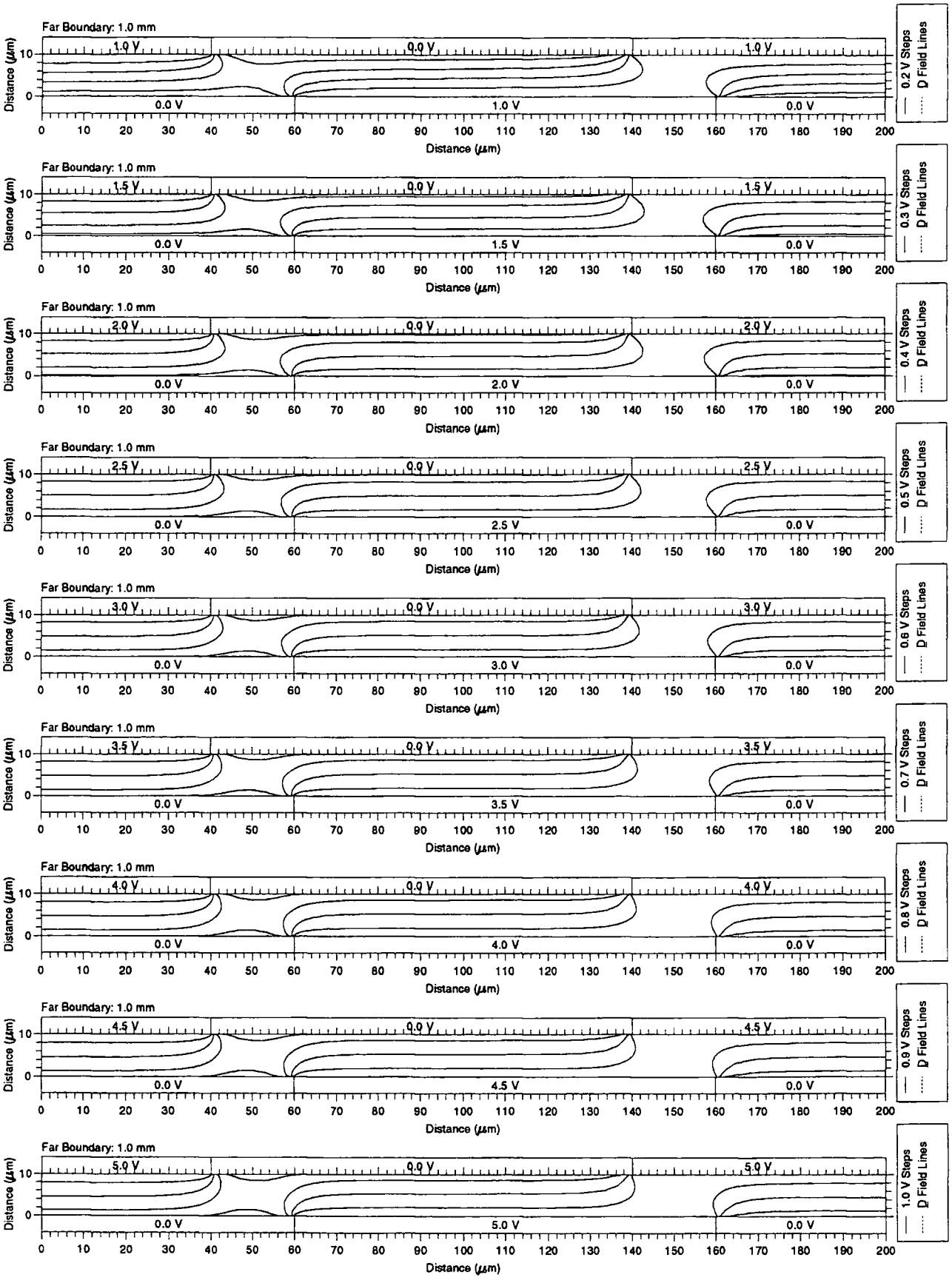

G.1.6 Increasing Boundary Pre-Tilt

Normalised Phase Distribution for a Periodic Liquid Crystal E44 Cell

Staggered Etched Earth Plate and Guard Plates

with Increasing Boudary Pre-Tilt

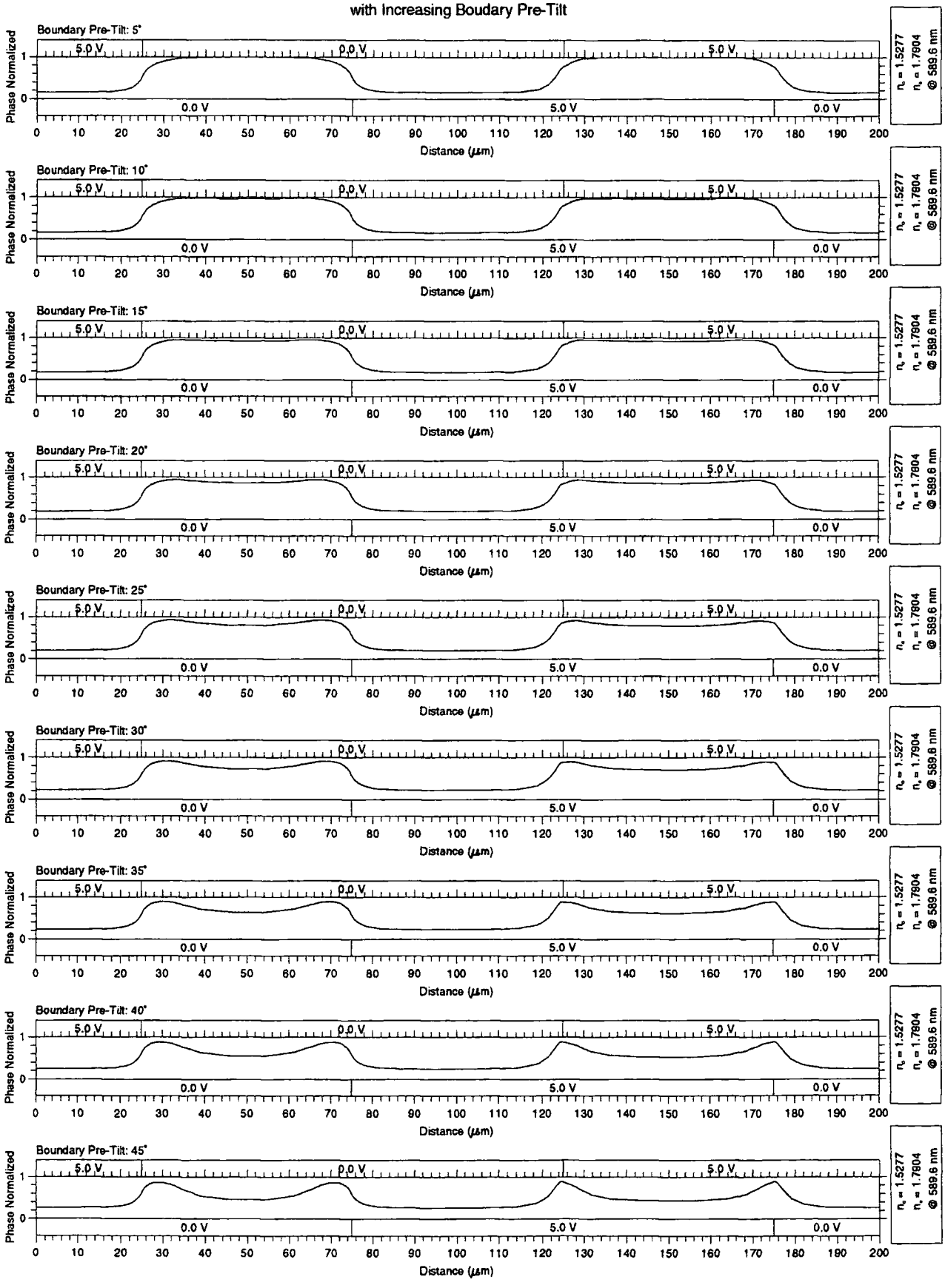

Director Orientation Distribution for a Periodic Liquid Crystal E44 Cell

Staggered Etched Earth Plate and Guard Plates

with Increasing Boudary Pre-Tilt

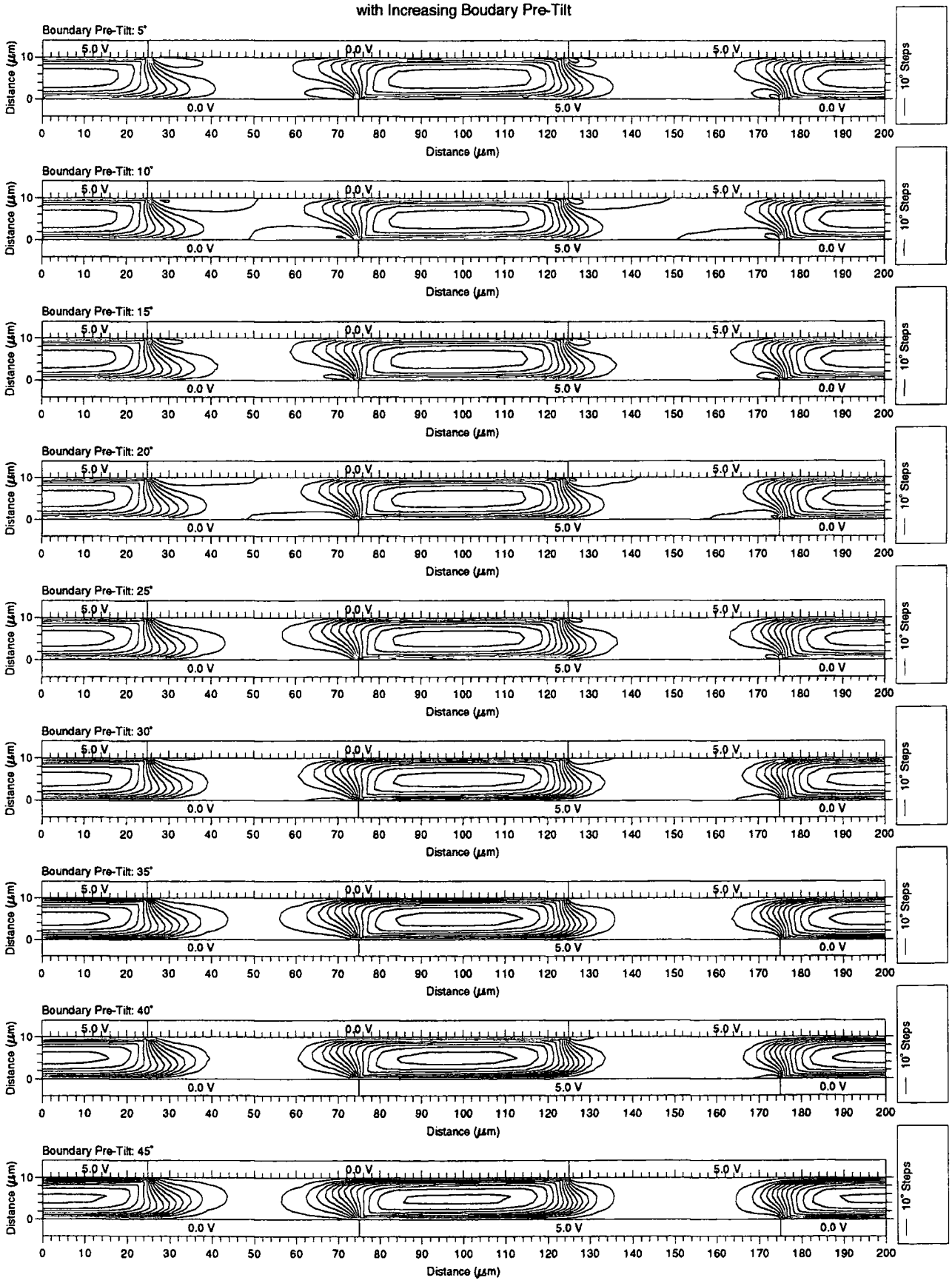

Potential Distribution and Displacement Field for a Periodic Liquid Crystal E44 Cell

Staggered Etched Earth Plate and Guard Plates

with Increasing Boudary Pre-Tilt

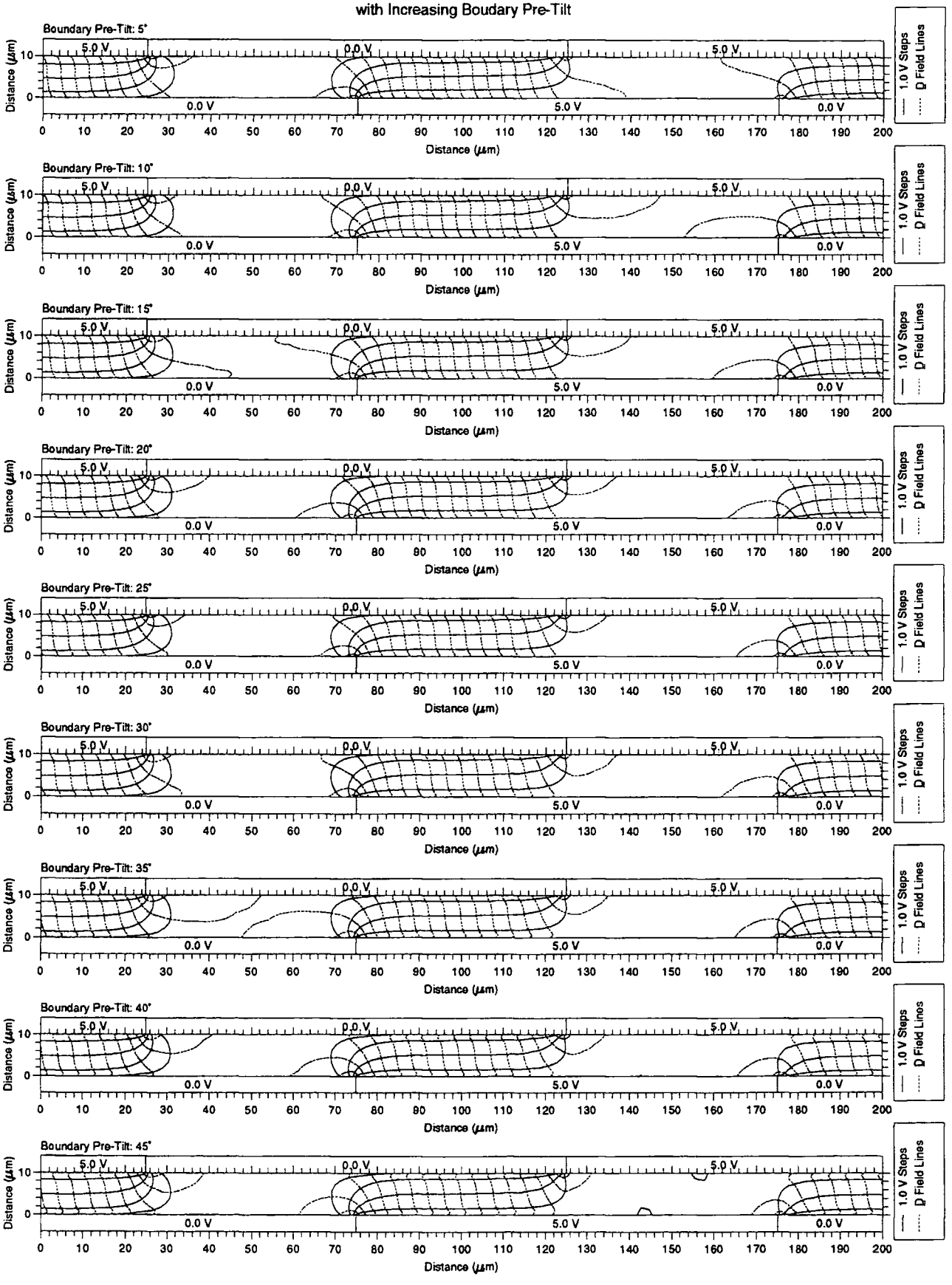

G.1.7 Broken Electrode

Normalised Phase Distribution for a Periodic Liquid Crystal E44 Cell

Staggered Etched Earth Plate and Guard Plates

with Broken Electrode

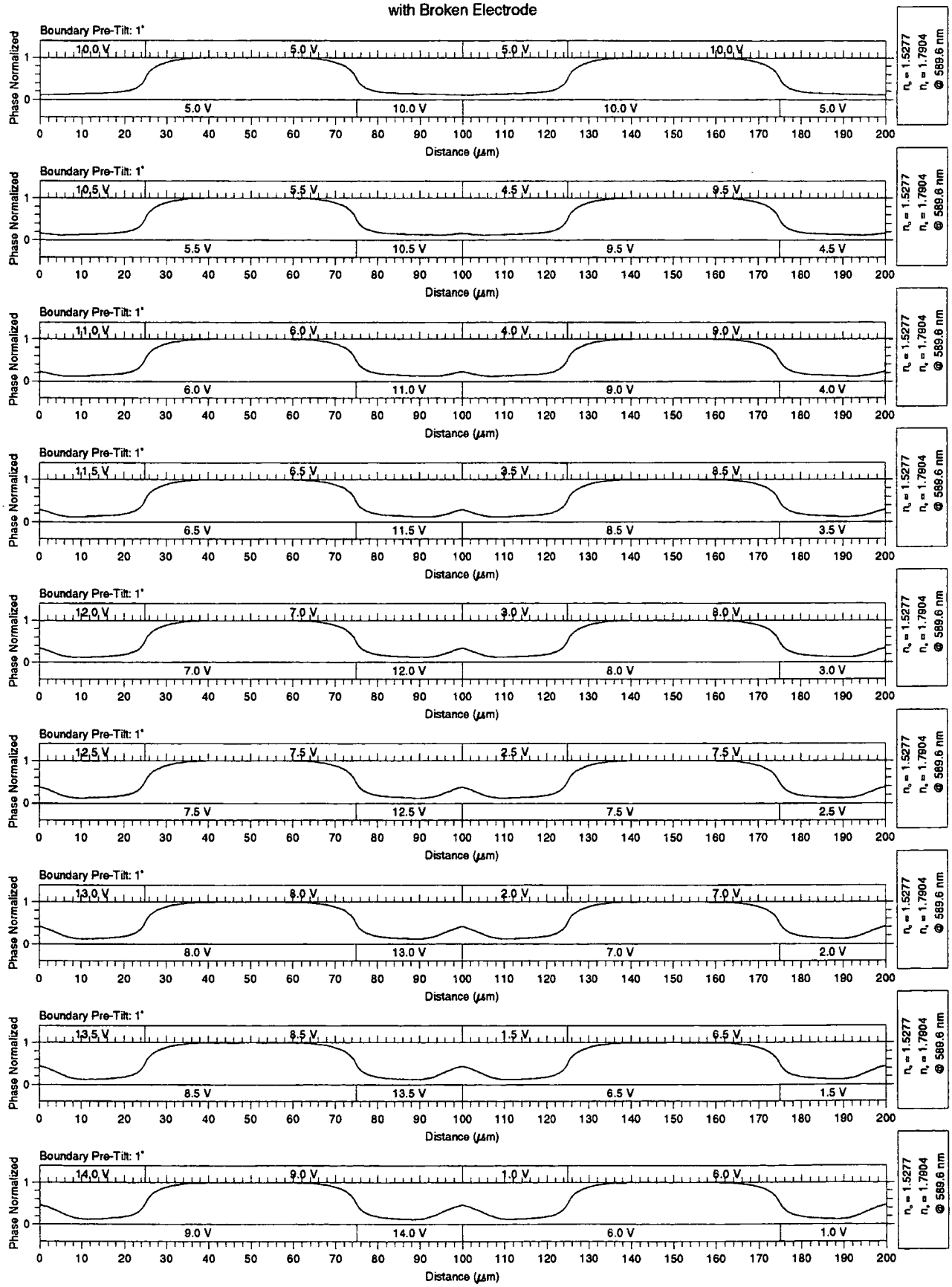

Director Orientation Distribution for a Periodic Liquid Crystal E44 Cell

Staggered Etched Earth Plate and Guard Plates

with Broken Electrode

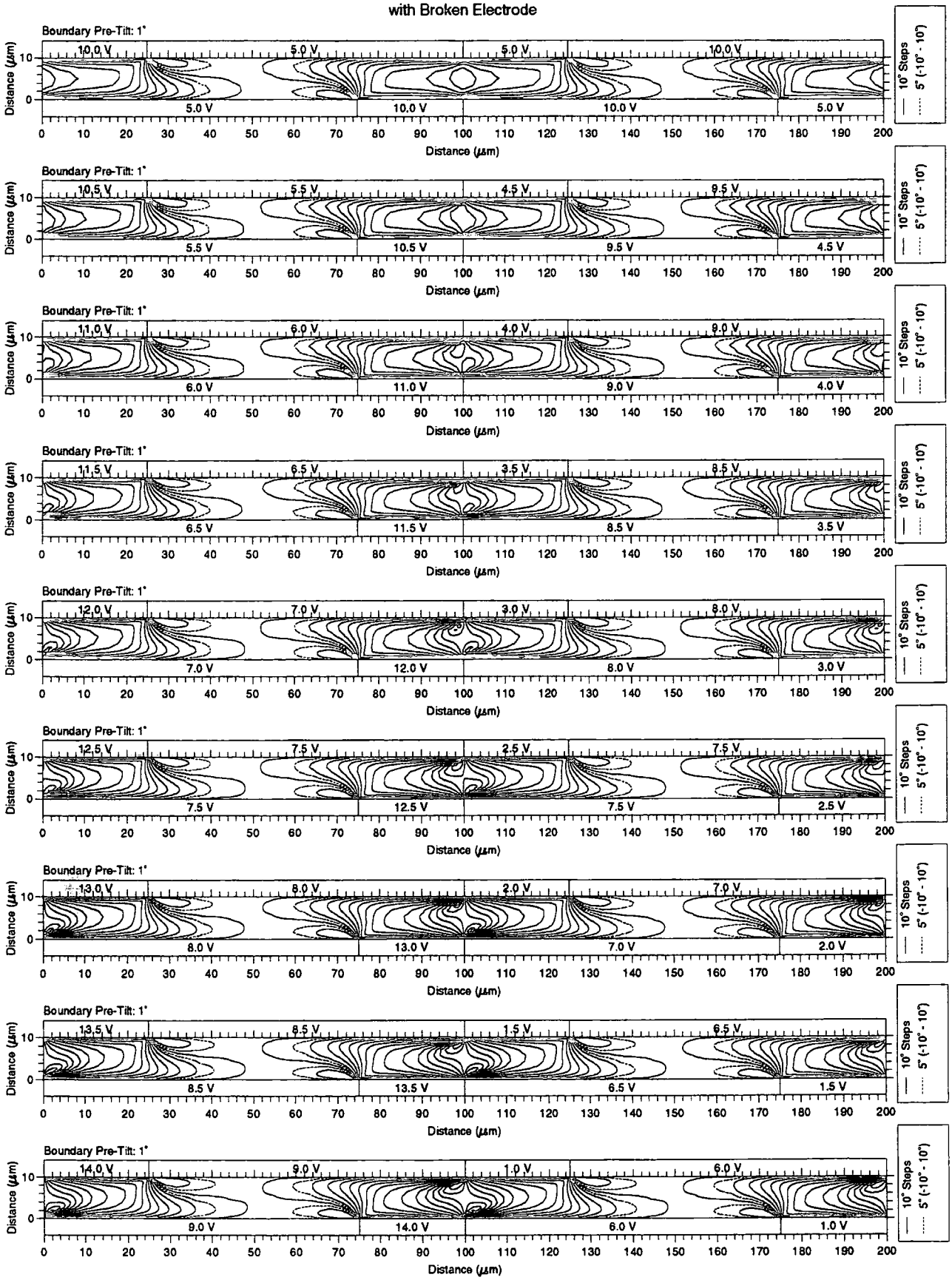

Potential Distribution and Displacement Field for a Periodic Liquid Crystal E44 Cell

Staggered Etched Earth Plate and Guard Plates

with Broken Electrode

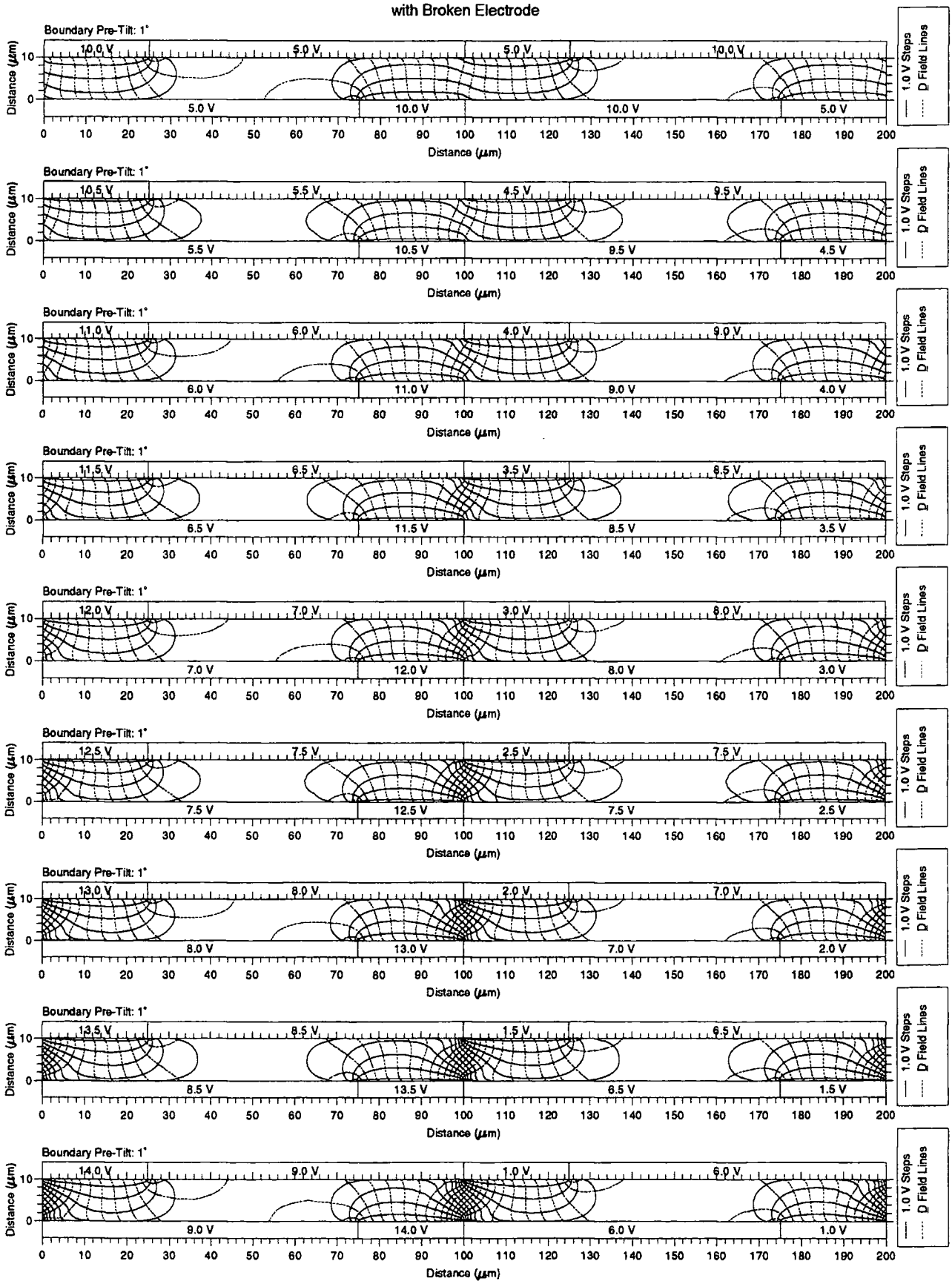

G.1.8 Broken Guard Plate

Normalised Phase Distribution for a Periodic Liquid Crystal E44 Cell

Symmetrical Etched Earth Plate and Guard Plates

with Broken Earth Plate

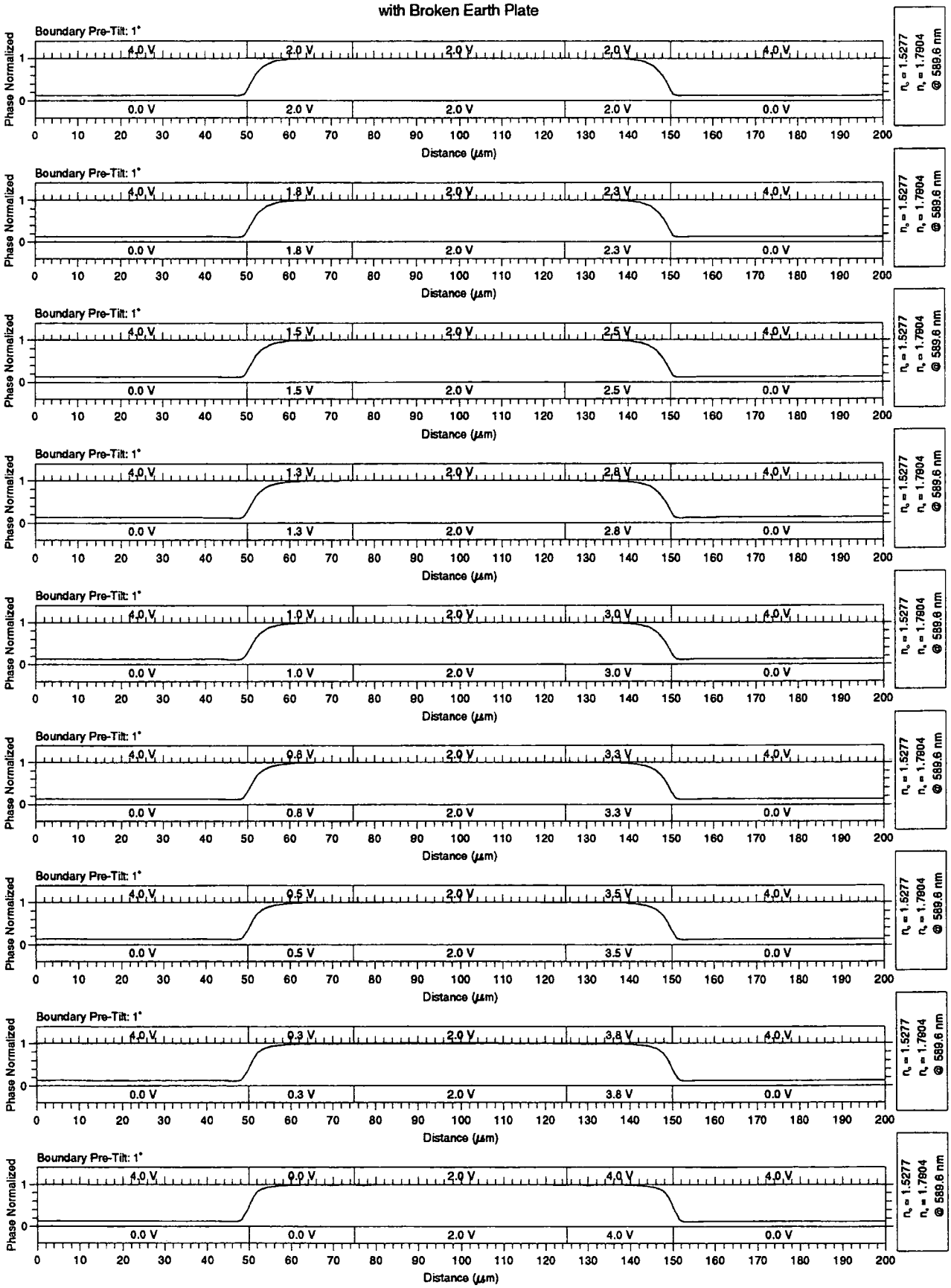

Director Orientation Distribution for a Periodic Liquid Crystal E44 Cell

Symmetrical Etched Earth Plate and Guard Plates

with Broken Earth Plate

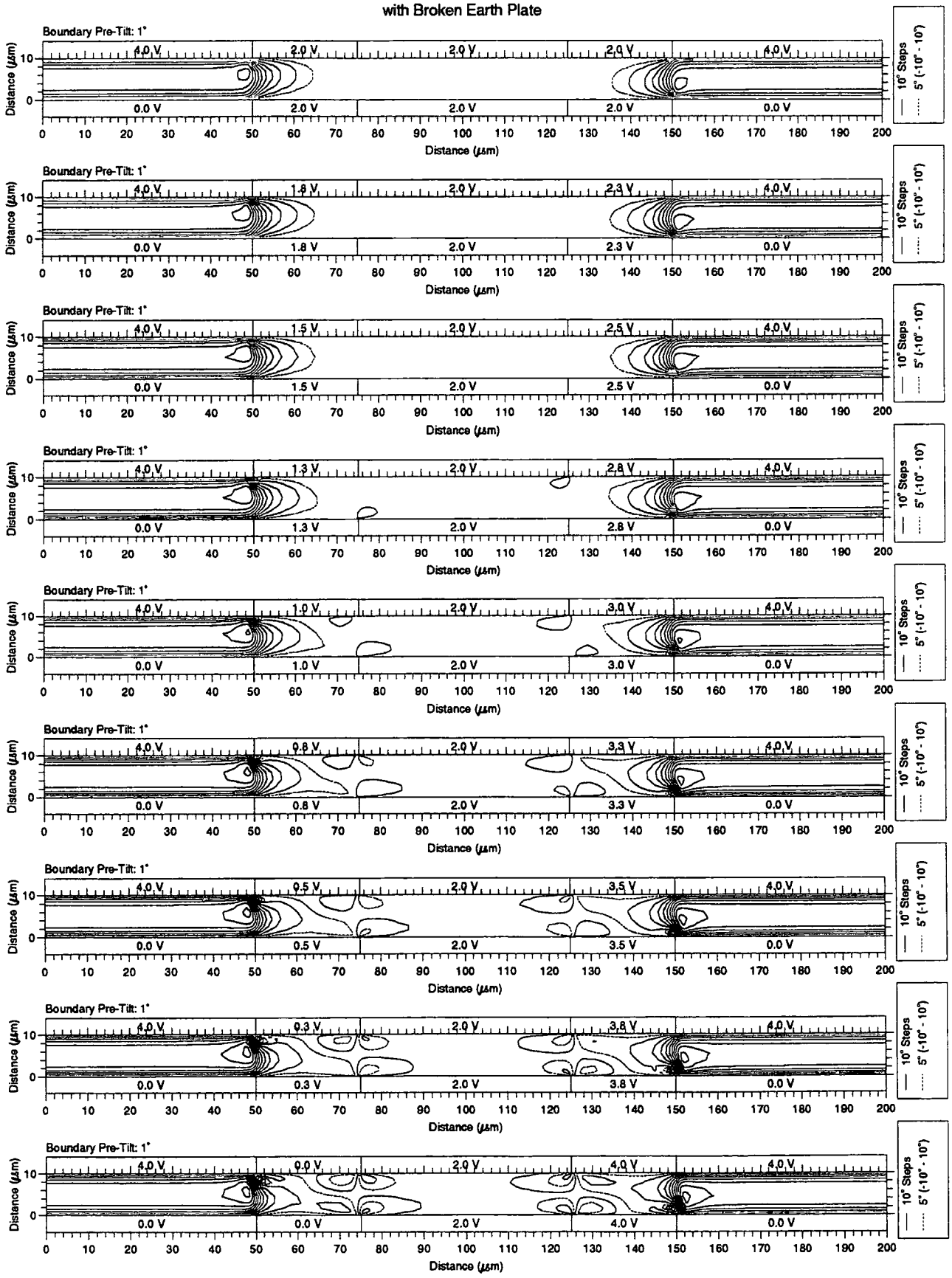

Potential Distribution and Displacement Field for a Periodic Liquid Crystal E44 Cell

Symmetrical Etched Earth Plate and Guard Plates

with Broken Earth Plate

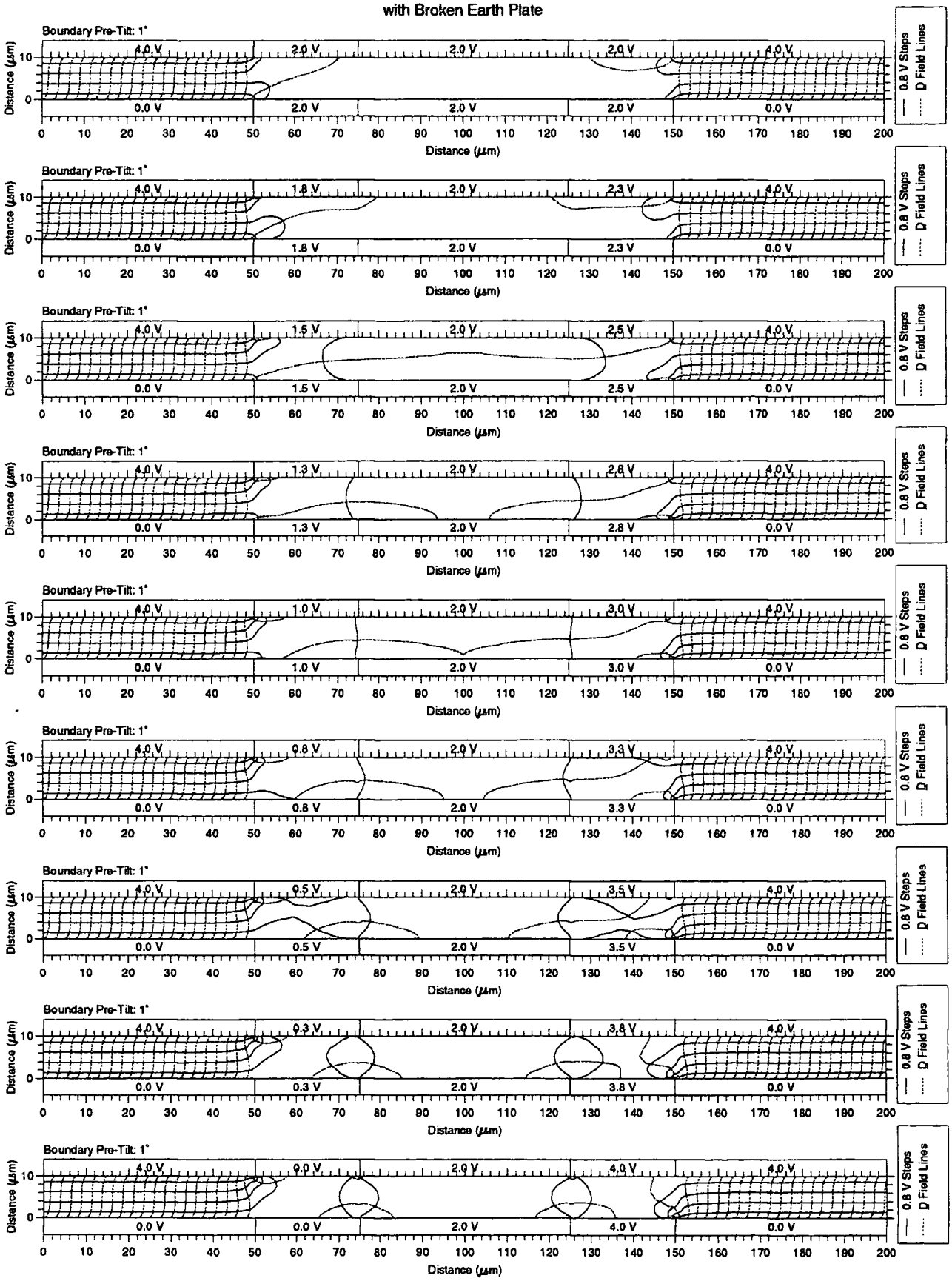

G.1.9 Shifted Broken Guard Plate I

Normalised Phase Distribution for a Periodic Liquid Crystal E44 Cell

Symmetrical Etched Earth Plate and Guard Plates

with Broken and Shifted Earth Plate

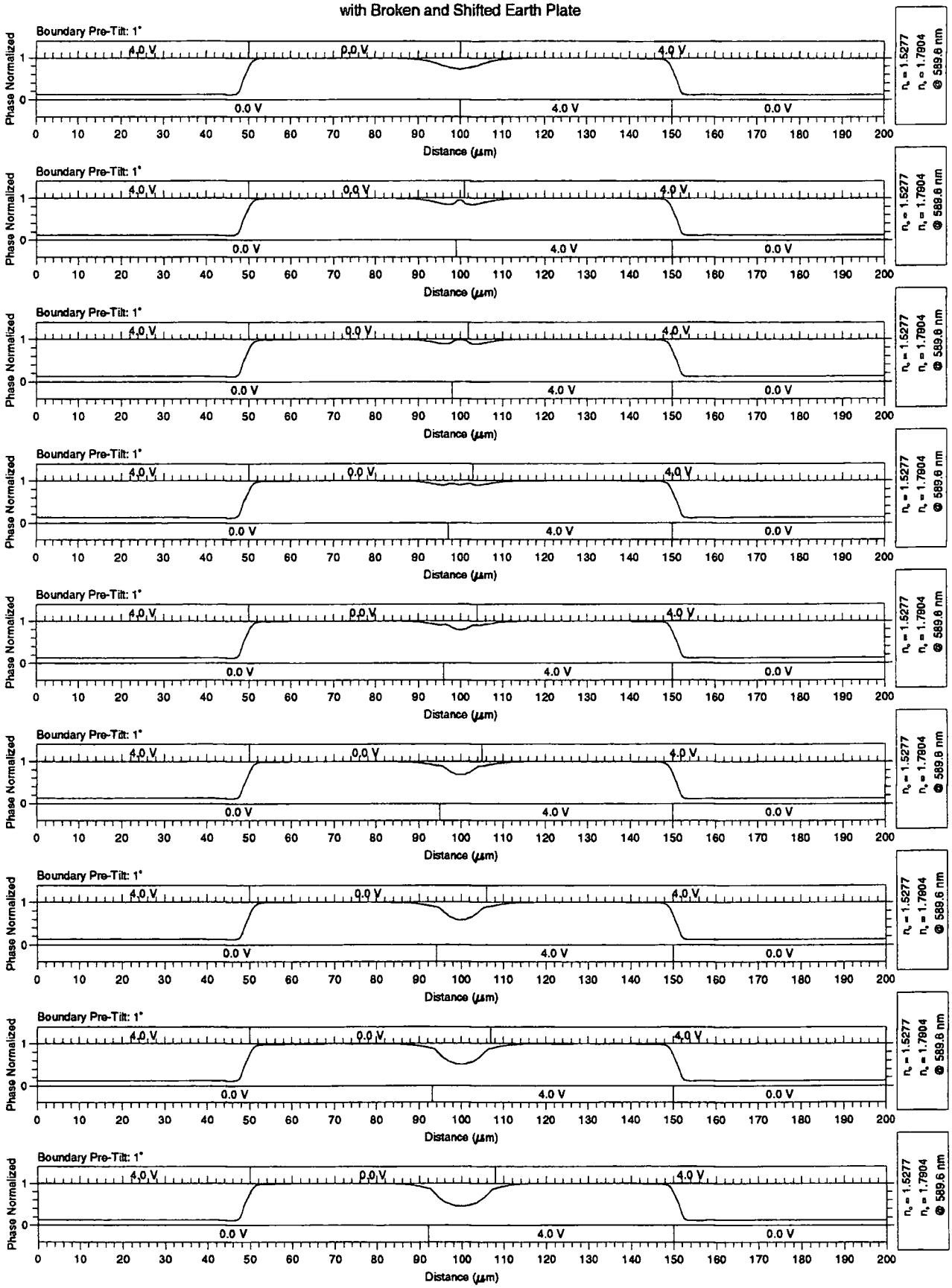

Director Orientation Distribution for a Periodic Liquid Crystal E44 Cell

Symmetrical Etched Earth Plate and Guard Plates

with Broken and Shifted Earth Plate

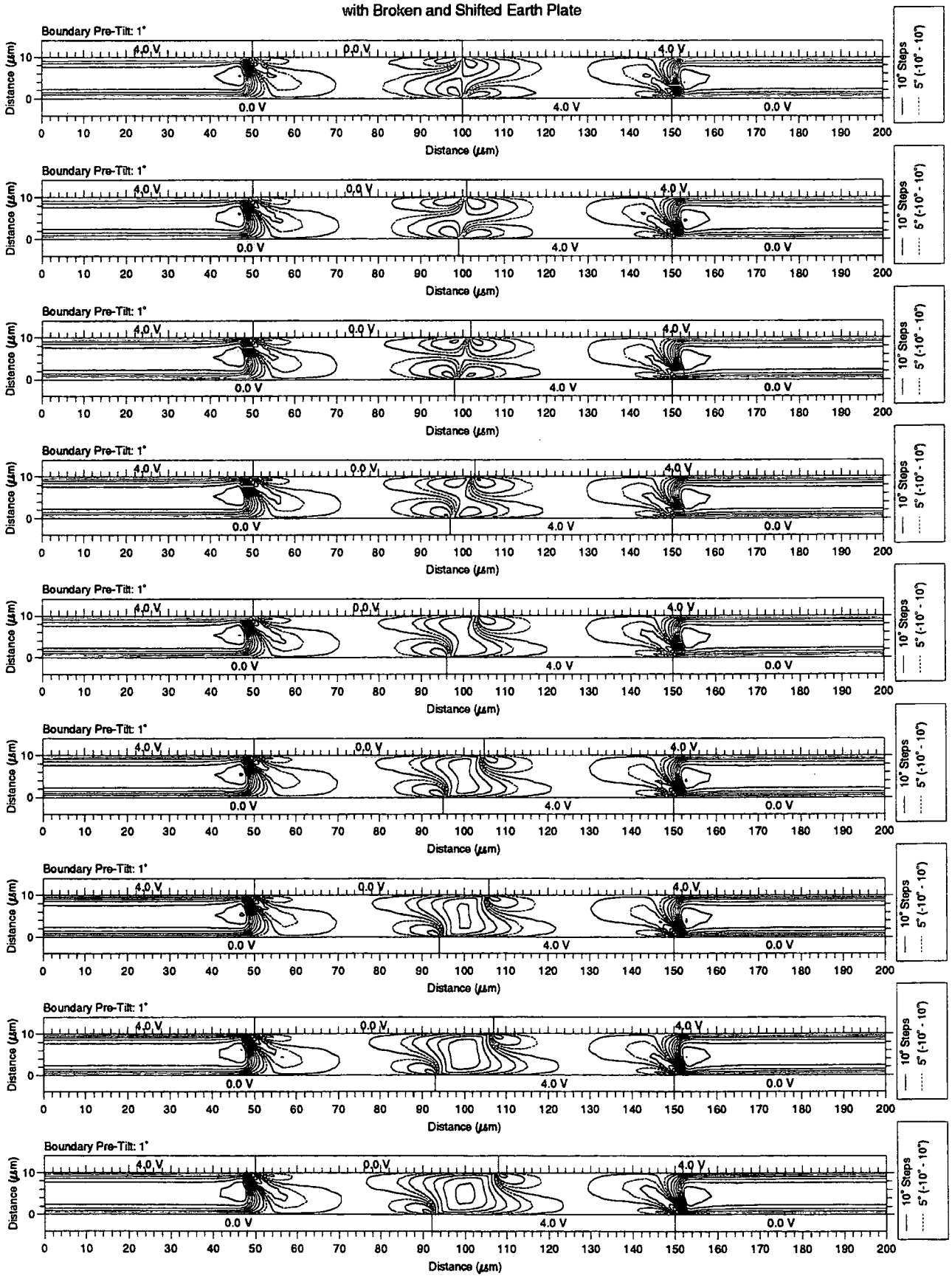

Potential Distribution and Displacement Field for a Periodic Liquid Crystal E44 Cell

Symmetrical Etched Earth Plate and Guard Plates

with Broken and Shifted Earth Plate

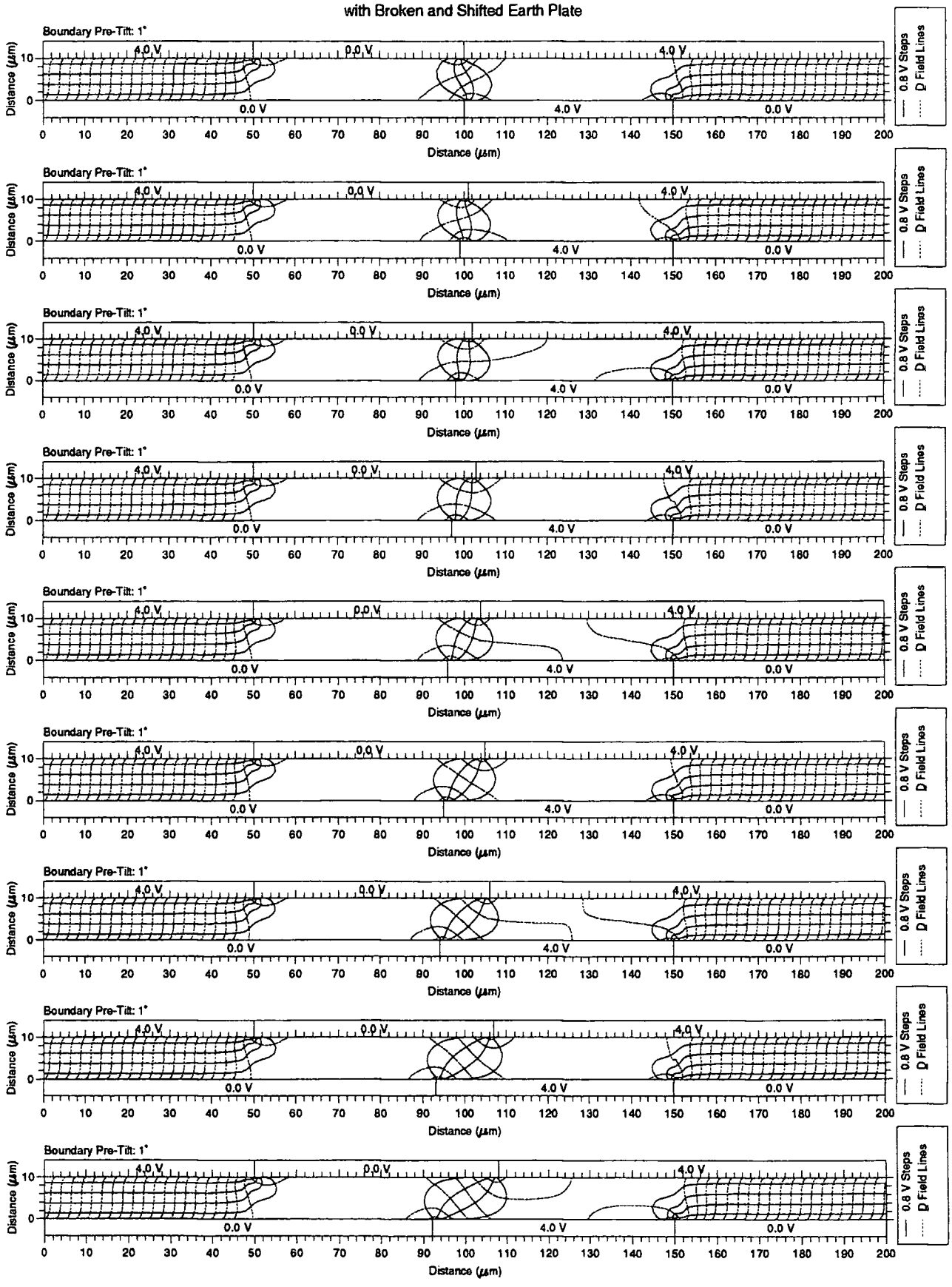

G.1.10 Shifted Broken Guard Plate II

Normalised Phase Distribution for a Periodic Liquid Crystal E44 Cell

Symmetrical Etched Earth Plate and Guard Plates

with Broken and Shifted Earth Plate II

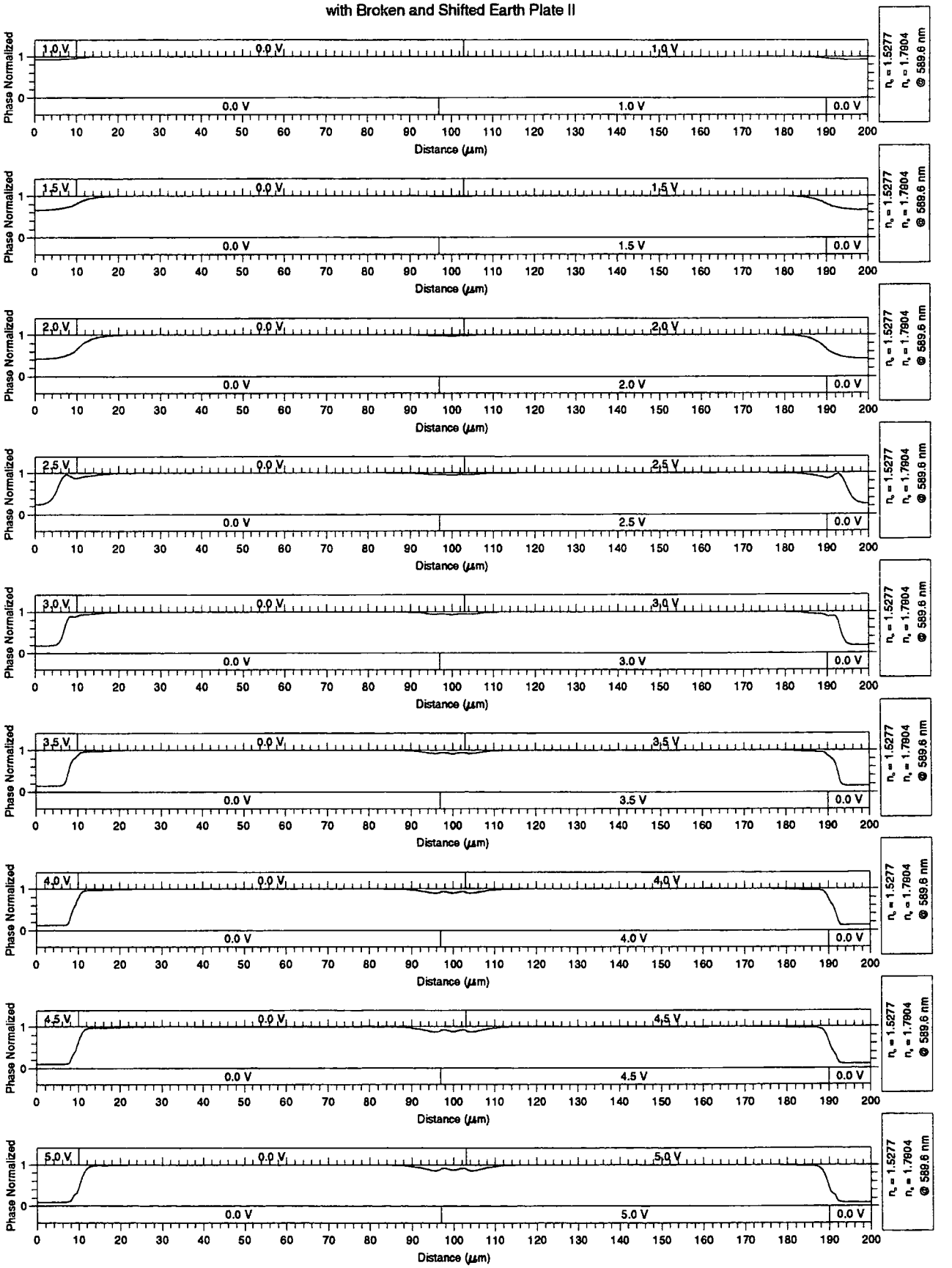

Normalised Phase Distribution for a Periodic Liquid Crystal E44 Cell

Symmetrical Etched Earth Plate and Guard Plates

with Broken and Shifted Earth Plate II

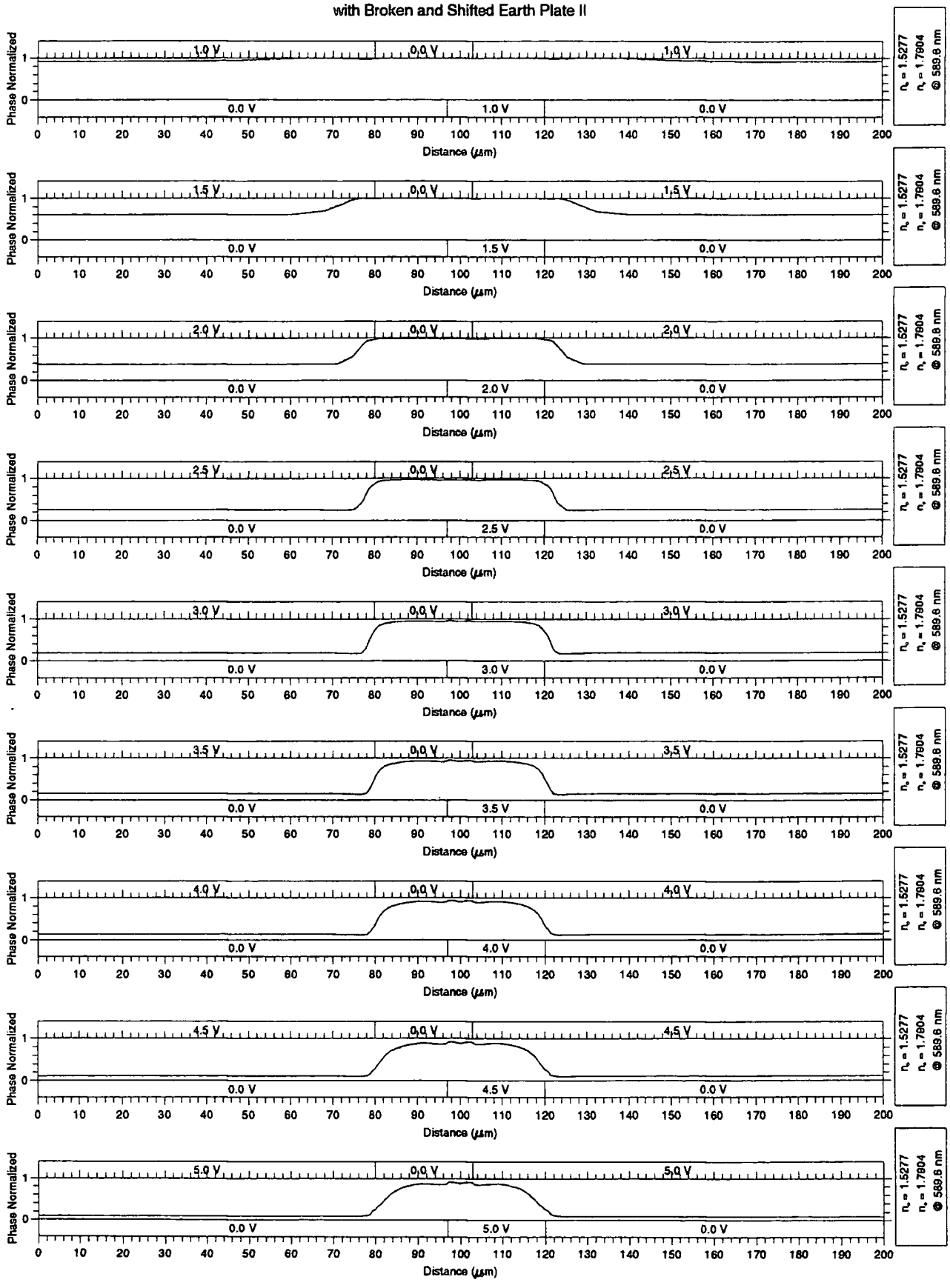

Normalised Phase Distribution for a Periodic Liquid Crystal E44 Cell

Symmetrical Etched Earth Plate and Guard Plates

with Broken and Shifted Earth Plate II

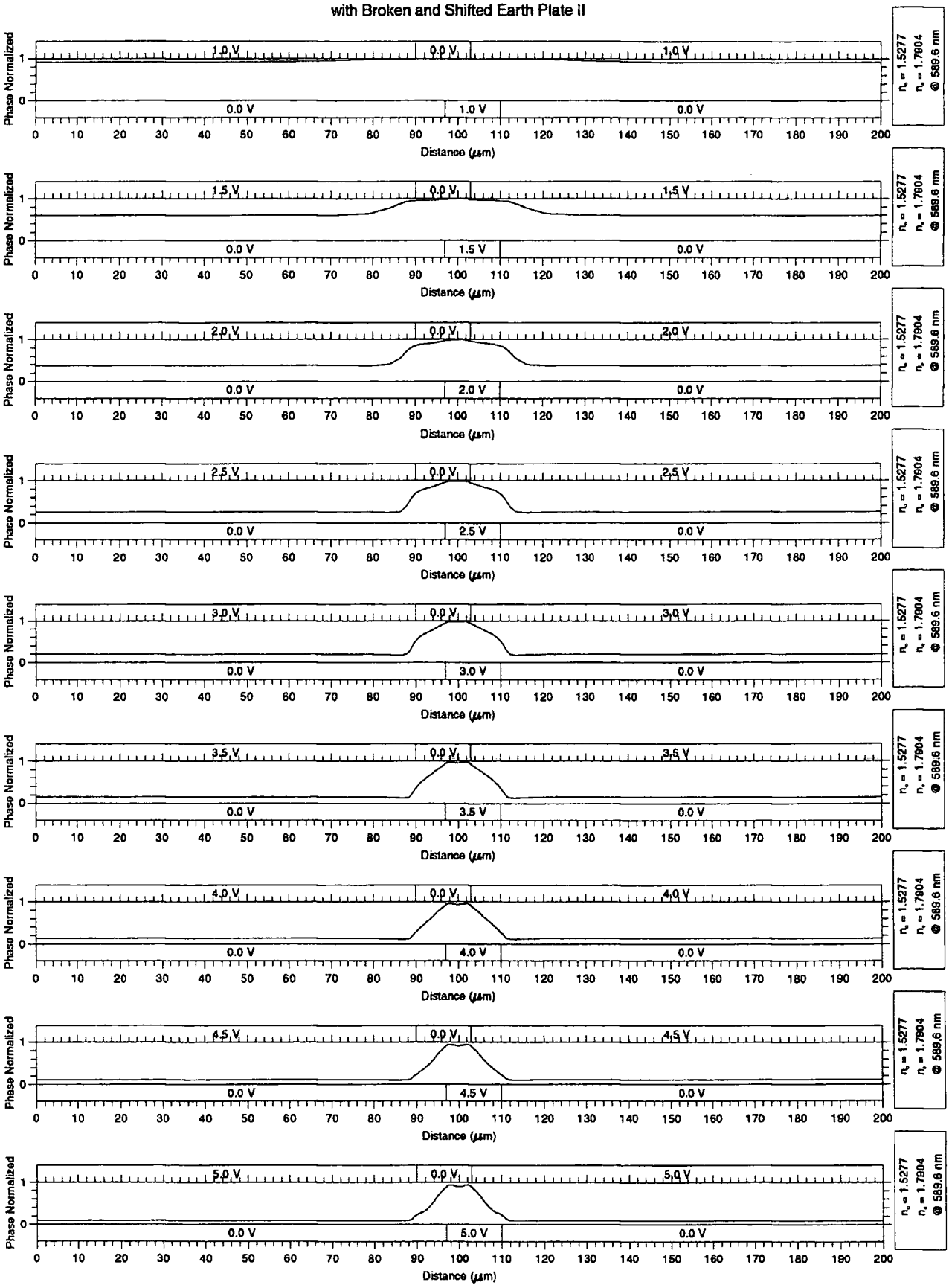

Director Orientation Distribution for a Periodic Liquid Crystal E44 Cell

Symmetrical Etched Earth Plate and Guard Plates

with Broken and Shifted Earth Plate II

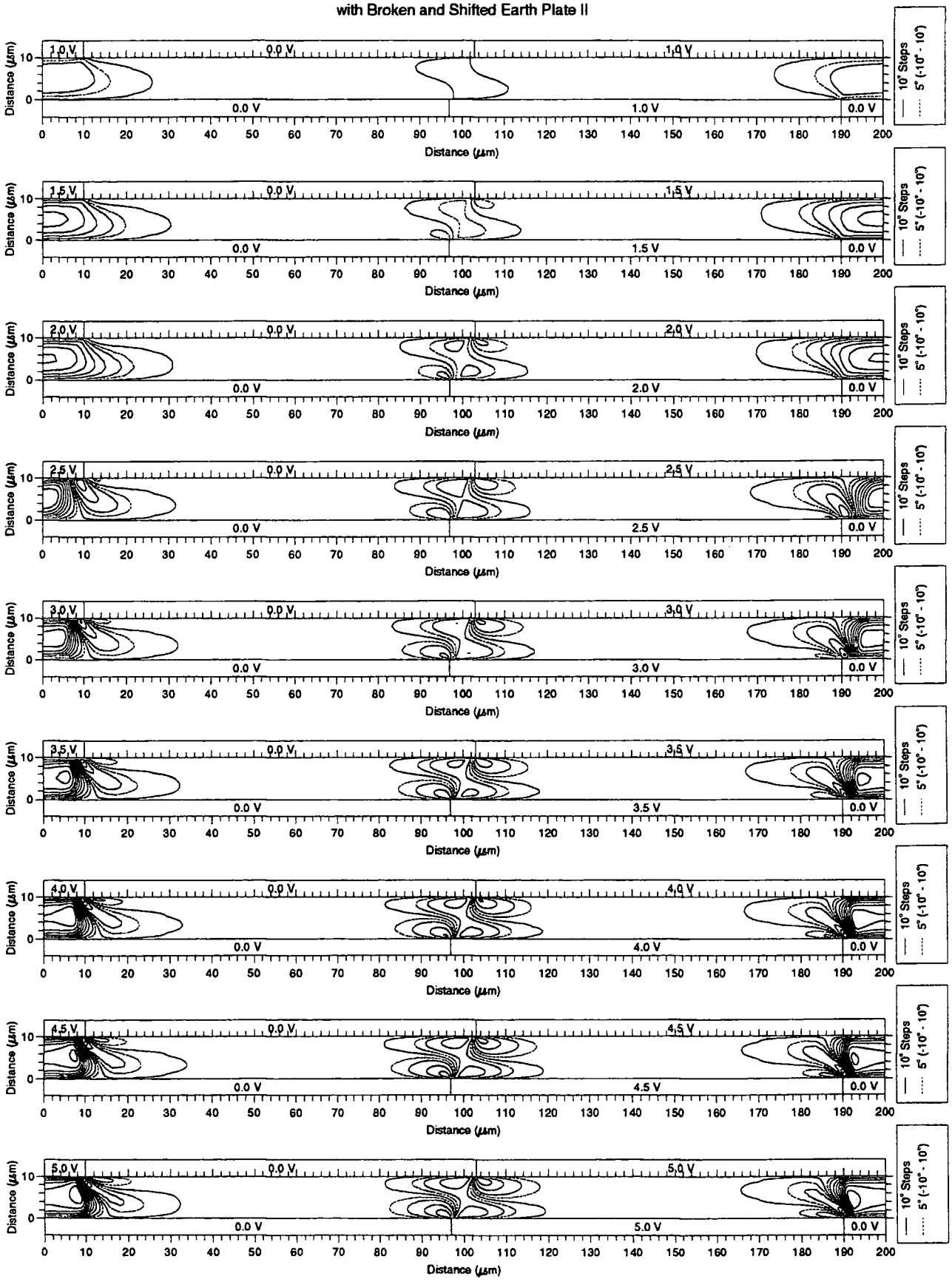

Director Orientation Distribution for a Periodic Liquid Crystal E44 Cell

Symmetrical Etched Earth Plate and Guard Plates

with Broken and Shifted Earth Plate II

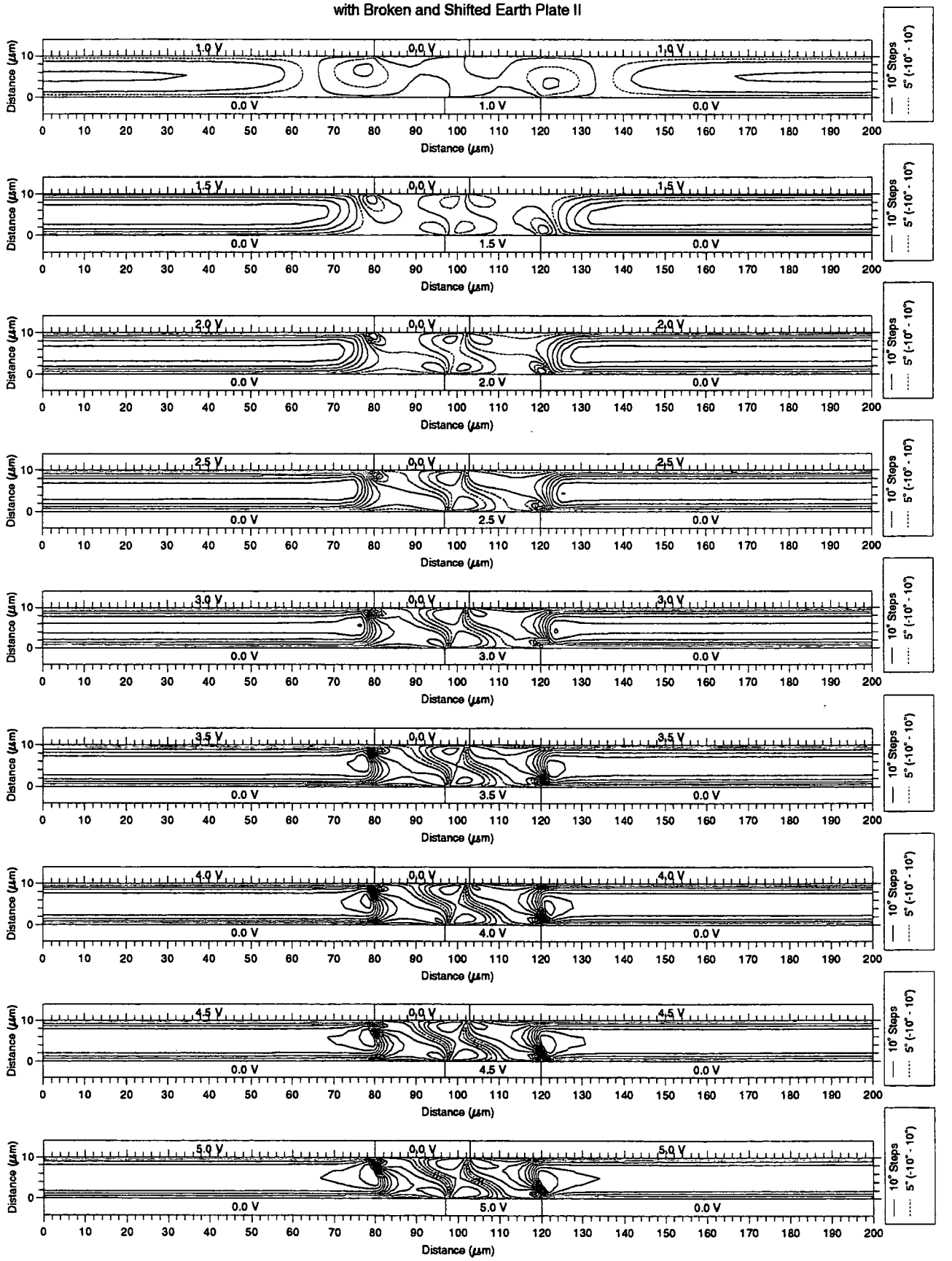

Director Orientation Distribution for a Periodic Liquid Crystal E44 Cell

Symmetrical Etched Earth Plate and Guard Plates

with Broken and Shifted Earth Plate II

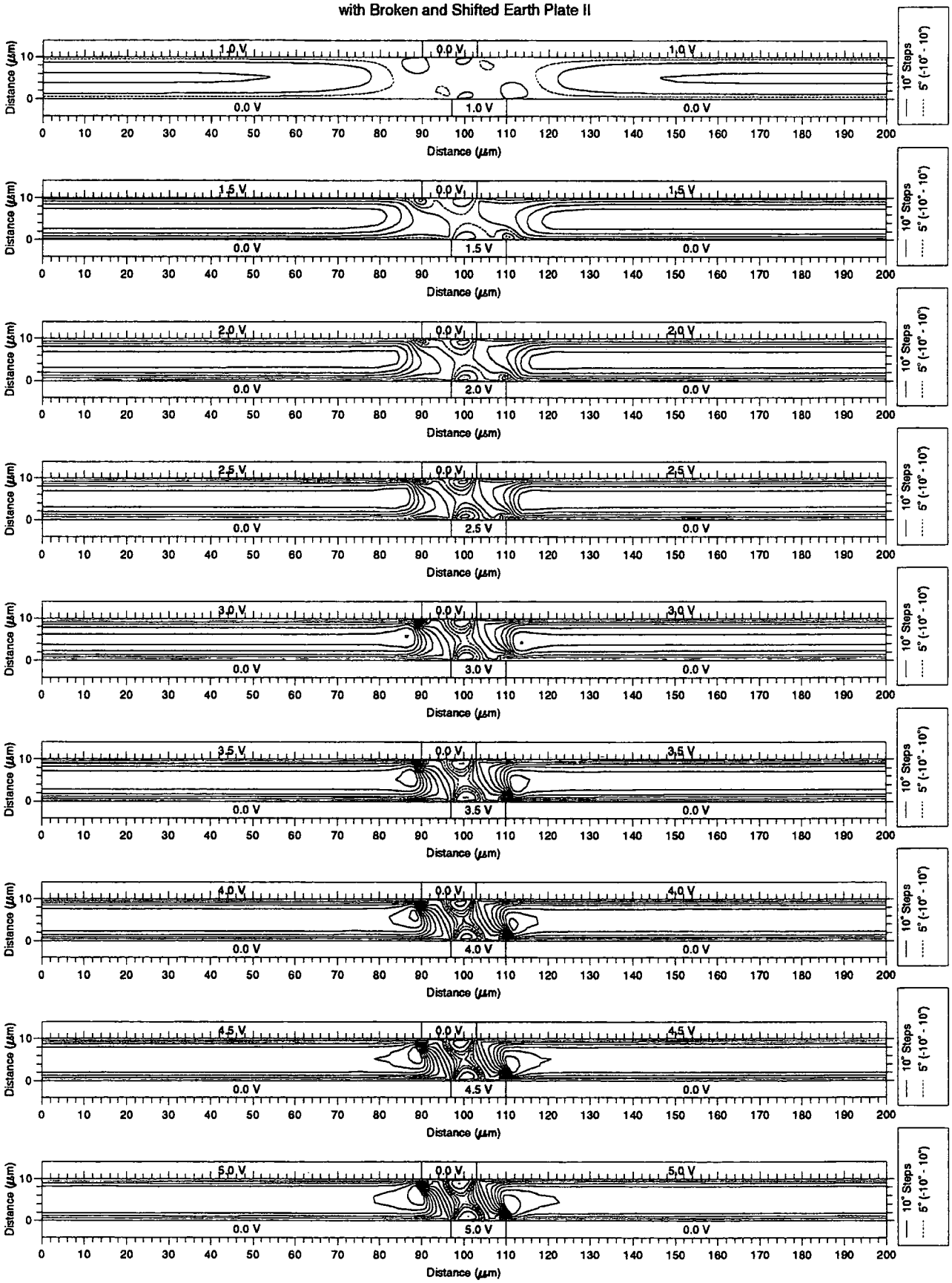

Potential Distribution and Displacement Field for a Periodic Liquid Crystal E44 Cell

Symmetrical Etched Earth Plate and Guard Plates

with Broken and Shifted Earth Plate II

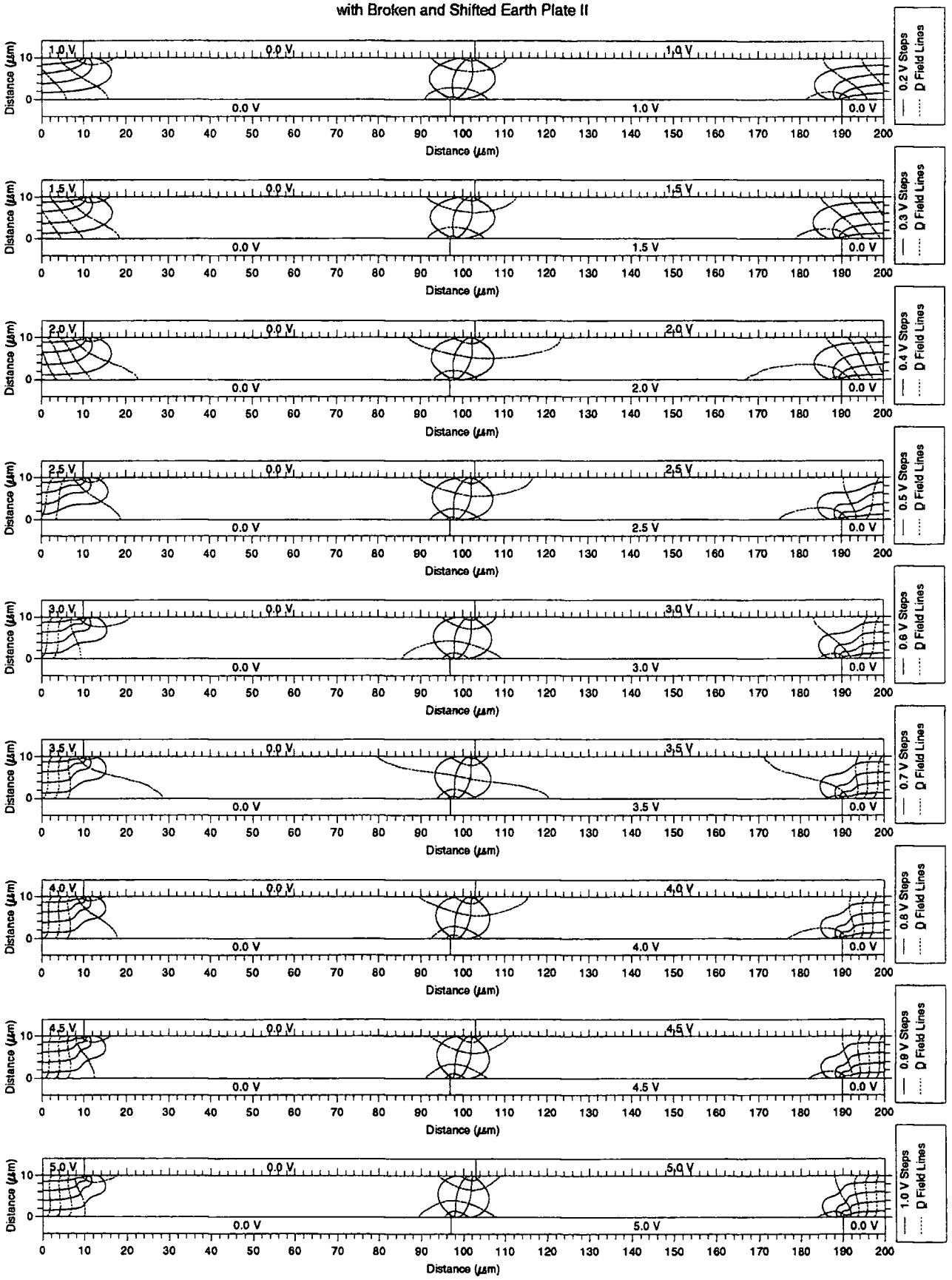

Potential Distribution and Displacement Field for a Periodic Liquid Crystal E44 Cell

Symmetrical Etched Earth Plate and Guard Plates

with Broken and Shifted Earth Plate II

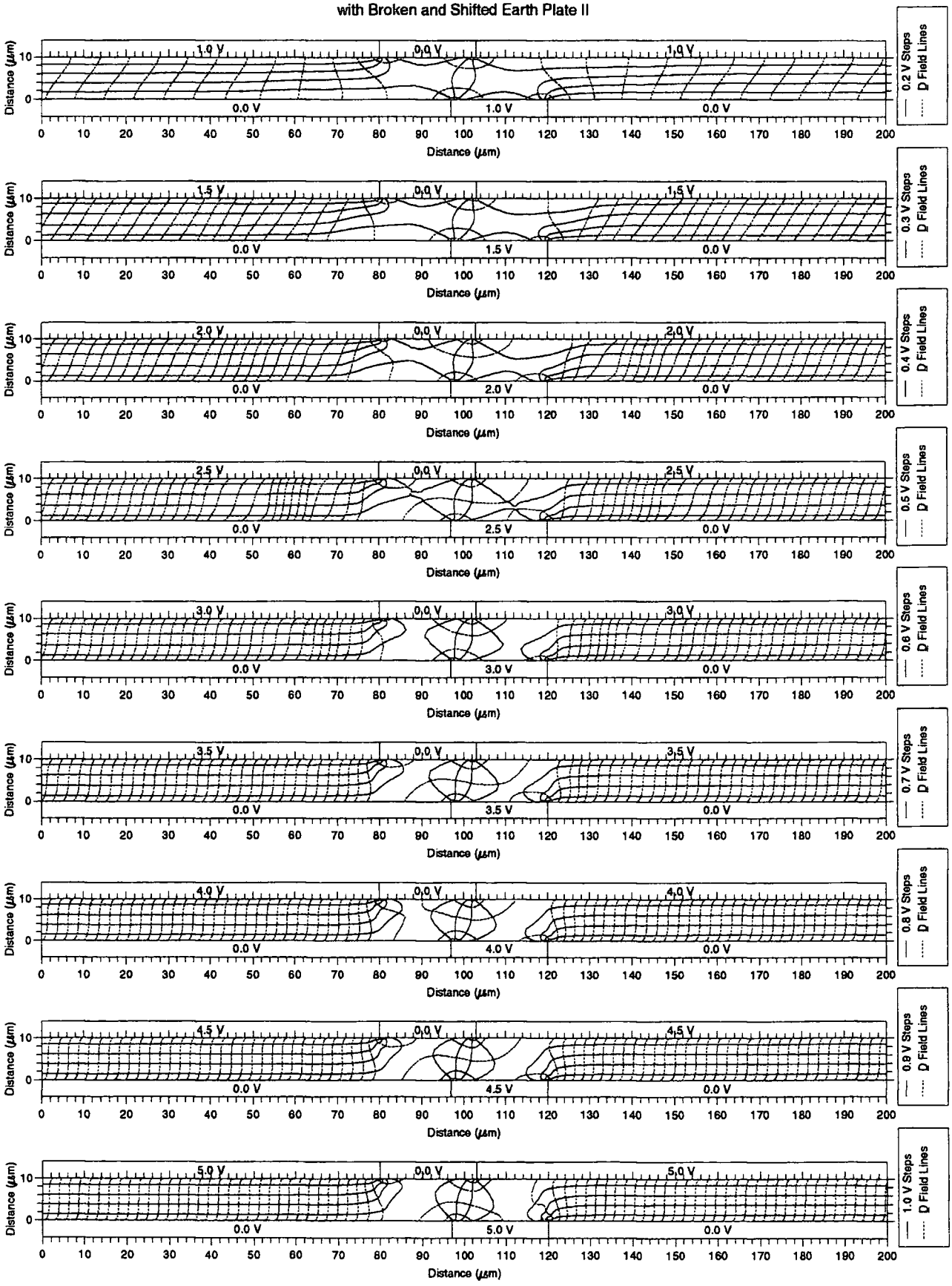

Potential Distribution and Displacement Field for a Periodic Liquid Crystal E44 Cell

Symmetrical Etched Earth Plate and Guard Plates

with Broken and Shifted Earth Plate II

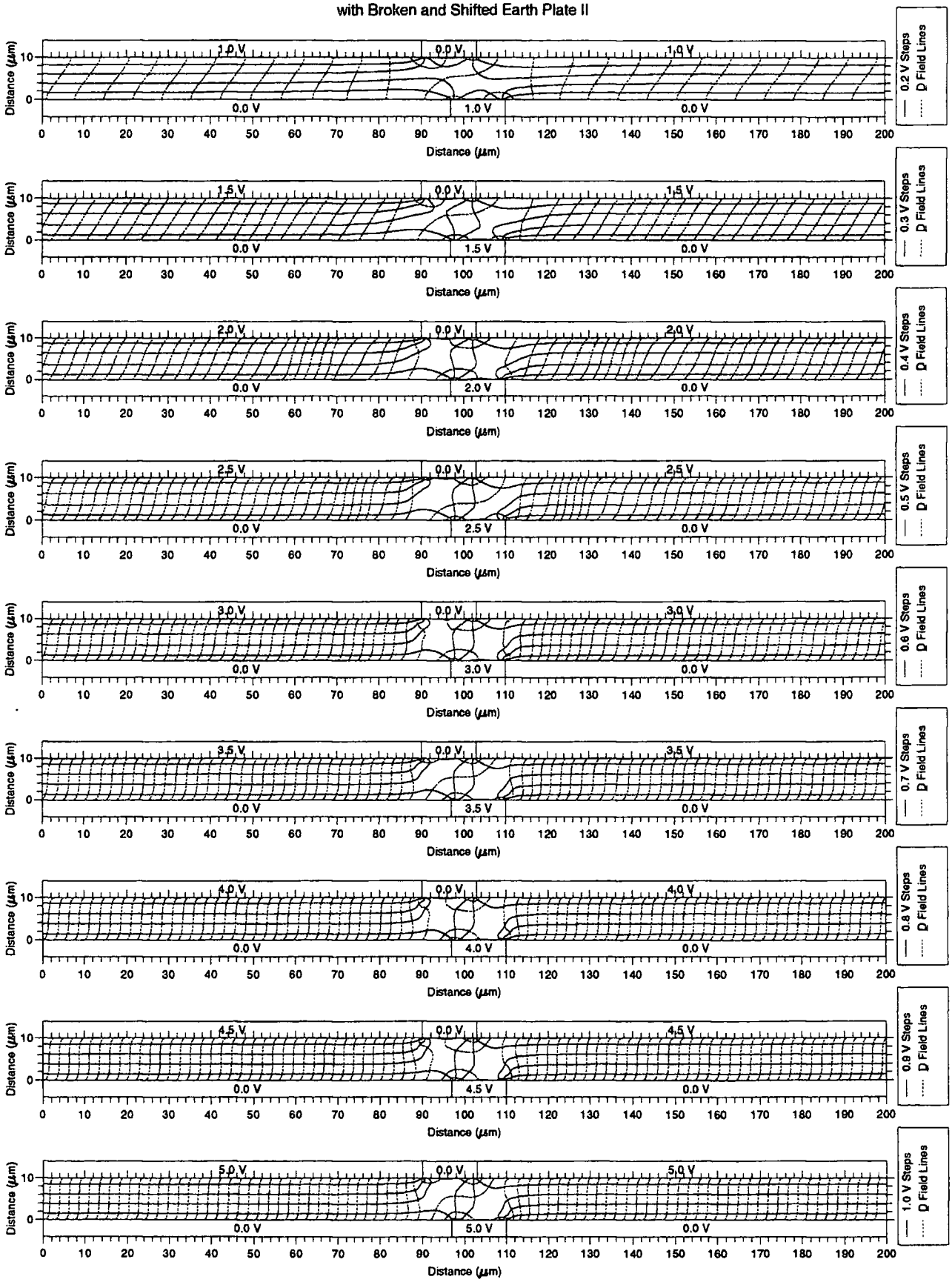

G.1.11 Shifted Broken Guard Plate III

Normalised Phase Distribution for a Periodic Liquid Crystal E44 Cell

Symmetrical Etched Earth Plate and Guard Plates

with Broken and Shifted Earth Plate III

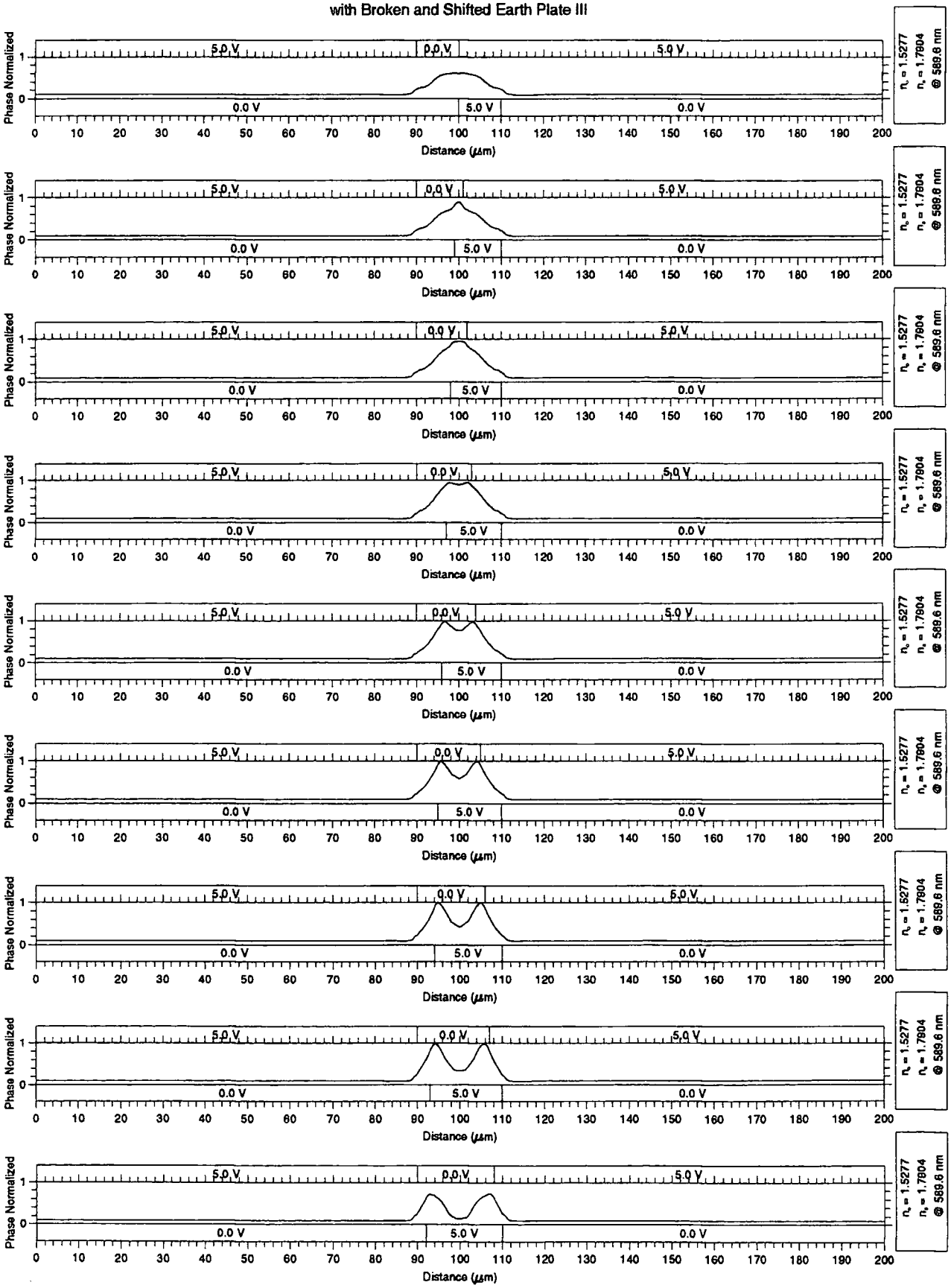

Director Orientation Distribution for a Periodic Liquid Crystal E44 Cell

Symmetrical Etched Earth Plate and Guard Plates

with Broken and Shifted Earth Plate III

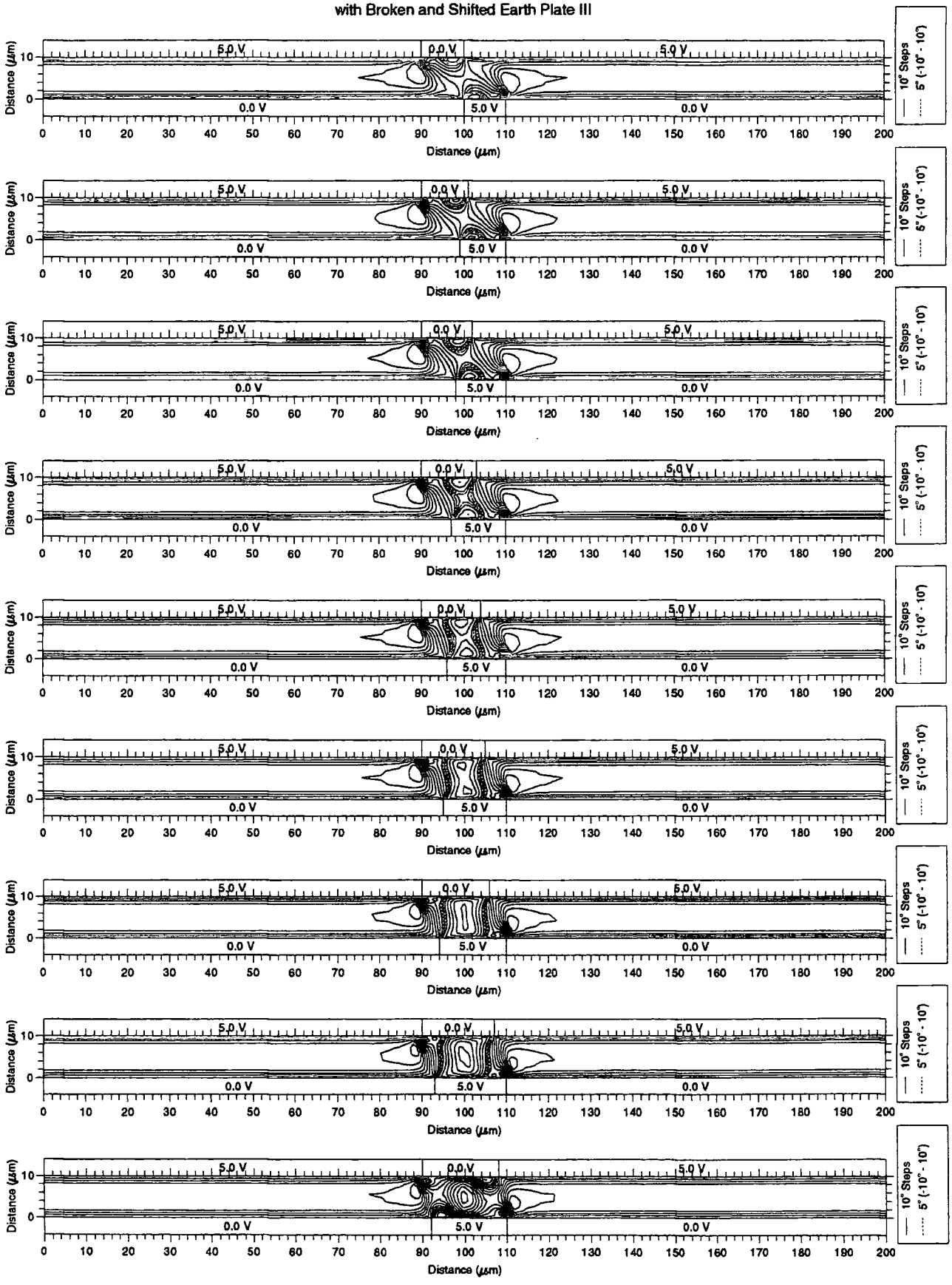

Potential Distribution and Displacement Field for a Periodic Liquid Crystal E44 Cell

Symmetrical Etched Earth Plate and Guard Plates

with Broken and Shifted Earth Plate III

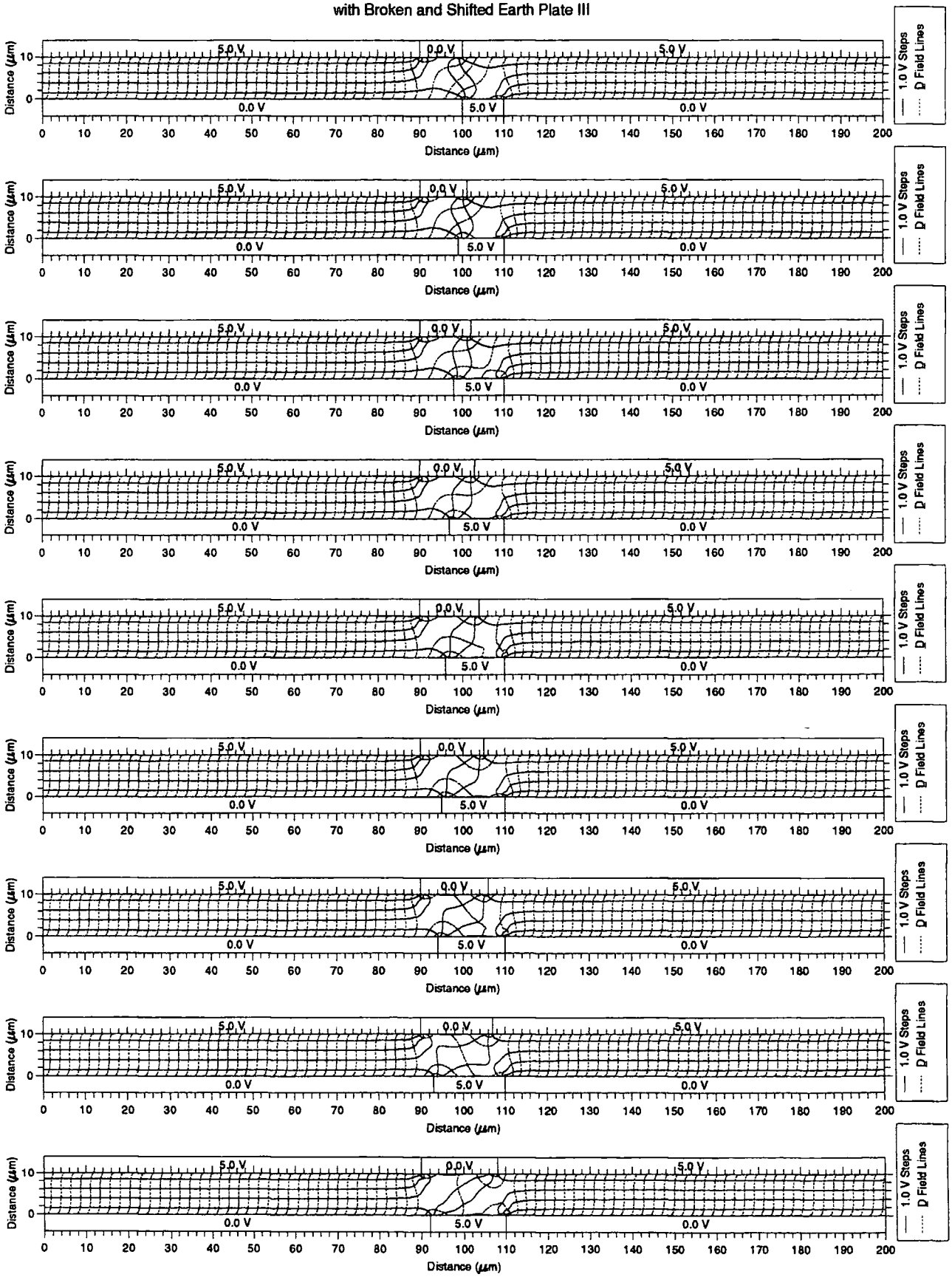

G.1.12 Staggered Guard Plate with Narrow Gaps

Normalised Phase Distribution for a Periodic Liquid Crystal E44 Cell

Staggered Etched Earth Plate and Guard Plates

with Narrow Gaps

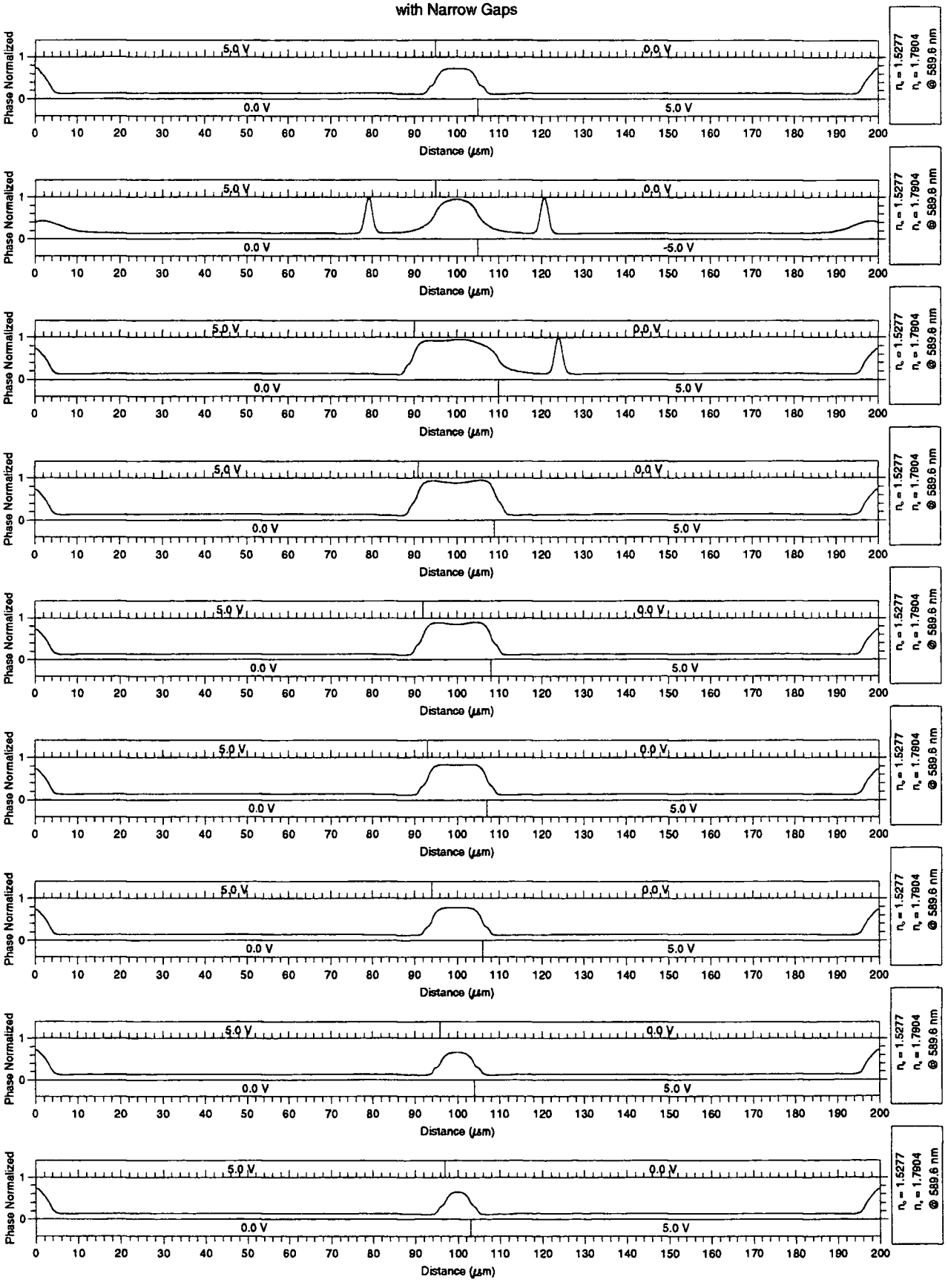

Director Orientation Distribution for a Periodic Liquid Crystal E44 Cell

Staggered Etched Earth Plate and Guard Plates

with Narrow Gaps

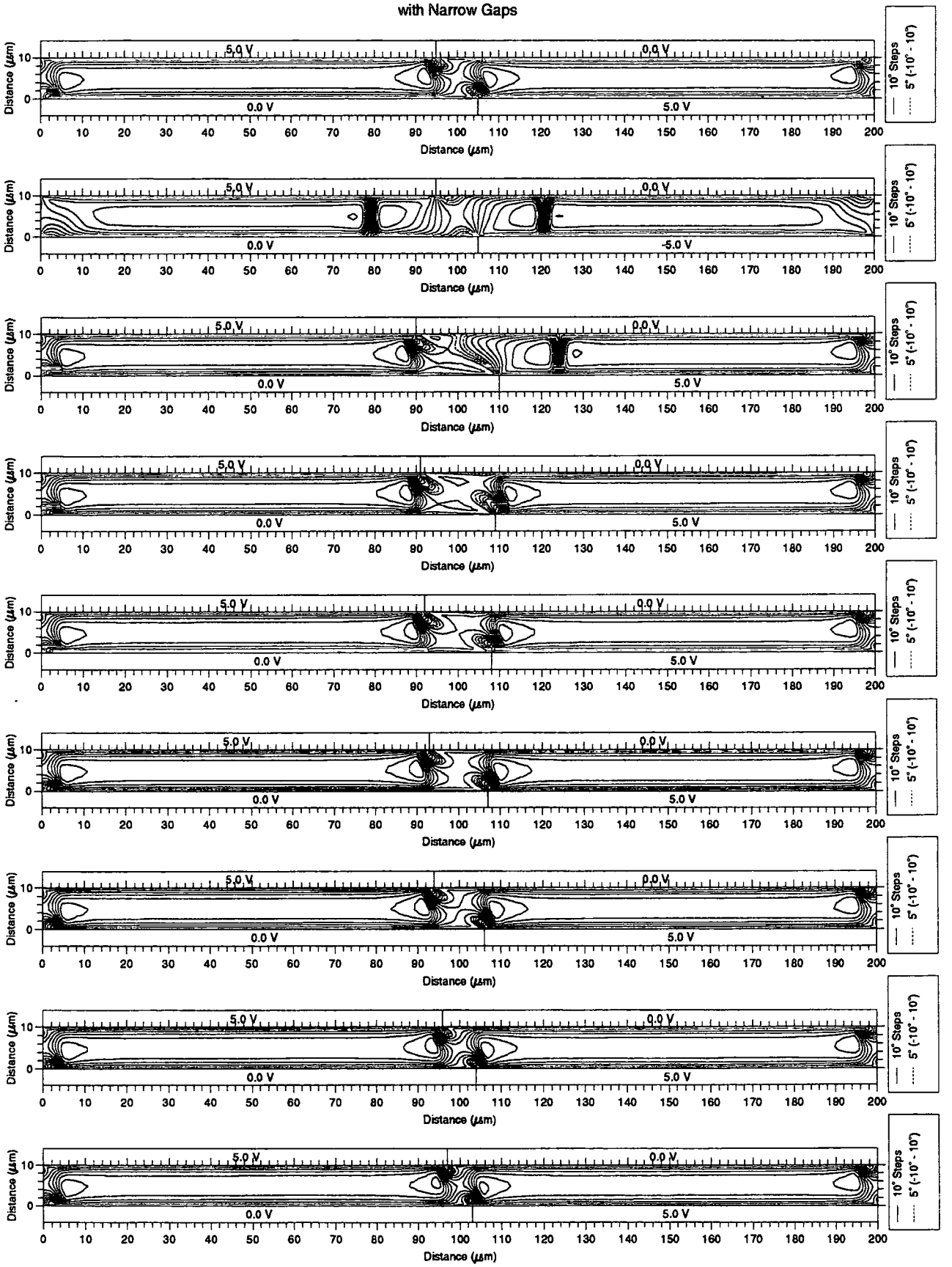

Potential Distribution and Displacement Field for a Periodic Liquid Crystal E44 Cell

Staggered Etched Earth Plate and Guard Plates

with Narrow Gaps

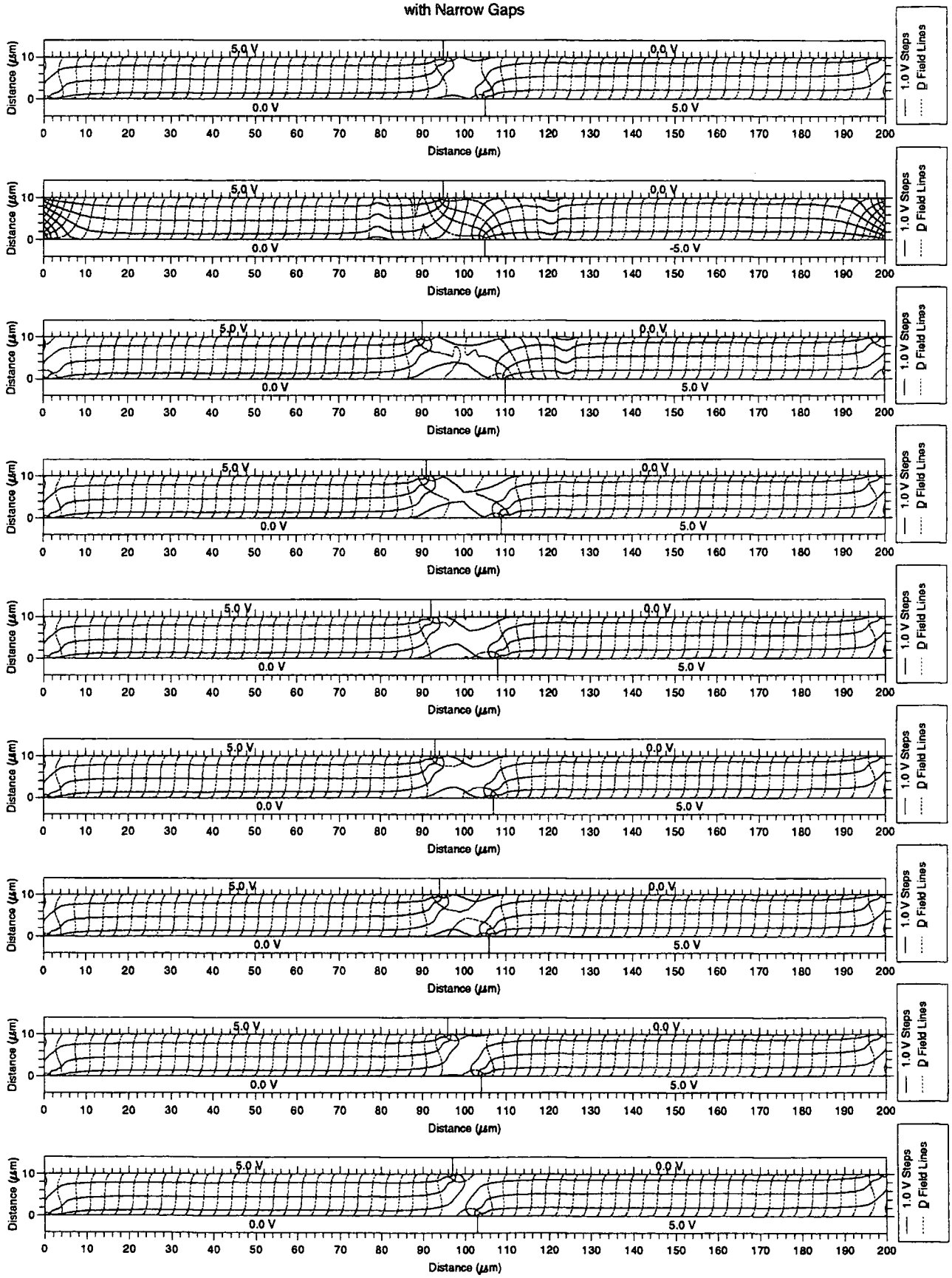

G.1.13 Vaiety of Electrode Structures with Narrow Gaps

Normalised Phase Distribution for a Periodic Liquid Crystal E44 Cell

A Variety of Electrode Structures

with Narrow Electrodes and Gaps

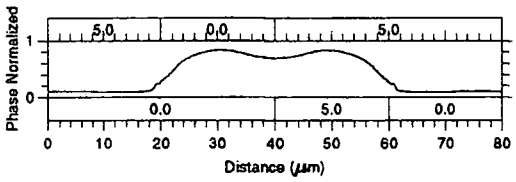

n_o = 1.5277
n_e = 1.7804
@ 589.6 nm

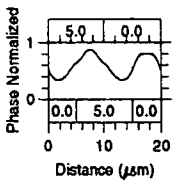

n_o = 1.5277
n_e = 1.7804
@ 589.6 nm

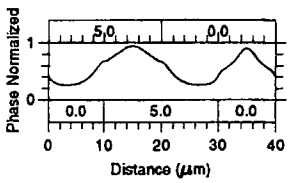

n_o = 1.5277
n_e = 1.7804
@ 589.6 nm

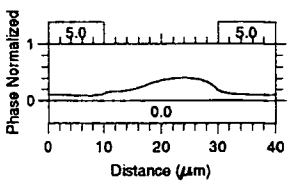

n_o = 1.5277
n_e = 1.7804
@ 589.6 nm

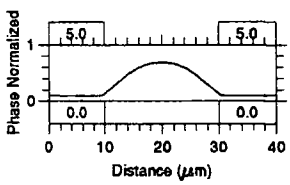

n_o = 1.5277
n_e = 1.7804
@ 589.6 nm

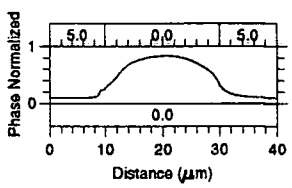

n_o = 1.5277
n_e = 1.7804
@ 589.6 nm

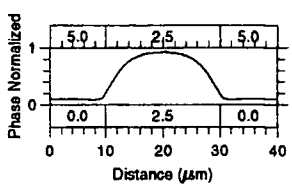

n_o = 1.5277
n_e = 1.7804
@ 589.6 nm

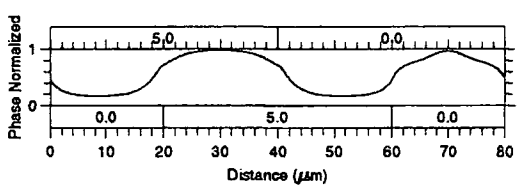

n_o = 1.5277
n_e = 1.7804
@ 589.6 nm

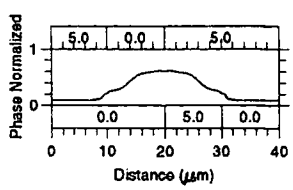

n_o = 1.5277
n_e = 1.7804
@ 589.6 nm

Director Orientation Distribution for a Periodic Liquid Crystal E44 Cell

A Variety of Electrode Structures

with Narrow Electrodes and Gaps

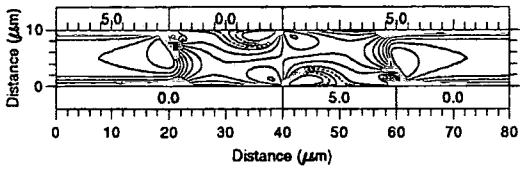

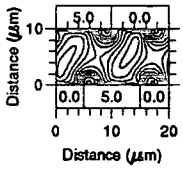

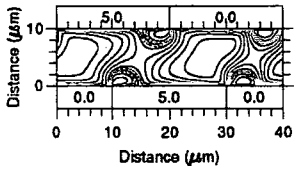

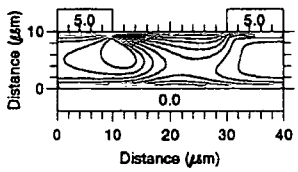

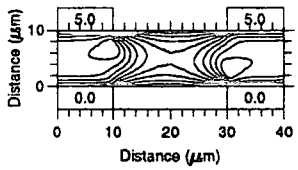

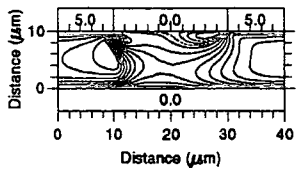

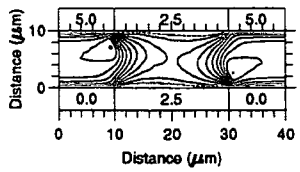

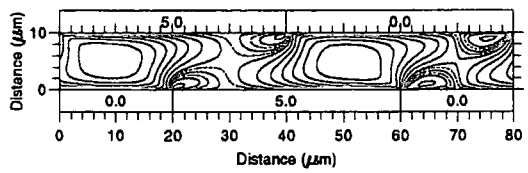

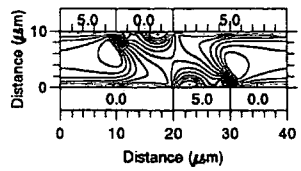

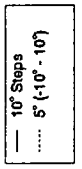

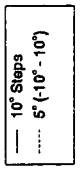

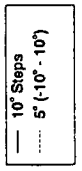

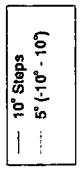

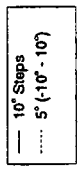

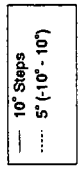

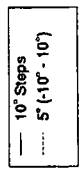

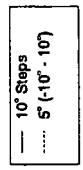

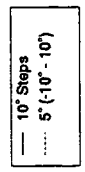

Potential Distribution and Displacement Field for a Periodic Liquid Crystal E44 Cell

A Variety of Electrode Structures

with Narrow Electrodes and Gaps

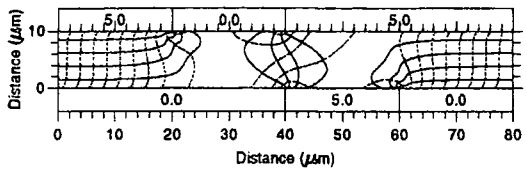

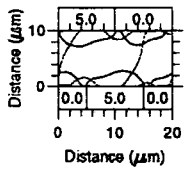

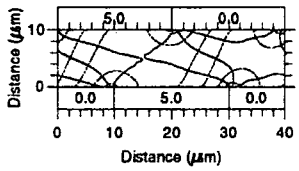

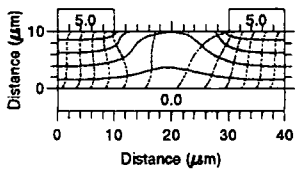

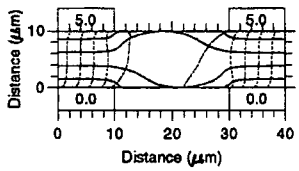

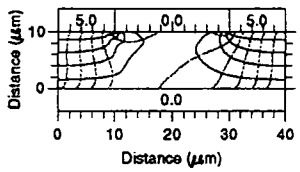

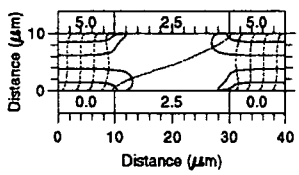

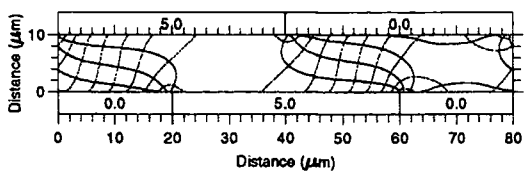

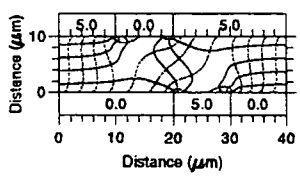

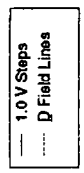

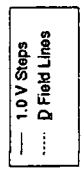

G.2 Refractive Structure

G.2.1 Simple Electrode Structure with Narrowing Gap

Normalised Phase Distribution for a Periodic Liquid Crystal E44 Cell

A Variety of Electrode Structures

with Narrow Electrodes and Gaps

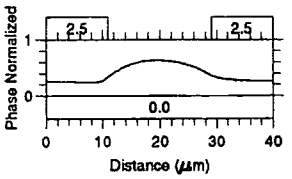

n_o = 1.5277
n_e = 1.7904
@ 589.6 nm

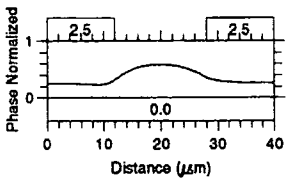

n_o = 1.5277
n_e = 1.7904
@ 589.6 nm

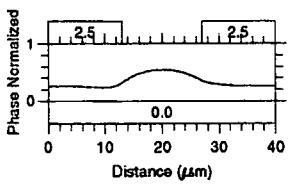

n_o = 1.5277
n_e = 1.7904
@ 589.6 nm

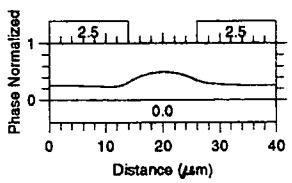

n_o = 1.5277
n_e = 1.7904
@ 589.6 nm

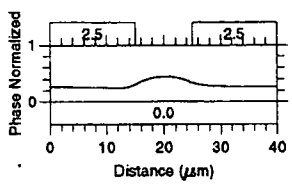

n_o = 1.5277
n_e = 1.7904
@ 589.6 nm

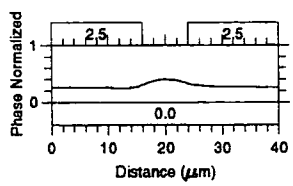

n_o = 1.5277
n_e = 1.7904
@ 589.6 nm

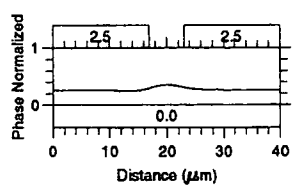

n_o = 1.5277
n_e = 1.7904
@ 589.6 nm

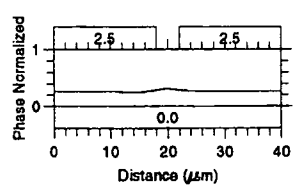

n_o = 1.5277
n_e = 1.7904
@ 589.6 nm

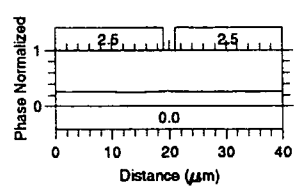

n_o = 1.5277
n_e = 1.7904
@ 589.6 nm

Director Orientation Distribution for a Periodic Liquid Crystal E44 Cell

A Variety of Electrode Structures

with Narrow Electrodes and Gaps

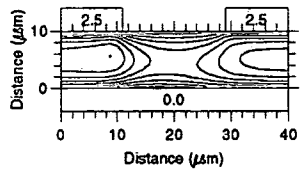

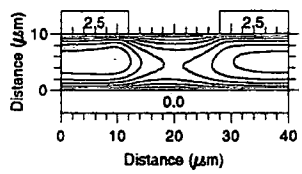

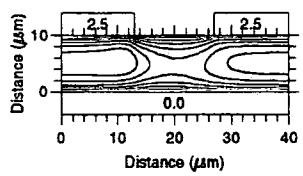

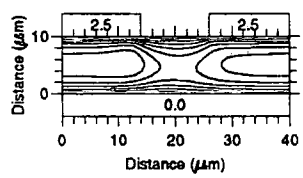

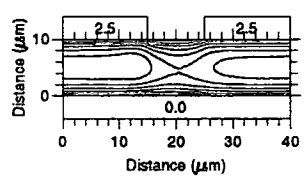

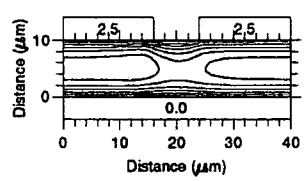

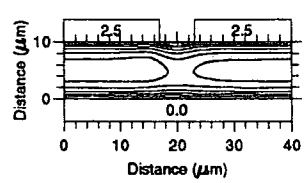

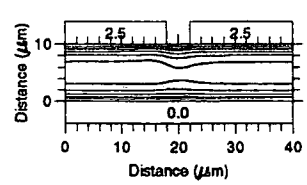

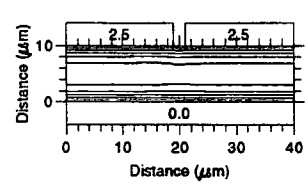

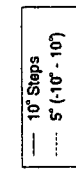

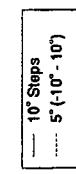

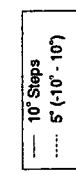

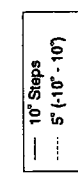

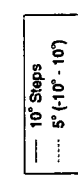

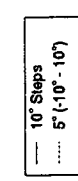

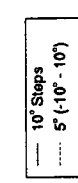

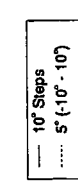

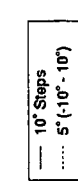

Potential Distribution and Displacement Field for a Periodic Liquid Crystal E44 Cell

A Variety of Electrode Structures

with Narrow Electrodes and Gaps

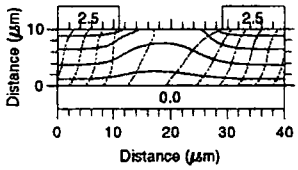

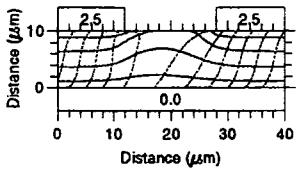

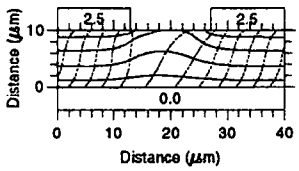

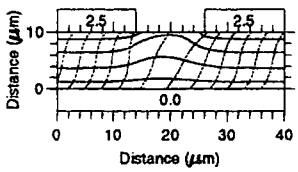

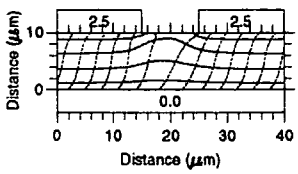

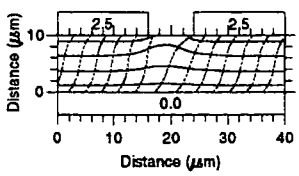

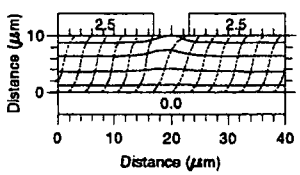

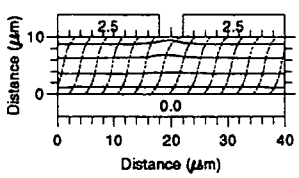

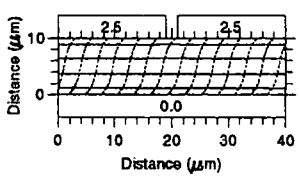

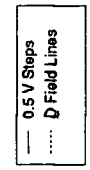

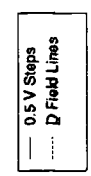

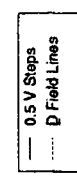

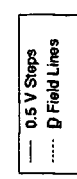

G.2.2 Buried Electrode Structure

Normalised Phase Distribution for a Periodic Liquid Crystal E44 Cell

Buried Electrode Structure

with Decreasing Depth

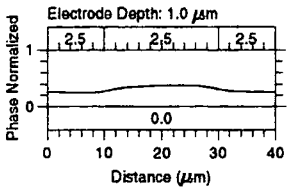

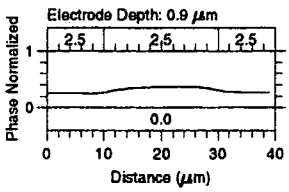

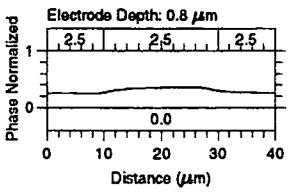

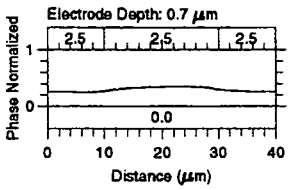

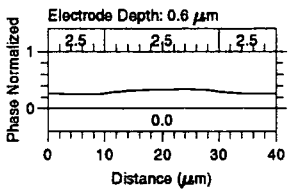

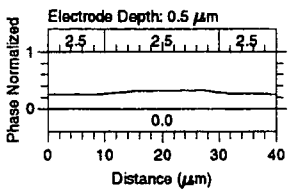

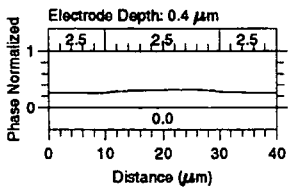

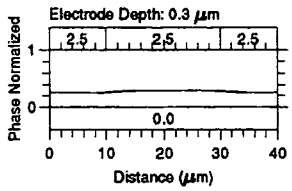

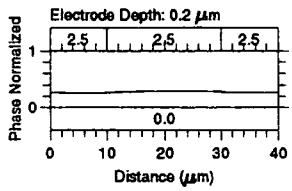

n_o = 1.5277
n_e = 1.7804
@ 589.6 nm

n_o = 1.5277
n_e = 1.7804
@ 589.6 nm

n_o = 1.5277
n_e = 1.7804
@ 589.6 nm

n_o = 1.5277
n_e = 1.7804
@ 589.6 nm

n_o = 1.5277
n_e = 1.7804
@ 589.6 nm

n_o = 1.5277
n_e = 1.7804
@ 589.6 nm

n_o = 1.5277
n_e = 1.7804
@ 589.6 nm

n_o = 1.5277
n_e = 1.7804
@ 589.6 nm

n_o = 1.5277
n_e = 1.7804
@ 589.6 nm

Director Orientation Distribution for a Periodic Liquid Crystal E44 Cell

Buried Electrode Structure

with Decreasing Depth

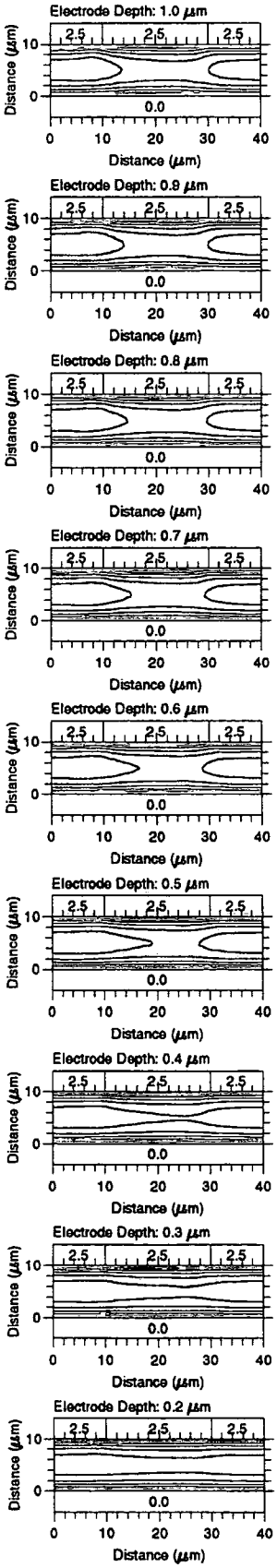

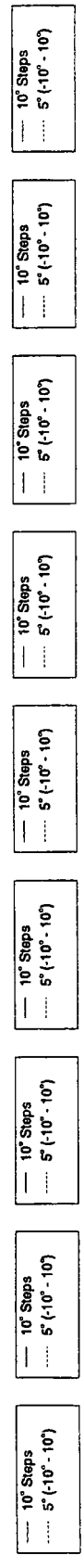

Potential Distribution and Displacement Field for a Periodic Liquid Crystal E44 Cell

Buried Electrode Structure

with Decreasing Depth

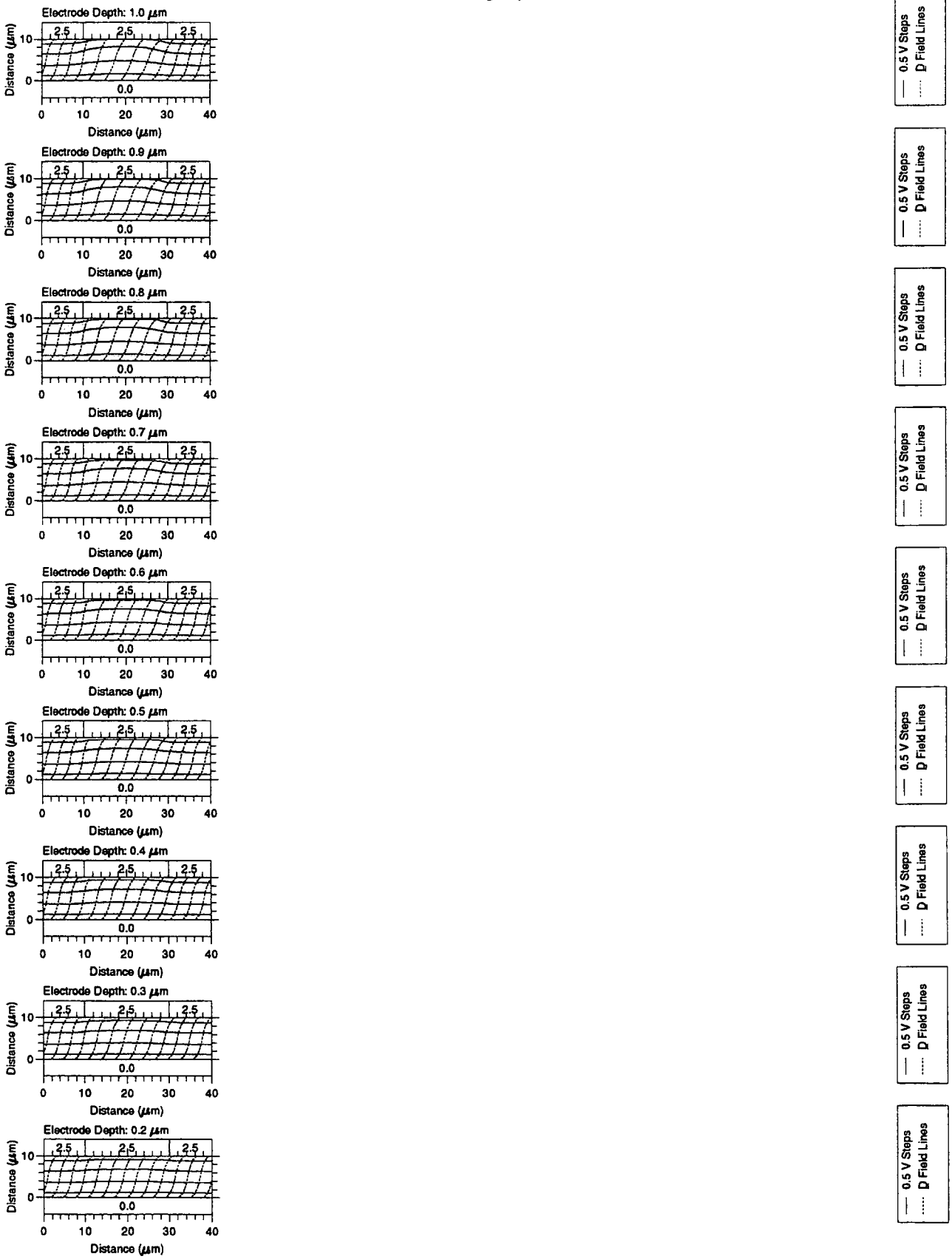

G.3 Diffractive/Refractive Structure

G.3.1 Linear Ramp Structures

Normalised Phase Distribution for a Periodic Liquid Crystal E44 Cell

Linear Ramp Structures

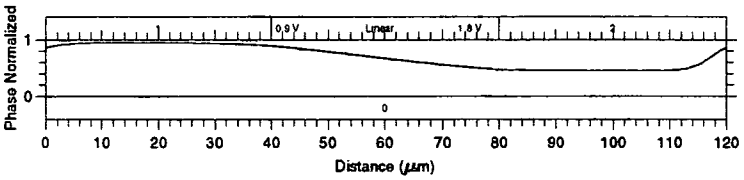

n_o = 1.5277
n_e = 1.7804
@ 589.6 nm

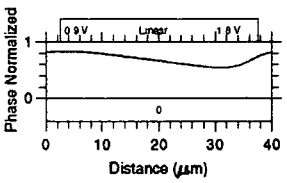

n_o = 1.5277
n_e = 1.7804
@ 589.6 nm

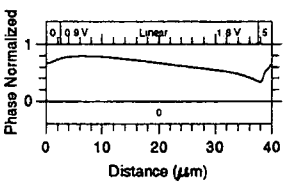

n_o = 1.5277
n_e = 1.7804
@ 589.6 nm

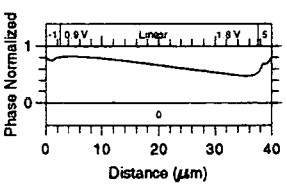

n_o = 1.5277
n_e = 1.7804
@ 589.6 nm

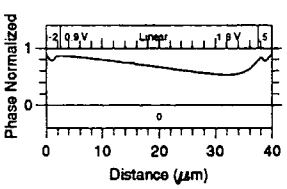

n_o = 1.5277
n_e = 1.7804
@ 589.6 nm

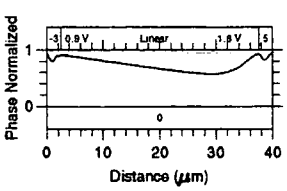

n_o = 1.5277
n_e = 1.7804
@ 589.6 nm

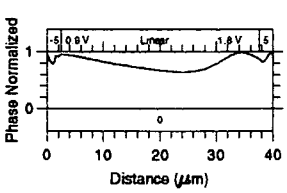

n_o = 1.5277
n_e = 1.7804
@ 589.6 nm

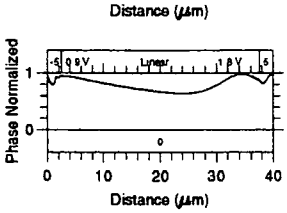

n_o = 1.5277
n_e = 1.7804
@ 589.6 nm

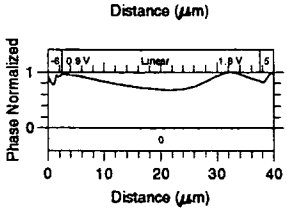

n_o = 1.5277
n_e = 1.7804
@ 589.6 nm

Director Orientation Distribution for a Periodic Liquid Crystal E44 Cell

Linear Ramp Structures

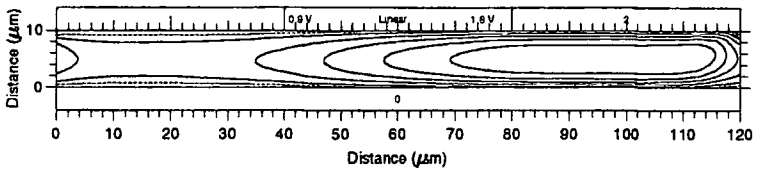

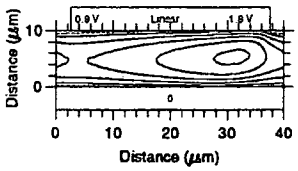

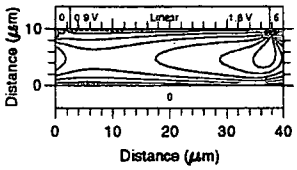

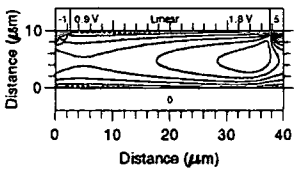

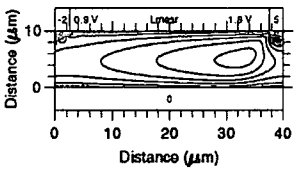

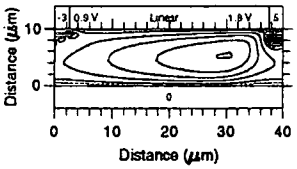

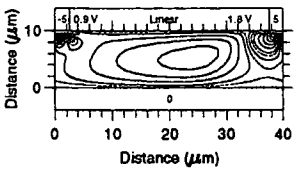

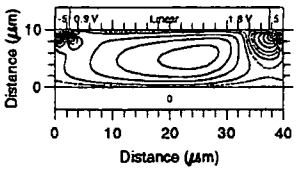

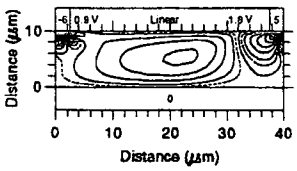

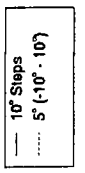

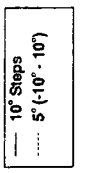

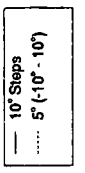

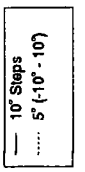

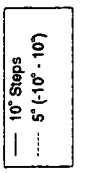

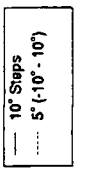

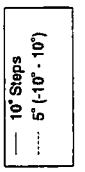

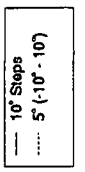

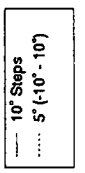

Potential Distribution and Displacement Field for a Periodic Liquid Crystal E44 Cell

Linear Ramp Structures

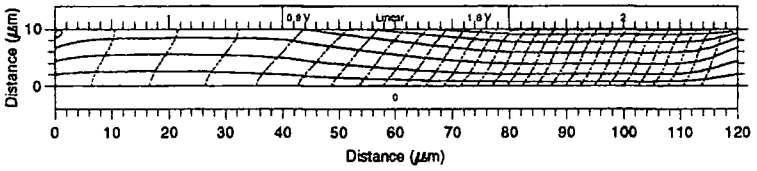

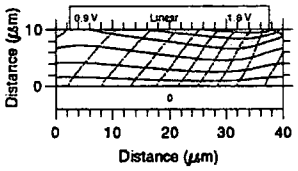

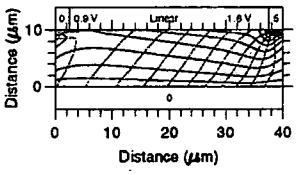

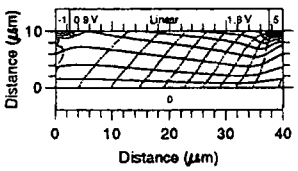

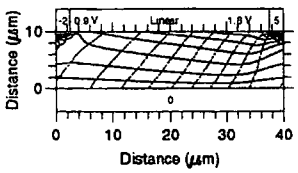

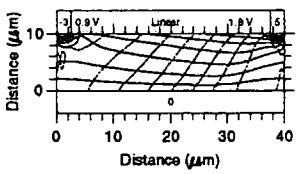

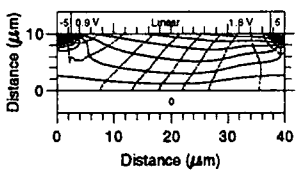

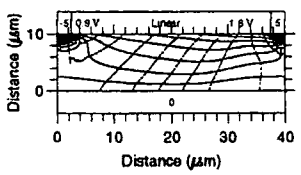

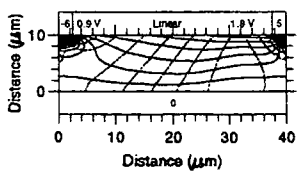

G.3.2 Narrowing Linear Ramp Structures

Normalised Phase Distribution for a Periodic Liquid Crystal E44 Cell

Narrowing Linear Ramp Structures

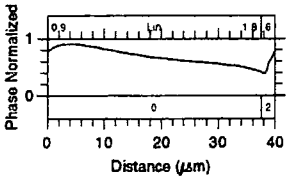

n_o = 1.5277
n_e = 1.7904
@ 589.6 nm

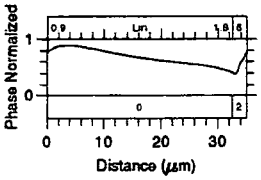

n_o = 1.5277
n_e = 1.7904
@ 589.6 nm

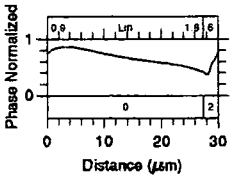

n_o = 1.5277
n_e = 1.7904
@ 589.6 nm

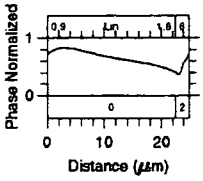

n_o = 1.5277
n_e = 1.7904
@ 589.6 nm

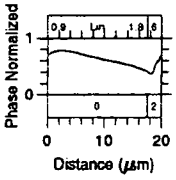

n_o = 1.5277
n_e = 1.7904
@ 589.6 nm

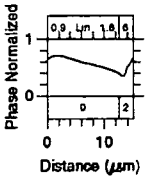

n_o = 1.5277
n_e = 1.7904
@ 589.6 nm

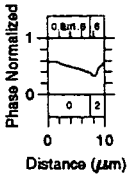

n_o = 1.5277
n_e = 1.7904
@ 589.6 nm

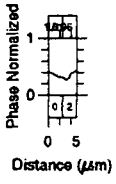

n_o = 1.5277
n_e = 1.7904
@ 589.6 nm

Director Orientation Distribution for a Periodic Liquid Crystal E44 Cell

Narrowing Linear Ramp Structures

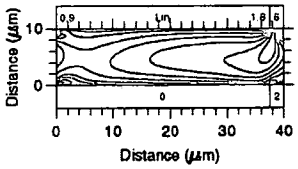

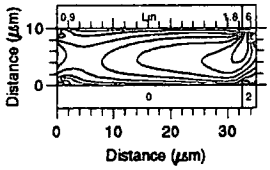

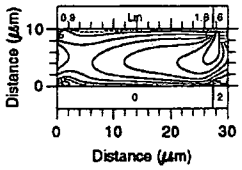

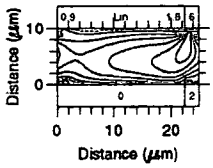

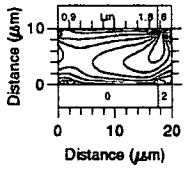

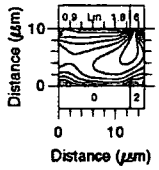

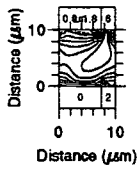

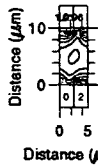

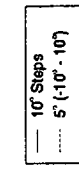

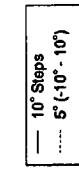

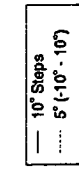

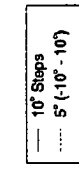

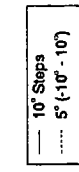

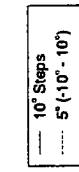

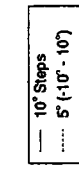

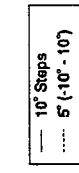

Potential Distribution and Displacement Field for a Periodic Liquid Crystal E44 Cell

Narrowing Linear Ramp Structures

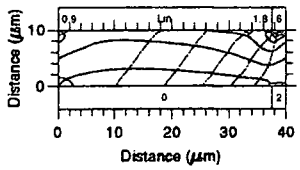

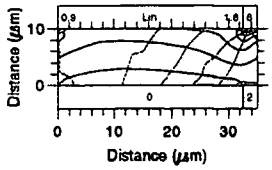

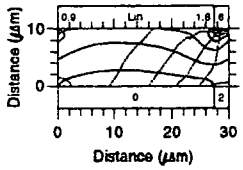

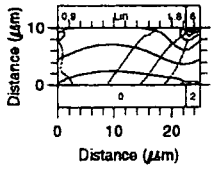

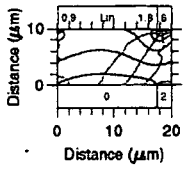

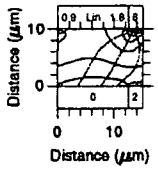

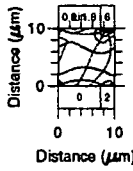

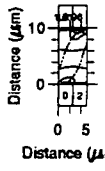

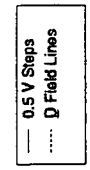

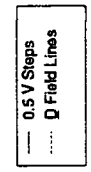

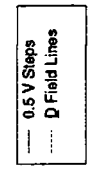

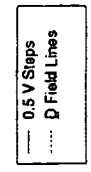

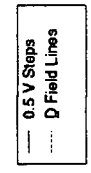

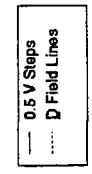

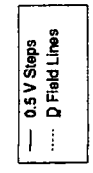

G.3.3 Electro-Static Ramp Structures

Normalised Phase Distribution for a Periodic Liquid Crystal E44 Cell

Electro-Static Ramp Structures

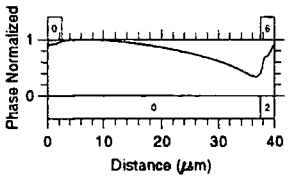

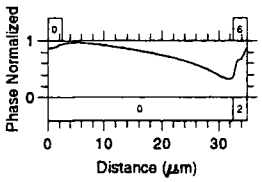

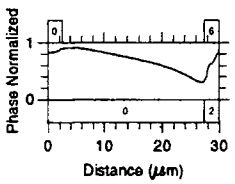

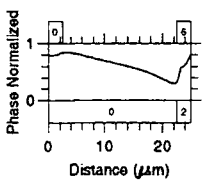

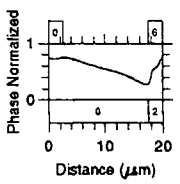

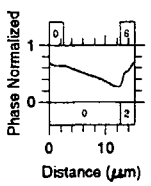

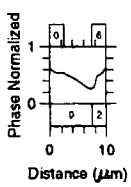

n_o = 1.5277
n_e = 1.7804
@ 589.6 nm

n_o = 1.5277
n_e = 1.7804
@ 589.6 nm

n_o = 1.5277
n_e = 1.7804
@ 589.6 nm

n_o = 1.5277
n_e = 1.7804
@ 589.6 nm

n_o = 1.5277
n_e = 1.7804
@ 589.6 nm

n_o = 1.5277
n_e = 1.7804
@ 589.6 nm

Director Orientation Distribution for a Periodic Liquid Crystal E44 Cell

Electro-Static Ramp Structures

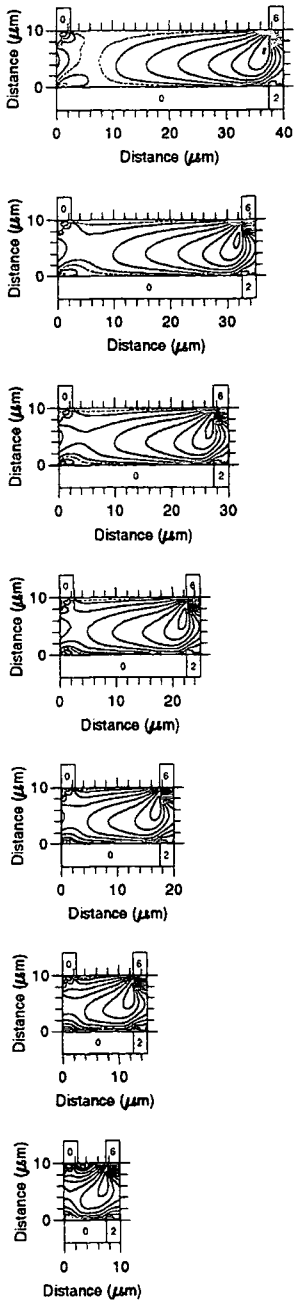

Potential Distribution and Displacement Field for a Periodic Liquid Crystal E44 Cell

Electro-Static Ramp Structures

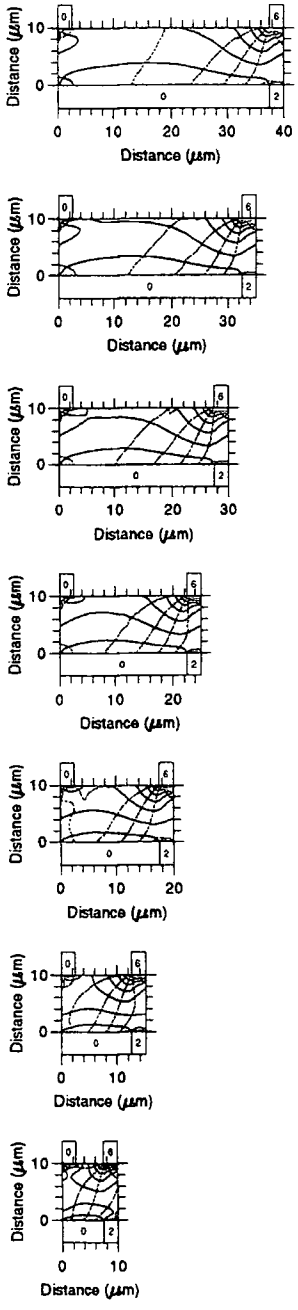

G.3.4 Combed Electrode Structure

Liquid Crystal: E44 Combed Electrode Structure

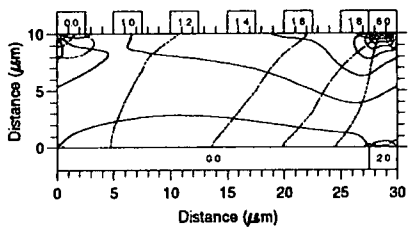

Equipotentials and Displacement Field Lines

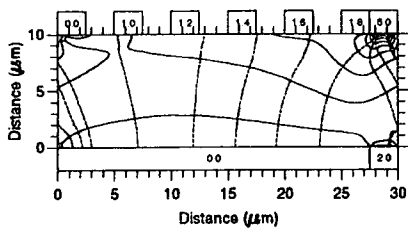

Equipotentials and Electric Field Lines

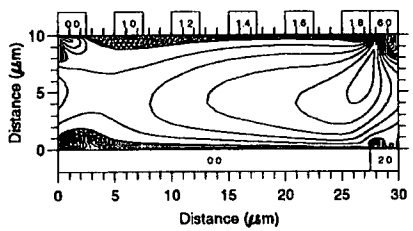

Director Orientation

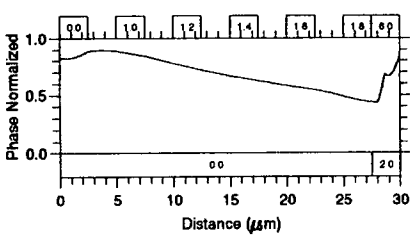

Normalized Phase Response

G.4 Driving Off Electrode Structures

Liquid Crystal: E44 Driving Off Electrode Structure: 1

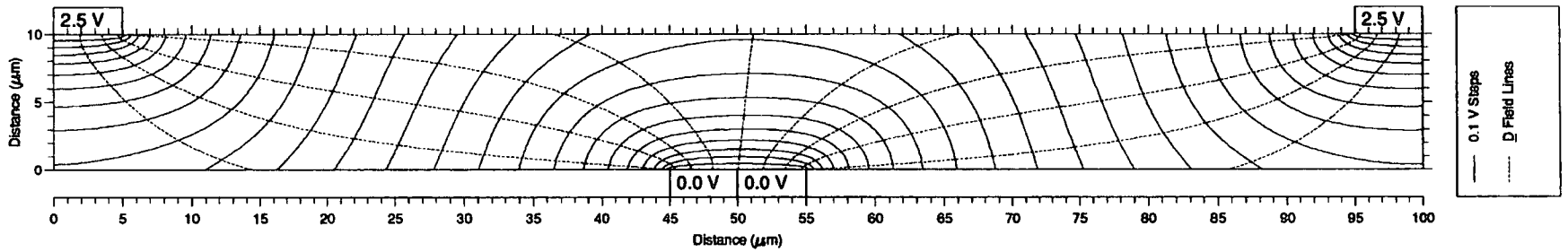

Equipotentials and Displacement Field Lines

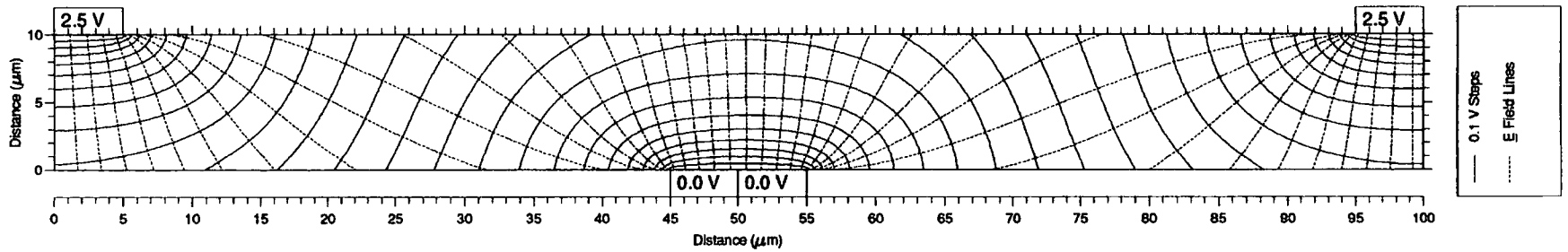

Equipotentials and Electric Field Lines

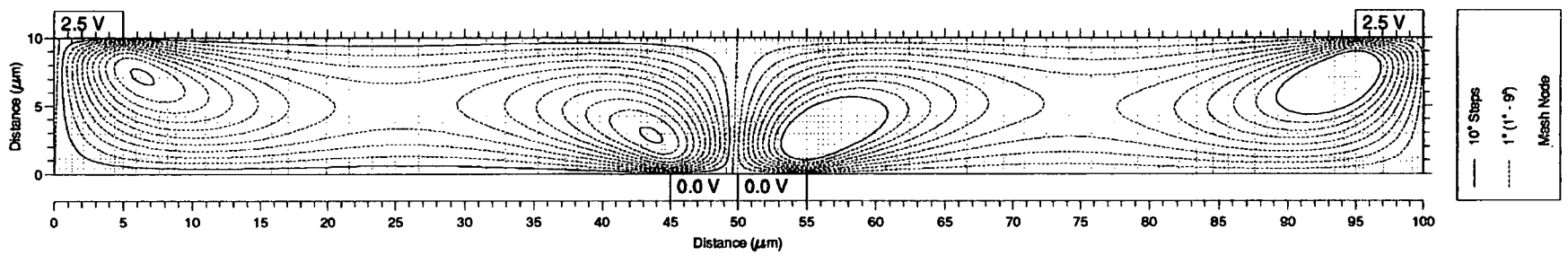

Director Orientation

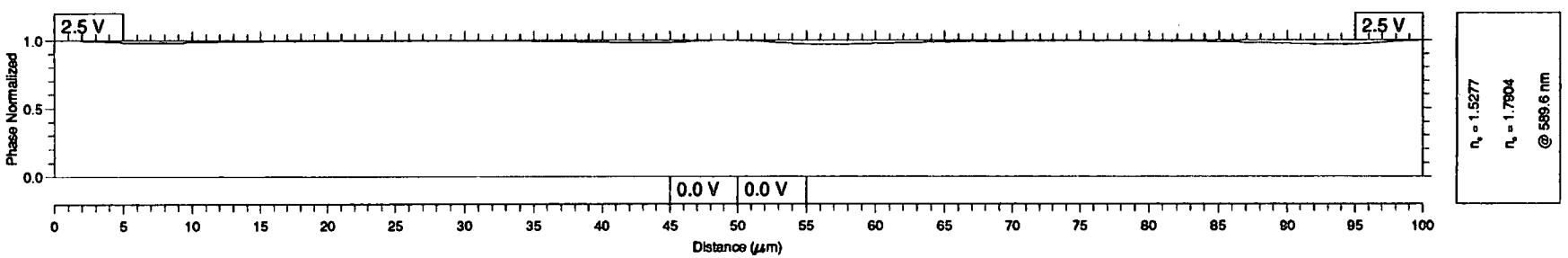

Normalized Phase Response

Liquid Crystal: E44 Driving Off Electrode Structure: 2

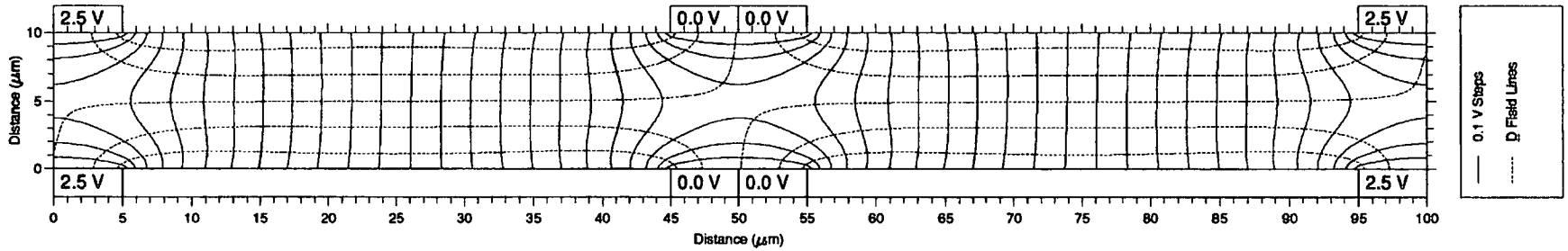

Equipotentials and Displacement Field Lines

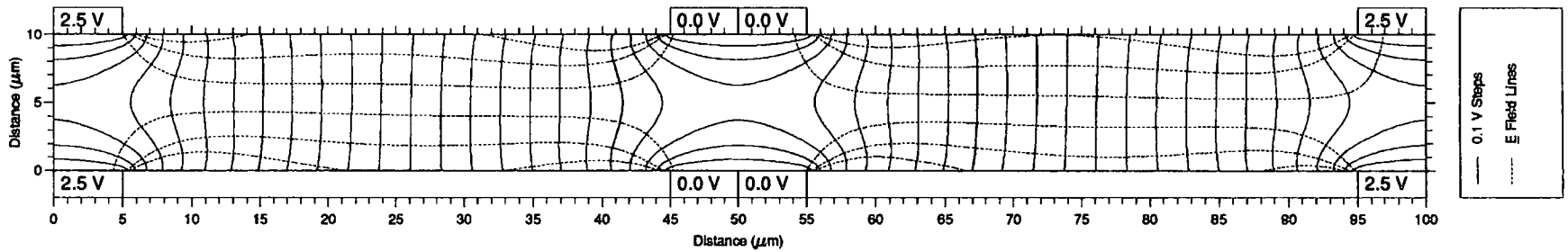

Equipotentials and Electric Field Lines

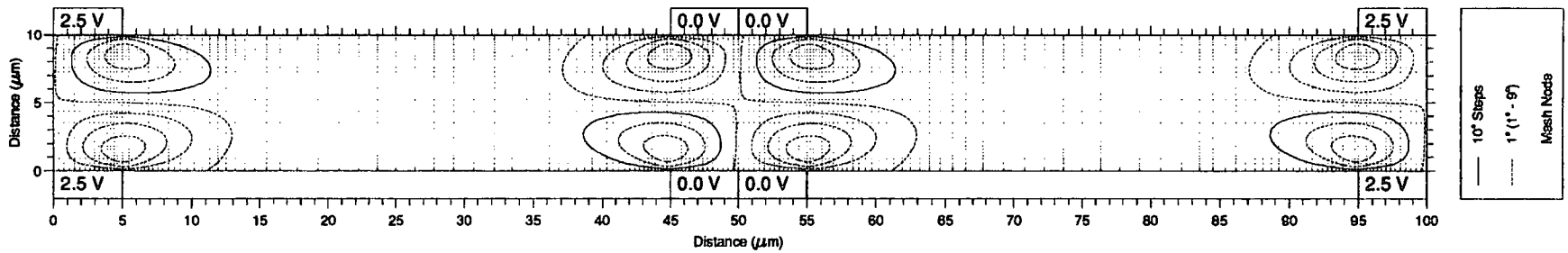

Director Orientation

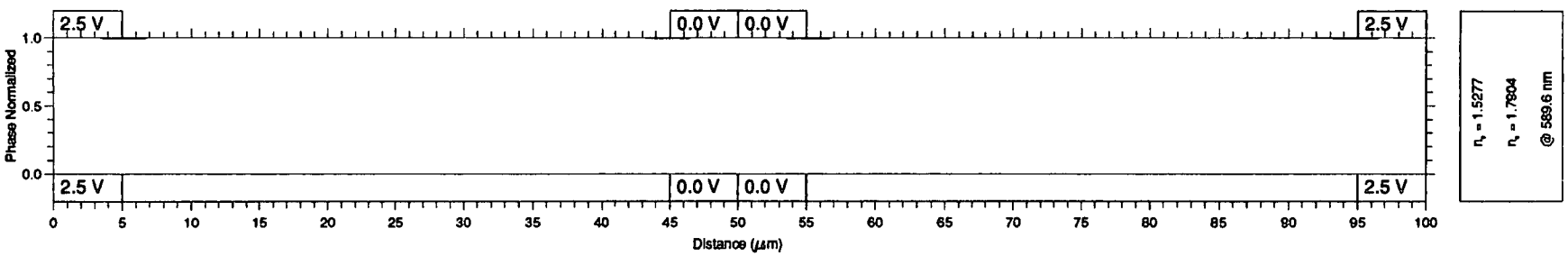

Normalized Phase Response

Liquid Crystal: E44 Driving Off Electrode Structure: 3

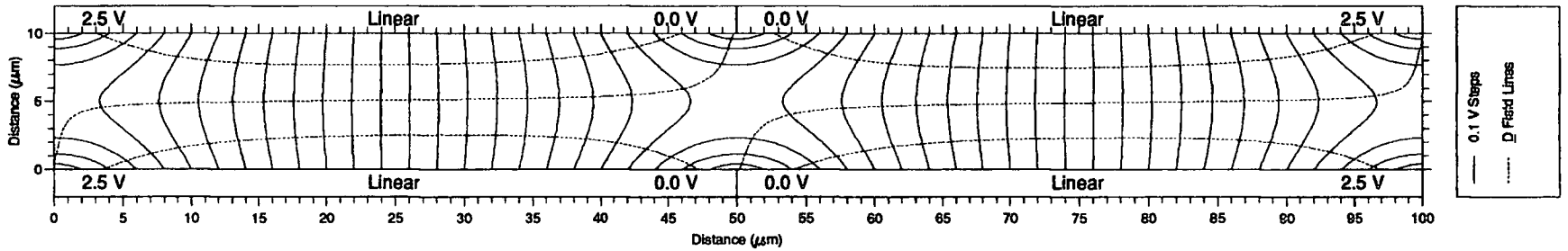

Equipotentials and Displacement Field Lines

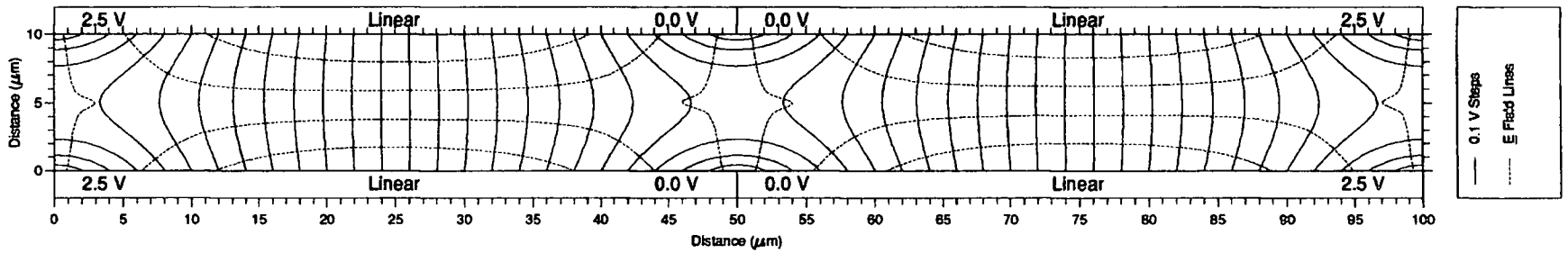

Equipotentials and Electric Field Lines

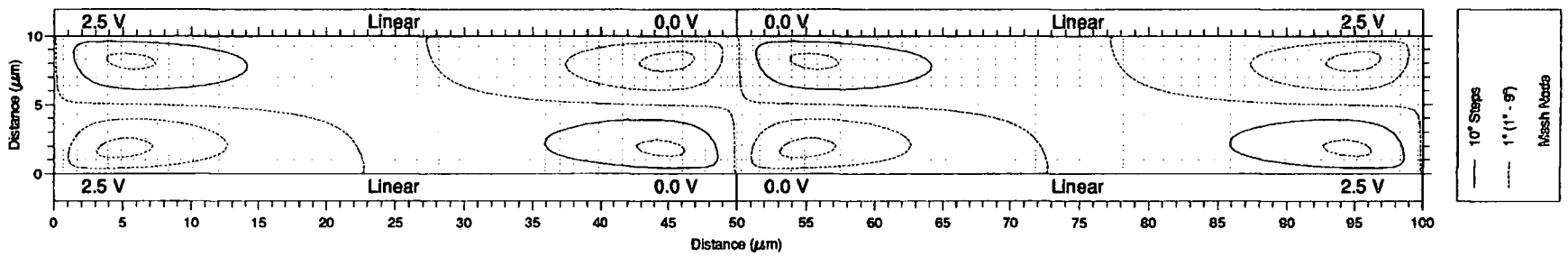

Director Orientation

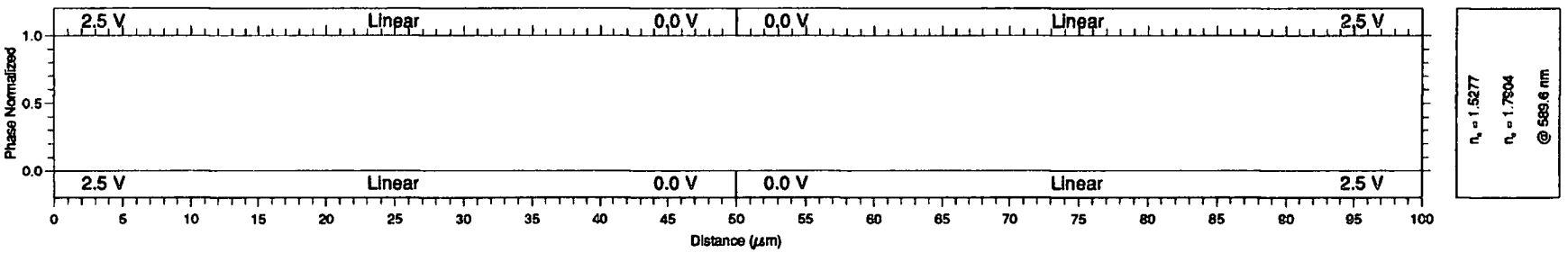

Normalized Phase Response

G.5 The Effects of Initial Conditions

Normalised Phase Distribution for a Periodic Liquid Crystal E44 Cell

The Effect of the Initial Condition on the Final Solution

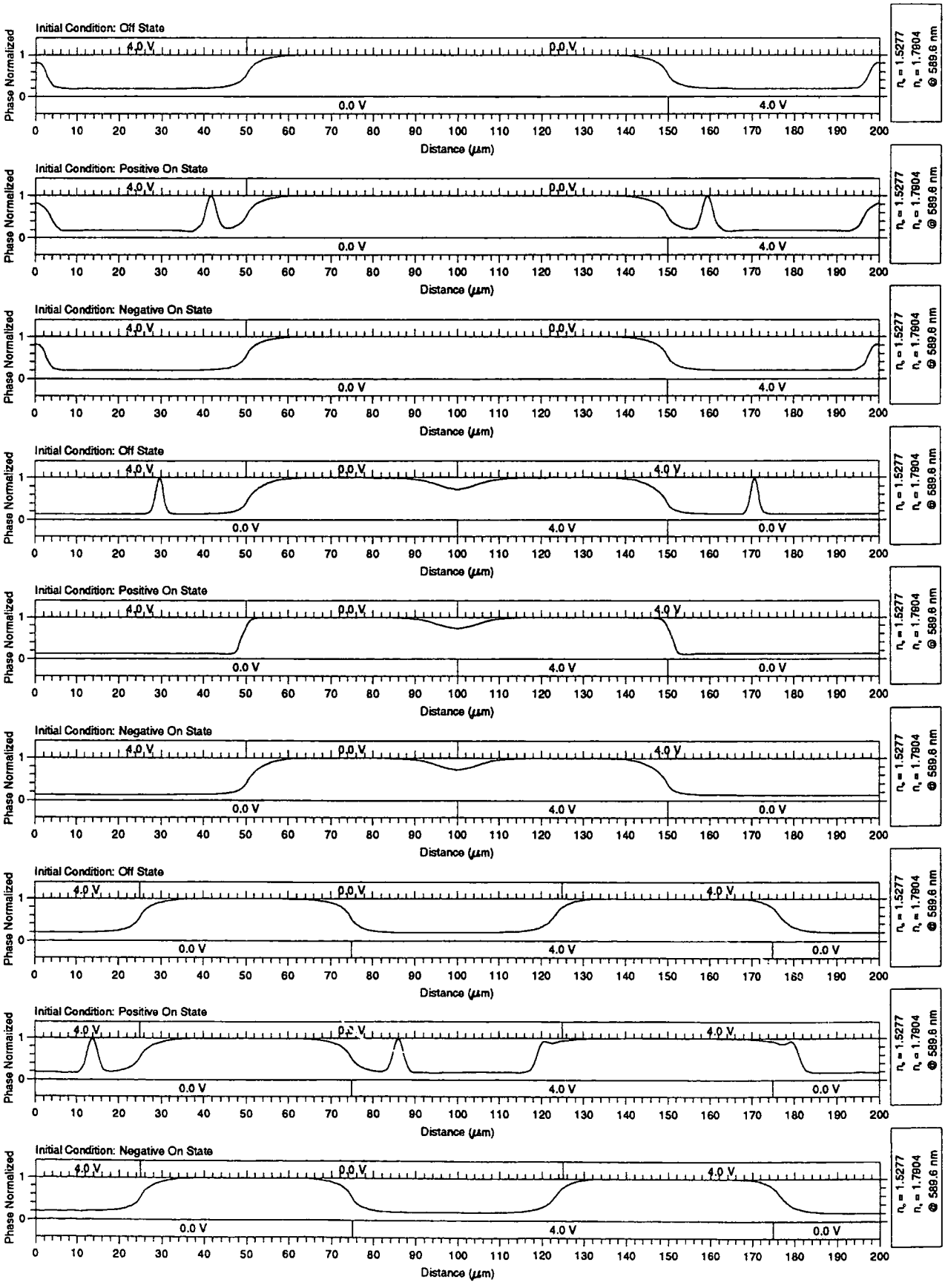

Director Orientation Distribution for a Periodic Liquid Crystal E44 Cell

The Effect of the Initial Condition on the Final Solution

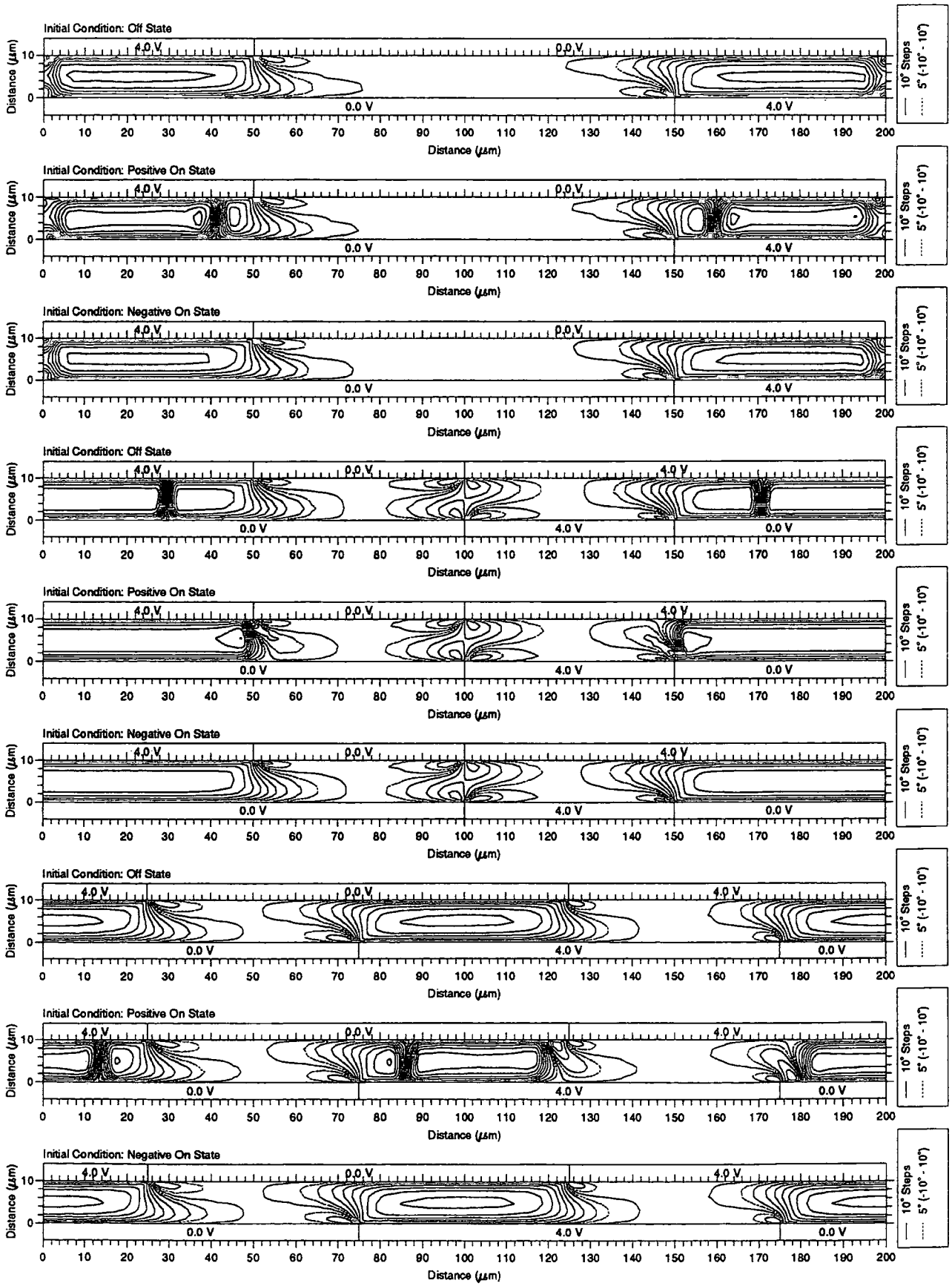

Potential Distribution and Displacement Field for a Periodic Liquid Crystal E44 Cell

The Effect of the Initial Condition on the Final Solution

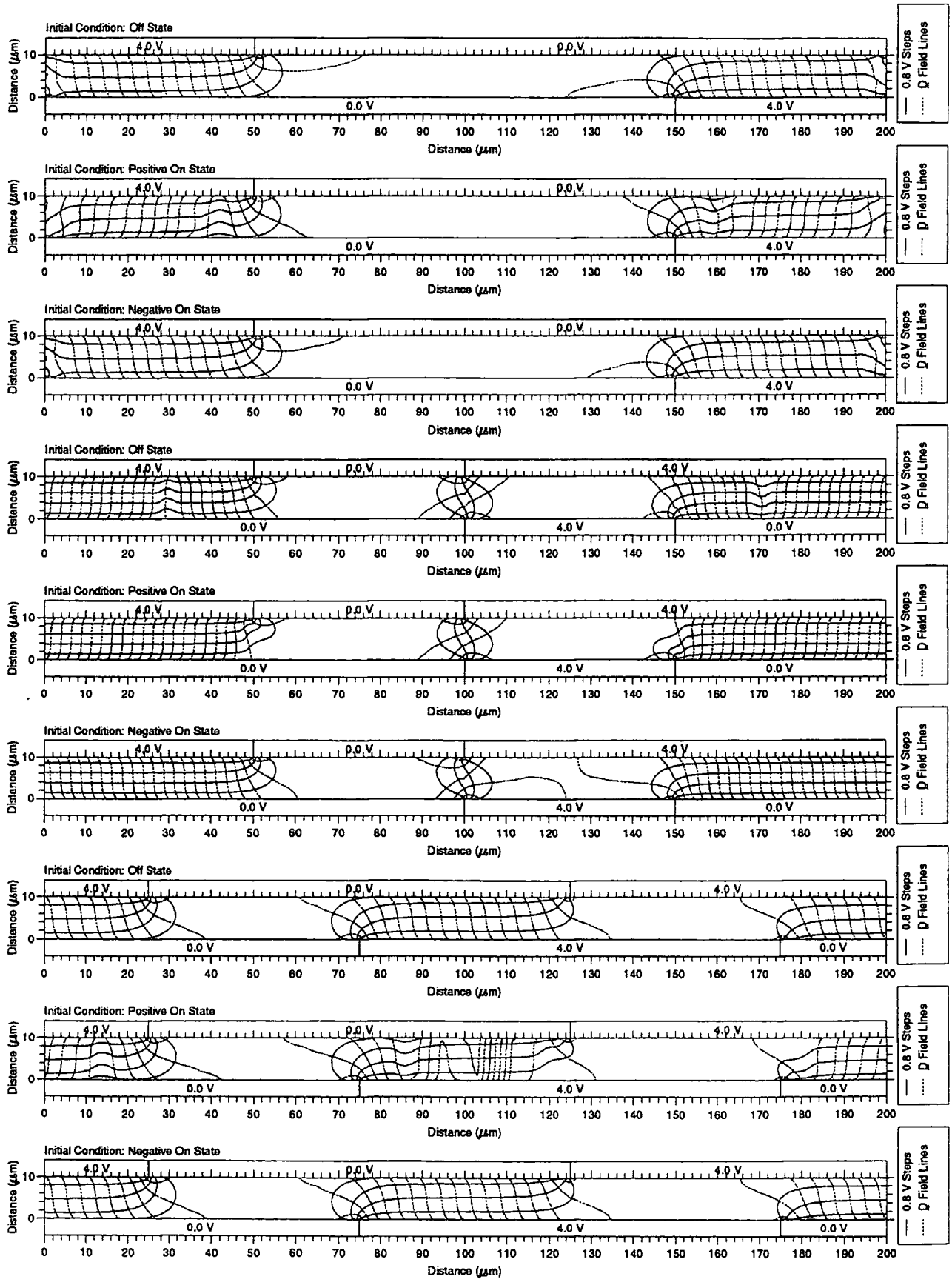

Appendix H

List of Publications

H.1 References

[1] N. J. Powell, R. W. Kelsall, G. D. Love and A. Purvis. 'An Investigation of Fringing Fields in Liquid Crystal Devices', *SPIE Proc.*, 1545 (1991).

[2] N. J. Powell, A. Purvis and M. C. K. Wiltshire. 'A Model of Fringing Fields in Liquid Crystal Devices', *Applied Optics and Opto-Electronics Digest, Leeds,* (1992) 226-228.

[3] G. Williams, N. J. Powell, A. Purvis and M. G. Clark. 'Electrically controllable LC Fresnel lens', *SPIE Proc.*, 1168 (1989) 352-357.

[4] A. Purvis, G. Williams, N. J. Powell, M. G. Clark and M. C. K. Wiltshire. 'Liquid crystal phase modulators for active micro-optic devices', *SPIE Proc.*, 1455 (1991) 145.

[5] A. Purvis, N. J. Powell and M. C. K. Wiltshire. 'Cascaded Liquid Crystal Fresnel Lenses', *Applied Optics and Opto-Electronics Digest, Leeds,* (1992) 229-233.

[6] M. G. Clark, M. C. K. Wiltshire, A. Purvis and N. J. Powell. 'Tapered - Electrode LC Prism.', *British Patent* No. 9 305 143.1 (1992).